Phase-coherent electron transport through metallic atomic-sized contacts and organic molecules

Zur Erlangung des akademischen Grades eines
DOKTORS DER NATURWISSENSCHAFTEN
von der Fakultät für Physik der Universität (TH)
Karlsruhe

genehmigte

DISSERTATION

von

Dipl.-Phys. Fabian Pauly
aus Bensheim

Tag der mündlichen Prüfung	02.02.2007
Referent	Prof. Dr. Gerd Schön
Korreferent	Prof. Dr. Reinhart Ahlrichs
Betreuer	Prof. Dr. Juan Carlos Cuevas

Contents

Chapter 1

Introduction

Since the last ten years there is a growing interest in nanophysics and nanoscience in general. The attention to this field is strongly encouraged by the ongoing miniaturization in the microelectronics industry. At the time of writing, an impressive number of more than a billion transistors on a chip with an area of less than 0.346 μm^2 can be realized industrially (see Fig. 1.1). Such devices involve transistor gate lengths of less than 35 nm. At such length scales we approach the extent of molecular systems. Nanophysics takes these developments to the absolute limit: the size of atoms and molecules. This means that we are dealing with atomic dimensions that are characterized by the Bohr radius of around 0.529 Å.

Physical laws at the atomic scale may differ substantially from those of the macroscopic world. Taking the example of the conduction properties, which are in the focus of the present work, the familiar Ohm's law, from which we learn that the resistance of a conductor is proportional to its length, breaks down [1]. The reason for this is that the distance that an electron travels between two scattering events is typically large compared with the atomic scale. Thus, electrons traverse an atomic-sized conductor ballistically, and the resistance becomes independent of length. Research in the field of nanoscience helps to understand, what modified physical properties may be met at the smallest scales.

At the nanometer scale the composition of materials plays an essential role. Often phenomena are non-generic and the rich variety of chemistry enters. By the very nature of this research the boundaries between the field of physics of small objects and chemistry are fading, making nanoscience a truly interdisciplinary research activity, where also aspects of materials science enter. Despite its complexity, the study of systems with atomic dimensions is attractive from another point of view. The fact that only few atoms are needed to describe the relevant device region makes possible a microscopic theoretical modeling, and a direct comparison between theory and experiment.

In order to investigate systems of atomic size experimental techniques for their characterization and manipulation are needed. Perhaps the most important tool in this respect is the scanning tunneling microscope (STM), developed by Binnig and Rohrer, for which they were awarded the Nobel prize in 1986 [2]. The STM is a very versatile tool. In its normal mode the topography and electronic properties of a metal or semiconductor surface can be

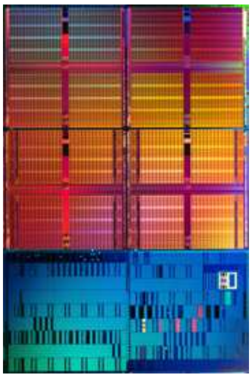

Figure 1.1: Dye photo of an Intel® 45 nm shuttle test chip including 153 Mbit SRAM and logic test circuits. More than 1 billion transistors are on this chip with an area of 0.346 μm^2 (http://www.intel.com).

studied with atomic resolution. Soon it became evident that the STM could also be used to modify samples on the atomic scale [3, 4, 5, 6, 7]. Furthermore the first metallic contact of atomic dimension was realized with an STM by indenting its tip into a metal surface [8]. Also nowadays the STM technique is frequently used to measure the conductance of atomic-sized contacts [9, 10, 11, 12, 13, 14, 15]. (See also Ref. [1] for related publications.)

Another very important technique for measuring the conduction properties of atomic-sized contacts is the mechanically controllable break junction (MCBJ) [16, 17, 18, 1]. As shown in the left panel of Fig. 1.2 a substrate is bent by means of a pushing rod. In this way a metallic wire, glued onto this substrate, can gently be broken with a sub-Ångström control over its elongation.

In order to investigate the conduction properties of metallic contacts, the conductance of an MCBJ can be measured simultaneously to its opening. An opening curve for the conductance, as depicted in the right panel of Fig. 1.2, is then obtained. Shortly before rupture of the junction, single atom contacts or even short atomic chain configurations can be studied [21, 22, 13]. The conductance curves in the right panel of Fig. 1.2 differ from one contact realization to the other. In order to obtain typical values of the conductance, a large number of such curves is assembled into a conductance histogram [11, 23, 24]. These histograms often show a peak structure, which is specific to the investigated metal (see also Figs. 2.1 and 2.2).

While the STM and MCBJ technique were initially used to measure the conductance of metallic contacts, recently they find application in the field of molecular electronics. The field of molecular electronics tries to understand the electronic transport properties of molecular structures. The visionary idea behind this activity is to use molecules as electronically active components in logic circuits.

Conductance measurements on molecular films, performed by Mann and Kuhn [25], date back to 1971. Since that time the aforementioned enhanced control at the atomic scale led to the measurement of conduction properties of single organic molecules [26, 27]. In these measurements, carried out by H.B. Weber *et al.* at the Institut für Nanotechnologie (INT), Forschungszentrum Karlsruhe (FZK), a metal contact is broken with the MCBJ technique. After rupture a droplet with a solution containing molecules is inserted into the junction. When the electrodes are approaching each other from large distances, the system eventually locks into a stable behavior, which allows the recording of several current-

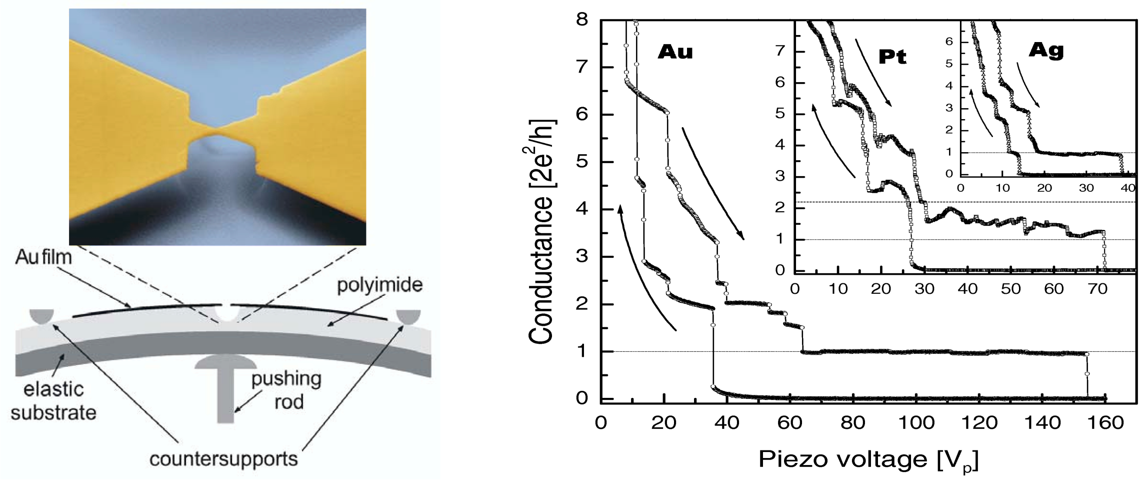

Figure 1.2: A typical break junction setup [19] is shown to the left. With the help of a pushing rod, controlled by a piezo voltage, a nanolithographically prefabricated wire can gently be broken. In this way the stretching of the nanowire, which is glued onto the flexible substrate, can be controlled at a sub-Ångström resolution. If the conductance is measured simultaneously to the bending of the substrate, conductance traces, as shown to the right, can be measured for different metals [20].

voltage (I-V) characteristics. This stable configuration is interpreted as a metal-molecule-metal (MMM) junction [26]. However, to contact a few organic molecules or even single molecules still remains a difficult task with many unknown features, just to mention the actual geometry of the MMM junction. Due to the importance of microscopic details, I-V characteristics commonly vary from one contact realization to the other. Therefore statistical measurements of single molecule junctions, similar to conductance histograms in metallic contacts, are another major step, in order to obtain reproducible data on the conduction properties of single-molecule junctions. Only recently Xu *et al.* [28] could present the statistical measurement of single-molecule junctions by means of the STM technique (see Fig. 1.3).

One essential task of molecular electronics is to understand the electron transport through a single molecule electrically wired to two electrodes. This requires knowledge about how the conductance is influenced by the device geometry, the electrode-molecule interfaces, and the chemical nature of the molecule [29]. As the precise device geometry is difficult to control, one may hope that due to the possibilities of molecular synthesis, relative differences in electron transport can be observed that depend on the intrinsic properties of the contacted molecule. Such differences in the chemical nature of a molecule may be caused by its side groups or its length.

Of central importance for the electrical conduction are delocalized electrons. In organic molecules the electrons of a conjugated system do not belong to a single atom, but they are shared by a group of atoms. For this reason Tour proposed thiophene ethynylene oligomers, which are conjugated linear molecules with an alternation of double and triple

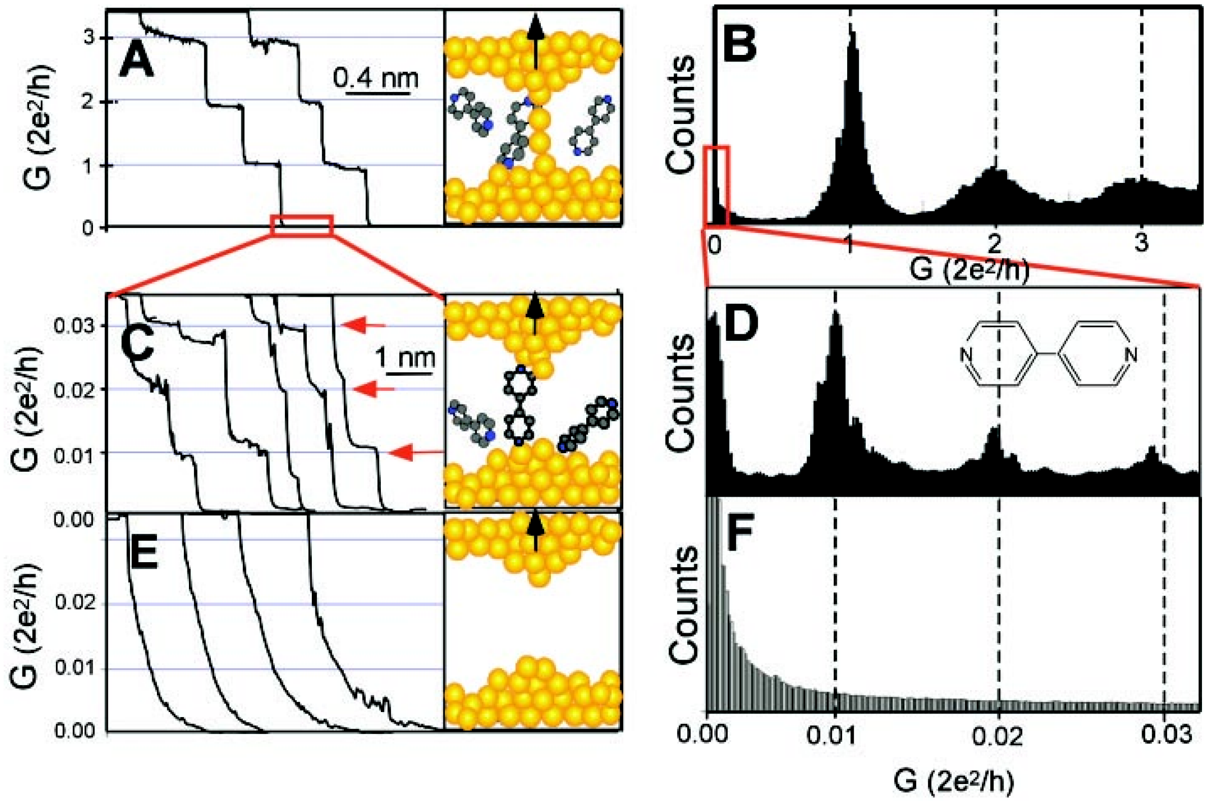

Figure 1.3: (A) Decreasing conductance of a gold contact formed between a gold STM tip and a gold substrate as the tip is pulled away from the substrate. (B) A corresponding conductance histogram is constructed from 1000 conductance curves as shown in (A). (C) When the contact displayed in (A) is completely broken, corresponding to the collapse of the last conductance plateau, a new series of conductance steps appears if molecules, such as bipyridine, are present in the solution. These steps are due to the formation of a stable molecular junction between the tip and the substrate electrodes. (D) A conductance histogram obtained from 1000 measurements, as displayed in (C), exhibits peaks near 1×, 2×, and $3 \times 0.01 G_0$ that are ascribed to one, two, and three molecules, respectively. (E and F) In the absence of molecules, no such steps or peaks are observed within the same conductance range [28].

bonds [30], as a prototype of a molecular wire. Due to this proposal such wires are often called "Tour wires". Generally, molecules with an extended π-system are of interest as organic conducting materials, as required for the visionary build-up of completely organic molecular electronics. In synthesizing such extended π-conjugated systems, the problem of a conjugation saturation is encountered that arises from an effective conjugated length (ECL) [31]. The ECL defines the extent of π-conjugated systems, in which the electronic delocalization is limited and at which point the optical, electrochemical or other physical properties reach a saturation level that is common with the analogous polymer [32]. A

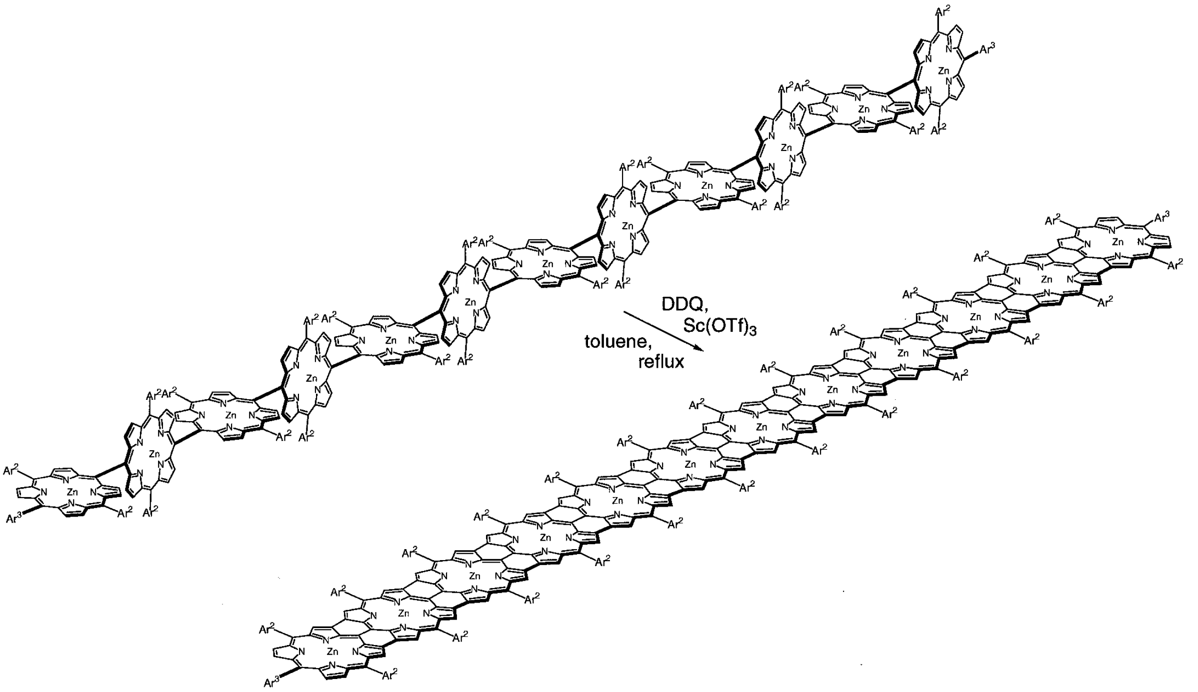

Figure 1.4: Rigid and giant molecular-size porphyrin arrays with extensively π-conjugated electron systems and a low HOMO-LUMO gap [31]. They may be used as conducting molecular wires in molecular-scale electronic devices.

straightforward synthetic strategy for maximizing the π-overlap and for avoiding a finite ECL may be to hold the π-system coplanar by means of appropriately chosen side groups. Recently it has been shown that in this manner fully conjugated porphyrin tapes with electronic bands that reach into the infrared can be synthesized (see Fig. 1.4) [31]. Such wires exhibit extremely low gaps between the highest occupied and lowest unoccupied molecular orbital (HOMO and LUMO), they are rigid and of giant molecular size. In addition they are stable in air and easy to manipulate so that conducting molecular wires for molecular-scale electronic devices seem to be realizable.

The chances that the research in the area of nanophysics, especially molecular electronics, leads to a large-scale fabrication of atomically engineered circuits that are replacing present day silicon technology should not be seen over-optimistically. Many barriers still need to be taken, including the long-term stability at room temperature and the time required for fabrication and design of giga-component circuits. However, there is no doubt that we should go ahead. While the allure of computing with molecules may perhaps never come true, many fundamental advances will be made on that way. The continuously improving control at the atomic scale serves as an example for such advances. Rephrasing R. P. Feynman's words, one might say that it is important to know "how much room is left at the bottom" [33].

Outline of this thesis Having given an introduction to the field of nanoscience, in particular the study of metallic atomic-sized contacts and molecular electronics, let us come to the outline of this thesis. Our work is concerned with physical properties of systems of atomic or molecular dimensions. In particular we are interested in conduction properties of atomic-sized contacts, which may either be purely metallic or consist of a molecule that bridges two metallic electrodes. From a methodological point of view the work is split into two main parts.

In the first part we will address mechanical and electrical properties of metallic nanowires (Chaps. 2 and 3). In Chap. 2 our focus is the theoretical understanding of conductance histograms, and we will try to explain their metal-specific peak structure. These investigations were carried out in collaboration with M. Dreher and Prof. P. Nielaba at Universität Konstanz. Subsequently we will study signatures of electron-vibration coupling on the conductance of gold atomic chains in Chap. 3. In both aforementioned studies a valence-electron tight-binding (TB) model is employed.

In the second part of the thesis we will analyze the conduction properties of metallic atomic contacts and organic molecules based on an ab-initio density functional theory (DFT) approach to quantum transport. This approach has been developed in this thesis and is presented in Chap. 4. The method is based on the implementation of DFT in the quantum chemistry package TURBOMOLE, developed by Prof. R. Ahlrichs at Universität Karlsruhe. Indeed this part of the work is a clear manifestation of the interdisciplinary research activities in the field of molecular electronics mentioned above, bringing together physics and chemistry. The subsequent analysis of metallic atomic contacts of gold and aluminum in Chap. 5 is rather meant as a test of the ab-initio transport scheme. Our main goal is the study of conduction properties of organic molecules, presented in the final Chap. 6. In that chapter the conductance of different series of oligophenylene molecules is studied. The main part of these molecules has been synthesized in the group of M. Mayor at INT, FZK as presented in the PhD thesis of M. Elbing [34]. For these molecules we will explore the importance of the conjugated π-system on the conductance. We will establish a clear relation between the molecule's internal structure and its conduction properties. Besides a study of the length dependence of the conductance and the influence of varied bonding positions, we will present a comparison with experimental data of Ref. [34].

Every chapter of this thesis will include a short introduction as well as a short summary. Finally a complete summary of all our results can be found following Chap. 6. Methodological details necessary for a thorough understanding of this thesis have been relegated to the extensive appendices. The appendices relevant for each chapter will be pointed out in the respective introduction. At the end of this thesis the complete list of abbreviations used throughout the different chapters is added for a quick reference.

Chapter 2

Metallic nanowires: Electrical and mechanical properties and the theoretical analysis of conductance histograms

In this chapter we will analyze the electrical and mechanical properties of atomic-sized contacts. The ultimate goal of the work in this chapter is to provide a better theoretical understanding of conductance histograms. Such histograms are a collection of many conductance curves and show a peak structure characteristic of the type of metal under investigation. Despite the enormous progress in the understanding of electronic transport in metallic nanowires, the origin of this peak structure is still a basic open problem. In order to analyze conductance histograms theoretically, extensive simulations of the breaking of nanocontacts are required as well as conductance calculations for systems, consisting of many hundred atoms. While the nanowire dynamics have been simulated by Markus Dreher in the Konstanz Computer Simulation Group of Prof. P. Nielaba at Universität Konstanz, the work in Karlsruhe concentrated on the development of an efficient computation scheme for their electron transport properties. From this effort two publications emerged. The first studies the conductance histograms of Au [35] and the second one the conductance histograms of Ag, Pt, and Ni [36]. The presentation below is a detailed discussion of these results.

After an Introduction 2.1, we present the details of our method for simulating the stretching of atomic wires and show how the conductance is subsequently computed in Sec. 2.2. Further technical details on the simulations can be found in the chapters D and E of the appendix. Studies of Ag, Au, Pt, Al, and Ni contacts follow in Secs. 2.4–2.7, respectively. In each of these sections we first discuss representative examples of the stretching processes of the nanocontacts, along with a comparison with experimental results in the case of Au. We then turn to the statistical analysis of the whole set of simulations for the different metals. This includes a discussion of the histograms of both the minimum cross-section (MCS) and the conductance as well as an analysis of the mean channel transmissions. Section 2.8 is devoted to the discussion of the mechanical properties of the different metals. We summarize the main conclusion of this work in Sec. 2.9.

While the results up to Sec. 2.9 have been obtained for bulk electrode Green's functions, we have subsequently implemented surface electrode Green's functions (see Chap. D), whose treatment is more involved. Their use should improve the quality of our results. Therefore we discuss in Sec. 2.10 the changes that arise, when the bulk Green's functions in the electrodes are replaced by surface Green's functions.

2.1 Introduction

The transport properties and mechanical characteristics of metallic atomic-scale wires have been the subject of numerous studies over the past ten years [1]. The analysis of these nanocontacts is nowadays possible due to experimental techniques such as the scanning tunneling microscope [9, 10] and mechanically controlled break junctions [18]. In both cases a metallic contact is stretched with a precision of a few picometers by use of piezoelectric elements, thus providing very detailed information about the formation and breaking of nanowires. A typical break junction setup is shown in Fig. 1.2.

The relative simplicity of the nanowires makes them ideal systems to perform extensive comparisons with microscopic theories. Such comparisons have made it possible, in particular, to elucidate the nature of the electrical conduction. The conduction in such systems is usually described in terms of the Landauer formula, according to which the low-temperature linear conductance of nonmagnetic contacts can be written as $G = G_0 \sum_n T_n$, where the sum runs over all the available conduction channels, T_n is the transmission for the nth channel, and $G_0 = 2e^2/h$ is the quantum of conductance (see Chap. C and Eq. (C.10)). As was shown in Ref. [19], the set of transmission coefficients is amenable to measurement in the case of superconducting materials. Using this possibility it has been established that the number of channels in a one-atom contact is determined by the number of valence electrons of the central atom, and the transmission of each channel is fixed by the local atomic environment [37, 38, 39].

The experiments show that in the stretching processes in which these metallic wires are formed, the conductance evolves in a steplike manner which changes from realization to realization. In order to investigate the typical values of the conductance, different authors introduced conductance histograms, constructed from a large number of individual conductance curves [11, 23, 24]. These histograms often show a peak structure, which is specific to the corresponding metal. In Figs. 2.1 and 2.2, we show experimentally measured conductance histogram for the metals Ag, Au, and Cu (Fig. 2.1) and Al, Pt, and Ni (Fig. 2.2). From Fig. 2.1, for instance, it is visible that for noble metals like Au and Ag, the conductance has a certain preference to adopt multiples of G_0. However, for a large variety of metals (see the histograms for Pt and Ni in Fig. 2.2), the peaks do not appear at multiples of G_0 (for a detailed discussion of the conductance histograms, see Sec. V D in Ref. [1]). It has become clear that the peak structure in the conductance histograms must be related to the interplay between electronic and mechanical properties. This interplay

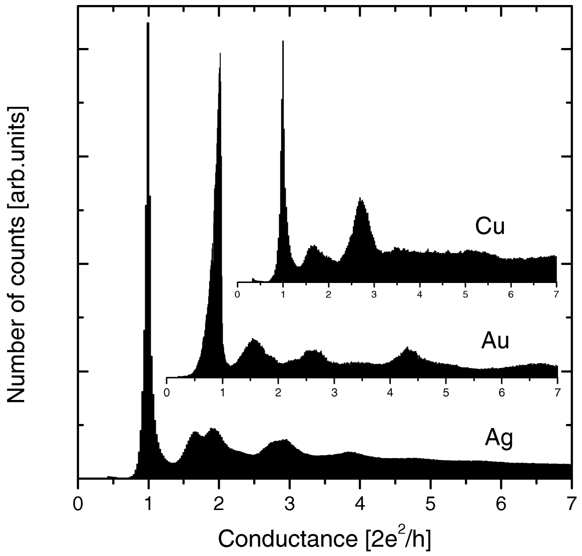

Figure 2.1: Experimentally measured conductance histograms for the noble metals Ag, Au, and Cu [20].

was nicely illustrated in the first simultaneous measurement of the conductance and strain force [40], but the precise origin of the differences between the various classes of metals remains to be understood. The solution of this basic open problem is precisely the central goal of the present work.

The analysis of the characteristic peaks of the conductance histograms of alkali and noble metals at relatively high temperatures has revealed the existence of exceptionally stable radii arising from electronic shell effects for thin wires and atomic shell effects for thicker wires [41, 42, 43, 44, 45]. Stable nanowires with thicknesses of several atoms could also be observed in transmission electron images [46, 47, 48, 49]. Commonly, the connection between the peaks in the conductance histograms and the radius of the contacts is established using semiclassical arguments based on the Sharvin formula or slight variations of it [50]

$$G = G_0 \left[\left(\frac{k_F R}{2} \right)^2 - \frac{k_F R}{2} + ... \right], \tag{2.1}$$

where k_F is the Fermi wave vector and R is the radius of the wire.[1] Using this type of formula, it was suggested in Ref. [52] that peaks found in the histogram of the MCS of Al contacts would directly translate into peaks in the conductance histograms. In other words, it was suggested that the conductance peaks would just be a manifestation of the existence of certain particularly stable contacts.

---

[1] Hard wall boundaries are assumed in this formula, and the inclusion of a work function alters the prefactor of the second term in Eq. (2.1) as explained in Ref. [51]. This effect is usually not taken into account.

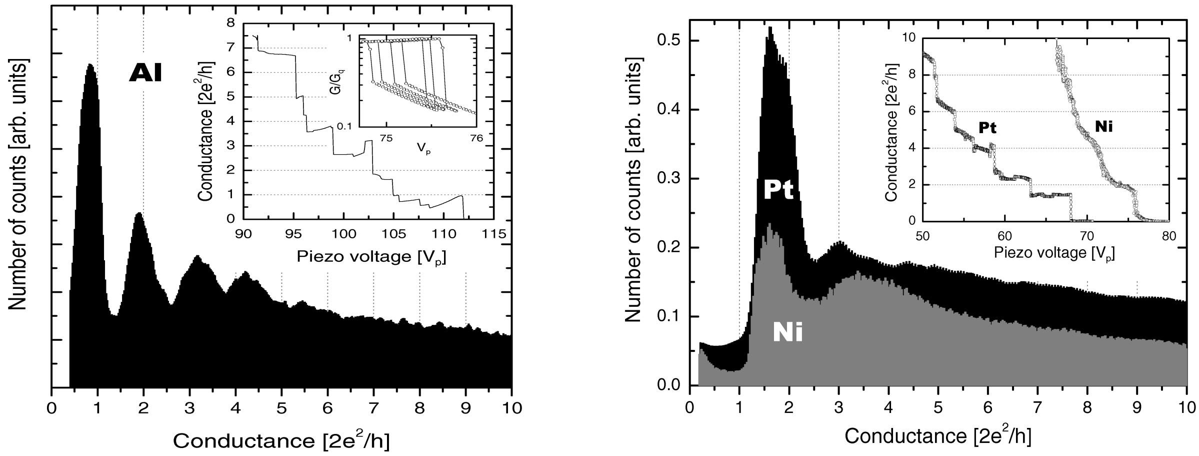

Figure 2.2: Experimentally measured conductance histograms for the metals Al, Pt, and Ni [20].

From the theory side, analyses of the conductance histograms are scarce in the literature. Mostly single stretching events have been investigated at various levels of sophistication [53, 54, 55, 56, 57, 58, 59, 60, 61, 62, 63, 64]. The analysis of conductance histograms, however, involves the statistical exploration of many different stretching events. Most such research is based on free-electron models, where particular nanowire dynamics are chosen [65], but there are practically no fully atomistic investigations of the conductance histograms. Three such studies have just recently appeared, where Hasmy *et al.* [66] studied Al contacts and Dreher *et al.* [35] and Pauly *et al.* [36] investigated atomic Ag, Au, Pt, and Ni contacts.

In order to elucidate the origin of the peak structure in the conductance histograms of metallic atomic-sized contacts, we will present a theoretical analysis of the conductance histogram for several metals with varying electronic structures. In particular, we study the cases of Ag and Au, two noble metals, Pt, a transition metal, and Ni, a ferromagnetic metal. We shall also briefly comment on our study of Al (an *sp*-like metal). Our theoretical approach is based on a combination of classical molecular dynamics (MD) simulations to describe the contact formation and a tight-binding (TB) model supplemented with a local charge neutrality condition for the atomistic computation of the conductance. The use of ab-initio methods is presently prohibited by the size of our nanocontacts consisting of several hundred atoms, in addition to the large number of configurations that need to be analyzed. The classical MD simulations in combination with the TB model allow us to obtain detailed information on the mechanical and electrical properties such as contact geometries, strain forces, the minimum cross-section (MCS), the conductance, the number and evolution of individual conductance channels, and, in the case of ferromagnetic contacts, the spin polarization of the current.

Concerning Ag and Au, we find a sharp peak in the conductance histogram at $1G_0$. This peak is due to the formation of single-atom contacts and dimers in the last stages of the breaking of the wires in combination with the fact that the transport in these noble metals is dominated by the *s* orbitals around the Fermi energy. With *single-atom contacts* we will refer throughout this chapter to junctions with a single atom in the narrowest constriction, in short a one-atom chain, while *dimer* means an atomic chain consisting of two atoms. For Au, also longer atomic chains contribute to the peak at $1G_0$. In the case of Pt, the first peak is broadened and shifted to a higher conductance value (above $1G_0$). This is due to the fact that in this transition metal the *d* orbitals play a fundamental role in the transport, providing extra conduction channels, as compared to Ag and Au. For Ni wires, we see that the *d* orbitals contribute to the electrical conduction for the minority-spin component, providing several partially open channels even in the last stages of the stretching process. As a consequence, we do not observe any type of conductance quantization. With respect to the polarization of the current, we find that there is a crossover from large negative values for thick contacts to positive values in the tunneling regime, right after the rupture of the contact.

From a more general point of view, the ensemble of our results allows us to conclude that the differences in the peak structure of the conductance histograms of metallic nanocontacts can be traced back to the following two ingredients. First, due to the different electronic structure of the various classes of metals, different atomic orbitals contribute to the transport. These orbitals determine in turn the number of conducting channels and therefore the conductance values. Thus, for similar structures a contact of a multivalent metal will have in general a higher conductance than one of a noble metal. Second, the different mechanical properties give rise to the formation of certain characteristic structures, which are finally reflected in the histograms. For instance, the formation of monoatomic chains in Au or Pt is responsible for the pronounced last conductance peak.

2.2 Theoretical approach

The goal of this study is the theoretical description of the mechanical and electrical properties of metallic nanojunctions as presented in [35, 36]. In order to analyze ferromagnetic Ni contacts, we present the spin-dependent formalism [36].

Our theoretical method is based on a combination of classical MD simulations for the determination of the geometric structure and mechanical properties of the nanowires and conductance calculations within a TB model. We proceed to explain these two types of calculations in the next subsections.

2.2.1 Geometric structure

The breaking of metallic nanocontacts is simulated by means of classical MD simulations. Forces and energies are calculated using semiempirical potentials derived from effective-medium theory (EMT) [67, 68]. These potentials have been shown to describe experimental bulk and surface properties [69] and have in addition successfully been used for simulating nanowires by Jacobsen *et. al.* [59, 61, 62, 70, 71].

Transmission electron microscopy shows that in the last stage of the stretching process, nanocontacts of Au are crystalline and atom rearrangements take place in such a way that one of the crystal directions [100], [110] or [111] lies in stretching direction of the wire, independent of the initial crystal orientation [46]. For this reason we choose as our starting configuration for the contacts a perfect fcc lattice of 112 atoms of length 2.65 nm (Au), 2.65 nm (Ag), 2.55 nm (Pt), 2.64 nm (Al), and 2.29 nm (Ni) oriented along the [001] direction (z direction) with a cross-section of eight atoms. This wire is attached at both ends to two slabs that are kept fixed, each consisting of 288 atoms. After equilibration, the stretching process is simulated by separating both slabs symmetrically by a fixed distance in every time step ($\Delta t = 1.4$ fs). Different time evolutions of the nanocontacts are obtained by providing the 112 wire atoms with random starting velocities. The stretching velocity of 2 m/s is much bigger than in the experiment, but it is small compared with the speed of sound in the investigated materials (of more than 2790 m/s). Thus the wire can reequilibrate between successive instabilities, while collective relaxation processes may be suppressed [55, 57]. The Newtonian equations of motion of the wire atoms are integrated via the velocity Verlet algorithm [72] with a time step of Δt. In all our calculations we assume an average temperature of 4.2 K, which is maintained in the simulations by means of a Nosé-Hoover thermostat [72]. We use periodic boundary conditions for the slabs in z direction and the minimum image convention for the slabs perpendicular to the z direction [73]. Before the stretching process, every atom of the wire gets a randomly chosen velocity and the wire is equilibrated for about 0.7 ns with periodic boundary conditions perpendicular to the z direction.

In order to test whether the conductance changes are correlated with atomic rearrangements in the nanocontact, we calculate the radius of the MCS perpendicular to the stretching direction as defined by Bratkovsky *et al.* [56]. For this purpose, every atom is represented by a sphere with the volume of the elementary cell in the fcc lattice. For a given configuration a slice with a width of about the interlayer distance[2] is taken perpendicular to the stretching direction. From the volume of the atomic spheres overlapping with the slice, the radius of a cylinder which would fill the same volume in that slice is computed. The procedure is repeated along the whole nanocontact and the smallest radius is taken as the radius of the MCS of a given configuration.

Finally, during the stretching process, every 1.4 ps a configuration is recorded and the strain force of the nanocontact is computed following Finbow *et al.* [74]. Every 5.6 ps the corresponding conductance is calculated using the method described below.

2.2.2 Conductance

We compute the conductance within the Landauer approach (see also Chap. C). In order to calculate the electronic structure of our atomic contacts a TB model is employed, which has been successful in describing the important qualitative features in the transport through metallic nanojunctions [37, 39]. This model is based on the following Hamiltonian written

---

[2] The width of the slice is $a_0/2$ for the [001]-direction, where a_0 is the lattice constant.

in a nonorthogonal local basis

$$\hat{H} = \sum_{i\alpha,j\beta,\sigma} H_{i\alpha,j\beta,\sigma} \hat{d}^{+}_{i\alpha,\sigma} \hat{d}_{j\beta,\sigma}, \tag{2.2}$$

where i and j run over the atomic sites, α and β denote different atomic orbitals, and $H_{i\alpha,j\beta,\sigma}$ are the on-site ($i = j$) or hopping ($i \neq j$) elements, which are spin-dependent ($\sigma =\uparrow, \downarrow$) in the case of ferromagnetic metals such as Ni. Additionally, we need the overlap integrals $S_{i\alpha,j\beta}$ of orbitals at different atomic positions.[3] We obtain the quantities $H_{i\alpha,j\beta,\sigma}$ and $S_{i\alpha,j\beta}$ from a parameterization that is designed to accurately reproduce the band structure of bulk materials [75, 76, 77, 79, 78].[4] The atomic basis is formed by nine valence orbitals, namely, the s, p, and d orbitals which give rise to the main bands around the Fermi energy. In this parameterization both the hoppings and the overlaps to a neighboring atom depend on the interatomic positions, which allows us to apply this parameterization in combination with the MD simulations. The overlap and hopping elements have a cutoff radius that encloses up to 5 (Au), 9 (Ag, Pt, and Al), or 12 (Ni) nearest-neighbor shells. The left (L) and right (R) electrodes are constructed such that all the hopping elements from the 112 wire atoms, which we will call the central part or center of our contact (C), to the electrodes are taken into account. This means that the electrodes in the conductance calculation are constituted of [001] layers containing even more than the 288 slab atoms used in the structure calculations (for details see Sec. E.3). Note that with the word electrode we will refer, throughout this chapter, to the fixed slab atoms (or the extended [001] layers used in the conductance calculations).

The local environment in the neck region is very different from that in the bulk material for which the TB parameters have been developed. This can cause large deviations from the approximate local charge neutrality that typical metallic elements must exhibit. Within the TB approximation we correct this effect by imposing a local charge neutrality condition on the atoms in the central part of the nanowire through a self-consistent variation of the Hamiltonian. This self-consistent procedure requires the computation of the electronic density matrix ϱ_{CC}, which is obtained by integrating the Green's function of the center up to the Fermi energy (for details see Sec. E.2)

$$\varrho_{CC} = -\frac{1}{\pi} \int_{-\infty}^{E_F} \mathrm{Im} \left[\sum_{\sigma} G^{r}_{CC,\sigma}(E) \right] dE. \tag{2.3}$$

In this expression $G^{r}_{CC,\sigma}$ is the retarded Green's function of the central part of the contact

$$G^{r}_{CC,\sigma}(E) = \left[(E + i\eta) S_{CC} - H_{CC,\sigma} - \Sigma^{r}_{L,\sigma} - \Sigma^{r}_{R,\sigma} \right]^{-1}, \tag{2.4}$$

---

[3] Note that the overlap elements $S_{i\alpha,j\beta}$ are spin independent for all the metals studied in this work. In principle, the formulation of the employed TB parameterization allows a spin dependence of the overlap integrals for ferromagnetic metals [75, 76, 77], but for the parameters used for Ni [78, 79], they are identical for the different spin components. This is expected, because the elements of the overlap matrix $S_{i\alpha,j\beta}$ should just be integrals over some (real) basis functions ϕ with orbital indices α and β at atomic positions $\vec{R}_i$ and $\vec{R}_j$ ($S_{i\alpha,j\beta} = \int \phi_\alpha \left(\vec{r} - \vec{R}_i \right) \phi_\beta \left(\vec{r} - \vec{R}_j \right) d^3r$).

[4] We use the parameter files au_par_99, ag_par, al_par, pt_par, and ni_ferro_par [77]. Note that for Au and Ni there are different parameterizations (au_par_99 or au_par and ni_ferro_par, ni_para_par, or ni_par).

where σ stands for the spin component, S_{CC} is the overlap matrix of the center, $H_{CC,\sigma}$ is the Hamiltonian, and $\Sigma_{X,\sigma}$ (with $X = L$ or R) are the self-energies that describe the coupling of the center to the electrodes. They are given by

$$\Sigma^r_{X,\sigma}(E) = (H_{CX,\sigma} - ES_{CX})\, g^r_{XX,\sigma}\, (H_{XC,\sigma} - ES_{XC})\,, \tag{2.5}$$

with the unperturbed retarded electrode Green's function $g^r_{XX,\sigma}$ and the overlap (hopping) matrices from the center to the electrodes S_{CX} ($H_{CX,\sigma}$). The unperturbed electrode Green's functions are assumed to be bulk Green's functions in all our calculations. (See Sec. 2.10 for a discussion of the influence of this approximation.) The charge on the atom i is then determined using a Mulliken population analysis

$$N_i = \sum_\alpha (\varrho_{CC} S_{CC})_{i\alpha,i\alpha}\,, \tag{2.6}$$

where only the contributions of the central part to the atomic charge are considered. The new Hamiltonian matrix elements $H_{i\alpha,j\beta,\sigma}$ are obtained from the original ones $H^{(0)}_{i\alpha,j\beta,\sigma}$ as [80]

$$H_{i\alpha,j\beta,\sigma} = H^{(0)}_{i\alpha,j\beta,\sigma} + S_{i\alpha,j\beta}\frac{\phi_i + \phi_j}{2}. \tag{2.7}$$

The shifts ϕ_i are determined such that no atom deviates from the charge neutrality by more than 0.02 electron charges ($|N_i - N_{\text{atom}}| < 0.02$, and N_{atom} stands for the electronic charge of the respective charge-neutral metal atom). Note that there is one shift parameter per central atom, also in the case of ferromagnetic metals.[5]

The low-temperature linear conductance is then computed using a Green's function formalism (see Chap. C for details), finally resulting in the Landauer formula

$$G^\sigma = \frac{e^2}{h}\sum_n T^\sigma_n(E_F) \tag{2.8}$$

with the Fermi energy E_F and the transmission T^σ_n of the nth transmission eigenchannel. The conductance is then given as the sum over the different spin contributions

$$G = \sum_\sigma G^\sigma, \tag{2.9}$$

which has the form

$$G = G_0 T(E_F) = G_0 \sum_n T_n(E_F) \tag{2.10}$$

---

[5] It should be mentioned that there is a slight inconsistency in our data concerning the implementation of the shift. While for Ag, Pt, and Ni the shift has been implemented as given in Eq. (2.7), we used a shift of the diagonal elements only, according to $H_{i\alpha,i\alpha,\sigma} = H^{(0)}_{i\alpha,i\alpha,\sigma} + \phi_i$ for Au and Al (see also Ref. [35]). The reason for this inconsistency is that first we implemented the shift for the diagonal elements of $H_{i\alpha,i\beta,\sigma}$. Only thereafter we became aware of the fact that for a uniform shift Eq. (2.7) gives a more meaningful limit by shifting all eigenvalues of the system uniformly (see Ref. [80] and Sec. E.2 for details). In Sec. E.2 we show, however, that the shift of only the diagonal elements and the use of Eq. (2.7) yield very similar results.

for the spin independent case. As explained in the Introduction, $G_0 = 2e^2/h$ is the quantum of conductance, and T is the total transmission.

To investigate the influence of a small bias voltage, we have computed for Ag and Pt the transmission $T(E)$ in an energy interval of width $2\Delta = 100$ meV around E_F.[6] The averaged conductance

$$\langle G \rangle = G_0 \langle T \rangle = G_0 \frac{1}{2\Delta} \int_{E_F-\Delta}^{E_F+\Delta} T(E) dE, \tag{2.11}$$

can then be compared to the conductance $G = G_0 T(E_F)$ (see Eq. (2.10)). This provides information on the nonlinearity of current-voltage (I-V) characteristics, although the formulas we use are, strictly speaking, only valid for the zero-bias situation.

2.2.3 Local density of states

To gain some insight into the electronic states relevant for the transport through our nanowires, we shall also compute the local density of states (LDOS) projected onto particular atoms. The computation of the LDOS requires the evaluation of the Green's function of the central part of the nanowire $G_{CC,\sigma}$ (see Eq. (2.4)). From $G_{CC,\sigma}$ we construct the LDOS via a Löwdin transformation [81]. The LDOS for a particular orbital α of atom i is then given by[7]

$$\mathrm{LDOS}_{i\alpha,\sigma}(E) = -\frac{1}{\pi} \mathrm{Im} \left[S_{CC}^{1/2} G_{CC,\sigma}^{r}(E) S_{CC}^{1/2} \right]_{i\alpha,i\alpha}. \tag{2.12}$$

In the case of the nonferromagnetic metals the LDOS will be given only for one spin component, because of the spin degeneracy.

2.3 Silver atomic contacts

We start the analysis of our results with the discussion of Ag nanowires. Ag is, like Cu and Au, a noble metal with a single s valence electron. Different experiments have shown that the conductance of Ag contacts exhibits a tendency towards quantized values in the last stages of the wire formation [82, 20, 83]. In fact, the most dominant feature in the experimental low-temperature conductance histogram is a pronounced peak at $1G_0$ (see Fig. 2.1) [82, 20].

2.3.1 Evolution of individual silver contacts

Let us first describe some typical examples of the breaking of Ag nanowires. In Fig. 2.3 we show the formation of a single-atom contact. In addition to the strain force we display the

---

[6] The averaged transmission $\langle T \rangle$ (see Eq. (2.11)) is determined as a sum over $T(E)$ on 11 equally spaced points in the energy interval $[E_F - \Delta, E_F + \Delta]$ around the Fermi energy ($\Delta = 50$ meV).

[7] For plots of the LDOS of an atom a broadening of $\eta = 10^{-3}$ Ry $= 0.0136$ eV is used in $G_{CC,\sigma}$ (see Eq. (2.4)), while for transport the broadening is chosen to be $\eta = 10^{-8}$ Ry $= 1.36 \times 10^{-7}$ eV.

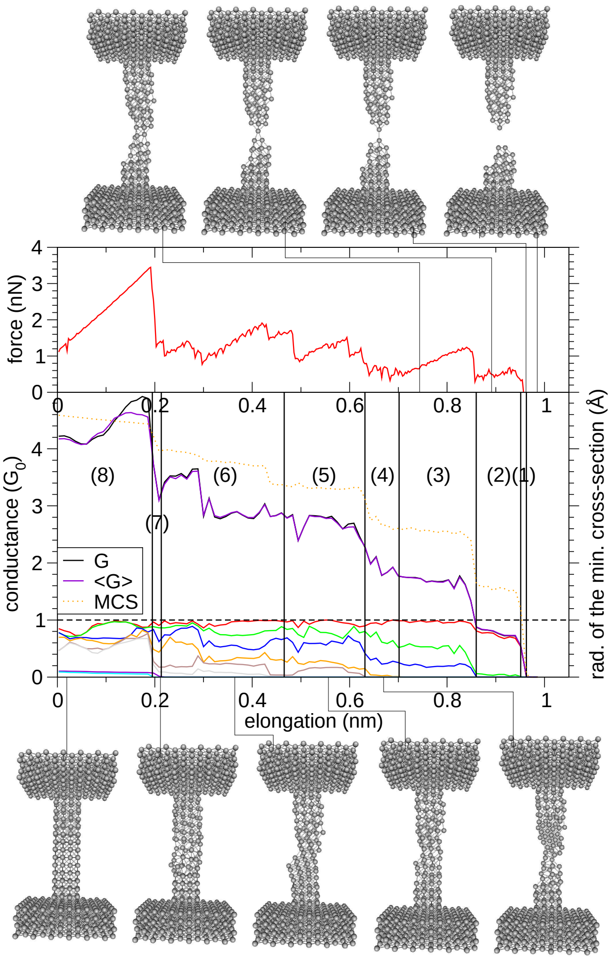

Figure 2.3: Formation of a single-atom contact for Ag (4.2 K, [001] direction). The upper panel shows the strain force as a function of the elongation of the contact. In the lower panel the conductance G, the averaged conductance $\langle G \rangle$, the MCS radius, and the channel transmissions are displayed. Vertical lines separate regions with different numbers of open channels ranging from 8 to 1. Above and below these graphs snapshots of the stretching process are shown.

conductance G, the averaged conductance $\langle G \rangle$ (see Eq. (2.11)), the MCS radius, and the channel transmissions. Let us point out that we consider a channel as being closed if its transmission is below 0.01.[8] As one can see, after an initial evolution up to an elongation of 0.2 nm (region with eight conduction channels), which is similar for all the 50 Ag contacts studied, the conductance starts decreasing in a steplike manner which changes from realization to realization. The jumps in the conductance usually occur at plastic deformations of the contact, i.e., when bonds break and sudden atomic rearrangements take place. Such sudden rearrangements are visible as a break-in of the strain force. The elastic stages, in which the atomic bonds are being stretched, are characterized by a linear increase of the strain force. In this case the conductance exhibits well-defined plateaus (see, for instance, the region with three channels, which occurs for elongations between 0.7 and

---

[8] For the division of a conductance trace into regions with different numbers of open conduction channels we use a criterion of $T_n^\sigma < 0.01$ to consider the nth channel to be closed. This division is only approximate: Due to fluctuations in the geometry, a channel transmission may fall temporarily below 0.01 but reenter later on. Often (especially in the metals Pt, Al, and Ni) many open conduction channels are present and, in order not to overload our pictures, we need to combine several channel-closing events into one.

0.83 nm). In the last stages of the breaking of the contact, displayed in Fig. 2.3, a stable single-atom contact is formed. In this region the conductance is mainly dominated by a single channel, although a second one is still visible (see two-channel region or elongations between 0.86 and 0.95 nm). Subsequently a dimer structure is formed, which survives for a short period of time, after which the contact finally breaks. In this region only a single transmission channel is observed.

It is worth noticing that there is practically no difference between the conductance G and the averaged conductance $\langle G \rangle$ (see Eq. (2.11)), demonstrating that the transmission as a function of the energy is rather flat around the Fermi energy (in the window $-\Delta \leq E - E_F \leq \Delta$). This can be seen explicitly in Fig. 2.5, which we shall discuss later in more detail. The flat transmission $T(E)$ is expected for a noble metal such as Ag because its DOS around E_F is mainly dominated by the contributions of the s and p bands, which are rather broad and vary slowly with energy (see also Fig. E.3).

Another example of a breaking curve for Ag is depicted in Fig. 2.4.In the beginning the conductance evolves similar to the contact discussed above (see Fig. 2.3). This time a stable dimer is finally formed. Prior to the formation of the dimer structure, which sustains a single transmission channel (see one-channel region or elongations from 1.06 to 1.19 nm), there also appears a single-atom contact, where two channels are still visible (see two-channel region or elongations from 0.97 to 1.06 nm), in analogy to what will be found for Au later (see Fig. 2.13). We observe for both configurations a single dominant transmission channel and a conductance of around $1G_0$. This result is consistent with first-principles calculations, where it has been shown for selected ideal contact geometries that the transmission of Ag chains is around $1G_0$ and the conductance is carried by a single transmission channel [84, 85].

Due to the appearance of a stable dimer structure there is now a long and flat last plateau before rupture in Fig. 2.4. Our simulations show that this type of dimer is the most common structure in the last stages of the contact formation.

A certain peculiarity can be observed if one has a closer look at the region with six open channels. Here, the conductance first drops abruptly and then increases again in the region with five open channels. Notice that this increase is accompanied by a steady decrease of the MCS. This type of reentrance of the conductance, which is often observed experimentally, cannot be explained in terms of semiclassical arguments, which are based on Eq. (2.1). According to this formula the conductance should be a monotonous function of the MCS, which, however, is not always the case. Such break-ins of the conductance have already been observed before in simpler TB calculations [56].

In order to explain the existence of a single channel in the final stages of breaking, we have plotted in Fig. 2.5 the LDOS of an atom in the narrowest part of the junction as a function of the energy together with the transmission. We have chosen a dimer configuration at an elongation of 1.16 nm, right before the rupture of the contact displayed in Fig. 2.4. The transmission around the Fermi energy is made up of a single channel, exhibiting only a tiny variation in the energy window $-\Delta \leq E - E_F \leq \Delta$. In the LDOS there are two dominant contributions, one coming from the s orbital, as expected, and the other one from the p_z orbital. Therefore, the transmission channel is expected to consist

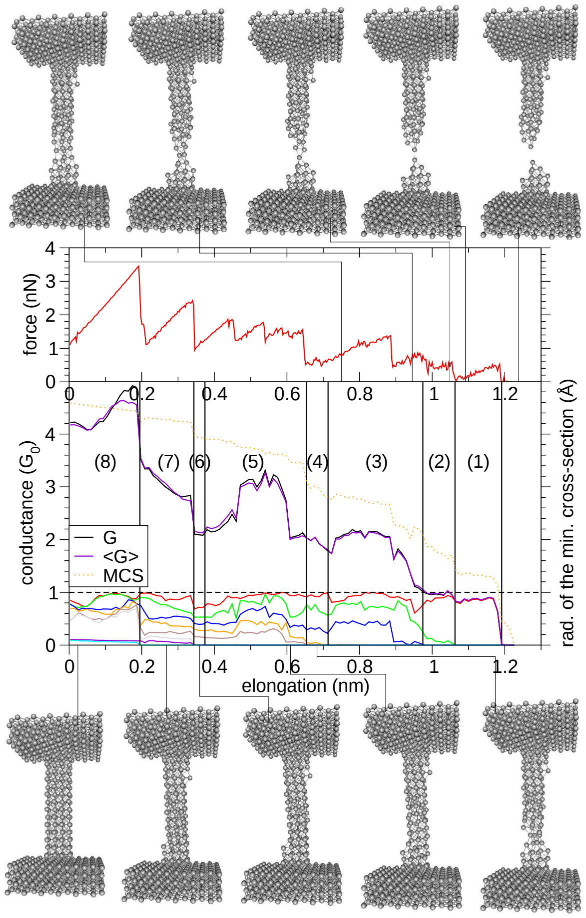

Figure 2.4: Formation of a dimer configuration for Ag (4.2 K, [001] direction). The upper panel shows the strain force as a function of the elongation of the contact. In the lower panel the conductance G, the averaged conductance $\langle G\rangle$, the MCS radius and the channel transmissions are displayed. Vertical lines separate regions with different numbers of open channels ranging from 8 to 1. Above and below these graphs snapshots of the stretching process are shown.

mainly of these two contributions, the other orbitals being of minor importance. As found before [39, 80], the s and p_z orbitals are then forming a radially isotropic transmission channel along the transport direction. If we denote by l_z the projection of the angular momentum onto the z axis (transport direction), this channel has the quantum number $l_z = 0$.

2.3.2 Statistical analysis of silver contacts

In Fig. 2.6 our MCS histogram as well as the computed conductance histogram are displayed.The histograms are obtained by collecting the results of the stretching of 50 Ag contacts oriented along the [001] direction at 4.2 K, as described in Sec. 2.2. In the case of the MCS histogram, the most remarkable feature is the appearance of very pronounced peaks, which indicate the existence of particularly stable contact radii. For the purpose of correlating these peaks with the structure in the conductance histogram, we have marked the regions around the peaks in the MCS histogram with different pattern styles. In the conductance histogram we indicate the counts for conductances belonging to a certain MCS

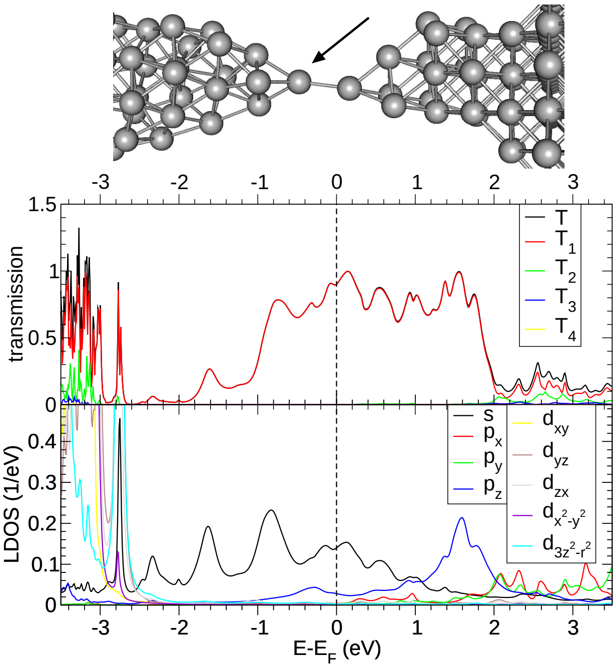

Figure 2.5: Ag contact of Fig. 2.4 at an elongation of 1.16 nm. The total transmission T is plotted as a function of the energy together with the contributions from the different transmission channels T_n. Additionally the LDOS is given for an atom in the narrowest part of the contact, where the different orbital contributions have been itemized. Above the figure the narrowest part of the Ag contact is displayed in a magnified fashion and the atom is indicated, for which the LDOS is shown.

region with the same pattern style, in order to establish the correlation between geometric structure and features in the conductance histogram.

With respect to the conductance histogram, our main result is the appearance of a pronounced peak at $1G_0$, in accordance with the experimental results [86, 20, 83] (see Fig. 2.1). This peak mainly stems from the contributions of contacts with MCS radii in the first (dimers) and second (single-atom contacts) region of the MCS histogram. Therefore, we can conclude that the peak at $1G_0$ is a consequence or manifestation of the formation of single-atom contacts and dimers in the last stages of the breaking of the Ag wires.

It is also important to stress that the contributions to the conductance histogram coming from the different regions of the MCS histogram clearly overlap. This means in practice that the MCS radius is not the only ingredient that determines the conductance, as one would conclude from semiclassical arguments (see Eq. (2.1)). In other words, the peak structure in the MCS histogram is not simply translated into a peak structure in the low-temperature conductance histogram, as suggested in Ref. [52].

At this stage, a word of caution is pertinent. In break junction experiments, contacts are opened and closed repeatedly, and the breaking processes start with a conductance as large as $100G_0$ [45]. Compared to this value, our simulations start with a very small conductance of around $4G_0$. Additionally, all the contacts are oriented along the [001] direction, which can be expected to have an influence on the structure of the conductance histogram. Even for rather thick contacts it has been shown experimentally that prefabricated wires cause a different peak structure in the conductance histograms [87].

The last three peaks of the MCS histogram (labeled 10, 11, and 12 in Fig. 2.6) are mainly dominated by the (arbitrarily) selected [001] starting configuration. It is interesting to observe that the MCS region labeled with a 10 has a large weight at conductances

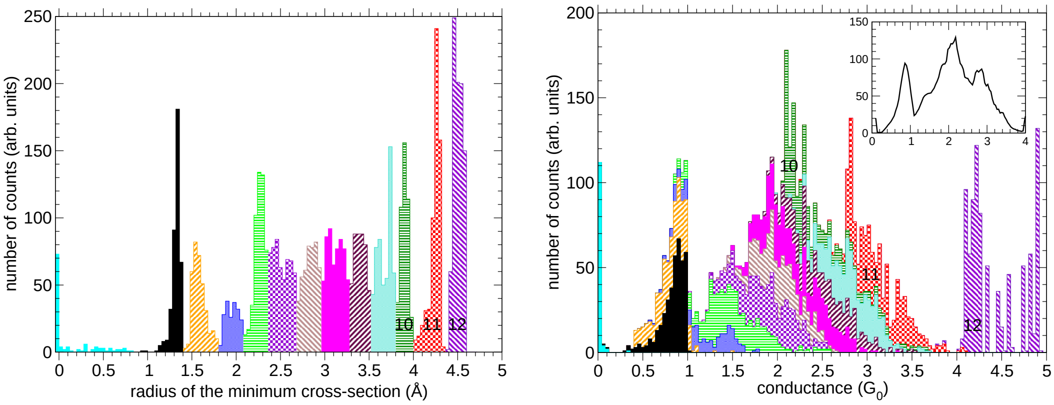

Figure 2.6: MCS histogram (left panel) and conductance histogram (right panel) for Ag (4.2 K, [001] direction, 50 contacts). In the MCS histogram different regions of frequently occurring radii have been marked with different pattern styles. The patterns in the conductance histogram indicate the number of counts for conductances belonging to the corresponding region of the MCS histogram. For better reference in the text, some regions in the MCS and conductance histogram have additionally been labeled with numbers. In the inset of the right panel the conductance histogram is displayed in the relevant region in a smoothed version by averaging over six nearest-neighbor points.

of somewhat above $2G_0$, although it should be expected to have contributions for large conductances because of its high MCS. The break-in of the conductance in Fig. 2.4 at the transition from the six- to five-channel region is an example showing the origin of the large weight of this MCS region. This observation illustrates that even conductance regions down to $2G_0$ are distorted due to the small size of our contacts. While we can be sure about the first peak in the conductance histogram at $1G_0$, all the higher peaks would require the study of bigger contacts with even more atoms in the central region.

It is important to remark that out of 50 simulations we have only observed the formation of three short chains with three, four, and five atoms in each case. This is in strong contrast to the case of Au, where chains are encountered much more frequently and with more chain atoms (see Sec. 2.4.1). Short atomic Ag chains of up to three atoms have also been observed in experiments [20, 83].

Another important piece of information can be obtained from the analysis of the mean channel transmission (averaged over all contacts) as a function of the conductance, which is shown in Fig. 2.7.[9] Here, one can see that the conductance region below $1G_0$ is largely

---

[9] The mean channel transmission $\langle T_n^\sigma \rangle$ as a function of the conductance is determined as follows: For all simulated contacts of a certain metal we consider the breaking curve of the conductance and all the channel transmissions T_n^σ. (For the nonferromagnetic contacts we will suppress the spin index σ.) Next we concentrate on a fixed conductance $G = G^\uparrow + G^\downarrow$ (within a bin-width of $0.04G_0$). We obtain the mean channel transmission $\langle T_n^\sigma \rangle$ of the nth channel as the mean value over all the corresponding individual channel transmissions $T_{n,j}^\sigma$ for this fixed conductance ($\langle T_n^\sigma \rangle = \sum_{j=1}^{N} T_{n,j}^\sigma / N$, where N is the number of values present in the average). The error of the mean channel transmission (as given in Figs. 2.15, 2.7, 2.21, and 2.27) is computed as the mean quadratic error $\tilde{\sigma} = \sqrt{\sum_j \left(T_{n,j}^\sigma - \langle T_n^\sigma \rangle\right)^2 / (N-1)}$ of the values

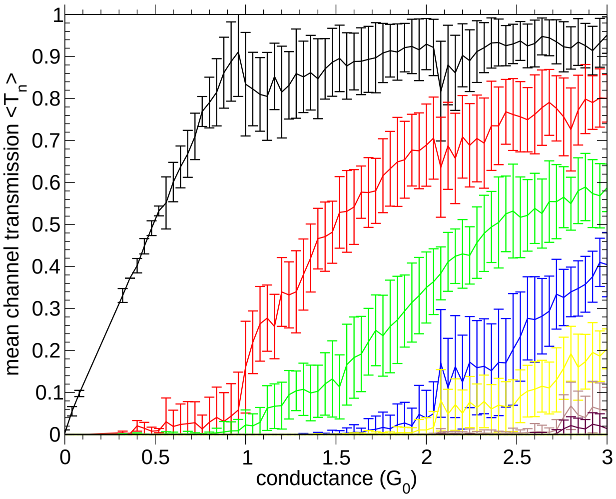

Figure 2.7: Mean value of the transmission coefficient $\langle T_n \rangle$ as a function of the conductance for Ag (4.2 K, [001] direction, 50 contacts). The error bars indicate the standard deviation $\tilde{\sigma}$.

dominated by a single channel. Above $1G_0$ a sharp onset of the second transmission channel can be observed, the third channel increasing more continuously. At $2G_0$ again an onset of the fourth and fifth channel is visible.

2.4 Gold atomic contacts

As another example of a noble metal with a single *s* valence electron we will analyze the conductance of Au nanowires. As for Ag different experiments have shown that the conductance of Au contacts exhibits a tendency towards quantized values in the last stages of the wire formation [82, 20, 87, 89]. Again the most dominant feature in the experimental low-temperature conductance histogram is a pronounced peak at $1G_0$ [82, 20] (see also Fig. 2.1).

2.4.1 Evolution of individual gold contacts

In this section we discuss in detail some of the typical features that we observe in single realizations of the Au contacts. In particular, we discuss the formation of both single-atom contacts and chains.

In Fig. 2.8 we show the formation of a dimer configuration. In order to give the complete picture of this process we have depicted the forces, the conductance, the radius of the MCS, and the transmissions of the different conduction channels. In this example the conductance evolves during the elongation process from a value close to $5G_0$ at the starting point to $1G_0$ in the last stages before breaking. The decrease of the conductance follows closely the evolution of the MCS. This correlation is particularly pronounced in the last stages when the contact has one or two atoms in the narrowest part. However,

---

$T^{\sigma}_{n,j}$, also called standard deviation [88]. (Note that in Ref. [36] we give the mean error of the arithmetic mean $\chi = 0.8\tilde{\sigma}/\sqrt{N}$, resulting in smaller error bars.)

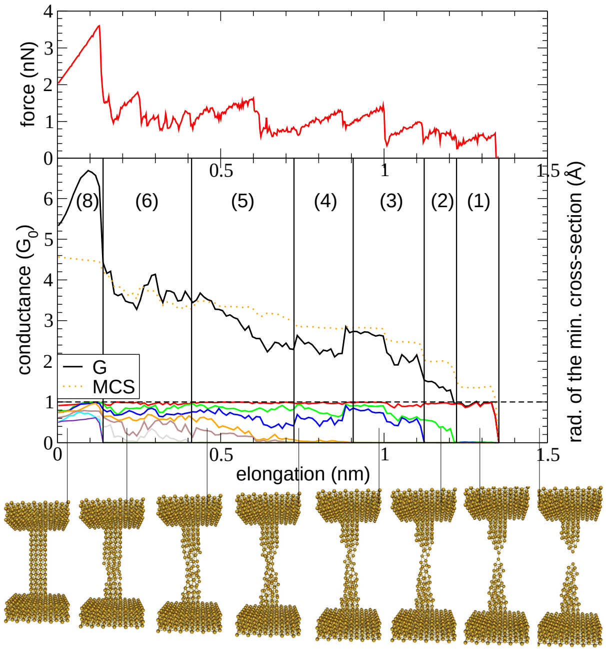

Figure 2.8: Formation of a dimer configuration for Au (4.2 K, [001] direction). The upper panel shows the strain force as a function of the elongation of the contact. In the lower panel the conductance G, the MCS radius, and the channel transmissions are displayed. Vertical lines separate regions with different numbers of open channels ranging from 8 to 1. Below these graphs snapshots of the stretching process are shown.

it is worth stressing that the conductance does not always follow the MCS. We made this observation for Ag before and see here another example in the elongation region between 0.75 and 1.0 nm. Sometimes there appear jumps in the conductance in regions where the MCS evolves smoothly. We interpret this fact as rearrangements of atoms away from the narrowest part of the wire. This interpretation is confirmed by the analysis of the forces, as we explain in the next paragraph.

As shown in the upper panel of Fig. 2.8, one can see in the forces a series of regions where they increase linearly and regions with abrupt jumps. As for Ag the first ones correspond to situations where the structure remains essentially unchanged (elastic stages), and the latter correspond to the breaking of bonds and subsequent sudden atomic rearrangements (plastic stages). Such evolutions of the forces have been measured for Au contacts at room temperature with the help of an atomic-force microscope [90]. The order of magnitude of the forces in Fig. 2.8 is in good agreement with this experiment. Notice that also in the cases where the jumps in the conductance are not correlated to abrupt changes in the MCS, one observes jumps in the forces. This indicates that plastic deformations in regions away from the narrowest part of the wire have also an influence on the conductance. Thus we see that in the determination of the conductance the MCS is an important ingredient, but it is by no means the only one.

Another interesting feature in Fig. 2.8 is the last conductance plateau. At these elongations the MCS corresponds to a contact with the cross-section of one atom. The configuration present is a dimer of gold atoms. Such dimer configurations are the most common geometries that we find in the last stages of the contact breaking. Notice also that in the last plateau, which is marked by a linear increase of the forces, the conductance is close to $1G_0$ and it is clearly dominated by a single conduction channel. As explained in

Refs. [37, 39, 38], this is due to the fact that the number of channels is controlled by the valence electrons in the narrowest part of the contact. In the case of Au the main contribution to the DOS at the Fermi energy comes from the single s valence orbital. This implies that in the dimer configuration of Fig. 2.8, there is only one possible path (conduction channel) which proceeds mainly through the s orbitals. It is also important to emphasize that during the elongation of the contact we observe that the channels disappear one by one in agreement with the experimental results reported in Ref. [38]. This will be discussed in more detail below, when we compare our results to the experimental measurements. We attribute the successive closing of the channels to the fact that in the stretching process the Au atoms leave the narrowest part one by one, and every Au atom contributes to the transport with one orbital, which in turn can give rise to one conduction channel.[10]

On occasion we observe that the Au contact does not break as in the configuration of Fig. 2.8, but continues to form chains of several atoms. This is illustrated in Fig. 2.9.Experimental evidence of the formation of Au chains was first reported independently by two groups [21, 22]. The formation of chains had already been suggested by different computer simulations before [59, 61, 74]. In the last ten years there has been an intense activity in this topic. Thus, for instance, there are now several experiments confirming the existence of gold chains [91, 47, 92], and the forces during the formation of a Au chain have been measured [70]. From the theoretical side, many authors have analyzed the formation, stability, and conductance of Au chains [93, 64, 80, 94, 95, 96, 97].[11]

In our simulations for the [001] direction we have observed 11 chains out of 50 stretching processes with different lengths: nine chains ranging from 3 to 6 atoms and three chains of 10, 12, and 14 atoms. Experimentally chains up to eight Au atoms have been reported [22]. The mechanism of the chain formation has been explained by Bahn and Jacobsen [71] in terms of many-body effects in metals. The main idea is that in certain metallic systems the binding energy per neighboring atom may increase as the number of neighbors decreases. Here, we want to illustrate how a chain is formed in real time. We show in Fig. 2.10 five snapshots of the dynamics of the nanocontact of Fig. 2.9. At 0.0 ps a contact is shown with a typical dimer structure in the middle. The atom number 2 has four nearest neighbors and the atom 1 only three. Due to the many-body interactions the bond between the atoms 2 and 3 breaks. After about 26.6 ps another bond breaks and the atom 2 moves into the chain. The atom 4 is now in a similar situation as the atom 2 was in the beginning, and the previous process can be repeated again.

Turning now to the transport properties of the chains, we see in Fig. 2.9 that during the chain formation the conductance ranges from $0.6G_0$ to $1.1G_0$, exhibiting a long flat plateau close to $1G_0$. With respect to the conductance value, this is in good agreement with experiment [98]. We observe that the conductance is mainly dominated by a single conduction channel. As in the case of the dimer contact shown before (see Fig. 2.8), the single dominant transmission channel is a consequence of the fact that Au is a monovalent

---

[10] For the MCS of the starting configuration with eight atoms one observes eight open conduction channels.

[11] For a more complete list of references, see Sec. XI in Ref. [1].

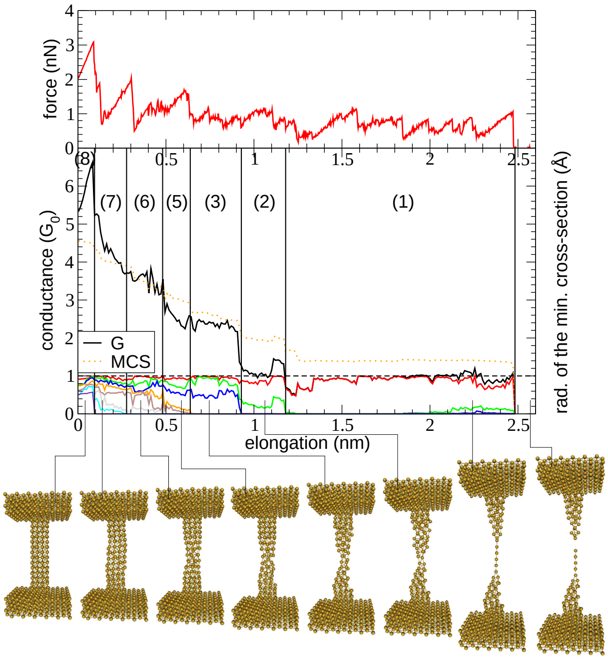

Figure 2.9: Formation of a six-atom chain for Au (4.2 K, [001] direction). The upper panel shows the strain force as a function of the elongation of the contact. In the lower panel the conductance G, the MCS radius, and the channel transmissions are displayed. Vertical lines separate regions with different numbers of open channels ranging from 8 to 1. Below these graphs snapshots of the stretching process are shown.

metal. At the end of the stretching process, when the chain is made up of four or more atoms, we typically observe the appearance of a second channel and sometimes even a third one (see Fig. 2.9). Our analysis shows that these additional channels are due to the contribution of the d orbitals [96]. With respect to the fluctuations of the conductance during the formation of the chains, we want to stress that they are not an artifact of our conductance calculations, but they are clearly related to fluctuations in the contact geometry. In Fig. 2.9 one can see that the structure in the conductance during the chain formation is accompanied by abrupt changes in the force values, i.e., by plastic deformations that correspond to the incorporation of additional atoms into the chain. We have calculated the conductance for all the configurations every 5.6 ps, including contact structures that could be unstable. In the experiment the stretching velocity is several orders of magnitude smaller and such unstable configurations should be averaged out.

2.4.2 Comparison with experimental results

In this section we show experimental results obtained following the technique of Refs. [38, 99, 100], where part of the experimental data has been presented. It is possible to extract the full information of the individual transmission coefficients in experiments. This is done by inducing proximity superconductivity in a Au contact and analyzing the superconducting I-V characteristics [101, 102]. We refer the reader to Ref. [100] for further details.

Fig. 2.11 shows the conductance and the transmission coefficients of a Au contact as a function of the elongation at 100 mK.[12]We can see how the channels disappear one by one

---

[12] The absolute value of the electrode distance is arbitrary, only relative distances could be measured.

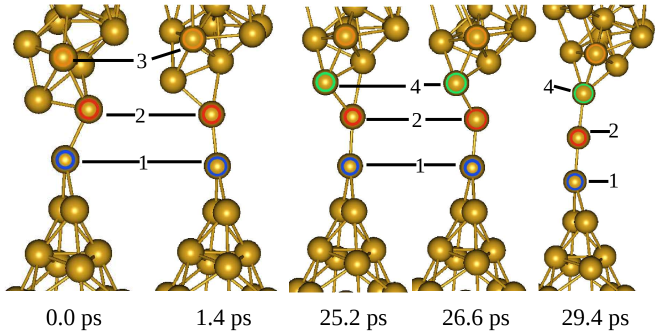

Figure 2.10: Snapshots of the chain formation for the contact displayed in Fig. 2.9. At an initial time of 0.0 ps the atom number 1 has three nearest neighbors and atom 2 has four neighbors. At 1.4 ps the bond between atoms 2 and 3 breaks. At 25.2 ps atom 2 is only connected to two atoms of the electrode. At 26.6 ps another bond breaks, and atom 2 moves into the chain. Atom 4 is now in a similar position as atom 2 was in the beginning and the process can repeat again.

as the contact is being stretched. Notice that there is a very long plateau of about 1 nm of length, which corresponds to the formation of a chain. In this plateau the conductance changes between $0.3G_0$ and $0.9G_0$ and it is dominated by a single channel. Notice also the abrupt changes of the conductance, which are most likely due to incorporations of new atoms into the chain.

In Fig. 2.12 we show another experimental conductance curve.As can be seen, there is a long plateau (about 0.7 nm of length), where the conductance is close to $1G_0$. Naively, one would expect the conductance to be dominated by a single conduction channel. However, the analysis reveals the presence of two channels, and only in the very last stages it reduces to one channel. In the two channel regime of the experiment in Fig. 2.12 the second channel has a transmission mainly below 0.2 and the total conductance is slightly below $1G_0$.

In our simulations we typically observe two open transmission channels in the last stages for geometries in which there are two atoms in the narrowest part displaced with respect to each other (see Fig. 2.13(a)). If there is only a single atom, the second channel gives only a small contribution to the conductance (see Fig. 2.13(b)). As soon as we observe a dimer (see Fig. 2.13(c)), the conductance is largely dominated by a single channel. Our analysis of the character of the channels suggests that for a single central atom like in Fig. 2.13(b) the second channel is due to direct tunneling between the electrodes. In the dimer configuration the distance between the electrodes is considerably larger, which leads to the disappearance of the second channel. The current then flows only through the s orbitals of the central atoms.

In the bottom panel of Fig. 2.11 all the highest measured transmission coefficients (circles) at each electrode distance are connected with straight lines, then the second highest transmission coefficients at each electrode distance are connected, and so on. The mapping of single transmission coefficients to certain transmission channels cannot be measured experimentally.

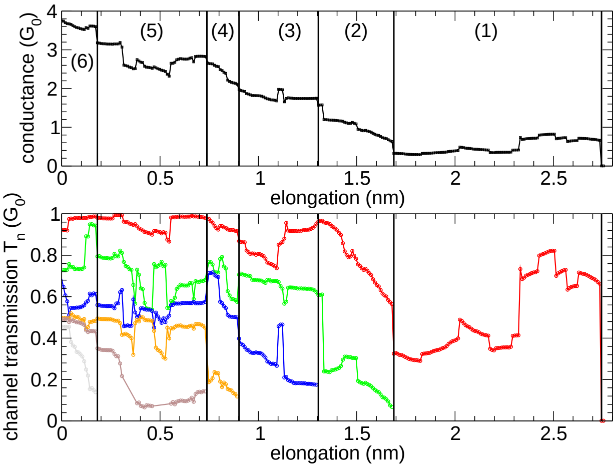

Figure 2.11: Measured total conductance (top panel) of a Au sample and single-channel contributions (bottom panel) as a function of the electrode distance. The vertical lines define regions with different numbers of transmission channels ranging from 6 to 1. The temperature was below 100 mK. For experimental details see Refs. [99, 100].

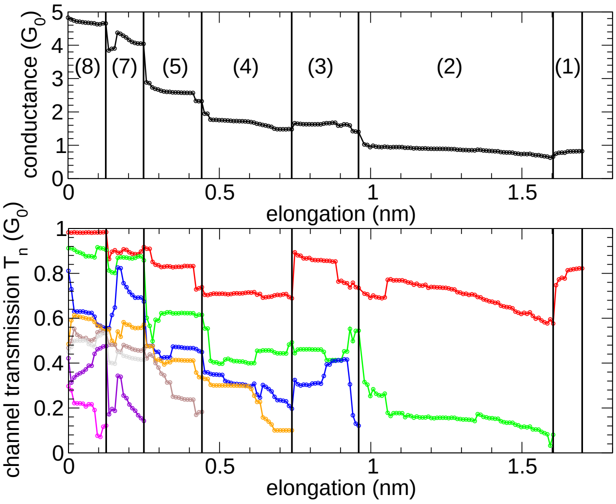

Figure 2.12: Same as Fig. 2.11. The vertical lines define regions with different numbers of transmission channels ranging from 8 to 1.

2.4.3 Statistical analysis of gold contacts

In order to study the origin of the characteristic peak structure in the conductance histogram for Au, we have collected the data of the conductance calculations for the stretching of 50 Au contacts oriented along the [001] direction at 4.2 K. The results are displayed in the conductance histogram of Fig. 2.14 (right panel). As one can see, the conductance histogram has a pronounced peak close to $1G_0$ and two further maxima above $2G_0$ and $3G_0$. In order to make a connection between the peak structure in the conductance histogram and the contact geometry, we show in the left panel of Fig. 2.14 the MCS histogram.

Clearly, the peak in the conductance histogram close to $1G_0$ is due to the contribution of contacts with the MCS of an atom, i.e., single-atom contacts, dimers, or chains of atoms. Concerning the peak structure above $2G_0$ and $3G_0$ it should be pointed out that we are simulating very thin contacts with a cross-section of only eight atoms. As visible in Figs. 2.8 and 2.9 a characteristic evolution of the conductance does only start below $3G_0$. Similarly to Ag a comparison with the experiment in this region is hampered.

Keeping the limitation of our thin geometries in mind, we want to point out that,

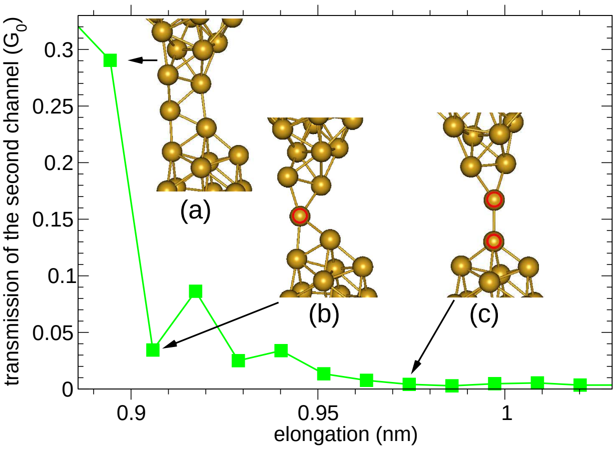

Figure 2.13: Transmission of the second channel during the last stages of the breaking of a typical Au contact (4.2 K, [001] direction). The transmission of the first channel is about $0.7G_0$ (not shown).

again, we do not observe a simple direct correlation between the MCS and the conductance histogram. The MCS regions overlap in the conductance histogram. And in addition the peaks of the MCS histogram, except for the first, are not reflected in the conductance histogram. The reason for this is that beside the MCS also the geometry of the narrowest part and the disorder in the contact play an important role. This means in practice that contacts with different radii can have similar values of the conductance. In particular this is true for small contacts such as the ones that we analyze here. Of course, the situation could be different for larger contacts, where semi-classical arguments are believed to provide a good description.

Another important piece of information can be obtained by analyzing the individual transmission coefficients. Fig. 2.15 shows the mean value of the channel transmissions $\langle T_n \rangle$ as a function of the total conductance for the conductance histogram of Fig. 2.14. Notice that below $1G_0$ the conductance is clearly dominated by a single channel. In particular, for a total conductance of $1G_0$ the second channel gives only a contribution of about $0.04G_0$. This is due to the fact that this region corresponds mainly to dimer configurations or chains of atoms, where all the current proceeds through the s orbital of Au, as explained in Sec. 2.4.1.

In the two channel regime of the experiment in Fig. 2.12 the second channel has a transmission mostly below $0.2G_0$ and the total conductance is slightly below $1G_0$. Similar values are obtained in the simulations. For example, in Fig. 2.15 we observe at a total mean conductance of about $1.1G_0$ a mean transmission of the second channel of about $0.16G_0$, while the third channel, with a mean transmission below $0.03G_0$, plays a negligible role. For higher conductance values the channels are not completely open, which explains the absence of conductance quantization in our conductance histogram (see Fig. 2.14).

The results for the transmission coefficient $\langle T_n \rangle$ for Ag and Au can be related to the experimental observation on noble metals made by Ludoph *et al.* [86, 82], namely, the principle of the "saturation of channel transmission". This principle says that there is "a strong tendency for the channels contributing to the conductance of atomic-size Au contacts to be fully transmitting, with the exception of one, which carries the remaining

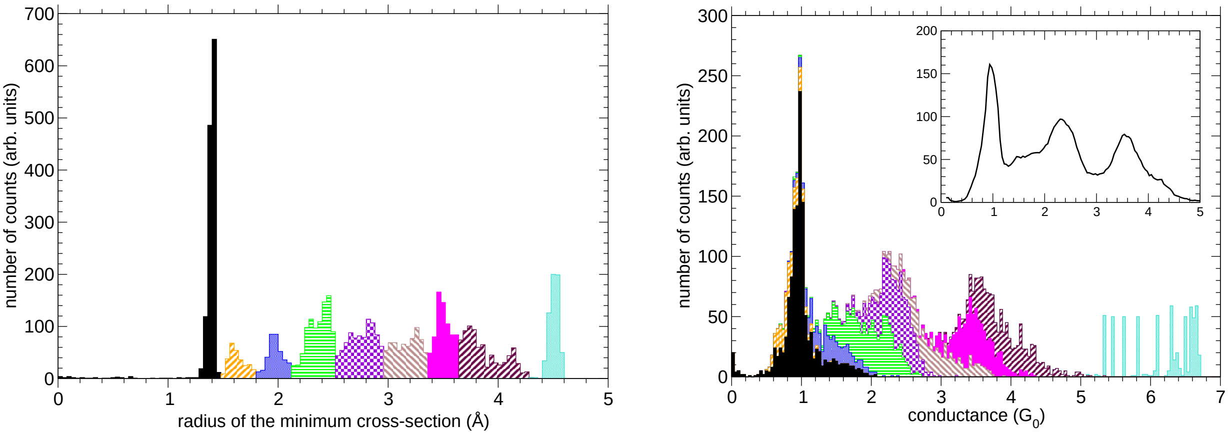

Figure 2.14: MCS histogram (left panel) and conductance histogram (right panel) for Au (4.2 K, [001] direction, 50 contacts). In the MCS histogram different regions of frequently occurring radii have been marked with different pattern styles. The patterns in the conductance histogram indicate the number of counts for conductances belonging to the corresponding region of the MCS histogram. In the inset of the right panel the conductance histogram is displayed in the relevant region in a smoothed version by averaging over six nearest-neighbor points.

fractional conductance" [86]. This tendency of the channels to open one by one is evident for the first channel from Figs. 2.7 and 2.15 and also experimentally the first peak in the conductance histogram for Ag and Au fulfills this principle best [82]. Concerning the higher conductances the finite size of our contacts plays an increasingly restrictive role, but we are well in line with the statement (made for Au, Ag, and Cu) that "particularly the second peaks in the histograms are also determined by other statistical (probably atomic) properties of the contact" [82].

2.5 Platinum atomic contacts

Now we turn to the analysis of Pt contacts. Pt is a transition metal with 10 valence electrons in the partially occupied $5d$ and $6s$ orbitals. The experiments reported so far show that in the case of Pt the last conductance plateau lies typically above $1G_0$. The conductance histogram is dominated by the presence of a broad peak centered around $1.5G_0$ [12, 20, 103] (see Fig. 2.2). Another remarkable feature of Pt contacts is the appearance of monoatomic chains (with up to six atoms), which have a conductance ranging from around $1.5G_0$ to $1.0G_0$ as the length increases [104, 98]. Moreover, complex oscillations of the conductance as a function of the number of chain atoms are superimposed on top of such a decay. Their origin has been explained in terms of a nearly half-filled s band and the additional conduction channels provided by the almost full d bands [105].

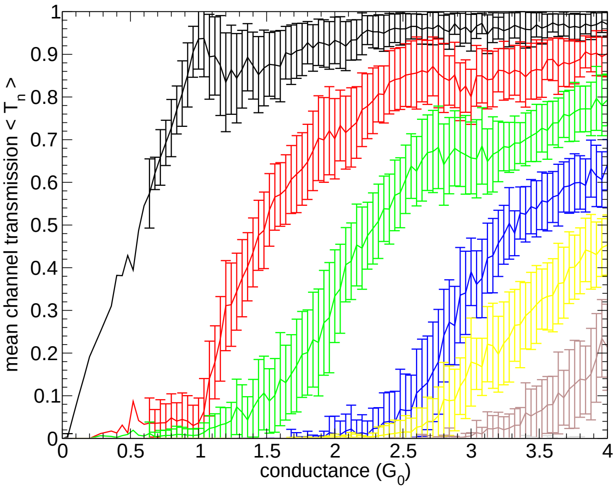

Figure 2.15: Mean value of the transmission coefficient $\langle T_n \rangle$ as a function of the conductance for Au (4.2 K, [001] direction, 50 contacts). The error bars indicate the standard deviation $\tilde{\sigma}$.

2.5.1 Evolution of individual platinum contacts

In Fig. 2.16 a typical example of the formation of a dimer configuration is shown. As before, in addition to the strain force, we display the conductance, the averaged conductance, the MCS radius, and the channel transmissions. The initial evolution is quite similar for all the 50 Pt contacts analyzed here. In this region, which corresponds to elongations below 0.17 nm, we observe between 11 and 10 open conduction channels. After this region, and as in the case of Ag and Au contacts, the conductance evolves in a series of jumps which coincide with plastic deformations (see the positions of break-ins in the sawtooth shape of the strain force). However, in contrast to the noble metals Ag and Au, now we find strong conductance fluctuations during the different elastic plateaus. The stretching of the contact of Fig. 2.16 ends with the formation of a dimer, which sustains three open channels and has a conductance above $1G_0$ (see the region with elongations between 1.12 and 1.22 nm). This is again in contrast to the Ag and Au junctions discussed above, where only a single dominant channel is observed in the final stages before rupture.

On the other hand, the comparison between the conductance G and the averaged conductance $\langle G \rangle$ shows certain deviations (see for instance the region with four channels). This fact indicates that for Pt there is a much stronger variation of the transmission as a function of the energy around the Fermi energy, as compared with Ag and Au. This is in agreement with the experimental finding of nonlinear I-V characteristics for Pt as opposed to linear ones for a noble metal such as Au [106].

The clear differences between the Pt and the noble metal contacts can be traced back to the difference in their electronic structure, as we now proceed to illustrate. We show in Fig. 2.17 the LDOS for an atom in the narrowest part of the junction as a function of the energy together with the transmission. We have chosen a dimer configuration at an elongation of 1.18 nm just before the rupture of the contact of Fig. 2.16. Notice the presence of a much more pronounced structure in the transmission around the Fermi energy as compared to Fig. 2.5, which can be attributed to the contribution of d states. This fact naturally explains the deviation between the conductance G and the averaged conductance

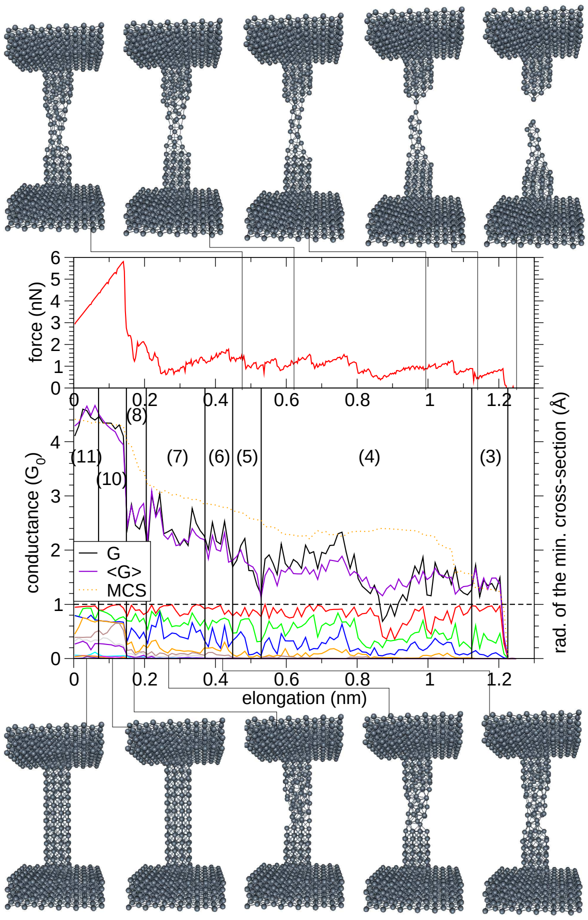

Figure 2.16: Formation of a dimer configuration for Pt (4.2 K, [001] direction). The upper panel shows the strain force as a function of the elongation of the contact. In the lower panel the conductance G, the averaged conductance $\langle G \rangle$, the MCS radius, and the channel transmissions are displayed. Vertical lines separate regions with different numbers of open channels ranging from 11 to 3. Above and below these graphs snapshots of the stretching process are shown.

$\langle G \rangle$ (see Fig. 2.16). At the same time, the partially occupied d orbitals are also responsible for the larger number of open transmission channels (three in the dimer region of Fig. 2.16), as they provide additional paths for electron transfer between the two electrodes [12].

From Fig. 2.17 it is evident that d states play a major role for the conductance in Pt contacts. The strong fluctuations of the conductance during the elastic stages of stretching, as observed in Fig. 2.16, point out a high sensitivity of these d states to the atomic configurations. Ultimately, the sensitivity of d states to atomic configurations can be attributed to the spatial anisotropy of the d orbitals as compared to the spatially isotropic s orbitals, which are mainly responsible for the conductance in Ag contacts.

Now we proceed to discuss the formation of chains in Pt contacts. In the last stages of our simulations we often observe the formation of special structures, namely linear chains of several atoms similarly to what we find for Au (see Sec. 2.4.1). In Fig. 2.18 we show the evolution of a Pt contact, which features a five-atom chain before rupture. As for the contact discussed previously, substantial fluctuations in the conductance are visible even during the elastic stages, demonstrating again the sensitivity of d orbitals to atomic positions. The conductance during the formation of the chain is mainly dominated by two

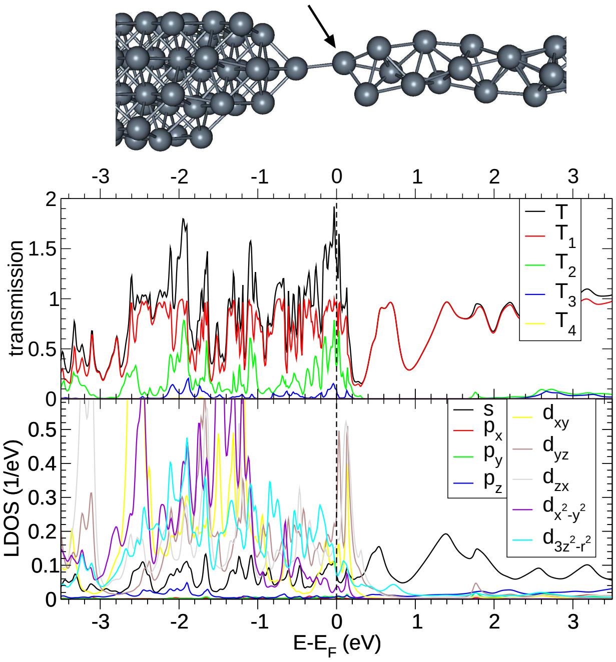

Figure 2.17: Pt contact of Fig. 2.16 at an elongation of 1.18 nm. The total transmission T is plotted as a function of the energy together with the contributions from the different transmission channels T_n. Additionally the LDOS is given for an atom in the narrowest part of the contact, where the different orbital contributions have been itemized. Above the figure the narrowest part of the Pt contact is displayed in a magnified fashion and the atom is indicated, for which the LDOS is shown.

channels, but also a third one is contributing slightly. The first two channels can be of nearly the same magnitude (see elongations above 1.1 nm). After the dimer has formed, the transmission fluctuates around $1G_0$. Compared with Ag, the conductance can, however, also be higher than $1G_0$ due to the presence of a second and a third open channel. The conductance of the last plateau is slightly below the typical experimental value of $1.5G_0$ [20, 106], and we will come back to this point later.

During the formation of the chain (see three-channel region or elongations above 0.8 nm), the strain force exhibits a clear sawtooth behavior. The abrupt jumps in the force after the long elastic stages signal the incorporation of a new atom into the chain. Such incorporations happen at elongations of 0.79 nm (dimer), 1.00 nm (three-atom chain), 1.05 nm (four-atom chain), and 1.27 nm (five-atom chain). Additional jumps at 0.83, 1.11, and 1.33 nm are due to bond breakings at the chain ends. Note that the incorporation of a new atom into an atomic chain does not always require long stretching distances of the order of the nearest-neighbor distance. Because of metastabilities depending on the geometry of the junction, they may actually be much shorter, as can be inferred from the transition from the three-atom chain to the four-atom chain.

In order to explore changes in the electronic structure and their influence on the transmission for the evolution from a dimer to a long atomic chain, we analyze these two kinds of structures now in more detail. In Fig. 2.19 we plot the transmission and LDOS as a function of the energy, considering as example the contact of Fig. 2.18. As can be seen in Fig. 2.19(a), for the case of the dimer the main contributions to the LDOS at the Fermi energy come from the s, d_{yz}, d_{zx}, and $d_{3r^2-z^2}$ orbitals. This is similar to the dimer structure investigated previously (see Fig. 2.17), where the d orbitals contribute significantly to the LDOS. While the energy dependence of the transmission looks qualitatively similar, the

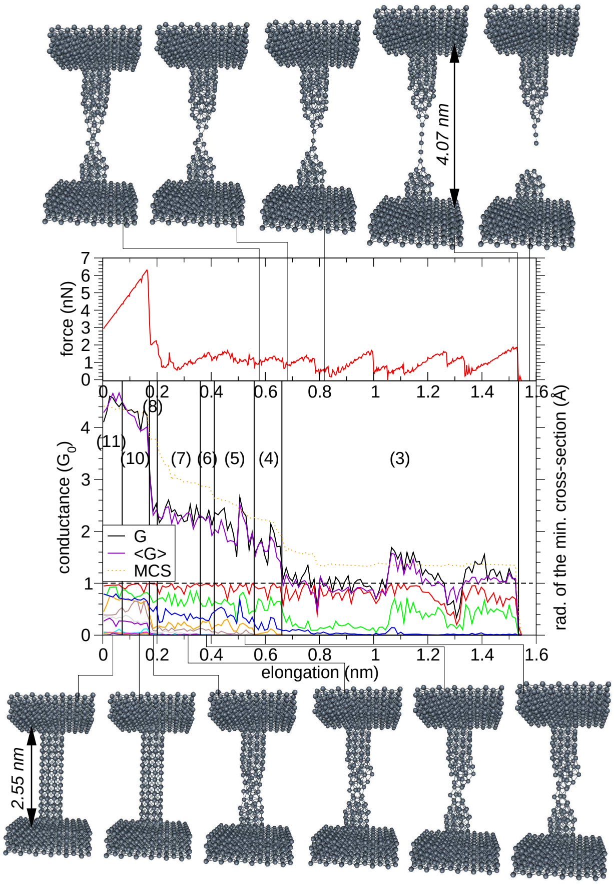

Figure 2.18: Formation of a five-atom chain for Pt (4.2 K, [001] direction). The upper panel shows the strain force as a function of the elongation of the contact. In the lower panel the conductance G, the averaged conductance $\langle G \rangle$, the MCS radius, and the channel transmissions are displayed. Vertical lines separate regions with different numbers of open channels ranging from 11 to 3. Above and below these graphs snapshots of the stretching process are shown.

LDOS changes dramatically when a long chain is forming (see Fig. 2.19(b)). We observe a pinning of the s and $d_{3r^2-z^2}$ states at the Fermi energy, where the s state is close to half filling corresponding to an electronic $5d^9 6s^1$ configuration of the Pt atom. (Notice also the change in scale for the LDOS when going from Fig. 2.19(a) to Fig. 2.19(b).) Comparing the energy dependence of the transmission channels and the LDOS in Fig. 2.19(b), we can infer that the first channel is a linear combination of s, p_z and $d_{3r^2-z^2}$ orbitals ($l_z = 0$), while the second and third seem to be dominated by d_{yz} and d_{zx} orbital contributions ($l_z = \pm 1$). These findings are perfectly in line with Ref. [105].

It is also noteworthy that when the d states have decayed 1 eV above the Fermi energy and the s contribution dominates in the LDOS, only a single channel is observed in the transmission for both the dimer and the chain configuration (see Figs. 2.17 and 2.19). This would correspond exactly to the situation described above for Ag wires, and demonstrates that the differences between these two metallic contacts (Ag and Pt) are mainly due to the different positions of their Fermi energy.

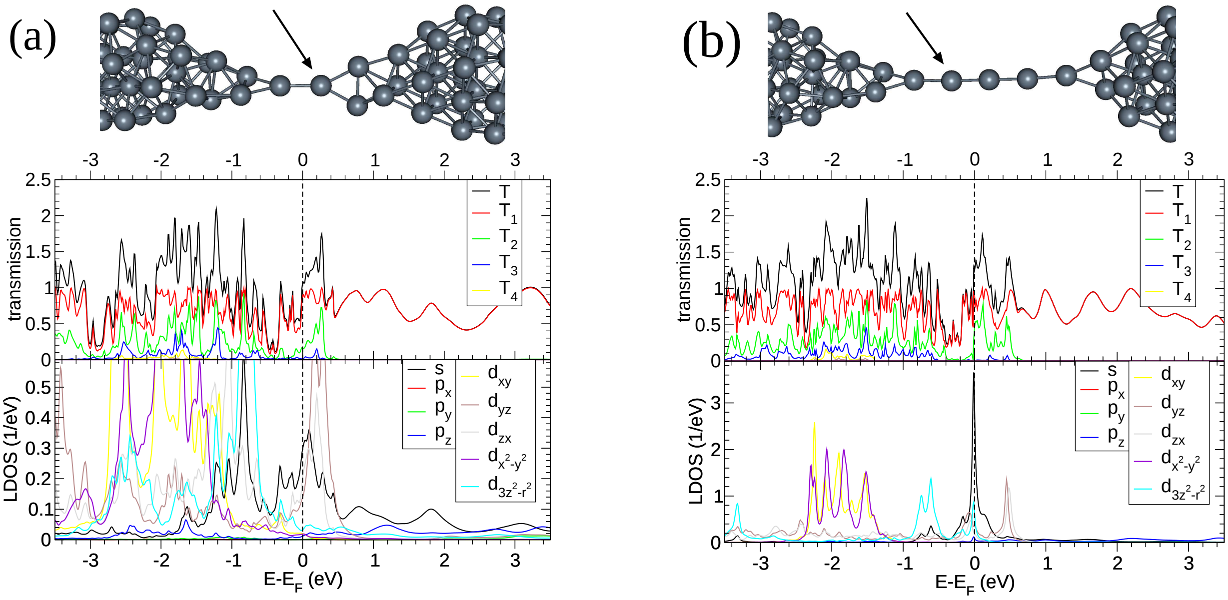

Figure 2.19: Pt contact of Fig. 2.18 at an elongation of 0.95 nm, when the contact is forming a dimer (a) and at an elongation of 1.44 nm, when the contact is forming a five-atom chain (b). In each case the total transmission T is plotted as a function of the energy together with the contributions from the different transmission channels T_n. Additionally the LDOS is given for an atom in the narrowest part of the contact, where the different orbital contributions have been itemized. Above each figure the narrowest part of the Pt contact is displayed in a magnified fashion and the atom is indicated, for which the LDOS is shown.

2.5.2 Statistical analysis of platinum contacts

Putting together the results for the 50 Pt contacts simulated, we obtain the histograms for the MCS and conductance shown in Fig. 2.20. The MCS histogram exhibits a very pronounced peak at radii corresponding to dimer contacts and chains of atoms. Out of 50 breaking events we obtain 18 chains, 17 chains ranging from 5 to 11 atoms and one with up to 19 atoms. The tendency of Pt to form atomic chains is consistent with experiments [20, 104], but the ratio of chain formation is obviously higher. This could partly be due to the thinness of the contacts that we investigate. There exists experimental evidence for the formation of chains with lengths up to six atoms [20], while longer chains become more and more unlikely. Therefore our chains with more than eight atoms seem somewhat artificial.

In the conductance histogram the low-lying MCS peak for dimers and atomic chains gives rise to a very broad peak in the conductance histogram. The position of this peak is centered around $1G_0$ rather than $1.5G_0$, as in the experiment [20, 107]. If we exclude the longest chains (chains with more than eight atoms), we obtain a conductance histogram with a very broad peak at $1.15G_0$ (see the inset in Fig. 2.20).

Experimentally it has been shown that the peak at $1.5G_0$ shifts to $1.8G_0$ for higher

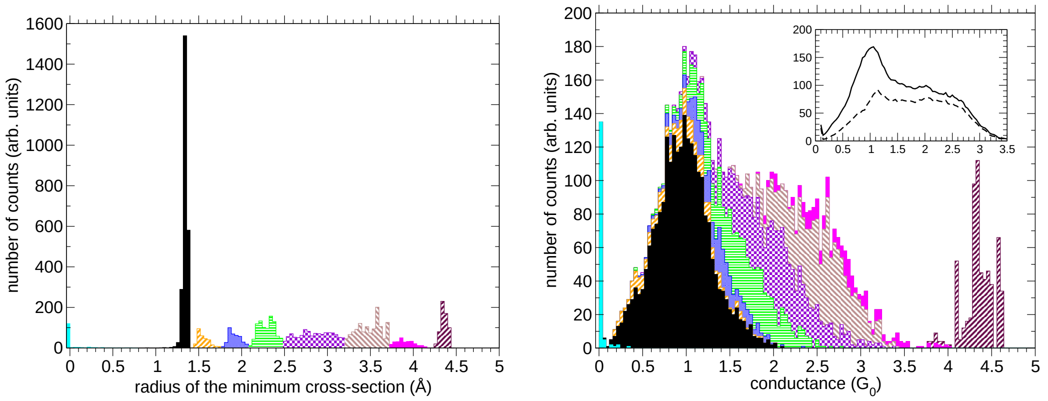

Figure 2.20: MCS histogram (left panel) and conductance histogram (right panel) for Pt (4.2 K, [001] direction, 50 contacts). In the MCS histogram different regions of frequently occurring radii have been marked with different pattern styles. The patterns in the conductance histogram indicate the number of counts for conductances belonging to the corresponding region of the MCS histogram. In the inset of the right panel the conductance histogram is displayed in the relevant region in a smoothed version by averaging over six nearest-neighbor points for all contacts (solid) and contacts with up to eight atoms in the chain (dotted).

bias voltages [107]. This has been attributed to a structural transition, where atomic chains are replaced by single-atom contacts. Thus, the conductance of dimers and chains should be around $1.5G_0$ and the conductance of single-atom contacts around $1.8G_0$. In Fig. 2 of Ref. [98] Smit *et al.* reported a decrease in the average conductance from $1.5G_0$ to around $1G_0$ for increasing chain lengths. This demonstrates that our broad distribution of conductances around $1G_0$ in the conductance histogram (see Fig. 2.20) is not unreasonable, although the transmission for dimers and short chains seems to be underestimated. A recent DFT study investigated ideal Pt chains consisting of two to five atoms in the [001] direction [108]. Conductances between $2G_0$ and $1G_0$ were obtained with a trend towards $1G_0$ for longer chains in agreement with the experiment. The structure of the chains, which in our case is linear, was zigzaglike. This could be another explanation for the lower transmissions in our study.[13]

Although the peak position in the conductance histogram in Fig. 2.20 is lower than in the experiments, we want to point out the strong qualitative differences in comparison to Ag and Au. While the first two MCS peaks in the Ag and Au histogram (see Figs. 2.6 and 2.14) are narrowly peaked around conductance values of $1G_0$, this is not the case for Pt. Instead, the first two peaks cover a range of conductance values from as low as $0.1G_0$ up to

---

[13] Further investigations are needed to find out, why the transmission of dimers and short chains is rather $1G_0$ than $1.5G_0$. Possible reasons could lie in the structural properties such as, for example, the high disorder of our thin contacts or linear instead of zigzag chains. The approximation of surface Green's functions by bulk Green's functions in the electrodes has been checked to have little influence on the transmission when chains have formed (see Sec. 2.10). Potentially the low transmission for dimers and short chains could also indicate limitations for the use of the Pt TB parameters in conductance calculations.

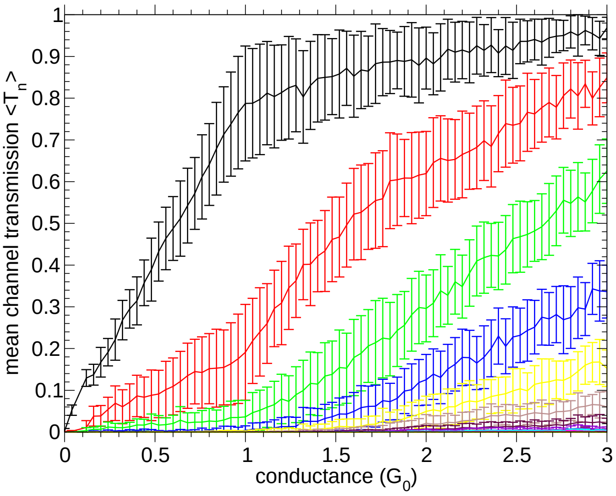

Figure 2.21: Mean value of the transmission coefficient $\langle T_n \rangle$ as a function of the conductance for Pt (4.2 K, [001] direction, 50 contacts). The error bars indicate the standard deviation $\tilde{\sigma}$.

$2G_0$ and are very broad. This is again due to the contribution of the d orbitals at the Fermi energy, which leads to a higher number of open channels in the case of Pt, as explained in Sec. 2.5.1. Let us recall that for Ag and Au there is a single dominant transmission channel (and a small second one), while for Pt there are usually three channels in the last stages before breaking, and the second channel can be comparable in magnitude to the first. As explained above, the extraordinary width of the first peak in the conductance histogram for Pt can be attributed to the sensitivity of d states to the atomic configuration of the contact.

This qualitative difference in the number of conduction channels is illustrated in Fig. 2.21, where we show the mean value of the transmission coefficients as a function of the conductance. Notice that as compared with the case of Ag and Au (see Figs. 2.7 and 2.15), there are contributions from the second and third channel already present for conductances below $1G_0$. For conductances of $1.5G_0$ there are four or five channels on average.

In conclusion, the different behavior of Ag, Au, and Pt contacts stems from the different electronic states present at the Fermi energy. While for noble metals such as Au and Ag it is located in the s band, its position is shifted downwards into the d bands for Pt. Therefore, in the latter case there are in general more open channels contributing to the conductance. This confirms the statements of Scheer *et al.* [38] that the number of transmission channels is determined by the chemical valence.

2.6 Aluminum atomic contacts

Al is an example of the so-called p-valent metals [20]. In the crystalline form there are three valence electrons occupying partly the $3s$ and $3p$ bands around the Fermi energy. In this respect, Al has a very different electronic structure as compared to Au, Ag, or Pt (e.g., see Fig. E.3), and in this section we study how this electronic structure is reflected in the conductance of Al atomic wires. Due to the technical problems detailed below, this analysis will be considerably shorter than for the other metals.

The experimental studies of the conductance of Al atomic-sized contacts have shown several peculiar features [109, 19, 110, 39, 20]. For instance, Scheer *et al.* [19], making use of superconducting current-voltage characteristics to extract the transmission coefficients, showed that usually three conduction channels contribute to the transport, although the conductance of the last plateau is typically below $1G_0$. This was explained in Ref. [37] in terms of the contribution of the p orbitals to the transport. Exploiting conductance fluctuations, the presence of several conduction channels for conductances above $0.5G_0$ could subsequently be confirmed by another independent experimental technique [82]. As an additional peculiarity, Al is one of the few multivalent metals which exhibits several pronounced peaks in the conductance histograms at low temperatures [110]. The first peak appears at around $0.8G_0$ and the next ones at $1.9G_0$, $3.2G_0$, and $4.5G_0$ (see Fig. 2.2). Furthermore, the conductance plateaus in Al have a positive slope upon stretching [109, 19], which is quite unique.

Again we simulated 50 breaking events. Although we always observe in the last stage of the nanocontacts either a single-atom contact (36 times), a dimer (13 times), or in one case a four-atom chain, the single-atom contacts and dimers are often very short-lived configurations and less stable than the corresponding Ag and Pt structures. We attribute this to shortcomings in the semiempirical potential employed for Al in this work. Previously it has been shown that this potential cannot reproduce adequately the mechanical properties of an infinite Al chain [111]. This underestimation of the stability of thin wires is quite apparent in our simulations, where the contacts break effectively at conductances well above $1.5G_0$ and with several atoms present in the MCS. This technical problem hindered the proper analysis of the statistical properties of Al contacts.

In Fig. 2.22 we show the evolution of a contact that effectively breaks at a conductance of $4G_0$. The dimer configuration occurring in the final stages is very short-lived and only appears to be an intermediate state (see the three-channel region).

However, we could recover a few sensible examples. One of the formations of a relatively stable dimer is displayed in Fig. 2.23. A region of three transmitting channels can be observed shortly before contact rupture, and the conductance of the dimer configuration is close to $1G_0$, which agrees nicely with the observations of Scheer *et al.* [19]. The origin of these three channels is, as explained in Ref. [37], the contribution of the partly occupied *sp*-hybridized valence orbitals of Al to the transport. Before this region, a nice plateau around $2G_0$ is visible. Both features agree well with the peaks in the experimental conductance histogram for Al close to $0.8G_0$ and $1.9G_0$ [110, 20]. More importantly, our results reproduce the peculiar positive slopes of the last plateaus of the stretching curves, in compliance with Refs. [109, 19, 39, 63].

2.7 Nickel atomic contacts

During the last few years a lot of attention has been devoted to the analysis of contacts of magnetic materials [112, 113, 114, 115, 116, 117, 118]. (For a more complete list of references see Refs. [1, 118].) In these nanowires the spin degeneracy is lifted, which

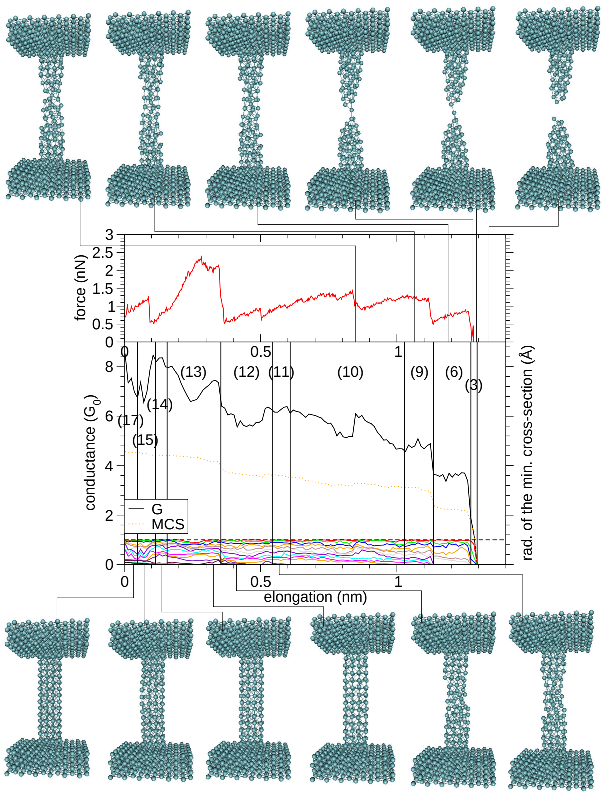

Figure 2.22: Formation of a short-lived dimer configuration for Al (4.2 K, [001] direction). The upper panel shows the strain force as a function of the elongation of the contact. In the lower panel the conductance G, the MCS radius and the channel transmissions are displayed. Vertical lines separate regions with different numbers of open channels ranging from 17 to 3. Above and below these graphs snapshots of the stretching process are shown.

can potentially lead to interesting spin-related phenomena in the transport properties. For instance, different groups have reported the observation of half-integer conductance quantization either induced by a small magnetic field [114] or even in the absence of a field [116, 117]. These observations are quite striking since such quantization requires simultaneously the existence of a fully spin-polarized current and perfectly open conduction channels.[14] With our present understanding of the conduction in these metallic junctions, it is hard to believe that these criteria can be met, in particular, in the ferromagnetic transition metals (Ni, Co and Fe). As a matter of fact, in a more recent study by Untiedt *et al.* [118], carried out at low temperatures and under cryogenic vacuum conditions, the complete absence of quantization in atomic contacts of Ni, Co, and Fe has been reported, even in the presence of a magnetic field as high as 5 T. Several recent model calculations support these findings [119, 120, 121, 122].

In this section we address the issue of the conductance quantization and the spin polarization of the current with a thorough analysis of Ni contacts. As described in Sec. 2.2.2 we apply our method to a Hamiltonian with spin-dependent matrix elements [78, 79].

---

[14] More generally, the half-integer conductance quantization could also arise from a perfectly polarized current, where the channel transmissions of the transmitted spin-component add up to 1.

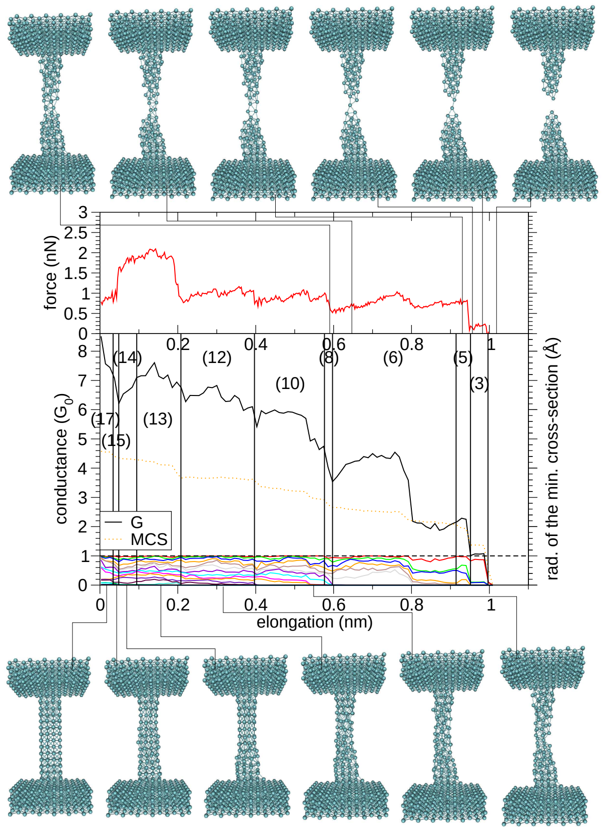

Figure 2.23: Formation of a dimer configuration for Al (4.2 K, [001] direction). The upper panel shows the strain force as a function of the elongation of the contact. In the lower panel the conductance G, the MCS radius, and the channel transmissions are displayed. Vertical lines separate regions with different numbers of open channels ranging from 17 to 3. Above and below these graphs snapshots of the stretching process are shown.

2.7.1 Evolution of individual nickel contacts

In Fig. 2.24 we show the evolution of the conductance during the formation of a Ni dimer structure, which is the most common geometry in the last stages of the breaking process. In addition to the evolution of the conductance and transmission eigenchannels for both spin components separately, we have plotted the MCS radius, strain force, spin polarization of the current, and contact configurations. The spin polarization of the current P, shown in the inset of the lower panel, is defined as

$$P = \frac{G^{\uparrow} - G^{\downarrow}}{G^{\uparrow} + G^{\downarrow}} \times 100\%, \tag{2.13}$$

where G^{σ} is the conductance of the spin component σ (see Eq. (2.8)). Here, spin up ($\sigma = \uparrow$) means majority spins and spin down ($\sigma = \downarrow$) minority spins. Notice that in the last stages of the stretching the conductance is dominated by a single channel for the majority spin, while for the minority spin there are still up to four open channels. In the final stages (see regions with three or one open channel(s) for $G^{\uparrow}$) the conductance for the majority spin lies below $1.2e^2/h$, while for the minority spin it is close to $2e^2/h$, adding up to a conductance of around 1.2–1.6 G_0.

With respect to the evolution of the spin polarization of the current, in the beginning of the stretching process it takes a value of around −40%, i.e., the conductance of the

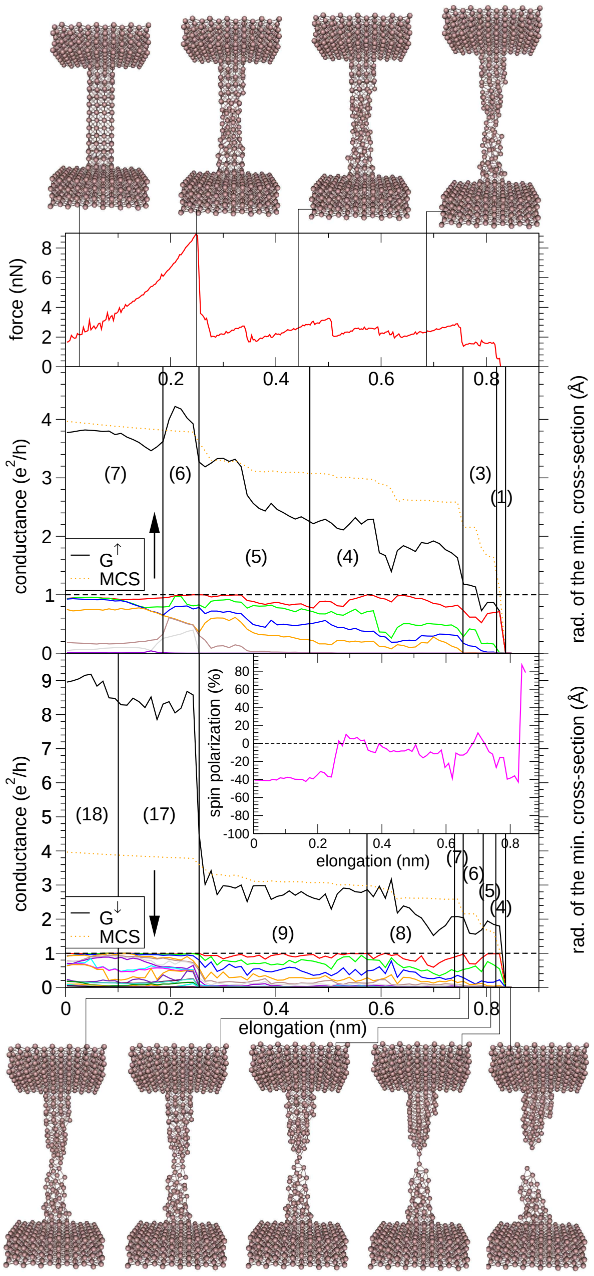

Figure 2.24: Formation of a dimer configuration for Ni (4.2 K, [001] direction). The upper panel shows the strain force as a function of the elongation of the contact. In the lower two panels the conductance G^σ, the MCS radius, and the channel transmissions are displayed for the respective spin component σ. Vertical lines separate regions with different numbers of open channels ranging from 7 to 1 and 18 to 4, respectively. An inset shows the evolution of the spin polarization. Above and below these graphs snapshots of the stretching process are shown.

minority-spin component outweighs that of the majority-spin component. This is expected from the bulk DOS of Ni (see Fig. E.3). For this transition metal the Fermi level lies right in the d band for the minority spin, while for the majority spin one is at the edge of the d band and the s and p bands contribute comparatively more strongly to the DOS. For this reason, there is a larger number of conduction channels for minority-spin component. The value of P is indeed quite close to the value of the spin polarization of the bulk DOS at the Fermi energy, which in our model is equal to -40.5%. As the contact geometry starts changing, the spin polarization of the current begins to fluctuate. It increases even to values above 0%, but keeps a tendency towards negative values, until it starts increasing to over +80% in the tunneling regime, when the contact is broken.

Let us now try to gain further insight into these findings. We show in Fig. 2.25 the transmission as a function of the energy together with the LDOS for an atom in the narrowest part of the constriction portrayed in the upper part of the figure.It can be observed that the Fermi energy, as in bulk, is located just at the edge of the d states for the majority-spin component, while it is inside the d states for the minority-spin component. The majority-spin component therefore exhibits a single transmission channel, behaving similar to a noble metal (see the results for Au and Ag in Sec. 2.4 and 2.3), while there are several open channels for the minority-spin component as in the case of a transition metal (see the results for Pt in Sec. 2.5).

Concerning the spin polarization of the current, the large DOS at E_F for the minority-spin component usually gives rise to a higher number of open channels for the minority-spin component than for the majority-spin component, which in turn leads to a negative spin polarization of the current. However, this argument is just qualitative, because the actual transmission of the channels cannot simply be predicted from the LDOS. The conductance depends also on the overlap of the relevant orbitals and on nonlocal properties like the disorder in the contact region. As a counter example, Fig. 2.24 shows that also intervals of positive P can be found, although the DOS of the minority-spin component is usually higher than for the majority-spin component. This is particularly dramatic in the tunneling regime at the end of the breaking process, where, for instance, in Fig. 2.24 we see that a value of $P = +80\%$ is reached. Such a reversal of the spin polarization is due to the fact that the couplings between the d orbitals of the two Ni tips decrease faster with distance than the corresponding s orbitals. As will be discuss further below, the result is typically a reduction of the minority-spin conductance and therefore a positive value of P.

We would like to point out that the contribution of the minority-spin component to the conductance is very sensitive to changes in the configuration. As is evident from Fig. 2.24, the minority spin shows stronger fluctuations than the majority spin as a function of the elongation. Again, this is a consequence of the fact that the minority-spin contribution is dominated by the d orbitals, which are anisotropic and therefore more susceptible to disorder than the s states responsible for the conductance of the majority spins. The sensitivity to atomic configurations is in agreement with the findings for Ag and Pt as discussed above, where stronger fluctuations of the conductance are seen for the transition metal Pt, as compared with the noble metal Ag.

2.7.2 Statistical analysis of nickel contacts

For the Ni contacts we did not observe the formation of any chain in the 50 simulated stretching processes. As a consequence, only a small first peak is visible in the MCS histogram (see Fig. 2.26). This peak originates from the dimer configurations, which usually form before the contacts break. In the conductance histogram there is a shoulder at around $1.3G_0$. Part of this first peak is buried under the subsequent conductance peak with its

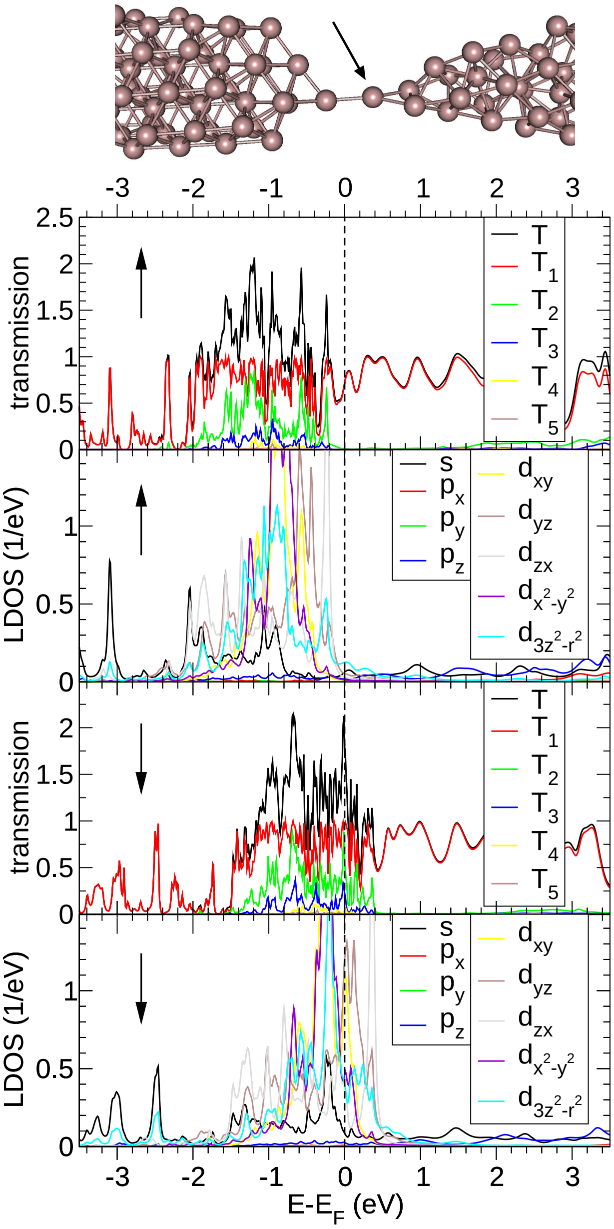

Figure 2.25: Ni contact of Fig. 2.24 at an elongation of 0.83 nm. The transmission is plotted as a function of the energy together with the contributions from the different transmission channels T_n^σ for the respective spin component σ. Additionally the LDOS is given for each spin component for an atom in the narrowest part of the contact, where the different orbital contributions have been itemized. Above the figure the narrowest part of the Ni contact is displayed in a magnified fashion and the atom is indicated, for which the LDOS is shown.

maximum at $2.5G_0$. This second very broad peak is mainly influenced by the starting configuration, which means that the small size of our contacts might hide part of the peak structure in the conductance histogram. According to the MCS regions contributing to the shoulder in the Ni conductance histogram, the first peak is mainly composed of thick contacts (with MCS radii of around 2 Å). This also explains the large broadening of the histogram peak, since for thick contacts, there is more configurational variability.

Concerning the comparison with measurements, the shoulder at $1.3G_0$ in our results is in agreement with the experimental conductance histogram, where a particularly broad peak between $1.1G_0$ and $1.6G_0$ is observed [118]. Our calculations indicate that this peak

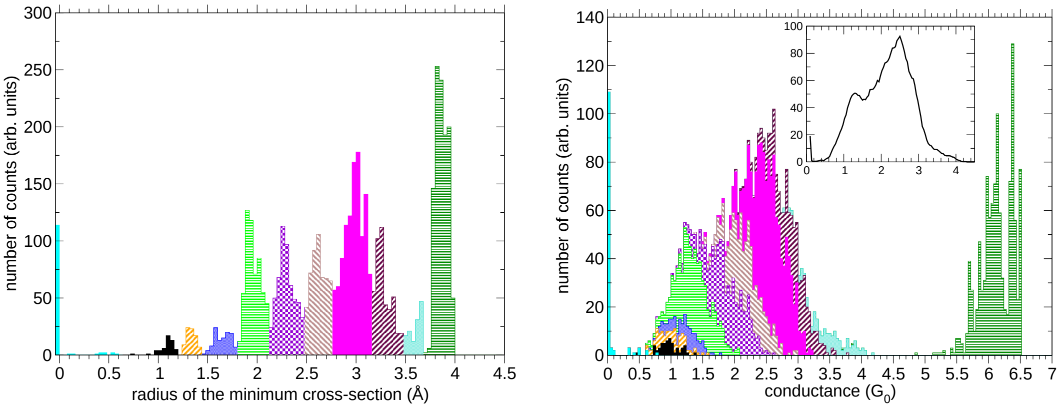

Figure 2.26: MCS histogram (left panel) and conductance histogram (right panel) for Ni (4.2 K, [001] direction, 50 contacts). In the MCS histogram different regions of frequently occurring radii have been marked with different pattern styles. The patterns in the conductance histogram indicate the number of counts for conductances belonging to the corresponding region of the MCS histogram. In the inset of the lower panel the conductance histogram is displayed in the relevant region in a smoothed version by averaging over six nearest-neighbor points.

contains contributions from high MCS regions. The remarkable width of the first peak in the experimental conductance histogram is then explained by the configurational variability of thick contacts in conjunction with the contribution of configurationally sensitive *d* states to the conductance of the minority-spin component. However, this interpretation requires further discussion. Usually the first peak in the experimental conductance histograms is believed to arise from single-atom contacts and dimers [38]. With respect to the problems encountered for Al (see Sec. 2.6), it may be that the employed EMT potential for Ni underestimates the stability of single-atom and dimer configurations in a similar manner. In contrast to our MCS histogram, García-Mochales *et al.* [123] obtain a decreasing peak height for higher MCS radii.[15] Although their results are obtained with a slightly different approach and for thicker contacts, their findings support the conjecture of a possible underestimation of the stability of single-atom contacts and dimers in our calculations. As a consequence the contribution of such configurations to the first peak in the conductance histogram may be too low. In addition, as mentioned above, this first peak in the conductance histogram is not well separated from contributions with a high MCS, which are influenced by our starting configuration. Simulations of thicker contacts and more sophisticated calculations of the contact geometry may be needed to clarify the robustness of our findings.

With regard to the mean channel transmission of the spin-components as a function of

---

[15] Note that in Fig. 4 of Ref. [123] the MCS histograms are plotted with counts vs. area and not counts vs. MCS radius as in our case. For a circular area $A = \pi r^2$ this means that according to $dA = 2\pi r dr$ for a constant dA the MCS radius sampling dr needs to decrease for growing r. However, in our calculations dr is fixed, to that the MCS histogram of Ref. [123] is not directly comparable to ours in Fig. 2.26.

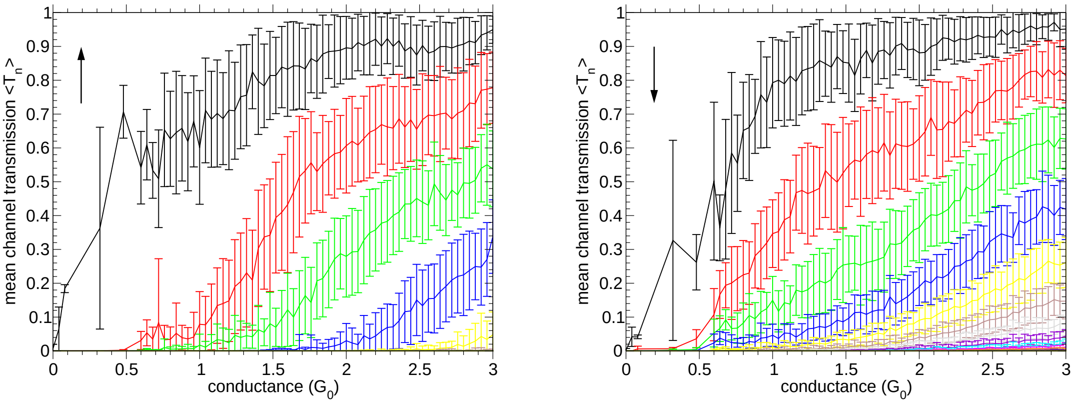

Figure 2.27: Mean value of the transmission coefficient $\langle T_n^\sigma \rangle$ for the respective spin component σ as a function of the conductance for Ni (4.2 K, [001] direction, 50 contacts). The error bars indicate the standard deviation $\tilde{\sigma}$.

the conductance, the minority-spin component exhibits more transmission channels than the majority-spin component (see Fig. 2.27). This further illustrates our previous argument, where we explained that the majority-spin component possesses an Ag-like character, while the minority-spin component behaves more Pt-like. Note also that the first channel for the majority-spin component opens up remarkably slowly compared with Ag or Au (see Figs. 2.7 and 2.15).

Now we want to address the question of how the spin polarization of the current is influenced by configurational changes. For this purpose, we show in Fig. 2.28 the spin polarization P as a function of the conductance for all the 50 simulated breaking events.[16] As already observed in the simulation of a single breaking event (see Fig. 2.24), the spin polarization of all the contacts starts at a value of -40%, when the contact is close to its starting configuration. As explained above, this value for the spin polarization of the current coincides rather well with the polarization of the bulk DOS at the Fermi energy (see Fig. E.3). As the contact is stretched, also the diversity of geometrical configurations increases and the spin polarization values are widely spread, ranging from around -60 to 20%. There is a tendency towards negative spin polarizations, as can be observed in the inset of Fig. 2.28. The average spin polarization varies between -30 and -10% for conductances above $0.6G_0$. As described in the previous subsection, these variations arise from the high sensitivity of the minority-spin conductance to atomic positions, as compared to the less sensitive majority-spin conductance. The trend towards negative P values can be explained by the higher number of states present at the Fermi energy for the minority-spin component as opposed to the majority-spin component.

In the region of conductances below $0.6G_0$ the number of points is comparatively lower, which explains the partly bigger error bars. Nevertheless, the number of realizations is still

---

[16] Note that bins (where a bin-width of $0.04G_0$ has been used) containing only a single data point are discarded in the inset of Fig. 2.28. The reason is that the calculation of the standard deviation $\tilde{\sigma}$ requires at least two data points.

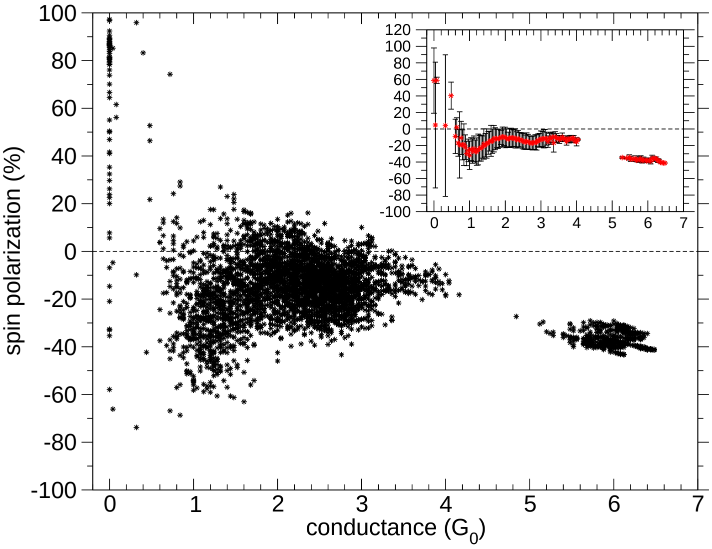

Figure 2.28: Spin polarization of the current P as a function of the conductance. All the data points for the spin polarization are plotted in the graph, while in the inset their arithmetic mean and the corresponding standard deviation $\tilde{\sigma}$ are displayed.

enough to see the spreading of P values over an even wider interval than in the contact regime, together with an average tendency towards positive values. We attribute this trend of reversed spin polarizations to the faster radial decay of the hoppings between the d orbitals that dominate the minority-spin contribution to the conductance, as compared with the s orbitals that dominate the majority-spin contribution. The faster decay with distance overcomes in the tunneling regime the effect of the higher DOS of the d states versus the s states.

2.8 Mechanical properties of metallic atomic contacts

Experimentally it is possible to measure simultaneously the conductance and the strain force during the breaking of nanowires [40]. Special attention has been devoted to the force in the very last stage of the stretching process [70]. For this reason, we present in this section a detailed analysis of this breaking force for the different metals discussed above. In addition, the exotic atomic chain structures will be investigated further.

Using the 50 contacts that we have simulated for the different metals, we construct histograms of the breaking force in the following way: We consider the last 30 recorded atomic configurations before the point of rupture of the contact. Out of them the 20 highest values of the strain force are assembled in a force histogram, combining the data from all 50 contacts.[17] The breaking force histograms obtained for the different metals are shown

---

[17] The choice of the 20 highest force values out of the last 30 recorded geometries before the point of rupture for each of the 50 simulated contacts can be justified as follows: To obtain enough statistics on the breaking force, and because of the evident fluctuations in the strain force (see Fig 2.4, for example) several geometries before breaking of a wire need to be considered in the breaking force histogram. This is why we take into account 30 recorded geometries before the point of rupture. However, the very tiny strain forces directly before and at the point of rupture (which is signaled by a negligible MCS radius of less than 0.3 Å) will produce artificial peaks at small force values. For this reason we select the 20 highest

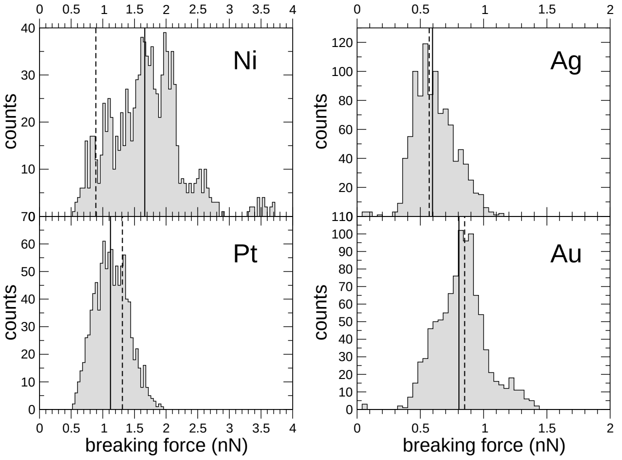

Figure 2.29: Histogram of the force needed to break atomic contacts of the metals Ag, Au, Pt, and Ni. For every contact the highest 20 force values of the last 30 recorded geometries before the point of rupture are gathered. The force data for 50 contacts of the respective metal are assembled in the respective histograms. Solid lines indicate the average breaking force as calculated from the respective histogram, while dashed lines correspond to the bulk breaking forces (see Table 2.1).

in Fig. 2.29. For all elements, except for Ni, a clear maximum is visible in the center of a broad distribution of force values. We will address later, why Ni forms an exception in our simulations.

It is elucidating to compare the values of the breaking force obtained in the simulations with the corresponding forces in bulk. For this purpose, we use the "universal" binding energy function, suggested in Ref. [124], to get a rough estimate for the breaking force expected for a bulk bond (see Sec. E.4 in the Appendix for details).

Values for the breaking forces are put together in Table 2.1.The expression for the breaking force in Eq. (E.24) needs to be considered as a rough estimate of the force necessary to break a bulklike bond. Concerning a comparison of this bulk estimate and the EMT results, it should be recalled that the EMT employed in the MD simulations considers by construction the experimentally verified increase of atomic bonding energies for low coordination [67]. Breaking forces for low-coordinated chains have been shown to be two to three times larger than bulklike bonds and bond breaking may take place at distances well before the inflection point of the bulk estimate [71] (see also Appendix E.4). Another difference is that the forces listed under "bulk" are estimates for breaking force of a single bond. This is not necessarily the case for the result called "EMT" (effective-medium theory). The EMT results are based on the stretching of the nanocontacts in our MD simulations. If the contact breaks while more than one atom resides in the MCS, several atomic bonds might be contributing to the breaking force of the contacts. This implies that the resulting force could be higher than the breaking force for a single bond.

For elements with a large peak in the MCS histogram at single-atom radii, like for the elements Au and Pt, which form chains, usually the contacts break after the formation of a dimer or atomic chain. As a consequence, for Ag, Au, and Pt single atomic bonds are probed in the EMT results. For all these elements, the force estimated from bulk

---

strain forces from the set of the 30 strain force values. (We have checked that our results are not altered qualitatively, when we select the 25 highest or only the 15 highest strain force values.) This is done for each of the 50 simulated contacts, and the data is assembled in the histogram of the breaking force.

metal	Ag	Au	Pt	Ni
EMT	0.60 ± 0.16	0.81 ± 0.20	1.12 ± 0.27	1.66 ± 0.55
bulk	0.57	0.85	1.31	0.89

Table 2.1: Breaking forces in nN for the metals Ag, Au, Pt, and Ni. The values in the column labeled "EMT" (effective-medium theory) are the average breaking force together with its standard deviation $\tilde{\sigma}$ as obtained from the force histograms in Fig. 2.29, and "bulk" refers to the force necessary to break a bulklike bond according to Eq. (E.24).

considerations agrees surprisingly well with the EMT results. For Ni, however, there is a discrepancy between the breaking force determined with EMT and the bulk prediction. We attribute this to the fact that its MCS histogram does not display a pronounced peak for dimer structures (see Fig. 2.26), indicating that Ni dimers are less stable than dimers of the other investigated metals (Ag, Au, and Pt). On account of this the breaking force typically contains contributions from more than a single atomic bond, and is therefore higher than the force of the bulk estimate. The contributions of several bonds also explain the broad distribution without a clear maximum for Ni in Fig. 2.29.

The absolute values of our breaking forces in Table 2.1 need not be quantitative, as the investigations of Rubio-Bollinger *et al.* [70] show. While our EMT-breaking force for Au coincides well with their value of "around 1 nN", they found that DFT calculations are in better agreement with the experimentally measured breaking force of 1.5 nN.

Coinciding with the DFT-simulations by Bahn *et al.* [71] the ordering of breaking force strengths for the different metals as predicted by the bulk estimate is $F_{\text{Ag}} < F_{\text{Au}} < F_{\text{Ni}} < F_{\text{Pt}}$, where F_x is the breaking force for the material x. The EMT results modify this ordering slightly by interchanging Pt and Ni.

Before we conclude, we want to investigate the appearance and structural properties of the peculiar atomic chain structures in more detail. The general mechanism behind the chain formation during a stretching process is an increase in bond strength between low-coordinated atoms [125, 71, 70, 35]. Independent of the metal under investigation, we observed that contacts, in which an atomic chain has formed, always break because of a bond rupture at the chain ends. The higher bond strength for low-coordinated atoms explains this phenomenon. Namely, the terminal atoms in the chain are connected with the thicker part of the contact, and possess a higher coordination number than the other chain atoms. As a consequence the bonds at the chain ends are weaker than the bonds in the interior of the chain [71].

We want to illustrate the mechanical properties of an atomic chain considering as example the Pt contact of Fig. 2.18. In Fig. 2.30 we plot the atomic displacements for this Pt contact projected onto the stretching direction (z axis) in the final elastic stage for elongations of $L_i = 1.37$ nm and $L_f = 1.49$ nm. The z-projected displacement is defined as $d_{z,j} = R_{z,j}(L_f) - R_{z,j}(L_i)$, where $R_{z,j}$ is the z-component of atom j, and L_f (L_i) is the final (initial) elongation. (Additionally we add an offset to $d_{z,j}$, such that the fourth layer in the lower electrode has zero displacement.) Due to the low coordination of the chain

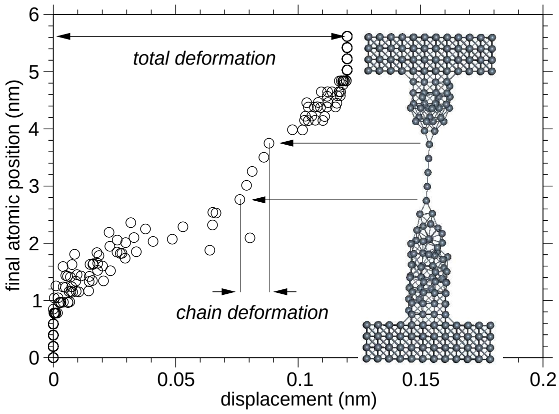

Figure 2.30: The atomic displacements for the Pt contact of Fig. 2.18 are shown in the last elastic stage before rupture (change in coordinates between initial and final elongations of $L_i = 1.37$ nm and $L_f = 1.49$ nm). On the abscissa the displacement of each atom is plotted, while on the ordinate the positions of the atoms can be seen at the end of the elastic stage (elongation L_f). To the right the final configuration is displayed. The atomic displacements and positions have both been projected onto the stretching direction (z axis).

atoms and the associated higher bond strength as compared to interatomic bonds of the other atoms in the central part of the nanowire, the chain is expected to be particularly stable. For this reason the chain atoms should stay close to each other in a displacement plot during an elastic stage of stretching. Instead, most of the displacement should take place in the regions of more highly coordinated atoms in the central part of the nanowire. Exactly this is visible in Fig. 2.30. Note that a similar analysis has been performed by Rubio-Bollinger *et al.* [70] for a Au chain.

Finally, we want to comment on experimental results of Ref. [104]. There, Smit *et al.* compare the tendency of formation of atomic chains for the neighboring $4d$ and $5d$ elements, namely, Rh, Pd, and Ag compared to Ir, Pt, and Au. They find a higher occurrence of chains for the $5d$ elements as compared to $4d$ elements, and explain this by a competition between s and d bonding. From their data we extract an enhancement factor of chain formation of 3.28 for Au compared to Ag.[18] Taking the ratio between the content of the first MCS peak in the histograms, which corresponds to dimers and atomic chains, for Ag and Au normalized by the complete area of the MCS histograms (see Figs. 2.14 and 2.6), we obtain a value of 3.09, in good agreement with their experiments. Bahn *et al.* [71] pointed out that the chain formation depends sensitively on the initial atomic configuration. In general we believe that chain formation in our thin geometries might be enhanced compared to experimental conditions. Nevertheless the chain enhancement factor, as it is a relative measure, might be robust.

---

[18] In Fig. 4 of Ref. [104] a fraction of long plateaus is given for Au and Ag respectively. Taking the ratio between the $P_{1.5}$-values for Au and Ag, an enhancement of chains by a factor of $P_{1.5}(\mathrm{Au})/P_{1.5}(\mathrm{Ag}) \approx 0.59/0.18 = 3.28$ is found for Au compared to Ag.

2.9 Conclusions

In summary, we have analyzed the mechanical and electrical properties of Au, Ag, Pt, and Ni nanojunctions. Using a combination of classical MD simulations and transport calculations based on a TB model supplemented with a local charge neutrality condition, we have studied the origin of the experimentally observed characteristic features in the conductance histograms of these metals. The ensemble of our results indicates that the peak structure of the low-temperature conductance histograms originates from an artful interplay between the mechanical properties and the electronic structure of the atomic-sized contacts.

In the case of Au and Ag wires, we observe a first peak in the conductance histogram at $1G_0$, resulting from single-atom contacts and dimers in good agreement with experiments [20]. For Au also long atomic chains contribute strongly to this first peak. In the last stages of the stretching process the transport is dominated by a single conduction channel, which arises mainly from the contribution of the $5s$ orbitals for Ag and the $6s$ orbitals for Au. Regarding the Au contacts our transmission channel analysis is in good agreement with experimental observations. The simulations indicate a small contribution of the second channel to the total conductance in single-atom contacts, i.e., if only a single atom is coupled to the electrodes. This finding can explain the number of channels of the experimental opening curve. Concerning contact geometries for Ag we find practically no formation of monoatomic chains, as opposed to Au. To be precise, for Ag the chain formation is found to be suppressed by a factor of 3 compared to Au, which is again consistent with the experimental observations [104].

In the case of Pt contacts, the first peak in the conductance histogram is mainly due to single-atom contacts and long atomic chains. However, it also contains some contributions from contacts with larger MCS radii. The peak is rather broad and centered around $1.15G_0$, which is somewhat below the experimental value of $1.5G_0$ [20, 103]. The differences in width and value of this conductance peak, as compared with Au and Ag, can be attributed to the key contribution of the $5d$ orbitals to the transport. First, the d orbitals provide additional conduction channels, and commonly there are three open transmission channels in the final stages of the Pt contacts. Second, these additional channels naturally give rise to higher conductance values. Third, caused by their spatial anisotropy the d orbitals are very sensitive to changes in the contact geometry, which results in a large width of the histogram features.

With respect to Al the statistical analysis of the contacts was hindered due to shortcomings in the employed EMT potential. However, for a sensible example a region of three transmitting channels is observed shortly before contact rupture, and the conductance of the dimer configuration is close to $1G_0$, which agrees nicely with experimental observations [19]. These three channels originate from the contribution of the partly occupied sp-hybridized valence electrons of Al to the transport. In addition, our results reproduce the peculiar positive slopes of the last plateaus of the stretching curves [109, 19, 37, 63].

In the case of ferromagnetic Ni, we have shown that the contacts behave, roughly speaking, as a mixture of a noble metal (such as Ag) and a transition metal (such as Pt).

While the $4s$ orbitals play the main role for the transport of the majority-spin electrons, the conduction of the minority-spin electrons is controlled by the partially occupied $3d$ orbitals. This follows from the position of the Fermi energy. While the minority spins are dominated by d states the contribution of s states is enhanced for the majority spins. In the conductance histogram we obtain a shoulder at $1.3G_0$, whose large width can again be attributed to the extreme sensitivity of the d orbitals to atomic configurations. On the other hand, we find that the spin polarization of the current in the Ni contacts is generally negative, increasing and fluctuating as the contacts narrow down and become disordered. In particular, large positive values are possible in the tunneling regime, right after the rupture of the wires. Once more, this behavior can be traced back to the fact that the d orbitals play a key role in the conductance of the minority-spin component.

The mechanical properties of our nanocontacts have been analyzed in detail with respect to breaking forces and the peculiar atomic chains. Concerning the breaking forces a simple estimate for the maximal force per bulk bond matches well the simulation results for Ag, Au and Pt. However, Ni shows deviations from the bulk estimate and an extraordinarily broad distribution of breaking force values, which we attribute to the generally larger thickness of the contacts at the breaking point, meaning that the breaking force contains contributions of several atomic bonds. Contacts with an atomic chain configuration were observed to always tear apart due to a bond rupture at the chain ends in agreement with previous simulations [125]. Pt atomic chains were illustrated to exhibit an enhanced stability as compared to the remaining atoms in thicker parts of the nanowire. In our simulations the most typical geometry in the last stages of the breaking are dimer configurations where two Au atoms are facing each other.

Another important observation is that, although we obtain for every metal a sequence of peaks in the minimum cross-section histogram, these peaks are smeared out in the conductance histograms. This indicates that not only the narrowest part of the constriction determines the conductance, but also the atomic configuration close to the narrowest part plays a role. This finding challenges the direct translation of peak positions in the conductance histogram into contact radii via the Sharvin formula. However, we should also point out the limitations of our modeling, in particular the small number of atoms present in the junctions. Classical molecular dynamics simulations might better describe atomic shell effects in thick junctions than electronic shell effects necessary for a reliable description of thin wires [126]. For this reason simulations of contacts with thick cross-sections are highly desirable. Moreover, let us remind that we have focused our analysis on low temperatures (4.2 K), where the atoms do not have enough kinetic energy to explore the low-energy configurations. Both the small number of atoms and the low temperature may cause an enhanced atomic disorder of the contacts in the stretching process.

The effects of higher temperatures, different crystallographic orientations of the contacts, a finite stiffness of the electrodes [59, 61] instead of the investigated infinitely rigid leads, or other protocols of the stretching process with different annealing, heating and relaxation times have not been addressed in our studies. A first-principles description of thick contacts, in which both the mechanics and the electronic structure of the contacts are treated at a higher level of accuracy and on an equal footing, should be a major goal for the theory in the future. Experiments in which, simultaneously to the recording of a conductance histogram, also the contact geometries are observed, could help to validate the correlation between conductance peaks and stable wire radii.

2.10 Surface versus bulk electrode Green's functions

The results in the previous Secs. 2.4–2.7 have been obtained with bulk electrode Green's functions (see Sec. 2.2). One may justify their use by arguing that the electrodes are just reservoirs, whose precise structure is not known, due to atomic disorder, for example. For this reason it is possible to describe them on a convenient level of sophistication and can improve their description if needed [127, 128]. Bulk Green's functions may constitute a reasonable approximation and the important characteristics of the system under investigation should be determined by the central part of the contact, which needs to be described properly. However, surface Green's functions are a more proper way of constructing the electrode Green's functions g_{XX} in the self-energies Σ_X (see Eq. (2.5)), because electrodes consitute a semi-infinite system as compared to the infinite crystal assumed in the construction of bulk Green's functions (see Chap. D for details on the construction of bulk and surface Green's functions). In addition to this the current is a nonlocal property and therefore the conductance will depend on the electrode description. For these reasons we wanted to overcome the approximation of bulk Green's functions and investigate the changes occurring, when we replace them by surface Green's functions. The results will be presented below. It should be mentioned that the major part of these results has been obtained after the publication of Ref. [36]. The numerical effort arising, when the electrode Green's functions are modeled as surface Green's functions, is even more demanding than when bulk Green's functions are being used.[19]

To anticipate the result of this section, it turns out that the conductance values are changed primarily for thick cross-section wires. These changes are, however, not relevant for the conductance histogram, as the results for thick wires are dominated by the chosen starting configuration (ideal fcc contact). Only for Ni there seems to be a systematic underestimation of the conductance of the majority spin component when bulk Green's functions are used to model the electrodes. This causes an increase of the spin polarization P to more positive values, while the shape of the spin polarization as a function of the total conductance remains rather unchanged. Nevertheless, apart from the systematic deviations detected for the spin polarization, all our conclusions remain unchanged.

We will concentrate on the materials Ag, Pt, and Ni. For each of these metals we will show a comparison of the results as obtained with surface and bulk electrode Green's functions. More concrete, we will compare (a) the evolution of the conductance for a stretching process and (b) the corresponding conductance histograms. With respect to Ni we will show in addition the changes in the spin polarization of the current as a function of the total conductance.

In Fig. 2.31 the breaking curve for the contact from Fig. 2.4 can be seen in the left panel, while in the right panel the conductance histogram is displayed as obtained for sur-

---

[19] The computation of surface Green's functions took so much time in the determination of a charge neutral Hamiltonian that it turned out to be necessary to compute all the surface Green's functions once, store them, and just read them at need. This procedure requires 15 GB hard disk space for unformatted Fortran data files per spin component. For Ni this resulted in a total of 30 GB of disk space per stretched contact.

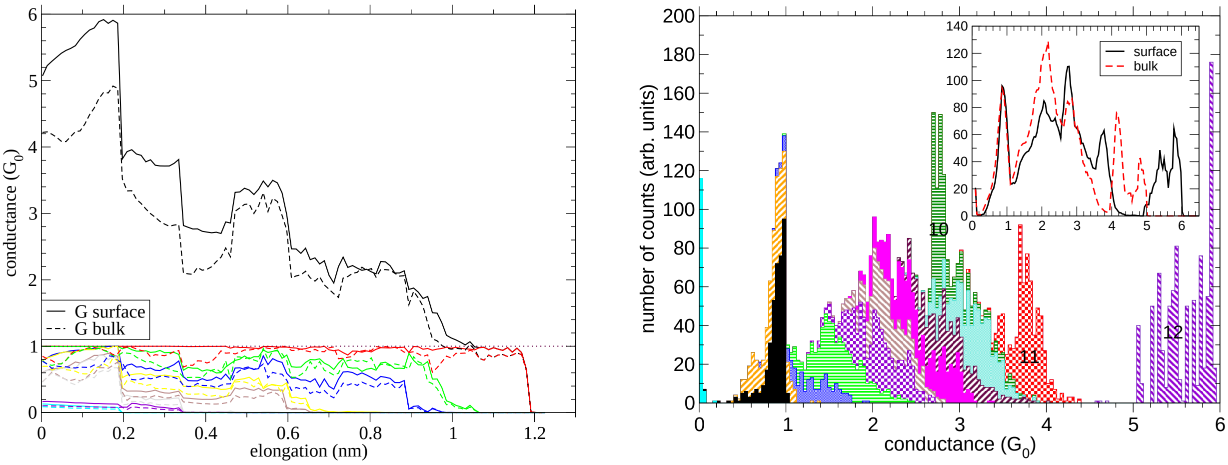

Figure 2.31: Comparison of results for surface and bulk electrode Green's functions in the case of Ag. To the left a comparison of the conductance curves for the contact of Fig. 2.4 is shown. To the right the conductance histogram of Ag, corresponding to Fig. 2.6, is depicted for surface electrode Green's functions. In the inset a direct comparison of the conductance histograms, as obtained for surface and bulk electrode Green's functions, is displayed in a smoothed version by averaging over six nearest-neighbor points.

face electrode Green's functions. The comparison of the breaking curves shows that the deviations of the conductance are biggest at small elongations, i.e., when the wire is close to its starting configuration, and the contact has a large cross-section. In general the conductance, as obtained with surface electrode Green's functions, exhibits a tendency towards a higher value. We explain this tendency by a reduced interface resistance between the central system and the electrode. Nevertheless the shape of the total conductance exhibits the same features, as for example the drops at around 0.2 and 0.34 nm. When comparing the conductance histograms (see the inset of Fig. 2.31), one observes that deviations mainly arise for high conductances, while the peak at $1G_0$ remains unchanged. The conductance histogram seems to be "stretched" to higher conductance values. This shows again that mainly thick MCS wires are affected by the choice of the electrode Green's functions.

Focussing on the peak belonging to the MCS region 10 in the conductance histogram, it is visible that this peak shifts towards conductance values of around $2.7G_0$, while it was located at around $2.2G_0$ previously (see Fig. 2.6). As argued before (see the discussion of Fig. 2.6), the peak position is due to such break-ins as visible for elongations between 0.34 and 0.47 nm in the left panel of Fig. 2.31. This argument can be confirmed by noticing that for the surface Green's functions the break-in is centered around a conductance of $2.7G_0$, in agreement with the new peak position in the conductance histogram in Fig. 2.31.

Let us now come to Pt. From Fig. 2.32 it can be inferred that the surface Green's functions have a similar influence on the results for Pt as they had on the results for Ag. Again we observe that the conductance for the surface and the bulk electrode Green's functions during the stretching of the contact only deviates in the beginning, while afterwards the differences between both are small (see the left panel of Fig. 2.32). Also the

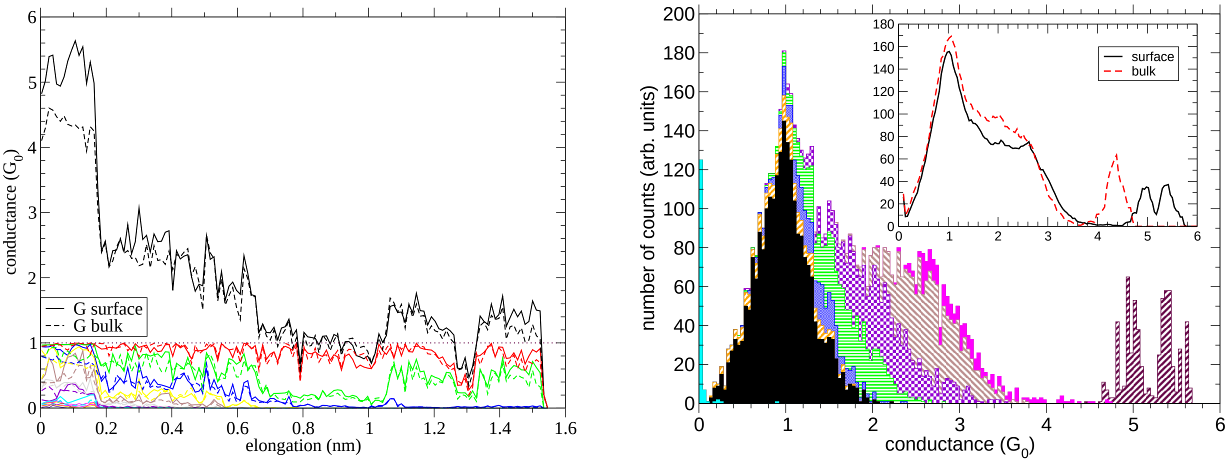

Figure 2.32: Comparison of results for surface and bulk electrode Green's functions in the case of Pt. To the left a comparison of the conductance curves for the contact of Fig. 2.18 is shown. To the right the conductance histogram of Pt, corresponding to Fig. 2.20, is depicted for surface electrode Green's functions. In the inset a direct comparison of the conductance histograms, as obtained for surface and bulk electrode Green's functions, is displayed in a smoothed version by averaging over six nearest-neighbor points.

trend towards higher conductance values is visible for the results obtained from the surface electrode Green's functions. As for Ag, the conductance histograms differ mainly for high conductance values (see the right panel of Fig. 2.32).

Concerning Ni, there seems to be a systematic increase of the conductance for the majority spins, while the minority-spin component shows only slight initial deviations between the bulk and surface electrode Green's function results (see Fig. 2.33). This increase of the conductance for the majority-spin component is in agreement with the observations made above for Ag and Pt, where a trend towards more positive total conductances was observed. As a result of the increase of the conductance for the majority-spin component and a mainly unchanged conductance of the minority-spin component, the spin polarization increases as well (see the inset in the right panel of Fig. 2.33). Now it is on average positive, as soon as the contact evolves in a characteristic fashion (elongations above 2.5 nm). The jump to a largely positive spin polarization in the tunneling regime, however, persists. In the conductance histogram the trend towards higher conductance values is evident again (see the left panel in Fig. 2.34). The conductance histogram for the surface Green's function with its first peak ranging from $1.2G_0$ to $1.8G_0$ possesses a striking similarity to the experimental histogram (see Fig. 2.2) [20, 118]. However, this similarity might be deceiving due to possible shortcomings in the employed EMT potential. As explained above (see the discussion of Fig. 2.26), the strong contribution of the high MCS regions as compared to single-atom contacts and dimer configurations seems to be in contradiction to the common wisdom that the first peak in the conductance histogram is due to single-atom contacts, dimers, and – depending on the investigated material – chain configurations. Looking at the spin polarization (see the left panel in Fig. 2.34), there is a systematic deviation from

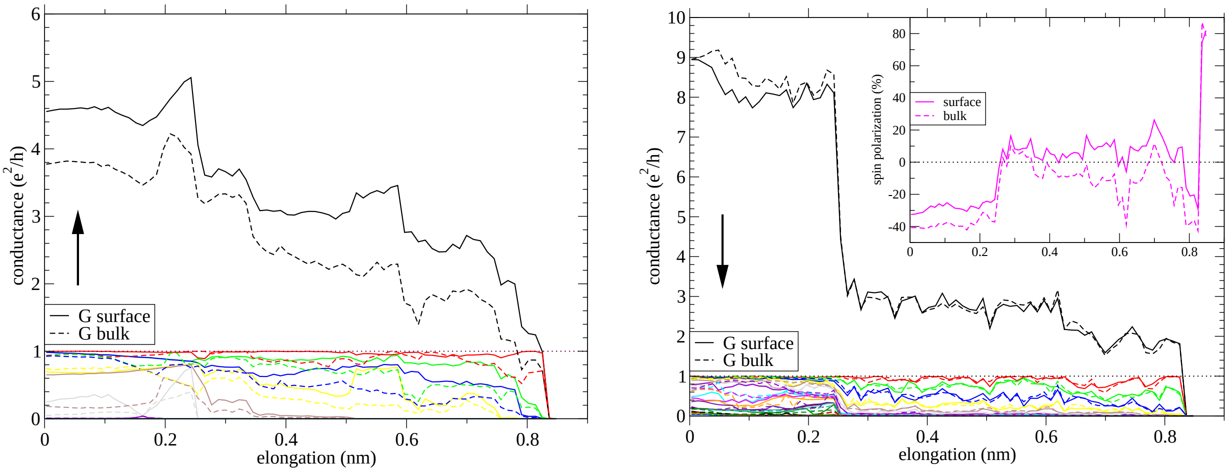

Figure 2.33: Comparison of results for surface and bulk electrode Green's functions in the case of Ni for the contact of Fig. 2.24. The different spin components σ are displayed in the left ($\sigma =\uparrow$) and the right ($\sigma =\downarrow$) panel. In the inset of the right panel a direct comparison of the spin polarization, as obtained for surface and bulk electrode Green's functions, is plotted.

the results of bulk Green's functions. The trend observed in Fig. 2.33 is clearly visible, namely the spin polarization is shifted to higher values by around 10%. The shape of the spin polarization as a function of the total conductance nevertheless stays the same, including the on average positive spin polarization in the tunneling regime.

To summarize, we have seen that the conductance is usually increased, when surface Green's functions are used instead of bulk Green's functions in the electrode description. We attribute this to a reduced interface resistance between the central system and the electrodes. The increase in the conductance affects mainly wires with large cross-sections. The first peaks in the conductance histograms remain unaffected for Ag and Pt. Only for Ni a clearer first broad peak arises. For the Ni contacts we observe a systematic enhancement of the conductance for the majority spins, while the minority spins stay rather unaffected. This causes a roughly constant increase in the spin polarization of the current with a constant shift of around 10% with respect to the results as obtained with bulk electrode Green's functions. Except for this slight modification in the spin polarization of the current for Ni, the use of surface Greens functions does not change the statements made in the Conclusions (see Sec. 2.9).

With regard to future investigations, especially with respect to investigations of wires with more atoms and bigger cross-sections (as proposed in the Conclusions (see Sec. 2.9)), the results of this paragraph recommend the use of surface Green's functions in the electrode description of quantum transport.

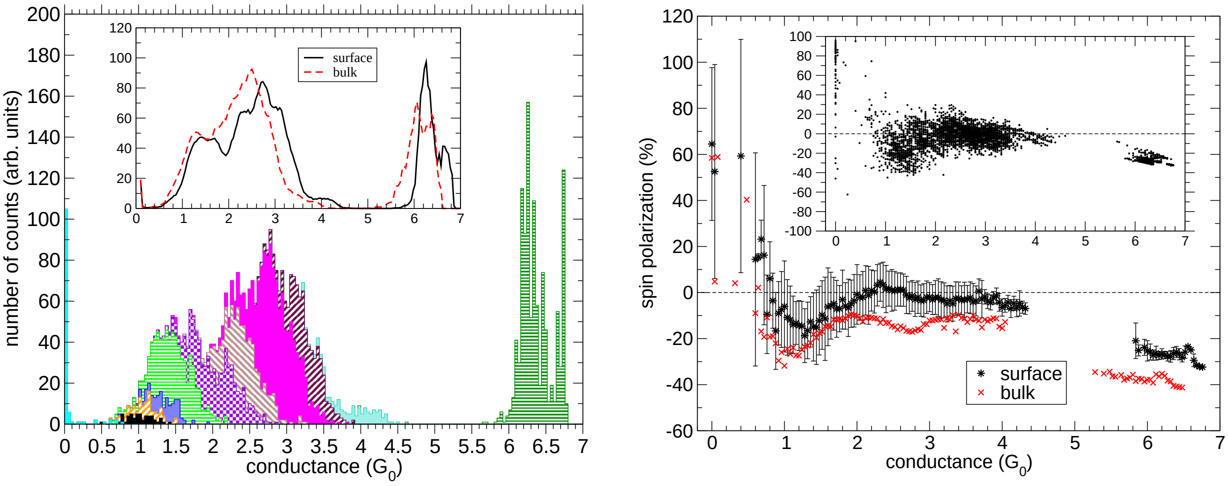

Figure 2.34: Comparison of results for surface and bulk electrode Green's functions in the case of Ni. To the left the conductance histogram of Ni, corresponding to Fig. 2.26, is shown for surface Green's functions. In the inset a direct comparison of the conductance histograms, as obtained for surface and bulk electrode Green's functions, is displayed in a smoothed version by averaging over six nearest-neighbor points. In the right panel, the spin polarization of the current as a function of the conductance is shown. All the data points of the spin polarization for surface electrode Green's functions can be found in the inset, while the main figure contains a direct comparison between the average value of the spin polarizations for bulk and surface electrode Green's functions. Error bars correspond to the standard deviation $\tilde{\sigma}$ introduced before (see Sec. 2.3).

Chapter 3

Electron-vibration interaction in transport through atomic gold wires

In this chapter we will shortly discuss the effects of electron-vibration coupling on the conductance of atomic gold wires. This work, as published in Ref. [129], has mainly been carried out by J. K. Viljas, and we will only shortly state the main results without going into the details. The interested reader is referred to the appendices of the aforementioned reference.

From the theoretical side the consideration of the influence of electron-vibration coupling on charge transport is an extension to the standard Landauer theory (see discussion of Eq. (C.6) in Chap. C). In addition to the elastic current, inelastic corrections due to vibrations need to be taken into account. From the experimental side there exist mainly two methods to detect signatures of inelastic effects on the electric current. The first is the point contact spectroscopy (PCS) and the second is the inelastic electron tunneling spectroscopy (IETS) [103]. Both methods are in principle very similar. In the PCS the differential conductance $G(V) = dI/dV$ is measured as a function of the dc bias voltage. The electrons in the contact are accelerated to an excess energy of eV. When this energy reaches that of the main phonon modes of the metal, inelastic scattering results in an enhanced probability for the electrons to scatter back through the contact, which is seen as a drop in $G(V)$. Opposed to this decrease of the current for PCS, an increase is observed in IETS.

Using PCS Agraït *et al.* [13] observed the onset of dissipation in atomic gold wires. Later Smit *et al.* [103] showed that PCS may be applied to reveal otherwise unaccessible information on configurations of molecules in atomic point contacts, namely hydrogen in platinum junctions. According to their analysis hydrogen is present in these contacts in molecular form as H_2 and not, as perhaps expected from the catalytic properties of platinum, in a dissociated form.

Both experiments show that important additional information about nanoscale systems may be gained from the signatures of electron-vibration interaction on the electric charge current. A theoretical model for the description of the experiment by Agraït *et al.* [13] is the subject of this chapter.

3.1 Introduction

In recent experiments, the conductance-voltage (I-V) characteristics $G(V)$ of gold wires formed by the STM technique were measured [13]. It was observed that the conductance often has a very pronounced single drop from G_0 at a critical voltage $V_{ph} = 10 - 20$ mV, marking the onset of a dissipative process. The size of the drop was on the order of $0.5\% - 2.0\%$ of G_0. It was also found that stretching of the wire typically leads to an increase in the step, and to a decrease in the critical voltage V_{ph}. Based on simple arguments for infinite single-orbital tight-binding (TB) chains, these findings were interpreted as a sign of the excitation of vibrational modes in the wire: only a single longitudinal mode with twice the Fermi wave vector can be excited, since this corresponds to the momentum which must be transferred from an electron to the vibrations in a single backscattering process. Although the validity of such arguments for a wire of finite length (of typically less than 10 atoms) can be questioned, the interpretation was backed up by first-principles calculations [130, 131]. The authors of Ref. [130] emphasize the importance of so-called alternating bond length (ABL) modes, and in particular the longitudinal mode of highest frequency. We also want to refer to the very recent ab initio study of the same authors in Ref. [132], where beside other systems the inelastic transport in gold wires is studied in more detail.

Below we aim at discussing possible answers to basic physical questions such as: When exactly does the electron-vibration coupling lead to a drop and when to an increase in the conductance? Why does there appear to be just a single drop in the experiments of Ref. [13], although the momentum conservation is not exact? What determines the height and width of this drop?

As mentioned above we concentrate on studying the I-V characteristics of gold wires. We use a Slater-Koster [133] type TB approach, where the parameters are taken from the non-orthogonal parameterization of Papaconstantopoulos and coworkers [134, 75, 135, 77]. The use of such a parameterization [136, 137, 80] makes the modeling of atomic wires computationally less intensive as compared with full *ab-initio* methods. The approach is still microscopic in that it takes into account the symmetries of the atomic s, p, and d valence orbitals, which, via hybridization, form the conduction channels. It is also general enough to allow one to model everything within the same framework: we use the parameters to compute the total energy of the wire, and thus to optimize the geometry. After this, the normal modes of oscillation and the electron-vibration coupling constants can be computed. Finally, we calculate the transport properties using the nonequilibrium Green's function (NEGF) approach. Our implementation is very similar to that of Ref. [80], and the present work is, in essence, an extension of that to inelastic transport. Beside the full *ab-initio* calculations [130, 132], the effect of electron-vibration interactions on transport through molecular wires has recently been studied by some simple single-level models [138, 139, 140]. The TB approach stands somewhere in between these two extremes.

We compute the conductance to lowest nontrivial order in the electron-vibration coupling constant. With our simple, self-contained method of optimizing the geometry, we obtain vibrational frequencies which are of the correct order of magnitude, usually to within a factor of two. We study how the conductance drops due to the electron-vibration cou-

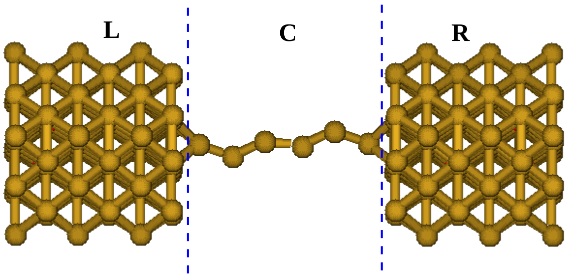

Figure 3.1: Geometry A, without "pyramids". A zigzag wire with $N_{ch} = 6$ atoms is shown.

pling and find a good overall agreement with the experiments of Ref. [13]. As observed in the earlier calculations [130], we find that the highest-frequency longitudinal modes usually couple most strongly, although there seems to be no fundamental reason for a bias toward the "ABL" modes. In contrast to previous theoretical results, the conductance drop is usually found to occur in two or more consecutive steps which are due to several close-lying longitudinal vibrational modes. Thus we find the "mode selectivity" to be only very approximate. However, the steps can be made to merge into a single one, when we introduce a large enough phenomenological broadening to the vibrational modes, such that the experimentally observed step widths of ~ 5 meV are accounted for.

The next sections are structured in the following way. In Sec. 3.2 we start by defining the problem, and discussing the electron-vibration coupling. In Sec. 3.3 we briefly discuss the calculation of the vibrational modes and the electron-vibration coupling constants, as well as our methods of computing the transport. After this, Sec. 3.4 introduces the important wide-band approximation to the full formalism. In Sec. 3.5 the signatures of vibrations in the conductance of atomic gold chains will be described. We end with the conclusions in Sec. 3.6. For most technical details we refer to the appendices of Ref. [129].

3.2 Definition of the problem

To model transport through atomic wires, we consider two idealized geometries, shown in Figs. 3.1 and 3.2. We call these geometry A and geometry B, respectively. Both involve a gold chain of N_{ch} atoms suspended between two gold leads. As the leads, we simply use semi-infinite "bars", where the repeat unit consists of two layers, with 12 and 13 atoms respectively, mimicking an infinite fcc [001] surface, where the z axis is always chosen parallel to the axis of the wire. The particular choice for the leads should not be very important, as long as they are infinite in one direction, and wider than the contact region. In geometry B, the chain connects to small clusters of atoms or "pyramids" on the surfaces (in our case consisting of 9 atoms), making it perhaps the more realistic one of the two. For technical reasons, the geometry is divided into three parts, the semi-infinite left (L) and right (R) leads, and the "central cluster" (C), which also includes the pyramids if any. These parts are indicated in the figures.

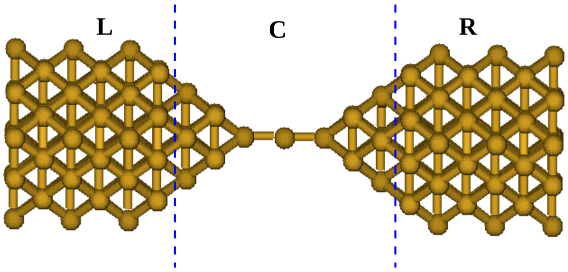

Figure 3.2: Geometry B, with "pyramids" and a linear wire of $N_{ch} = 3$ atoms.

Our objective is to model the effect of vibrations (or "phonons") of the wire on the transport, when a voltage is applied over the contact. Within a TB picture, the system of electrons coupled to vibrational modes is described by the Hamiltonian

$$\hat{H} = \hat{H}_e + \hat{H}_{vib} + \hat{H}_{e-vib},$$

where

$$\begin{aligned}
\hat{H}_e &= \sum_{ij} \hat{d}_i^+ H_{ij} \hat{d}_j \\
\hat{H}_{vib} &= \sum_{\alpha} \hbar\omega_\alpha \hat{b}_\alpha^+ \hat{b}_\alpha \qquad (3.1) \\
\hat{H}_{e-vib} &= \sum_{ij} \sum_{\alpha} \hat{d}_i^+ \lambda_{ij}^\alpha \hat{d}_j (\hat{b}_\alpha^+ + \hat{b}_\alpha).
\end{aligned}$$

Here ω_α are the vibrational frequencies, $H_{ij} = \langle i|H|j\rangle$ are the matrix elements of the equilibrium single-electron Hamiltonian H in the atomic-orbital basis $\{|i\rangle\}$, and λ_{ij}^α are the electron-vibration coupling constants. The index i denotes collectively the atomic sites and orbitals, and α runs from 1 to $3N_{vib}$, where N_{vib} is the number of atoms in the system that are allowed to vibrate. The creation and annihilation operators for vibrational modes $\hat{b}_\alpha^+$,$\hat{b}_\alpha$ satisfy the bosonic commutation relation $[\hat{b}_\alpha, \hat{b}_\beta^+] = \delta_{\alpha\beta}$. The electronic basis is in general non-orthogonal, with overlap matrix elements $S_{ij} = \langle i|j\rangle$. Thus the anticommutator for electron operators $\hat{d}_i^+$,$\hat{d}_i$ is given by $\{\hat{d}_i, \hat{d}_j^+\} = (S^{-1})_{ij}$ (see Eq. B.9).

The matrices H, S, and λ^α are all symmetric in our case. In the *spd* TB model, the matrix elements H_{ij} and S_{ij} are obtained directly from the parameterization [77]. These can also be used to calculate the vibrational frequencies ω_α and the coupling constants λ^α, as we shall now describe.

3.3 Methods

The solution of the inelastic transport problem involves a few rather separate sub-problems: the optimization of the geometry and evaluation of the vibrational modes, estimation of the electron-vibration coupling constants, and finally the calculation of the transport. The technical details have been worked out in Ref. [129]. We will only give a brief description of each of these steps as far as needed to understand the final results. Our basic approach is to solve for the elastic transmission problem exactly, and then to take the electron-vibration coupling into account in a slightly modified version of lowest-order perturbation theory. Other works have considered the so-called self-consistent Born approximation [130, 140], where some of the terms in the perturbation expansions are effectively summed to infinite order. However, this is not essential for describing the basic physics which is involved in the present problem.

3.3.1 Vibrational modes and the electron-vibration coupling constants

The calculation of the vibrational modes requires knowledge of the total (ground-state) energy of the system as a function $E(\vec{R}_k)$ of the ionic coordinates $\vec{R}_k$ with $k = 1, \ldots, N_{vib}$. This energy must be minimized to find the equilibrium configuration $\vec{R}_k^{(0)}$. Now consider small displacements $\vec{Q}_k = \vec{R}_k - \vec{R}_k^{(0)}$ around the equilibrium. The Hamiltonian describing the oscillations of the ions around $\vec{R}_k^{(0)}$ is given by

$$H_{ion} = \frac{1}{2}\sum_{k\mu} M_k \dot{Q}_{k\mu}^2 + \frac{1}{2}\sum_{k\mu,l\nu} \mathcal{H}_{k\mu,l\nu} Q_{k\mu} Q_{l\nu},$$

where M_k are the ionic masses, $\mu, \nu = x, y, z$ denote cartesian components of vectors and $\mathcal{H}$ is the Hessian matrix ($\mathcal{H}_{k\mu,l\nu} = \partial^2 E/\partial R_{k\mu}\partial R_{l\nu}$). This can be diagonalized by the transformation $Q_{k\mu} = \sum_{\alpha=1}^{3N_{vib}} A_{k\mu,\alpha} q_\alpha$, where q_α are the normal coordinates. Thus, we obtain $H_{ion} = \frac{1}{2}\sum_\alpha (\dot{q}_\alpha^2 + \omega_\alpha^2 q_\alpha^2)$, where ω_α ($\alpha = 1, \ldots, 3N_{vib}$) are the vibrational frequencies. The transformation matrix A is normalized according to $A^T M A = 1$, M being the mass matrix. In our case M is simply a scalar giving the mass of a gold atom. Upon using the canonical quantization prescription $q_\alpha = (\hbar/2\omega_\alpha)^{1/2}\,(b_\alpha^+ + b_\alpha)$, $\dot{q}_\alpha = i\,(\hbar\omega_\alpha/2)^{1/2}\,(b_\alpha^+ - b_\alpha)$, one finally obtains $\hat{H}_{vib}$ in Eq. (3.1).

The electron-vibration interaction may be derived as follows [141, 142]. Assume that the electronic single-particle Hamiltonian H is a function of the ionic coordinates, denoted collectively as $\vec{R}$. Then we may expand $H(\vec{R}^{(0)} + \vec{Q}) \approx H(\vec{R}^{(0)}) + \sum_k \vec{Q}_k \cdot \vec{\nabla}_k H|_{\vec{Q}=0}$. Defining $\hat{H}'_e = \sum_{ij} \hat{d}_i^+ \langle i|H(\vec{R}^{(0)} + \vec{Q})|j\rangle \hat{d}_j$, inserting the expansion, and using the canonical quantization for q_α again, one finds $\hat{H}'_e = \hat{H}_e + \hat{H}_{e-vib}$ [cf. Eq. (3.1)], where $H \equiv H(\vec{R}^{(0)})$, and the electron-vibration coupling constants are given by

$$\lambda_{ij}^\alpha = \lambda_0 \left(\frac{\hbar}{2\omega_\alpha}\right)^{1/2} \sum_{k\mu} M_{ij}^{k\mu} A_{k\mu,\alpha}, \tag{3.2}$$

where $M_{ij}^{k\mu} = \langle i|\nabla_{k\mu} H|_{\vec{Q}=0}|j\rangle$. In Eq. (3.2) we have added a dimensionless factor λ_0 to describe the strength of the coupling — in the physical case $\lambda_0 = 1$.

3.3.2 Propagator formalism

The use of a local basis allows one to partition the electronic Hamiltonian and the overlap matrices into parts according to the division in L, C and R regions:

$$H = \begin{pmatrix} H_{LL} & H_{LC} & H_{LR} \\ H_{CL} & H_{CC} & H_{CR} \\ H_{RL} & H_{RC} & H_{RR} \end{pmatrix}, \; S = \begin{pmatrix} S_{LL} & S_{LC} & S_{LR} \\ S_{CL} & S_{CC} & S_{CR} \\ S_{RL} & S_{RC} & S_{RR} \end{pmatrix}.$$

Although the dimension of the problem is infinite, its single-particle nature allows for very effective methods of solution, as long as we may assume that $Y_{RL} = Y_{LR}^T = 0$ ($Y = H$ or S), which we shall do. We shall use the NEGF method. In this method, one can restrict the problem to the C part only by introducing energy-dependent lead self-energies which take into account the presence of the semi-infinite L and R leads in an exact way (see the formalism presented in Sec. C.4).

The quantity from which all elastic transport properties may be extracted, is the retarded Green's function of the C part in the absence of electron-vibration coupling. We call it $\tilde{G}^r$, and it may be written as $\tilde{G}^r(E) = (E^+ S_{CC} - H_{CC} - \Sigma_L^r - \Sigma_R^r)^{-1}$. The lead self-energy Σ_L^r is given by $\Sigma_L^r = t_{CL} g_{LL}^r t_{LC}$, and $\Gamma_L = i\,(\Sigma_L^r - \Sigma_L^a)$, where we define $t_{CL} = H_{CL} - ES_{CL}$. The matrix $g_{LL}^r(E) = ((E + i\gamma_L/2)\, S_{LL} - H_{LL})^{-1}$ is the lead (surface) Green's function, where $\gamma_L = 0^+$. Similar equations hold for Σ_R^r. The lead Green's functions g_{LL}^r and g_{RR}^r are "surface" Green's functions for the semi-infinite leads. The electron-vibration interaction gives rise to further self-energies, as will be discussed below.

The vibrational modes should in principle be treated in an analogous way, by introducing lead self-energies for their propagators. However, here we restrict the modes strictly to the wire of N_{ch} atoms within the C region (i.e. $N_{vib} = N_{ch}$) and use the corresponding normal-mode basis for them. Thus the number of modes which we have to consider is $3N_{ch}$, and their "lead coupling" is taken into account only in a phenomenological way. For further details on the propagator technique, including the expressions for the phonon propagators and all self-energy diagrams, we refer to Ref. [129].

3.3.3 Calculation of current

The most important physical observable, which we are interested in, is the electric (charge) current through the atomic wire, when a voltage V is applied. We denote $eV = \mu_L - \mu_R$, where $\mu_{L,R}$ are the L and R side electrochemical potentials, and $e > 0$ is the absolute value of electron charge. We also define $f_{L,R}(E) = f(E - \mu_{L,R})$, where $f(E) = 1/[\exp(\beta E) + 1]$ is the Fermi function, and $\beta = 1/k_B T$ is the inverse temperature.

It can be shown that the current flowing through the interface from L to C (C to R) in the stationary state is given by (see Eq. C.4)

$$I^{\Omega} = \pm \frac{2e}{\hbar} \int \frac{dE}{2\pi} \mathrm{Tr}[G_{C\Omega}^{<}(E) t_{\Omega C}(E) - t_{C\Omega}(E) G_{\Omega C}^{<}(E)], \tag{3.3}$$

where $\Omega = L$ (R) is chosen with the upper (lower) sign, and the factor 2 accounts for spin degeneracy. The Green's functions $G^<$ are defined as in Sec. A.3.2. Developing Eq. (3.3) further, it is convenient to split it into two parts: $I^{L,R} = I_{el} + I^{L,R}_{inel}$, where

$$\begin{aligned} I_{el} &= \frac{2e}{\hbar}\int \frac{dE}{2\pi}\mathrm{Tr}[G^r\Gamma_R G^a \Gamma_L](f_L - f_R) \\ I^{L,R}_{inel} &= \mp\frac{2e}{\hbar}i\int \frac{dE}{2\pi}\mathrm{Tr}\{G^a\Gamma_{L,R}G^r[(f_{L,R}-1)\Sigma^<_{e-vib} - f_{L,R}\Sigma^>_{e-vib}]\}. \end{aligned} \tag{3.4}$$

Here we define the full retarded and advanced Green's functions $G^{r,a}$, where $G^r = (E^+S_{CC} - H_{CC} - \Sigma^r_L - \Sigma^r_R - \Sigma^r_{e-vib})^{-1}$ and $G^a = (G^r)^+$. The new self-energies Σ^r_{e-vib} and $\Sigma^{<,>}_{e-vib}$ are due to the electron-vibration interaction. Since they vanish in the absence of λ^α, we call the $I^{L,R}_{inel}$ part an "inelastic" current, while I_{el} is the "elastic" part [140].

If we do lowest-order perturbation theory with respect to λ^α, we may expand $G^r = \tilde{G}^r + \tilde{G}^r\Sigma^r_{e-vib}\tilde{G}^r + \cdots$. In this way the elastic current is split into two parts as $I_{el} = I^0_{el} + \delta I_{el}$, where δI_{el} is an "elastic correction". We find

$$\begin{aligned} I^0_{el} &= \frac{2e}{\hbar}\int \frac{dE}{2\pi}\mathrm{Tr}[\tilde{G}^r\Gamma_R\tilde{G}^a\Gamma_L](f_L - f_R) \\ \delta I_{el} &= \frac{4e}{\hbar}\int \frac{dE}{2\pi}Re\{\mathrm{Tr}[\Gamma_L\tilde{G}^r\Sigma^r_{e-vib}\tilde{G}^r\Gamma_R\tilde{G}^a]\}(f_L - f_R) \\ I^{L,R}_{inel} &= \mp\frac{2e}{\hbar}i\int \frac{dE}{2\pi}\mathrm{Tr}\{\tilde{G}^a\Gamma_{L,R}\tilde{G}^r[(f_{L,R}-1)\Sigma^<_{e-vib} - f_{L,R}\Sigma^>_{e-vib}]\} \end{aligned} \tag{3.5}$$

For these expressions the current conservation $I^L = I^R = I$ can be proven [129].

Besides the charge current, other interesting observables would be the heat current (or power dissipation) [130], the current noise [143], and possibly the spin current in case of magnetic materials. We only consider the charge current here, as it is the only one which can easily be measured. More specifically, we shall be interested in the differential conductance $G(V) = dI/dV$ and its derivative, since these quantities reveal the signatures of the vibrational-mode coupling most clearly.

3.4 Wide-band limit

Even in the case of the perturbative current formulas [Eqs. (3.5)], the expressions will involve double energy integrals which can be very cumbersome to evaluate. However, the existence of different energy scales in the problem allows us to make an important simplification.

The energies of the vibrational modes are on the order of 10 meV, so that we are only interested in the differential conductance for voltages up to $V \approx 40$ mV, at most. Together with the temperature $T \approx 4.2$ K, this determines the width of the energy window around the Fermi energy E_F which is important for transport. However, for the atomic wires which we are considering, the electronic density of states (DOS) tends to vary at much larger energy scales ~ 1 eV around E_F. Thus, to a good approximation, we may neglect this energy dependence, and simply evaluate all the electronic Green's functions at E_F. This approximation is often called the "wide-band limit" (WBL).

In the WBL approximation, the expressions for the current (Eqs. (3.5)) may be simplified considerably, since some of the energy integrals may be done analytically. In order to understand the results in the following, we need to state that in the expressions for the current the vibrational DOS ρ_α appears together with the mode distribution N_α. We approximate ρ_α here by using the imaginary part of d^r_α, the unperturbed phonon propagator. It then acquires the form

$$\rho_\alpha(\epsilon) = \frac{1}{\pi}\frac{\eta/2}{(\epsilon - \hbar\omega_\alpha)^2 + \eta^2/4} - \frac{1}{\pi}\frac{\eta/2}{(\epsilon + \hbar\omega_\alpha)^2 + \eta^2/4}, \tag{3.6}$$

where we take η as a finite phenomenological parameter, describing the effect of coupling the vibrational modes to an external bath. This bath is provided by the leads [140]. However, we are neglecting any renormalizations of the bare frequencies ω_α, so that the main purpose of η here is to broaden the vibrational DOS. As in the expression for ρ_α the bath-coupling parameter η also enters the voltage-dependent mode distribution function

$$N_\alpha(E) = \frac{1}{2}\frac{\mathrm{Im}\Pi^<_\alpha(E) - n(E)\eta E/\hbar\omega_\alpha}{\mathrm{Im}\Pi^r_\alpha(E) - \eta E/2\hbar\omega_\alpha} \tag{3.7}$$

where $n(\epsilon) = 1/[\exp(\beta\epsilon) - 1]$ is the Bose distribution, and $\mathrm{Im}\Pi^<_\alpha$ and $\mathrm{Im}\Pi^r_\alpha$ are imaginary parts of the phonon polarizations (see Ref. [129]).

In the expression for the distribution function, the limit $\eta \to 0^+$ corresponds to the case where the vibrational modes are uncoupled from leads. Supposing that one also wishes to take the phonon polarizations to zero, which is formally accomplished by taking $\lambda_0 \to 0$ (see Eq. (3.2)), one discovers that these two limits do not commute.

If we take first the limit $\eta \to 0$, then the result actually becomes independent of λ_0, since $\Pi^r_\alpha, \Pi^<_\alpha \propto \lambda_0^2$ and the λ_0^2-factors cancel. A physical interpretation can be described as follows. If the vibrational modes are not coupled to any external bath, then even an infinitesimally small coupling constant can eventually lead to a *stationary state* with a strongly nonequilibrium mode occupation. Here emission and absorption of phonons are in balance, and hence there is no net energy transfer between the electrons and the vibrations. Following Ref. [130], we call this the *externally undamped limit.* In this case the voltage-dependence of $N_\alpha(eV)$ shows a sharp kink at $V = \hbar\omega_\alpha/e$, and a subsequent linear increase [130].

In the opposite case, where $\lambda_0 \to 0$ first, the expression becomes independent of η, and we recover the Bose distribution $n(E)$. This corresponds to the limit where the vibrational modes are strongly damped by coupling to a heat bath which is in equilibrium. This is the *externally damped limit.* However, for a finite λ^α this limit can only be reached with a large enough finite η. Thus the externally damped limit should also imply a considerable broadening of the vibrational modes.

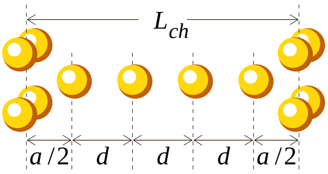

Figure 3.3: Dimensions of the unoptimized geometry with $N_{ch} = 4$. The fcc lattice constant a_0 is $a_0 = 4.08$ Å. Only the coordinates of the N_{ch} chain atoms are optimized.

3.5 Signatures of vibrations in the conductance of atomic gold chains

In this section we describe a TB approach to the problem of electron-vibration coupling in atomic gold wires. We use the nine-orbital *spd* parameterization of Papaconstantopoulos *et al.* [134, 75, 135, 77]. This type of *spd* TB approach is known to reproduce very well some nontrivial *ab-initio* results, like the numbers of conduction channels and the formation of zigzag Au chains [96, 64, 35]. Thus we can be confident that the method gives at least good order-of-magnitude estimates for all of the quantities which we shall be interested in.

However, since the parameters are extracted from first-principles *bulk* calculations, they cannot be exactly correct for atomic point contacts, where the important atoms of the structure are significantly less coordinated than in bulk. It has thus become customary in the method to "correct" the parameters in the central cluster in order to satisfy local charge neutrality as was explained in Sec. 2.2.2. Doing this typically brings the central cluster levels better in resonance with the lead orbitals.[1]

3.5.1 Geometry optimization and vibrational modes

We consider two types of ideal geometries, the "A" and "B" ones, shown in Figs. 3.1 and 3.2, respectively. As mentioned, the leads are assumed to be of fcc type with the [001] axis in the transport (or z) direction. Before geometry optimization, the chain atoms are positioned as described in Fig. 3.3. The "length of the wire" L_{ch} is defined as $L_{ch} = a_0 + d(N_{ch} - 1)$, where N_{ch} is the number of atoms in the chain, d the distance between them, and $a_0 = 4.08$ Åis the equilibrium lattice constant of the bulk fcc lattice. We only optimize the geometry of the N_{ch} chain atoms – also in geometry B which has the "pyramids". Thus, although the interatomic distances change slightly from those of Fig. 3.3, L_{ch} remains fixed.

To estimate the total energy $E(\vec{R}_k)$, we simply take a cluster which includes the wire and some atoms from the leads, solve for the electronic eigenstates ϵ_α, and then occupy the states according to charge neutrality. This energy, as a function of the $3N_{ch}$ wire coordinates, is then optimized with standard library routines. As shown previously [96], it is often energetically favorable for the gold chains to exist in a zigzag-like pattern instead

---

[1] The results of this chapter are generated using finite lead broadenings $\gamma_{L,R} \approx 1.0$ eV. The limit $\gamma_{L,R} \to 0^+$ can in principle be taken without affecting the results in any essential way.

of a linear one. Only after a sufficient amount of stretching (i.e., with a larger d) does the linear configuration become stable, after which it remains linear until the wire breaks. We find that the maximum d at breaking is, depending on the geometry, typically something between 2.70–2.85 Å.

After the geometry is optimized, the energy function is used to compute the Hessian matrix $\mathcal{H}$. The eigenvalues k_α ($\alpha = 1, \ldots, 3N_{ch}$) are all positive, and the vibrational frequencies are simply given by $\omega_\alpha = \sqrt{k_\alpha / M}$. With both geometries, A and B, we obtain quite similar vibrational frequencies and modes. For a linear wire, the modes can be classified as longitudinal or transverse in character. The highest-frequency modes are then always longitudinal ones, and the highest of them is of the ABL type [130].

3.5.2 Elastic transmission

Perhaps the most characteristic experimental property of gold chains is that they appear to have a conductance very close to the quantum of conductance G_0. In the present TB method there is usually only a single open channel, which consists of s, p_z, and $d_{3z^2-r^2}$ orbitals. Sometimes, a small contribution is seen arising from a second channel, involving the other p and d orbitals. The transmission around E_F varies between $0.7 \lesssim T_0 \lesssim 1.0$. The present method is known to reproduce experimental conductance histograms rather well [35] (see also the discussion in Sec. 2.4). In particular, the conductance peak somewhat below $G = 1G_0$ is a very robust feature.

3.5.3 Longitudinal and transverse modes

Let us first discuss the basic observations using a simple example, namely, a linear chain of four atoms in geometry A. A schematic illustration of the vibrational modes is shown in Fig. 3.4 for $d = 2.62$ Å. There are four longitudinal modes and eight transverse modes. However, due to the fourfold rotational symmetry of the geometry around the axis of the wire, the transverse modes are all doubly degenerate. The zero-bias conductance is due to two partially open channels. The main contribution (about 98% of G_0) is due to a channel (C_1) formed from s, p_z, and $d_{3z^2-r^2}$ orbitals, which have the symmetry of the geometry. In addition, there is a small (less than 1% of G_0) contribution from a second, doubly degenerate channel (C_2), which consists of d_{xz}, d_{yz}, p_x, and p_y orbitals, which have a lower symmetry. Thanks to the symmetry of the C_1 channel, only longitudinal modes have a finite coupling constant in its subspace ($\lambda^\alpha_{C_1,C_1}$). In the subspace of the C_2 channel, also the transverse modes have a finite coupling ($\lambda^\alpha_{C_2,C_2}$). Thus we might expect that also the transverse modes give a small signal in the current.

Figure 3.5 shows an analysis of the contribution from the different modes to the differential conductance $G(V) = dI/dV$. We divide this conductance into three parts according to the three current contributions: $G(V) = G_0 T_0 + \delta G_{inel}(V) + \delta G_{ec}(V)$. Here $G_0 = 2e^2/h$, $\delta G_{inel} = dI_{inel}/dV$, and $\delta G_{ec} = d\delta I_{ec}/dV$. It is seen that δG_{inel} gives always positive contributions to the conductance steps, while δG_{ec} gives negative ones. As expected, we find that there is a finite step in both δG_{inel} and δG_{ec} due to all of the vibrational modes,

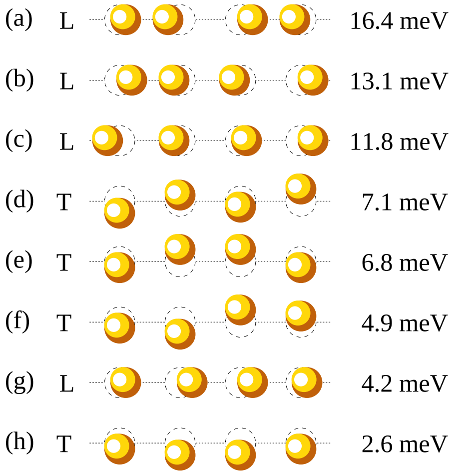

Figure 3.4: A sketch of the vibrational eigenmodes of a linear four-atom gold wire, with energies corresponding to $d = 2.62$ Åin geometry A. The longitudinal modes (L) are all nondegenerate, whereas the transverse modes (T) are all doubly degenerate.

also the transverse ones, although the latter are quite small. However, the contributions of δG_{inel} and δG_{ec} for the transverse modes almost perfectly cancel each other, such that only steps due to the longitudinal modes are seen in the total $G(V)$. This cancellation is apparently due to the exact fourfold rotation symmetry, and the mirror symmetry with respect to the plane cutting the wire in the middle. In less symmetric geometries the transverse modes can also give finite contributions to $G(V)$.

In the case of zigzag wires, the distinction between longitudinal and transverse modes does not really exist, and all modes are always seen as steps in $G(V)$. An example of this is shown below.

Thus, we find that the conductance features depend in an intricate way on the symmetries of the geometry, the symmetries of the vibrational modes, the coupling constants, as well as the symmetries of the electronic states which are relevant at the Fermi energy.

3.5.4 Conductance curves of linear gold wires

Here we discuss in more detail, how our I-V curves for linear wires look like. Figure 3.6 shows an example for geometry B with a wire of $N_{ch} = 11$ atoms. The left-hand panels are calculated at $T = 4.2$ K and with a small η, such that they are more or less in the externally undamped regime. The right-hand panels show two examples of the experimental results for a wire of approximately 7 atoms taken at the temperature $T = 4.2$ K [13]. Comparing these to the theoretical curves on the left-hand side, one immediately notices that if the conductance drop is to be due to a single mode, then the ~ 5 meV width of the peak in the experimental dG/dV cannot be explained by temperature alone [130]. On the other hand, the energy distance between the vibrational modes is rather large $\gtrsim k_B T$, so that at $T = 4.2$ K a peak consisting of several sub-peaks can in general easily be recognized.

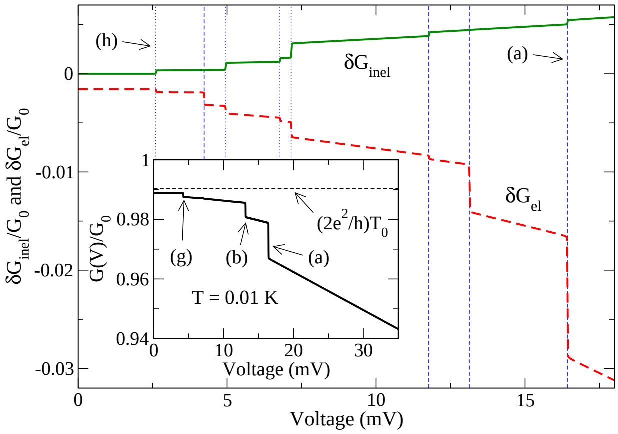

Figure 3.5: Decomposition of the conductance $G(V)$ into $G_0 T_0$, an "inelastic" contribution δG_{inel}, and an "elastic correction" δG_{ec} for a four-atom wire in geometry A. The geometry and the labels (a)–(h) correspond to those of Fig. 3.4. Other parameters are $T = 0.01$ K, $\eta = 0.002$ meV. The solid step-like curve shows δG_{inel}, and the dashed one shows δG_{ec}. The increases of δG_{inel} due to transverse modes are exactly canceled by decreases in δG_{ec}. The inset shows the elastic transmission (dashed line), and the total conductance $G(V)$ (solid line). In $G(V)$ only drops due to longitudinal modes are seen.

For example, the highest-frequency peak in Fig. 3.6 actually consists of two peaks, and it is still not wide enough.

Thus we conclude that in the experiment there are probably other broadening mechanisms at play besides temperature. In the right panels of Fig. 3.6 we use the parameter η to broaden the peaks. In the latter, the system is already in the externally damped regime, with very little local heating: in addition to the broadening, the damping is signified by a smaller slope after the drop. The peaks due to individual modes are smoothed out to form a single one, with a width comparable to that seen in experiments. In this way, it is possible to obtain a rather good quantitative correspondence between theory and experiment.

3.6 Conclusions

We have studied the onset of dissipation by excitation of vibrational modes in atomic gold wires, using a tight-binding model. In doing so we investigated two different geometries, which yield qualitatively similar results and find a reasonable agreement with experiments.

Our results for the linear chains agree rather well with experiments and previous *ab-initio* calculations, apart from the incomplete "mode selectivity". In this context, we have pointed out the importance of taking into account the broadening of vibrational modes due to their coupling to the leads, especially in the limit where the vibrational mode distribution is assumed to be strongly damped. We derived equations in the wide-band limit, which take this into account in a phenomenological manner. The wide-band limit combined with the lowest-order perturbation approach appears to provide a sufficiently

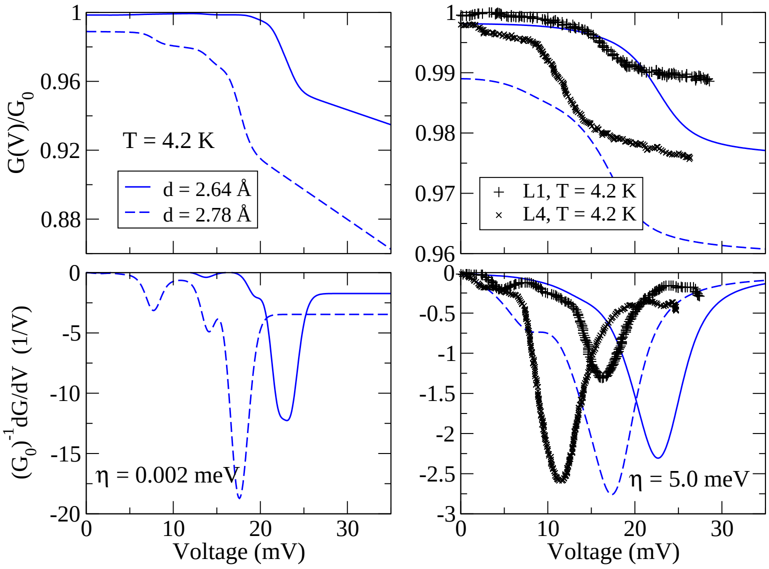

Figure 3.6: Comparison between theory and experiment for $N_{ch} = 11$ in geometry B. All results are at $T = 4.2$ K. The solid and dashed curves correspond to theoretical results for $d = 2.64$ Åand $d = 2.78$ Å, respectively. On the left-hand panels $\eta = 0.002$ meV, whereas on the right-hand panels the curves have been broadened with a bath-coupling $\eta = 5.0$ meV. The experimental results L1 (+) and L4 (×) correspond to the notation and results of Fig. 1(d) of Ref. [13] with $V > 0$. They are obtained for a 7-atom chain at $T = 4.2$ K.

good description of the phenomenology of electron-vibration interaction in atomic wires. To make further progress, more detailed calculations of the lead-coupling of the vibrational modes are needed.

Studying different materials (Pt and Ir) with this same method would be straightforward in principle. However, it seems that the parameters available for these materials are not very good for geometry optimizations of the wires. This is because the overlap matrices easily lose their positive definiteness when the validity range of the parameterization is exceeded.[2] Thus, as already implied in Ref. [80], one should probably use more general *ab-initio* methods, or at least parameters which have been specifically fit to work for chain geometries with a large span of interatomic distances. Currently an extension of the DFT transport method, presented in Chap. 4, is envisaged to include also the effects of electron-phonon coupling.

---

[2] With the gold parameters au_par_99 [77], such problems never appeared.

Chapter 4

Ab-initio density functional approach to molecular electronics

Advances in the experimental techniques for manipulating and contacting individual molecules, and the prospect of simple organic molecules as basic building blocks in electronically active devices have recently intensified the interest in electron transport at the nanoscale [144, 145, 21, 146, 26, 103, 28]. It is clear that from the theoretical side a systematic understanding is required in order to support the experimental efforts and to stimulate further technological advances. In order to do so an accurate modeling of the structural, electronic, and transport properties is required. Microscopic approaches are needed to account correctly for the quantum-mechanical phenomena affecting the physical properties at the nanoscale.

In today's physics and chemistry electronic structure calculations are an important tool for investigating new materials and molecules. An essential factor for the success of these techniques is the development of first-principles methods that allow the reliable modeling of a wide range of systems, without introducing system dependent parameters. It is natural that quantum transport theories, aiming at a realistic description of nanoscale devices in the field of molecular electronics, will rely on the established approaches developed over the recent years in the fields of theoretical physics and quantum chemistry. While in early attempts semiempirical extended-Hückel parameters were used to model the quantum transport [147, 148], soon self-consistent schemes like the Hartree-Fock level of description were employed [149]. Nowadays most models are based on density functional theory (DFT) [150, 151, 152, 128, 153, 154, 155, 63, 156, 157, 158, 159]. For an overview on the atomistic theory of transport in nanostructures we recommend the review by Peccia *et al.* [160].

The description of quantum transport from first principles is very challenging. Most electronic structure calculations are limited in two aspects: (i) the geometry is either restricted to finite or to periodic systems, (ii) the electronic system must be in equilibrium. If a molecule is, however, contacted by two metallic electrodes a method is needed to treat an infinite, nonperiodic system. The whole system – electrodes and the molecule[1] – should

---

[1] Indeed we mean the central part of the system, often referred to as the extended molecule.

be treated at the same level of theory in a consistent basis set. In addition a finite bias voltage may be applied to the electrodes. In this case the electronic subsystem of the molecule is not in equilibrium [152].

The requirements (i) and (ii) are not easy to fulfill, and within the aforementioned references there exist large differences in the level of sophistication. Often the electrodes are treated only approximately or the developed program is not capable of handling finite bias voltages. Thus for example, Xue *et al.* [150] use electrode parameters obtained from a tight-binding parameterization as given elsewhere [161], Palacios *et al.* [128] use Bethe lattices to model the electronic reservoirs, and Evers *et al.* [162] approximate the electrode description by using bulk instead of surface Green's functions. In the approaches by Xue and Palacios a minimal basis set is employed for the description of the electrode atoms. Other more accurate programs [155, 154] currently do not have the ability to treat the nonequilibrium finite bias situation that allows the computation of current-voltage (I-V) characteristics. Very complete implementations of the above requirements are presented in Refs. [152, 159]. The program of Ref. [152] is even commercially available under the name TRANSIESTA, and that of Ref. [159], called SMEAGOL, offers the possibility to treat magnetic structures. Both of the last two references are based on the electronic structure program SIESTA.

Generally it can be observed that there are two approaches concerning the practical implementations. One comes from the field of quantum chemistry and is based on packages like GAUSSIAN [150, 128, 163] or TURBOMOLE [162]. When using this approach the electrodes are usually described in an approximate fashion. The presently most advanced quantum transport packages are based on DFT programs, such as SIESTA, that can treat periodic systems. The central system is then described as a long supercell such that the electron density has converged to the bulk value in the electrodes [152]. In this way, no mismatch problems arise, when the electrode surface Green's functions are constructed from bulk parameters, and are finally coupled to the central system. Instead, the quantum chemistry approach suffers from surface effects. But apparently also the SIESTA-like approaches have their drawbacks. The supercell involved in a description of the central system is rather limited in its transverse dimensions. This hinders the description of molecules with a large lateral extent. In addition the convergence of transport results with respect to the transverse dimension has, to the best of our knowledge, not yet been shown for the supercell approach, and also the finite bias situation is only described approximately. Instead of a solution of the Poisson equation in real space one commonly solves the electrostatic problem in reciprocal space, even though the finite bias situation clearly breaks the translational symmetry in the transport direction. So there does not yet seem to exist a completely satisfactory solution to all the challenges that the ab-initio modeling of quantum transport poses. We will come back to some of these complications in the course of this chapter.

On the one hand these details may be very important in order to determine, what DFT really predicts with respect to the conduction properties of molecules, for example. On the other hand one may, from a more general point of view, perhaps say that they are minor points. In DFT-based transport methods not only the total electron density is used, but the Kohn-Sham (KS) wave functions are taken as single-particle wave functions, when calculating the electronic current [152]. In this sense DFT is a bona fide approach to quantum transport. Due to its meanfield-like structure DFT cannot capture pronounced many-body effects. For this reason new methods have been proposed very recently that shall improve the description of the open system quantum many body-problem [164, 165]. But also from the DFT side there are further developments, where time-dependent DFT is applied to quantum transport [166, 167, 168, 169, 170, 171].

Concerning our work let us mention that we use the quantum chemistry approach, namely the software package TURBOMOLE. As could be anticipated by the analysis of the literature (see above), the electrode description turned out to be the most difficult part due to the lack of periodic boundary conditions that facilitate the solid state description of the infinite metallic electrodes. Our basic ideas to describe the electrodes follow Ref. [153]. However, compared to that work we could make progress in some essential points, as will be outlined in the course of this chapter. Our present implementation of quantum transport is only able to describe the equilibrium zero bias situation. It is based on the separate calculation of an electrode and a contact cluster. From this fact an uncertainty concerning the position of the Fermi energy arises. A self-consistent treatment of the electrodes plus the central system could help to eliminate this uncertainty. Such a procedure has been tried without success, and we will give the reasons for the problems encountered. However, due to TURBOMOLE's ability to compute very large atomic clusters, we arrived at a transport scheme, where the electrodes are described at the same level of sophistication as the central system. In particular we use the same nonorthogonal basis set for both of them. For this reason the aforementioned uncertainty can, in principle, be eliminated by computing large enough cental systems. Indeed we show for metallic Au and Al systems that our method yields converged results perfectly in line with experimental expectations. Also the direct comparison between our method and the DFT-based studies of other theoretical approaches, i.e., TRANSIESTA, turns out to be very satisfactory. In this sense we have developed a quantum transport description that is equivalent to other transport methods. It has the additional advantage that it can be applied to systems with large transverse dimensions.

We want to mention that another implementation of a transport code based on TURBOMOLE was published in the course of our studies [162]. However, due to the shortness of the presentation in Ref. [162], uncertainties about the details of the employed method remain. (In particular Ref. 28 of Ref. [162] has to the best of our knowledge not yet been published.) Contrary to the method proposed in paragraph III.A of Ref. [162] the group of F. Evers currently makes use of "absorbing boundary conditions" in the electrode description [172].[2] These circumstances justify the development of our own methodology in order to describe the electron transport with the help of TURBOMOLE.

Let us give the outline of this chapter. First we will give an introduction to the fundamentals of DFT in Sec. 4.1. Second, Sec. 4.2 will present the implementation scheme for

---

[2] With the language of Ref. [172] "absorbing boundary conditions" refer to energy independent, purely imaginary electrode self energies.

quantum transport within TURBOMOLE, as developed in this thesis. Thereafter we will explain the major steps of the electrode description in Sec. 4.3, and come to unsuccessful studies of the electronic structure of open quantum systems in Sec. 4.4. In Sec. 4.5 we show a comparison between results of our method and that of Ref. [152] for a three-atom Au chain, before we end with the Conclusions in Sec. 4.6. The presentation given below involves details that can be found in Chaps. B, C, D, and F of the Appendix.

4.1 Electronic structure calculation in density functional theory

The goal of DFT is the approximate solution of the time-independent (non-relativistic) Schrödinger equation

$$\hat{H}\Psi_\mu(\vec{x}_1, ..., \vec{x}_N, \vec{R}_1, ..., \vec{R}_M) = E_\mu \Psi_\mu(\vec{x}_1, ..., \vec{x}_N, \vec{R}_1, ..., \vec{R}_M) \tag{4.1}$$

with the Hamiltonian

$$\hat{H} = -\frac{\hbar^2}{2m_e}\sum_{\mu=1}^{N}\nabla_\mu^2 - \frac{\hbar^2}{2}\sum_{A=1}^{M}\frac{1}{M_A}\nabla_A^2 - \sum_{\mu=1}^{N}\sum_{A=1}^{M}\frac{Z_A e^2}{4\pi\varepsilon_0 r_{\mu A}} + \sum_{\mu=1}^{N}\sum_{\nu>\mu}^{N}\frac{e^2}{4\pi\varepsilon_0 r_{\mu\nu}} + \sum_{A=1}^{M}\sum_{B>A}^{M}\frac{Z_A Z_B e^2}{4\pi\varepsilon_0 R_{AB}}. \tag{4.2}$$

Here, A and B run over the M nuclei, while i and j denote the N electrons in the system, m_e is the electron mass, $e = |e|$ is the elementary charge, ε_0 the electric constant, and $r_{pq} = |\vec{r}_p - \vec{r}_q|$ ($R_{pq} = \left|\vec{R}_p - \vec{R}_q\right|$) is the distance between the particles p and q. The first two terms in this expression describe the kinetic energy of the electrons and nuclei, respectively, and M_A is the mass of nucleus A. The remaining three terms define the potential part of the Hamiltonian and represent the attractive electrostatic interaction between the nuclei and the electrons and the repulsive potential due to the electron-electron and nucleus-nucleus interaction. E_μ is the energy of the states, described by the wave function $\Psi_\mu(\vec{x}_1, ..., \vec{x}_N, \vec{R}_1, ..., \vec{R}_M)$ of the μth state of the system. The wave function depends on $3N$ spatial coordinates $\{\vec{r}_i\}$ and N spin coordinates $\{s_i\}$ of the electrons, which are collectively termed $\{\vec{x}_i\}$, and the $3M$ spatial coordinates $\left\{\vec{R}_i\right\}$ of the nuclei. As usual, the wave functions Ψ_μ contain all the information that can possibly be known about the quantum system at hand. The presentation in the following is almost completely based on Ref. [173].

In order to solve the basic electronic Schrödinger problem of Eq. (4.1) the Born-Oppenheimer approximation is made, leading to a separation of electronic and nuclear degrees of freedom. One arrives at the electronic Schrödinger equation

$$\hat{H}_{el}\psi = E_{el}\psi$$

where ψ depends on the electronic coordinates, while the nuclear coordinates enter only parametrically and the electronic Hamiltonian has been defined as

$$\hat{H}_{el} = -\frac{\hbar^2}{2m_e}\sum_{\mu=1}^{N}\nabla_\mu^2 - \sum_{\mu=1}^{N}\sum_{A=1}^{M}\frac{Z_A e^2}{4\pi\varepsilon_0 r_{\mu A}} + \sum_{\mu=1}^{N}\sum_{\nu>\mu}^{N}\frac{e^2}{4\pi\varepsilon_0 r_{\mu\nu}} = \hat{T} + \hat{V}_{Ne} + \hat{V}_{ee}. \tag{4.3}$$

The total energy

$$E_{tot} = E_{el} + E_{nuc} \tag{4.4}$$

is then given as the sum of the electronic energy E_{el} and the nuclear repulsion term

$$E_{nuc} = \sum_{A=1}^{M}\sum_{B>A}^{M}\frac{Z_A Z_B e^2}{4\pi\varepsilon_0 R_{AB}}. \tag{4.5}$$

The attractive potential exerted on the electrons by the nuclei, obtained as the expectation value of $\hat{V}_{Ne}$ in Eq. (4.3), is often termed the external potential V_{ext}. From now on we will only consider the electronic problem as described by Eqs. (4.3)–(4.5).

From a wave function ψ the electron density ρ, central to DFT, is obtained as

$$\rho(\vec{r}) = N\int\cdots\int|\psi(\vec{x}_1,\vec{x}_2,...,\vec{x}_n)|^2\, ds_1 d^4x_2\cdots d^4x_N.$$

ρ determines the probability of finding any of the N electrons within the volume element d^3r with arbitrary spin s, while the state of the other $N-1$ electrons (both in space and spin) is arbitrary. The electron density is normalized to the number of electrons N in the system ($\int d^3r\rho = N$).

4.1.1 Hohenberg-Kohn theorems

DFT, as we know it today, was born in 1964 when a landmark paper by Hohenberg and Kohn appeared in Physical Review [174]. The theorems proven in this report represent the major theoretical pillars, on which all modern DFTs are erected.

The first Hohenberg-Kohn theorem provides the proof that the electron density in fact uniquely determines the Hamiltonian operator and thus all properties of the system. Quoting directly from Ref. [174] this theorem states that "the external potential $V_{ext}(\vec{r})$ is (to within a constant) a unique functional of $\rho(\vec{r})$; since, in turn $V_{ext}(\vec{r})$ fixes $\hat{H}$ we see that the full many particle ground state is a unique functional of $\rho(\vec{r})$".

More pictorially we can summarize this as

$$\rho_0 \Rightarrow \left\{N, Z_A, \vec{R}_A\right\} \Rightarrow \hat{H}_{el} \Rightarrow \psi_0 \Rightarrow E_0 \quad \text{(and all other properties)}$$

By this we mean that once the ground state density ρ_0 is known, this determines the total number N of electrons, the charges $Z_A e$ of the nuclei, and their spatial coordinates $\vec{R}_A$. This information in turn fixes V_{ext}, meaning that the Hamiltonian $\hat{H}_{el}$ can be constructed. Once the electronic Hamiltonian is known all information about the system is in our hand

and we can – at least in principle – determine the ground state wave function ψ_0, the ground state energy E_0, and all other properties of the system.

Since the complete ground state energy is a functional of the ground state electron density, so must be its individual components, thus we can write (see Eq. (4.3))

$$E_0[\rho_0] = T[\rho_0] + E_{ee}[\rho_0] + E_{Ne}[\rho_0].$$

It is convenient at this point to separate this energy expression into those parts that depend on the actual system, i.e., the potential energy due to the nuclei-electron attraction $E_{Ne}[\rho_0] = \int d^3r \rho_0(\vec{r}) V_{Ne}$, and those which are universal in the sense that their form is independent of N, R_A and Z_A, namely $T[\rho_0]$ and $E_{ee}[\rho_0]$. Collecting the system independent parts into the Hohenberg-Kohn functional

$$F[\rho] = T[\rho] + E_{ee}[\rho] \tag{4.6}$$

the energy is given as

$$E_0[\rho_0] = \int d^3r \rho_0(\vec{r}) V_{Ne} + F[\rho_0].$$

Up to now we have established that the ground state density is in principle sufficient to obtain all properties of interest. But how can we be sure that a certain density is really the ground state density that we are looking for? A formal prescription, for how this problem should be tackled, has been given through the second Hohenberg-Kohn theorem [174]. It states that the functional $E[\rho]$ that delivers the ground energy of the system delivers the lowest energy E_0, if and only if the input density $\tilde{\rho}$ is the true ground state density ρ_0. More formally this means that the following inequality holds

$$E_0 = E[\rho_0] < E[\tilde{\rho}],$$

where the electron densities all fulfill the boundary conditions $\tilde{\rho}(\vec{r}) \geq 0$ and $\int d^3r \tilde{\rho}(\vec{r}) = N$.

4.1.2 Kohn-Sham approach

Let us now show how the Hohenberg-Kohn theorems are put to work. The approach we are discussing has its origin in the second major paper of modern DFT [175]. In this paper Kohn and Sham suggested an avenue for how the hitherto unknown universal functional $F[\rho]$ can be approached. At the center of this idea is the insight that most of the problems with direct density functionals, like the Thomas-Fermi method, are connected to the way the kinetic energy is determined. In order to alleviate the situation and by realizing that orbital based approaches such as the Hartree-Fock method perform much better in this respect, Kohn and Sham introduced the concept of a noninteracting reference system built from a set of orbitals (i.e., one electron functions) such that the major part of the kinetic energy can be computed to good accuracy. The remainder is merged with the non-classical contributions to the electron-electron repulsion – which are also unknown but usually fairly small. By this method as much information as possible is computed exactly, leaving only a small part of the total energy to be determined by an approximate functional.

It is customary to separate the universal functional $F[\rho]$ of Eq. (4.6) into individual contributions of the kinetic energy $T[\rho]$, the classical Coulomb interaction

$$J[\rho] = \frac{e^2}{8\pi\varepsilon_0} \int \int \frac{\rho(\vec{r}_1)\rho(\vec{r}_2)}{r_{12}} d^3r_1 d^3r_2$$

and the non-classical contributions to the Coulomb interaction

$$E_{ncl}[\rho] = E_{ee}[\rho] - J[\rho].$$

The functionals $T[\rho]$ and $E_{ncl}[\rho]$ are unknown and the finding of explicit expressions for them constitutes the essential challenge in DFT. It turns out that a functional for $T[\rho]$ is particularly difficult to find.

Kohn and Sham found out that a more accurate way to determine the kinetic energy is by defining a noninteracting reference system with a Hamiltonian

$$\hat{H}_S = -\frac{\hbar^2}{2m_e} \sum_{\mu=1}^{N} \nabla_i^2 + \sum_{\mu=1}^{N} V_S(\vec{r}_\mu) \tag{4.7}$$

and an effective local potential $V_S(\vec{r})$. The wave functions in this noninteracting reference system are given as Slater determinants constructed from Kohn-Sham (KS) orbitals φ_μ in analogy to the Hartree Fock method. The orbitals φ_μ are determined by

$$\hat{f}^{KS} \varphi_\mu = \varepsilon_\mu \varphi_\mu \tag{4.8}$$

with the KS operator

$$\hat{f}^{KS} = -\frac{\hbar^2}{2m_e} \nabla^2 + V_S(\vec{r}). \tag{4.9}$$

The connection of this artificial system to the one we are really interested in is now established by choosing the effective potential V_S such that the density of the noninteractring reference system exactly equals the ground state density of our target system of interacting electrons

$$\rho_S(\vec{r}) = \sum_{\mu=1}^{N} \sum_{s_i=-1/2}^{1/2} |\varphi_\mu(\vec{r}, s)|^2 = \rho_0(\vec{r}).$$

In this way the functional $F[\rho]$ is brought into the form

$$F[\rho] = T_S[\rho] + J[\rho] + E_{XC}[\rho]$$

where

$$T_S = -\frac{\hbar^2}{2m_e} \sum_{\mu=1}^{N} \langle \varphi_\mu | \nabla^2 | \varphi_\mu \rangle$$

and E_{XC}, the so called exchange-correlation energy, is defined as

$$E_{XC}[\rho] = (T[\rho] - T_S[\rho]) + (E_{ee}[\rho] - J[\rho]) = T_C[\rho] + E_{ncl}[\rho].$$

The residual part of the true kinetic energy T_C, which is not recovered by T_S, is simply added to the non-classical electrostatic contributions. The exchange correlation energy E_{XC} is the functional, which contains everything that is unknown. It is a kind of a junkyard, where everything is stowed away that we do not know how to handle exactly. In spite of its name E_{XC} contains not only the non-classical effects of self-interaction correction, exchange and correlation, which are contributions to the potential energy of the system, but also a portion belonging to the kinetic energy.

Finally the total energy is

$$E[\rho] = T_S[\rho] + J[\rho] + E_{XC}[\rho] + E_{Ne}[\rho]$$

and V_S of Eqs. (4.7) and (4.9) can be shown to be

$$V_S(\vec{r}_1) = \frac{e^2}{4\pi\varepsilon_0} \int \frac{\rho(\vec{r}_2)}{r_{12}} d^3r_2 + V_{XC}(\vec{r}_1) - \frac{e^2}{4\pi\varepsilon_0} \sum_{A=1}^{M} \frac{Z_A}{r_{1A}}. \tag{4.10}$$

The exchange-correlation potential $V_{XC} = \delta E_{XC}/\delta\rho$ is the functional derivative of E_{XC}. Up to this point the KS approach is exact. Unfortunately the explicit form of E_{XC} and thus V_{XC} is unknown and the approximations enter, when we decide on an explicit form for them. The central goal of research in DFT is to find better and better approximations to E_{XC} and V_{XC}.

4.1.3 Basic machinery of density functional theory

In this paragraph we turn to the practical problem, of how the strategies of DFT, developed so far, can be mapped onto computational schemes. First we will discuss the linear combination of atomic orbitals (LCAO) ansatz, which is by far the most dominant way to make the iterative self-consistent field procedure for solving the one-electron KS equations computationally accessible. Next we will say, how the basis sets used in TURBOMOLE look like, before we end with a particularly efficient way on how to compute the Coulomb term, known as RI-J approximation or density fitting.

4.1.3.1 LCAO ansatz in the Kohn-Sham equations

The KS approach to DFT, developed so far, requires the solution of Eqs. (4.8), (4.9), and (4.10). These KS equations represent a complicated system of coupled integro-differential equations and we need to find a computationally efficient way of solving them. At the end of this process we obtain as solutions the KS molecular orbitals (MOs) $\{\varphi_\mu\}$, which yield the ground state density associated with the particular choice of V_{XC}.

A frequently used strategy in order to solve the KS equations is the LCAO expansion of the KS MOs

$$\varphi_\mu = \sum_{i=1}^{L} c_{i\mu}\phi_i \tag{4.11}$$

within a set of L basis functions $\{\phi_i\}$. In real applications L is finite, and it is of crucial importance to choose the basis set $\{\phi_i\}$ such that the LCAO provides an approximation of the exact KS orbitals as accurate as possible. By using the LCAO ansatz in the KS equations the originally highly nonlinear optimization problem has been simplified into a linear one, with the coefficients $\{c_{i\mu}\}$ being the only variables.

With the LCAO ansatz applied to Eq. (4.8), we finally arrive at the matrix equation

$$F^{KS}(C)C = SC\varepsilon \tag{4.12}$$

with the KS Fock matrix

$$F_{ij}^{KS} = \int \phi_i(\vec{r}_1)\hat{f^{KS}}\phi_j(\vec{r}_1)d^3r_1, \tag{4.13}$$

the overlap matrix

$$S_{ij} = \int \phi_i(\vec{r}_1)\phi_j(\vec{r}_1)d^3r_1,$$

the expansion coefficient matrix

$$C_{i\mu} = c_{i\mu}$$

and the matrix of eigenenergies

$$\varepsilon_{\mu\nu} = \delta_{\mu\nu}\varepsilon_\mu.$$

Notice that, in case of real basis functions, all the matrices just defined are symmetric. In Eq. (4.12) we have written $F^{KS} = F^{KS}(C)$ because the KS matrix depends nonlinearly on the expansion coefficients $c_{i\mu}$. An iterative solution of Eq. (4.12) is possible in analogy to the Hartree-Fock theory.

The different terms appearing in the KS Fock matrix are

$$F_{ij}^{KS} = h_{ij} + J_{ij} + V_{ij}^{XC}$$

with the single-particle integrals

$$h_{ij} = \int \phi_i(\vec{r}_1)\left[-\frac{\hbar^2}{2m_e}\nabla^2 - \sum_{A=1}^{M}\frac{Z_A e^2}{4\pi\varepsilon_0 r_{iA}}\right]\phi_j(\vec{r}_1)d^3r_1, \tag{4.14}$$

the Coulomb part

$$J_{ij} = \sum_{m=1}^{L}\sum_{n=1}^{L} P_{mn}\int\int \phi_i(\vec{r}_1)\phi_j(\vec{r}_1)\frac{1}{r_{12}}\phi_m(\vec{r}_2)\phi_n(\vec{r}_2)d^3r_1d^3r_2, \tag{4.15}$$

and the exchange correlation part

$$V_{ij}^{XC} = \int \phi_i(\vec{r}_1)V_{XC}(\vec{r}_1)\phi_j(\vec{r}_1)d^3r_1. \tag{4.16}$$

In Eq. (4.15) the density matrix

$$P_{ij} = \sum_{\mu=1}^{N} c_{i\mu} c_{j\mu}$$

has been defined, from which we obtain

$$\rho(\vec{r}) = \sum_{\mu=1}^{N} |\varphi_\mu(\vec{r})|^2 = \sum_{i=1}^{L} \sum_{j=1}^{L} \phi_i(\vec{r}) P_{ij} \phi_j(\vec{r}).$$

Note that the Coulomb part J_{ij} is particularly expensive to evaluate as it involves four-center-two-electron integrals.

4.1.3.2 Basis sets

As mentioned before one tries to use the most efficient and accurate functions possible in the LCAO expansion of Eq. (4.11) in the sense that the expansion will require the fewest possible terms for an accurate representation of the KS MOs φ_μ. From these considerations one may try to use Slater type orbitals (STOs) of the form

$$\phi^{\mathrm{STO}} = \aleph r^{n-1} e^{-\alpha r} Y_{lm}$$

with a normalization constant $\aleph$, the principal quantum number n, the orbital exponent α, and spherical harmonics Y_{lm}. This choice is physically natural as the simple exponentials ϕ^{STO} mimic the exact eigenfunctions of the hydrogen atom. However, many-center integrals, as needed in Eqs. (4.14)–(4.16), are notoriously difficult to evaluate.

On the other hand there exist very efficient integration schemes for Gaussian type orbitals (GTOs) [81] of the form

$$\phi^{\mathrm{GTO}} = \aleph x^m y^p z^q e^{-\alpha r^2}. \tag{4.17}$$

Again $\aleph$ is a normalization constant. The orbital exponent α determines how compact (large α) or diffuse (small α) the resulting function is. $L = m + p + q$ is used to classify the GTO as s function ($L = 0$), p function ($L = 1$), d function ($L = 2$), etc..

In an attempt to approximate the STO basis set as closely as possible, one uses contracted GTO basis sets in which n primitive Gaussian functions as in Eq. (4.17) are summed up in a fixed linear combination to give one contracted Gaussian function (CGF)

$$\phi_i^{\mathrm{CGF}} = \sum_{a=1}^{n} d_{ai} \phi_a^{\mathrm{GTO}}.$$

with appropriate expansion coefficients d_{ai}. Such CGF basis functions are used in TURBOMOLE.

Concerning the classification of the CGFs and GTOs one should note that for $L > 1$ the number of cartesian GTO functions exceeds the number of $2l + 1$ physical functions of angular momentum l. For example, among the six cartesian functions with $L = 2$ one is spherically symmetric and is therefore not a d orbital but an s orbital. One can distinguish between cartesian atomic orbitals of the form of Eq. (4.17) or transform to a spherical atomic orbital (SAO) representation, where the angular symmetry is that of the spherical harmonics combined linearly to get a basis set of real angular functions (see Eqs. (F.5) and (F.7)). If we talk about s, p and d orbitals we will always refer to this SAO representation.

4.1.3.3 Calculation of the Coulomb term

As pointed out before the coulomb term J_{ij} in Eq. (4.15) is particularly difficult to evaluate as it involves four-center-two-electron integrals. In order to reduce the effort to compute this term the electron density can be expanded in an auxiliary basis set

$$\rho(\vec{r}) \approx \tilde{\rho}(\vec{r}) = \sum_{\kappa=1}^{K} c_\kappa \omega_\kappa(\vec{r}). \tag{4.18}$$

This leads to an approximated Coulomb term

$$\tilde{J}_{ij} = \sum_{\kappa=1}^{K} c_\kappa \int\int \frac{\phi_i(\vec{r}_1)\phi_j(\vec{r}_1)\omega_\kappa(\vec{r}_2)}{r_{12}} d^3r_1 d^3r_2,$$

which can be handled more efficiently, as it involves only three-center-two-electron integrals. This technique has been implemented into different ab-initio programs, in particular TURBOMOLE, where it has the name "RI-J", or Gaussian, where it is called "density fitting" due to Eq. (4.18).

The RI-J approximation speeds up calculations roughly by a factor of 10 compared to standard DFT and is equally accurate. In our studies we exclusively rely on the RI-DFT method of TURBOMOLE as implemented in the module ridft [176, 177].

4.2 Molecular electronics – the system and its description

In this paragraph we want to present the basic problems that need to be solved, when one tries to describe the phase-coherent electron transport in a nanoscale system from first principles. By first principles we mean a theory with a minimal number of free parameters. Such an ab-initio description of electron transport is of high interest in the field of molecular electronics.

The quantum chemistry software TURBOMOLE, in particular its DFT implementation in the module ridft, has been developed to deal with finite systems, such as molecules or big metal clusters.[3] In contrast in quantum transport a molecule is, for example, coupled

---

[3] For a detailed list of options used with TURBOMOLE in our calculations and the proper citation of this method we refer the reader to Sec. F.4.

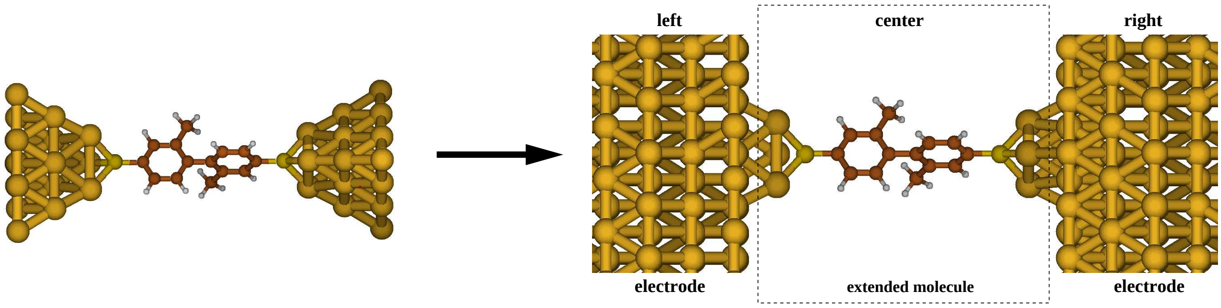

Figure 4.1: Transition from a finite system, as displayed to the left, to an infinite system on the right. For the system on the right a partitioning is indicated. The system is divided into a left part (L), a center (C), and a right part (R). The parts L and R are semi-infinite electrodes. The central part C is often called the extended molecule. (The word extended arises from the fact that usually some metal atoms are included in C.)

to semi-infinite metallic electrodes. Thus the challenges encountered are (i) an ab-initio description of the electronic structure of an infinite system and (ii) the calculation of the transport through the determined electronic states. Within the quantum chemistry approach a practicable strategy to make this transition from a finite to an infinite system has been developed at the beginning of this century [149, 150, 178, 127, 153]. In Fig. 4.1 we give a sketch of this strategy. A finite system has been computed as sketched in the left panel. We need to make the transition to a system as indicated on the right, where the finite clusters of metal atoms are replaced by semi-infinite electrodes. The contact is divided into the left (L) and right (R) electrodes and the center (C), central part, or extended molecule.

Now we want to calculate the electric charge current within the Green's functions formalism (see Chap. C and Sec. B.3.1). As for the TB models presented in the preceeding chapters, the use of a local basis allows for a partitioning of the electronic Hamiltonian and overlap matrices into parts according to the division into L, C, and R regions:

$$H = \begin{pmatrix} H_{LL} & H_{LC} & H_{LR} \\ H_{CL} & H_{CC} & H_{CR} \\ H_{RL} & H_{RC} & H_{RR} \end{pmatrix}, \; S = \begin{pmatrix} S_{LL} & S_{LC} & S_{LR} \\ S_{CL} & S_{CC} & S_{CR} \\ S_{RL} & S_{RC} & S_{RR} \end{pmatrix}.$$

Although the dimension of the problem is infinite due to the L and R regions, its single-particle nature allows for very effective methods of solution, as long as we may assume that $Y_{RL} = Y_{LR}^T = 0$ ($Y = H$ or S). This can always be achieved by choosing a large enough central region. We shall use the method of nonequilibrium Green's functions (NEGF) in order to compute the electrical current as worked out in the Appendices (see in particular Sec. B.3.1). In this method, one can restrict the problem to the C part only by introducing energy-dependent lead self-energies which, take into account the presence of the semi-infinite L and R leads in an exact way.

The quantity of central importance is the retarded Green's function of the C part

$$G_{CC}^r = \left(E^+ S_{CC} - H_{CC} - \Sigma_L^r(E) - \Sigma_R^r(E)\right)^{-1}$$

with the self-energies

$$\Sigma^r_X(E) = (H_{CX} - ES_{CX})g^r_{XX}(H_{XC} - ES_{XC}) \tag{4.19}$$

and the electrode Green's functions

$$g^r_{XX} = (E^+S_{XX} - H_{XX})^{-1}$$

where $X = L$ or R (see Eqs. (B.26) and (B.27)) and $E^+ = E + i0^+$. The self-energies Σ_X of Eq. (4.19) describe the effect of the coupling of C to semi-infinite electrodes. Their construction will be the major concern of this whole chapter. The self-energies require two ingredients, namely (a) the coupling matrices S_{CX} and H_{CX} and (b) the electrode Green's function g^r_{XX}.

Once Σ^r_X and G^r_{CC} have been constructed the transmission $T(E)$ can be computed as

$$T(E) = \mathrm{Tr}\left[\Gamma_L G^r_{CC} \Gamma_R G^a_{CC}\right] = \mathrm{Tr}\left[t^+ t\right], \tag{4.20}$$

where we have introduced the scattering matrix

$$\Gamma_X = (H_{CX} - ES_{CX})\, i\,(g^r_{XX} - g^a_{XX})\,(H_{XC} - ES_{XC}) = i\,(\Sigma^r_X - \Sigma^a_X) = -2\mathrm{Im}\left[\Sigma^r_X\right] \tag{4.21}$$

and the transmission matrix[4]

$$t(E) = \sqrt{\Gamma_L} G^a_{CC} \sqrt{\Gamma_R}. \tag{4.22}$$

The zero-bias, zero temperature conductance G is then obtained as

$$G = G_0 T(E_F) = G_0 \mathrm{Tr}\left[t^+ t\right] = G_0 \sum_n T_n(E_F), \tag{4.23}$$

where $G_0 = 2e^2/h$ is the unit of conductance (see Eqs. (C.7), (B.42), (C.8), and (C.10)).

For the Hamiltonian H we will use the matrix elements of the KS Fock operator of Eq. (4.13). As discussed in the introduction it is a bona fide assumption that we can use the KS orbitals as single-particle wave functions, when calculating the electronic current [152]. The validity of this assumption is under debate, and we will not discuss this any further [162, 166, 165].

Let us now address the question of how we can obtain the self-energies Σ^r_X. We will follow the ideas of Damle *et al.* [153]. However, in the construction of the electrode Green's functions as proposed in that reference, we encountered major problems. We will discuss them in detail later. But let us state already now that the use of just nearest neighbor couplings in the construction of electrode Green's functions as suggested in Ref. [153] does not work for reasons of overlap definiteness problems, at least not in nonorthogonal basis sets. Even an analytical model (see Sec. 4.3.1) shows these problems clearly. This is

---

[4] The positive definiteness of Γ_X, necessary for the possibility to take the square root of this matrix, is proven in Sec. C.2.

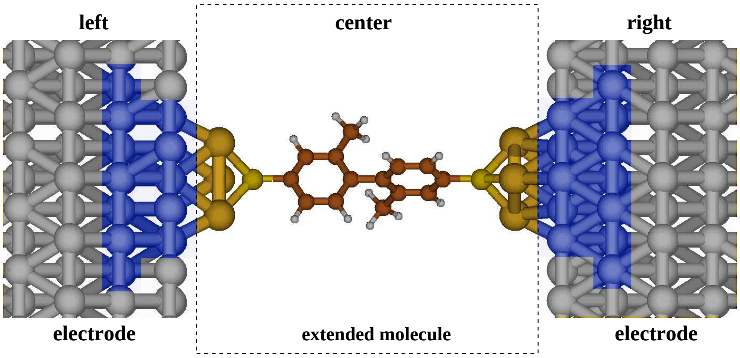

Figure 4.2: The extended molecule coupled to surface Green's functions. A finite system consisting of the blue-shaded atoms plus the center is cut into L, C, and R parts. From the blue atoms the coupling matrix elements S_{CX} and H_{CX} ($X = L$ or R) are extracted. The blue atoms are replaced by atoms embedded into semi-infinite surfaces displayed in grey.

likely to be the reason, why in that particular paper, despite the compelling concepts, the authors finally resorted to energy independent self-energies evaluated at the Fermi energy ($\Sigma_X^r(E) = \Sigma_X^r(E_F)$).

As seen in Eq. (4.19) we need the coupling matrices S_{CX} and H_{CX}. In order to obtain them, we compute a large contact with metallic clusters on either side, which are as large as possible (see the contact system on the left side of Fig. 4.1). Then the finite contact cluster with overlap and Hamiltonian matrices $S^{contact}$ and $H^{contact}$ is partitioned into the L, C, and R regions. As the matrix elements for the complete finite system $L + C + R$ are known, the couplings $S_{CX} = S_{CX}^{contact}$ and $H_{CX} = H_{CX}^{contact}$ can be extracted from this calculation [153]. (Of course we set $S_{CC} = S_{CC}^{contact}$ and $H_{CC} = H_{CC}^{contact}$.)

As a next step the electrode Green's functions g_{XX}^r of Eq. (4.19) needs to be constructed. As proposed in Ref. [153] we use parameters extracted from finite metal clusters that are calculated with the same basis set as the metal atoms of the contact system. In doing so we obtain electrode parameters at the same level of theory as those of the central system. From them we construct electrode Green's functions as explained in Chaps. D and F. Having constructed the electrode Green's functions, we couple them via the previously determined couplings to the central system.

In Fig. 4.2 we illustrate this procedure. The contact system consists of the center plus the blue atoms in the left and right electrodes. The coupling matrices S_{CX} and H_{CX} are obtained as the matrix elements connecting the center to the blue atoms. Next the finite L and R parts are replaced by the grey-shaded semiinfinite surface. We then determine a surface Green's function g_{XX}^r from bulk parameters S_{0j} and H_{0j} (see the explanations in Sec. D.2). The atoms in blue will be replaced by surface atoms, as described by the matrix elements of the surface Green's function g_{XX}^r.

It is obvious in this procedure that (i) for too few blue atoms in the region L or R not all relevant couplings to the surface are included, (ii) there may be a mismatch problem between the bulk parameters used to construct the surface Green's function and the couplings H_{CX} due to surface effects.

Indeed in Gaussian basis sets the overlaps between atoms are very big and fall off slowly with distance. Let us consider a simple s orbital function

$$\phi_s^{\mathrm{GTO}}(\vec{r}-\vec{R}_j) = \left(\frac{2\alpha}{\pi}\right)^{3/4} e^{-\alpha\left|\vec{r}-\vec{R}_j\right|^2} \tag{4.24}$$

(see Eq. (4.17)) with a typical minimal exponent of $\alpha = 0.05/b_0^2$ where b_0 is the Bohr radius $b_0 = 0.52918$ Å. Then the overlap element between two atoms a distance d apart is given by

$$S(d) = \int_{-\infty}^{\infty} d^3r \phi_s^{\mathrm{GTO}}(\vec{r}-\vec{d})\phi_s^{\mathrm{GTO}}(\vec{r}) = e^{-\alpha d^2/2}. \tag{4.25}$$

A decay of the overlap to 10^{-10} – a typical TURBOMOLE cutoff – requires a distance $d = 16.06$ Å. In an fcc geometry oriented along the [100], [110] or [111] direction with interlayer distances of $d_{n,n+1} = a/2$, $d_{n,n+1} = a/\sqrt{8}$, and $d_{n,n+1} = a/\sqrt{3}$ this means that 7, 11, and 6 layers are coupled due to the overlap $S(d)$ for Au with a lattice constant of $a_0 = 4.08$ Å. For this reason it is at present not possible for us to come to the real DFT limit of description by including such a big number of surface atoms (blue-shaded atoms in Fig. 4.2) that all electrode atoms are coupled to the central system, namely more than 6 layers of electrode atoms.[5] DFT programs capable of treating periodic boundary conditions (PBCs), seem to perform better in this respect. Very long supercells can be computed with them and the metalicity of the systems does not appear to be problematic in these cases [151, 152]. As the atoms at the end of the supercell are surrounded again by other atoms one can also get rid of surface effects at the outer layers and avoid coupling mismatch problems, when surface Green's functions constructed by bulk parameters are coupled to the central system [151, 152]. In Fig. 4.3 we display this situation, when PBCs are used (see also Fig. 5 of Ref. [152]).

Let us, however, mention as positive points that for the blue-shaded atoms in Fig. 4.2 we have included all connections to central atoms and not just a few, as it is also done in the literature [179]. In addition our central systems are not limited in their transverse extend, whereas the supercell approach of Fig. 4.3 cannot easily cope with such systems. For large transverse sizes of the center a strongly increasing number of electrode atoms need to be computed.

The only point to decide about in our method is, how to divide the system into the L, C, and R regions. Otherwise there are no free parameters. In this sense our method fulfills the criterion of being an ab-initio theory without adjustable fit parameters.

To end this section, we summarize the complete method pictorially in Fig. 4.4. The

---

[5] Going one step further and seeing things from the correctness of the coupling elements H_{CX}, the couplings require correct onsite energies of the atoms in X. That means that also they should be saturated with all atoms coupled to them, implying a doubling of the previously mentioned layer numbers in the blue-shaded region of Fig. 4.2. Thus more than 12 electrode layers might be needed to converge to the DFT limit.

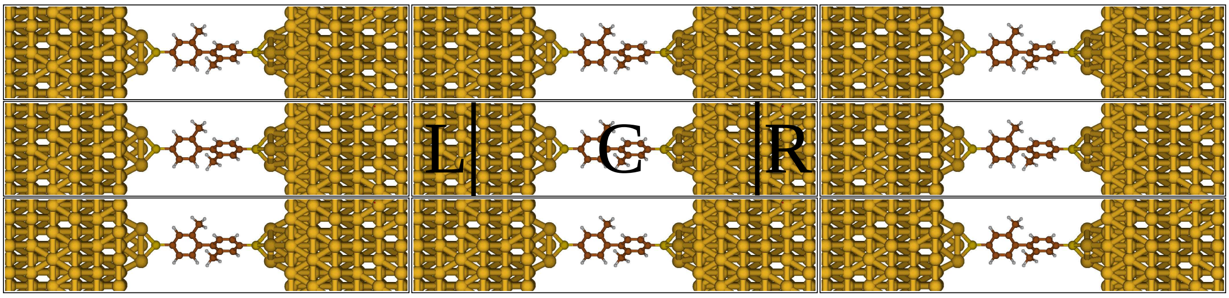

Figure 4.3: System as computed by use of PBCs. The effective DFT potentials in the regions L and R are very well at bulk values, because of the surrounding atoms due to the three dimensional PBCs.

picture already includes the construction of the electrode parameters S_{0j} and H_{0j}, needed to determine the surface electrode Green's functions g^r_{XX} (see the explanations in Sec. D.2). The electrode description will be the subject of the next section.

4.3 Electronic structure of the electrodes

In this section we will explain the construction of the parameters S_{0j}, H_{0j}, and H^{orth}_{0j} introduced in Fig. 4.4 (procedure 1 and 2). For this purpose we will explain, how the electrode clusters are constructed, from which we extract the electrode parameters. In particular we will present a size requirement that needs to be fulfilled, if meaningful parameters are to be obtained for an electrode Green's function construction in a nonorthogonal basis set. Next we will discuss, how we impose the fcc space group on the Hamiltonian. In this thesis we consider only electrode materials with an fcc crystal structure, namely Au and Al. For this reason it is sufficient to concentrate on the fcc space group symmetry.

4.3.1 Constructing electrode clusters and size requirements

Our aim is the construction of bulk parameters. Ideally we would now perform a solid state calculation with periodic boundary conditions and obtain a solid state Hamiltonian directly. Unfortunately this possibility does not exist in TURBOMOLE. However, TURBOMOLE is specialized on the calculation of large systems. In particular good results could be obtained with the functional BP-86 for large metal clusters [180, 181, 182, 183].

Therefore we set out to construct bulk parameters from clusters. As we will work exclusively with metals that exhibit an fcc structure in their crystalline form, we construct spherical fcc clusters, henceforth called fcc balls, $\{\vec{R}\,\big|\,\vec{R} = \sum_{l=1}^{3} i_l \vec{a}^{std}_l \wedge R \leq R_{ball}\}$ with the fcc standard primitive lattice vectors $\vec{a}^{std}_1 = (0, a_0/2, a_0/2)^T$, $\vec{a}^{std}_2 = (a_0/2, 0, a_0/2)^T$, and $\vec{a}^{std}_3 = (a_0/2, a_0/2, 0)^T$, the lattice constant a_0, and a radius R_{ball}.[6] We did not relax these

---

[6] We will usually use the vector of integer indices $i = (i_1, i_2, i_3)^T$ to characterize the vector $\vec{R} = \sum_{l=1}^{3} i_l \vec{a}_l = \vec{R}_i$.

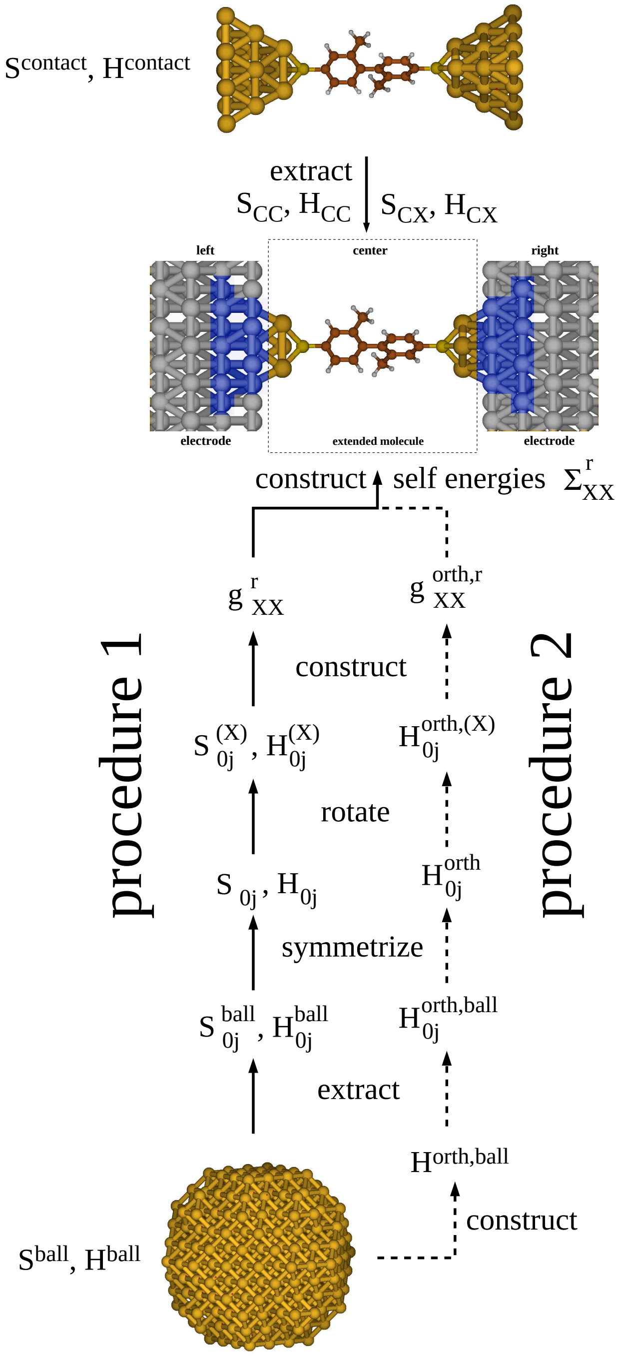

Figure 4.4: Pictorial representation of the quantum transport method developed in this work. Procedure 1 is a construction of electrode Green's function consistently in a nonorthogonal basis set. Procedure 2 uses orthogonal parameters and involves some uncontrolled basis set manipulation.

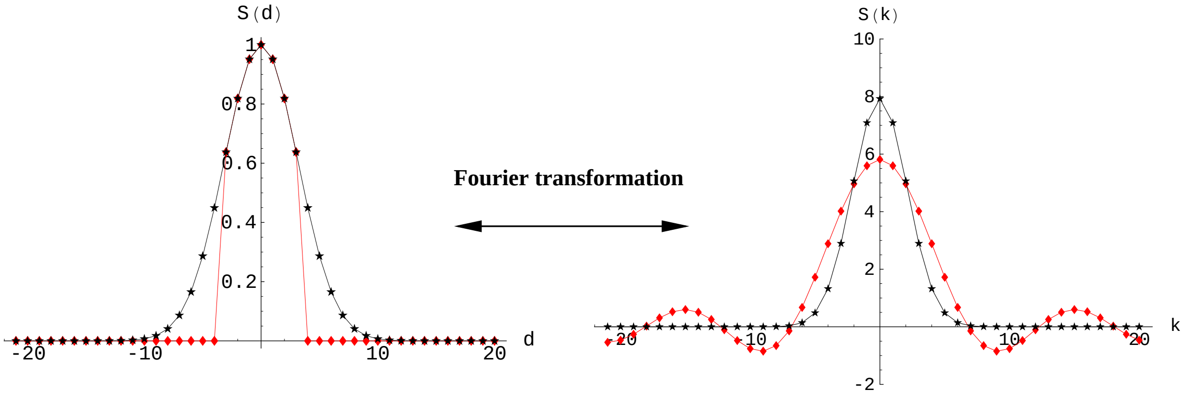

Figure 4.5: Discrete Fourier transformation for a simple s orbital model. In black (indicated with $\star$ symbols) the overlap $S(d)$ from a central atom to all its nearest neighbors is given. It is a simple Gaussian and a Fourier transformation gives back a Gaussian. In case that too few overlap elements have been extracted in direct space (red curve or symbols $\blacklozenge$), the overlap in k space becomes negative at certain k values. This behavior needs to be avoided as any physical overlap matrix needs to be positive definite.

structures and set the lattice constant to its literature value [184, 77]. The idea behind the choice of fcc balls is that the atom at the origin 0 is surrounded by a large number of nearest neighbor shells. Increasing the radius R_{ball} should finally lead to a central atom that possesses an electronic structure close to an atom in a crystal. From these clusters we want to extract the overlap and Hamiltonian parameters S_{0j}^{ball} and H_{0j}^{ball}, connecting the central atom to all the other atoms of the fcc ball. These parameters will serve as an approximation for bulk that is of an increasing accuracy for increased cluster sizes. It is suggested in Ref. [153] that a cluster with nearest (at most second nearest) neighbor interaction is sufficient for the construction of reasonable bulk parameters. We will show now that this is not the case, at least not in a nonorthogonal basis.

What happens to the overlap matrix, when we want to extract parameters from a finite cluster? Let us for this reason study a simple s orbital model as introduced before (see Eq. (4.24) and (4.25)). It has been shown that the overlap between two s orbitals a distance d apart is just a simple Gaussian function $S(d) = \exp(-\alpha d^2/2)$ with an orbital exponent α. Our cluster shall be a one-dimensional chain with atoms at equally spaced positions and Born-von-Kármán PBCs (see Chap. D). The overlap from a central atom, located in the middle of the chain, to its nearest neighbors will then drop off exponentially (see Fig. 4.5). The discrete Fourier transform will again result in a Gaussian with purely positive values $S(k)$. If, however, only few overlap matrix elements are taken into account, corresponding to the situation sketched in red, a rough $\sin(k)/k$-behavior results and $S(k)$ becomes negative at certain values in k space. This indicates an unphysical behavior, because overlap matrices need to be positive definite in real space [81] and this cannot be changed by a unitary transformation like the Fourier transformation.[7] As Gaussian basis

---

[7] The fact that the overlap in k space is positive definite can be seen with the help of the con-

functions have very long tails this implies that the electrode clusters need to be, depending simply on the basis chosen, of very large radius R_{ball}.

Of course in a quantum chemistry basis set the situation is not as simple as just discussed, because higher angular momentum functions such as p and d orbitals appear in these basis sets. The basis function with the smallest orbital exponent α_{min} will finally determine the large-distance behavior. The positive definiteness of the overlap is easily analyzed for very large fcc balls. This will give information on how large the fcc balls need to be in order to obtain a physically meaningful overlap behavior from the extracted parameters. For this reason we construct

$$S_k = S(\vec{k}_k) = \sum_j S(\vec{0}, \vec{R}_j) e^{-i\vec{k}_k \vec{R}_j} = \sum_j S_{0j} e^{-i\vec{k}_k \vec{R}_j}$$

according to Eq. (D.14). Next we diagonalize it with respect to the orbital dimensions, which have been dropped, and determine the minimum eigenvalue over all k. Thus we define the quantity

$$\xi = \min_k (\mathrm{eigval}(S(\vec{k}_k)_{\alpha,\beta}) \tag{4.26}$$

with orbtial indices α and β. ξ should be positive, otherwise the fcc ball was not big enough, and we should try to increase R_{ball}. (Note that ξ depends somewhat on the period assumed in the Born-von-Kármán PBCs.)

We concentrate now on the basis sets relevant for this work, namely the standard basis sets al SVP, au SVP, the additional basis sets al SVP-wsp-opt, and au SVP-wsp, where the most diffuse basis functions are eliminated, and al hw-min (see Sec. F.4). Investigations will be made at a periodicity length of $N_i = 16$ (see Eq. (D.8)), and the fcc balls were constructed using a lattice constant $a_0 = 4.05$ Åfor Al and $a_0 = 4.08$ Åfor Au. For these basis sets we plot in Fig. 4.6 the behavior of ξ as a function of the nearest neighbor shell. It is clearly visible in this figure that ξ is positive for a single atom (0 nearest neighbor shells), but negative for small fcc balls. With increasing nearest neighbor shell number ξ approaches 0 from below or becomes even positive at some stage. As expected, those basis sets with diffuse functions (such as au SVP) need more nearest neighbors for recovering the positive definiteness ξ of the k space overlap than the basis sets, where these functions are dropped (such as au SVP-wsp). For these basis sets we also determined, as given in Table 4.1, the number of nearest neighbor shells and total atom number of the fcc ball necessary to arrive at a positive ξ and for ξ to converge to a fixed value.[8] Note the extremely large number of atoms necessary to obtain a converged ξ in the SVP basis sets. This outlines the importance of overlap contributions and confirms the common statement that Gaussian basis functions possess long tails.

---

volution theorem. We work in three dimensions, and writing $S(\vec{y}) = \int d^3x \phi(\vec{x})\phi(\vec{x} - \vec{y})$, we get $S(\vec{k}) = \int d^3y e^{-i\vec{k}\cdot\vec{y}} S(\vec{y}) = \left|\phi(\vec{k})\right|^2 \geq 0$.

[8] For all elements in Table 4.1 the values "nn shells" and N_{atoms} in the row "ξ converged" are due to the TURBOMOLE cutoffs for the overlap matrix elements, except for al SVP-wsp-opt. There, the cutoff of the basis set is at "nn shells " 13, corresponding to a total number of atoms N_{atoms} of 321.

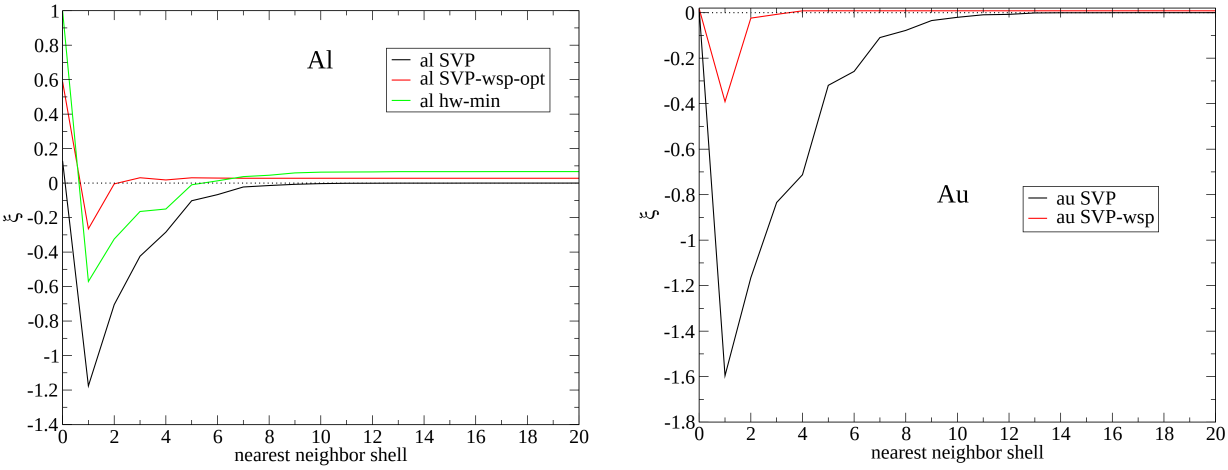

Figure 4.6: The positive definiteness measure ξ is plotted for the metals Al and Au as a function of the nearest neighbor shell for various basis sets (see the legends). Details on the basis sets are given in Sec. F.4, the periodicity length is $N_i = 16$ (see Eq. (D.8)), and the fcc balls are constructed with a lattice constant $a_0 = 4.05$ Åfor Al and $a_0 = 4.08$ Åfor Au.

It is at the moment not possible for us, to calculate clusters of more than 555 atoms in the basis sets al SVP and al SVP-wsp-opt, 683 in the basis set al hw-min, and 429 atoms in the basis sets au SVP and au SVP-wsp. Comparing to the data listed in Table 4.1, the al SVP-wsp-opt, the al hw-min, and the au SVP-wsp basis sets correspond to "ξ converged" electrode clusters. For al SVP we have reached the region of positive k space overlap, but for au SVP negative eigenvalues of the k space overlap need to be tolerated to some extend.

In Figs. 4.7 and 4.8 we show the relevant electrode fcc balls studied in this work. The small clusters may be used for checks regarding the convergence of certain properties such as the bulk DOS. By switching to another basis set, the basis set dependence of the results can be checked. For the HOMO energies of the biggest clusters we get -4.261 eV for Al_{555} in the basis al SVP, -4.039 eV for Al_{555} in the basis al SVP-wsp, -5.487 eV for Al_{683} in the basis al hw-min, -5.013 eV for Au_{429} in the basis au SVP, -3.891 eV for Au_{429} in the basis au SVP-wsp. Due to the cutting out of the most diffuse basis functions the electronic structure may differ substantially in the basis sets of SVP-wsp quality. Also for al hw-min the HOMO is at a very different position as compared to the al SVP results. It would of course be desirable to improve the basis set quality instead of reducing it by cutting out the diffuse basis functions. With respect to the data of Table 4.1 the positive definiteness property would require the study of even bigger fcc balls well beyond our present computer[9] resources.[10]

---

[9] We used Opteron 64bit architectures with a main memory of up to 16 GB.

[10] These problems should also arise in the study of solids in Gaussian basis sets even if PBCs are available. The smallest orbital exponents of the basis functions need to be increased in studies of solids with Gaussian basis sets, as seems to be the case in studies with the program CRYSTAL [185, 186, 187, 188, 189, 190].

	$\xi > 0$		ξ converged	
basis set	nn shells	N_{atoms}	nn shells	N_{atoms}
al SVP	17	459	25	791
al SVP-wsp-opt	3	43	11	225
al hw-min	6	87	19	555
au SVP	24	767	28	959
au SVP-wsp	4	55	10	201

Table 4.1: Number of nearest neighbor shells (nn shells) needed for ξ to become positive and to converge to a constant value. The total number of atoms (N_{atoms}) of these fcc balls is also indicated. As in Fig. 4.6, the periodicity length is $N_i = 16$ (see Eq. (D.8)) and the fcc balls were constructed with a lattice constant $a_0 = 4.05$ Å(Al) and $a_0 = 4.08$ Å(Au).

From the clusters shown in Figs. 4.7 and 4.8 we extract the parameters from the center at position 0 to the neighboring atoms at position j yielding the matrix elements $S^{ball}_{0\alpha,j\beta}$ and $H^{ball}_{0\alpha,j\beta}$ where α and β stand for the basis functions of the atoms at 0 and j. We choose the elements from the center to the surrounding atoms because the center has the highest number of nearest neighbors. We will, for reasons of brevity, often suppress the orbital indices and write S^{ball}_{0j} and H^{ball}_{0j}, which are then matrices with appropriate orbital dimensions.

If orthogonal parameters shall be extracted according to procedure 2 of Fig. 4.4, we orthogonalize the basis via a Löwdin orthogonalization with the full cluster overlap S^{ball} [81]. In this way we come to the Hamiltonian $H^{orth,ball} = \left(S^{ball}\right)^{-1/2} H^{ball} \left(S^{ball}\right)^{-1/2}$ from which we can extract the orthogonal parameters $H^{orth,ball}_{0j}$ from the center to all its nearest neighbors.

The matrix elements $S_{0,j}$, $H_{0,j}$, and H^{orth}_{0j} as employed in the construction of surface (or bulk) Green's functions need to be conform with the fcc space group of the crystal. In the following paragraphs we will study how we come to such parameters.

4.3.2 Imposing the fcc space group on the electrode Hamiltonian

With the help of Eq. (F.11) we can generate parameters $Y_{0,j}$ ($Y = S$, H, or H^{orth}) that obey the fcc space group $(O_h, T_{\vec{R}})$. As the fcc ball clusters possess O_h point group symmetry (see Figs. 4.7 and 4.8), this symmetry is also contained in the elements S^{ball}_{0j} and H^{ball}_{0j}.[11] It seems that also $H^{orth,ball}_{0j}$ fulfills this O_h symmetry within the numerical error. Concerning the translational symmetry this is necessarily fulfilled for $S_{0,j}$ because the overlap only depends on the relative distance between two atoms. However, the elements of the Fock operator are computed self-consistently and surface effects are included in their calculation. For this reason the translational symmetry needs to be imposed (see Fig. F.4). We observe generally that the deviations $\Delta Y_{0j} = \max(\left|Y_{0j} - Y^{ball}_{0j}\right|)$ between the symmetrized parameters Y_{0j}

---

[11] Indeed we exploit this point group symmetry in TURBOMOLE to accelerate the computation. The effort decreases with the order of the group, which is $N_G = 48$ for O_h.

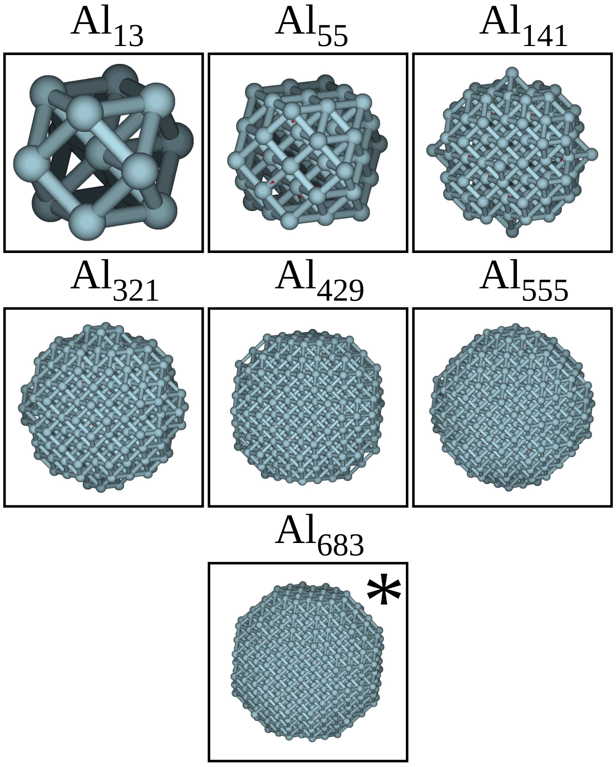

Figure 4.7: Fcc balls for the metal Al. All clusters, except the biggest marked with a star, were computed in the basis sets al SVP, al SVP-wsp-opt, and al hw-min. Al_{683} could only be computed in the basis set al hw-min.

and the parameters of the original unsymmetrized Y_{0j}^{ball} decrease with increasing cluster size ($Y = H$ or H^{orth}).[12] In Table 4.2 we list these deviations for the different clusters of Figs. 4.7 and 4.8. The clear trend of decaying ΔY_{0j} with cluster size of the fcc ball can be observed.

We summarize the steps of procedure 1 that works with nonorthogonal parameters and procedure 2 that works with orthogonal parameters (see Fig. 4.4):

- procedure 1:

  $$\left\{S_{i,j}^{ball}; H_{i,j}^{ball}\right\} \overset{\text{extract}}{\Longrightarrow} \left\{S_{0,j}; H_{0,j}^{ball}\right\} \overset{\text{impose fcc symmetry}}{\Longrightarrow} \left\{S_{0,j}; H_{0,j}\right\}$$

  The overlap and Hamiltonian parameters S_{0j} and H_{0j} are in the standard orientation of the fcc lattice. In order to use them for a computation of the surface Green's functions of the left and right electrodes g_{LL}^r and g_{RR}^r a transformation to the lattice orientation of the corresponding electrode may be required. This gives the set of parameters $S_{0j}^{(X)}$ and $H_{0j}^{(X)}$ with $X = L$ or R. The self-energy is then given by Eq. (4.19), where the Green's functions g_{XX}^r are surface electrode Green's functions

---

[12] For S_{0j} the differences ΔS_{0j} are less than 10^{-14}, independent of the cluster size.

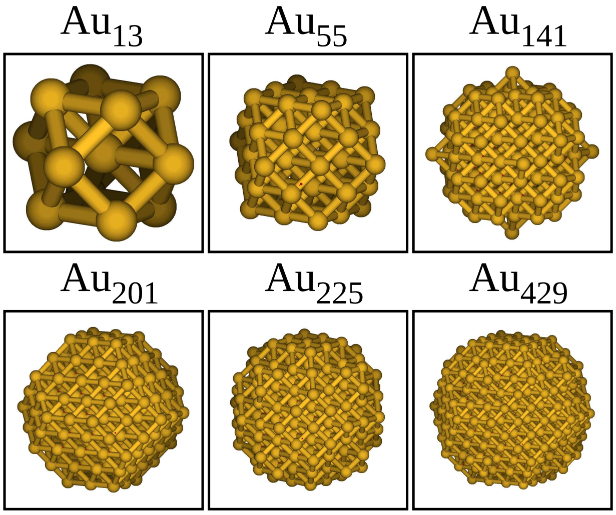

Figure 4.8: Fcc balls for the metal Au. All clusters were computed in the basis sets au SVP and au SVP-wsp-opt.

(constructed as explained in Sec. D.2).[13] Their computation is described in Sec. D.1. In this way we have constructed a self-energy consistently in a nonorthogonal basis set. We call this recipe procedure 1.

- procedure 2:

$$\left\{S_{i,j}^{ball}; H_{i,j}^{ball}\right\} \overset{\text{Lwdin orthogonalization}}{\Longrightarrow} \left\{\mathbb{1}_{i,j}; H_{i,j}^{orth,ball}\right\} \overset{\text{extract}}{\Longrightarrow} \left\{\mathbb{1}_{0,j}; H_{0,j}^{orth,ball}\right\}$$

$$\overset{\text{impose fcc symmetry}}{\Longrightarrow} \left\{\mathbb{1}_{0,j}; H_{0,j}^{orth}\right\}$$

In this way we arrive at the parameters H_{0j}^{orth}. From these parameters we can then construct, after appropriate rotations, the parameters $H^{orth,(X)}$ and orthogonal surface or bulk Green's functions. In order to construct a self-energy in a nonorthogonal basis from these orthogonal Green's functions we need to orthogonalize the coupling elements to the electrodes. We do this by a Löwdin transformation with the overlap matrices $S_{XX}^{contact}$ of the contact system to get

$$\Sigma_X^r(E) = (H_{CX} - ES_{CX})S_{XX}^{-1/2} g_{XX}^{orth,r} S_{XX}^{-1/2}(H_{XC} - ES_{XC}).$$

We call this recipe procedure 2.

It should be clear this procedure, which works with orthogonal parameters as compared to the nonorthogonal ones in procedure 1, contains an uncontrolled approximation, namely the transformation to an orthogonal basis set. The Löwdin transformations depend on the concrete overlap structure and thus cluster geometry. Therefore

---

[13] For testing purposes, also bulk Green's functions may be chosen for g_{XX}^r (see also the discussion in Sec. 5.1.5).

Al						
	al SVP		al SVP-wsp		al hw-dz	
N_{atoms}	ΔH_{0j}	ΔH_{0j}^{orth}	ΔH_{0j}	ΔH_{0j}^{orth}	ΔH_{0j}	ΔH_{0j}^{orth}
13	2E-2	4E-2	2E-3	8E-3	7E-3	8E-3
55	9E-4	3E-2	3E-4	2E-3	3E-4	9E-4
141	6E-4	7E-3	2E-4	6E-4	5E-4	4E-4
321	4E-4	5E-3	2E-4	2E-4	3E-4	3E-4
429	2E-4	3E-3	5E-5	4E-5	6E-4	3E-3
555	2E-4	3E-3	7E-5	7E-5	2E-4	2E-4
683	–	–	–	–	8E-5	1E-4

Au						
	au SVP		au SVP-wsp		–	
N_{atoms}	ΔH_{0j}	ΔH_{0j}^{orth}	ΔH_{0j}	ΔH_{0j}^{orth}	–	–
13	3E-2	9E-2	3E-3	4E-2	–	–
55	3E-3	3E-1	6E-4	3E-2	–	–
141	4E-4	3E-1	3E-4	1E-2	–	–
201	5E-4	8E-2	8E-5	7E-3	–	–
225	9E-4	8E-2	6E-4	7E-3	–	–
429	5E-4	4E-2	4E-5	3E-3	–	–

Table 4.2: Comparison of deviations $\Delta Y_{0j} = \max(|Y_{0j} - Y_{0j}^{ball}|)$ between parameters Y_{0j} in fcc symmetry and the unsymmetrized parameters Y_{0j}^{ball} for different basis sets and cluster sizes. Given is the lowest upper bound to the error. The errors have been determined in the set of rational numbers of the form $n \times 10^{-m}$ with $n \in [1, ..., 9]$ and $m \in \mathbb{Z}$.

the multiplication with $\left(S^{ball}\right)^{-1/2}$ in the orthogonalization of $H^{orth,ball}$ uses different orthogonal orbitals than the orthogonalization of the contact couplings, which involves a multiplication with $S_{XX}^{-1/2}$.

We want to point out that an unexpectedly slow radial decay is observed for the Hamiltonian H_{0j}^{orth}. To demonstrate this, we analyze the fcc ball Au_{429} in the basis sets au SVP and au SVP-wsp. We divide the cluster into its nearest neighbor shells and plot for every shell the maximum absolute value $\max(|Y_{0j}|)$ (with $Y = S$, H and H^{orth}). The plot is shown in Fig. 4.9. While the maximum absolute values of the overlap and Hamiltonian elements S_{0j} and H_{0j} start to decay similarly and roughly exponentially from a certain nearest neighbor shell on, this is different for H_{0j}^{orth}. It can be observed that after an initial decay H_{0j}^{orth} seems to stay constant. This shows that a Löwdin orthogonalization changes the radial dependence of the Hamiltonian matrix elements strongly.

The identification of the Hamiltonian elements of two orthogonal basis sets that have been generated by Löwdin transformations with different overlap structures should be avoided because such basis set identifications result in uncontrolled errors. This points out that procedure 1, working consistently in a nonorthogonal basis set, should be preferred to

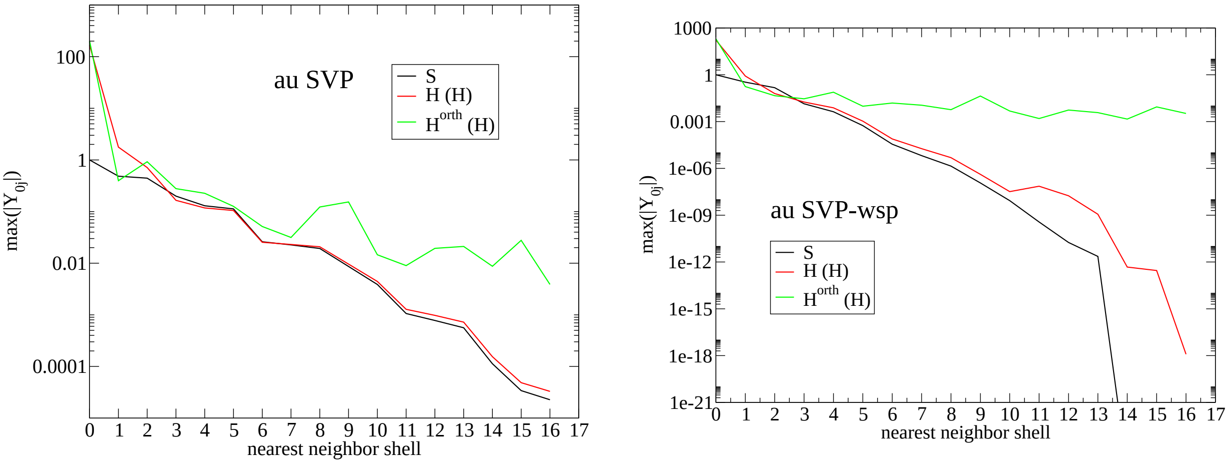

Figure 4.9: Maximum absolute value $\max(|Y_{0j}|)$ (with $Y = S$, H and H^{orth}) as a function of the nearest neighbor shells. The parameters are obtained from fcc balls Au_{429} in the basis sets au SVP and au SVP-wsp.

procedure 2. Unfortunately procedure 1 might not be applicable, if the positive definiteness ξ of the overlap is difficult to achieve for practical limitations of the cluster size (see Eq. (4.26) and Table 4.1).

4.3.3 Convergence of bulk densities of states

The bulk DOS can be used as a measure for the convergence to a good solid state description. For large enough systems we observe the equivalence of the DOS construction with respect to the three different orthogonal Hamiltonians H_k^{orth}, which are constructed either via procedure 2 or by use of Eqs. (D.18) and (D.19) for the nonorthogonal parameters of procedure 1. If the positive definiteness property is not completely fulfilled due to a too small cluster size, as it is the case for the SVP basis sets, then the construction of the DOS from the orthogonal parameters is of a higher quality than that resulting from the nonorthogonal constructions (Eqs. (D.18) and (D.19)). For this reason we show in Fig. 4.10 the DOS as obtained with parameters constructed via procedure 2 and as extracted from different Al and Au fcc balls of Figs. 4.7 and 4.8. The basis sets employed are al SVP and au SVP, the number of k points is 32^3, and the broadening for Al is $\eta = 0.02$ H, while for Au it is $\eta = 0.01$ H. These parameters will also be used for the electrode broadening in conductance calculations.[14] We observe both for Al and Au that the bulk DOS seems well converged with respect to the fcc balls' size. In the figure also the Fermi energy is indicated. It is set roughly into the middle of the HOMO and LUMO energy of the biggest cluster calculated. For Al we get $E_F = -4.25$ eV (al SVP), $E_F = -4.02$ eV (al SVP-wsp-opt) and $E_F = -5.46$ eV (al hw-min), and for Au $E_F = -5.00$ eV (au SVP) or $E_F = -3.87$ eV (au SVP-wsp).

---

[14] As explained in Sec. D.1.1 we choose the broadening conveniently so that the DOS looks smooth for a certain number of employed k points.

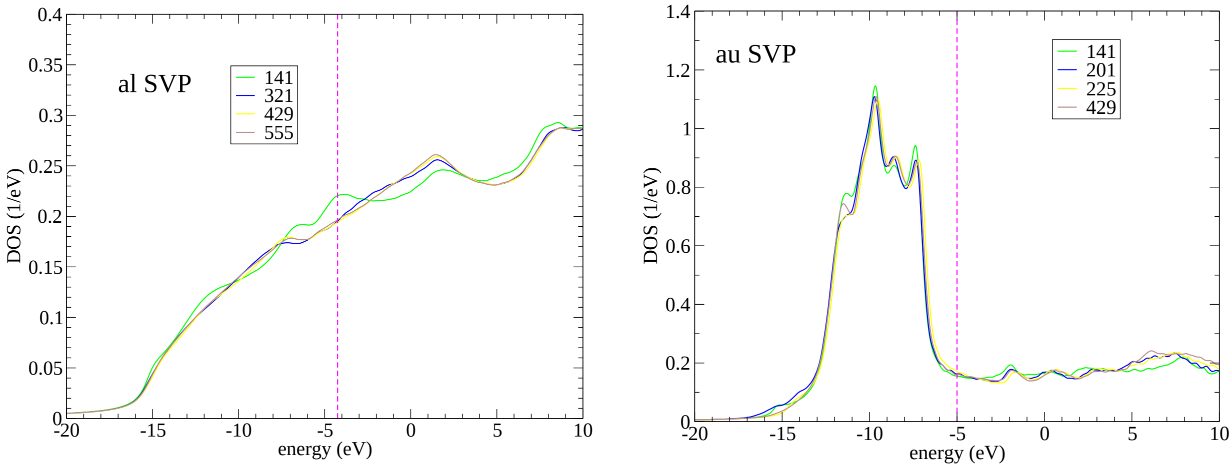

Figure 4.10: Bulk DOS for Al and Au in the basis sets al SVP and au SVP for some selected clusters of Figs. 4.7 and 4.8. The broadening parameter η is 0.02 and 0.01 H for Al and Au, respectively. The number of k points involved in the construction is 32^3.

4.4 Self-consistent calculation of the electronic structure of infinite systems

In the present scheme displayed in Fig. 4.4 we perform two separate calculations of finite systems. The parameters extracted are "put together" and we compute the conductance. There arises some uncertainty about the position of the Fermi energy E_F. In principle a Fermi energy does not even exist for finite systems and we should talk about HOMO and LUMO levels. Due to the finiteness of the two separate systems their HOMO and LUMO levels will be separated by a certain gap and their HOMO and LUMO positions will not be the same. So where should be the Fermi energy needed in a conductance calculation? Currently we set this energy to an energy in the HOMO-LUMO gap of the fcc ball, which is very metallic. The Fermi energy in our formalism is just the point, where we read off the conductance in a transmission curve, and it enters at no other point.

In order to eliminate the uncertainty of the position of E_F completely, it has been proposed that fully self-consistent DFT calculations of the infinite coupled system should be carried out [151, 150, 152, 127, 153, 128, 191, 192]. In this way the electronic structure is computed for the coupled system, and also the nonequilibrium situation of a bias applied over a junction can be analyzed. It is thus highly desirable to develop such a scheme and in particular references [150, 127, 128, 153, 191] suggest that this should also be possible for the quantum chemistry approach. All our attempts were, however, unsuccessful and we will show in short why. Analysing Refs. [150, 127, 128, 153, 191] we want to point out that in all of them approximations in the electrode description (or the coupling of the central system to the electrodes) are made. In Ref. [153] one finally resorts to energy independent self-energies, whereas Refs. [150, 127, 128, 191] all describe their electrodes in a minimal basis tight-binding model with an orthogonal basis set. Already from this orthogonal basis

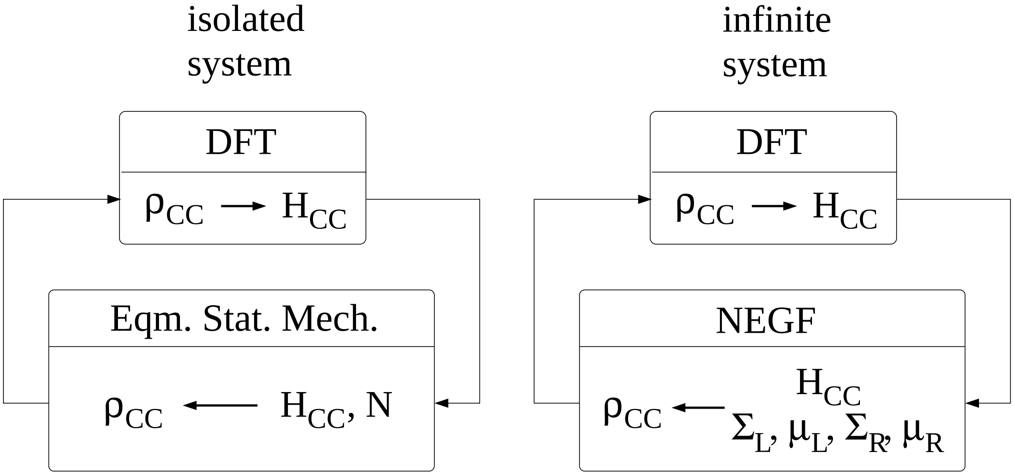

Figure 4.11: Sketch of schemes for the determination of the electronic structure of a finite system (left panel) and an infinite system (right panel) [153]. For the isolated system, the density matrix is constructed by occupying the states of the Hamiltonian H_{CC} from the lowest to the highest energy, where N levels are occupied according to the number of electrons in the system. For an infinite system the nonequilibrium Green's function (NEGF) formalism is employed. In the construction of the density matrix ϱ_{CC} the self-energies Σ_X and chemical potentials μ_X ($X = L$ or R) of the electrodes enter.

set an uncontrolled approximation results. In this sense these latter references on the quantum chemistry approach do not appear to be real first principles calculations due to the semiempirical parameters employed in the electrode description.

Another class of references [151, 152, 192, 159], including the commercially available code TRANSIESTA, uses software with the capability of PBCs. Recently these groups work very successfully, and we believe that only with PBCs, that offer the possibility to eliminate surface effects, a real ab-initio description of the molecular junctions is possible. Let us now argue, how we come to this point of view.

4.4.1 The self-consistent scheme

There is a nice pictorial representation in Ref. [153] of the way, in which the electronic structure of finite systems is determined in conventional DFT, and how this procedure should be changed for infinite systems. We show the idea in Fig. 4.11. On the left the scheme for isolated systems can be seen. We start with a guess of the overlap and Hamiltonian (or KS Fock operator) S_{CC} and H_{CC} of a finite system, called C. Next we construct the density matrix ϱ_{CC}, and iterate until convergence is achieved. In the Green's function formalism this scheme is analogous. We get S_{CC} and a guess for H_{CC}, construct the retarded Green's function $G^r_{CC}(E) = (E^+ S_{CC} - H_{CC})^{-1}$. The density matrix ϱ_{CC} is determined as the integral over the imaginary part of G^r_{CC} up to an energy, where the system is charge neutral (this corresponds to the occupation of the lowest eigenvalues in order to construct ϱ_{CC}), so that

$$\varrho_{CC}^{(new)} = -\frac{1}{\pi}\int_{-\infty}^{E_N} dE \mathrm{Im}\left[G_{CC}^r(E)\right] \tag{4.27}$$

with the equation $N = \mathrm{Tr}\left[\varrho_{CC}^{(new)} S_{CC}\right]$ for the determination of E_N. As explained in Sec. B.3.3 (see in particular Eq. (B.48) and Fig. (B.2)) this integration can be carried out in the complex plane in order to save integration points, if this is convenient [150, 152, 127].

We implemented the above scheme for an isolated system, and there was no problem to converge the system to an energy close to that determined by TURBOMOLE. Here we used a simple density mixing of the form $\varrho_{CC}^{(n+1)} = (1-g)\,\varrho_{CC}^{(n)} + g\varrho_{CC}^{(new)}$ and a damping constant g. Hence, for isolated systems there are no problems.

Let us now come to the infinite system in equilibrium. Here the self-energies are added and G_{CC}^r becomes

$$G_{CC}^r = \left(ES_{CC} - H_{CC} - \Sigma_L^r - \Sigma_R^r\right)^{-1}$$

Again Eq. (4.27) is used to determine ϱ_{CC}. This density matrix is then given back to the quantum chemistry routine that shall determine the Hamiltonian. A first question arises here on the role of E_N. There are charge contributions from the outside that one might need to include ($N_C = \sum_{X=L,C,R} \mathrm{Tr}\left[\varrho_{CX} S_{XC}\right]$). Indeed we found out that the numerical routine becomes unstable, if electrode charge contributions are included, because TURBOMOLE will then compute with a density matrix ϱ_{CC} of slightly different charge $N = \mathrm{Tr}\left[\varrho_{CC} S_{CC}\right]$, depending on the iteration. The problem is that TURBOMOLE has only information about the finite system C in the construction of H_{CC} and not about the system LCR. Therefore E_N should be fixed to the charge of the central system.

Thinking further about this point there appear more problems. The system C is embedded into the system LCR. A calculation of the complete LCR system will use basis functions of L and R to describe states in C, more so due to the long tail of Gaussian basis functions. The construction of H_{CC} from the density ϱ_{CC} will make a severe basis set superposition error. But even more severe should be the effect of neglected contributions of the L and R regions to the Kohn-Sham Fock operator of system C, especially the Coulomb terms. It is a well known fact from the implementation of PBCs with Gaussian basis sets that these electrostatic contributions from far away atoms are very important and that their accurate determination plays a crucial role in a proper convergence of an total energy calculation [193, 185, 189]. Due to the finiteness of our systems and the fact that the step $\varrho_{CC} \rightarrow H_{CC}$ involves only the system C these contributions are completely neglected if no special precautions are taken. The TRANSIESTA community seems to be aware of these problems. They state that the calculation of their "density matrix correct part" needs a "Hamiltonian correct part" in a bigger region containing the "density matrix correct part" [152].

Assume we had PBCs as sketched in Fig. 4.3. After a computation of ϱ_{CC} the DFT procedure will compute H_{CC} with PBCs applied. The missing contributions to the Hamiltonian are then included (at least approximately), because the PBC makes the system be surrounded by other atoms. This explains, why PBC software should be more appropri-

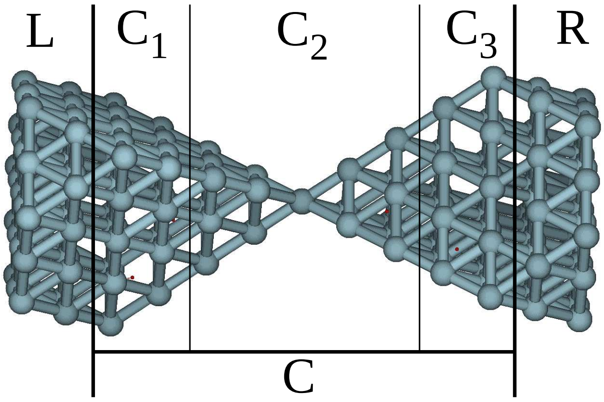

Figure 4.12: Al test system for checking the self-consistent procedure for the calculation of the electronic structure. As usual, the system is divided into parts L, C, and R. As shown, the region C may be subdivided into further regions C_1, C_2, and C_3.

ate for self-consistent calculations of infinite systems than software, where these boundary conditions are missing.

4.4.2 A minimal test system

We want to illustrate the problems mentioned previously at a simple test system. For this purpose we calculate a large LCR system in TURBOMOLE. As test system we used a pyramid of Al atoms with the basis set al hw-min, displayed in Fig. 4.12. So we know the complete DFT Hamiltonian for the LCR system and all its parts when we choose a concrete partitioning into regions L, C, and R. In this way we know, how the Hamiltonian of the system C embedded into the finite system LCR looks like. By using $g^r_{XX} = (ES_{XX} - H_{XX})^{-1}$ of the finite clusters ($X = L$ and R) we can construct the exact self-energies $\Sigma^r_X = (H_{CX} - ES_{CX})\, g^r_{XX}\, (H_{XC} - ES_{XC})$. The self-consistent procedure applied to the system C coupled via the exact self-energies Σ^r_X of the finite L and R regions should not change the Hamiltonian H_{CC}.

Our findings are in contrast to this. When we carry out the integration scheme, the energies of the C part of the system start increasing by several Hartree (several ten eV)! Let us point out that from the technical side we checked all our routines carefully. In addition a contour integration of the previous kind has already been implemented by us in the context of the TB models (see Eq. (2.3)), where we developed an adaptive integration scheme of the closed Newton-Cotes form (see Sec. E.2). Within the TB formalism no problem related to the charge neutrality loop ever appeared in the sense that we could not converge a system. Due to the well tested routines, their modular structure directly usable in the DFT formalism, and careful checks, we can virtually exclude any error.

Due to the remark of Ref. [152], where it is stated that a "density correct region" requires a larger "Hamiltonian correct region" in which the density correct region is contained, we started subdividing the central system C further into subregions C_1, C_2, and

C_3. The idea was to fix the Hamiltonian of the regions C_1 and C_3, because in these regions the error due to the neglect of contributions of the L and R regions to the KS DFT Hamiltonian should be more severe than for region C_2. But even with fixed Hamiltonian contributions $H_{C_1C_1}$ and $H_{C_3C_3}$ we obtained a final total energy more than 10 H= 272 eV above the starting point of -137.394 H. In this sense the fixing of parts C_1 and C_3 did not help solving the problems encountered before.

In conlusion, these results show that substantial errors are made if the step $H_{CC} \rightarrow \varrho_{CC}$ in Fig. 4.11 is done for the infinite system by including self-energies without properly accounting for contributions to the KS Hamiltonian from atoms outside of the central system C in the step $\varrho_{CC} \rightarrow H_{CC}$. The accurate inclusion of electrostatic terms is known to be crucial in the calculation of infinite systems [193, 185, 189]. An approximate accounting for them seems possible, when software with the capability of PBCs is used.

For these reasons the self-consistent determination of the electronic structure of the infinite system, namely a contact region coupled to semi-infinite electrodes on both sides, is currently hindered due to the missing ability to use periodic boundary conditions in TURBOMOLE. Therefore, it will unfortunately not be possible in this work to compute device characteristics out of equilibrium.[15]

Nevertheless, we will show that due to TURBOMOLE's ability to compute clusters consisting of many atoms even our present transport scheme yields very satisfactory results. Indeed we will demonstrate in Chap. 5 at the example of metallic atomic contacts that our results exhibit some kind of convergence. In addition they are completely in line with experimental observations and the results of previous DFT based theoretical studies. In this sense the self-consistent determination of the electronic structure of the infinite system does not appear to be urgently required for the determination of the conductance.

4.5 Evaluation of the method

In the previous section we outlined a problem of our present scheme, namely that the electronic density of the infinite system is not computed self-consistently. In contrast our method calculates separate electrode and contact parameters and puts them together to determine the transmission curve (see Fig. 4.4). This causes some uncertainty about the position of the Fermi energy. For large enough contact and electrode fcc ball clusters their HOMO and LUMO levels should converge to a common value so that the self-consistent determination of the Fermi energy may not be needed. In practice of course it may be difficult to reach this limit due to computer hardware limitations.

We will demonstrate now that, despite the technical problems detailed above, our method yields results that are in perfect agreement with experiments and other more established quantum transport methods. For this purpose we show a direct comparison

---

[15] Also from the point of view of avoiding surface effects and parameter mismatch problems in the self-energy construction, periodic boundary conditions, as shown in Fig. 4.3, are highly desirable for the implementation of a quantum transport scheme.

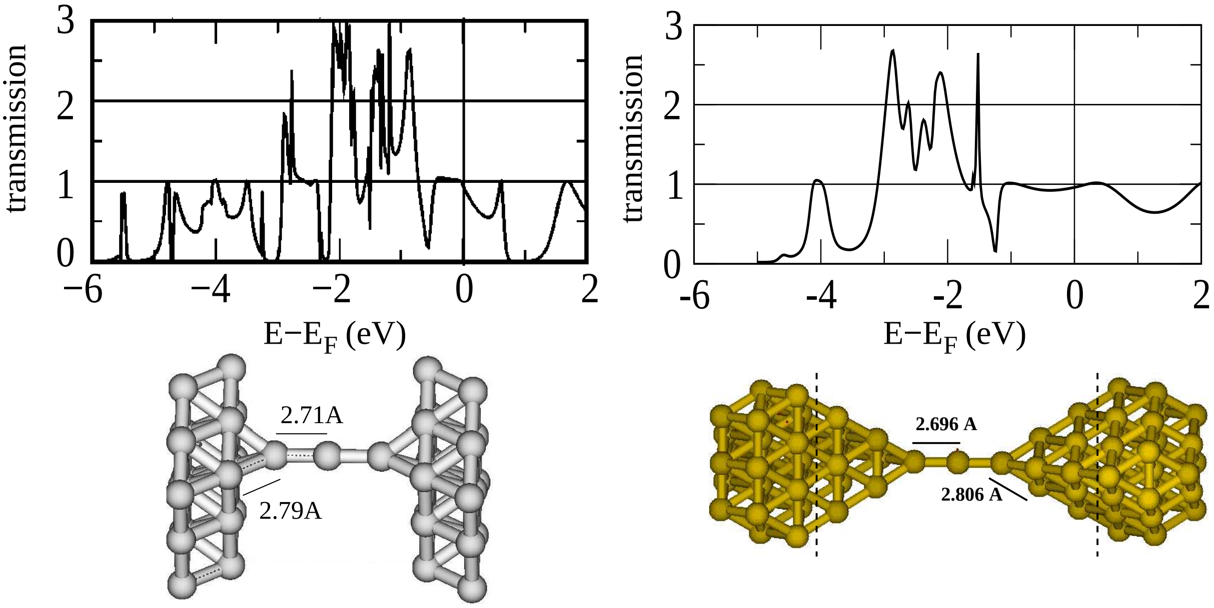

Figure 4.13: Comparison between results of Ref. [152] (left panel) and those obtained with the method developed in this work (right panel). In both cases the atomic contact consists of a three-atom chain with very similar interatomic distances and electrodes oriented in the [111] direction.

with results of the commercially available TRANSIESTA program [152]. As test system we choose a three atom Au chain and an electrode oriented in the [111] direction.

Different experiments have shown that the conductance of Au contacts exhibits a tendency towards integer values in the last stages of the wire formation [82, 20, 87, 89]. As discussed in Sec. 2.4, the most dominant feature in the experimental low-temperature conductance histogram is a pronounced peak at $1G_0$, which is due to single atom contacts or chains of atoms (see Fig. 2.1) [82, 20]. On the theoretical side this result has been confirmed in various DFT calculations [152, 84, 85].

In Fig. 4.13 we show now the comparison between our result and those of Ref. [152] (see Fig. 9d therein). We use procedure 1 with surface Green's functions (see Fig. 4.4). The fcc ball used is a Au_{429} cluster with a HOMO energy of -5.01 eV and we set the Fermi energy to $E_F = -5.00$ eV. The contact calculation involves an Au contact of 77 atoms as shown in the right lower part of the figure. Also indicated is the partitioning into the left, central and right regions. For reasons of better comparison with Ref. [152] we shifted E_F to the origin. We observe that all the basic features in our transmission curve are the same as in the TRANSIESTA calculation. After the d band with a high final peak there comes in both cases a dip in the transmission. $T(E)$ recovers after that, and a flat region with a transmission of around 1 is visible. In both cases the conductance is close to $1G_0$ at the Fermi energy E_F. To be precise we obtain a transmission $T(E_F) = 0.96G_0$.

We will come back to a more careful analysis of these results in Sec. 5.1. For the moment let us conclude that the method developed in this work is very well compatible with the experimental expectations for the conductance of a Au atomic chain. Furthermore our method compares favorably to the results of other ab-initio methods.

4.6 Conclusions

In this chapter we presented the details of a first-principles method to compute the electric charge current in nanoscale systems. The method is based on the implementation of density functional theory in the quantum chemistry package TURBOMOLE.

We developed two practical schemes, called procedures 1 and 2, by which we model the electronic structure of an infinite system such as a molecule coupled to two semi-infinite electrodes. The schemes differ slightly in the construction of the electrode self-energies. In both cases the contact region and the electrodes are treated within the same basis set. The contact and electrode description are performed using large atomic clusters. We showed, how electrode parameters can be extracted from finite clusters involving a symmetrization procedure. For these electrode parameter clusters we pointed out a size requirement arising from the physically required positive definiteness of extracted overlap matrix elements. While procedure 1 works consistently in a nonorthogonal basis set, procedure 2 involves an orthogonalization step in the electrode description that makes this scheme more approximate. Procedure 1 should therefore be preferred to procedure 2. However, one may need to resort to procedure 2, if the positive definiteness requirement for the overlap in the nonorthogonal basis cannot be fulfilled for reasons of practical computer hardware limitations. For the electrode parameters extracted from finite fcc balls, we presented the convergence of the bulk density of states with respect to the fcc ball's cluster size.

Subsequently we commented on unsuccessful tests of the implementation of a self-consistent procedure by which the electronic structure of a truly infinite system is calculated. We pointed out a deficiency in the naive application of the standard scheme by which these calculations should be carried out. This deficiency is the neglect of contributions of atoms in the electrodes to the Hamiltonian of the central system, if no periodic boundary conditions are used. As such periodic boundary conditions are currently not available in TURBOMOLE we could not implement an ab-initio self-consistent procedure for the determination of the electronic structure of an infinite system.

From the deficiency an uncertainty with respect to the position of the Fermi energy of the central system results. It may be overcome by computing contact geometries comprising a large number of electrode atoms. We demonstrated for a gold atomic contact that the method in its present form (procedure 1 combined with surface Green's functions) gives results perfectly in line with experimental expectations. In addition our results compare very well with results of more established transport methods that perform a self-consistent calculation of the electronic structure of an infinite system. Within our method the only "free parameter" is the partitioning of the contact system into a left, central, and right region. For this reason we believe that the proposed procedure can be called an ab-initio description of electron transport.

Chapter 5

Ab-initio calculations of the transmission of metallic atomic contacts

In the last chapter we presented a first-principles method for the prediction of conduction properties of infinite systems. In Sec. 4.5 we already applied it to a Au contact, namely a chain of three Au atoms, in order to validate the results of our method. Indeed they turned out to be in line with experimental expectations and other theoretical studies present in the literature. In this chapter we will explore further metallic atomic contacts, namely Au and Al metallic contacts, which will serve as further test systems for our method. After the study of these metallic test systems we will be in a position to apply our method in the field of molecular electronics (see the following Chap. 6), the ultimate goal behind our effort of developing an ab-initio approach to quantum transport.

In this chapter we will start out by discussing the conduction properties of Au systems, in particular a Au four-atom chain, a three-atom chain, and a two-atom chain. For them we will discuss the transmission, the channel decomposition of the transmission, and the local density of states (LDOS) for the atoms in the narrowest part of the contact. Even more important, we will demonstrate that our transmission curves converge, if contact geometries are chosen large enough. In addition we will compare the performance of the procedures 1 and 2 of Fig. 4.4, and investigate the differences in the transmission properties arising from an exchange of surface by bulk electrode Green's functions. Finally we will discuss ideal Al contacts. We will follow basically the same agenda as for Au. This means that we will look at the transmission, the channel decomposition of the transmission, the local density of states (LDOS) for the atoms in the narrowest part of the contact, and show again the convergence of the obtained transmission curves. Furthermore we will compare the results of a high quality quantum chemistry basis to the predictions of a minimal basis model.

In the subsequent sections we will use the basis sets au SVP for the description of Au, and al SVP and al hw-min for Al. Electrode parameters will be taken from the biggest fcc ball clusters computed (see Figs. 4.7 and 4.8), namely Al_{555} for al SVP, Al_{683} for al

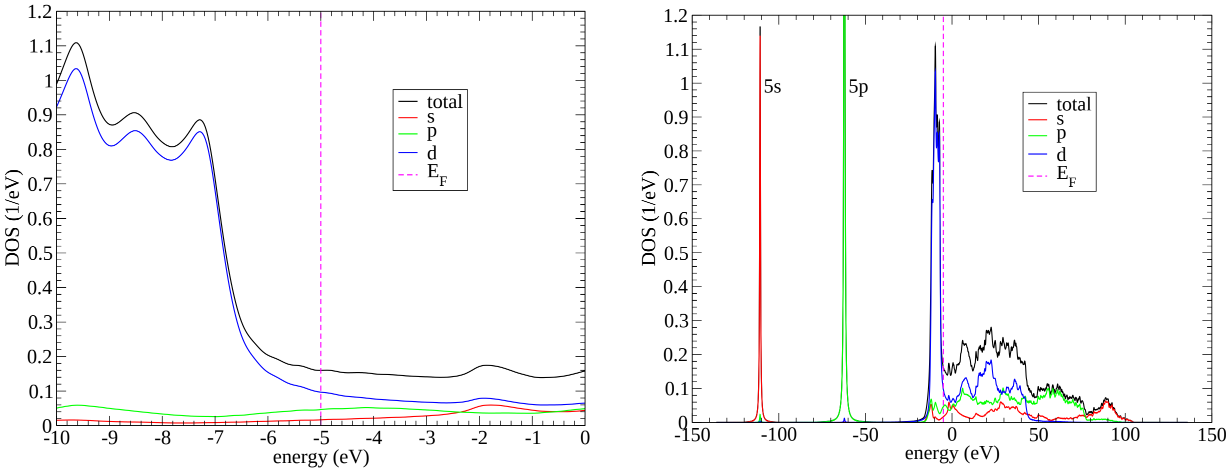

Figure 5.1: DOS for a bulk Au atom resolved in its orbital contributions. On the left the DOS is shown in a region around E_F, while the right panel displays a large energy interval. As indicated the first peak in the right panel corresponds to the 5s orbitals, the second one to the 5p orbitals, and only after that the electronic conduction band is visible, starting mainly with d contributions.

hw-min, and Au_{429} for au SVP. As explained before we choose the Fermi energy to be in the HOMO-LUMO (highest occupied/lowest unoccupied molecular orbital) gaps of these fcc balls, resulting in $E_F = -4.25$ eV (al SVP), $E_F = -5.46$ eV (al hw-min), and $E_F = -5.00$ eV (au SVP). In Chap. F.4 of the appendix the basis sets of relevance for the following sections are described.

5.1 Conduction properties of gold atomic chains

In this section we want to study the conduction properties of Au contacts, in particular a Au four-atom chain, a Au three-atom chain, and a Au two-atom chain. As mentioned in Sec. 4.5 one expects a conductance of around $1G_0$ for these structures from experimental measurements [82, 20, 87, 89] as well as from density functional theory (DFT) calculations [152, 84, 85]. This value of the conductance should be due to a dominant single transmission channel arising mainly from the s valence of the noble metal Au.

Let us first discuss the DOS for a bulk Au atom as visible in Fig. 5.1. The Fermi energy E_F for Au is located in a fairly structureless flat region of the DOS, located somewhat above the d band (see the left panel of Fig. 5.1). From the atomic point of view Au has an electronic configuration $5s^2 5p^6 5d^{10} 6s^1$ and one might have expected a strong contribution of the s orbitals at the Fermi energy. But also due to the higher multiplicity of the p and d states the DOS at E_F is dominated by their contributions. This signifies that in the bulk metal a strong hybridization of all the states from valence orbitals takes place.

All the systems studied in this section have been analyzed with two different basis sets, namely au SVP and au SVP-wsp. As stated before (see Secs. 4.3.1 and 4.8) the Fermi

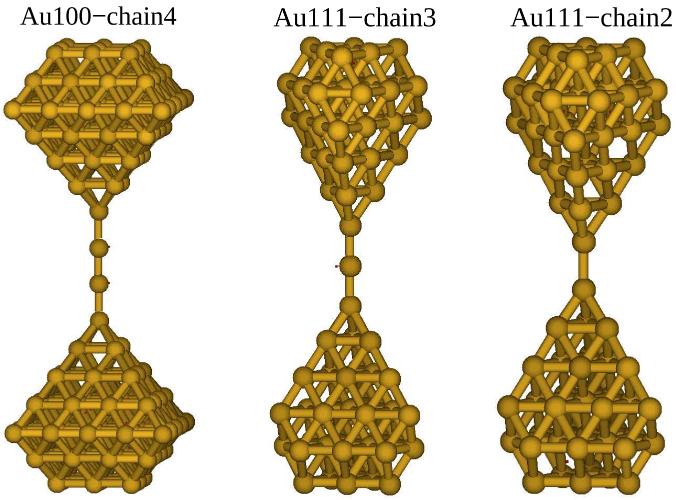

Figure 5.2: Au contact geometries as investigated further below. The geometry Au100-chain4 is a four-atom Au chain with electrodes oriented in the [100] direction, Au111-chain3 is a three-atom Au chain with [111] electrodes, and Au111-chain2 is a two-atom Au chain with [111] electrodes.

energy of Au_{429} in these two basis sets differs a lot. We obtain Fermi energies of $E_F = -5.00$ eV (au SVP) and $E_F = -3.87$ eV (au SVP-wsp). In the analysis of our data we found that the conductances, as obtained in the basis set au SVP-wsp, deviated substantially from $1G_0$, in contrast to experimental observations. This is not unexpected because in the basis set au SVP-wsp the most diffuse functions s and p functions are omitted. This should result in a poor description of a metal with delocalized electrons. We will therefore only discuss the results as obtained with au SVP.

5.1.1 Determination of contact geometries

The ideal behind the study of Au chains is to check the results of our method. In the literature exists a consensus that the conductance of Au atomic chains is around $1G_0$ as discussed above. However, finite size effects play a certain role, and also the experimental values for the conductance of Au chains vary in a certain range around $1G_0$. Therefore it is important to construct some reference geometries that have been studied with a well established transport method. We choose to compare with results as obtained with TRANSIESTA [152]. The geometries investigated by us are shown in Fig. 5.2. The four-atom Au chain with [100] electrodes, called Au100-chain4, corresponds to a geometry given in Ref. [130] (see Fig. 1b therein). The three atom Au chain Au111-chain3 is chosen in analogy to Ref. [152] (see Fig. 9d therein). In addition, we studied a Au dimer contact, where a two atom chain is present at the narrowest part of the contact.

Let us shortly state, how we determine these geometries, which shall all be oriented along the z axis. For Au100-chain4 we construct two ideal Au [100] pyramids, with two atoms in between. The pyramids end with the layer consisting of 25 atoms. The distance between the layers containing 4 atoms is set to 12.68 Å[130]. Then we relax the inner four atoms in symmetry C_1, keeping all other atoms fixed. After convergence we put the atoms into a D_{4h} symmetry, by slightly manipulating their positions. Furthermore we add two more layers with 16 and 9 atoms on each side. This geometry consists now of 162 atoms. Finally we perform a single point calculation exploiting the point group symmetry D_{4h}. For Au111-chain3 we proceed similarly. We start with two perfect Au [111] pyramids, set the z distance between the Au layers with 3 atoms to 9.91 Å[152], and cut the pyramid off at a layer with 10 atoms. Next we add one atom in the middle, relax the 3 chain atoms, put them back into symmetric positons, add two layers on each side with 12 and 6 atoms, and make a single point calculation in symmetry D_{3d}. Au111-chain3 contains 77 atoms in total. For the Au111-chain2 we did this a little bit different in the sense that we relaxed the innermost eight atoms. The z distance between the first fixed layers with 6 atoms is 12.12 Å. Otherwise the steps are the same as for Au111-chain3. This contact was computed in the point group symmetry C_{2h} and consists of 76 atoms.

5.1.2 Four-atom gold chain

Let us now study the conduction properties of the contact Au100-chain4. There are many different possibilities to partition the contact into the left (L), central (C), and right (R) parts. We will refer to such partitionings as "cuts". It is clear that the cuts should be done such that L and R are unconnected ($S_{LC} = 0$ and $H_{LC} = 0$), which is required by the formalism by which we compute the conductance. This requires a large enough C region. In addition it is sensible, if there are several layers in the L and R regions. Otherwise a substantial mismatch problem due to surface effects will result. In such cases the transmission as a function of the energy $T(E)$ shows many artificial wiggles. We observe that at minimum two layers in the L and R regions are necessary to obtain reasonable $T(E)$ curves. For two different cuts $T(E)$ is plotted in Fig. 5.3 for the contact Au100-chain4. For the two different cuts shown in the left panel $T(E)$ is very much identical, indicating some kind of robustness of our method and a convergence with respect to the size of C. The transmissions at the Fermi energy are $T(E_F) = 0.93$ and 0.98 for cuts 1 and 2, respectively. These values correspond well to the results of Ref. [130], where $T(E_F) = 0.99$.

Next we want to study the channel decomposition of $T(E)$ at E_F (see Fig. 5.4). There is clearly a single channel at E_F again in perfect agreement with experimental observations [38] and previous theoretical studies [152, 84].

In general the electronic structure in the narrowest part should be responsible for the conductance of an atomic point contact [38]. In order to gain more insight into the electronic structure of the Au chain we plot in the right panel of Fig. 5.4 the LDOS of the atom indicated by an arrow in Fig. 5.3. As compared to the bulk DOS of Fig. 5.1 the contributions of s orbitals are enhanced at E_F signaling that the single transmission channel should mainly be due to the s orbitals.[1]

---

[1] Note that the contribution of the s orbitals in the DOS is obtained by summing over all s basis

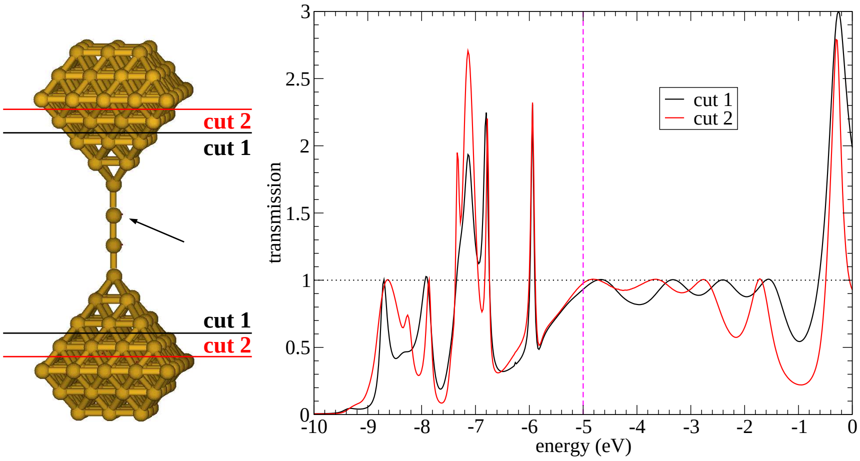

Figure 5.3: The transmission as a function of the energy for the contact Au100-chain4. Two different partitionings of the contat into the LCR parts are indicated by cut 1 and 2 to the left. The corresponding $T(E)$ curves are displayed to the right.

5.1.3 Three-atom gold chain

Exactly the same analysis will now be carried out for the contact Au111-chain3, a three atom Au chain. This system was already under investigation in Sec. 4.5, where we directly compared our transmission curve to a study with TRANSIESTA. Now we will show more details on this contact system. While the contact Au100-chain4 did not require a rotation of the electrode parameters, the [111] electrode planes aligned with the z axis make such a transformation necessary (see Sec. F.1). So from the methodological point of view the system Au111-chain3 is more complicated than the geometry Au100-chain4.

In Fig. 5.5 the analysis of the three-atom chain Au111-chain3 is shown. Again we observe a flat region in $T(E)$ with transmissions close to 1. At the Fermi energy cuts 1 and 2 predict $T(E_F) = 0.96$ and 0.99, respectively. We see in the lower left of the figure that the transmission at E_F is dominated by a single transmission channel. The LDOS indicates a dominant contribution of s orbitals. For the d states in the LDOS we observe very sharp peak structures that are also reflected in the transmission. This phenomenon is also apparent in Fig. 5.4.

5.1.4 Two-atom gold chain

Another system often discussed in the literature (see also Sec. 2.4) is a Au chain of two atoms, also called a dimer configuration. Such a system, contact Au111-chain2, is displayed in Fig. 5.6. Similar to the plots before we analyze the channel decomposition of $T(E)$. Again we observe a dominant channel. But $T(E)$ is partly over 1 around E_F, so that, as compared to Au100-chain4 and Au111-chain3, the contribution of other channels becomes

---

functions, the p contribution is a summation over all p functions of the basis set and so on. For au SVP we combine $6s$, $3p$, and $5d$ functions into the contributions s, p, and d, respectively.

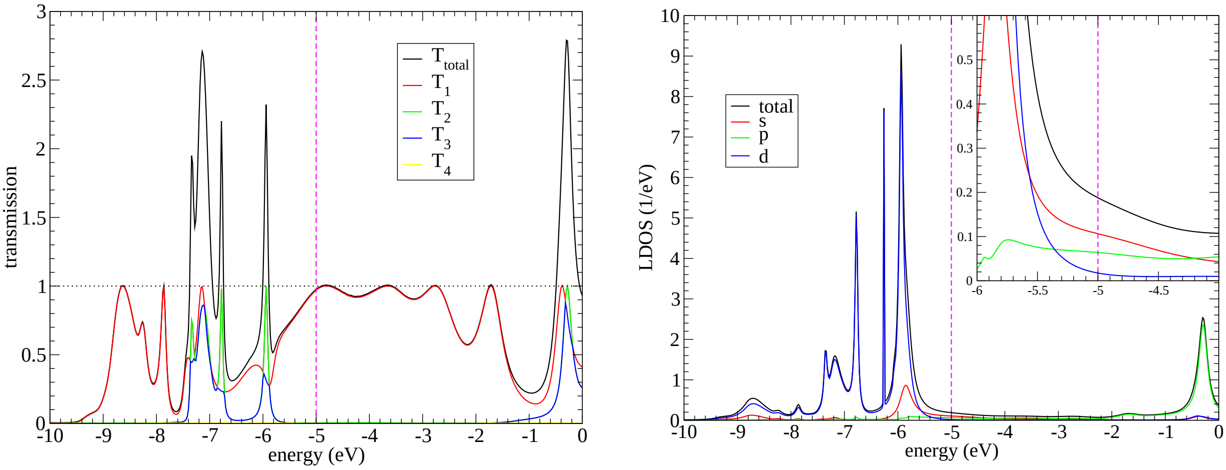

Figure 5.4: In the left panel $T(E)$ is plotted for the contact Au100-chain4 partitioned with cut 2. In addition to the total transmission also the transmission channel decomposition of $T(E)$ is shown, as indicated in the legend. To the right the LDOS of a Au atom in the four atom chain is displayed (see the atom pointed at by the arrow in Fig. 5.3). The LDOS is also resolved in the contributions of s, p, and d orbitals by summing over the respective s, p, and d functions of the basis set.

already visible. We find that $T(E_F) = 0.96$. In the left panel of the figure we also depict the LDOS for an atom in the narrowest part of the constriction (see the arrow in the contact geometry in Fig. 5.6). Presumably due to the higher coordination number of the atom, the structure of the d states has changed as compared to Figs. 5.4 and 5.5. Also the p contributions are increased at E_F, possibly indicating that the $6s^1$ electronic character of the Au atom is diminished due to the high coordination number.

5.1.5 Role of the self-energies: orthogonal versus nonorthogonal parameters and bulk versus surface Green's functions

Before we switch to another metal, namely Al, let us compare the performance of the procedures 1 and 2, as depicted in Fig. 4.4. We will refer to these two procedures as p1 and p2 throughout this paragraph. In addition we will study the difference between the $T(E)$ curves obtained with surface or bulk Green's functions. We show this comparison in Fig. 5.7 for the contacts Au100-chain4 and Au111-chain3 . For both these chain configurations we compare the cuts 1 and 2 in the corresponding Figs. 5.3 and 5.5.

We can observe that all procedures produce qualitatively similar transmission curves with an initial "peaky" region from energies of -9 to -6 eV, corresponding to the d states of Au. Also the increase of the transmission at -1 eV is a common feature in all plots. However, there appear to be strong oscillations of $T(E)$ around E_F, depending on the method chosen. The procedure performing best, in the sense that the transmission resides on a stable plateau of $T(E) \approx 1$ at E_F, is the method p1, surface. This is the method

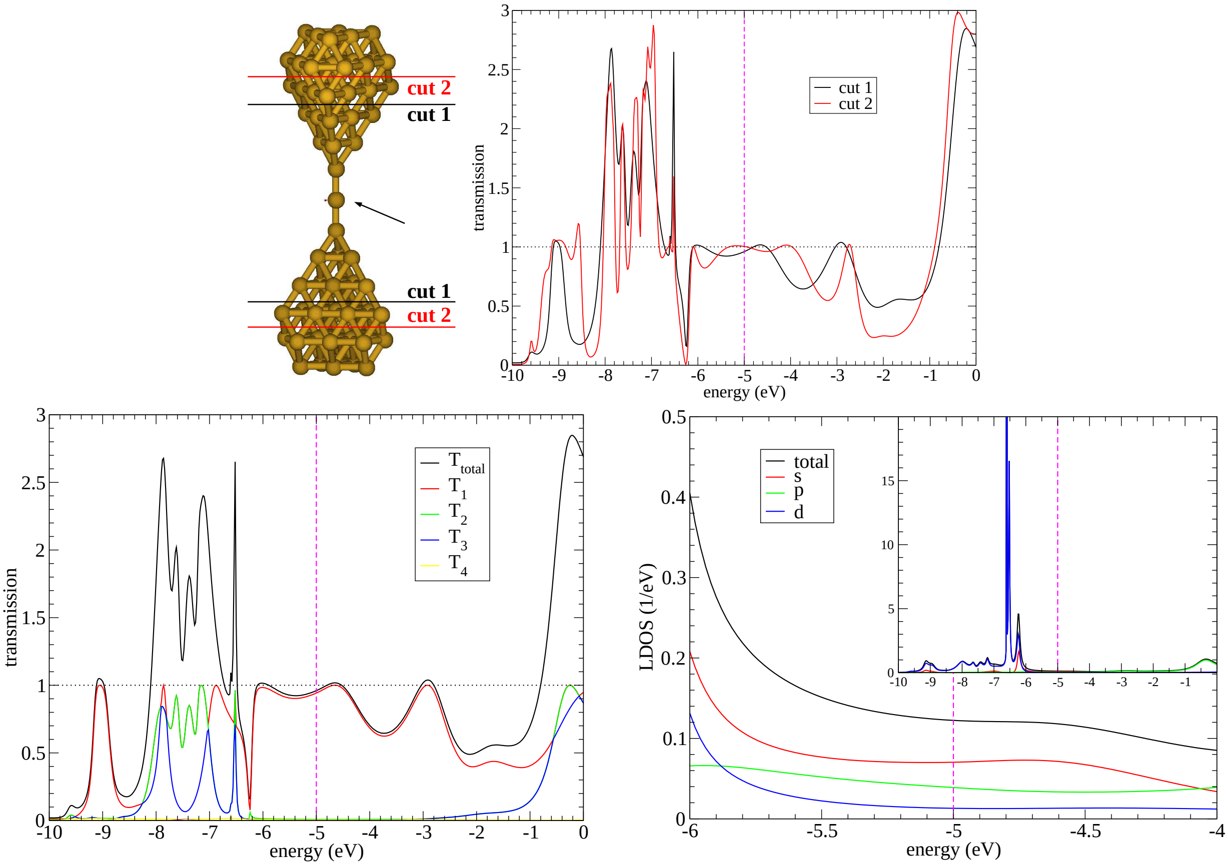

Figure 5.5: In the upper right $T(E)$ is shown for two different cuts of the contact Au111-chain3. These cuts are indicated in the contact geometry to the left of these curves. In the lower left panel the decomposition of the total transmission into transmission channels is depicted for cut 1. To the lower right the LDOS of the central Au atom in the three-atom chain is shown (see the atom pointed at by the arrow in the contact geometry). The LDOS is resolved in its orbital contributions.

that we used up to now, namely nonorthogonal electrode parameters combined with surface electrode Green's functions. The results for Au111-chain3 show that the use of bulk Green's functions combined with nonorthogonal electrode parameters does not seem to be a good approximation. Also the method p2, surface performs quite badly in this particular case. Instead p2, bulk, the use of orthogonal electrode parameters combined with the use of bulk Green's functions seems to be a reasonable approximation.

There is a clear message from this analysis: Nonorthogonal electrode parameters should be used with surface electrode Green's functions, and there is no other method that performs equally well.

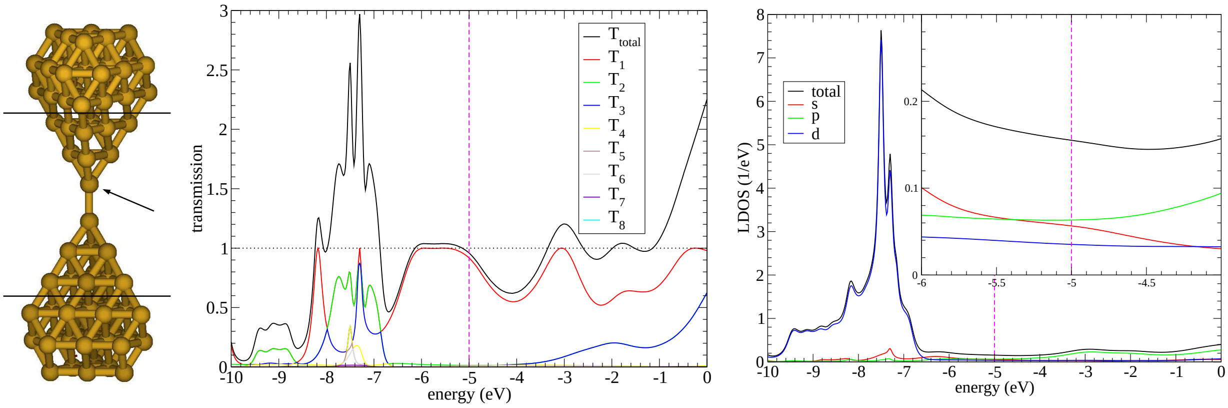

Figure 5.6: In the left panel $T(E)$ is shown for the contact Au111-chain2 together with the transmissions of the different transmission channels. The right panel diplays the LDOS of an atom in the narrowest part of the contact (see the atom pointed at by the arrow in the contact geometry). The LDOS is resolved in its orbital contributions.

5.2 Conductance of ideal aluminum atomic contacts

In this paragraph we want to investigate Al contacts. As it is visible from the bulk DOS in Fig. 5.8 the electronic structure of Al is quite different to that of Au. While Au is a noble metal with an s valence, the Al atom has an open p shell and the metal is considered as a p-valent metal (see also Sec. 2.6).

For Al we will study an ideal fcc [111] pyramid consisting of 251 atoms. Ideal means that none of the atoms have been relaxed. Instead the geometry is cut out of an fcc lattice with the experimental lattice constant $a = 4.05$ Å. The calculations presented below are therefore rather meant as a demonstration that our method is applicable to other metals than Au. We want to point out that S. Wohlthat [194] studied the transport in atomic Al contacts in the presence of gas molecules, based on the methods developed in this work.

In this section we will compare the results of the conductance for different basis sets. These basis sets will be al SVP and al hw-min. From the biggest fcc balls calculated for them we extract Fermi energies $E_F = -4.25$ eV (al SVP) and $E_F = -5.46$ eV (al hw-min).

5.2.1 Aluminum single-atom contact

Let us start with the discussion of the transmission in the basis set al SVP. The contact considered, called Al111-251, is shown in Fig. 5.9 together with the total transmission, the individual transmission channel contributions, and the LDOS of the atom in the narrowest part of the contact. From the plot of $T(E)$ it is obvious that the transmission channel structure has changed a lot compared to Au. Now there are three transmission channels at E_F that contribute to the total conductance. Due to the D_{3d} symmetry of the contact structure two of the channels are exactly degenerate and T_2 lies directly on top of T_3. These additional channel contributions, as compared to the single dominant channel in the Au

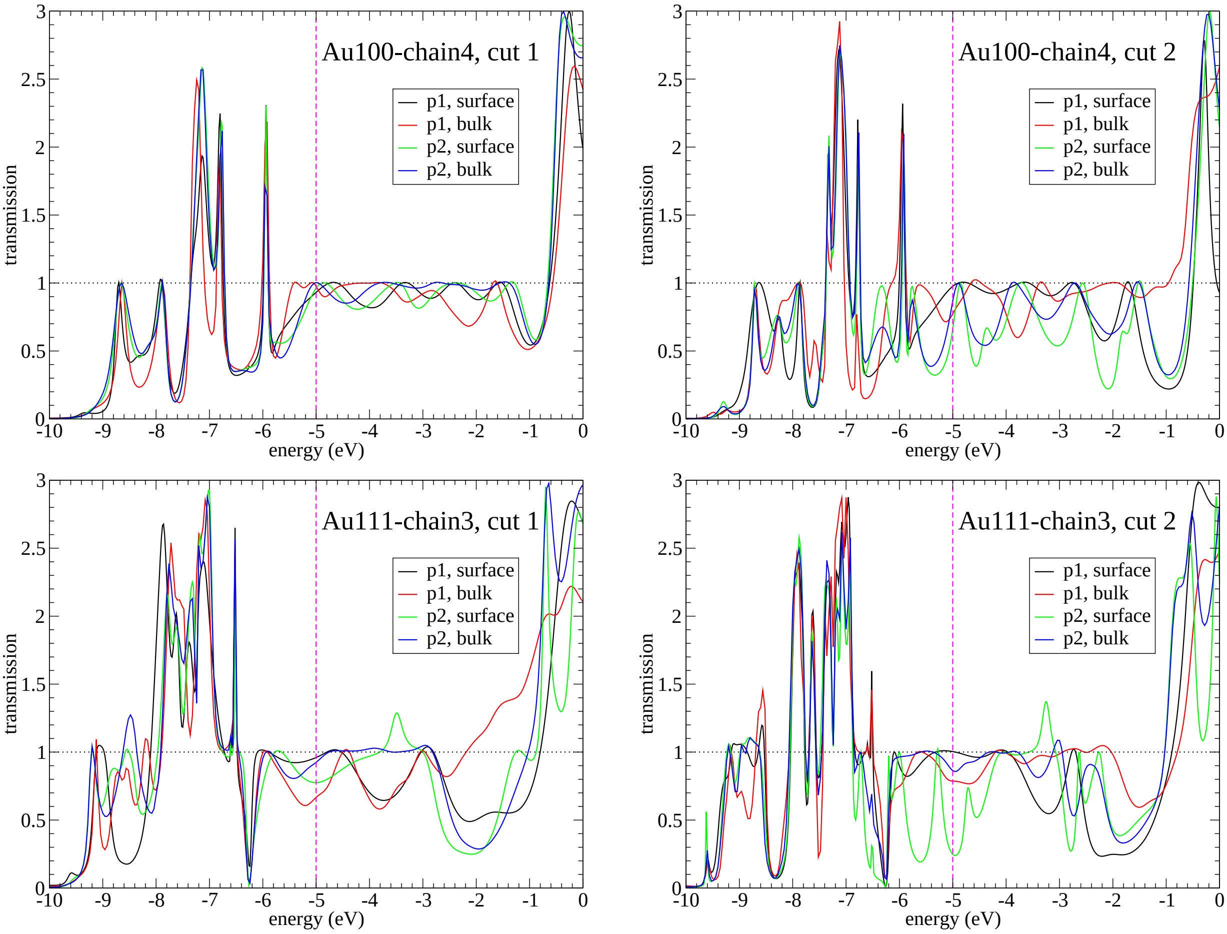

Figure 5.7: Comparison of the $T(E)$ curves as predicted by procedure 1 (p1) and 2 (p2) of Fig. 4.4. In addition the results with surface electrode Green's function (surface) are compared to bulk electrode Green's functions (bulk). In the upper panel this comparison is shown for the Au four-atom chain of Fig. 5.3, while the lower two panels are for the Au three atom chain of Fig. 5.5. The left and right panels in each row correspond to the cuts 1 and 2 of the corresponding Figs. 5.3 and 5.5.

chains, can mainly be attributed to the p orbitals. Also the LDOS in the narrowest part shows the clear dominance of these p contributions. The existence of three conduction channels is perfectly in line with the experimental observations of Scheer *et al.* [19, 38]. For the transmission we get $T(E_F) = 1.88$.

5.2.2 Basis set dependence of the transmission

Finally we want to explore, how our results vary when the basis set is changed. In particular, often minimal basis sets are used for the description of the electrodes in the field of molecular electronics [163, 128]. For this purpose we consider, beside the basis al SVP, the minimal basis al hw-min. For three different cuts we show in Fig. 5.10 the $T(E)$ curves

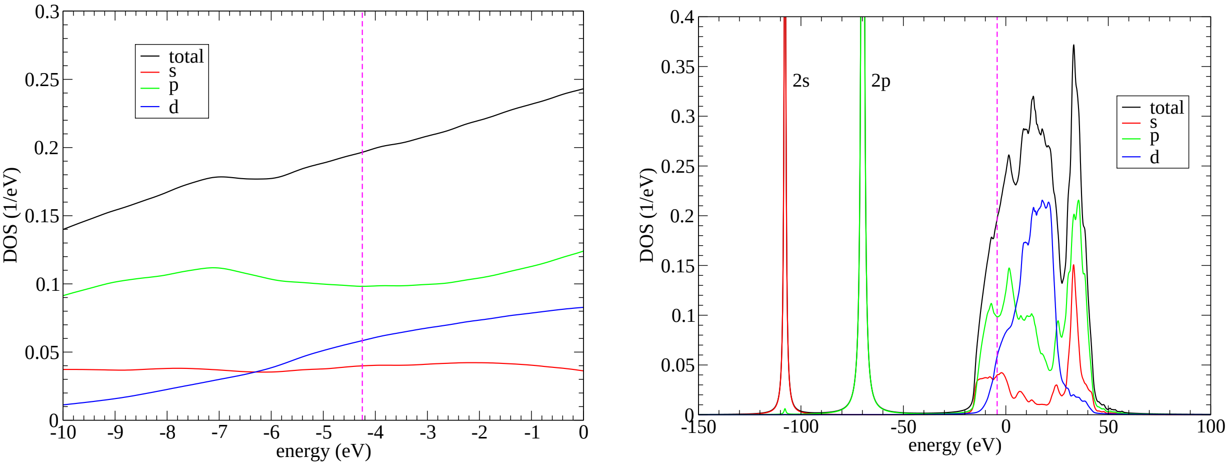

Figure 5.8: DOS for a bulk Al atom resolved in its orbital contributions. On the left the DOS is shown in a region around E_F, while the right panel displays a large energy interval. As indicated, the first peak in the right panel corresponds to the $2s$ orbitals, the second one to the $2p$ orbitals, and only after that the electronic conduction band is visible, starting mainly with s and p contributions.

for the two different basis sets. Up to the Fermi energy E_F (which is quite different for these two basis sets) there are no big differences visible between the curves for the different cuts. The results for the basis set al SVP look very robust with respect to the cut, even above E_F. Unfortunately just at the Fermi level some differences between the three cuts arise and $T(E_F) = 2.36$ (cut 1), 1.88 (cut 2), and 2.23 (cut 3). For Al hw-min the visual impression is a stronger sensitivity of the $T(E)$ curves to the cut. However, directly at E_F the deviations between the different transmission curves are not much bigger than for the, from a quantum chemical point of view, much more elaborate basis set al SVP. For al hw-min we get $T(E_F) = 1.76$, 2.18, and 2.45. Above E_F the transmission differs strongly for the minimal basis set. It is interesting to observe that the results for the minimal basis set are – at least in this case – very close the predictions of the much more sophisticated basis set al SVP.

5.3 Conclusions

In this chapter we used metallic atomic contacts to test the ab-initio transport scheme as developed in Chap. 4. The different metals studied were Au and Al.

For Au we found that our results coincide with experimental observations of a conductance close to $1G_0$, where we studied a two-, a three-, and a four-atom Au chain with varied electrode lattice orientations. In addition, the results for the three- and four-atom Au chains could be compared to other DFT based approaches to quantum transport, and were in close agreement. Concerning the methodology, there were usually at least two different partitionings of the system that led to similar transmission curves, demonstrat-

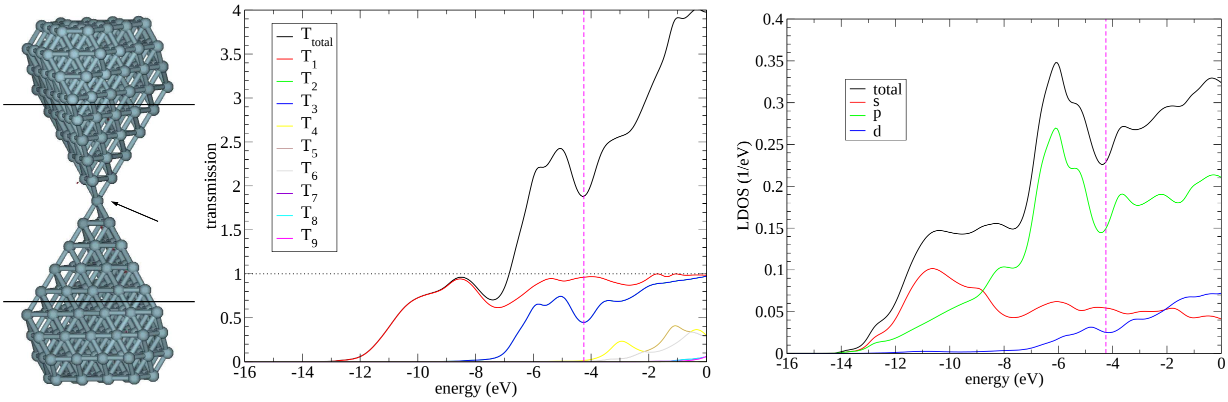

Figure 5.9: In the left panel the transmission $T(E)$ for an Al-pyramid with planes oriented along the [111] direction is displayed. We call this contact Al111-251. The transmission eigenchannels are shown for the cut indicated in the picture of the contact geometry. The right panel shows the LDOS of the atom in the narrowest part of the contact.

ing the robustness or convergence of our results with respect to the predicted conduction properties. Furthermore, we investigated the different transport schemes as proposed in Fig. 4.4. While procedure 1 employs nonorthogonal electrode parameters, procedure 2 uses orthogonal ones (see also Sec. 4.3). For them, in turn, we studied the changes resulting from a replacement of surface by bulk Green's function. We saw that the nonorthogonal electrode parameters combined with surface Green's functions indeed perform best.

Next we investigated an ideal Al single atom contact. In this case the transmission channel structure changed compared to Au. But again the finding of three open transmission channels is in agreement with experimental results. Also for Al we could demonstrate a reasonable robustness of our results with respect to the partitioning.

In conclusion we have shown that our quantum transport method is applicable to different electrode materials. Moreover it possesses a certain predictive power. These successful tests open up the possibility to apply our method in the field of molecular electronics (see the following Chap. 6).

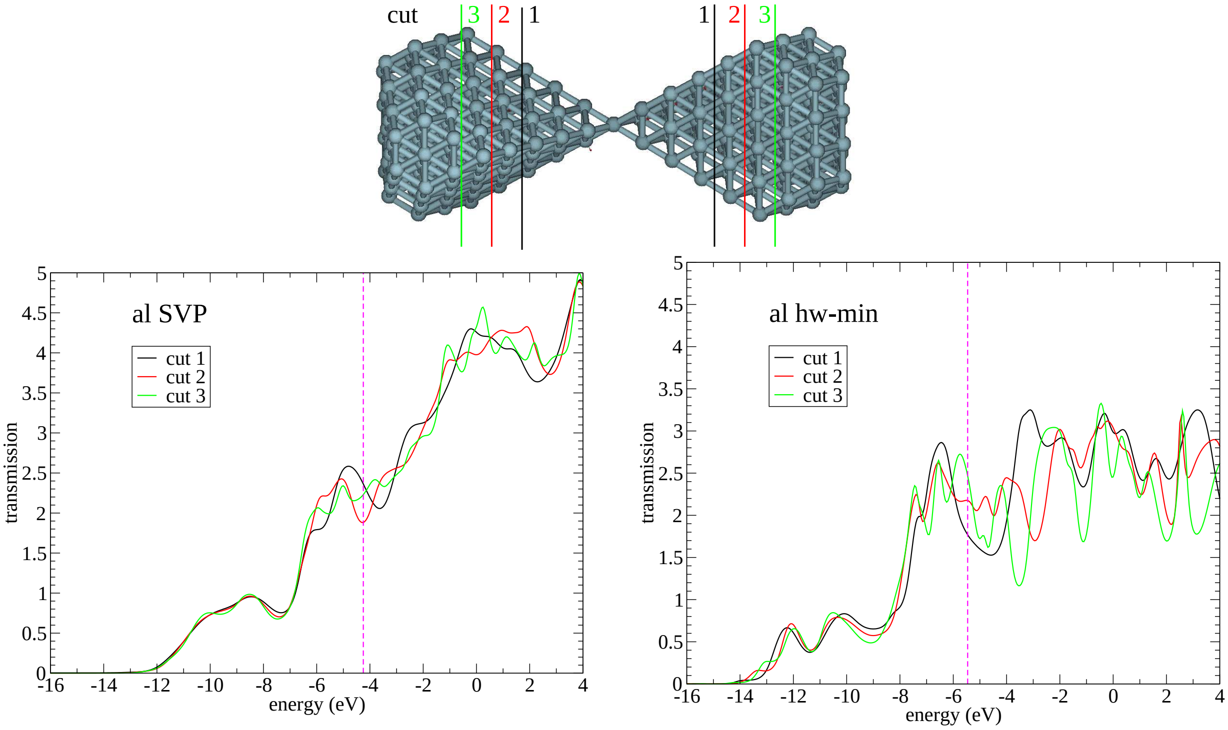

Figure 5.10: Comparison between the basis sets al SVP and al hw-min. In the left panel $T(E)$ is plotted for different cuts using the basis set al SVP, while on the right the same is done for the minimal basis set al hw-min.

Chapter 6

Molecular electronics with organic molecules

In this chapter the conduction properties of different series of oligophenylene molecules will be analyzed theoretically. The main part of the molecules studied here has been synthesized in the group of M. Mayor at the Institut für Nanotechnologie (INT), Forschungszentrum Karlsruhe (FZK) (see PhD thesis of M. Elbing [34]). Oligophenylene molecules consist of phenyl rings as basic building blocks, and several of these rings with varied side groups make up the complete molecule. The basic idea persued in the chemical synthesis at the INT was to study the importance of the conjugated π-electron system for the conductance as well as the behavior of the conductance with respect to the number of phenyl ring units. Partly, the conductance has been measured for the molecules in the groups of H.B. Weber at the INT or the group of M. Rampi at Universita di Ferrara, Italy, which offers to us the possibility to compare our results to experimental ones [34]. Very recently we were informed that the conductance measurements on the molecules of Ref. [34] have been redone in an improved way at the IBM Research Laboratories in Zürich, Switzerland [195]. At present we are looking forward to the comparison between the results of our theory and these new experimental results. In a recent paper Venkataraman *et al.* [196] published experimental data for molecules very similar to the ones investigated in this work. Only the bonding group is altered, and terminal sulfur endgroups are replaced with amines.

In the first part of this chapter, Sec. 6.1, we will give a survey of the molecules analyzed in this work. Their different properties will both be discussed for the free molecules and molecules in contact to Au electrodes. In Sec. 6.2 we study the length dependence of the conductance for three different families of oligophenylenes. These three families differ in their side groups and allow either a large extent of the π-electron system or force it to be broken. In addition, variations of the electron transport properties for different bonding positions will be explored. A simple analytic wire model will help to understand better the length dependence of the conductance as well as the influence of molecular orbitals on the transport. Furthermore the profound influence of the electrode coupling on the energetic structure of the metal-molecule-metal (MMM) system is demonstrated. We conclude with Sec. 6.3. In that section we start out with the investigation of a family of planar biphenyl molecules. Next we compare part of our results to the experiment. We show that from the theoretical side strong variations of the conduction properties of molecules can be due to different bonding positions, but also changed intermolecular conformations. After this we investigate in a more conceptual study the influence of ring tilts on the conductance. For this purpose we force the phenyl rings of biphenyl molecules to adopt a certain tilt angle and study both the conductance and the total energy as a function of the tilt angle. Considering the different tilting positions as a thermally occupied configurational space, we calculate the temperature behavior of the conductance and find qualitative differences with respect to the molecules studied.

6.1 Oligophenylenes

We will now present the complete series of molecules investigated. First these molecules are studied in isolation in Sec. 6.1.1. Ultimately, we want to contact them and determine their electrical conduction properties. For this reason we need to determine the geometrical structure of the molecule connected to Au electrodes. Results on this can be found in Sec. 6.1.2.

6.1.1 Oligophenylenes in isolation

In this work we have investigated the molecules displayed in Fig. 6.1.[1] All of them are oligophenylene molecules where the different rings are connected at the para positions. The family of rings R1–R4 represents the basic structure. R1–R4 are simple phenyl rings with one, two, three, and four ring units. Starting from these basic structures side groups may be introduced in the ortho positions with respect to the ring connecting carbon atoms. If the H atom in the ortho position is replaced by a single methyl group we come to the molecules S2–S4. The series of molecules D2–D4 emerges if both H atoms in the ortho position are substituted by a methyl group. In the additional biphenyl molecules B1–B3 the two phenyl rings are connected via an alkyl-bridge of the form C_1H_2, C_2H_2, or C_2H_4, respectively.

The idea behind introducing different side groups to the molecules becomes immediately obvious from Fig. 6.1. By means of them the tilt angle between adjacent phenyl ring units can be controlled. For the molecules R2–R4 there is an interplay between conjugation and steric repulsion of the H atoms in the ortho position. While the conjugation tends to make the geometry planar, the H atoms in the ortho position prevent this [197], resulting in tilt angles of 33°–37° (see Table 6.1). The steric repulsion may be increased by introducing methyl groups in ortho position. For the S series this leads to inter-ring tilt angles of 72°–90°, depending on whether the relaxation of the molecules is started with the two

---

[1] All structures are fully relaxed as obtained at the level of density functional theory (DFT). We use TURBOMOLE V5.7 with the standard basis set SVP, the functional BP-86 and the options RI, scfconv 6 and gcart 4. See Sec. F.4 for further TURBOMOLE specific details. As these options are the same throughout this chapter, we will not mention them again.

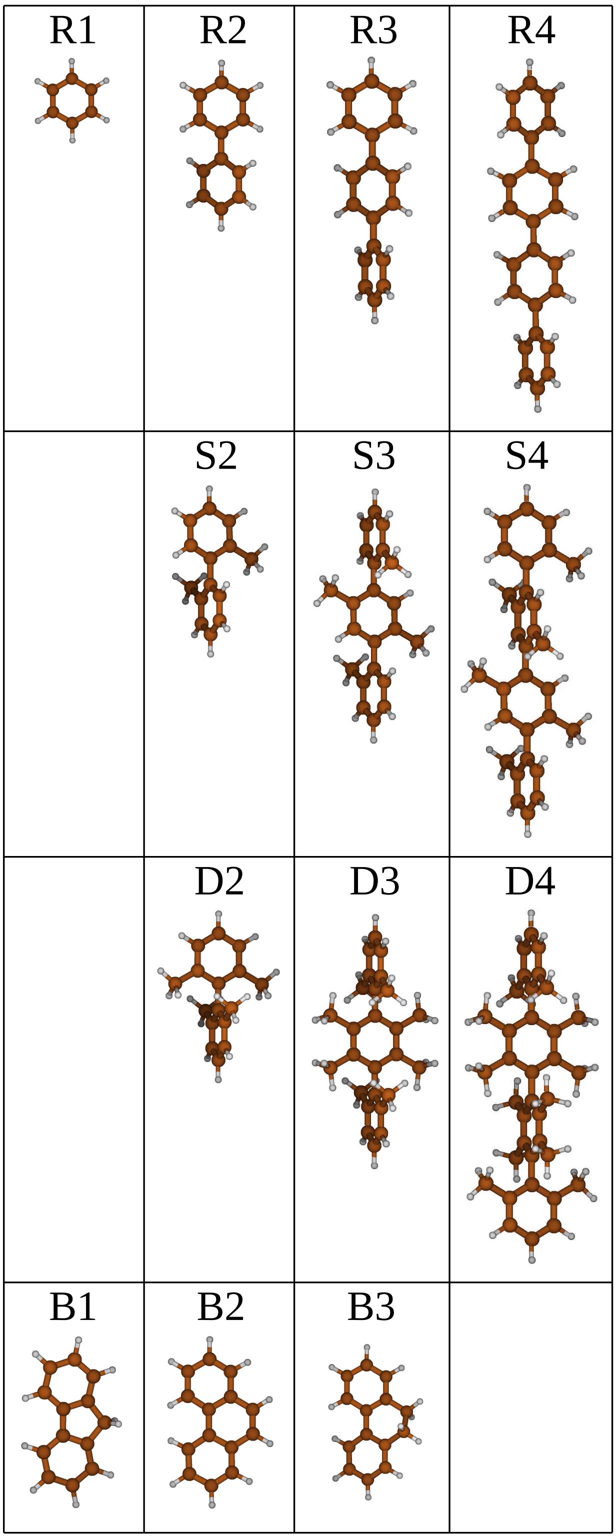

Figure 6.1: Different families of oligophenylene molecules as investigated in this work. The first family R1–R4 consists of phenyl rings of up to four units connected via the C atoms in the para position. In the series S2–S4 one of the two H atoms in the ortho position has been replaced by a methyl group, while in the series D2–D4 both H atoms are replaced by methyl groups. Finally the series of molecules B1–B3 consists of biphenyl molecules whose rings are connected by alkyl bridges.

methyl side groups touching each other (resulting in ring tilt angles close to 90°) or not

molecule	E_{HOMO}(eV)	E_{LUMO} (eV)	Δ (eV)	$\lvert\varphi_1\rvert$ (°)	$\lvert\varphi_2\rvert$ (°)	$\lvert\varphi_3\rvert$ (°)	$d(\mathrm{C}-\mathrm{C})$ (Å)
R1	−6.266	−1.125	5.141	–	–	–	2.812
R2	−5.684	−1.830	3.854	36.39	–	–	7.175
R3	−5.441	−2.218	3.313	35.39	35.81	–	11.538
R4	−5.312	−2.295	3.017	34.82	33.44	35.16	15.901
S2	−5.913	−1.177	4.736	89.96	–	–	7.154
S3	−5.681	−1.245	4.436	89.06	84.78	–	11.497
S4	−5.652	−1.225	4.427	88.99	89.79	85.37	15.837
D2	−5.786	−1.088	4.698	89.97	–	–	7.147
D3	−5.447	−1.056	4.391	89.20	89.11	–	11.497
D4	−5.401	−1.103	4.298	89.91	88.94	88.74	15.844
B1	−5.430	−1.813	3.617	0.02	–	–	6.965
B2	−5.425	−2.087	3.338	0.24	–	–	7.169
B3	−5.423	−1.885	3.538	20.40	–	–	7.161

Table 6.1: Energetic and structural data for the organic molecules displayed in Fig. 6.1. The highest occupied molecular orbital (HOMO) and lowest unoccupied molecular orbital (LUMO) energies are given together with the resulting HOMO-LUMO gap $\Delta = E_{\mathrm{LUMO}} - E_{\mathrm{HOMO}}$. The angles $|\varphi_i| \in [0°, ..., 90°]$ correspond to the tilt angles between the different phenyl units. In addition the distance $d(\mathrm{C}-\mathrm{C})$ between the terminal carbon atoms is specified.

(which may lead to angles as low as 72°). In Table 6.1 we concentrate on molecules of family S with tilt angles above 84°. (We will come back to the analysis of molecules with smaller ring tilt angles in Sec. 6.3.2). Having observed that the ring tilts for the molecules S2–S4 may vary by up to 20° we decided to study in addition the structures D2–D4, which were not synthesized in Ref. [34]. By introducing a second methyl group in the ortho position, the molecule is stiffened further, and the variations in ring tilt angles are reduced to 2°. We obtain tilt angles between 88°–90°.[2] Additionally the molecules B1–B3 have been synthesized in Ref. [34].[3] By means of the alkyl bridge the ring tilts can be controlled, resulting in inter-ring tilts of 0°, 0°, and 20° for B1, B2, and B3, respectively.

We believe that for molecular electronics it is crucial to work with molecular structures, whose geometry is fixed to the best extent possible. Due to stress in the contacts and the heating due to the electrical current, the molecule is most likely not in its equilibrium configuration. In the case of small rotational barriers for phenyl ring tilts the angle between adjacent phenyl units may differ substantially from the equilibrium tilt angles. If the

---

[2] At the time when we started to study the series D2-D4 we were not sure, whether the chemical synthesis of these molecules may not be hampered for practical reasons. But in Ref. [196] the molecule D2 has been synthesized (with amino end groups), so that we believe that the complete series D2–D4 can be synthesized as well (with sulfur end groups).

[3] Note that we changed the order of the molecules with respect to Ref. [34]. B2 and B3 of this work correspond to the molecules B3 and B2 in Ref. [34].

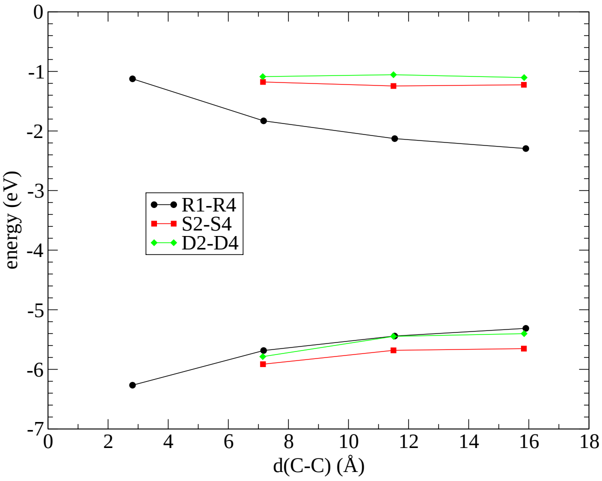

Figure 6.2: Evolution of the HOMO-LUMO gap for the species R1–R4, S2–S4, and D2–D4 according to Fig. 6.1 and Table 6.1. Plotted are the energies of the HOMO and LUMO states E_{HOMO} and E_{LUMO} on an absolute scale. (The upper curves, closer to the vacuum level at 0 eV, correspond to E_{LUMO}, while the lower ones are E_{HOMO}.)

conductance depends decisively on this angle, it is of paramount importance to make the molecule as inflexible as possible. In this sense the molecules R2–R4 do not seem to be very adequate for the study in molecular electronics due to a missing control of inter-ring fixation. The series of molecules D2–D4 seems indeed better suited for the study in molecular electronics than S2–S4 in the sense that their structure allows less flexibility with respect to inter-ring tilts. This gives rise to the conjecture that experimental measurements of the conductance of molecules D2–D4 should show a better reproducibility than those of S2–S4. The family B fulfills the criterion of a good control over the extent of the conjugated π-system, because rigid ring connectors stabilize them. The variations in the inter-ring tilt angles observed in Table 6.1 for the different series of molecules motivated us to study the height of rotational barriers and the dependence of the transport on the inter-ring tilt angles (see Sec. 6.3).

In order to illustrate the evolution of the HOMO-LUMO gap $\Delta = E_{\mathrm{LUMO}} - E_{\mathrm{HOMO}}$ with respect to the molecular length, we plot in Fig. 6.2 the highest occupied molecular orbital (HOMO) and lowest unoccupied molecular orbital (LUMO) energies as a function of the terminal carbon atom distance for the series R1–R4, S2–S4, and D2–D4. It can be seen that Δ is reduced for R1–R4 most strongly, where both the HOMO and LUMO levels come closer to each other. For the series S2–S4 and D2–D4 the LUMO level remains fixed at a value corresponding to the LUMO level of R1 and only the HOMO moves up. Just from the inspection of the gap energies, the molecules R2–R4 should be better conductors than S2–S4 or D2–D4.

It would be interesting to know the effective conjugated length (ECL) for the different series of molecules. The ECL defines the extent of π-conjugated systems, in which the electronic delocalization is limited [32]. From Fig. 6.2 it is apparent that such an analysis would require the study of longer molecules with more than four ring units, because the distance, at which the HOMO-LUMO gap saturates, has not yet been reached.

6.1.2 Oligophenylenes in a gold contact

The aim of this work is the study of molecular electronics, or more specifically the analysis of conduction properties of organic molecules coupled to metallic electrodes. In this chapter the electrodes will be Au electrodes, which are frequently used in experiments due to the chemical inertness of noble metals. Experimentally the contact between the molecule and the Au electrodes is most often established by covalent S-Au bonds. For this purpose acetate-protected thiol-functionalized molecules are prepared that split off their acetate protection group upon contact to Au. A covalent S-Au bond will then connect the molecule to the electrode at both sides [26, 27]. All the molecules presented in Ref. [34] have therefore been prepared with acetyl-protected sulfur functionalities on both ends.

When a molecule is present in a break junction, the length between the metallic electrodes is a free parameter. It may be that the molecule is stretched or squeezed depending on this external control parameter. For this reason it is necessary to think of a protocol, on how to set the electrode length appropriately in the theoretical determination of a contact structure. We intend to prepare a junction with the least external influence on the molecule, because we are interested in how the molecular properties translate into conduction properties. In this study we are not interested in the conduction through, for example, strongly distorted molecular structures due to the break junction's external length control.

There are different possibilities on how the molecule is connected to the electrodes. In Ref. [198] different bonding situations of S-C_6H_5 on a Au_{29} cluster have been studied. The two-fold bonding position was the most stable one, but also other bonding positions were found to be stable, namely a bond to a single Au tip atom or a bond of S to three Au atoms. For a contact realization in the real world one can only speculate, which bonding situation between Au and S will actually be realized, because the equilibrium structure need not be present in the MMM junction due to the influence of external stress or the heat dissipated in the molecule as a result of an electrical current.

We decided to analyze two particular bonding situations, namely the "hollow" bonding situation and the "top" bonding situation. In the hollow situation the molecule's S atom is connected symmetrically to three surface Au atoms, while in the top situation it is bond to only a single tip surface Au atom. We decided to simulate Au electrodes, oriented along the [111] direction, where the [111] direction shall coincide with the z axis. In order to determine the length of our break junction, we followed the protocols given in Fig. 6.3. For the complete series of molecules of Fig. 6.1 we determined the fully relaxed structures of molecules with an S-Au group at the terminal carbon atoms.[4] In a next step we set up a Au [111] pyramid with Au bulk distances including (excluding) a tip Au atom in the case of the hollow (top) bonding situation, corresponding to a Au_{19} (Au_{20}) cluster. These

---

[4] We do not list the precise data for these molecules here, because the structural data, namely tilt angles and terminal carbon distances are very similar to the data listed in Table 6.1.

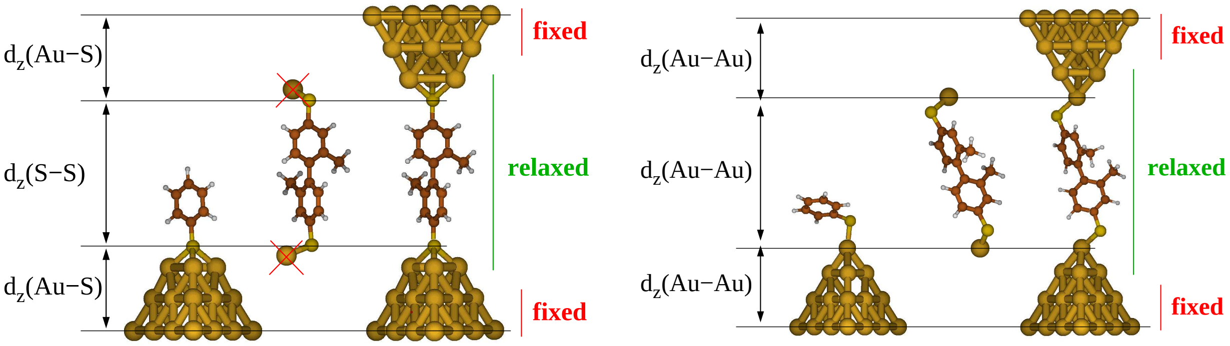

Figure 6.3: Protocols followed in the construction of geometries for the "hollow" (left panel) and "top" (right panel) bonding situations.

pyramids are then fully relaxed, while the last two layers are kept fixed at the Au bulk bond distance as required for a later computation of electron transport for these structures (see the description of the electrode construction in Sec. D.2).

In agreement with Ref. [198] we observe stable hollow and top bonding situations on these clusters, where the molecule stands up in the hollow situation (meaning that the terminal carbon-sulfur axis stands in a right angle to the Au [111] planes) and in the top situation there is a tilt angle of 104.55° between the tip Au atom, the sulfur atom and the terminal carbon. From the relaxed pyramids we extract the distance $d_z(\mathrm{Au}-\mathrm{S}) = 6.20$ Åbetween the lowest Au layer and the sulfur atom projected onto the z axis for the hollow geometry, while for the top geometry we do the same for the z projected distance between the lowest Au layer and the tip Au atom, and get $d_z(\mathrm{Au}-\mathrm{Au}) = 6.80$ Å. For the hollow and top geometry the total length L_z of our junction is set to $L_z = 2d_z(\mathrm{Au}-\mathrm{S}) + d^{\mathrm{mol}}(\mathrm{S}-\mathrm{S})$ or $L_z = 2d_z(\mathrm{Au}-\mathrm{Au}) + d^{\mathrm{mol}}(\mathrm{Au}-\mathrm{Au})$ for the top and hollow geometries, respectively. With d^{mol} we refer to the distances as obtained for the molecule with a S-Au termination. Finally a Au [111] double pyramid is generated, where the distances of the terminal Au layers are L_z apart. The molecule is placed appropriately into the junction as exemplified for the molecule S2 in Fig. 6.3. Keeping L_z fixed together with the Au-Au-distances of the last two layers on both sides, the interior of the contact is fully relaxed.

Equipped with the previously described protocol for the determination of Au-molecule-Au junctions, we compute contacts for the complete series of molecules given in Fig. 6.1 for the hollow and top bonding configurations. The geometries as obtained for hollow and top bonding positions are displayed in Figs. 6.4 and 6.5, respectively. We will refer to the Au-molecule-Au clusters as Au-h-Z or Au-t-Z where Au shall symbolize the presence of Au clusters, h (t) stands for hollow (top) and Z is a particular molecule, e.g. Z=S2.[5] The most important energetic data and structural properties of these junctions are listed in Tables 6.2 and 6.3 for the hollow bonding position, and in Tables 6.4 and 6.5 for the top bonding positions.

---

[5] We want to note here that the relaxation of one of the structures Au-h-Z or Au-t-Z took something between two weeks and a month on fast personal computers with more then 2 GHz of processor speed.

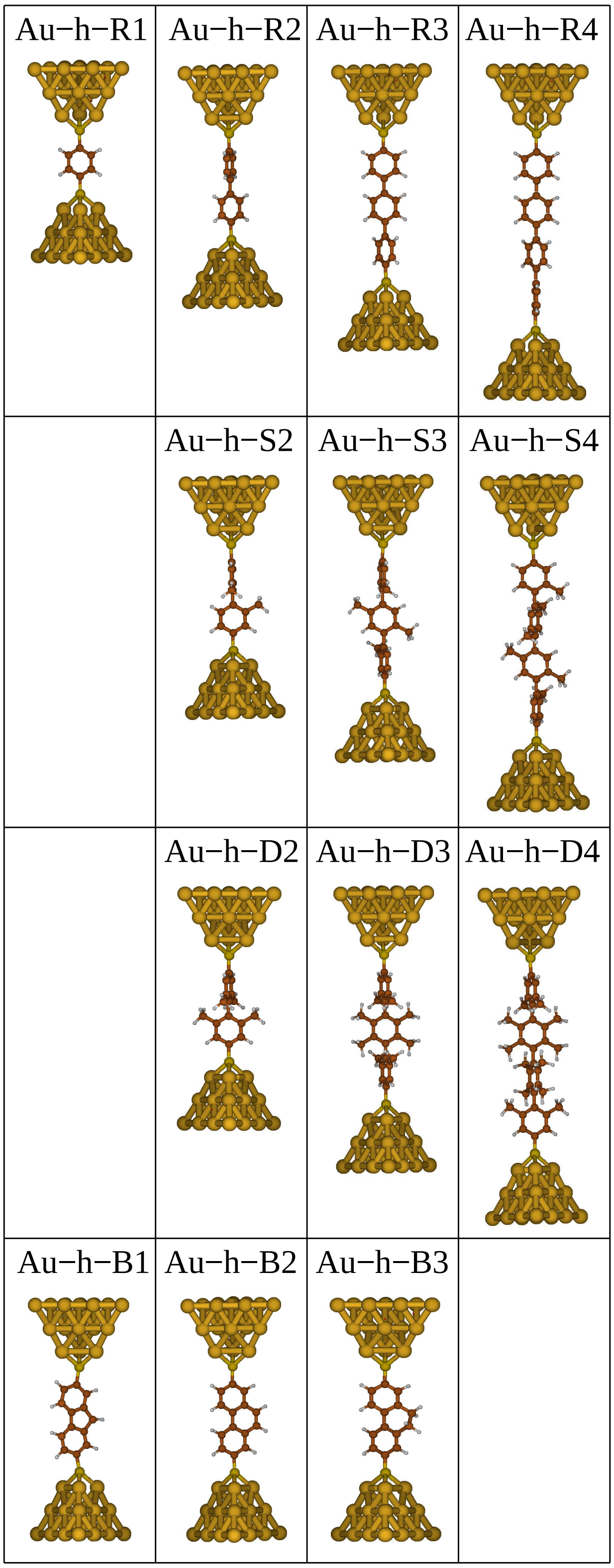

Figure 6.4: Different families of oligophenylene molecules covalently bond to Au_{19} clusters with the last two layers oriented along the [111] crystallographic axis. The molecule is connected to the Au electrodes at both sides with a symmetric covalent bond of a sulfur atom to three Au atoms, a bonding situation which we refer to as the hollow position. The contacts are labeled Au-h-Z, where Au stands for the Au clusters, h indicates the hollow position, and Z can be a particular molecule (Z=R1–R4, S2–S4, D2–D4, or B1–B3).

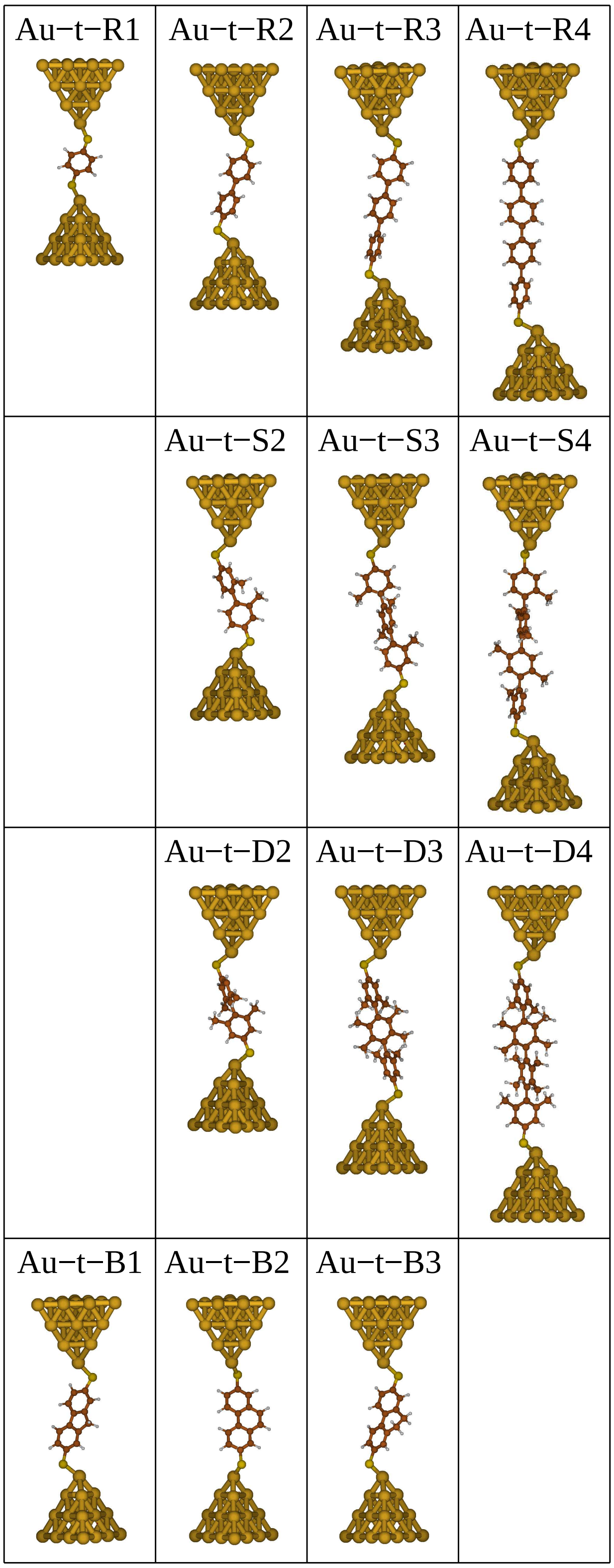

Figure 6.5: Different families of oligophenylene molecules covalently bond to Au_{20} clusters with the last two layers oriented along the [111] crystallographic axis. The molecule is connected to the Au electrodes at both sides with a single covalent bond of a sulfur atom to the tip Au atom, a bonding situation which we refer to as the top position. These contacts are labeled Au-t-Z, where Au stands for the Au clusters, t indicates the top position and Z can be a particular molecule (Z=R1–R4, S2–S4, D2–D4, or B1–B3).

molecule	E_{HOMO}(eV)	E_{LUMO}(eV)	$E_{\mathrm{LUMO+1}}$(eV)	Δ(eV)	Δ_1 (eV)
Au-h-R1	−5.725	−4.306	−4.289	1.419	0.017
Au-h-R2	−5.680	−4.254	−4.254	1.426	0.000
Au-h-R3	−5.629	−4.227	−4.227	1.402	0.000
Au-h-R4	−5.573	−4.209	−4.209	1.364	0.000
Au-h-S2	−5.737	−4.236	−4.235	1.501	0.001
Au-h-S3	−5.693	−4.201	−4.201	1.492	0.000
Au-h-S4	−5.670	−4.181	−4.181	1.489	0.000
Au-h-D2	−5.717	−4.222	−4.221	1.495	0.001
Au-h-D3	−5.655	−4.181	−4.180	1.474	0.001
Au-h-D4	−5.629	−4.157	−4.157	1.472	0.000
Au-h-B1	−5.608	−4.251	−4.238	1.357	0.013
Au-h-B2	−5.683	−4.256	−4.255	1.427	0.001
Au-h-B3	−5.618	−4.242	−4.241	1.376	0.001

Table 6.2: Energetic data for the organic molecules displayed in Fig. 6.4 bond to Au clusters in the hollow position (contact geometries Au-h-Z). The HOMO, LUMO, and LUMO+1 energies are given together with the resulting HOMO-LUMO gap $\Delta = E_{\mathrm{LUMO}} - E_{\mathrm{HOMO}}$ and the energy difference $\Delta_1 = E_{\mathrm{LUMO+1}} - E_{\mathrm{LUMO}}$.

molecule	$\lvert\varphi_1\rvert$ (°)	$\lvert\varphi_2\rvert$ (°)	$\lvert\varphi_3\rvert$ (°)	$d(\mathrm{C}-\mathrm{C})$ (Å)
Au-h-R1	–	–	–	2.808
Au-h-R2	33.82	–	–	7.174
Au-h-R3	34.51	34.31	–	11.519
Au-h-R4	34.05	33.57	34.13	15.882
Au-h-S2	89.28	–	–	7.153
Au-h-S3	84.95	88.73	–	11.487
Au-h-S4	85.11	89.00	87.91	15.817
Au-h-D2	89.66	–	–	7.146
Au-h-D3	89.51	89.42	–	11.485
Au-h-D4	89.07	89.37	89.67	15.820
Au-h-B1	0.07	–	–	6.945
Au-h-B2	0.18	–	–	7.163
Au-h-B3	19.78	–	–	7.157

Table 6.3: Structural data for the organic molecules displayed in Fig. 6.4 bond to Au clusters in the hollow position (contact geometries Au-h-Z). The angles $|\varphi_i| \in [0°, ..., 90°]$ correspond to the tilt angles between the different phenyl units. In addition the distance $d(\mathrm{C}-\mathrm{C})$ between the terminal carbon atoms is specified.

molecule	E_{HOMO}(eV)	E_{LUMO}(eV)	$E_{\text{LUMO+1}}$(eV)	Δ(eV)	Δ_1 (eV)
Au-t-R1	−5.569	−5.256	−4.264	0.313	0.992
Au-t-R2	−5.444	−5.246	−4.234	0.198	1.012
Au-t-R3*	−5.365	−5.194	−4.226	0.171	0.968
Au-t-R4	−5.226	−5.155	−4.154	0.071	1.001
Au-t-S2	−5.412	−5.311	−4.212	0.101	1.099
Au-t-S3	−5.290	−5.280	−4.207	0.010	1.073
Au-t-S4*	−5.216	−5.199	−4.177	0.017	1.022
Au-t-D2	−5.336	−5.295	−4.213	0.041	1.082
Au-t-D3*	−5.219	−5.212	−4.163	0.007	1.049
Au-t-D4	−5.167	−5.166	−4.153	0.001	1.013
Au-t-B1	−5.435	−5.216	−4.208	0.219	1.008
Au-t-B2	−5.446	−5.243	−4.213	0.203	1.030
Au-t-B3	−5.426	−5.208	−4.221	0.218	0.987

Table 6.4: Energetic data for the organic molecules displayed in Fig. 6.5 bond to Au clusters in the top position (contact geometries Au-t-Z). The HOMO, LUMO, and LUMO+1 energies are given together with the resulting HOMO-LUMO gap $\Delta = E_{\text{LUMO}} - E_{\text{HOMO}}$ and the energy difference $\Delta_1 = E_{\text{LUMO+1}} - E_{\text{LUMO}}$. For the molecules marked with * negative HOMO-LUMO gaps occurred in standard closed shell calculations of −0.166 eV for Au-t-R3, −0.001 eV for Au-t-S4, and −0.008 eV for Au-t-D3. As explained in the text we have chosen a fractional occupation number of 1 electron in the previously inverted HOMO and LUMO levels. Therefore for Au-t-Z* the HOMO is actually the singly occupied HOMO−1-level, the LUMO is the singly occupied HOMO, and LUMO+1 is the actual LUMO.

All calculations in this chapter are based on closed shell calculations with doubly occupied shells. While in the hollow bonding position convergence was very unproblematic, some contacts did not converge in the self-consistent field (SCF) runs. A higher orbital shift was then used and the geometries converged again without problems.[6] For some molecules the Au-t-Z structures exhibited, however, negative HOMO-LUMO gaps. This was the case for Au-t-R3 ($\Delta = -0.166$ eV), Au-t-S4 ($\Delta = -0.001$ eV), and Au-t-D3 ($\Delta = -0.008$ eV). For this reason we decided to recompute the structure of these molecules with a fractional occupation number of one electron in the previously inverted HOMO and LUMO levels. For these new occupations we relaxed the structures, and we shall refer to them as Au-t-Z*. In doing so no further inversions of electronic levels occurred. Concerning the changes on the conductance data presented later, we want to state here, that there are only marginal differences visible between the transmission curves of Au-t-S4 and Au-t-S4* and also Au-t-D3 and Au-t-D3* as suggested by the very small level inversion. For Au-t-R3

---

[6] TURBOMOLE option $scforbitalshift automatic 0.5, instead of the default option $scforbitalshift automatic 0.1.

molecule	$\lvert\varphi_1\rvert$ (°)	$\lvert\varphi_2\rvert$ (°)	$\lvert\varphi_3\rvert$ (°)	$d(\mathrm{C}-\mathrm{C})$ (Å)
Au-t-R1	–	–	–	2.846
Au-t-R2	19.99	–	–	7.189
Au-t-R3	28.84	30.76	–	11.515
Au-t-R4	28.94	31.36	30.41	15.836
Au-t-S2	55.70	–	–	7.137
Au-t-S3	81.32	83.29	–	11.469
Au-t-S4	79.86	88.05	87.19	15.770
Au-t-D2	79.62	–	–	7.136
Au-t-D3	89.54	89.23	–	11.456
Au-t-D4	88.10	89.18	89.04	15.761
Au-t-B1	0.15	–	–	6.962
Au-t-B2	0.87	–	–	7.162
Au-t-B3	17.85	–	–	7.158

Table 6.5: Structural data for the organic molecules displayed in Fig. 6.5 bond to Au clusters in the top position (contact geometries Au-t-Z). The angles $|\varphi_i| \in [0°, ..., 90°]$ correspond to the tilt angles between the different phenyl units. In addition the distance $d(\mathrm{C}-\mathrm{C})$ between the terminal carbon atoms is specified.

and Au-t-R3* bigger differences are visible, because here molecular orbitals change their energetic positions more strongly (around 0.1 eV near the HOMO and LUMO levels) as compared to the previous two cases. So in conclusion only the molecule Au-t-R3 seems somewhat difficult to treat, concerning its electronic structure in the top position.[7] In the following we will replace the three junctions Au-t-R3, Au-t-S4, and Au-t-D4 by the junctions Au-t-R3*, Au-t-S4*, and Au-t-D4*. For reasons of brevity, and as already done in Fig. 6.5 and Table 6.5, we refer to Au-t-Z* as Au-t-Z (Z=R3, S4, D3) from now on.

There are some important differences, when one compares the data of the hollow and top bonding positions. It is apparent from Tables 6.2 and 6.4 that the HOMO levels are shifted upwards by up to 0.4 eV, when going from the hollow to the top bonding configuration. In addition there is a HOMO-LUMO gap Δ of around 1.5 eV for the hollow geometry and the energetic difference between the LUMO and LUMO+1 level $\Delta_1 = E_{\mathrm{LUMO+1}} - E_{\mathrm{LUMO}}$ is negligible. In contrast there exists a LUMO state slightly above the HOMO for the top geometry, causing Δ to be small in this case. The electronic gap shows up for the transition from the LUMO to the LUMO+1 level. Now the gap Δ_1 is around 1 eV. Concerning the gap energies $\Delta + \Delta_1 = E_{\mathrm{LUMO+1}} - E_{\mathrm{HOMO}}$ for the hollow and top geometries, this sum is bigger for the hollow geometry than for the top geometry, suggesting a better conducting behavior for the junctions Au-t-Z than Au-h-Z, as will also be observed later.[8]

---

[7] Of course open shell calculations could cure the problem of negative HOMO-LUMO gaps without the need to resort to fractional occupation numbers. But all calculations in this work used the closed shell formalism so that we considered this solution most consistent.

[8] Notice that due to the position of the LUMO level below the Fermi energy of Au ($E_F = -5.0$ eV),

As regards the geometrical structure, the Au-t-Z geometries corresponds to junctions under a higher internal stress then the Au-h-Z contacts. The reason is that the S atom tries to be positioned right on top of the pyramid as visible in Fig. 6.3. As the Au electrodes are placed opposite to each other the tilt angle between the Au-S-C bond between the top Au tip atom and the molecule's sulfur and terminal carbon atom does not allow the axis of the Au-S axis to stand perpendicular to the Au [111] planes (see Fig. 6.5). This demonstrates the existence of internal stress in these structures.[9] The internal stress may now cause molecules to deflect from their equilibrium structure, if they are not stiff enough. This is clearly visible for the molecule Au-t-S2, for which we determine an inter-ring tilt angle of only 55.70° (see Table 6.5) instead of 89.96° for the isolated S2 (see Table 6.1). In contrast the tilt angle for the nearly stressfree Au-h-S2 configuration is close to the angle for the isolated S2, namely 89.28° (see Table 6.5). Also for S3 we could observe similarly strong deviations from equilibrium tilt angles in the top geometry. For an isolated S3 system (not shown in the Tables), relaxed from a different starting position than the S3 molecule depicted in Fig. 6.1, we obtain tilt angles $|\varphi_1|$ and $|\varphi_2|$ of 72.10° and 73.65°. These angles remain more or less unchanged in the hollow geometry, taking values 70.62° and 69.98°. For the top geometry, however, the tilt angles of 55.11° and 66.11° deviate strongly with respect to those of the isolated S3 variant. Thus the clear message to any experimentalist in the field of molecular electronics is that, in order to obtain reproducible results in conductance measurements, the employed molecules should be designed such that configurational changes due to external stress, as caused by the electrodes, are minimal. We will come back to this issue in Sec. 6.3.

From the study of Au and Al metallic contacts, as presented in Chap. 5, we know that two layers in the left and right electrode, as present in the Au-h-Z and Au-t-Z geometries of Figs. 6.4 and 6.5, are just the minimum number of layers needed to get meaningful results for the transmission. For this reason we tried to add more layers to the Au pyramids. Unfortunately these attempts turned out to be unsuccessful. The Au-h-Z geometries with increased numbers of Au cluster atoms did not converge anymore in DFT's SCF loop, a purely TURBOMOLE-related problem. For this reason we will present in the following the results for the conductance with two electrode layers in the left and right electrode. We do not have the possibility to check a convergence of the transmission results with respect to different "cuts", as it was done in Chap. 5. Nevertheless the results in the following sections give a physically consistent picture and show good agreement with the results of other theory groups, wherever such a comparison is possible. This justifies the confidence in our studies in spite of the relatively small Au electrode clusters employed in the Au-h-Z and Au-t-Z geometries.

---

results on the conduction properties for the top position need to be considered with reservations. More atoms in the Au clusters are needed to confirm their validity.

[9] This stress also gives a rational for the inverted HOMO-LUMO gaps, occurring in particular for the long molecules. The longer the molecule the more is the S atom away from its preferred position on top of the Au tip. As these structures are no real equilibrium geometries of a free standing Au-molecule-Au system, but correspond to relaxed structures under the constraint of two fixed electrode layers and a fixed length of the complete junction, this may cause problems with the DFT's SCF procedure.

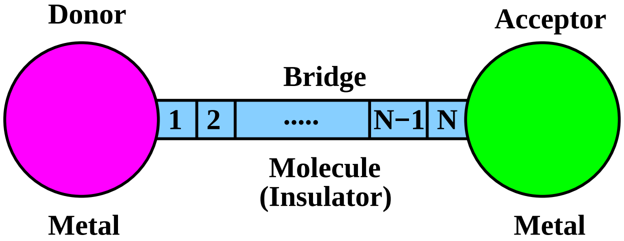

Figure 6.6: Sketch of a DBA system.

For the construction of the electrode Green's functions g_{XX} for the last two layers on both sides of the Au-h-Z and Au-t-Z contacts we use the same procedure as in Sec. 5.1. The electrode parameters stem from a Au_{429} cluster, with a Fermi energy of $E_F = -5.00$ eV. Let us point out again that the Fermi energy merely serves to read off the conductance when the transmission is plotted as a function of the energy. It has no influence on the shape of the transmission curve itself.

6.2 Length-dependent conductance

In this section we will study the length dependence of the conductance for different families of organic molecules. A large amount of work has been devoted to the study of this subject, both experimentally [199, 200, 201, 202, 28, 203, 196] and theoretically [204, 205, 147, 30, 206, 179, 207, 208, 209], just to mention a few of them. While the references quoted look at the electrical conduction properties of organic molecules more from the physicist's point of view in terms of current, resistance and conductance, this topic is intimately related to the established field of electron transfer in chemistry. In chemistry one characterizes the electron transfer rather in terms of transfer rates than in terms of conductance. Again a vast amount of experimental and theoretical work, probably even more than in the young field of molecular electronics, exists on this subject [210, 211, 212, 213]. In particular we recommend the review articles of Salomon *et al.* [214], which is written more from a physicist's point of view, Refs. [215, 216], which adopt the chemist's perspective, and the review by Adams *et al.* [203] that brings together the fields of chemistry and physics.

In essence two different characterizations of electron transport through molecules exist, namely as (i) an incoherent sequential transfer process or as (ii) a coherent tunneling process [213, 203]. In a donor-bridge-acceptor system (DBA) as displayed in Fig. 6.6 the electron transfer reaction reads

$$DBA \rightarrow \left\{ \begin{array}{c} D^{+}B^{-}A \\ DB^{+}A^{-} \end{array} \right\} \rightarrow D^{+}BA^{-} \tag{6.1}$$

where the intermediate states are either $D^{+}B^{-}A$ or $DB^{+}A^{-}$. In MMM junctions the electrodes correspond to the donor (D) and acceptor (A), while the molecule constitutes the bridge (B).

In the first case of sequential electron transfer the electron (or hole) resides on the bridge and the intermediate states D^+B^-A or DB^+A^- are rather real than virtual. The distance dependence of this electron transfer is ohmic, which means that the conductance is inversely proportional to the length L of the bridge $G \propto L^{-1}$. Instead in the second mechanism of quantum tunneling the intermediate states are not populated. In the chemistry community this kind of transfer process is called superexchange mechanism. Depending on the actual energetic situation in the DBA system the length dependence of the conductance for the superexchange mechanism is either (a) exponential, if there are no molecular orbitals present at the injection energy of the tunneling electron, (b) oscillatory, if there are levels present at the injection energy, or (c) it may be inversely proportional to the squared distance in special cases [205].

In reality electron transport will be a mixture of the sequential and superexchange mechanism. We will only consider the superexchange mechanism in this work. The reason is that we assume that the molecule is rather short, shorter than the energy relaxation length (see Chap. C), and strongly coupled to metallic electrodes. In such a case the charge carriers (electrons) will not reside on the molecule for a long time, and the picture of quantum tunneling applies. The transport can then be described as an elastic and coherent process.

Organic molecules usually possess a gap at the Fermi energy so that the distance dependence of the conductance can be expected to be exponential [147] (see Fig. 6.7) according to situation (a) of the superexchange mechanism.[10] Using the text book formula for the tunneling through a rectangular potential barrier one gets the exponential decay law for the conductance

$$G/G_0 \propto e^{-\gamma L} \tag{6.2}$$

with the length L of the molecule and the attenuation factor γ [217]

$$\gamma = \sqrt{8m\left(V_0 - E_I\right)/\hbar^2}. \tag{6.3}$$

In the attenuation factor γ the energy E_I is the energy of the injected electron and $V_0 > E_I$ is the energetic height of the potential barrier (see Fig. 6.7). The energy of the injected electrons is the Fermi energy $E_I = E_F$. Following Ref. [147] $V_0 - E_I$ will be chosen to be $\Delta/2$ for analytic estimates of γ. This corresponds to the situation, when the Fermi energy is in the middle of the electronic gap of the molecule. This situation is sketched in Fig. 6.7.

6.2.1 Length dependence of the conductance for oligophenylene molecules

We will now present an analysis of the length dependence of the conductance for the families of molecules R, S, and D. In doing so we will study both the hollow and top bonding positions (see Figs. 6.4 and 6.5).

In Fig. 6.8 the transmission of the molecules of the series R, S, and D is displayed.

---

[10] See also Table 6.1 where molecules all exhibit HOMO-LUMO gaps between 3 and 5 eV.

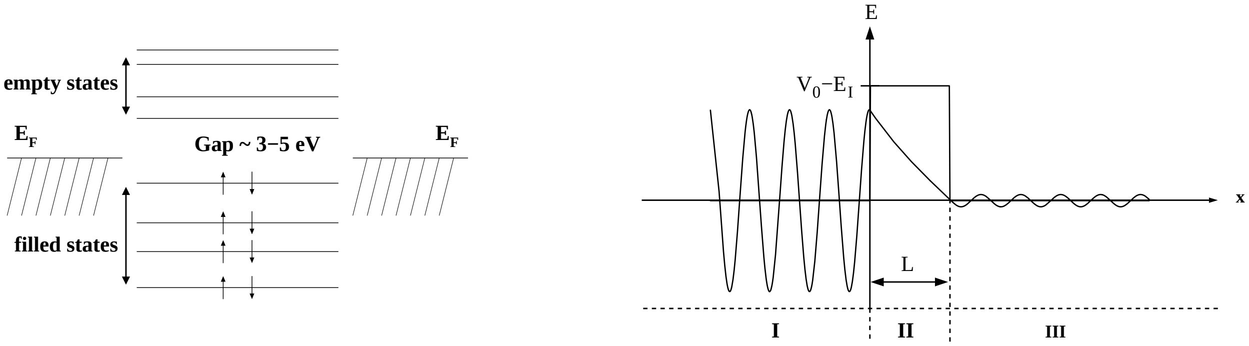

Figure 6.7: In the left panel a schematic diagram shows the molecular energy levels and the Fermi energy E_F in the electrodes. The right panel depicts the tunneling through an energetically forbidden region of length L. Also indicated is the effective height $V_0 - E_I$ of the potential well as measured from the energy E_I of the injected electron.

In all transmission curves a gap is opening up around the Fermi energy E_F. This gap is smallest for the molecules of series R (around 3 eV) and is increased for molecules of series S and D. Generally the conductance decreases within each family of molecules with increasing numbers of phenyl rings irrespective of the bonding position. The molecules of series R are the best conductors. Strikingly the conductance for R4 is higher than that of S2 and D2. In S2 and D2 the conjugated π-system is broken due to methyl side groups. This shows the extreme impact of the extent of the conjugated π-electron system for the conduction properties of organic molecules. An additional observation in Fig. 6.8 is that the transmissions of the molecules of series S and D behave similarly. This is more obvious for the hollow position. The discrepancies noticeable, especially between the transmission curves for S2 and D2 in the top bonding position, can be explained as arising from differences in tilt angles between the S and D molecules (see Table 6.5). These differences can be attributed to the internal stress in the junctions Au-t-Z (see Sec. 6.1.2).

In Table 6.6 we list the precise data for the conductance read off from the transmission curves at a value of $E_F = -5.00$ eV. With respect to the different bonding positions, it can be observed that the conductances increase by an order of magnitude, when going from the hollow to the top position. With the data from Tables 6.2 and 6.4 this phenomenon can be explained by a shift of the HOMO level to higher energies in the top bonding position. In addition to this shift of around 0.4 eV there resides an additional LUMO level above the HOMO and is only around 0.1 eV away from it. The electronic gap of roughly 1 eV is observed between the levels of the LUMO and LUMO+1. This is in contrast to the hollow configuration, where an electronic gap of 1.5 eV is present directly between the HOMO and LUMO levels. The combined effect of the shift of the HOMO levels to higher energies and the by around 0.5 eV reduced electronic gap can explain, why the contacts Au-t-Z exhibit a better conducting behavior than the contacts Au-h-Z.

We will see later that the experimentally measured conductance seems to agree better with the results for the hollow position than with those of the top position (see in particular Fig. 6.14 and its discussion). The changes between the two bonding configurations may

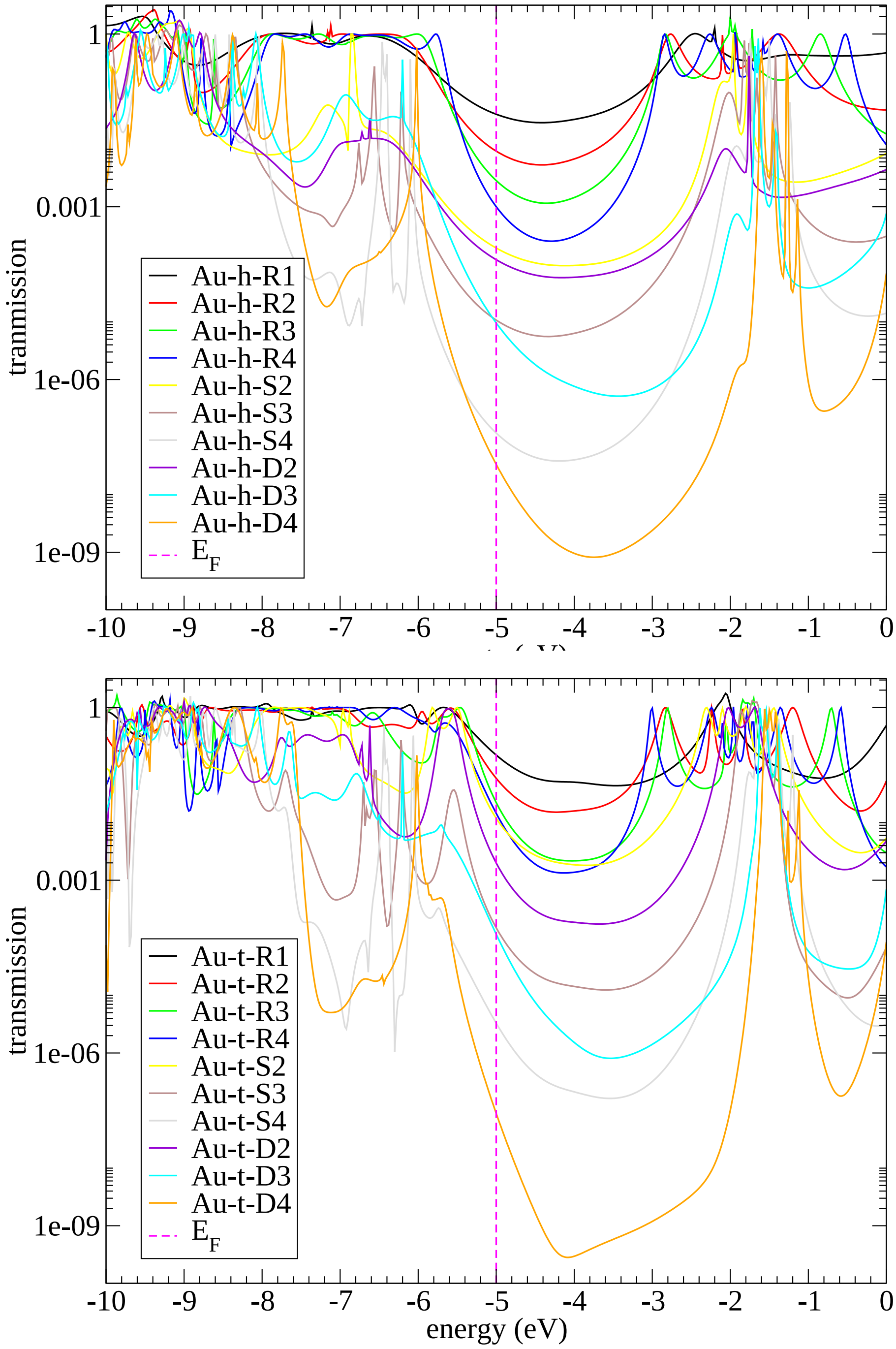

Figure 6.8: Transmission as a function of energy for the molecules of series R, S, and D. The transmission curves for both the hollow (Au-h-Z) and top (Au-t-Z) bonding positions are shown as a function of the energy.

eventually point out a fundamental problem in the use of DFT for the computation of the conductance. It should, however, be taken into account that also in the experiments the

	conductance (G_0)	
molecules	hollow	top
R1	4.04×10^{-2}	1.49×10^{-1}
R2	9.24×10^{-3}	5.89×10^{-2}
R3	2.85×10^{-3}	3.42×10^{-2}
R4	1.00×10^{-3}	1.45×10^{-2}
S2	1.92×10^{-4}	1.19×10^{-2}
S3	1.08×10^{-5}	1.50×10^{-4}
S4	1.18×10^{-7}	3.30×10^{-6}
D2	1.20×10^{-4}	2.00×10^{-3}
D3	9.59×10^{-6}	1.16×10^{-4}
D4	3.36×10^{-8}	8.94×10^{-8}

Table 6.6: Conductance of molecules R1–R4, S2–S4, and D2–D4 as read off from the curves in Fig. 6.8 at a Fermi energy $E_F = -5.0$ eV.

	γ (Å^{-1})	
molecules	hollow	top
R	0.28	0.18
S	0.85	0.95
D	0.94	1.16

Table 6.7: Attenuation factor γ for the length dependence of the conductance (see Eq. (6.2)) as determined from the least-squares fits of Fig. 6.9.

measured conductance changes from one contact realization to the other, which indicates that details of the molecule-metal bonding play a crucial role for the conduction properties (see also the discussion in Sec. 6.3.2).

In order to analyze the length dependence of the conductance we have plotted in Fig. 6.9 the conductance as a function of the length of the molecules of the families R, S, and D for the two bonding positions. The length of the molecules has been measured as the distance between the carbon atoms bonded to the terminal sulfur functions of each molecule. In addition to the data points least-squares fits, according to the expected exponential length dependence of Eq. (6.2), have been plotted. The attenuation factors γ, as determined from these slopes, are listed in Table 6.7.

As discussed before, Fig. 6.9 demonstrates that the conductance for the top position is generally higher than for the hollow position. However, the length dependence within a family of molecules compares well between hollow and top bonding positions, meaning that their least-squares fits run approximately parallel to each other. The molecules of series R are the best conductors, since the conductance decays slowest for them. The attenuation factors for molecules of series S and D are bigger by at least a factor of 3 as compared to R.

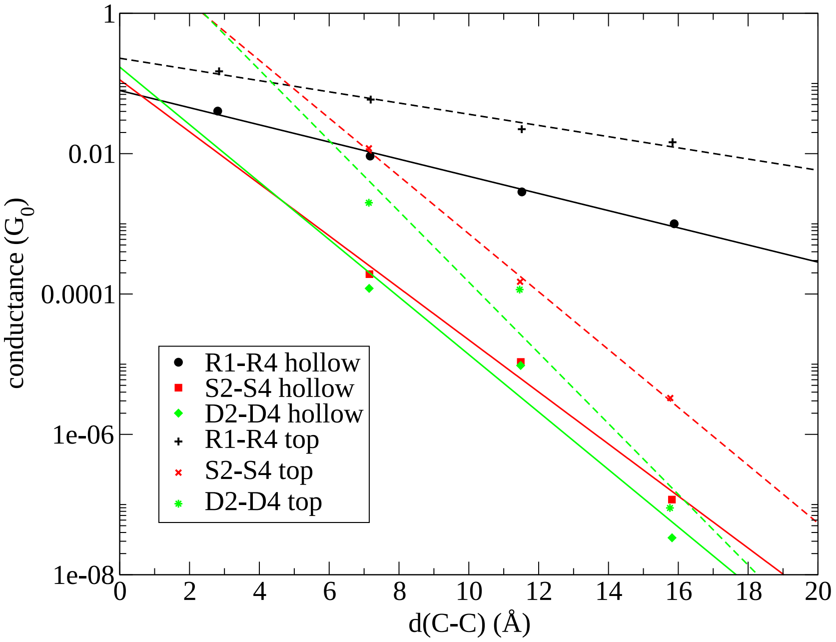

Figure 6.9: Length dependence of the conductance for the different families of molecules R, S, and D. In addition to the data from Table 6.6 least-squares fits are shown according to the exponential decay law of Eq. (6.2).

Comparisons to experimental results are presently difficult. We are not aware of a study of precisely the dithiolated oligophenylenes of the series R, S, or D. Oligophenylene thiolate self-assembled monolayers have, however, been measured in Ref. [202]. In the oligophenylene thiolate molecules of series R, the second terminal sulfur is replaced by a hydrogen atom, resulting in a bad contact to one side. Attenuation factors of $\gamma = 0.35$–0.50 Å^{-1} have been measured experimentally [202]. A subsequent theoretical study for these thiolate molecules reports $\gamma = 0.5$ Å^{-1} [206]. Or attenuation factors of $\gamma = 0.28$ or 0.18 Å^{-1} for the hollow and top geometries of molecules in series R are somewhat lower than these values, presumably due to the different bonding situation at one end of the molecule. Nevertheless we note a reasonable agreement with the experimental data of Ref. [202]. From the theory side Kondo *et al.* [179] studied exactly the series R with up to five rings in a DFT approach. They obtained – although with a less accurate electrode model – an attenuation factor of $\gamma = 0.256$ Å^{-1}, well in line with our findings.

With the help of Eq. (6.3) a simple estimate of the attenuation factor is possible. From Table 6.1 we can extract that the molecules of series R exhibit HOMO-LUMO gaps Δ of around 3 eV, while for the series S and D Δ is around 4.5 eV. Assuming the mid-gap situation as explained in the context of Eq. (6.3) we obtain with $V_0 - E_I = \Delta/2$ the attenuation factors $\gamma = 1.25$ Å^{-1} ($\Delta = 3$ eV) and $\gamma = 1.54$ Å^{-1} ($\Delta = 4.5$ eV). Although a very rough estimate, these values are close to the attenuation factors of the families S and D. The attenuation factor of the molecules R, instead, is drastically lower. This difference in attenuation factors cannot simply be explained by the smaller electronic gap of the molecules R. Again this observation points out the significance of the conjugated π-electron system for the conductance in organic molecules. The better the delocalization of electrons is, the better will the molecule be conducting, and the smaller will be the decay of the conductance with distance.

6.2.2 The role of molecular orbitals in the regime of exponential conductance decay

In the field of molecular electronics an attempt is often made to quantify the importance of a particular molecular orbital for the conductance of a MMM junction [163, 179]. One tries to make a statement, for example, whether the HOMO plays a more important role for the conductance than the LUMO. In order to clarify the importance of a particular orbital of a molecular wire we will analyze in this chapter the conductance of a homogeneous wire model as established in Refs. [218, 204, 205].

We start from the Hamiltonian for the homogeneous wire with nearest neighbor interaction

$$H = \begin{pmatrix} \varepsilon & -t & 0 & \cdots & 0 \\ -t & \varepsilon & & & \vdots \\ 0 & & \ddots & & 0 \\ \vdots & & & \varepsilon & -t \\ 0 & \cdots & 0 & -t & \varepsilon \end{pmatrix}, \tag{6.4}$$

where ε is the onsite element and t is the nearest neighbor coupling. All matrices will be assumed to be of dimension $N \times N$ in the following. Each onsite element shall effectively describe a certain site (atom) of a homogeneous wire. Like in the sketch of the DBA system in Fig. 6.6 the N sites describe the units of a molecular bridge between two electrodes. In an orthogonal basis the inverse Green's function is

$$G^{-1}(E) = E\mathbb{1} - \begin{pmatrix} \varepsilon+\Sigma & -t & 0 & \cdots & 0 \\ -t & \varepsilon & & & \vdots \\ 0 & & \ddots & & 0 \\ \vdots & & & \varepsilon & -t \\ 0 & \cdots & 0 & -t & \varepsilon+\Sigma \end{pmatrix}$$

with some scalar self-energies Σ that are, for reasons of simplicity, assumed to be equal for both the left and the right side and energy independent. For a single orbital model the conductance is given by (see Eqs. C.7 and C.10) [205]

$$G = G_0\Gamma^2 \left|G_{1N}(E_F)\right|^2 . \tag{6.5}$$

In this expression G_0 is the unit of conductance, $\Gamma = -2\mathrm{Im}\,[\Sigma]$ is the transfer rate and G_{1N}

is the propagator between site 1 and N of the wire.[11] From simple determinantal rules [218, 204] it can be shown that

$$G_{1N} = \frac{t^{N-1}}{D_{1N} - D_{2N}\Sigma - D_{1(N-1)}\Sigma + D_{2(N-1)}\Sigma^2}.$$

In this expression D_{pq} refers to the determinant of the matrix $g^{-1}(E) = E\mathbb{1} - H$ obtained by taking out rows and columns only in the range from p to q. Thus $D_{1N} = \det\left[g^{-1}(E)\right]$ is the determinant of $g^{-1}(E)$ and by definition $D_{pq} = 1$ for $p = q = 0$ and $D_{pq} = 0$ if either p or q are negative. With the help of the explicit form of the Chebyshev polynomial of the second kind

$$U_N(x) = \frac{1}{2}\frac{\left(x + \sqrt{x^2-1}\right)^{N+1} - \left(x - \sqrt{x^2-1}\right)^{N+1}}{\sqrt{x^2-1}} \tag{6.6}$$

we can write

$$G_{1N}(E_F) = \frac{g_{1N}}{1 - 2\left(\Sigma/t\right)U_{N-1}(x)/U_N(x) + \left(\Sigma/t\right)^2 U_{N-2}(x)/U_N(x)} \tag{6.7}$$

with the argument $x = \left(E_F - \varepsilon\right)/2t$ and the propagator

$$g_{1N}(x) = \frac{1}{tU_N(x)} \tag{6.8}$$

of the uncoupled system without self-energies.

Let us now look at the behavior of the conductance for increasing chain lengths $N \rightarrow \infty$. According to Eq. (6.5) we need to study the behavior of G_{1N} in Eq. (6.7). We will study the off-resonant situation $|x| \gg 1$. For large x the Chebyshev polynomial in Eq. (6.6) is approximately $U_N(x) \approx (2x)^N$. The denominator in Eq. (6.7) is then $d = 1 - \Sigma/tx + \left(\Sigma/2tx\right)^2$ and does not depend on the length of the wire. As x is assumed to be big, we approximate the denominator by $d = 1$, and get $G_{1N} \approx g_{1N}$. The distance dependence of G_{1N} is completely characterized by the distance dependence of g_{1N} belonging to the homogeneous wire of the uncoupled system. Exploiting Eq. (6.8) we get

$$G_{1N} \rightarrow t^{-1}\left(2x\right)^{-N} \quad \text{for } |x| \gg 1 \text{ and } N \rightarrow \infty, \tag{6.9}$$

and the conductance in Eq. (6.5) becomes

$$G \rightarrow G_0\left(\Gamma/t\right)^2\left(2x\right)^{-2N}.$$

This shows that an exponential length dependence of the conductance is observed for a homogeneous wire in the offresonant situation $|x| \gg 1$, caused by the exponential length dependence of the propagator g_{1N}.

---

[11] Note that in order not to confuse the conductance G with the Green's functions $G(E)$ we will keep the energy argument of the Green's function. The propagator G_{1N} can, however, not be confused with G and we drop its energy argument.

In order to quantify the role of certain molecular orbitals of the wire on the conductance we adopt now a different point of view in terms of the spectral representation of the propagator G_{1N}. In the previous discussion we have seen that in the limit of long wire lengths the length dependence of G_{1N} is the same as that of the uncoupled homogeneous wire g_{1N}. For this reason we will, in the following, concentrate on systems described by the Hamiltonian of Eq. (6.4). This means that we will neglect the role of self-energies in the following.

For a homogeneous wire with a Hamiltonian, as given in Eq. (6.4), the eigenvalues

$$e_\mu = \varepsilon - 2t\cos(\frac{\pi}{N+1}\mu)$$

and eigenvectors

$$v_\mu^{(n)} = \pm\sqrt{\frac{2}{N+1}}\sin(\frac{\pi n}{N+1}\mu)$$

are known analytically [208]. By $v_\mu^{(n)}$ we mean the nth component of the eigenvector with eigenvalue e_μ. Equipped with these relations the propagator g_{1N} can be written

$$\begin{aligned} g_{1N}(E_F) &= \sum_{\mu=1}^{N} \frac{2}{N+1} \frac{\sin(\frac{\pi}{N+1}\mu)\sin(\frac{\pi N}{N+1}\mu)}{E_F - \left(\varepsilon - 2t\cos(\frac{\pi}{N+1}\mu)\right)} \qquad (6.10)\\ &= \sum_{\mu=1}^{N} \frac{1}{N+1} \frac{\sin(\frac{\pi}{N+1}\mu)\sin(\frac{\pi N}{N+1}\mu)}{t\left(x + \cos(\frac{\pi}{N+1}\mu)\right)}, \end{aligned}$$

where we can now see the role of the different molecular orbitals explicitly as compared to the equivalent expression in Eq. (6.8).

For the length dependence to be exponential, we need to be in the off-resonant situation as above ($|x| = |(E_F - \varepsilon)/2t| \gg 1$). The exponential length dependence of g_{1N}, as seen from the point of view of the spectral representation in Eq. (6.10), needs to arise from the summation over different orbitals. The reason is that for $|x| \gg 1$ the denominator is roughly $(N+1)\,tx$. For the summation over the numerator alone the relation

$$\sum_\mu \sin(\frac{\pi}{N+1}\mu)\sin(\frac{\pi N}{N+1}\mu) = \sum_\mu \left\{\cos(\pi\frac{N-1}{N+1}\mu) - (-1)^\mu\right\} = 0 \quad \text{for } N > 1$$

holds. As a crude approximation for very large $|x|$ we get

$$g_{1N} \approx \frac{1}{N+1}\frac{1}{tx}\sum_\mu \sin(\frac{\pi}{N+1}\mu)\sin(\frac{\pi N}{N+1}\mu) = 0 \quad \text{for } N > 1. \qquad (6.11)$$

It is thus difficult to observe the exponential length dependence of g_{1N} from the spectral representation, Eq. (6.10), due to the oscillations in the numerator and denominator. We interpret Eq. (6.11) such that the exponential decay of g_{1N} in the off-resonant situation (outside the energy interval $\varepsilon \pm 2t$) can only arise from a destructive interference of *all* molecular orbitals of the wire.

This interpretation can be made more explicit by considering the length dependence as predicted by Eq. (6.10) for a particular orbital. We consider the contributions of levels at three different energies, namely $\mu_1 = 1$, $\mu_2 = (N+1)/2$, and $\mu_3 = N$. All other molecular orbitals will be neglected in the summation over μ in Eq. (6.10). In this way we get

$$\begin{aligned} g_{1N}^{(\mu_1)} &\rightarrow \frac{1}{N+1} \frac{\left(\frac{\pi}{N+1}\right)\left(\frac{\pi}{N+1}\right)}{tx} = \frac{\pi^2}{(N+1)^3\, tx} \\ g_{1N}^{(\mu_2)} &\rightarrow \frac{1}{(N+1)\, tx} \\ g_{1N}^{(\mu_3)} &\rightarrow \frac{1}{N+1} \frac{\left(\frac{\pi}{N+1}\right)\left(\frac{\pi}{N+1}\right)}{tx} = \frac{\pi^2}{(N+1)^3\, tx} \end{aligned}$$

where $g_{1N}^{(\mu_i)}$ stands for the contribution of the orbital μ_i to the propagator. It is apparent that the propagator exhibits a power law dependence, when particular orbital levels of the homogeneous wire are considered. This is in contrast to the correct exponential length dependence of Eq. (6.4).

In conclusion the spectral representation, where the molecular orbitals are explicitly visible, does not appear to be particularly suited for observing the exponential length dependence of the conductance for systems with a gap in the electronic states. In this off-resonant situation the exponential decay of the conductance appears to arise from a destructive interference of *all* molecular orbitals. The consideration of just a particular molecular orbital, e.g. the HOMO or LUMO level, cannot explain the exponential decay, but only results in a power law dependence of the conductance.

6.2.3 Influence of the electrode coupling on the molecular orbitals of isolated systems

In this paragraph we will analyze, how the charge transfer properties and the electronic structure of the isolated Au-molecule-Au junction translate to the conduction properties and LDOS of this junction, when the junction is coupled to semi-infinite electrodes at both ends. We will refer to the uncoupled cluster as the isolated system, while the system with semi-infinite electrodes attached to both ends will be called the coupled system. In the following, we will concentrate on the example of the contact Au-h-S2. All ideas illustrated here have been checked to be equally valid for all other junctions.

A lot of work in the field of chemistry has been devoted to intermolecular charge transfer. Commonly a DBA system is studied with an electron transfer reaction as given in Eq. (6.1). In order to make theoretical predictions on the charge transfer rate an electronic transition matrix element, also often called effective electronic coupling element, is needed as discussed in Refs. [210, 219, 218, 204, 205, 220, 203]. As reasoned in these references the electronic transition matrix element for an electron to go from the donor site

D to the acceptor site A in the superexchange mechanism is approximately proportional to the propagator g_{DA}.

In order to study the transition probability of an electron to cross a molecule, we will consider the Frobenius norm of the propagator g_{DA}, namely

$$F(E) = \sum_{i \in A, j \in D} \left| g^r_{ij}(E) \right|^2 = \mathrm{Tr}_D \left[g^r_{DA} \left(g^r_{DA} \right)^+ \right] \tag{6.12}$$

In this formula the summations $i \in A$ ($j \in D$) mean that we sum over all orbitals of atoms in region A (D).

As illustrated in the left panel of Fig. 6.10 we consider the gold electrode clusters to be the donor (D) and acceptor (A) regions. To the right the plot of $F(E)$ is shown. The Frobenius norm exhibits clear peaks at energies that coincide with the molecular orbital (MO) energies of the system. Only with few exceptions most molecular orbital energies are degenerate, where two or more MOs have the same energy. For the peaks of $F(E)$ selected in Fig. 6.10 there are two degenerate MOs for each peak position, and the shape of the wave function associated with one of them is depicted above, the other one below the plot.

The exact correspondence between molecular orbital energies and peaks in $F(E)$ is readily explained by recalling the spectral representation of a Green's function. With Eq. (B.20) we can write

$$g^r_{ij}(E) = \sum_{\mu} \frac{c_{i\mu} c_{j\mu}}{E + i\eta - \varepsilon_{\mu}} \tag{6.13}$$

where the summation runs over all molecular orbitals μ with eigenvalues ε_{μ}, η is a small broadening parameter, and the coefficients $c_{i\mu}$ are the solutions to the generalized eigenvalue problem Eq. (B.21). If the coefficients $c_{i\mu}$ or $c_{j\mu}$ with $i \in A$ and $j \in D$ are not all zero for a certain MO, which is unlikely to occur, then at the energy $E = \varepsilon_{\mu}$ there occurs a singularity in g_{DA} and consequently also in $F(E)$. (Finite peak heights in Fig. 6.10 are therefore an artefact of a finite broadening η and a finite number of energy points.) Depending on the weight of the molecular orbital in both A and D one may perhaps expect peaks of high or low magnitude. However we can note that the peak heights of wavefunctions, seemingly localized on one side of the electrode (see the peaks at energies of -6.38 and -3.40 eV), are of equal height as the wave functions corresponding to delocalized wave functions (see the peaks at energies of HOMO and LUMO level at -5.74 and -4.24 eV). Commonly our experience tells us that if low enough isovalues are chosen, when plotting the wave function of a particular MO, the wave function appears to be delocalized over the entire system. This was at least true for all molecular orbitals in the vicinity of the HOMO or LUMO level, which we inspected.

When looking at the plot of $F(E)$ another remarkable feature is the gap visible in the center. This gap resembles the gap in the transmission curve of the coupled system Au-h-S2 in Fig. 6.8. We will now investigate the connection between the transmission and the electronic structure of the isolated system, represented by the Frobenius norm.

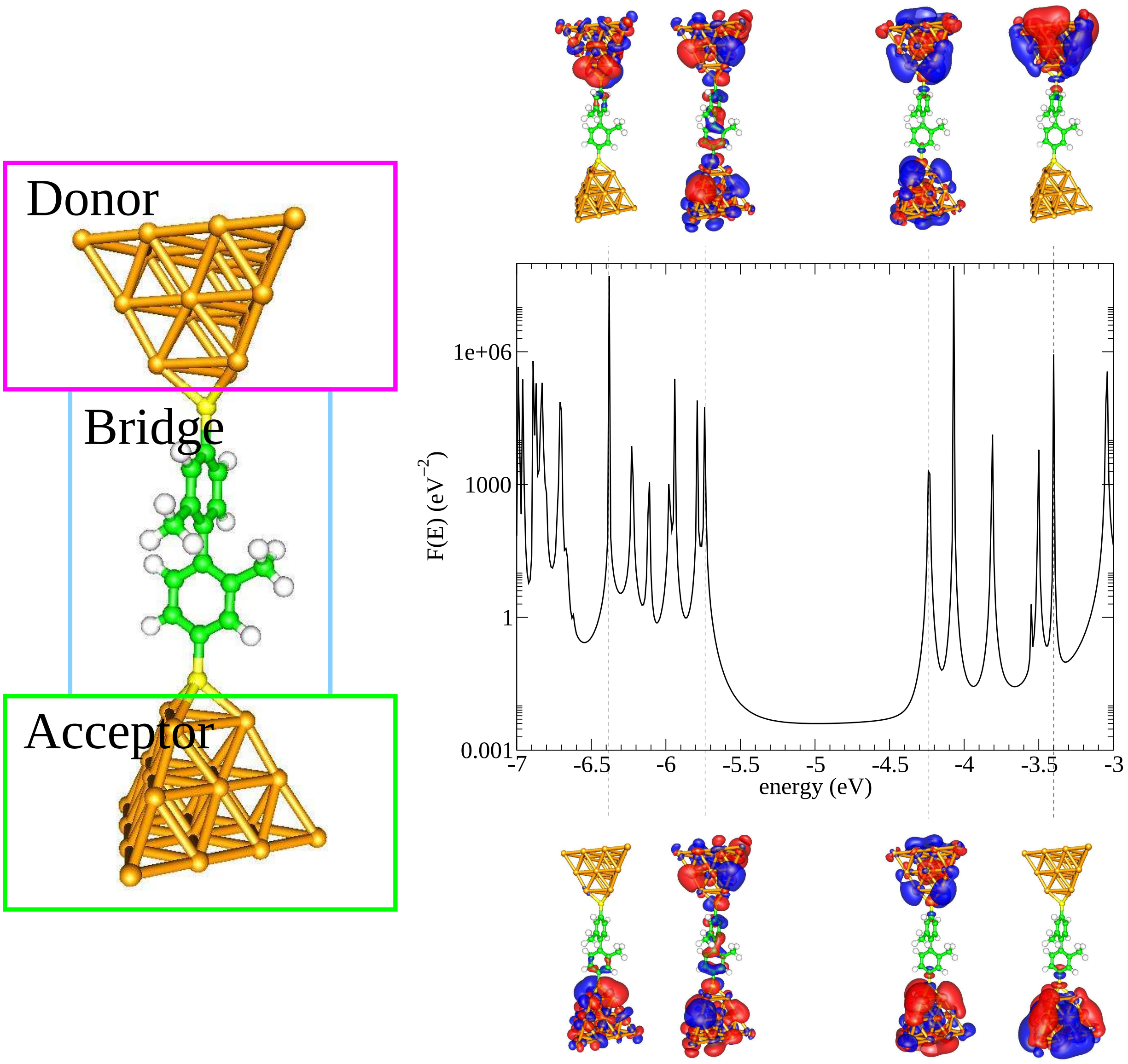

Figure 6.10: In the left panel the partitioning of the uncoupled contact Au-h-S2 into a DBA system is shown. To the right the Frobenius norm $F(E)$ of the propagator g_{DA} between the donor (D) and acceptor (A) regions is displayed. Also indicated are the molecular orbitals, to which the peaks can be attributed, as visible above and below the plot. All molecular orbital wave functions have been plotted with the same contour isovalue of ± 0.01, where red corresponds to the positive and blue to the negative sign. A broadening parameter of $\eta = 10^{-8}$ H$= 2.7 \times 10^{-7}$ eV has been used for the Green's function g^r_{DA} in this plot.

In Fig. 6.11 we display the transmission of the coupled system Au-h-S2 and the LDOS for three different regions in the central part of the contact. The three regions contain different numbers of atoms. The first one comprises only carbon and hydrogen atoms of

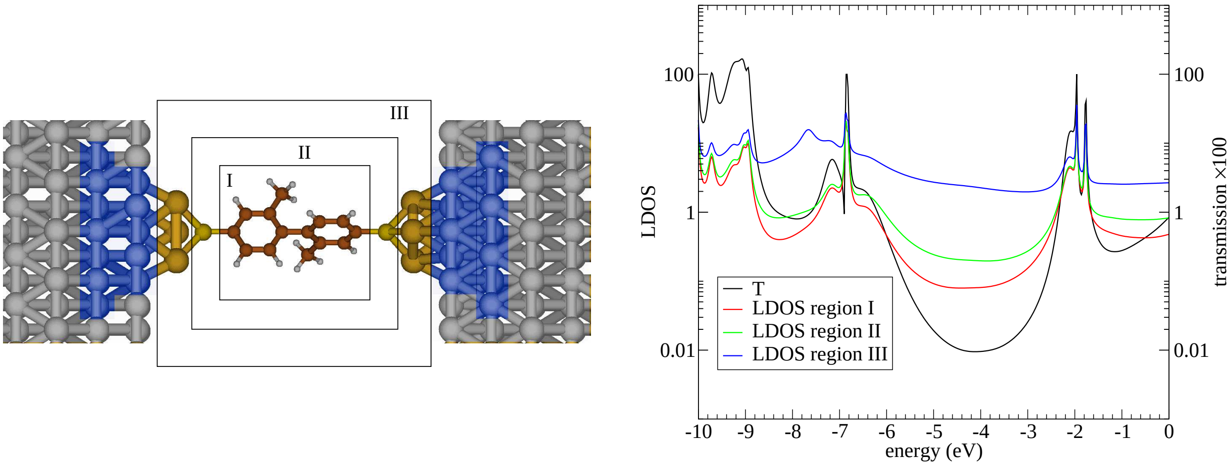

Figure 6.11: Comparison of the transmission and the LDOS for the coupled junction Au-h-S2. To the left the three different regions are indicated for which the LDOS has been computed according to Eq. (B.38). The first one contains the atoms of the center with the bonding sulfur excluded, the second region adds the two sulfur atoms, and in the third region three additional gold atoms on each side are included. To the right the LDOS is overlayed with the transmission T, which has been multiplied by a factor of 100.

the molecule, while in the second region the terminal sulfur atoms are added. The region number III contains the additional three gold atoms on each side of the contact. In each case the LDOS has been computed with the help of Eq. (B.38).

It becomes obvious from Fig. 6.11 that the transmission follows all the features that the LDOS of regions I and II exhibits. Both the LDOS of regions I and II possess a gap in their center. When the Au atoms are included in the LDOS, the gap is closed. This observation is indeed not surprising, because the Au atoms are directly coupled to semi-infinite Au electrodes with a continuous DOS without gaps at the Fermi energy.

Now we may compare the transmission of Fig. 6.11 to the Frobenius norm in Fig. 6.10, which can be interpreted as being proportional to the energy-dependent transition probability for electrons to go from D to A [220, 203].[12] While $F(E) = \mathrm{Tr}_D \left[g_{DA} g_{DA}^{+} \right]$ (see Eq. (6.12)) contains only the bare propagators, the transmission $T(E) = \mathrm{Tr}\left[\Gamma_L G_{CC}^r \Gamma_R G_{CC}^a\right]$ (see Eq. (C.7)) is weighted by the transition rates Γ_L and Γ_R and the Green's function G_{CC} contains additional self-energy terms Σ_L and Σ_R in the denominator (see Eq. (B.26)). In the comparison of $T(E)$ with $F(E)$ we observe that the peak structure in the transmission has vanished. More interestingly the level structure seems to have changed drastically. Thus the gap in $T(E)$ appears to be between -6.4 and -2.1 eV, while in $F(E)$ the HOMO and LUMO level at positions of -5.74 and -4.24 eV border the gap. We interpret this fact as a strong modification of the electronic structure due to the coupling of semi-infinite electrodes to the contact. The level shifts seem to be of magnitudes up to 2 eV. This stresses the importance of the construction of accurate self-energies Σ (see Sec. 4.2).

---

[12] Note that $F(E)$ is by no means bounded and that this analogy is for this reason somewhat vague.

	conductance (G_0)	
molecule	hollow	top
R2	9.24×10^{-3}	5.89×10^{-2}
B1	1.71×10^{-2}	7.07×10^{-2}
B2	1.07×10^{-2}	7.20×10^{-2}
B3	1.38×10^{-2}	8.22×10^{-2}

Table 6.8: Conductance of different biphenyl molecules in the hollow and top bonding position ($E_F = -5.00$ eV).

Indeed the strong modification of the electronic structure is not too surprising. As visible in Fig. 6.11 the last two blue-shaded atomic layers are replaced by surface Green's functions. This means that 32 out of 38 atoms of the Au clusters are replaced, explaining a strong change in the properties of the isolated system Au-h-S2. While the finite system still exhibits a gap in the electronic structure, the incorporated surface Green's functions possess a continuous DOS without a gap at the Fermi energy. The vanishing of the gap in the DOS is visible from the LDOS of region III in Fig. 6.11. We conclude by stating that, with respect to these observations, an interpretation of the properties of the fully coupled system in terms of the level structure of the isolated system appears to be hampered.

6.3 Tailoring the conductance by controlling the degree of electronic conjugation

In this section, we will first present the analysis of electron transport through biphenyl junctions of series R and B (see Figs. 6.4 and 6.5). Then we will address the question, how molecular structures look like in an experimental realization of a junction. We will observe that many different conformations may be present, depending on the molecule contacted. Additionally we will compare our results to experimental ones of Ref. [34]. Finally, we will address in a more conceptual study the influence of varied inter-ring tilt angles in three different biphenyl junctions. We will show, how the total energy and conductance depends on this tilt angle. Considering the ring tilts as the most important degree of freedom, we will study the temperature dependence of the conductance and obtain qualitatively different temperature behaviors for the three different biphenyl systems investigated.

6.3.1 Conductance of biphenyl derivatives

This paragraph is devoted to the study of biphenyl molecules with a high degree of electronic conjugation. Besides the molecule R2 this includes the molecules of series B (B1–B3), which has not been discussed yet. In Fig. 6.12 we display the transmission of these molecules for both the hollow and top position (see Figs. 6.4 and 6.5). The precise values of the conductance are listed in Table 6.8 As visible in the figure all molecules feature quan-

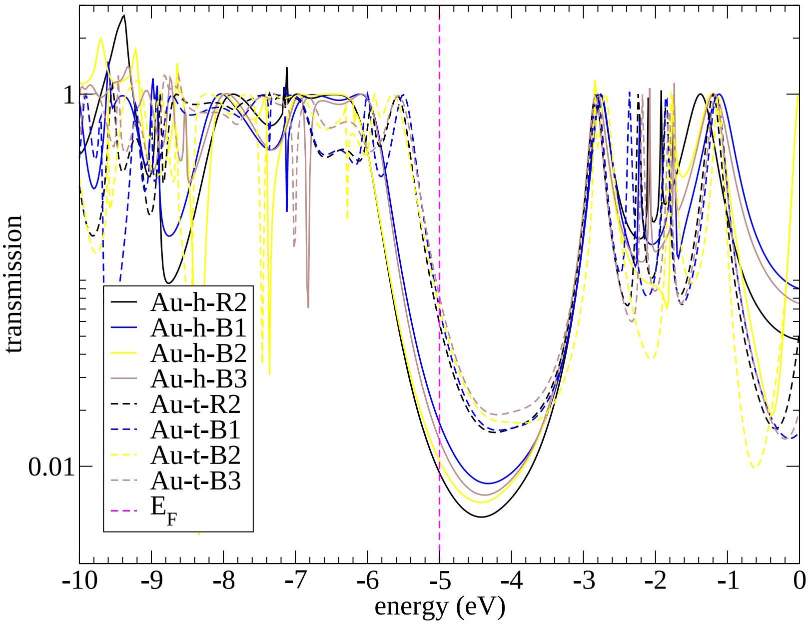

Figure 6.12: Transmission of biphenyl junctions with an extended π-electron system. The curves displayed correspond to R2 and B1–B3. As indicated in the legend, solid lines correspond to the hollow geometries Au-h-Z (see Fig. 6.4), while broken lines are for geometries Au-t-Z (see Fig. 6.5) in the top bonding position.

titatively similar transmission curves. There are, however, substantial differences between the hollow and top bonding position. Between these two conformations a difference in the conductance of up to one order of magnitude can be read off from Table 6.8, similar to what has been observed before (see Table 6.6). From the tilt angles given in Tables 6.3 and 6.5 one might have expected that the conductances of the various molecules are ordered as $G_{\mathrm{R2}} < G_{\mathrm{B3}} < G_{\mathrm{B1}} \approx G_{\mathrm{B2}}$, because the tilt angles between the phenyl rings increase (and the extent of the conjugated π-system reduces) in this sequence. Of course this simple reasoning neglects the effect of the side groups. The ordering that we can read off from Table 6.8 is $G_{\mathrm{R2}} < G_{\mathrm{B2}} < G_{\mathrm{B3}} < G_{\mathrm{B1}}$ for the hollow geometries and $G_{\mathrm{R2}} < G_{\mathrm{B1}} < G_{\mathrm{B2}} < G_{\mathrm{B3}}$ for the top bonding. The expectation that R2 is the worst conductor in this set of four molecules is fulfilled. However, B3 is a better conductor than B2. We are not sure, whether our method is precise enough to resolve the differences in the conductance of the molecules B1, B2, and B3 correctly. Let us conclude by stating that the conductances of the molecules R2, and B1–B3 are very similar. This coincides with intuitive expectations, because all these molecules possess a similarly extended conjugated π-electron system.

6.3.2 Geometric configurations of contacted molecules

Let us now compare the results of our method to experimental results of Ref. [34]. We start with the single phenyl ring R1. This molecule has a long history in the young field of molecular electronics. It was one of the first molecules, for which it was claimed that single molecule measurements have been performed [221]. To date many more experimental [222, 34] as well as theoretical studies [150, 223, 162, 179] have been carried out, of which we list here only a small part.

In Fig. 6.13 we compare the predictions of our method for the differential conductance of the molecule R1 to experimental results by Elbing *et al.* [34] and Xiao *et al.* [222].At zero bias the conductance G can be read off. Strictly speaking, we can only give a value for this zero bias conductance. In order to obtain a dI/dV-curve that can be compared with experimental data, we use the simple model by W. Tian *et al.* [224]. In this model one starts from Eq. (C.6) generalized to finite bias

$$I = \frac{2e}{h} \int_{-\infty}^{\infty} dE T(E,V) \left[f(E-\mu_L) - f(E-\mu_R) \right].$$

We assume that the electrochemical potentials in the two contacts can be written

$$\mu_L = E_F + \nu e V$$

and

$$\mu_R = E_F - (1-\nu)\, eV.$$

The free parameter ν describes, how the electrostatic potential difference is divided between the left and right electrode. Neglecting the voltage dependence of the transmission and considering low temperatures, we arrive at an expression for the conductance

$$G = \frac{dI}{dV} \approx G_0 \left[\nu T(\mu_L) + (1-\nu)\, T(\mu_R) \right].$$

It is immediately obvious that for $\nu = 0$ the conductance G has the same shape as the original transmission $T(E)$, while it is mirrored with respect to $V = 0$ for $\nu = 1$. The value $\nu = 0.5$ corresponds to a symmetric average of the transmission with respect to the Fermi energy at any bias voltage V.

For R1 we compute a conductance of $G = 4.04 \times 10^{-2} G_0$ and $G = 1.49 \times 10^{-1} G_0$ for the hollow and top bonding positions, respectively. We observe that the transmission for the hollow geometry is a factor of around 4 smaller than the transmission for the top geometry. The experimental measurements both show transmissions below the results of the hollow geometry. In order to compare better to experimental results, we reproduce only the results for the hollow position in Fig. 6.13. Comparing to the results of Ref. [34] the overestimation of the conductance G could lead to despair. The dI/dV-curve of the experiments is hardly visible at the bottom of the right panel. However, the measurements of Xiao *et al.* [222] stand in strong contrast to the results of Ref. [34]. In the former reference a conductance of $0.011 G_0$ is obtained in statistical measurements that suggest results of better reproducibility. In Ref. [34] the following comments are made on the measurements of the conductance of molecule R1, namely (i) that "only asymmetric I-V curves have been measured", (ii) that the measurements on molecule R1 "turned out to be

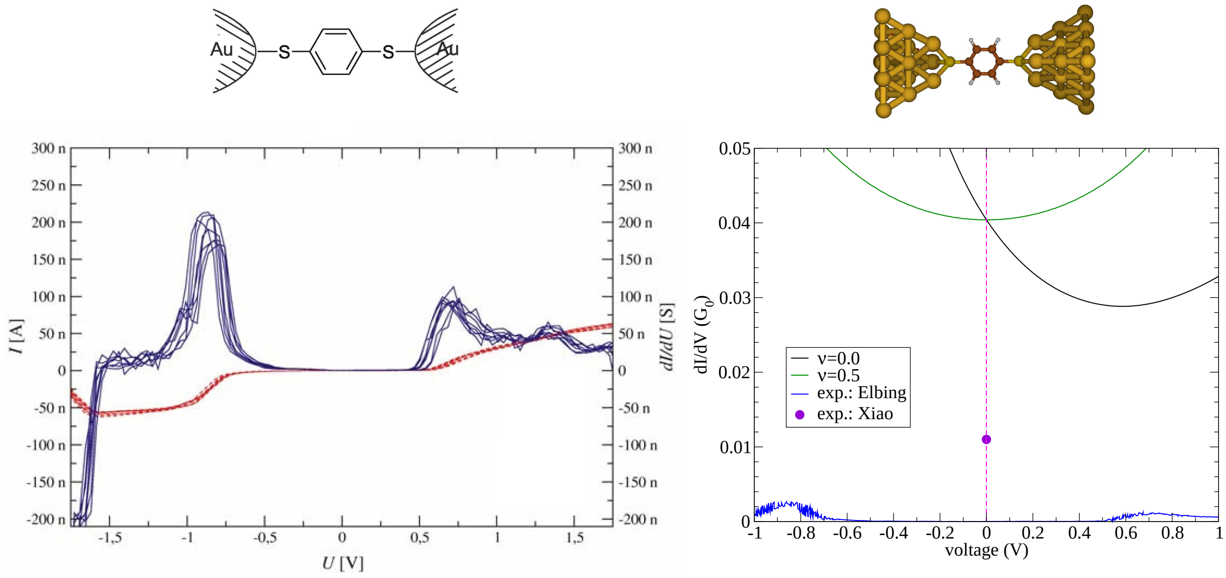

Figure 6.13: Comparsion of experimental measurements and theoretical predictions for the conductance of benzenedithiol, called R1 in this work. The experimental data refers to results by Elbing *et al.* [34] and Xiao *et al.* [222]. In the left panel the original data of Ref. [34] is reproduced. In the right panel the comparison between the theoretical data as obtained with the method developed in this work and the experiments is displayed.

rather challenging, which can probably be attributed to the short length of the molecule". With respect to the second point it seems that the molecule R1 is not the right one to make a conclusive comparison between theory and experiment. In addition to experimental uncertainties we want to mention that, also theoretically, the calculation of the conductance of R1 are more problematic than for longer molecules. We still observe elements in the Hamiltonian (overlap) matrices H_{LR} (S_{LR}) of up to 2×10^{-7} H (1.4×10^{-7}) in absolute values. Thus longer electrode cluster are required in order to completely separate the left and right electrode from each other, as assumed in the formalism for the calculation of the conductance.[13]

The next molecule that we compare to experimental data is the molecule S2. For S2 our method yields conductances of $1.92 \times 10^{-4} G_0$ and $1.19 \times 10^{-2} G_0$ for the hollow and top positions. This means that there are roughly two orders of magnitude difference in the prediction for both bonding situations, with the value for the top position substantially above the result for the hollow position. The comparison to the experimental results of Ref. [34] is shown in Fig. 6.14. Again we suppressed the results for the top position in the figure, which seem to overestimate the conductance of the molecule S2 by a factor of

---

[13] Note that although such elements seem small, there are many of them. In such cases we often observe that the conductance is not going down to zero outside the energy bands but, unphysically, remains finite. Although the main features of a transmission curve are usually well reproduced, a slight overestimation of the conductance results from this fact.

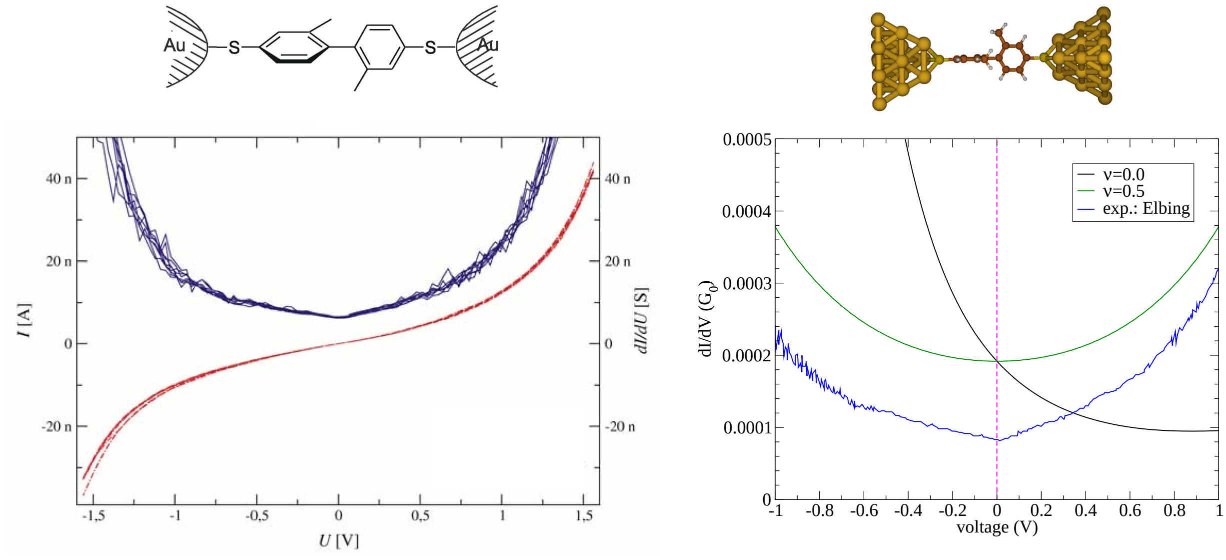

Figure 6.14: Comparsion of experimental measurements and theoretical predictions for the conductance of the molecule S2. The experimental data refers to results by Elbing *et al.* [34], the theoretical data is obtained by means of the method developed in this work. To the left the original data of Ref. [34] is reproduced, while on the right a comparsion of our theoretical results with this data is shown.

60. The difference between the experimental data and our zero bias conductance in the hollow bonding position is, however, only a factor of 2. The dI/dV-curve for the symmetric voltage division ($\nu = 0.5$) is much closer to the experiment than the asymmetric curve for $\nu = 1$. This confirms the statement made in Ref. [224] that in experiments typical values of ν are around 0.5. We want to point out that the measurements on molecule S2 could be performed more reliably as compared to R1 [34].

Results for the molecules S3 and S4 are also presented in Ref. [34]. However the conductance is so small that it was not possible to extract the data with such an accuracy that it could have been compared on a logarithmic scale to our results. Therefore we stop this comparison here and look forward to systematic measurements of the molecules S2–S4 at the IBM Research Laboratories in Zürich, Switzerland [195].

Before we come to a conclusion on the comparison between our DFT conductance results and the experiments let us return to an observation made in the beginning, namely that tilt angles for certain molecules of the S family can deviate from the 90° tilt angle. The tilt angle depends on the initial configuration at the start of the relaxation.[14] But more important is the internal stress in the contact geometry, when the molecule is bonded to Au (see for example Au-t-S2 in Table 6.5). For this reason we relaxed molecules S2 and

---

[14] If in the beginning methyl groups of adjacent rings are at an angle of less than 90° from each other the relaxation usually increases this angle to something close to 90°. If instead hydrogen atoms are at an angle of less than 90° to the methyl groups, relaxed geometries exhibit angles of less than 90° due to the smaller steric repulsion of the hydrogen atom.

molecule	$\lvert\varphi_1\rvert$ (°)	$\lvert\varphi_2\rvert$ (°)
S2	89.96°	–
S2’	83.70°	–
Au-h-S2	89.28	–
Au-h-S2’	80.06	–
Au-t-S2	55.70	–
Au-t-S2’	49.69	–
S3	89.06	84.78
S3’	72.10	73.65
Au-h-S3	84.95	88.73
Au-h-S3’	70.62	69.98
Au-t-S3	81.36	83.29
Au-t-S3’	55.11	66.11

Table 6.9: Ring tilt angles for different minimum energy configurations of the molecules S2 and S3. While S2 and S3 are obtained from starting configurations, where both methyl groups have an angle of less than 90°, the primed molecules result from a starting configuration, where this angle is smaller than 90° for a methyl group and a hydrogen atom on adjacent phenyl rings. Tilt angles are generally smaller for the primed structures.

S3 in the top and hollow geometries with different starting geometries. In the first case the methyl groups of all adjacent rings were at an angle of less than 90°, while in the second case at every connection between two rings a hydrogen atom was at an angle of less than 90° to a methyl group. The first case corresponds to the molecules S2 and S3 discussed up to now, while the two new molecules will be called S2’ and S3’. The tilt angles of the isolated molecules S2, S3 and their primed variants together with the data for the structures in contact with gold clusters can found in Table 6.9. Generally the primed molecules possess smaller inter-ring tilt angles due to the reduced steric repulsion. It is clear from the data of Table 6.9 that the molecules S2’ and S3’ should be better conductors than S2 and S3 due to an increased overlap of the electronic π-system. Their conductance properties for the top and hollow geometries can be seen in Fig. 6.15. The expectations concerning the better conducting behavior of S2’ and S3’ are completely fulfilled. The fact that the molecules S2’ and S3’ are minimum energy configurations suggests that in experiments several conformations of the molecules may be present. The assignment of a unique conductance to ”the molecule” S2 or S3 is thus impossible. Taking this into account the good agreement between the experimental dI/dV-curve for molecule S2 and our result should be seen in the right light. For a molecule in conformation S2’ the overestimation of the conductance, even for the hollow position, increases from a factor of 2 to a factor of 6.

In agreement with Ref. [162] we thus observe that, generally speaking, the conductance of the molecular contacts seems to be overestimated by the DFT-based methods. While this effect is very dramatic for the top bonding position, we see, however, a much better agreement for the hollow bonding situation with very reasonable agreement for the reproducibly measurable molecule S2.[15] While this relativizes the statement of Evers *et al.* [162] that DFT often overestimates the molecular conductance by orders of magnitude,

---

[15] As observed in the discussion of the junctions Au-t-Z (see discussion of Table 6.4), the data for the top bonding position requires further analysis due to the position of the LUMO level well below $E_F = -5.0$ eV.

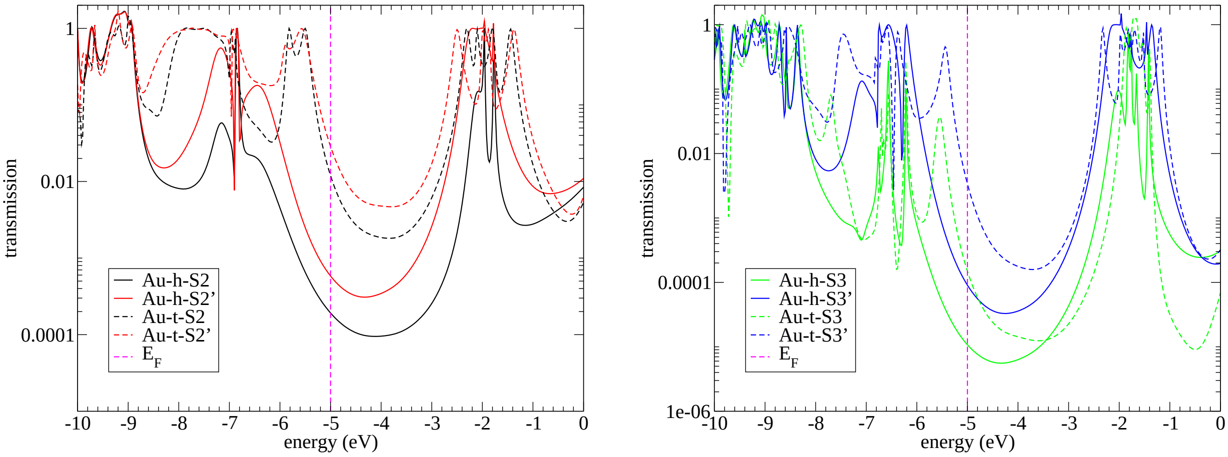

Figure 6.15: Transmission curves for the different molecules S2 and S2' (left panel) and S3 and S3' (right panel). The primed molecules have smaller tilt angles than the unprimed molecules (see Table 6.9). The precise values for the conductance are $1.92 \times 10^{-4} G_0$ for Au-h-S2, $5.83 \times 10^{-4} G_0$ for Au-h-S2', $1.19 \times 10^{-2} G_0$ for Au-t-S2, $2.86 \times 10^{-2} G_0$ for Au-t-S2', $1.08 \times 10^{-5} G_0$ for Au-h-S3, $9.06 \times 10^{-5} G_0$ for Au-t-S3', $1.50 \times 10^{-4} G_0$ for Au-t-S3, $3.38 \times 10^{-3} G_0$ for Au-t-S3'.

we agree that the observed discrepancies, especially in the top bonding position, require further investigations.

The studies presented in this section point out that the reproducibility of conductance measurements in experiments depends crucially on the molecules chosen. For too short molecules reproducible measurements are hampered, as observed here at the example of molecule R1 with very contradictory results in Refs. [222] and [34]. Also conformational changes of the molecular geometry can play a decisive role as illustrated at the example of the two and three ring molecules S2 and S3. For them the tilt angles between different rings could differ, depending on the initial geometry in the search for the minimum energy configurations. Physically this indicates that in a real junction the molecules may adopt different geometries, depending on the actual realization of the contacting process. The configurational changes are observed to cause big changes in the conductance. In order to improve a comparison between predictions of theoretical and experimental results, such uncontrollable configurational variations of the molecular geometry should best be prevented by use of appropriate side groups in future experiments.

6.3.3 Controlling the degree of electronic conjugation

Until now we have already seen many examples for the importance of the extent of the delocalized π-system for the electron transport through molecules. All structures studied so far have been minimum-energy configurations. In this paragraph we will force the rings to adopt other tilt angles, keeping the rest of the structure frozen. In this way we can analyze the dependence of the conductance on continously varying angles. We will do so for the

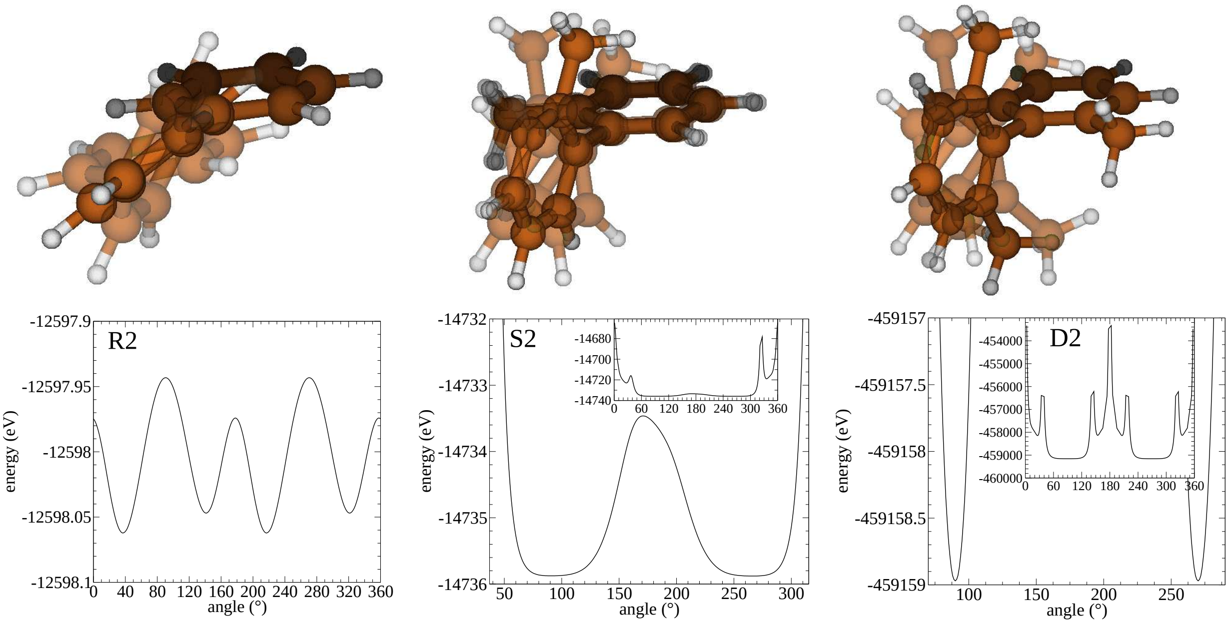

Figure 6.16: In the first row equilibrium structures of the molecules R2, S2, and D2 (from left to right) are displayed. Faintly overlayed on each plot are geometries with ring tilts ±30° away from the equilibrium structure. In each case only the orientation of the phenyl ring unit in the front of the image is changed, while that of the ring in the back of the image is kept fixed. Below these plots the energy landscape $E(\varphi)$ for otherwise frozen structures of the molecules R2, S2, and D2 with respect to varied angles φ of their phenyl rings is shown. This landscape is resolved in steps of $\Delta\varphi = 1°$. For the molecules S2 and D2 the main panel displays $E(\varphi)$ for the two important energetic minima, while the inset shows the complete energy landscape. Note the different scales of energies on the y axes.

molecules R2, S2, and D2. Ultimately the temperature dependence of the conductance for these three kind of molecules will be studied.

As a first step we start out by analyzing the energy landscape for ring tilts $E(\varphi)$ of the isolated molecules, where φ is the inter-ring tilt angle. In Fig. 6.16 the molecules R2, S2, and D2 can be seen in their equilibrium position. Faintly overlayed are structures with tilt angles ±30° away from the equilibrium structure. Also shown are the energy landscapes $E(\varphi)$, namely the total energy as a function of φ. While the curves for the molecules S2 and D2 exhibit energetic minima approximately at right tilt angles of 90° and 270°,[16] for R2 there are four minima at 37°, 141°, 217°, and 321°.[17] In principle one would expect a

---

[16] To be precise, within the resolution of $\Delta\varphi = 1°$ we find the local minima of S2 at 91° and 267° and a central local maximum at 171°. The energy difference between these two local minima and the maximum at $\varphi = 171°$ is $\Delta E = 2.4$ eV. For D2 the minima are located at $\varphi = 90°$ and 270°.

[17] Local maxima for R2 are located at angles φ of 91°, 178°, 271°, and 358°. Energetic differences between the local minimum at $\varphi = 37°$ (and equivalently 217°) and the maxima at 90° (or 270°) and 178° (or 358°) are $\Delta E = 0.12$ eV and $\Delta E = 0.09$ eV. The differences for the local minimum at $\varphi = 141°$ (and equivalently 321°) and the maxima at 90° (or 270°) and 178° (or 358°) are $\Delta E = 0.10$ eV and $\Delta E = 0.07$

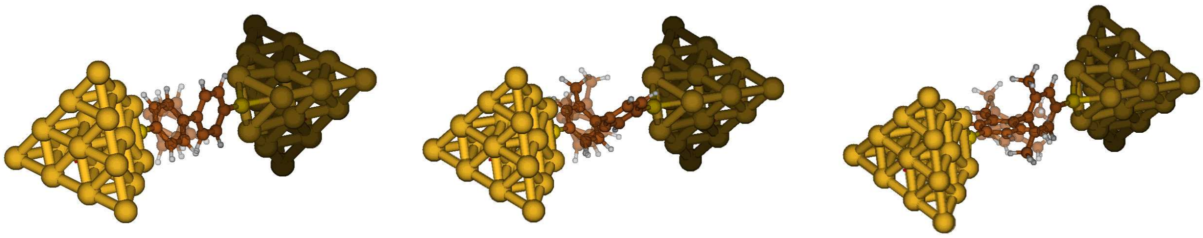

Figure 6.17: Equilibrium structures of the contact configurations Au-h-R2, Au-h-S2, and Au-h-D2 from left to right. Faintly overlayed on each plot are geometries with ring tilts ±30° away from the equilibrium structure. In each case only the orientation of the phenyl ring unit in the front of the image is changed, while the rest of the structure remains unchanged.

periodicity of 90° for $E(\varphi)$ for molecule R2. Due to slight distortions of atoms out of the phenyl ring planes (mainly the ortho hydrogen atoms at the ring connecting carbons) there are deviations from this behavior. Instead the curve is only periodic after 180°. Similar deviations from an expected 180° periodicity in the total energy landscape of molecules S2 and D2 are mainly due to analogous distortions of the methyl side groups. It should be noted that the energy axes in all plots have quite different scales.

In principle theses energy landscapes provide information on the existence of atropisomers, i.e., rotational isomers. In Ref. [34] such rotational isomers have been observed for terphenyl and quaterphenyl compounds. In NMR (nuclear magnetic resonance) measurements the coalescence temperature T_C was determined to be around 325 K.[18] In terms of energies this translates to an approximate energy difference of 0.028 eV between the maximum and minimum in $E(\varphi)$ for the compound S2. Instead we observe an energy difference of around 2.5 eV. This substantial overestimation stems from the frozen structure of the molecule, where side groups have no possibility to avoid each other by, for example, elongated bond distances of the ring connecting carbons. While this is unrealistic, these calculations were done in order to get a rough idea, about which angles may be accessible to the molecules R2, S2, and D2. In a molecular junction the length of the molecule may actually be fixed due to the external boundary conditions set by the electrodes, and the situation may correspond better to the frozen molecular structure as simulated here.

Let us now come to the discussion of the conductance as a function of the tilt angle. For this purpose we studied the hollow bonding configurations Au-h-R2, Au-h-S2, and Au-h-D2 shown in Fig. 6.17. Due to the simulations of the energy landscape $E(\varphi)$ of the isolated molecules R2, S2, and D2 just discussed (see Fig. 6.16), we decided to explore the tilt angle intervals of $\varphi \in [0°, ..., 360°]$ for Au-h-R2, $\varphi \in [60°, ..., 300°]$ for Au-h-S2,

---

eV.

[18] The coalescence temperature is that temperature, for which only one isomer can be measured in the NMR spectra, suggesting that the phenyl rings are rotating so fast that the isomers cannot be distinguished anymore on the NMR time-scale [34]. This means that the energetic barrier between the two configurations has largely been overcome by the thermal energy $E_C = k_B T_C$ with the Boltzmann constant k_B.

and $\varphi \in [60°, ..., 120°]$ for Au-h-D2. In each case the angular resolution was $\Delta\varphi = 2°$. The results for the total energy as a function of the tilt angle $E(\varphi)$ together with the conductance $G(\varphi)$ are shown in Fig. 6.18. As for the isolated molecules (see Fig. 6.16) $E(\varphi)$ exhibits deviations from expected mirror symmetries at 90° for Au-h-R2 and at 180° for Au-h-S2. The reason are again small distortions of the ortho-positioned side groups, which stand slightly away from the ring planes. The presence of the pyramidal gold clusters is an additional factor, why the rotational potentials of Au-h-R2 and Au-h-S2 are not mirror symmetric with respect to 180°.

Concerning the total energy curve for Au-h-D2, there is a minimum at 90°, and the conductance at this point is $1.20 \times 10^{-4} G_0$. For Au-h-S2 the total energy $E(\varphi)$ exhibits two minima at 94° and 268° connected by a local maximum at 174°. The energy difference between the minima and this maximum is $\Delta E = 2.2$ eV. In the minima the conductance is $2.24 \times 10^{-4} G_0$ and $2.18 \times 10^{-4} G_0$ for $\varphi = 94°$ and 268°, respectively. For Au-h-D2 and Au-h-S2 the minimum energy configurations coincide with minima of the conductance curves. This is different for the contact Au-h-R2. Analogously to the isolated molecule, this junction exhibits four minima at angles of $\varphi = 34°$, 144°, 214°, and 324° and four maxima at $\varphi = 90°$, 178°, 270°, and 358°. These local extrema are not visible in the conductance curve $G(\varphi)$, which possesses only two maxima at 0° and 180° and two minima at 90° and 270°. In the maxima the conductance is $1.38 \times 10^{-2} G_0$ and in the minima $2.01 \times 10^{-4} G_0$. Thus an "on-off" ratio of around 70 is obtained, when switching from the planar configurations to the minimum π-overlap geometry.

Especially the results for molecule R2 show the importance of the extent of the conjugated π-electron system for the conduction properties of biphenyl molecules. While in the planar geometry the p orbitals perpendicular to the phenyl ring plane overlap to a large degree, the overlap of these p orbitals will be strongly reduced, when $\varphi = 90°$. The coupling of the p orbitals perpendicular to the phenyl ring planes should be the dominant intermolecular coupling element for the transport. One observes that it is proportional to $\cos(\varphi)$ (see the sketch in Fig. 6.19). This angular dependence can quickly be derived by noting that the wave function of those p orbitals is proportional to $\cos(\phi)$ in the plane perpendicular to the transport direction, where cylinder coordinates are assumed and the angle ϕ is measured in the x-y plane around the z axis. The effective coupling element between the two rings rotated by an angle φ is then proportional to

$$\int_0^{2\pi} d\phi \cos(\phi) \cos(\phi - \varphi) = \pi \cos(\varphi).$$

This coupling element will appear in the transition amplitude or propagator G_{CC} in the trace expression for the current (see Eq. (C.7)). As in turn the propagator appears twice in this expression, the conductance can be expected to be proportional to $\cos^2(\varphi)$ [196].

For this reason we show in Fig. 6.18 a fit to the conductance curve $G(\varphi)$ of molecule R2 to a function of the form $\alpha + \beta \cos^2(\varphi)$. From a least-squares fit we obtain the fit parameters $\alpha = 5.95 \times 10^{-5} G_0$ and $\beta = 1.35 \times 10^{-2} G_0$. The agreement between $G(\varphi)$ and the fitted curve appears to be very convincing with both curves falling nearly on top of each other. This demonstrates that the p orbital coupling is indeed the dominant

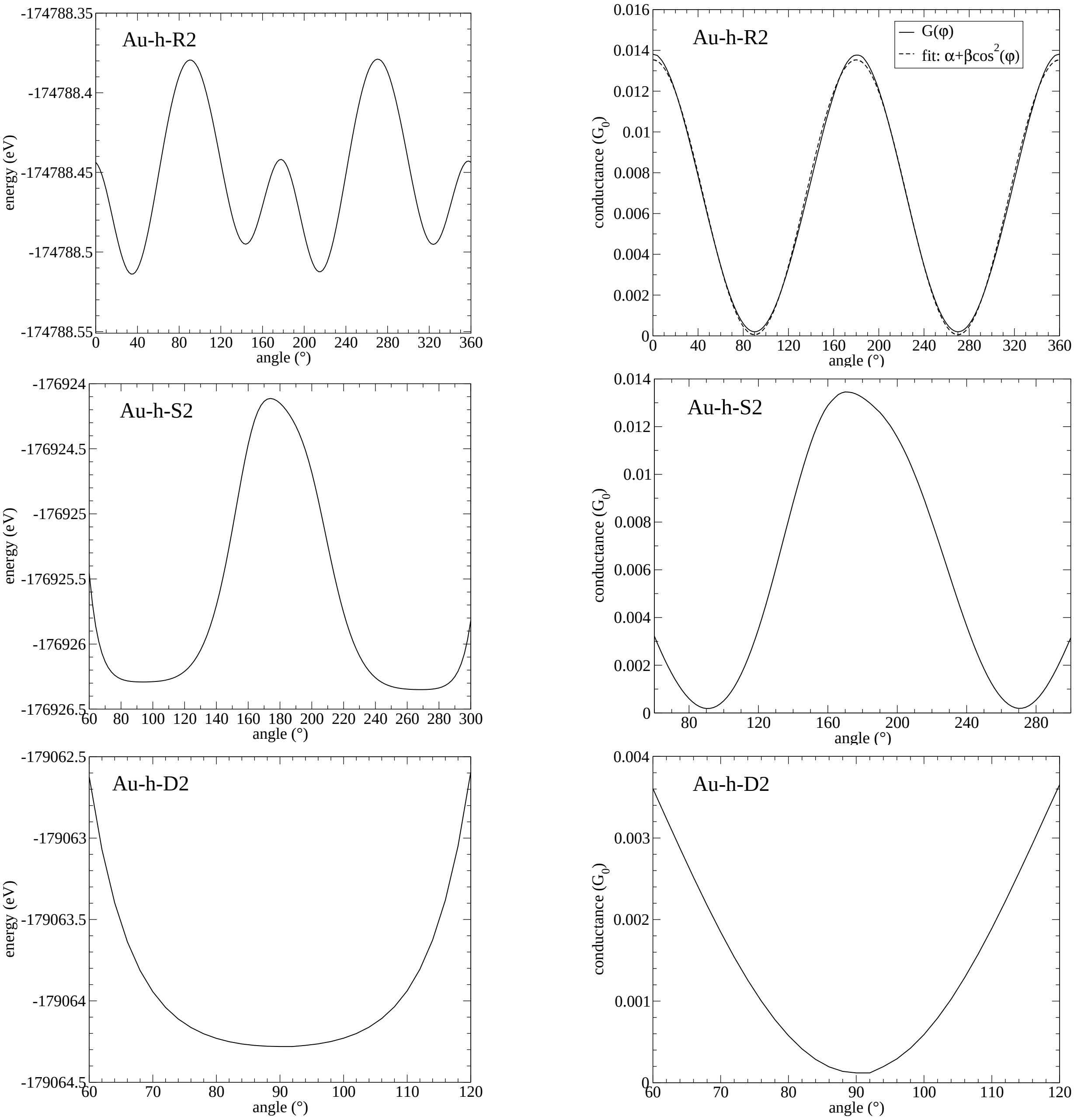

Figure 6.18: Total energy E and conductance G as a function of the tilt angle φ between adjacent rings of the molecules R2, S2, and D2. The geometries correspond to those displayed in Fig. 6.17. A fit to the conductance curve of molecule R2 with a function of the form $\alpha + \beta \cos^2(\varphi)$ is presented as indicated in the legend. From a least-squares fit we obtain the fit parameters $\alpha = 5.95 \times 10^{-5} G_0$ and $\beta = 1.35 \times 10^{-2} G_0$.

mechanism that determines the conduction properties of the molecule R2. However some slight deviations at the extrema of $G(\varphi)$ are observable. Actually the small offset coefficient $\alpha = 5.95 \times 10^{-5} G_0$ indicates an important point. If G would indeed be proportional to

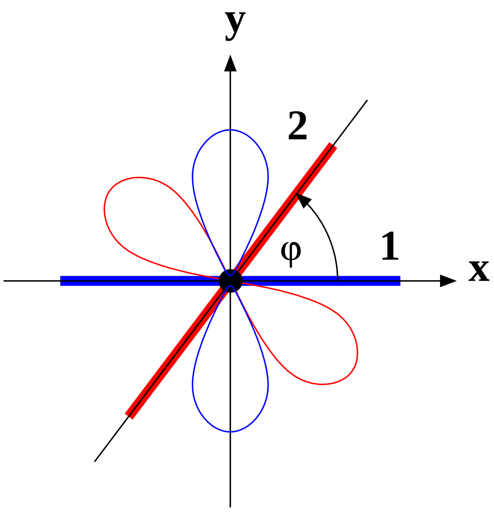

Figure 6.19: The planes of two phenyl rings, called 1 and 2, are tilted by an angle φ with respect to each other. The p orbitals that stand perpendicular to the ring plane are indicated. Their overlap will give rise to an effective coupling element that is proportional to $\cos(\varphi)$ as explained in the text.

$\cos^2(\varphi)$, an infinite on-off ratio would be the result, because in the minima of G the conductance would vanish. This is not the case in our simulations, where an on-off ratio of around 70 is observed as discussed above. At the point of complete π-orbital decoupling some other coupling elements, presumably σ couplings, prevent a complete blockade of the electron transport.

Finally we analyze the behavior of the conductance with respect to temperature. As proposed by Troisi *et al.* [225] in the context of conformational molecular rectifiers, we thermally average the conductance over different tilt angles φ in order to get the temperature dependent conductance[19]

$$\bar{G}(T) = \frac{\sum_i G(\varphi_i) e^{-E(\varphi_i)/k_B T}}{\sum_i e^{-E(\varphi_i)/k_B T}}. \tag{6.14}$$

In this expression T is the temperature and k_B is Boltzmann's constant. The thermal average is based on the energy and conductance landscapes $E(\varphi)$ and $G(\varphi)$ of the Au-molecule-Au contacts as shown in Fig. 6.16.

In Fig. 6.20 the behavior of $\bar{G}$ for the molecules R2, S2, and D2 is shown for temperatures between 0 and 400 K. The temperature behavior exhibits main qualitative differences between the different molecules. While for R2 we observe a decrease of $\bar{G}$ with increasing temperature, this trend is reversed for S2 and D2. For them the thermally averaged conductance increases for elevated temperatures. The reason for these phenomena can be explained via Fig. 6.18. The equilibrium configurations for S2 and D2 correspond to conformations with minimal conductances. Elevated temperatures give access to conformations with reduced tilt angles and increased conductance values. This causes $\bar{G}$ to increase. Opposed to this, the molecule R2 with an equilibrium tilt angle of 37° is already a good conductor. An increased temperature therefore reduces the conductance on average, because conformations with increased inter-ring tilt angles will contribute to the average.

---

[19] Due to our numerical grid with a finite $\Delta\varphi$ this average is written as a discrete sum and not as an integral.

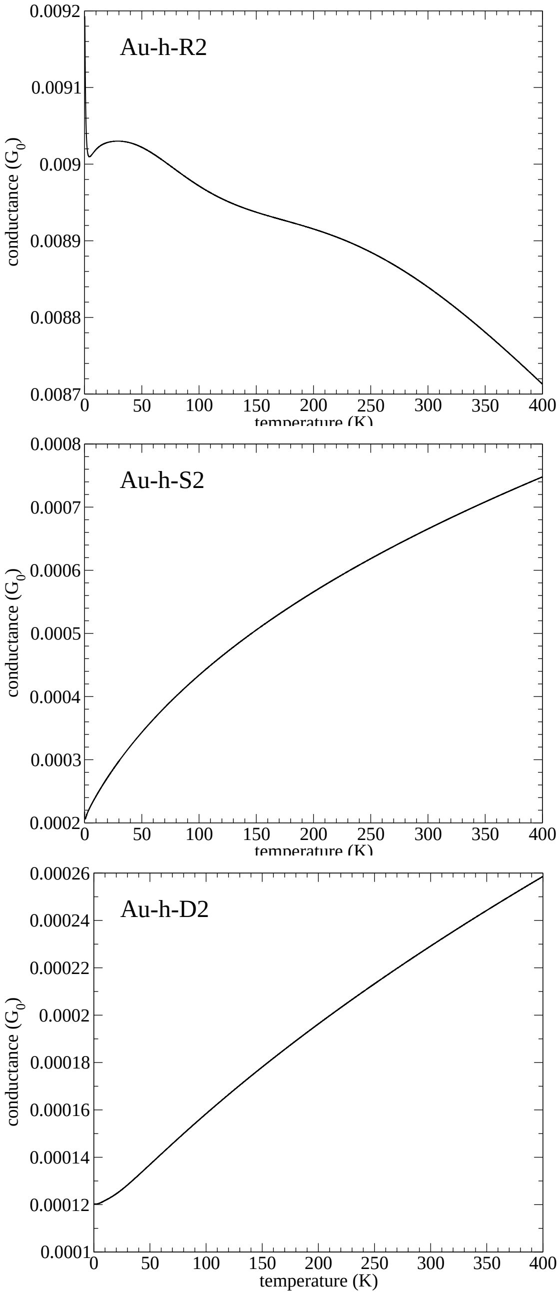

Figure 6.20: Behavior of the conductance $\bar{G}(T)$ for the molecules R2, S2, and D2 for temperatures T between 0 and 400 K.

Of course it should be kept in mind that the calculations in Fig. 6.20 take only thermal averages over different tilt angles into account. Altough definitely an important degree of freedom, there may be reconfigurations that have a larger impact on the temperature behavior of the conductance, e.g., a change of the bonding position from top to hollow. Ramachandran *et al.* [226] explain their measured stochastic on-off switching of thiolated molecules at 333 K by the mobility of molecules tethered to gold via thiol linkage. From this point of view the study of the temperature dependence of the thermally averaged conductance may be considered to be conceptual.

The measurement of the dependence of the conductance on tilt angles between phenyl rings is experimentally most likely best performed by synthesizing molecules with side groups that fix the tilt angles to a predefined value. This is exactly the concept behind the synthesis of the molecules of the series R, S, D, and B. The concept has successfully been realized in the work of Venkataraman *et al.* [196]. Further studies of this kind with more continuous variations of tilt angles may help to demonstrate in more detail the influence of the extent of a delocalized π-electron system on the conductance.

6.4 Conclusions

In this section we have studied the conduction properties of organic molecules bond to Au electrodes. The molecules all belonged to the family of oligophenylenes and carried sulfur functionalities at their ends that established covalent bonds to the Au electrodes on both sides. Their investigation was motivated by recent research activities at the INT, FZK [34].

The idea behind the study of different families of oligophenylene molecules was to provide a deeper theoretical insight into the importance of the conjugated π-electron system for the conduction properties of single molecules. For this reason we analyzed the length dependence of the conductance for three different families of oligophenylenes (R, S, and D). While the first family (R) exhibited an extended delocalized π-electron system, methyl groups hindered the electronic delocalization in the other two families (S and D). Within each family the number of phenyl ring units was varied between one and four. In agreement with previous experimental and theoretical studies of similar molecules, we observed an exponential decay of the conductance for an increased number of phenyl rings.

The attenuation factors for the family R agreed well with previous experimental and theoretical studies. Compared to the other series S and D, where the conjugated π-electron system was completely broken due to two methyl side groups, the attenuation factor for the molecules of series R turned out to be substantially lower. (These side groups forced adjacent phenyl rings to stand at almost 90° to each other for families S and D.) This demonstrates that the intuitive expectation is correct that molecules with a conjugated π-electron system of large extent are better conductors than those, for which the electron delocalization is hindered.

In addition we investigated two kinds of bonding situations, which we called hollow and top. By and large the attenuation factors turned out to be independent of the bonding situation. However, the absolute values of the conductance were roughly an order of magnitude higher in the top than in the hollow position.

In order to gain more insight into the length dependence of the conductance, we studied analytically a single orbital wire model. We could show that the exponential decay of the conductance with length can only be explained as a complex interference of *all* molecular orbitals of the wire.

After the analysis of the length dependence we studied the family B of planar biphenyl molecules. They showed a very similar conductance that was rather independent of the alkyl-bridges employed to stabilize the conjugated π-system.

We continued with a comparison between experimental and theoretical results, demonstrating that reproducible experimental data is needed for a judgment of the correctness of a theoretical description. Particular molecules, namely a single thiolated phenyl ring may just be too short for reproducible conductance measurements. For a biphenyl molecule of the S series, which could be measured reproducibly in the experiments, we obtain a fair agreement with the experiment. In the hollow configuration our results deviate from the experimental ones by a factor of 2–6, while for the top position the conductance is substantially overestimated by a factor of 60. We demonstrated that the actual geometry of the molecule connected to Au electrodes may deviate substantially from the equilibrium structure of the isolated molecule with regard to tilt angles between adjacent phenyl rings. These tilt angles were demonstrated to be a very important ingredient in the determination of the molecule's electronic transport properties. We concluded that a reproducible measurement of the conductance of molecules requires an appropriate design of the molecules. This design needs to insure that the molecule is hindered to adopt different internal conformations when contacted by metallic electrodes. In the case of the oligophenylenes this can be achieved by use of appropriate side groups.

Finally we investigated in a more conceptual study the effect of forced ring tilts for three different biphenyl molecules in the hollow configuration. For the simple biphenyl molecule we obtain a $\cos^2$ dependence of the conductance with respect to the tilt angle, as predicted in previous studies and recently confirmed experimentally. Remarkably, the conductance is never fully suppressed, but differs by two orders of magnitude between the minimum and maximum conductance for the planar and perpendicular ring configurations, respectively. From the tilt angle dependence of the total energy and the conductance we determined the temperature dependence of the conductance for three different biphenyl molecules, and found qualitative differences. While for the molecules of families S and D with a broken π-system the conductance increases, the opposite is observed for the conjugated molecule of series R.

In summary our results are a further demonstration of the elaborate interplay between geometric configuration and transport properties. By an appropriate chemical design of the geometric structure of a molecule it is indeed possible to tailor the conductance of metal-molecule-metal junctions.

Summary

The present work is concerned with the theoretical description of systems at the nanoscale. In particular the electric charge current through atomic-sized metallic contacts and organic molecules, bridging two metallic electrodes, is in the focus of our research.

In the first part of this work a valence electron tight-binding approach is used to study metallic atomic contacts. We addressed the question, on how the characteristic peak structure, as observed in the conductance histograms of different classes of metals, can be explained. Combining classical molecular dynamics simulations performed at the Universität Konstanz with a tight-binding model for the conductance, we studied two noble metals, namely silver and gold, a transition metal, platinum, and nickel, a ferromagnetic metal. With the help of an extensive statistical analysis of fifty stretching events for contacts of the respective metal we could illustrate that the differences in the peak structure of the conductance histograms arise from the very different electronic structure of the analyzed metals as well as their different mechanical properties. These mechanical properties may lead to the formation of special structures, such as monoatomic chains for the metals gold and platinum. For nickel we could demonstrate, how the polarization of the current evolves on average from negative values in thick contacts to even positive values in the tunneling regime after rupture of the contact. Moreover we analyzed the forces before rupture of a contact using breaking force histograms.

Next we explored the effect of electron-vibration coupling on the conductance in atomic gold wires. While the formalism applied in the analysis of conductance histograms was based on the elastic current alone, the determination of the signature of vibrations on the conductance required the inclusion of inelastic corrections. We treated the electron-vibration coupling to the first nontrivial order, and found that this lowest-order perturbation approach provides a sufficient description of the phenomenology of electron-vibration interactions in atomic wires.

In the second part of the thesis we developed an ab-initio method for predicting the conduction properties of atomic-sized contacts. This method is based on density functional theory as implemented in the quantum chemistry package TURBOMOLE. For developing this method, we had to overcome a major obstacle. The description of the metallic electrodes turned out to be problematic due the lack of periodic boundary conditions in TURBOMOLE that would allow a solid state description. We decided to extract electrode parameters from finite clusters instead. Due to the long tails of Gaussian basis functions it turned out that extremely large cluster sizes are required to achieve a meaningful electrode description within the nonorthogonal Gaussian basis sets used by TURBOMOLE. By means of a measure for the positive definiteness of the overlap matrix, we could give a criterion, on how big the clusters need to be, in order to extract electrode parameters that yield physically relevant results. Due to TURBOMOLE's ability to compute very large metal clusters it was finally possible to fulfill this criterion, so that the central contact system and the electrodes can be described on an equal footing within the same nonorthogonal

basis set.

At the example of gold and aluminum metallic atomic contacts we demonstrated a kind of convergence of our transmission curves. In addition we showed that our method agrees with the present literature and reproduces the results of other established theoretical methods in the field of molecular electronics.

Subsequently we applied our ab-initio method in studies of organic molecules. Inspired by recent activities in the group of M. Mayor at the Institut für Nanotechnologie, Forschungszentrum Karlsruhe [34], we analyzed different series of oligophenylene molecules. In these molecules the conjugated π-electron system was either stabilized or broken by means of side groups. In this way the degree of the electron delocalization was controlled. We explored the conductance as a function of the number of phenyl ring units for three different series of such oligophenylene molecules, which consist of one to four ring units. We found an exponential decrease of the conductance for all of them, however with a much lower damping for the molecules with an extended π-system. In addition we studied different bonding positions and showed that, while the absolute value of the conductance may differ substantially (roughly by an order of magnitude), the attenuation factors are by and large unaffected.

We compared our results to experimental data and found out that the conductance for the hollow bonding position seems to be in better compliance with experiments than those of the top position. We pointed out that the sensible comparison between theory and experiment requires the measurement of molecules with an appropriately designed geometric structure. This design should aim at a stabilization of the molecule's internal structure, such that its configuration cannot deviate from the equilibrium structure of the isolated molecule, when the molecule is brought into contact with metallic electrodes.

Furthermore we analyzed the dependence of the conductance on enforced interphenyl-ring tilts for three different biphenyl molecules. The observed functional dependence of the conductance on the tilt angle agrees well with predictions of a simple effective π-electron coupling model. Treating the tilt angle as a classical variable, we determined the temperature dependence of the conductance. Qualitative differences could be observed between the three different biphenyl molecules analyzed.

The concept of molecular electronics envisages the use of single molecules as smallest building blocks in electronic circuitry, hopefully leading to further miniaturization and reduced production costs in the chip industry. However, the use of individual molecules as electronically active components requires the possibility to tailor their conduction properties at will. Correlations between the geometric structure and the electron transport behavior of a molecule may serve as a basic design principle to achieve this goal. Our analysis of oligophenylene molecules is a further confirmation that such correlations exist, and tailor-made molecular electronic circuitry may indeed be possible.

Appendix A

Contour-ordered Green's functions and Keldysh formalism

This appendix is devoted to the study of Green's functions, in particular contour-ordered single-particle Green's functions as they appear in the context of the Keldysh formalism [227]. By now, there exists excellent literature devoted to the powerful Keldysh Green's function technique [228, 229, 230, 231]. As this formalism, however, constitutes the fundamental tool of this thesis and is employed for the computation of transport and other physical quantities like densities of states etc., this appendix on the Keldysh nonequilibrium Green's functions is included for reasons of completeness. The presentation of the formalism given here follows closely the review by Rammer et al. [228] and Appendix A of the PhD thesis by J.C. Cuevas [232].

In his original paper Keldysh developed a diagrammatic technique for calculating Green's functions for particles in a statistical system which, under the action of an external field, deviates to an arbitrary extent from the state of thermodynamic equilibrium [227]. This technique has the advantage that it is completely analogous to the usual Feynman technique in field theory, with the only difference that the number of Green's functions appearing in it is increased. Since its invention it has found applications in numerous fields of physical research like superconductivity, Fermi liquid theory, surface physics, but also in nuclear and particle physics and optics (see Refs. [228, 229] for a survey of the literature). The particular application we are interested in is electron transport (see for instance Refs. [233, 234, 235, 236, 152]).

This chapter is organized as follows: In Sec. A.1, we recall the different pictures of time-evolution as known in quantum mechanics due to their importance for the perturbative expansion of Green's functions. In Sec. A.2 equilibrium Green's functions and their properties will be studied, before, in Sec. A.3, we come to the concept of nonequilibrium contour-ordered Green's functions, in particular the Keldysh formalism. The concepts encountered in the study of nonequilibrium situations will appear as a natural generalization of the equilibrium theory.

A.1 Different pictures of time evolution

In quantum mechanics there exist mainly three equivalent pictures for the time evolution of a quantum system. They differ in the way that states $|\psi(t)\rangle$ and measurement operators $\hat{O}(t)$ of a quantum mechanical system evolve with time. The three different pictures of time evolution can be summarized as follows [237, 217, 229], where all pictures shall coincide at time t_0:

Schrödinger picture: The states $|\Psi_S(t)\rangle = \hat{U}_H(t,t_0)\,|\Psi_S(t_0)\rangle$ are time-dependent, while the operator O_S is constant (except for its own explicit time dependence $\frac{d}{dt}\hat{O}_S = \frac{\partial}{\partial t}\hat{O}_S$). The time evolution operator $\hat{U}_H(t,t_0)$ from time t_0 to t obeys the differential equation $i\hbar\frac{d}{dt}\hat{U}_H(t,t_0) = \hat{H}\hat{U}_H(t,t_0)$.

Heisenberg picture: The states $|\Psi_H\rangle = |\Psi_S(t_0)\rangle$ are constant ($i\hbar\frac{d}{dt}\,|\Psi_H(t)\rangle = 0$), while the operator $\hat{O}_H(t) = \hat{U}_H^{+}(t,t_0)\hat{O}_S(t)\hat{U}_H(t,t_0)$ evolves with time. The time evolution operator $\hat{U}_H(t,t_0)$ is defined as in the Schrödinger picture ($i\hbar\frac{d}{dt}\hat{U}_H(t,t_0) = \hat{H}\hat{U}_H(t,t_0)$).

Interaction picture: The states $|\Psi_I(t)\rangle = \hat{U}_I(t,t_0)\,|\Psi_I(t_0)\rangle$ evolve with time as determined by the time-evolution operator in the interaction picture, which is $\hat{U}_I(t,t_0) = \hat{U}_{H_0}^{+}(t,t_0)\hat{U}_H(t,t_0)$. Here we used that $|\Psi_I(t_0)\rangle = |\Psi_S(t_0)\rangle$. The operators of the Schrödinger and interaction picture are related by $\hat{O}_I(t) = \hat{U}_{H_0}^{+}(t,t_0)\hat{O}_S(t)\hat{U}_{H_0}(t,t_0)$. The behavior of $\hat{U}_I(t,t_0)$ – as will be discussed further below – is controlled by the "complicated" (possibly time-dependent) interaction part $\hat{H}'$ of the Hamiltonian $\hat{H} = \hat{H}_0 + \hat{H}'$ ($i\hbar\frac{d}{dt}\hat{U}_I(t,t_0) = \hat{H}_I'(t)\hat{U}_I(t,t_0)$ and $\hat{H}_I'(t) = \hat{U}_{H_0}^{+}(t,t_0)\hat{H}'\hat{U}_{H_0}(t,t_0)$ is $\hat{H}'$ in the interaction picture). The time evolution operators $\hat{U}_H(t,t_0)$ and $\hat{U}_{H_0}(t,t_0)$ are defined as in the Schrödinger picture ($i\hbar\frac{d}{dt}\hat{U}_H(t,t_0) = \hat{H}\hat{U}_H(t,t_0)$ and $i\hbar\frac{d}{dt}\hat{U}_{H_0}(t,t_0) = \hat{H}_0\hat{U}_{H_0}(t,t_0)$).

Which picture for the time evolution is chosen in a description of a quantum mechanical system is a matter of convenience and the intended application. In the context of perturbation theory, the interaction picture turns out to be the most useful representation. Below, the form of the time evolution operator appropriate for a perturbative treatment will be given.

Generally a time evolution operator $\hat{U}_H(t,t_0)$, obeying the differential equation

$$i\hbar\frac{d}{dt}\hat{U}_H(t,t_0) = \hat{H}(t)\hat{U}_H(t,t_0),$$

may be expressed in different ways depending on the time-dependence of $\hat{H}(t)$. For (i) a time-independent Hamiltonian ($\frac{d}{dt}\hat{H} = 0$)

$$\hat{U}_H(t,t_0) = \exp\left(-\frac{i}{\hbar}\hat{H}(t-t_0)\right),$$

for (ii) time-dependent $\hat{H} = \hat{H}(t)$ with a Hamiltonian that commutes for different times ($\left[\hat{H}(t_i), \hat{H}(t_j)\right] = 0$ for arbitrary t_i and t_j)

$$\hat{U}_H(t,t_0) = \exp\left(-\frac{i}{\hbar}\int_{t_0}^{t} dt'\hat{H}(t')\right),$$

whereas for (iii) time-dependent $\hat{H} = \hat{H}(t)$, where the commutator of the Hamiltonian at different times does not vanish for all times ($\left[\hat{H}(t_i), \hat{H}(t_j)\right] \neq 0$ for some t_i and t_j)

$$\hat{U}_H(t,t_0) = \sum_{n=0}^{\infty}\left(\frac{-i}{\hbar}\right)^n \int_{t_0}^{t} dt_1 \int_{t_0}^{t_1} dt_2 \cdots \int_{t_0}^{t_{n-1}} dt_n \hat{H}(t_1)\hat{H}(t_2)\cdots\hat{H}(t_n). \qquad \text{(A.1)}$$

Here the zeroth term is the unit operator [238, 237, 141]. This series is sometimes known as Dyson series. With the introduction of the time ordering operator T, which acts on a group of operators and arranges the operators with the earliest time to the right, Eq. (A.1) many then formally be written as [238, 141]

$$\hat{U}_H(t,t_0) = T\exp\left(-\frac{i}{\hbar}\int_{t_0}^{t} dt'\hat{H}(t')\right).$$

Note that for all the time evolution operators defined above $\hat{U}_X(t,t_0)$ (with $X = H$, H_0 or I) the following relations are fulfilled, namely the group property

$$\hat{U}_X(t_1,t_2)\hat{U}_X(t_2,t_3) = \hat{U}_X(t_1,t_3), \qquad \text{(A.2)}$$

the boundary condition

$$\hat{U}_X(t_1,t_1) = 1, \qquad \text{(A.3)}$$

and the unitarity

$$\hat{U}_X^{+}(t,t_0) = \hat{U}_X^{-1}(t,t_0) = \hat{U}_X(t_0,t). \qquad \text{(A.4)}$$

In order to obtain an expression for the time evolution operator in the interaction picture, we assume a Hamiltonian of the form $\hat{H} = \hat{H}_0 + \hat{H}'(t)$. $\hat{H}_0$ shall be the "simple" time-independent part of the Hamiltonian for a certain system, while $\hat{H}'(t)$ may contain complicated time-dependent interaction parts. With the definitions above, the time-evolution operator in the interaction picture is given by[1]

$$\hat{U}_I(t,t_0) = \hat{U}_{H_0}^{+}(t,t_0)\hat{U}_H(t,t_0) = \hat{U}_{H_0}(t_0,t)\hat{U}_H(t,t_0) \qquad \text{(A.5)}$$

and obeys the differential equation

$$i\hbar\frac{d}{dt}\hat{U}_I(t,t_0) = \hat{H}_I'(t)\hat{U}_I(t,t_0), \qquad \text{(A.6)}$$

---

[1] Exploiting the time independence of $\hat{H}_0$ this may be written more explicitly as $\hat{U}_I(t,t_0) = \exp\left(\frac{i}{\hbar}\hat{H}_0(t-t_0)\right)\hat{U}_H(t,t_0)$.

where $\hat{H}'_I(t) = \hat{U}^+_{H_0}(t, t_0)\hat{H}'(t)\hat{U}_{H_0}(t, t_0)$ is $\hat{H}'(t)$ in the interaction picture. This means that $\hat{U}_I$ is only changing with time due to the presence of $\hat{H}'(t)$, suggesting that the interaction picture is the appropriate one for a perturbative treatment of the interaction part $\hat{H}'(t)$.

In the most general case of a time-dependent $\hat{H}'_I(t)$ with a noncommuting Hamiltonian for different times the time-evolution operator in the interaction picture may now be brought into the form

$$\hat{U}_I(t, t_0) = T \exp\left(-\frac{i}{\hbar}\int_{t_0}^{t} dt' \hat{H}'_I(t')\right). \tag{A.7}$$

A.2 Equilibrium Green's functions at zero and finite temperature

In classical physics Green's functions are used as a powerful method for solving inhomogeneous differential equations. The Green's functions obey a certain differential equation with a singular inhomogeneity. Similarly one can introduce Green's functions in many-body physics, which, because of their construction, obey a wave equation with a singular inhomogeneity. These Green's functions turn out to provide a very powerful technique for evaluating properties of many-body systems both in thermal equilibrium and in nonequilibrium situations. The usefulness of the Green's functions stems from the possibility to extract experimentally relevant properties from their knowledge. Their definitions allow a systematic perturbation theory. In this paragraph we will start by describing briefly the equilibrium Green's function formalism both for zero and finite temperature, before the concept will be generalized and unified in the context of contour-ordered nonequilibrium Green's functions (see Sec. A.3).

A.2.1 Definitions and relations

Commonly, the different equilibrium Green's functions are defined as [228, 229]

$$\begin{aligned}
G^c(\vec{x}_1, t_1; \vec{x}_2, t_2) &= -i\left\langle T\left(\hat{\psi}_K(\vec{x}_1, t_1)\hat{\psi}^+_K(\vec{x}_2, t_2)\right)\right\rangle && \text{(A.8)}\\
G^r(\vec{x}_1, t_1; \vec{x}_2, t_2) &= -i\Theta(t_1 - t_2)\left\langle\left\{\hat{\psi}_K(\vec{x}_1, t_1), \hat{\psi}^+_K(\vec{x}_2, t_2)\right\}\right\rangle && \text{(A.9)}\\
G^a(\vec{x}_1, t_1; \vec{x}_2, t_2) &= i\Theta(t_2 - t_1)\left\langle\left\{\hat{\psi}_K(\vec{x}_1, t_1), \hat{\psi}^+_K(\vec{x}_2, t_2)\right\}\right\rangle && \text{(A.10)}\\
G^<(\vec{x}_1, t_1; \vec{x}_2, t_2) &= i\left\langle\hat{\psi}^+_K(\vec{x}_2, t_2)\hat{\psi}_K(\vec{x}_1, t_1)\right\rangle && \text{(A.11)}\\
G^>(\vec{x}_1, t_1; \vec{x}_2, t_2) &= -i\left\langle\hat{\psi}_K(\vec{x}_1, t_1)\hat{\psi}^+_K(\vec{x}_2, t_2)\right\rangle && \text{(A.12)}
\end{aligned}$$

The Green's functions G^c, G^r, G^a, $G^<$, and $G^>$ are called the causal, retarded, advanced, lesser, and greater Green's functions. The operators $\hat{\psi}_K(\vec{x}, t)$ and $\hat{\psi}^+_K(\vec{x}, t)$ are the field operators in the Heisenberg picture. As we are dealing with many-particle states and statistical ensembles, we have defined the grand canonical Hamiltonian of the system $\hat{K} = \hat{H} - \mu\hat{N}$ [238]. This means that single-particle energies are measured with respect to the chemical potential.[2] All the equations for the time evolution in Sec. A.1 are valid for $\hat{H}$ replaced by $\hat{K}$. Especially

$$\hat{\psi}_K(\vec{x},t) = \hat{U}_K^+(t,t_0)\hat{\psi}(\vec{x},t_0)\hat{U}_K(t,t_0) \qquad \hat{\psi}_K^+(\vec{x},t) = \hat{U}_K^+(t,t_0)\hat{\psi}^+(\vec{x},t_0)\hat{U}_K(t,t_0)$$

where $\hat{\psi}(\vec{x},t_0)$ and $\hat{\psi}^+(\vec{x},t_0)$ are the field operators at time t_0

$$\hat{\psi}(\vec{x},t_0) = \sum_n \phi_n(\vec{x},t_0)\hat{c}_n(t_0) \qquad \hat{\psi}^+(\vec{x},t_0) = \sum_n \phi_n^*(\vec{x},t_0)\hat{c}_n^+(t_0). \tag{A.13}$$

The operators $\hat{c}_n(t_0)$ ($\hat{c}_n^+(t_0)$) act in the abstract occupation-number Hilbert space and annihilate (create) a particle in a state n. The wavefunctions $\phi_n(\vec{x},t_0)$ form a complete set of single-particle eigenfunctions for the Hamiltonian $\hat{K}(t_0)$ with quantum labels n, where n may comprise for example momentum and spin quantum numbers. In the definition of the Green's functions G^r and G^a (see Eqs. (A.9) and (A.10)), and throughout this work, $\left\{\hat{A},\hat{B}\right\}$ ($\left[\hat{A},\hat{B}\right]$) shall be the anticommutator (commutator) of the operators $\hat{A}$ and $\hat{B}$. The step function $\Theta(x)$ appearing in G^r and G^a, is defined as[3]

$$\Theta(x) = \left\{ \begin{array}{ll} 1 & x > 0 \\ 0 & x < 0 \end{array} \right. . \tag{A.14}$$

As introduced in the previous chapter and needed in the definition of G^c (see Eq. (A.8)) T is the time ordering operator, which arranges the operators with the earliest time to the right, when acting on a group of operators. More generally the T product of several operators orders them from right to left in ascending time order and adds a factor $(-1)^P$, where P is the number of interchanges of fermion operators from the originally given order. For two operator this means explicitly

$$\begin{aligned} T\left(\hat{\psi}_K(1)\hat{\psi}_K^+(2)\right) &= \Theta(t_1-t_2)\hat{\psi}_K(1)\hat{\psi}_K^+(2) - \Theta(t_2-t_1)\hat{\psi}_K^+(2)\hat{\psi}_K(1) \\ &= \left\{ \begin{array}{ll} \hat{\psi}_K(1)\hat{\psi}_K^+(2) & t_1 > t_2 \\ -\hat{\psi}_K^+(2)\hat{\psi}_K(1) & t_1 < t_2 \end{array} \right. , \end{aligned}$$

where we used the short-hand notation $1 = (\vec{x}_1,t_1)$. The negative sign in this definition for the case $t_1 < t_2$ arises from the anticommutator relation for fermion creation and annihilation operators. These are $\left\{\hat{\psi}(\vec{x}_1,t_0),\hat{\psi}^+(\vec{x}_2,t_0)\right\} = \delta(\vec{x}_1-\vec{x}_2)$ and

---

[2] We assume in the following that the particle number (fermion number) is conserved in time, so that $\left[\hat{H},\hat{N}\right] = 0$. The same shall be true for all the individual components of the Hamiltonian $\hat{H}$ like for example $\hat{H}_0$ or $\hat{H}'$.

[3] The step function $\Theta(x)$ is not defined for $x = 0$, which implies that G^c, G^r, and G^a are not defined for equal times (see Eqs. (A.8), (A.9), and (A.10)).

$\left\{\hat{\psi}(\vec{x}_1,t_0),\hat{\psi}(\vec{x}_2,t_0)\right\} = \left\{\hat{\psi}^+(\vec{x}_1,t_0),\hat{\psi}^+(\vec{x}_2,t_0)\right\} = 0$ for the field operators at time t_0 and follow from the corresponding relations between the annihilators $c_n(t_0)$ and creators $c_n^+(t_0)$ of states with quantum numbers n ($\left\{\hat{c}_n(t_0),\hat{c}_{n'}^+(t_0)\right\} = \delta_{n,n'}$ and $\{\hat{c}_n(t_0),\hat{c}_{n'}(t_0)\} = \left\{\hat{c}_n^+(t_0),\hat{c}_{n'}^+(t_0)\right\} = 0$) together with the completeness of the basis functions $\phi_n(\vec{x},t_0)$ ($\sum_n \phi_n^*(\vec{x}_1,t_0)\phi_n(\vec{x}_2,t_0) = \delta(\vec{x}_1-\vec{x}_2)$).[4]

The brackets $\langle\rangle$ in Eqs. (A.8)–(A.12) shall signify the quantum mechanical average. For (i) zero temperature ($T=0$) this is the average over the interacting many-particle ground state $|\Psi_0\rangle$. The causal Green's function is then given as

$$G^c(1,2) = -i\,\langle\Psi_0|\,T\left(\hat{\psi}_K(1)\hat{\psi}_K^+(2)\right)|\Psi_0\rangle \,/\, \langle\Psi_0|\,\Psi_0\rangle\,. \tag{A.15}$$

For (ii) finite temperature ($T>0$) the average $\langle\rangle$ shall signify the statistical average in the grand canonical ensemble with the density matrix

$$\hat{\varrho} = \frac{\exp(-\beta\hat{K})}{\mathrm{Tr}\left[\exp(-\beta\hat{K})\right]} = \frac{\exp(-\beta\hat{K})}{Z} = \exp(\beta(\Omega-\hat{K})), \tag{A.16}$$

where the grand canonical partition function $Z = \exp(-\beta\Omega)$ has been introduced. Thus for finite temperature G^c is given as

$$G^c(1,2) = -i\mathrm{Tr}\left[\hat{\varrho}T\left(\hat{\psi}_K(1)\hat{\psi}_K^+(2)\right)\right]. \tag{A.17}$$

Directly from the definition of the Green's functions, some relations between them follow, for example

$$\begin{aligned}
G^r(1,2) &= \Theta(t_1-t_2)\left(G^>(1,2)-G^<(1,2)\right) && \text{(A.18)}\\
G^a(1,2) &= -\Theta(t_2-t_1)\left(G^>(1,2)-G^<(1,2)\right) && \text{(A.19)}\\
G^r(1,2)-G^a(1,2) &= G^>(1,2)-G^<(1,2) && \text{(A.20)}\\
G^c(1,2) &= \Theta(t_1-t_2)G^>(1,2)+\Theta(t_2-t_1)G^<(1,2) && \text{(A.21)}
\end{aligned}$$

Despite of the connections between the various Green's functions, each has its own advantages [229] (as will become obvious further below):

1. G^c has a systematic perturbative expansion.
2. $G^{r,a}$ have a handy analytic structure with poles only in one half-plane. They contain information about spectral properties, densities of states, and scattering rates and are well-suited for calculating a physical response.
3. $G^{<,>}$ are directly linked to observables and kinetic properties such as particle densities or currents.

---

[4] Note that the time ordering operator T is not defined for equal times. Instead, one needs to think about how t_1 and t_2 need to approach each other, such that the physically relevant limit is obtained.

Roughly speaking the Green's functions describe the propagation of holes and particles in a system. For example the probability amplitude in the many-particle ground state to create a particle at space point $2 = (\vec{x}_2, t_2)$ and to find it later at space point $1 = (\vec{x}_1, t_1)$ is $\langle \Psi_0 | \hat{\psi}_K(1) \hat{\psi}_K^+(2) | \Psi_0 \rangle / \langle \Psi_0 | \Psi_0 \rangle$, whereas $\langle \Psi_0 | \hat{\psi}_K^+(1) \hat{\psi}_K(2) | \Psi_0 \rangle / \langle \Psi_0 | \Psi_0 \rangle$ is the propability amplitude for the same process with the hole generated first.

The direct connection of the Green's functions to physical observables will be illustrated at two examples, namely the electron density and the current operator [238, 230]. The operator for the electron density is

$$\hat{\varrho}(\vec{x}, t) = \hat{\psi}^+(\vec{x}, t) \hat{\psi}(\vec{x}, t). \tag{A.22}$$

Therefore the electron density in a quantum system is obtained as[5]

$$\varrho(\vec{x}, t) = \langle \hat{\varrho}(\vec{x}, t) \rangle = -iG^<(\vec{x}, t; \vec{x}, t) = -iG^c(\vec{x}, t; \vec{x}, t^+). \tag{A.23}$$

Another example is the current operator

$$\hat{\vec{j}}(\vec{x}, t) = \frac{i}{2m} \left(\left(\nabla \hat{\psi}^+(\vec{x}, t) \right) \hat{\psi}(\vec{x}, t) - \hat{\psi}^+(\vec{x}, t) \left(\nabla \hat{\psi}(\vec{x}, t) \right) \right), \tag{A.24}$$

which may be expressed in terms of Green's functions as

$$\begin{aligned} \hat{\vec{j}}(\vec{x}, t) &= \frac{i}{2m} \lim_{\vec{x}' \to \vec{x}} \left\langle \left(\nabla_{\vec{x}'} - \nabla_{\vec{x}} \right) \hat{\psi}^+(\vec{x}', t) \hat{\psi}(\vec{x}, t) \right\rangle \qquad \text{(A.25)} \\ &= \frac{1}{2m} \lim_{\vec{x}' \to \vec{x}} G^<(\vec{x}', t; \vec{x}, t). \end{aligned}$$

The aforementioned direct relation of $G^{<,>}$ to physically observable quantities becomes apparent from these examples.

Looking at the equation of motion, it can be noticed that G^c, G^r, and G^a all obey the same differential equation, however with different boundary conditions [239]. Denoting $G^\alpha(1,2) = \gamma^\alpha_{\hat{\psi}(\vec{x}_1);\hat{\psi}^+(\vec{x}_2)}(t_1, t_2)$ ($\alpha = c$, a, or r) the equation of motion is

$$i\hbar \frac{\partial}{\partial t_1} \gamma^\alpha_{\hat{\psi}(\vec{x}_1);\hat{\psi}^+(\vec{x}_2)}(t_1, t_2) = \hbar \delta(t_1 - t_2) \left\langle \left\{ \hat{\psi}_K(1), \hat{\psi}_K^+(2) \right\} \right\rangle + \gamma^\alpha_{\left[\hat{\psi}(\vec{x}_1), \hat{K}\right];\hat{\psi}^+(\vec{x}_2)}(t_1, t_2) \tag{A.26}$$

with the following boundary conditions for the different Green's functions

$$\begin{aligned} G^r(1,2) &= 0 \qquad \text{for } t_1 < t_2, \\ G^a(1,2) &= 0 \qquad \text{for } t_1 > t_2, \\ G^c(1,2) &= \left\{ \begin{array}{ll} G^<(1,2) & \text{for } t_1 < t_2, \\ G^>(1,2) & \text{for } t_1 > t_2. \end{array} \right. . \end{aligned}$$

The Green's function $\gamma^\alpha_{\left[\hat{\psi}, \hat{K}\right];\hat{\psi}^+(\vec{x}_2)}(t_1, t_2)$ appearing in Eq. (A.26) is a new Green's function because $\left[\hat{\psi}_K(1), \hat{K} \right]$ is itself an operator. Generally it is a so-called n-particle Green's

---

[5] The notation t^+ (t^-) means a time infinitesimally bigger (smaller) than t ($t^\pm = \lim_{\varepsilon \to 0} t \pm \varepsilon$).

function, which means that it contains more field operators than the original single-particle Green's function $G^\alpha(1,2)$. Also for this n-particle Green's function an equation of motion may be written down, with further n-particle Green's functions emerging. This procedure may lead to an infinite chain of equations of motion, which needs to be truncated at some point to obtain an approximate solution. However, in this work we will only use effective single-particle Hamiltonians, and consequently no other Green's functions than the single-particle Green's functions need to be discussed.

For a Hamiltonian without an explicit time dependence the Green's functions are homogeneous functions of time, namely they depend only on time differences

$$\frac{\partial \hat{K}}{\partial t} = 0 \Rightarrow G^\alpha(1,2) = G^\alpha(\vec{x}_1, \vec{x}_2, t_1 - t_2). \tag{A.27}$$

Here G^α may stand for any of the Green's functions introduced above ($\alpha = c$, r, a, $<$, and $>$; see Eqs. (A.8)–(A.12)). The statement of Eq. (A.27) can be proved by showing that the correlation functions $\left\langle \hat{\psi}_K(1)\hat{\psi}_K^+(2)\right\rangle$ or $\left\langle \hat{\psi}_K^+(2)\hat{\psi}_K(1)\right\rangle$ depend only on the time difference [239]. Denoting $\hat{A}(t) = \hat{\psi}_K(\vec{x}, t)$ and $\hat{B}(t) = \hat{\psi}_K^+(\vec{x}, t)$ it follows that

$$\begin{aligned}
\mathrm{Tr}\left[e^{\beta(\Omega-\hat{K})}\hat{A}(t)\hat{B}(t')\right] &= \mathrm{Tr}\left[e^{\beta(\Omega-\hat{K})}e^{i\hat{K}(t-t_0)/\hbar}\hat{A}(t_0)e^{-i\hat{K}(t-t')/\hbar}\hat{B}(t_0)e^{-i\hat{K}(t'-t_0)/\hbar}\right] \\
&= \mathrm{Tr}\left[e^{\beta(\Omega-\hat{K})}e^{i\hat{K}(t-t')/\hbar}\hat{A}(t_0)e^{-i\hat{K}(t-t')/\hbar}\hat{B}(t_0)\right] \\
&= \mathrm{Tr}\left[e^{\beta(\Omega-\hat{K})}\hat{A}(t-t'+t_0)\hat{B}(t_0)\right].
\end{aligned} \tag{A.28}$$

This means that

$$\left\langle \hat{A}(t)\hat{B}(t')\right\rangle = \left\langle \hat{A}(t-t'+t_0)\hat{B}(t_0)\right\rangle \tag{A.29}$$

and thus depends only on the time difference. With a similar proof for $\left\langle \hat{B}(t')\hat{A}(t)\right\rangle = \left\langle \hat{B}(t_0)\hat{A}(t-t'+t_0)\right\rangle$ this finally demonstrates the translational invariance of G^α with respect to its time arguments.

For time independent Hamiltonians G^α may thus be diagonalized via a Fourier transformation

$$\begin{aligned}
G^\alpha(\vec{x}_1, \vec{x}_2, E) &= \int_{-\infty}^{\infty} \frac{d(t_1-t_2)}{\hbar} G^\alpha(\vec{x}_1, \vec{x}_2, t_1-t_2) \exp\left(\frac{i}{\hbar}E\,(t_1-t_2)\right) \\
G^\alpha(\vec{x}_1, \vec{x}_2, t_1-t_2) &= \int_{-\infty}^{\infty} \frac{dE}{2\pi} G^\alpha(\vec{x}_1, \vec{x}_2, E) \exp\left(-\frac{i}{\hbar}E\,(t_1-t_2)\right).
\end{aligned}$$

In this way Eq. (A.26) becomes an an algebraic equation

$$E\gamma^\alpha_{\hat{\psi}(\vec{x}_1);\hat{\psi}^+(\vec{x}_2)}(E) = \left\langle\left\{\hat{\psi}_K(\vec{x}_1, t_0), \hat{\psi}_K^+(\vec{x}_2, t_0)\right\}\right\rangle + \gamma^\alpha_{\left[\hat{\psi}(\vec{x}_1),\hat{K}\right];\hat{\psi}^+(\vec{x}_2)}(E). \tag{A.30}$$

We define now the spectral function $\rho(\vec{x}_1, \vec{x}_2, E)$ as

$$\rho(\vec{x}_1, \vec{x}_2, E) = \frac{i}{2\pi}\left(G^r(\vec{x}_1, \vec{x}_2, E) - G^a(\vec{x}_1, \vec{x}_2, E)\right) = \frac{i}{2\pi}\left(G^>(\vec{x}_1, \vec{x}_2, E) - G^<(\vec{x}_1, \vec{x}_2, E)\right). \tag{A.31}$$

Due to the equal-time anticommutation rule, this function has the property

$$\int_{-\infty}^{\infty} dE \rho(\vec{x}_1, \vec{x}_2, E) = \int d(t_1 - t_2)\delta(t_1 - t_2)\left\langle\left\{\hat{\psi}_K(\vec{x}_1, t_0), \hat{\psi}_K^+(\vec{x}_2, t_0)\right\}\right\rangle = \delta(\vec{x}_1 - \vec{x}_2). \tag{A.32}$$

Written explicitly the spectral density is found to be

$$\begin{aligned}\rho(\vec{x}_1, \vec{x}_2, E) &= \sum_{n,m} \langle E_n|\, \hat{\psi}_K^+(\vec{x}_1, t_0)\, |E_m\rangle \langle E_m|\, \hat{\psi}_K(\vec{x}_2, t_0)\, |E_n\rangle \qquad \text{(A.33)}\\ &\quad \cdot e^{\beta(\Omega - E_n + \mu N_n)}\left(e^{\beta E} + 1\right)\delta(E - (E_n - E_m - \mu))\end{aligned}$$

With the help of the representation of the step function

$$\Theta(t - t') = \frac{i}{2\pi}\int_{-\infty}^{\infty} dx \frac{\exp(-ix(t - t'))}{x + i0^+}$$

the retarded and advanced Green's function can be brought into their spectral representation, also known as Lehmann representation [239]

$$G^{\substack{r\\a}}(\vec{x}_1, \vec{x}_2, E) = \int_{-\infty}^{\infty} dE' \frac{\rho(\vec{x}_1, \vec{x}_2, E')}{E \pm i0^+ - E'}. \tag{A.34}$$

As $\rho(\vec{x}, \vec{x}, E)$ is purely real, the following relations hold

$$G^r(\vec{x}, \vec{x}, E) = \left(G^a(\vec{x}, \vec{x}, E)\right)^* \tag{A.35}$$

and

$$\rho(\vec{x}, \vec{x}, E) = \mp\frac{1}{\pi}\mathrm{Im}\left[G^{\substack{r\\a}}(\vec{x}, \vec{x}, E)\right]. \tag{A.36}$$

Eq. (A.36) may be obtained by applying Eq. (A.35) in the definition of ρ (see Eq. (A.31)) or by using the Dirac-identity

$$\frac{1}{x - x_0 \pm i0^+} = \mathcal{P}\frac{1}{x - x_0} \mp i\pi\delta(x - x_0), \tag{A.37}$$

in which $\mathcal{P}$ stands for the Cauchy principle value. Note that while generally $\rho(\vec{x}, \vec{x}, E)$ is purely real,[6] for the offdiagonal elements of $\rho(\vec{x}_1, \vec{x}_2, E)$ with $\vec{x}_1 \neq \vec{x}_2$ this need not be the case. Otherwise the given relations also hold for the off diagonal elements.

---

[6] This is the case, because the density ρ in Eq. (A.31) may be written $\rho(\vec{x}_1, \vec{x}_2, E) = \frac{1}{2\pi}\left\langle\left\{\hat{\psi}_K(\vec{x}, t_0), \hat{\psi}_K^+(\vec{x}, t_0)\right\}\right\rangle$ and $\left\{\hat{\psi}_K(\vec{x}_1, t_0), \hat{\psi}_K^+(\vec{x}_2, t_0)\right\}$ is a hermitian operator for $\vec{x}_1 = \vec{x}_2$.

Similar expressions as for the spectral function $\rho(\vec{x}_1, \vec{x}_2, E)$ in Eq. (A.33) for $G^<$ and $G^>$ yield a relation between these two Green's function components in energy space [229]

$$G^>(\vec{x}_1, \vec{x}_2, E) = -e^{\beta E} G^<(\vec{x}_1, \vec{x}_2, E), \tag{A.38}$$

from which the fluctuation-dissipation theorem can be derived. With the introduction of the Fermi function $f(E) = \left(e^{\beta E} + 1\right)^{-1}$ one obtains

$$\begin{aligned} G^<(\vec{x}_1, \vec{x}_2, E) &= 2\pi i f(E) \rho(\vec{x}_1, \vec{x}_2, E) && \text{(A.39)} \\ G^>(\vec{x}_1, \vec{x}_2, E) &= -2\pi i \left(1 - f(E)\right) \rho(\vec{x}_1, \vec{x}_2, E). && \text{(A.40)} \end{aligned}$$

The fluctuation-dissipation theorem (see Eq. (A.39)) establishes a connection between the correlation function $G^>$ and the dissipative part ρ. The spectral function ρ is called dissipative part, because – as explained above – ρ is related to the imaginary part of G^r. As G^r determines decays in the time domain, it describes the dissipation. The fluctuation-dissipation theorem states that the hole propagation is proportional to the spectral density times the propability of creating a hole. The companion relation, Eq. (A.40), expresses the fact that the particle propagation is proportional to the spectral density times the probability of creating a particle [229].

A more elegant derivation of Eqs. (A.39) and (A.40) may be done as follows: Denoting, as before, $\hat{A}(t) = \hat{\psi}_K(\vec{x}, t)$ and $\hat{B}(t) = \hat{\psi}_K^+(\vec{x}, t)$ and using the cyclic invariance of the trace Tr, it follows that

$$\begin{aligned} \mathrm{Tr}\left[e^{\beta(\Omega - \hat{K})} \hat{A}(t) \hat{B}(t')\right] &= e^{\beta\Omega} \mathrm{Tr}\left[\hat{B}(t') e^{-\beta\hat{K}} \hat{A}(t)\right] && \text{(A.41)} \\ &= e^{\beta\Omega} \mathrm{Tr}\left[e^{-\beta\hat{K}} e^{\beta\hat{K}} \hat{B}(t') e^{-\beta\hat{K}} \hat{A}(t)\right] \\ &= \mathrm{Tr}\left[e^{\beta(\Omega - \hat{K})} \hat{B}(t' - i\beta\hbar) \hat{A}(t)\right], \end{aligned}$$

which means that

$$\left\langle \hat{A}(t) \hat{B}(t') \right\rangle = \left\langle \hat{B}(t' - i\beta\hbar) \hat{A}(t) \right\rangle. \tag{A.42}$$

Using Eq. (A.20) one may write

$$G^r(1,2) - G^a(1,2) = G^>(1,2) - G^<(1,2) = G^>(1,2) + G^>\left((t_1 - i\beta\hbar, \vec{x}_1), 2\right).$$

A Fourier transformation yields

$$\begin{aligned} -2\pi i \rho(\vec{x}_1, \vec{x}_2, E) &= \int_{-\infty}^{\infty} \frac{d(t_1 - t_2)}{\hbar} \left(G^>(\vec{x}_1, \vec{x}_2, t_1 - t_2) + G^>(\vec{x}_1, \vec{x}_2, t_1 - t_2 - i\beta\hbar)\right) e^{\frac{i}{\hbar} E (t_1 - t_2)} \\ &= G^>(\vec{x}_1, \vec{x}_2, E) \left(1 + e^{-\beta E}\right) \\ &= G^>(\vec{x}_1, \vec{x}_2, E) \left(1 - f(E)\right)^{-1}, \end{aligned}$$

which is just Eq. (A.40). The analogous expression

$$G^r(1,2) - G^a(1,2) = -G^<(1, (t_2 - i\beta\hbar, \vec{x}_2)) - G^<(1,2)$$

yields

$$-2\pi i\rho(\vec{x}_1,\vec{x}_2,E) = -G^<(\vec{x}_1,\vec{x}_2,E)\left(1+e^{\beta E}\right) = -G^<(\vec{x}_1,\vec{x}_2,E)f(E)^{-1},$$

which is Eq. (A.39).

A.2.2 Perturbation theory

In order to evaluate the Green's functions introduced in Eqs. (A.8)–(A.12) for a nontrivial many-body problem, perturbation theory is the general method of attack. The system of interest is supposed to have a time-independent Hamiltonian $\hat{K} = \hat{K}_0 + \hat{H}_i$. In this expression $\hat{K}_0 = \hat{H}_0 - \mu\hat{N}$ shall be the simple, exactly solvable non-interacting part of the Hamiltonian, while $\hat{H}_i$ is the complicated interaction part, which shall be treated perturbatively. We want to sketch the procedure only briefly, so that the generalizing ideas in the context of contour-ordered nonequilibrium Green's functions can be appreciated. For more extensive explanations the following books may be consulted [238, 229, 141, 239], for example. First the procedure for zero temperature $T = 0$ will be presented, before we will come to the ideas, how to treat finite temperatures $T > 0$, known as the Matsubara technique.

Perturbation theory at zero temperature The perturbation theory is most easily carried out in the interaction picture, where the various terms are enumerated systematically with the help of Wick's theorem [240, 238]. For $T = 0$ the Green's function consists of a matrix element of Heisenberg operators in the interacting ground state. This form is inconvenient for perturbation theory, where it turns out, that G^c (see Eq. (A.15)) has a systematic perturbative expansion. With the help of the Gell-Mann and Low theorem the ground state of the interacting system $|\Psi_0\rangle$ is then expressed in terms of the noninteracting ground state $|\Phi_0\rangle$. For this purpose the interaction is switched on adiabatically, when coming from t at $-\infty$ and going over to t_0. After that point the interaction is switched off again. This means that a Hamiltonian of the form

$$\hat{K} = \hat{K}_0 + \hat{H}_i e^{-\varepsilon|t-t_0|} \tag{A.43}$$

is considered, where $\varepsilon \longrightarrow 0$. At $t = t_0$ the system is the fully interacting quantum system, while at $\pm\infty$ it is just the noninteracting system (see Fig. A.1). The procedure of adiabatically switching on (and off) an interaction represents a mathematical device that generates exact eigenstates of the interacting system from those of the non-interacting system. The Gell-Mann and Low theorem states that if $|\Phi_0\rangle$ is an eigenstate of the noninteracting system ($\hat{K}_0|\Phi_0\rangle = E_0|\Phi_0\rangle$) the state

$$\left|\widetilde{\Psi}_0\right\rangle = \frac{|\Psi_0\rangle}{\langle\Phi_0|\,\Psi_0\rangle} = \lim_{\varepsilon\to 0}\frac{\hat{U}_I(t_0,-\infty)\,|\Phi_0\rangle}{\langle\Phi_0|\,\hat{U}_I(t_0,-\infty)\,|\Phi_0\rangle} = \lim_{\varepsilon\to 0}\frac{\hat{U}_I(t_0,\infty)\,|\Phi_0\rangle}{\langle\Phi_0|\,\hat{U}_I(t_0,\infty)\,|\Phi_0\rangle}$$

is an eigenstate of the interacting system ($\hat{K}\left|\widetilde{\Psi}_0\right\rangle = E\left|\widetilde{\Psi}_0\right\rangle$). Here, $\hat{U}_I$ is the time-evolution operator in the interaction picture (see Eq. (A.7)) for the Hamiltonian in Eq. (A.43),

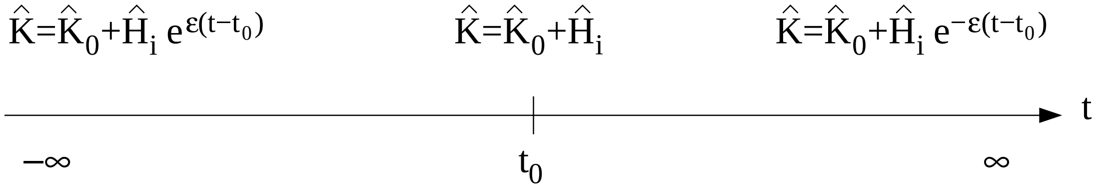

Figure A.1: Method of adiabatically switching on (and off) the interaction $\hat{H}_i$ in a Hamiltonian of the form $\hat{K} = \hat{K}_0 + \hat{H}_i$.

which depends explicity on ε. This dependence has been suppressed. If $|\Phi_0\rangle$ is the noninteracting ground state, the state $\left|\widetilde{\Psi}_0\right\rangle$ obtained from the adiabatic switching on is usually taken to be the ground state of the interacting system. However, this need not be true. The Gell-Mann and Low theorem merely asserts that it is an eigenstate of the interacting system.

Using the Gell-Mann and Low theorem the causal Green's function can be written as

$$G^c(1,2) = -i\frac{\langle\Phi_0|\, T\left(\hat{U}_I(\infty,-\infty)\hat{\psi}_I(1)\hat{\psi}_I{}^+(2)\right)|\Phi_0\rangle}{\langle\Phi_0|\,\hat{U}_I(\infty,-\infty)\,|\Phi_0\rangle},$$

where the ground state of the interacting many-body system has been expressed by the ground-state of the noninteracting system. The subscript I means that the operators are in the interaction picture. Expanding the numerator as well as the denominator with the help of Wick's theorem, the following result is finally obtained [238, 229]

$$\begin{aligned} G^c(1,2) &= -i\sum_{n=0}^{\infty}\left(-\frac{i}{\hbar}\right)^n\frac{1}{n!}\int_{-\infty}^{\infty}dt_1\cdots\int_{-\infty}^{\infty}dt_n \\ &\quad\cdot\langle\Phi_0|\,T\left(\hat{H}_{i;I}(t_1)\cdots\hat{H}_{i;I}(t_n)\hat{\psi}_I(1)\hat{\psi}_I^+(2)\right)|\Phi_0\rangle_{\text{connected}}\,. \end{aligned} \tag{A.44}$$

The index "connected" means that no diagrams are contained in the summation, which possess subunits that are not connected to the rest of the diagram by any lines. In Fig. A.2 the zeroth-order and the two connected first-order diagrams are displayed.

Perturbation theory at finite temperature At nonzero temperature ($T > 0$) one must average not only over the ground state, but over all possible configurations of the system, weighted with the density matrix (see Eq. (A.17)). In order to perform perturbation theory, it needs to be realized that the interaction $\hat{H}_i$ for a time-independent Hamiltonian $\hat{K} = \hat{K}_0 + \hat{H}_i$ not only appears in the time evolution of the field operators $\hat{\psi}_K(1)$ and $\hat{\psi}_K^+(1)$, but also in the density matrix $\hat{\varrho}$ (see Eq. (A.16)). For $T = 0$ the ground-state of the interacting system could be expressed via time-evolution operators in terms of the noninteracting ground state. To arrive at a practicable perturbative expansion the idea is that both in the field operators and the density matrix the Hamiltonian enters as an exponential factor. So the factor $\beta = 1/kT$ in $\hat{\varrho} = \exp(\beta(\Omega - \hat{K}))$ can be considered

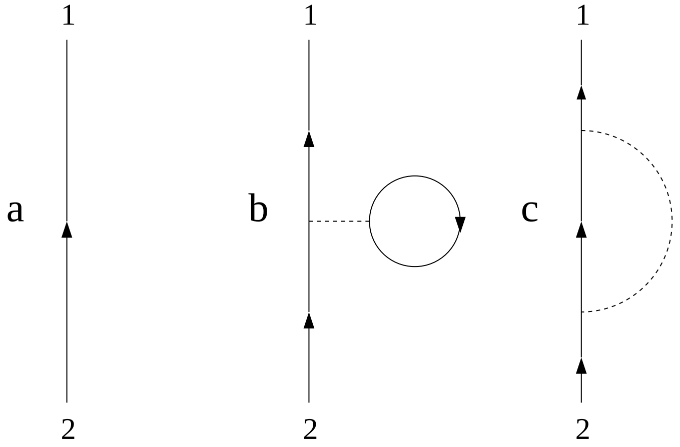

Figure A.2: The zeroth-order (a) and the two connected first-order diagrams (b and c) are displayed, as occurring in the perturbative expansion of $G^c(1,2)$ (see Eq. (A.44)).

to be a complex time. This point of view will be adopted in the study of contour-ordered Green's functions in the following Sec. A.3. The Matsubara technique does the reverse and treats the time as a complex temperature.

In the finite temperature formalism for any operator $\hat{O}_S$ in the Schrödinger picture, the (modified) interaction picture $\hat{O}_I(\tau)$ and the (modified) Heisenberg picture $\hat{O}_K(\tau)$ are defined by the equations [238]

$$\begin{aligned}\hat{O}_I(\tau) &= e^{\hat{K}_0\tau/\hbar}\hat{O}_S e^{-\hat{K}_0\tau/\hbar}\\ \hat{O}_K(\tau) &= e^{\hat{K}\tau/\hbar}\hat{O}_S e^{-\hat{K}\tau/\hbar}.\end{aligned}$$

These relations follow from the conventional Heisenberg picture by a replacement $t = -i\tau$ in the time-evolution operator, which is also known as the Wick rotation. The two pictures are related via

$$\hat{O}_K(\tau) = \hat{\mathcal{U}}(0,\tau)\hat{O}_I(\tau)\hat{\mathcal{U}}(\tau,0),$$

where $\hat{\mathcal{U}}$ is defined by

$$\hat{\mathcal{U}}(\tau_1,\tau_2) = e^{\hat{K}_0\tau_1/\hbar}e^{-\hat{K}(\tau_1-\tau_2)/\hbar}e^{-\hat{K}_0\tau_2/\hbar}.$$

Note that $\hat{\mathcal{U}}$ is not unitary, but still satisfies the group property (see Eq. (A.2))

$$\hat{\mathcal{U}}(\tau_1,\tau_3) = \hat{\mathcal{U}}(\tau_1,\tau_2)\hat{\mathcal{U}}(\tau_2,\tau_3)$$

and the boundary condition (see Eq. (A.3))

$$\hat{\mathcal{U}}(\tau,\tau) = 1.$$

The single-particle temperature Green's function is defined as

$$\mathcal{G}(1,2) = -\mathrm{Tr}\left[\hat{\varrho}T_\tau\left(\hat{\psi}_K(1)\hat{\psi}_K^+(2)\right)\right]$$

where $1 = (\vec{x}_1, \tau_1)$ and T_τ orders the operators according to their value of τ, with the smallest to the right. T_τ also includes the signature factor $(-1)^P$, where P is the number of permutations of fermion operators needed to restore the original ordering. Exploiting the cyclic invariance of the trace, it can be shown that $\mathcal{G}$ depends only on the time difference $\tau_1 - \tau_2$. In addition $\mathcal{G}$ is antiperiodic in each time variable with period $\beta\hbar$ in the range $0 \leq \tau_1, \tau_2 \leq \beta\hbar$, namely $\mathcal{G}(\vec{x}_1, \vec{x}_2, \tau_1 - \tau_2 < 0) = -\mathcal{G}(\vec{x}_1, \vec{x}_2, \tau_1 - \tau_2 + \beta\hbar)$. This periodicity allows a Fourier expansion

$$\begin{aligned}
\mathcal{G}(\vec{x}_1, \vec{x}_2, \tau) &= \frac{1}{\beta\hbar} \sum_n e^{-i\omega_n \tau} \mathcal{G}(\vec{x}_1, \vec{x}_2, i\omega_n) \\
\mathcal{G}(\vec{x}_1, \vec{x}_2, i\omega_n) &= \int_0^{\beta\hbar} d\tau e^{i\omega_n \tau} \mathcal{G}(\vec{x}_1, \vec{x}_2, \tau),
\end{aligned}$$

where $\omega_n = (2n+1)\,\pi/\beta\hbar$ for fermions.

In order to perform a perturbation expansion of the temperature Green's function the interaction picture is used. A generalized version of Wick's theorem is needed for evaluating the ensemble average of operators. It relies on the detailed form of the statistical operator $e^{-\beta\hat{K}_0}$, where $\beta\hat{K}_0$ can be any single-particle operator [241], and thus differs from Wick's original theorem, which is an operator identity valid for arbitrary matrix elements. The final result of the perturbation analysis is

$$\begin{aligned}
\mathcal{G}(1,2) &= -\frac{\mathrm{Tr}\left[e^{-\beta\hat{K}_0} T_\tau \left(\hat{\mathcal{U}}(\beta\hbar, 0) \hat{\psi}_I(1) \hat{\psi}_I^+(2)\right)\right]}{\mathrm{Tr}\left[e^{-\beta\hat{K}_0} \hat{\mathcal{U}}(\beta\hbar, 0)\right]} \\
&= -\sum_{n=0}^{\infty} \left(-\frac{1}{\hbar}\right)^n \frac{1}{n!} \int_0^{\beta\hbar} d\tau_1 \cdots \int_0^{\beta\hbar} d\tau_n \\
&\quad \cdot \mathrm{Tr}\left[e^{\beta(\Omega_0 - \hat{K}_0)} T_\tau \left(\hat{H}_{i;I}(\tau_1) \cdots \hat{H}_{i;I}(\tau_n) \hat{\psi}_I(1) \hat{\psi}_I^+(2)\right)\right]_{\text{connected}} . \qquad \text{(A.45)}
\end{aligned}$$

in analogy to what has been found for zero temperature (see Eq. (A.44)). Since the algebraic structure of the finite-temperature Wick's theorem is identical to that at zero-temperature, the temperature Green's function $\mathcal{G}$ has the same set of Feynman diagrams as G^c at zero temperature. Note also that the finite-temperature formalism never needed the assumption of the adiabatic switching on. This eleminates some uncertainty, because, as stated above, it is not necessary that the ground state of the interacting system is obtained, when the interaction is turned on starting from the ground state of the noninteracting system. One might as well arrive at an excited state. Instead it has been show for the Matsubara formalism that the limiting case $T \to 0$ results in the ground state of the interacting system [175, 239].

Once the finite temperature function $\mathcal{G}$ is known, the retarded and advanced functions follow with an analytic continuation $\mathcal{G}^{r}_{a}(\vec{x}_1, \vec{x}_2, \omega) = \mathcal{G}(\vec{x}_1, \vec{x}_2, \omega \pm i\eta)$. See the following books for further details [238, 141, 229, 239].

A.3 Contour-ordered nonequilibrium Green's functions

Although the techniques presented in Sec. A.2 are extremely powerful with regard to the determination of thermodynamic properties, these approaches are evidently unable to cope with kinetic problems, which are very important in condensed matter theory. For example they cannot describe the response of a system to a time-dependent external perturbation. However, there exists an elegant extension of the Green's function technique to nonequilibrium situations, which reduces to standard quantum field theory for systems in equilibrium [227, 242].

The Hamiltonian considered in nonequilibrium is

$$\hat{K}(t) = \hat{\mathcal{K}} + \hat{V}(t)\Theta(t - t_0). \tag{A.46}$$

The time-independent part of the Hamiltonian $\hat{\mathcal{K}} = \hat{K}_0 + \hat{H}_i$ (where $\hat{K}_0 = \hat{H}_0 - \mu\hat{N}$) is split into two parts, namely the "simple" part $\hat{K}_0$, for which Wick's theorem applies, and the "complicated" part $\hat{H}_i$, which contains many-body aspects and thus requires a special treatment. The nonequilibrium part $\hat{V}(t)$, arising, e.g., from an electric field or a light excitation pulse, is assumed to vanish for $t < t_0$.

Before the perturbation is turned on, the system is described by the thermal equilibrium density matrix

$$\hat{\rho}(\hat{\mathcal{K}}) = \frac{e^{-\beta\hat{\mathcal{K}}}}{\mathrm{Tr}\left[e^{-\beta\hat{\mathcal{K}}}\right]}.$$

Note the use of the equilibrium density matrix $\hat{\rho}(\hat{\mathcal{K}})$ instead of some time-dependent $\hat{\rho}$, in which the influence of $\hat{V}(t)$ is included. Before the time t_0 the physical system is assumed to be in thermodynamic equilibrium with a reservoir. At t_0 it is then disconnected from the reservoir and exposed to a disturbance represented by the contribution $\hat{V}(t)$ [228]. Physically this means that the thermodynamic degrees of freedom contained in $\hat{\mathcal{K}}$ do not follow the rapid variations contained in $\hat{V}(t)$. Other choices could be possible [229].

A.3.1 Contour-ordered Green's functions and perturbation theory

The equilibrium Green's function methods cannot be applied to obtain the Green's function for a Hamiltonian with a time-dependent perturbation. The reason for this is the fact that no state in the future may be identified with any of the states in the past. This is done for example in the zero temperature formalism, where the initial state in the infinitely remote past is related to a state in the infinitely remote future. Instead, the idea behind the nonequilibrium technique is to refer only to the initial state of the system at t_0.

As in equilibrium we define the correlation functions

$$\begin{aligned} G^{<}(1,2) &= i\left\langle \hat{\psi}_K^{+}(2)\hat{\psi}_K(1)\right\rangle \\ G^{>}(1,2) &= -i\left\langle \hat{\psi}_K(1)\hat{\psi}_K^{+}(2)\right\rangle, \end{aligned}$$

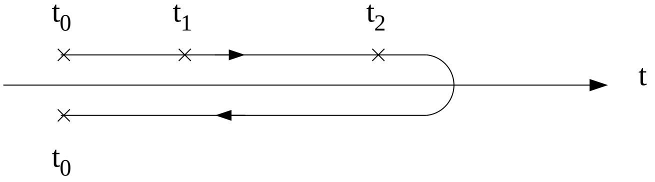

Figure A.3: The "closed time path" contour c.

where the brackets $\langle\rangle$ mean the statistical average $\left\langle \hat{O}_K(t) \right\rangle = \mathrm{Tr}\left[\hat{\rho}(\hat{\mathcal{K}})\hat{O}_K(t)\right]$ and the field operators are in the Heisenberg picture. The central quantity of the nonequilibrium technique is the contour-ordered Green's function

$$G(1,2) = -i\left\langle T_c\left(\hat{\psi}_K(1)\hat{\psi}_K^+(2)\right)\right\rangle, \tag{A.47}$$

which possesses a simple perturbative expansion. The subscript c refers to a contour along the real-time axis starting at t_0 and passing through $t_1$and t_2 once. Such a contour is displayed for the case $t_1 <_c t_2$ in Fig. A.3, where $t_1 <_c t_2$ ($t_1 >_c t_2$) means that t_1 is before (after) t_2 on the contour c. T_c is the time-ordering operator along the contour c. In terms of the correlation functions the contour-ordered Green's function is given by

$$G(1,2) = \Theta_c(t_1 - t_2)G^>(1,2) + \Theta_c(t_2 - t_1)G^<(1,2),$$

where $\Theta_c(t_1 - t_2) = \begin{cases} 1 & t_1 >_c t_2 \\ 0 & t_1 <_c t_2 \end{cases}$.

To motivate, why a contour as displayed in Fig. A.3 is introduced, consider the expectation value of an operator in the Heisenberg picture $\left\langle \hat{O}_K(t) \right\rangle = \mathrm{Tr}\left[\hat{\rho}(\hat{\mathcal{K}})\hat{O}_K(t)\right]$. In this expression

$$\hat{O}_K(t) = \hat{u}_I^+(t,t_0)\hat{O}_{\mathcal{K};I}(t)\hat{u}_I(t,t_0),$$

$\hat{O}_{\mathcal{K};I}(t)$ is the operator $\hat{O}_K(t)$ in the interaction picture with respect to $\hat{\mathcal{K}}$, and $\hat{u}_I(t,t_0) = T\exp\left(-\frac{i}{\hbar}\int_{t_0}^{t} dt'\hat{V}_{\mathcal{K};I}(t')\right)$. As in the equilibrium formalism T denotes the time-ordering operator and $\hat{V}_{I;\mathcal{K}}(t')$ is the perturbation in the interaction picture with respect to $\hat{\mathcal{K}}$. Thus the transformation between the Heisenberg and the interaction picture can be expressed as [228]

$$\hat{O}_K(t) = T_c\left(\exp\left(-\frac{i}{\hbar}\int_c dt'\hat{V}_{\mathcal{K};I}(t')\right)\hat{O}_{\mathcal{K};I}(t)\right)$$

and the contour-ordering appears naturally as an elegant way of connecting these two pictures.

For a perturbative expansion of the contour-ordered Green's function G, or in other words for Wick's theorem to apply, one needs to (i) express the density matrix $\hat{\rho}(\hat{\mathcal{K}})$ of the interacting system $\hat{\mathcal{K}}$ in terms of the noninteracting density $\hat{\rho}(\hat{K}_0)$ and (ii) express the field operators in terms of annihilation and creation operators of the noninteracting system. The solution to problem (ii) can be achieved by changing from the Heisenberg picture to

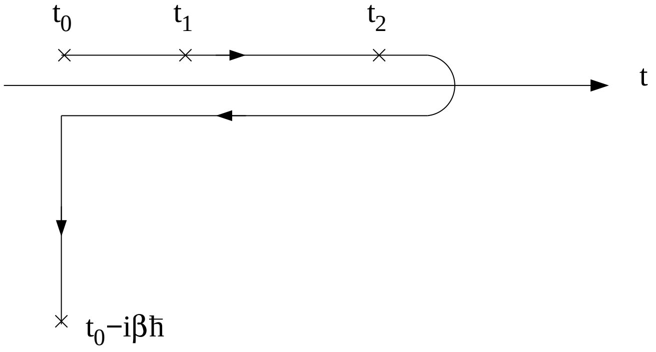

Figure A.4: The "interaction" contour c_i.

the interaction picture in the time dependence of the field operators. In the interaction picture the time evolution of the field operators is then due to the noninteracting system $\hat{K}_0$. The solution to problem (i) can be obtained by formally considering temperatures as imaginary times, as explained in the context of finite temperature Green's functions above. The appropriate time-evolution operator, connecting the Heisenberg picture and the interaction picture with respect to the nonperturbative part $\hat{K}_0$, is

$$\hat{w}(t, t_0) = T \exp\left(-\frac{i}{\hbar}\int_{t_0}^{t} dt' \hat{W}_{K_0;I}(t')\right),$$

where $\hat{W}_{K_0;I}(t)$ is the interaction picture operator belonging to $\hat{W}(t) = \hat{H}_i + \hat{V}(t)\Theta(t - t_0)$. Noting that $\hat{W}(t) = \hat{H}_i$ for $t < t_0$ and

$$e^{-\beta\hat{\mathcal{K}}} = e^{-\beta\hat{K}_0}\hat{w}(t_0^- - i\beta, t_0^-),$$

the contour-ordered Green's function G can be brought into a form, for which Wick's theorem applies

$$G(1,2) = -i\frac{\mathrm{Tr}\left[e^{-\beta\hat{K}_0}T_{c_i}\left(\hat{w}_{c_i}\hat{\psi}_{K_0;I}(1)\hat{\psi}^{+}_{K_0;I}(2)\right)\right]}{\mathrm{Tr}\left[e^{-\beta\hat{K}_0}T_{c_i}\left(\hat{w}_{c_i}\right)\right]}. \tag{A.48}$$

The symbol $\hat{w}_{c_i}$ stands for $\hat{w}_{c_i} = \exp\left(-\frac{i}{\hbar}\int_{c_i} dt'\hat{W}_{K_0;I}(t')\right)$, and the interaction contour c_i is displayed in Fig. A.4.

If one considers a system starting at $T = 0$ one might also think about adiabatically switching on the interaction H_i, such that

$$\hat{K} = \hat{K}_0 + \hat{H}_i\Theta(t_0 - t)e^{\varepsilon(t-t_0)} + \left(\hat{H}_i + \hat{V}(t)\right)\Theta(t - t_0).$$

and choose the contour c_i' depicted in Fig. A.5. In this case the contour-ordered Green's

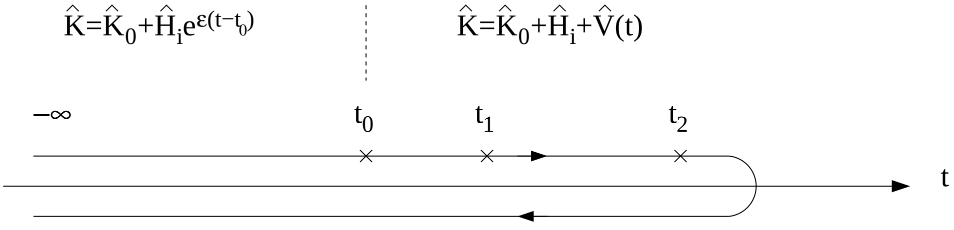

Figure A.5: The "interaction" contour c_i' for $T=0$.

function is

$$G(1,2) = -i\frac{\langle\Phi_0|\, T_{c_i'}\left(\hat{w}_{c_i'}\hat{\psi}_{K_0;I}(1)\hat{\psi}^{+}_{K_0;I}(2)\right)|\Phi_0\rangle}{\langle\Phi_0|\, T_{c_i'}\left(\hat{w}_{c_i'}\right)|\Phi_0\rangle}. \tag{A.49}$$

We are now in a position to apply Wick's theorem to Eqs. (A.48) and (A.49), just as in equilibrium, to get to a perturbation expansion for G. Again the denominator in Eqs. (A.48) and (A.49) will cancel all the disconnected diagrams and thus only contributions due to connected diagrams of the numerator need to be considered, which results in the following formula

$$\begin{aligned} G(1,2) &= -i\sum_{n=0}^{\infty}\left(-\frac{i}{\hbar}\right)^n \frac{1}{n!}\int_{\tilde{c}} dt_1 \cdots \int_{\tilde{c}} dt_n \qquad \text{(A.50)} \\ &\quad \cdot \left\langle T_{\tilde{c}}\left(\hat{W}_{K_0;I}(t_1)\cdots\hat{W}_{K_0;I}(t_n)\hat{\psi}_{K_0;I}(1)\hat{\psi}^{+}_{K_0;I}(2)\right)\right\rangle_{\text{connected}}. \end{aligned}$$

where $\left\langle\hat{X}\right\rangle = \mathrm{Tr}\left[e^{\beta(\Omega_0-\hat{K}_0)}\hat{X}\right]$ and $\tilde{c}=c_i$ in the context of Eq. (A.48), whereas $\left\langle\hat{X}\right\rangle = \langle\Phi_0|\,\hat{X}\,|\Phi_0\rangle$ and $\tilde{c}=c_i'$ in the context of Eq. (A.49).

The only difference between the nonequilibrium and the equilibrium formalism is the appearance of the integration over a contour in the nonequilibrium situation, whereas in the equilibrium theory an integration over the real time axis for $T=0$ (see Eq. (A.44)) or an inverse temperature interval for $T>0$ (see Eq. (A.45)) was necessary. Consequently the contour-ordered Green's function is mapped onto its Feynman diagrams precisely as in the equilibrium theory. It can be concluded, that equilibrium and nonequilibrium statistical mechanics are formally and structurally equivalent and that this equivalence is demonstrated by introducing a contour ordering to play the role of the usual time ordering [228].

A.3.2 The Keldysh formulation

With the theory described so far (see Eq. (A.48) and the contour c_i in Fig. A.4) we can describe exactly the temporal evolution of a system initially in thermodynamic equilibrium. In the transport problems, relevant for this work, no transient effects are considered. For this reason we let t_0 in c_i (see Fig. A.4) approach $-\infty$. We assume that the Green's function falls off sufficiently rapidly as a function of the separation of its time arguments. Then, we

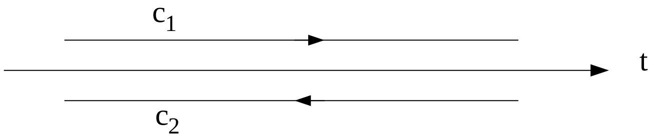

Figure A.6: The Keldysh contour $c_K = c_1 \cup c_2$.

can also neglect the part on the contour c_i from t_0 to $t_0 - i\beta\hbar$, which takes into account initial correlations [228, 242, 229]. The contour c_i therefore reduces to the contour c (see Fig. A.3), both of which start and end at $-\infty$ now. By use of the unitarity of the time evolution operator the contour c can be extended beyond the largest time considered, and the Keldysh contour c_k is obtained, when the turning point of the contour c is approaching ∞ [227]. As depicted in Fig. A.6 the Keldysh contour c_K consists of two parts: c_1 extending from $-\infty$ to ∞ and c_2 extending from ∞ to $-\infty$.

It is more convenient to deal with Green's functions defined on the real time axis than on a contour. As G has two time arguments, which can be on the different parts of the Keldysh contour c_1 or c_2, there are altogether 4 different Green's functions with real time arguments. They can be grouped into a 2 × 2-matrix form

$$\tilde{G}(1,2) = \begin{pmatrix} G_{11}(1,2) & G_{12}(1,2) \\ G_{21}(1,2) & G_{22}(1,2) \end{pmatrix},$$

where G_{ij} means that t_1 is on c_i and t_2 on c_j.[7] Writing out the different components, we observe (see Eqs. (A.8), (A.11), and (A.12)) that

$$\begin{aligned} G_{11}(1,2) &= -i\left\langle T\left(\hat{\psi}_K(1)\hat{\psi}_K^+(2)\right)\right\rangle = G^c(1,2) && \text{(A.51)} \\ G_{12}(1,2) &= i\left\langle \hat{\psi}_K^+(2)\hat{\psi}_K(1)\right\rangle = G^<(1,2) && \text{(A.52)} \\ G_{21}(1,2) &= -i\left\langle \hat{\psi}_K(1)\hat{\psi}_K^+(2)\right\rangle = G^>(1,2) && \text{(A.53)} \\ G_{22}(1,2) &= -i\left\langle \tilde{T}\left(\hat{\psi}_K(1)\hat{\psi}_K^+(2)\right)\right\rangle. && \text{(A.54)} \end{aligned}$$

In Eq. (A.54) the anti-time-ordering operator $\tilde{T}$ has been introduced for G_{22}, when both components are on the lower contour c_2. $\tilde{T}$ orders the operators from right to left in descending order, or more explicitly for two field operators

$$\tilde{T}\left(\hat{\psi}_K(1)\hat{\psi}_K^+(2)\right) = \begin{cases} -\hat{\psi}_K^+(2)\hat{\psi}_K(1) & t_1 > t_2 \\ \hat{\psi}_K(1)\hat{\psi}_K^+(2) & t_1 < t_2 \end{cases}.$$

As in the equilibrium formalism, the Green's functions are not linearly independent. In particular

$$\begin{aligned} G_{11}(1,2) &= \Theta(t_1-t_2)G^>(1,2) + \Theta(t_2-t_1)G^<(1,2) && \text{(A.55)} \\ G_{22}(1,2) &= \Theta(t_1-t_2)G^<(1,2) + \Theta(t_2-t_1)G^>(1,2) && \text{(A.56)} \\ G_{11}(1,2) + G_{22}(1,2) &= G_{12}(1,2) + G_{21}(1,2), && \text{(A.57)} \end{aligned}$$

---

[7] Note, that if transient effects are considered, one needs to employ a 3 × 3-matrix formalism [242].

where Eq. (A.57) directly follows from Eqs. (A.55) and (A.56). By performing a rotation in Keldysh space, it is possible to remove part of the redundancy. Besides the retarded and advanced Green's functions G^a and G^r, defined as in the equilibrium case (see Eqs. (A.9), (A.10), and (A.18), (A.19))

$$\begin{aligned} G^r(1,2) &= \Theta(t_1 - t_2)\left(G^>(1,2) - G^<(1,2)\right) && \text{(A.58)} \\ G^a(1,2) &= -\Theta(t_2 - t_1)\left(G^>(1,2) - G^<(1,2)\right), && \text{(A.59)} \end{aligned}$$

the Keldysh Green's function

$$\begin{aligned} G^K(1,2) &= -i\left\langle \left[\hat{\psi}_K(1), \hat{\psi}_K^+(2)\right] \right\rangle \\ &= G^>(1,2) + G^<(1,2) \end{aligned}$$

is encountered.

Following Larkin and Ovchinnikov [243, 228, 230], a slightly modified rotation in Keldysh space will be used here as compared to Keldysh's original work [227]. First a transformation in Keldysh space is performed

$$\check{G} = \sigma_3 \tilde{G} \tag{A.60}$$

followed by a rotation

$$\bar{G} = L\check{G}L^+, \tag{A.61}$$

where

$$L = \frac{\sigma_0 - i\sigma_2}{\sqrt{2}} = \frac{1}{\sqrt{2}}\begin{pmatrix} 1 & -1 \\ 1 & 1 \end{pmatrix}.$$

In these formulas the matrices σ_i $(i = 0, 1, 2, 3)$ are the Pauli matrices[8]

$$\sigma_0 = \begin{pmatrix} 1 & 0 \\ 0 & 1 \end{pmatrix}, \ \sigma_1 = \begin{pmatrix} 0 & 1 \\ 1 & 0 \end{pmatrix}, \ \sigma_2 = \begin{pmatrix} 0 & -i \\ i & 0 \end{pmatrix}, \ \sigma_3 = \begin{pmatrix} 1 & 0 \\ 0 & -1 \end{pmatrix}.$$

With the help of the relations

$$\begin{aligned} G^r(1,2) &= G_{11}(1,2) - G_{12}(1,2) = G_{21}(1,2) - G_{22}(1,2) && \text{(A.62)} \\ G^a(1,2) &= G_{11}(1,2) - G_{21}(1,2) = G_{12}(1,2) - G_{22}(1,2) && \text{(A.63)} \\ G^K(1,2) &= G_{12}(1,2) + G_{21}(1,2) = G_{11}(1,2) + G_{22}(1,2) && \text{(A.64)} \end{aligned}$$

(which are consistent with Eqs. (A.51)–(A.54)) we obtain a matrix representation for $\bar{G}$ with an upper triangular matrix

$$\bar{G} = \begin{pmatrix} G^r & G^K \\ 0 & G^a \end{pmatrix}.$$

---

[8] Notice the useful property $(\sigma_i)^2 = 1$.

For manipulations within the Keldysh formalism the inverse relations to Eqs. (A.62)–(A.64) are helpful

$$\begin{aligned}
G_{11}(1,2) &= \left(G^r(1,2) + G^a(1,2) + G^K(1,2)\right)/2 \\
G_{12}(1,2) &= \left(-G^r(1,2) + G^a(1,2) + G^K(1,2)\right)/2 \\
G_{21}(1,2) &= \left(G^r(1,2) - G^a(1,2) + G^K(1,2)\right)/2 \\
G_{22}(1,2) &= \left(-G^r(1,2) - G^a(1,2) + G^K(1,2)\right)/2.
\end{aligned}$$

When the self-energy Σ is written in its matrix representation

$$\tilde{\Sigma}(1,2) = \begin{pmatrix} \Sigma_{11}(1,2) & \Sigma_{12}(1,2) \\ \Sigma_{21}(1,2) & \Sigma_{22}(1,2) \end{pmatrix}$$

a similar relationship between the Σ_{ij} as the one in Eq. (A.57) for the G_{ij} is found. This relation can be derived from the Dyson equation [238, 229, 230] of the contour-ordered Green's function

$$G(1,1') = g(1,1') + \int_c dt_2 \int d^3x_2 \int_c dt_3 \int d^3x_3 g(1,2)\Sigma(2,3)G(3,1'). \tag{A.65}$$

In this expression g is the unperturbed contour-ordered Green's function and the self-energy Σ is, similar to the equilibrium case, the sum over all topologically distinct proper self-energy diagrams. In this integral, times t_i are integrated along the contour c. In the transformed and rotated matrix representation of the Dyson equation, times run only along the real axis

$$\bar{G}(1,1') = \bar{g}(1,1') + \int_{-\infty}^{\infty} dt_2 \int d^3x_2 \int_{-\infty}^{\infty} dt_3 \int d^3x_3 \bar{g}(1,2)\bar{\Sigma}(2,3)\bar{G}(3,1'). \tag{A.66}$$

The self-energy $\bar{\Sigma} = L\tilde{\Sigma}\sigma_3 L^+$ is transformed with σ_3 from the right. Exploiting the upper triangular form of the Green's functions, it can be shown that

$$\Sigma_{11} + \Sigma_{22} = -\left(\Sigma_{12} + \Sigma_{21}\right). \tag{A.67}$$

Exploiting this relation and by defining the retarded, advanced, and Keldysh self-energy components

$$\Sigma^r(1,2) = \Sigma_{11}(1,2) + \Sigma_{12}(1,2) = -\left(\Sigma_{21}(1,2) + \Sigma_{22}(1,2)\right) \tag{A.68}$$

$$\Sigma^a(1,2) = \Sigma_{11}(1,2) + \Sigma_{21}(1,2) = -\left(\Sigma_{12}(1,2) + \Sigma_{22}(1,2)\right) \tag{A.69}$$

$$\Sigma^K(1,2) = \Sigma_{11}(1,2) + \Sigma_{22}(1,2) = -\left(\Sigma_{12}(1,2) + \Sigma_{21}(1,2)\right) \tag{A.70}$$

the matrix representation of the self-energy $\bar{\Sigma}$ is

$$\bar{\Sigma}(1,2) = \begin{pmatrix} \Sigma^r & \Sigma^K \\ 0 & \Sigma^a \end{pmatrix}.$$

For reasons of completeness we also state the inverse relations to Eqs. (A.68)-(A.70)

$$\begin{aligned}
\Sigma_{11}(1,2) &= \left(\Sigma^r(1,2)+\Sigma^a(1,2)+\Sigma^K(1,2)\right)/2 \\
\Sigma_{12}(1,2) &= \left(\Sigma^r(1,2)-\Sigma^a(1,2)-\Sigma^K(1,2)\right)/2 \\
\Sigma_{21}(1,2) &= \left(-\Sigma^r(1,2)+\Sigma^a(1,2)-\Sigma^K(1,2)\right)/2 \\
\Sigma_{22}(1,2) &= \left(-\Sigma^r(1,2)-\Sigma^a(1,2)+\Sigma^K(1,2)\right)/2
\end{aligned}$$

Now it is easy to see that the following Dyson equations hold for the different Green's functions

$$\begin{aligned}
G^r &= g^r + g^r\Sigma^r G^r = g^r + G^r\Sigma^r g^r && \text{(A.71)} \\
G^a &= g^a + g^a\Sigma^a G^a = g^a + G^a\Sigma^a g^a && \text{(A.72)} \\
G^K &= g^K + g^r\Sigma^r G^K + g^r\Sigma^K G^a + g^K\Sigma^a G^a && \text{(A.73)} \\
&= g^K + G^r\Sigma^r g^K + G^r\Sigma^K g^a + G^K\Sigma^a g^a
\end{aligned}$$

In these equations the integration over intermediate arguments is understood. This convention is adopted for the rest of this section in order to simplify the notation. It should be noted that the Dyson equation for the contour-ordered Green's function G may also be written with the unperturbed Green's function to the right $G = g + G\Sigma g$. From this relation the left-hand Dyson equation follows (as compared to the right-hand Dyson equation (see Eq. (A.66)))

$$\bar{G} = \bar{g} + \bar{G}\bar{\Sigma}\bar{g} \tag{A.74}$$

and the second relations in Eqs. (A.71)–(A.73) are obtained.

By transforming Eqs. (A.66) and (A.74) one obtains an alternative form of the Dyson equations [228]

$$\begin{aligned}
\left[\left(g^{-1}-\bar{\Sigma}\right)G\right](1,2) &= \delta(1-2) && \text{(A.75)} \\
\left[G\left(g^{-1}-\bar{\Sigma}\right)\right](1,2) &= \delta(1-2), && \text{(A.76)}
\end{aligned}$$

where the unperturbed inverse Green's function is given by

$$g^{-1}(1,2) = \left[i\hbar\partial_{t_1} - K_0(\vec{x}_1)\right]\delta(1-2) \tag{A.77}$$

and $K_0(\vec{x}_1)$ is the onsite element of the noninteracting single-particle operator $\hat{K}_0$ (see Eq. (A.46) and notice that $\hat{K}_0$ is an operator, which is diagonal in its space representation $\langle\vec{x}_1|\,\hat{K}_0\,|\vec{x}_2\rangle = K_0(\vec{x}_1)\delta(\vec{x}_1-\vec{x}_2)$).[9]

---

[9] Notice that, most conveniently, the self-energy in Eqs. (A.75) and (A.76) is split into two components, namely the irregular and regular parts Σ^{irreg} and Σ^{reg} [242, 231]. Here the irregular part consists of all single-particle contributions to the self-energy. Such contributions are local in time, so that the matrix representation $\bar{\Sigma}^{\text{irreg}}$ is diagonal, because self-energy components with times on different contour branches vanish. This self-energy then transform in the same way and Σ^{irreg} may be added to g^{-1}, yielding the modified inverse Green's function operator $g_0^{-1}(1,2) = [i\hbar\partial_{t_1} - K_0(x_1)]\,\delta(1-2) - \Sigma^{\text{irreg}}(1,2)$ and the relations $\left[\left(g_0^{-1}-\bar{\Sigma}^{\text{reg}}\right)G\right](1,2) = \delta(1-2)$. (See also the discussion in Sec. A.3.3.)

Eqs. (A.71)–(A.73) form the complete set of equations that needs to be solved for each concrete problem. The number of independent equations that need to be considered is actually only two, because G^a and G^r are Hermitian conjugates [227]. While G^r and G^a characterize dynamical properties and spectral densities, G^K contains information about the distribution function.

With the help of the Dyson equations (see Eqs. (A.71) and (A.72)) more detailed connections between the self-energy components Σ_{ij} as compared to the sum rule in Eq. (A.67) can be derived [242]. These equations are[10]

$$\begin{aligned}
\Sigma_{11}(1,2) &= \begin{cases} -\Sigma_{21}(1,2) & t_1 > t_2 \\ -\Sigma_{12}(1,2) & t_1 < t_2 \end{cases} \\
\Sigma_{22}(1,2) &= \begin{cases} -\Sigma_{12}(1,2) & t_1 > t_2 \\ -\Sigma_{21}(1,2) & t_1 < t_2 \end{cases}
\end{aligned}$$

As opposed to the relations for the Green's function components G_{ij} the self-energy components Σ_{ij} have an opposite sign in the mixed components Σ_{12} and Σ_{21}, arising from the time reversed contour integration on path c_2 as compared to path c_1 (see Fig. (A.6)).[11] These differences in signs of the mixed self-energy components could already be noticed in Eq. (A.67), where a negative sign appeared as compared to Eq. (A.57) for the Green's function components G_{ij}. For this reason one defines

$$\Sigma^{<} = -\Sigma_{12} \tag{A.78}$$
$$\Sigma^{>} = -\Sigma_{21} \tag{A.79}$$

and obtains the relations

$$\Sigma_{11}(1,2) = \Theta(t_1-t_2)\Sigma^{>}(1,2) + \Theta(t_2-t_1)\Sigma^{<}(1,2) \tag{A.80}$$
$$\Sigma_{22}(1,2) = \Theta(t_1-t_2)\Sigma^{<}(1,2) + \Theta(t_2-t_1)\Sigma^{>}(1,2) \tag{A.81}$$
$$\Sigma_{11}+\Sigma_{22} = \Sigma^{<} + \Sigma^{>} \tag{A.82}$$

---

[10] The derivation of these relations goes as follows: Starting from the Dyson equation for G^r (see Eq. (A.71)) one can write it as

$$G^r(1,1') = g^r(1,1') + g^r(1,2)\left(\Sigma_{11}(2,3)+\Sigma_{12}(2,3)\right)G^r(3,1').$$

(As above an integration is understood over the dummy arguments 2 and 3.) From Eq. (A.58) it follows that for $t_1 < t_{1'}$

$$0 = g^r(1,2)\left(\Sigma_{11}(2,3)+\Sigma_{12}(2,3)\right)G^r(3,1').$$

For times $(t_1 < t_2) \vee (t_3 < t_{1'})$ this equation is fulfilled due to the vanishing retarded Green's functions $g^r(1,2)$ and $G^r(3,1')$. Therefore times $(t_1 > t_2) \wedge (t_3 > t_{1'})$ together with the first assumption $t_1 < t_{1'}$ yield a relation between Σ_{11} and Σ_{12}. One obtains that $\Sigma_{11}(2,3) = -\Sigma_{12}(2,3)$ if $t_2 < t_1 < t_{1'} < t_3$ or more compactly $t_2 < t_3$. Using Eq. (A.67) one obtains $\Sigma_{22}(2,3) = -\Sigma_{21}(2,3)$. An analogous procedure for G^a(see Eq. (A.72)) yields $\Sigma_{11}(2,3) = -\Sigma_{21}(2,3)$ and $\Sigma_{22}(2,3) = -\Sigma_{12}(2,3)$ for $t_3 < t_2$.

[11] In Σ_{22} negative signs due to the integration path on c_2 appear twice, such that they cancel and Σ_{22} behaves like G_{22} concerning the signs.

in analogy to Eqs. (A.55)–(A.57). Equipped with these relations Σ^r, Σ^a and Σ^K can be expressed as

$$\begin{aligned}\Sigma^r(1,2) &= \Theta(t_1-t_2)\left(\Sigma^>(1,2)-\Sigma^<(1,2)\right)\\ \Sigma^a(1,2) &= -\Theta(t_2-t_1)\left(\Sigma^>(1,2)-\Sigma^<(1,2)\right)\\ \Sigma^K(1,2) &= \Sigma^<(1,2)+\Sigma^>(1,2)\end{aligned}$$

Below we will use the lesser ($<$) and greater ($>$) components of G and Σ instead of the 12- and 21-components because of their completely analogous expressions (see Eqs. (A.55)–(A.57) and Eqs. (A.80)–(A.82)), which allow the use of the Langreth rules [244, 229, 231].

Eq. (A.73) can be solved for G^K. Exploiting the relation $(1+G^r\Sigma^r)(1-g^r\Sigma^r)=1$, which follows from Eq. (A.71), the solution for G^K is

$$G^K=(1+G^r\Sigma^r)\,g^K\,(1+\Sigma^aG^a)+G^r\Sigma^KG^a. \tag{A.83}$$

More frequently, especially in the context of the computation of electron transport, the functions $G^<=G_{12}$ and $G^>=G_{21}$ are needed. For this reason the Dyson equation and corresponding solution for these components is also given below. The former can simply be obtained by taking the offdiagonal matrix elements in the expression

$$\check{G}=\check{g}+L^+\bar{g}\bar{\Sigma}\bar{G}L.$$

This yields

$$\begin{aligned}G^< &= g^<+g^<\Sigma^aG^a+g^r\Sigma^rG^<+g^r\Sigma^<G^a &\text{(A.84)}\\ &= g^<+G^<\Sigma^ag^a+G^r\Sigma^rg^<+G^r\Sigma^<g^a\\ G^> &= g^>+g^>\Sigma^aG^a+g^r\Sigma^rG^>+g^r\Sigma^>G^a &\text{(A.85)}\\ &= g^>+G^>\Sigma^ag^a+G^r\Sigma^rg^>+G^r\Sigma^>g^a\end{aligned}$$

with solutions very similar to Eq. (A.83)

$$\begin{aligned}G^< &= (1+G^r\Sigma^r)\,g^<\,(1+\Sigma^aG^a)+G^r\Sigma^<G^a &\text{(A.86)}\\ G^> &= (1+G^r\Sigma^r)\,g^>\,(1+\Sigma^aG^a)+G^r\Sigma^>G^a. &\text{(A.87)}\end{aligned}$$

A.3.3 Feynman diagrams

In this last paragraph, the Feynman rules in Keldysh space shall be established. They will be illustrated for the most simple example, namely the coupling to an external potential[12]

$$\hat{V}_{K_0;I}(t)=\int d^3x\hat{\psi}^+_{K_0;I}(\vec{x},t)V(\vec{x},t)\hat{\psi}^+_{K_0;I}(\vec{x},t). \tag{A.88}$$

---

[12] Here, $\hat{V}_{K_0;I}(t)$ is written in the interaction picture I and its time evolution is governed by the unperturbed Hamiltonian $\hat{K}_0$.

Similar presentations can be found in Refs. [228, 232]. As we will mainly cope with such single-particle perturbations in the calculations of the current, this example is, however, relevant for the studies in this work.

To the standard Feynman rules the additional features brought about by the contour need to be added. In Fig. A.7 the diagrammatic expansion of G is shown with the crosses denoting the external potential. In order to discuss the Feyman rules, it is sufficient to consider simple diagrams. The first order $G^{(1)}$ in the perturbation expansion of the contour-ordered Green's function G is obtained from Eq. (A.50)

$$\begin{aligned} G^{(1)}(1,1') &= -\frac{1}{\hbar}\int_{c_K} dt_2 \int d^3x_2 \int_{c_K} dt_3 \int d^3x_3 g(1,2)U(2,3)g(3,1') && \text{(A.89)} \\ &= -\frac{1}{\hbar}\int_{c_K} dt_2 \int d^3x_2 g(1,2)V(2)g(2,1'), && \text{(A.90)} \end{aligned}$$

where the time integration runs along the Keldysh contour c_K (see Fig. A.6) and $g = G^{(0)}$ is the unperturbed Green's function. While in the first line of Eq. (A.89) a general two-particle potential U has been used, the special shape of

$$U(1,2) = V(1)\delta(t_1 - t_2)\delta(\vec{x}_1 - \vec{x}_2) \tag{A.91}$$

(see Eq. (A.88)) has been exploited in Eq. (A.90). Often such one-body external potentials are treated separately from truly many-body interactions [241, 229, 231]. Danielewicz and van Leeuwen [241, 231] call these single-particle contributions singular part of the self energy $\Sigma(1,2) = \Sigma^{\delta}(1)\delta(1-2) + \Theta_c(t_1-t_2)\Sigma^{>}(1,2) + \Theta_c(t_2-t_1)\Sigma^{<}(1,2)$. It is immediately clear, that due to the locality of U for single-particle terms (see Eq. (A.91)) such kinds of self-energies are on the diagonal of $\tilde{\Sigma}$, because no contributions to Σ_{12} of Σ_{21} can arise [242].

In Eq. (A.90) we first split the integration along the contour into integrations along the real time axis

$$\int_{c_K} dt = \int_{-\infty}^{\infty} dt + \int_{\infty}^{-\infty} dt = \int_{-\infty}^{\infty} dt - \int_{-\infty}^{\infty} dt$$

and second we use the matrix representation to write $G^{(1)}$ in its components in Keldysh space (with indices that take the values 1 and 2)

$$G_{ij}^{(1)}(1,1') = \int_{-\infty}^{\infty} dt_2 \int d^3x_2 \sum_{k,l} g_{ik}(1,2)V_{kl}(2)g_{lj}(2,1').$$

The perturbation

$$V_{ij}(2) = V(2)\left(\sigma_3\right)_{ij}$$

gives a clear motivation for introducing the Green's functions $\check{G}$ transformed with σ_3 (see Eq. (A.60)). We have shown that the external potential in Keldysh space couples to particles through σ_3. Suppressing integrations over intermediate arguments, we can write

$$\tilde{G}^{(1)}(1,2) = \tilde{g}(1,2)\tilde{V}(2)\tilde{g}(2,1'). \tag{A.92}$$

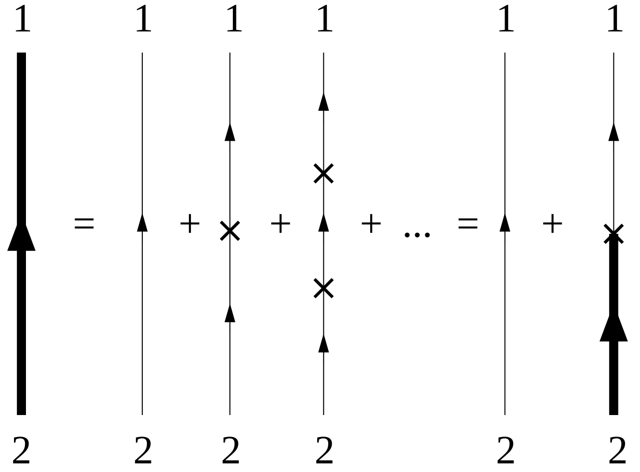

Figure A.7: Perturbation expansion of the contour-ordered Green's function G for an external single-particle potential $\hat{V}(t)$ (see Eq. (A.88)).

The diagrammatic expansion of G is the same as in equilibrium. The first-order term of G in V, given in Eqs. (A.90) and (A.92), corresponds to the second diagram of the infinite series shown in Fig. A.7. The Dyson equation for G is therefore

$$\tilde{G} = \tilde{g} + \tilde{g}\tilde{V}\tilde{G}$$

where the self-energy can be identified to be

$$\tilde{\Sigma} = \tilde{V} = V\sigma_3.$$

As mentioned above, it can be seen that this self-energy is diagonal, meaning that $\Sigma_{12} = \Sigma_{21} = 0$ and $\Sigma_{11}(1,2) = V(1)\delta(1-2) = -\Sigma_{22}$. With the help of Eqs. (A.68) and (A.69) this means that $\Sigma^r(1,2) = \Sigma^a(1,2) = V(1)\delta(1-2)$, while $\Sigma^< = \Sigma^> = 0$.

Therefore the self-energies $\Sigma^< = -\Sigma_{12}$ and $\Sigma^> = -\Sigma_{21}$ vanish for any single-particle potential and will only be non-zero for true many-body interactions as for example electron-electron or electron-phonon interactions. See Ref. [228, 230] for the Feynman rules in Keldysh space for such more complicated interactions.

Appendix B

Nonorthogonal basis sets

In usual text books on quantum mechanics [237, 217] physical systems are described in therms of orthonormal basis sets. They naturally arise, when quantum systems are represented in terms of eigenstates of some hermitian operator, like for example in terms of energy or momentum eigenstates. In such cases the basis vectors belonging to different eigenvalues are orthogonal, and if degeneracies should occur, the degenerate subspace can again be orthogonalized by procedures like Gram-Schmidt.

In quantum chemistry efficient descriptions of the electronic structure of a system often involve nonorthogonal, local basis sets. In particular, the technique of linear combination of atomic orbitals (LCAO) [81, 173, 245] spans a basis of a Hilbert space by means of atomic basis functions. These atomic basis functions are commonly located at the atomic positions, in order to describe well the electrons, which are close to the positively charged atomic nuclei. The LCAO technique finds wide applications for efficiency reasons, because only a small number of such atomic basis functions may be needed to achieve a good description of the electronic states, if they are chosen such that they resemble atomic orbitals of the isolated atoms. However, the atomic basis functions of different atoms are usually not orthogonal to each other so that one needs to work in a nonorthogonal basis.

While it has been proposed recently to describe quantum systems with nonorthogonal basis states by means of embedding them into a "new Hilbert space in which they are by definition mutually orthogonal" [246, 247], a proper description of systems with a nonorthogonal basis is formulated in terms of a tensorial formalism [248, 249, 250, 251, 252, 253]. While in Refs. [248, 249] the tensor calculus is nicely demonstated in the three-dimensional Euclidean space, Ref. [251] presents a more general formulation applicable also to the complex domain and also considers second quantization. As the basis functions in chemistry are constructed such that the atomic basis functions are real, the formalism presented by Artacho et al. [251] will be simplified somewhat below, by restricting our discussion to the real domain.

B.1 Dual basis set and tensorial representations

Let us assume that our (one-particle) Hilbert space $\mathcal{H}_1$, associated with a given physical system, is spanned by the basis $\{|\phi_i\rangle\}$. (The set $\{|\phi_i\rangle\}$ may be the set of atomic basis functions.) This basis will be called the covariant basis. There exists a unique set of vectors $\{|\phi^i\rangle\}$, called the contravariant basis set or dual basis, defined by its relation to the covariant basis

$$\left\langle\phi^i \left|\phi_j\right\rangle = \langle\phi_i \left|\phi^j\right\rangle = \delta^i_j, \tag{B.1}$$

where

$$\delta^i_j = \delta^j_i = \begin{cases} 1 & \text{if } i = j \\ 0 & \text{if } i \neq j \end{cases} .$$

The co- and contravariant components of the metric tensor are defined by the transformation between the co- and contravariant basis sets

$$\left|\phi^i\right\rangle = g^{ij}\left|\phi_j\right\rangle \quad \text{and} \quad \left|\phi_i\right\rangle = g_{ij}\left|\phi^j\right\rangle .$$

With this definition of the metric tensor its components can be obtained as

$$g_{ij} = \langle\phi_i \left|\phi_j\right\rangle = S_{ij} \quad \text{and} \quad g^{ij} = \left\langle\phi^i \left|\phi^j\right\rangle = \left(S^{-1}\right)_{ij},$$

where the overlap matrix $S_{ij} = \langle\phi_i \left|\phi_j\right\rangle$ has been introduced to show the connection to quantum chemistry. As $S = S^T$ (where S^T shall be the transposed overlap matrix), the metric tensor is symmetric, which will be used below. For the metric tensor the relations

$$g^{ij}g_{jk} = g_{ij}g^{jk} = \delta^i_k$$

hold. For any tensor $\hat{T}$ of order two there exist four different representations, namely a covariant representation

$$\hat{T} = \left|\phi^i\right\rangle T_{ij}\left\langle\phi^j\right|,$$

two mixed representations

$$\hat{T} = \left|\phi^i\right\rangle T_i^{\ j}\left\langle\phi_j\right|$$

$$\hat{T} = \left|\phi_i\right\rangle T^i_{\ j}\left\langle\phi^j\right|,$$

and a contravariant representation

$$\hat{T} = \left|\phi_i\right\rangle T^{ij}\left\langle\phi_j\right| .$$

In all these expressions the Einstein convention of summation over repeated indices has been assumed. The coefficients T_{ij}, $T^i_{\ j}$ ($T_i^{\ j}$), and T^{ij} are the covariant, mixed, and contravariant representation of the tensor $\hat{T}$ in the contravariant, mixed and covariant basis. All the different tensor components are connected by the corresponding metric tensors, e.g.,

$$T_i^{\ j} = T_{il}g^{lj} = g_{ik}T^{kj} = g_{ik}T^k_{\ l}g^{lj}.$$

If one applies this formalism to represent the unity, then one obtains the different representations

$$\hat{1} = |\phi_i\rangle\, \delta^i_j \,\langle\phi^j| = |\phi^i\rangle\, g_{ij}\, \langle\phi^j| = |\phi_i\rangle\, g^{ij}\, \langle\phi_j| \,.$$

We also want to state the transformation of co- and contravariant tensor components in case of a change of the basis [249]. Let us assume that two nonorthogonal basis sets $\{|\phi_i\rangle\}$ and $\{|\overline{\phi}_i\rangle\}$ with their corresponding dual basis sets $\{|\phi^i\rangle\}$ and $\left\{\left|\overline{\phi}^i\right\rangle\right\}$ and metric tensors $g_{ij} = \langle\phi_i\,|\phi_j\rangle = S_{ij}$ and $\overline{g}_{ij} = \langle\overline{\phi}_i\,|\overline{\phi}_j\rangle = \overline{S}_{ij}$ are given. The transformation between the two basis sets shall be given by $|\overline{\phi}_i\rangle = \underline{a}^j_i\,|\phi_j\rangle$ and $|\phi_i\rangle = \overline{a}^j_i\,|\overline{\phi}_j\rangle$, where the bar is at the height of the index belonging to the basis $\{|\overline{\phi}_i\rangle\}$. It can then be shown that the following relations hold

$$\begin{aligned} |\phi_i\rangle = \overline{a}^j_i\,|\overline{\phi}_j\rangle\,,\ |\overline{\phi}_i\rangle = \underline{a}^j_i\,|\phi_j\rangle \quad &\text{with} \quad \underline{a}^k_i\overline{a}^j_k = \delta^j_i \\ |\phi^j\rangle = \underline{a}^j_i\left|\overline{\phi}^i\right\rangle,\ \left|\overline{\phi}^j\right\rangle = \overline{a}^j_i\,|\phi^i\rangle \quad &\text{with} \quad \overline{a}^k_i\underline{a}^j_k = \delta^j_i . \end{aligned} \tag{B.2}$$

From the requirement of the invariance of the tensor $\hat{T}$ with respect to the change of basis it follows that

$$\begin{aligned} \overline{T}^{mn} = \overline{a}^m_k T^{kl}\overline{a}^n_l \quad &\text{and} \quad T^{mn} = \underline{a}^m_k\overline{T}^{kl}\underline{a}^n_l \\ \overline{T}_{mn} = \underline{a}^k_m T_{kl}\underline{a}^l_n \quad &\text{and} \quad T_{mn} = \overline{a}^k_m\overline{T}_{kl}\overline{a}^l_n . \end{aligned} \tag{B.3}$$

If the basis set $\{|\overline{\phi}_i\rangle\}$ is orthogonal ($\langle\overline{\phi}_i\,|\overline{\phi}_j\rangle = \delta^j_i$), then covariant, mixed, and contravariant indices in this basis set do not need to be distinguished.[1] This is why one commonly avoids nonorthogonal basis sets and uses orthogonal ones instead, which considerably simplifies the notation. Note that the generalization of these formulations in the complex domain necessitates the introduction of an additional "property of the indices" [251]. In such a case proper and improper indices may exist. This additional complication arises from the anticommutativity of the scalar product in a complex Hilbert space.

B.2 Second quantization

Starting from the basis set $\{|\phi_i\rangle\}$, spanning the single-particle Hilbert space $\mathcal{H}_1$ and the corresponding dual basis $\{|\phi^i\rangle\}$, one may construct a basis and dual basis of the complete Fock space $\mathcal{F}$ of a physical system. Here we will focus solely on fermionic systems. In Ref. [251] also bosonic systems are studied.

Quoting from Ref. [251], the set $\{|D^i_N\rangle\}$ of all possible tensorial products of N one-particle basis vectors, conveniently antisymmetrized, constitutes a complete basis of the

---

[1] From the definition of the dual basis Eq. (B.1) it follows that the dual basis is identical to the original basis $\{|\overline{\phi}_i\rangle\}$ with $\overline{g}_{ij} = \langle\overline{\phi}_i\,|\overline{\phi}_j\rangle = \delta^j_i$. Hence no distinction between co- and contravariant indices needs to be made.

Hilbert space $\mathcal{H}_N$ of N fermions. The Fock space $\mathcal{F}$ may then be constructed as the direct sum of all N-particle Hilbert spaces

$$\mathcal{F} = \oplus_{N\geq 0}\mathcal{H}_N,$$

where $\mathcal{H}_0$ is the one-dimensional space generated by the vacuum vector $|0\rangle$. If $|0\rangle$ is chosen as the direct and dual basis of $\mathcal{H}_0$ then, the union

$$\cup_{N\geq 0}\left\{\left|D_N^i\right\rangle\right\}$$

will be a basis of $\mathcal{F}$, nonorthogonal for vectors with the same number of particles and orthogonal for the others.

The creation and annihilation operators in the Fock space $\mathcal{F}$ can be defined by their action on the basis vectors. In standard occupation-number notation these definitions can be written as

$$\begin{aligned} \hat{c}_i \left|n_i\right\rangle &= (-1)^{\sum_i}(1-n_i)\left|n_i+1\right\rangle \\ \hat{c}^i \left|n_i\right\rangle &= (-1)^{\sum_i} n_i \left|n_i-1\right\rangle, \end{aligned}$$

where $\sum_i$ stands for the number of occupied one-particle states with indices smaller than i. The creation and annihilation operators obey the following anticommutation relations

$$\left\{\hat{c}_i, \hat{c}_j\right\} = \left\{\hat{c}^i, \hat{c}^j\right\} = 0 \tag{B.4}$$

$$\left\{\hat{c}^i, \hat{c}_j\right\} = \delta^i_j. \tag{B.5}$$

As opposed to orthogonal basis sets $\hat{c}_i$ and $\hat{c}^i$ are not Hermitian conjugates of one another. Instead the Hermitian conjugation of the creation (annihilation) operator in the covariant basis results in the annihilation (creation) operator in the dual basis, i. e.,

$$\begin{aligned} \left(\hat{c}_i\right)^+ \left|n^i\right\rangle &= (-1)^{\sum_i} n_i \left|n^i-1\right\rangle \\ \left(\hat{c}^i\right)^+ \left|n^i\right\rangle &= (-1)^{\sum_i}(1-n_i)\left|n^i+1\right\rangle. \end{aligned}$$

It can be shown [251] that

$$\hat{c}_i = g_{ji}\left(\hat{c}^j\right)^+$$

and

$$\hat{c}^i = g^{ij}\left(\hat{c}_j\right)^+.$$

Clearly, different choices of creation and annihilation operators make different formulations of the second quantization possible. The choice of $\hat{c}^i$ and $\hat{c}_i$ as creation and annihilation operators has the advantage of the simple commutation rules of Eqs. (B.4) and (B.5). However, the hermiticity relation between the creation and annihilation operators does not hold then. Another choice, which will be adopted below is a description with $(\hat{c}^i)^+$ and $\hat{c}^i$. This has the advantage that the hermiticity relation holds, but now the commutation relation will look more complicated, as will be detailed below. The presented formalism renders any transformation between the different formulations of the second quantization formally trivial. These transformations require the simple use of the appropriate metric tensors.

We will now focus on one-particle operators. Most often we will use the representation, in which the matrix elements are in covariant form and $\hat{T}$ reads

$$\hat{T} = T_{ij} \left(\hat{c}^i\right)^+ \hat{c}^i. \tag{B.6}$$

For reasons of brevity we define

$$\hat{d}_i = \hat{c}^i \quad \text{and} \quad \hat{d}_i^+ = \left(\hat{c}^i\right)^+. \tag{B.7}$$

This provides the possibility to write $\hat{T} = T_{ij}\hat{d}_i^+\hat{d}_i$, which looks more familiar to the usual notation of a single-particle operator in second quantized form than Eq. (B.6). The anti-commutation relations are now

$$\begin{aligned} \left\{\hat{d}_i, \hat{d}_j\right\} &= \left\{\hat{d}_i^+, \hat{d}_j^+\right\} = 0 && \text{(B.8)} \\ \left\{\hat{d}_i, \hat{d}_j^+\right\} &= g^{ij} = \left(S^{-1}\right)_{ij}. && \text{(B.9)} \end{aligned}$$

Finally we state the equation of motion for the operator $\hat{d}_i$, which may also be found in Refs. [129, 194]. The corresponding equation for $\hat{d}_i^+$ may be obtained by a hermitian conjugation of the equation for $\hat{d}_i$. Starting from the Heisenberg equation of motion and a single-particle Hamiltonian $\hat{H} = H_{ij} d_i^+ d_j$ one obtains

$$i\hbar \frac{d}{dt}\hat{d}_i = \left[\hat{d}_i, \hat{H}\right] = H^i_{\ k}\hat{d}_k = g^{il} H_{lk}\hat{d}_k$$

or slightly rewritten

$$i\hbar \frac{d}{dt} g_{ij}\hat{d}_j = i\hbar \frac{d}{dt} S_{ij}\hat{d}_j = H_{ij}\hat{d}_j.$$

Analogously one gets for $\hat{d}_i^+$ by Hermitian conjugation

$$-i\hbar \frac{d}{dt}\hat{d}_i^+ S_{ij} = \hat{d}_i^+ H_{ij}.$$

So the time derivatives of $\hat{d}_i$ and $\hat{d}_i^+$ are

$$\begin{aligned} i\hbar \frac{d}{dt}\hat{d}_i &= \left(\sum_j H_{ij} - i\hbar \sum_{j\neq i} S_{ij}\frac{d}{dt}\right)\hat{d}_j && \text{(B.10)} \\ -i\hbar \frac{d}{dt}\hat{d}_i^+ &= \left(\sum_j H_{ij} + i\hbar \sum_{j\neq i} S_{ij}\frac{d}{dt}\right)\hat{d}_i^+ && \text{(B.11)} \end{aligned}$$

We also want to note, as another example, that the particle number operator $\hat{N}$ in this representation is

$$\hat{N} = \hat{c}_i\hat{c}^i = \hat{d}_j^+ S_{ji}\hat{d}_i.$$

B.3 Single-particle Green's functions

In chapter A we have introduced Green's functions as expectation values of field operators $\hat{\psi}(1)$ and $\hat{\psi}^{+}(1)$ that obey the following anticommutation relations $\left\{\hat{\psi}(\vec{x}_1,t_0),\hat{\psi}^{+}(\vec{x}_2,t_0)\right\} = \delta(\vec{x}_1-\vec{x}_2)$ and $\left\{\hat{\psi}(\vec{x}_1,t_0),\hat{\psi}(\vec{x}_2,t_0)\right\} = \left\{\hat{\psi}^{+}(\vec{x}_1,t_0),\hat{\psi}^{+}(\vec{x}_2,t_0)\right\} = 0$ (see Eqs. (A.8)–(A.12), or Eq. (A.47)). These Heisenberg field operators may be expanded in terms of the nonorthogonal basis states as $\hat{\psi}_H(\vec{x},t) = \sum_n \alpha_n(\vec{x},t_0)\hat{d}_n(t)$, where the $\alpha_n(\vec{x},t_0)$ are space-dependent expansion coefficients. This expansion leads to the definition of nonorthogonal Green's functions as expectation values of the $\hat{d}_i(t)$ and $\hat{d}_i^{+}(t)$ such as

$$G^r_{ij} = -i\Theta(t_1-t_2)\left\langle\left\{\hat{d}_i(t_1),\hat{d}_i^{+}(t_2)\right\}\right\rangle .$$

From the equation of motion (see Eq. (A.30))[2] for the retarded, advanced and causal Green's function ($\alpha = r$, a or c) it follows that

$$EG^{\alpha}_{ij}(E) = \left(S^{-1}\right)_{ij} + \left(S^{-1}\right)_{ik} H_{kl}G^{\alpha}_{lj}(E)$$

or rewritten

$$\left(ES-H\right)_{ij} G^{\alpha}_{jk}(E) = \mathbb{1}_{ij}. \tag{B.12}$$

The matrix $G_0^{-1}(E) = (ES-H)$ is thus the inverse operator for the Green's functions $G^{\alpha}(E)$. The components of $G_0^{-1}(E)$ are the covariant matrix elements of S and H. Instead, G^{α}_{ij} should better be written $(G^{\alpha})^{ij}$, because it has been defined as the expectation value of operators $\hat{d}_i$ and $\hat{d}_i^{+}$, which possess contravariant transformation properties (see Eq. (B.7)). A proper notation of Eq. (B.12) in the tensor formalism is thus

$$\left(ES-H\right)_{ij} \left(G^{\alpha}\right)^{jk}(E) = \delta_i^k. \tag{B.13}$$

From Eq. (B.12) the contravariant components of the retarded and advanced Green's functions can be written

$$G^{\overset{r}{a}}(E) = \left[\left(E \pm i\eta\right)S - H\right]^{-1} \tag{B.14}$$

with a small broadening $\eta = 0^{+}$. This demonstrates that the inverse of the covariant components of S and H results in the contravariant components of the retarded or advanced Green's function [250, 252]. Due to the overlap, which appears in the Eq. (B.14) we will also refer to this Green's function as the "nonorthogonal" Green's function $G^{\overset{r}{a}}$.

Another access to the Green's functions is the Schrödinger equation

$$i\hbar\frac{d}{dt}\left|\psi(t)\right\rangle = \hat{H}\left|\psi(t)\right\rangle$$

(with time-independent $\hat{H}$). The Schrödinger equation can be solved easily, when the energy eigenstates $|\psi_i\rangle$ are known, which fulfill the equation

$$\hat{H}\left|\psi_\mu\right\rangle = \varepsilon_\mu\left|\psi_\mu\right\rangle . \tag{B.15}$$

---

[2] Use Eq. (A.30) with $\hat{\psi}$ replaced by $\hat{d}$ and recall the commutation relations Eq. (B.8)-(B.9).

In this orthogonal basis (where no distinction between co- and contravariant components needs to be made) the equation of motion (see Eq. (A.30))[3] yields the matrix equation

$$(E \pm i\eta - \varepsilon_\mu)\, G^{\substack{r\\a}}_{\mu\nu} = \delta_{\mu\nu}$$

or solved for $G^{\substack{r\\a}}$ this is

$$G^{\substack{r\\a}} = \left[(E \pm i\eta)\,\mathbb{1} - \varepsilon\right]^{-1}$$

where ε is the diagonal matrix of orbital eigenenergies. Other ways of representing $G^{\substack{r\\a}}$ are the operator form

$$G^{\substack{r\\a}}(E) = \sum_\mu \frac{|\psi_\mu\rangle\,\langle\psi_\mu|}{E \pm i\eta - \varepsilon_\mu} \tag{B.16}$$

or in real space

$$G^{\substack{r\\a}}(\vec{x}_1, \vec{x}_2, E) = \sum_\mu \frac{\psi_\mu(\vec{x}_1)\psi_\mu(\vec{x}_2)}{E \pm i\eta - \varepsilon_\mu}. \tag{B.17}$$

Here and in the following, all basis functions are assumed to be real. Notice that Eq. (B.17) is nothing else but the discrete spectral representation given in Eq. (A.34) with spectral density

$$\rho(\vec{x}_1, \vec{x}_2, E) = \sum_\mu \delta(E - \varepsilon_\mu)\psi_\mu(\vec{x}_1)\psi_\mu(\vec{x}_2). \tag{B.18}$$

With the help of the Dirac identity, Eq. (A.37), we get from this last expression the result stated in Eq. (A.36) that $\rho(\vec{x}_1, \vec{x}_2, E) = \mp\mathrm{Im}\left[G^{\substack{r\\a}}(\vec{x}_1, \vec{x}_2, E)\right]/\pi$, where $\rho(\vec{x}_1, \vec{x}_2, E)$ fulfills the integral property given in Eq. (A.32).

Expanding the $|\psi_\mu\rangle$ in terms of the local atomic basis functions $|\phi_i\rangle$ as

$$|\psi_\mu\rangle = \sum_i c_{i\mu}\,|\phi_i\rangle \tag{B.19}$$

the Green's function in operator form becomes

$$G^\alpha(E) = \sum_{ij} |\phi_i\rangle \left(G^\alpha(E)\right)^{ij} \langle\phi_j|\,,$$

which is

$$G^\alpha(\vec{x}_1, \vec{x}_2, E) = \sum_{ij} \left(G^\alpha(E)\right)^{ij} \phi_i(\vec{x}_1)\phi_j(\vec{x}_2).$$

in real space ($\alpha = a$ or r). The contravariant components $\left(G^{\substack{r\\a}}\right)^{ij}$ are

$$\left(G^{\substack{r\\a}}(E)\right)^{ij} = \sum_\mu \frac{c_{i\mu}c_{j\mu}}{(E \pm i\eta) - \varepsilon_\mu} \tag{B.20}$$

---

[3] Use Eq. (A.30) with $\hat{\psi}$ replaced by $\hat{d}$ and replace all metric tensors with unity in the commutation relations Eq. (B.8)–(B.9) ($g^{ij} = g_{ij} = \delta_i^j$), because the basis of energy eigenstates is orthonormal.

Writing the energy eigenvalue problem of Eq. (B.21) in the local basis [81, 127] one obtains

$$\sum_j H_{ij} c_{\mu j} = \varepsilon_\mu \sum_j S_{ij} c_{j\mu} \tag{B.21}$$

with[4]

$$S_{ij} = \langle \phi_i \left| \phi_j \right\rangle = \int d^3x \phi_i\left(\vec{x}\right) \phi_j\left(\vec{x}\right) \tag{B.22}$$

and

$$H_{ij} = \langle \phi_i \right| \hat{H} \left| \phi_j \right\rangle = \int d^3x \phi_i\left(\vec{x}\right) H(\vec{x}) \phi_j\left(\vec{x}\right). \tag{B.23}$$

Exploiting the orthogonality relation between energy eigenstates

$$\delta_{\mu\nu} = \langle \psi_\mu \left| \psi_\nu \right\rangle = \sum_{ij} c_{i\mu} S_{ij} c_{j\nu} = \left(CSC^T\right)_{\mu\nu},$$

Eq. (B.13) for the Green's functions $\left[\left(E \pm i\eta\right) S - H\right]_{ij} \left(G^{\substack{r\\a}}(E)\right)^{jk} = \delta_i^k$ is recovered. This means that Eq. (B.20) is an explicit representation of the retarded and advanced nonorthogonal Green's functions.

In quantum chemistry several ways are known, how to transform nonorthogonal basis functions to orthogonalized ones. The most frequently adopted choice is the Löwdin-orthogonalized set of basis functions. They originate from the set $\{|\phi_i\rangle\}$ with the metric tensor $g_{ij} = S_{ij}$ by going over to the set $\left\{\left|\overline{\phi}_i\right\rangle\right\}$, where [81]

$$\left|\overline{\phi}_i\right\rangle = \sum_j \left(S^{-1/2}\right)_{ij} \left|\phi_j\right\rangle.$$

It is immediately obvious that $\left\langle \overline{\phi}_i \left| \overline{\phi}_i \right\rangle\right. = \delta_{ij}$. The use of $S^{-1/2}$ is also called symmetric orthogonalization, but other transformations leading to an orthogonal basis set are possible [81]. In this basis no distinction between covariant, mixed and contravariant indices needs to be made. With the help of Eqs. (B.2)–(B.3) it can be seen that the transformation $\underline{a}_i^j$ between the different coordinate systems is given by

$$\underline{a}_i^j = \left(S^{-1/2}\right)_{ij}.$$

According to the requirement that $\underline{a}_i^k \overline{a}_k^j = \delta_i^j$ and it follows that

$$\overline{a}_j^i = \left(S^{1/2}\right)_{ij}$$

Using that $S = S^T$ or $S^{-1/2} = \left(S^{-1/2}\right)^T$, the (covariant) Hamiltonian $\overline{H}$ in the Löwdin-orthogonal basis sets reads

$$\overline{H} = S^{-1/2} H S^{-1/2},$$

---

[4] As before all basis functions are assumed to be real.

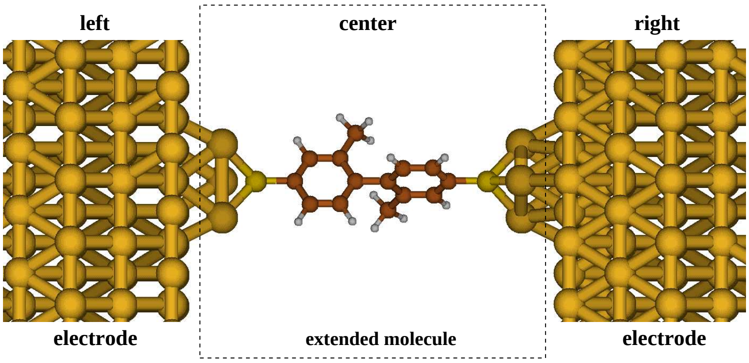

Figure B.1: Molecular electronic device: A molecule is coupled via linking groups to semi-infinite electrodes. The system can be separated into the three parts indicated, namely the left electrode (L), the center (C), also called "extended molecule", and the right electrode (R).

whereas the (contravariant) Green's function is

$$\overline{G}^{\overset{r}{a}}(E) = S^{1/2}G^{\overset{r}{a}}(E)S^{1/2} = \left[(E \pm i\eta)\,\mathbb{1} - \overline{H}\right]^{-1}$$

Thus the difference in the kind of tensorial components of H and G, namely co- and contravariant, naturally explains their different transformational properties (with $S^{-1/2}$ and $S^{1/2}$), when going over from the nonorthogonal basis set to the orthogonal one.

From now on and throughout this work we will mostly use the usual lax notation, in which all matrices appear to be covariant, because indices will be denoted as subscripts and no more as superscripts. However, it simplifies the notation, because one does not need to keep track of indices and can write G^r_{CC} instead of $(G^r)^{CC}$ for example. Generally, it should be kept in mind that for an orthogonal basis, no distinction between the index notations needs to be made. For a nonorthogonal basis, we will usually talk about covariant components of the overlap $S_{ij} = \langle \phi_i \, | \phi_j \rangle$ and the Hamiltonian $H_{ij} = \langle \phi_i | \, \hat{H} \, | \phi_j \rangle$, while Green's functions, defined as the inverse of covariant components $G^{\overset{r}{a}}_{ij}(E) = \left(\left[(E \pm i\eta)\, S - H\right]^{-1}\right)_{ij}$, are contravariant components despite their index appearance. All quantities directly connected to the Green's functions are also contravariant components except if they are multiplied by overlap or better metric tensor contributions. Only in cases of need, we will come back to the proper tensorial formulation. Unfortunately, the lax notation may then lead to some "confusion" in what we mean. But the careful reader should be able to trace back the source for this "confusion" with the help of the relations of this paragraph.

B.3.1 Perturbation theory for single-particle Green's functions

Let us now consider the perturbation theory for a system which is split into three different parts, as we encounter it in the context of molecular electronics (see Fig. B.1). If the center is long enough, there should be no overlap elements in S or H between the left and the right electrode ($S_{LR} = (S_{RL})^T = 0$ and $H_{LR} = (H_{RL})^T = 0$). Thus the (nonorthogonal)

Green's function[5] will obey the matrix equation

$$\begin{pmatrix} E^+S_{LL}-H_{LL} & E^+S_{LC}-H_{LC} & 0 \\ E^+S_{CL}-H_{CL} & E^+S_{CC}-H_{CC} & E^+S_{CR}-H_{CR} \\ 0 & E^+S_{RC}-H_{RC} & E^+S_{RR}-H_{RR} \end{pmatrix} \begin{pmatrix} G^r_{LL} & G^r_{LC} & G^r_{LR} \\ G^r_{CL} & G^r_{CC} & G^r_{CR} \\ G^r_{RL} & G^r_{RC} & G^r_{RR} \end{pmatrix} = \begin{pmatrix} I_{LL} & 0 & 0 \\ 0 & I_{CC} & 0 \\ 0 & 0 & I_{RR} \end{pmatrix} \tag{B.24}$$

Treating the system described by the overlap S and the Hamiltonian H perturbatively, the offdiagonal components $Y_{LC} = (Y_{CL})^T$ and $Y_{CR} = (Y_{RC})^T$ ($Y = S$ or H) may be regarded as the perturbations. The unperturbed Green's functions are

$$\begin{aligned} g^r_{LL} &= \left(E^+S_{LL} - H_{LL}\right)^{-1} \\ g^r_{CC} &= \left(E^+S_{CC} - H_{CC}\right)^{-1} \\ g^r_{RR} &= \left(E^+S_{RR} - H_{RR}\right)^{-1} \end{aligned}$$

As opposed to standard perturbation theory, there is not only a perturbation in the Hamiltonian, but also in the overlap, such that the perturbations are

$$t_{CX}(E) = H_{CX} - ES_{CX} = \left(t_{XC}(E)\right)^T \tag{B.25}$$

(with $X = L$ or R) [250, 252]. (Notice that the limit $\eta \to 0$ has been taken explicitly in t.) In terms of the Keldysh formalism $t_{CX}(E)$ plays the role of the retarded and advanced self-energies (see Sec. A.3.3).

In transport it turns out that the component G^r_{CC} is needed. Solving for it, one obtains

$$G^r_{CC}(E) = \left(E^+S_{CC} - H_{CC} - \Sigma^r_L(E) - \Sigma^r_R(E)\right)^{-1} \tag{B.26}$$

$$\Sigma^r_X(E) = \left(H_{CX} - E^+S_{CX}\right) g^r_{XX} \left(H_{XC} - E^+S_{XC}\right) = t_{CX} g^r_{XX} t_{CX}, \tag{B.27}$$

where $\Sigma^r_X(E)$ is the self-energy belonging to lead X ($X = L$ or R), also called "embedding self-energy" [231], and g^r_{XX} are the unperturbed electrode Green's functions. The electrode self-energies Σ_X describe the influence of the respective electrodes on the central system.

The following interesting observation about the self-energies can now be made, namely for $E \to \infty$ they behave as

$$\Sigma_X(E) \to ES_{CX} \left(S_{XX}\right)^{-1} S_{XC} \quad \text{for} \quad E \to \infty. \tag{B.28}$$

The interpretation of this behavior is that not only the Hamiltonian of the center is renormalized due to the coupling, but also the overlap. This is understandable if one recalls that the perturbations t_{CX} contain not only a perturbation in the Hamiltonian H_{CX}, but also in the overlap S_{CX}.

Concerning the perturbation theory, the solution for G^r_{CC} in Eq. (B.26) is exact. This means that G^r_{CC} contains all perturbative contributons t_{CX} summed to infinite order.

---

[5] Let us concentrate on the retarded Green's function G^r, but results are equally valid for G^a by making the replacement $E^+ = E + i\eta \to E^- = E - i\eta$.

B.3.2 Density of states

In order to interpret the behavior of physical quantities like the conductance, it is interesting to know, where energy eigenstates of a system are located. For example a localized state may give no contribution to the conductance, while a state extending from the left to the right electrode will lead to a substantial feature in the transmission. In this sense the information about the energetics of a system may help to identify the conduction mechanisms, when the transmission is investigated as a function of energy. It is therefore of interest to define quantities from Green's functions such that this information can be obtained. In this respect the spectral density $\rho(\vec{x}_1, \vec{x}_1, E)$ has been seen to be an important quantity, because it contains information on the energy eigenstates of a particular system (see Eqs. (A.33) and (B.18)). For this reason we will investigate the spectral density further in this section.

In Eq. (A.32) the spectral density has been shown to fulfill an integral equation. We will investigate now, how these integral equations are modified when co- and contravariant components of the Green's function are considered. Starting from the operator form in the orthogonal basis of the energy eigenstates (see Eq. (B.16)) one observes for a nonorthogonal basis $|\phi_i\rangle$ with $|\psi_\mu\rangle = \sum_i c_{i\mu} |\phi_i\rangle$ that

$$\begin{aligned} G^{\overset{r}{a}}_{ij}(E) &= \langle\phi_i| G^{\overset{r}{a}}(E) |\phi_j\rangle = \sum_\mu \frac{\langle\phi_i |\psi_\mu\rangle \langle\psi_\mu |\phi_j\rangle}{E \pm i\eta - \varepsilon_\mu} \\ \left(G^{\overset{r}{a}}(E)\right)^{ij} &= \langle\phi^i| G^{\overset{r}{a}}(E) |\phi^j\rangle = \sum_\mu \frac{\langle\phi^i |\psi_\mu\rangle \langle\psi_\mu |\phi^j\rangle}{E \pm i\eta - \varepsilon_\mu} = \sum_\mu \frac{c_{i\mu} c_{j\mu}}{E \pm i\eta - \varepsilon_\mu}. \end{aligned}$$

If we now exploit the Dirac identity (see Eq. (A.37)) we get

$$\mp\mathrm{Im}\left[G^{\overset{r}{a}}_{ij}(E)\right]/\pi = \sum_\mu \langle\phi_i |\psi_\mu\rangle \delta(E - \varepsilon_\mu) \langle\psi_\mu |\phi_j\rangle \tag{B.29}$$

$$\mp\mathrm{Im}\left[\left(G^{\overset{r}{a}}(E)\right)^{ij}\right]/\pi = \sum_\mu \langle\phi^i |\psi_\mu\rangle \delta(E - \varepsilon_\mu) \langle\psi_\mu |\phi^j\rangle \tag{B.30}$$

An integration of the components of the Green's functions over all energies gives

$$\mp\int_{-\infty}^{\infty} \frac{dE}{\pi} \mathrm{Im}\left[G^{\overset{r}{a}}_{ij}(E)\right] = \sum_\mu \langle\phi_i |\psi_\mu\rangle \langle\psi_\mu |\phi_j\rangle = g_{ij} = S_{ij} \tag{B.31}$$

$$\mp\int_{-\infty}^{\infty} \frac{dE}{\pi} \mathrm{Im}\left[\left(G^{\overset{r}{a}}(E)\right)^{ij}\right] = \sum_\mu \langle\phi^i |\psi_\mu\rangle \langle\psi_\mu |\phi^j\rangle = g^{ij} = \left(S^{-1}\right)_{ij} \tag{B.32}$$

This shows that the components of the Green's function get an "overlap weight" in a nonorthogonal basis.

For the central quantity in the computation of the transmission G_{CC} (see Eq. (B.26), which is actually a contravariant component, and we better write $G^{CC} = (ES_{CC} - H_{CC})^{-1}$, this weight is $\mp\int_{-\infty}^{\infty}\frac{dE}{\pi}\mathrm{Im}\left[G^{CC}(E)\right] = \left(S^{-1}\right)_{CC}$. Using the structure of the overlap, where $S_{LR} = \left(S_{RL}\right)^{T} = 0$, it can be shown that

$$\left(S^{-1}\right)_{CC} = \left(S_{CC} + \sum_{X=L,R} S_{CX}\left(S_{XX}\right)^{-1}S_{XC}\right)^{-1} \tag{B.33}$$

in a similar manner to the solution for G^{CC} in Eq. (B.24) (see Eq. (B.26)).

This overlap weight is also obvious by looking at G^{CC} (see Eq. (B.26)) in the limit $E\to\infty$ and recalling the asymptotic behavior of Σ_X (see Eq. (B.28)), which leads to

$$G^{CC} \to \left(E\left(S_{CC} + \sum_{X=L,R} S_{CX}\left(S_{XX}\right)^{-1}S_{XC}\right)\right)^{-1} \quad \text{for} \quad E\to\infty.$$

This result shows that the energy dependent self-energy Σ_X has an influence on the overlap structure. The usual interpretation in the orthogonal case, where in $\Sigma_X(E) = \mathrm{Re}\left[\Sigma_X(E)\right] + i\mathrm{Im}\left[\Sigma_X(E)\right]$ the real part of the self-energy ($\mathrm{Re}\left[\Sigma_X(E)\right]$) describes the shift of the energies of the Hamiltonian and the imaginary part ($\mathrm{Im}\left[\Sigma_X(E)\right]$) provides a broadening in the energy domain, is therefore more complicated in a nonorthogonal basis. The renormalization of the overlap is due to the perturbation t_{CX} (see Eq. (B.25)) that contains an overlap contribution in addition to the energy-independent perturbation of the Hamiltonian.

We want to note now some properties for the imaginary part of the contravariant component of the Green's function, visible in Eq. (B.30).[6] One observes that the diagonal components are positive

$$\mp\mathrm{Im}\left[\left(G^{\substack{r\\a}}(E)\right)^{ii}\right] \geq 0 \tag{B.34}$$

and $\mp\mathrm{Im}\left[\left(G^{\substack{r\\a}}(E)\right)^{ij}\right]$ is positive definite. This is obvious by multiplying from both sides with an arbitrary vector with components v_i. It is immediately obvious that this can only yield positive numbers

$$\begin{aligned}\mp\sum_{i,j} v_i\mathrm{Im}\left[\left(G^{\substack{r\\a}}(E)\right)^{ij}\right]v_j &= \sum_{i,j,\mu} v_i\left\langle\phi^i\left|\psi_\mu\right.\right\rangle\delta(E-\varepsilon_\mu)\left\langle\psi_\mu\left|\phi^j\right.\right\rangle v_j \\ &= \sum_{\mu}\delta(E-\varepsilon_\mu)\left|\sum_i\left\langle\psi_\mu\left|\phi^i\right.\right\rangle v_i\right|^2 \\ &\geq 0.\end{aligned} \tag{B.35}$$

In order to get information on the energetic states of a system, we analyse the local density of states (LDOS). For this purpose we plot

$$\mathrm{LDOS}_{i\alpha}(E) = \mp\frac{1}{\pi}\left(S_{CC}^{1/2}\mathrm{Im}\left[\left(G^{\substack{r\\a}}(E)\right)^{CC}\right]S_{CC}^{1/2}\right)_{i\alpha,i\alpha} \tag{B.36}$$

---

[6] Similar results hold for the covariant component (see Eq. (B.29)), but we will not need them in this work.

as a function of energy. The indices $i\alpha$ have replaced the index i from before ($i \rightarrow i\alpha$), where i shall now indicate some atom at position i and α is the orbital or basis function at that particular atom. As $\mathrm{Im}\left[\left(G^{\substack{r\\a}}(E)\right)^{CC}\right]$ is positive definite, also this $\mathrm{LDOS}_{i\alpha}(E)$ is positive definite. The positive definiteness of $\mathrm{LDOS}_{i\alpha}(E)$ is also a reason, why we choose the symmetric Löwdin like orthogonalization of Eq. (B.36) instead of the equally possible Mulliken analysis, where $\widetilde{\mathrm{LDOS}}_{i\alpha}(E) = \mp\left(\mathrm{Im}\left[\left(G^{\substack{r\\a}}(E)\right)^{CC}\right] S_{CC}/\pi\right)_{i\alpha,i\alpha}$. In terms of the overlap weight, the property $\int_{-\infty}^{\infty} dE \mathrm{LDOS}_{i\alpha}(E) = 1$ is only approximately fulfilled. This is due to the fact, that we multiply with $S_{CC}^{1/2}$ instead of $\left((S^{-1})_{CC}^{-1}\right)^{1/2} = \left(S_{CC} + \sum_{X=L,R} S_{CX}\left(S_{XX}\right)^{-1} S_{XC}\right)^{1/2}$. This means that the self-energy contributions to the overlap are neglected. However, one is usually interested in the LDOS of atoms in the center of a system and not at the surface. As $\sum_{X=L,R} S_{CX}\left(S_{XX}\right)^{-1} S_{XC}$ constitutes a surface correction, its neglect may be justified for atoms in the center of the contact. In terms of charges Eq. (B.36) may be seen as an approximation to the Löwdin charge of the atom i from basis function α

$$\int_{-\infty}^{E_F} dE \mathrm{LDOS}_{i\alpha}(E) = \left(S_{CC}^{1/2} \varrho^{CC} S_{CC}^{1/2}\right)_{i\alpha,i\alpha},$$

where again charges from outside the central system are neglected. (For a proof that the electron density is connected with $\mathrm{Im}\left[\left(G^{\substack{r\\a}}(E)\right)^{CC}\right]$ via $\mp\int_{-\infty}^{E_F} dE \mathrm{Im}\left[\left(G^{\substack{r\\a}}(E)\right)^{CC}\right] = \varrho^{CC}$ see Eq. (B.48) in the next section.)

The summation of $\mathrm{LDOS}_{i\alpha}(E)$ over all basis functions α is the LDOS of the atom i

$$\mathrm{LDOS}_{i}(E) = \sum_{\alpha} \mathrm{LDOS}_{i\alpha}(E) = \mp\frac{1}{\pi}\mathrm{Tr}_{\alpha}\left[S_{CC}^{1/2}\mathrm{Im}\left[\left(G^{\substack{r\\a}}(E)\right)^{CC}\right] S_{CC}^{1/2}\right]. \tag{B.37}$$

By summing over a particular set of atoms Λ, we get the LDOS of the region Λ as

$$\mathrm{LDOS}_{\Lambda}(E) = \sum_{i\in\Lambda} \mathrm{LDOS}_{i}(E). \tag{B.38}$$

B.3.3 Electron density

In order to obtain a locally charge neutral Hamiltonian of a system or in order to do self-consistent calculations of a cluster embedded into a semiinfinite system, it is necessary, to compute the density matrix of the system under investigation (see Secs. 2.2.2, E.2 or Refs. [127, 152]). As it has been noted before (see Eq. (A.23)), the electron density $\varrho(\vec{r},t)$ is directly connected to the lesser Green's function via the relation $\varrho(\vec{x},t) = -iG^{<}(\vec{x},t;\vec{x},t)$. For the time-independent case this means that

$$\varrho(\vec{x}) = \int \frac{dE}{2\pi i} G^{<}(\vec{x},\vec{x},E).$$

The Keldysh formalism provides a means to compute $G^<(\vec{x},t,\vec{x},t)$ (see Eq. (A.52)). It has been noticed in Sec. A.3.3 that for our single-particle perturbations the lesser and greater self-energies $\Sigma^<$ and $\Sigma^>$ vanish. From Eq. (A.86) we therefore find

$$G^< = (1 + G^r\Sigma^r)\, g^< \,(1 + \Sigma^a G^a) \tag{B.39}$$

One is usually only interested in the electron density of the central part of the system. By expanding both ϱ and $G^<$ in a local basis set

$$\varrho(\vec{x}) = \sum_{ij} \varrho_{ij}\phi_i(\vec{x})\phi_j(\vec{x}) = \sum_{ij} \int \frac{dE}{2\pi i} G^<_{ij}(E)\phi_i(\vec{x})\phi_j(\vec{x}) = \int \frac{dE}{2\pi i} G^<(\vec{x},\vec{x},E),$$

we obtain the following matrix formulation between the (contravariant) components of ϱ and $G^<$

$$\varrho_{ij} = \int \frac{dE}{2\pi i} G^<_{ij}(E)$$

Focussing on ϱ_{CC} we need to obtain an expression for $G^<_{CC}$ from Eq. (B.39) and want to derive the final result that

$$G^<_{CC} = iG^r_{CC}\left(\Gamma_L f_L + \Gamma_R f_R\right) G^a_{CC}, \tag{B.40}$$

where we have suppressed the energy dependence of all the arguments in this expression and

$$f_X = f(E-\mu_X) = \left(e^{\beta(E-\mu_X)}+1\right)^{-1} \tag{B.41}$$

is the Fermi function in the lead X ($X = L$, R) measured with respect to the electrochemical potential μ_X. In addition, Γ_X is the scattering matrix defined as

$$\begin{aligned} \Gamma_X &= (H_{CX} - ES_{CX})\, i\left(g^r_{XX} - g^a_{XX}\right)(H_{XC} - ES_{XC}) = i\left(\Sigma^r_X - \Sigma^a_X\right) \\ &= -2\mathrm{Im}\left[\Sigma^r\right] = 2\pi t_{CX}\rho_{XX}t_{XC} \end{aligned} \tag{B.42}$$

with the spectral function ρ defined as in Eq. (A.31).

The derivation of Eq. (B.40) will now be presented. Starting from Eq. (B.39) we note that

$$G^<_{CC} = \sum_{W=L,C,R} (1 + G^r\Sigma^r)_{CW}\, g^<_{WW}\, (1 + \Sigma^a G^a)_{WC} \tag{B.43}$$

The term with $W = C$ may be rephrased by noting that $(1 + G^r\Sigma^r)_{CC} = G^r_{CC}\left(g^r_{CC}\right)^{-1}$ and similarly $(1 + \Sigma^a G^a)_{CC} = \left(g^a_{CC}\right)^{-1} G^a_{CC}$ from Eqs. (A.71) and (A.72). As $g^<_{CC}$ is the unperturbed lesser Green's function of the center, it is an equilibrium Green's function and Eq. (A.39) in combination with Eq. (A.31) can be applied in the form $g^<_{CC} = -f_C\left(g^r_{CC} - g^a_{CC}\right)$, where f_C is the Fermi or better occupation function of the unperturbed center. Taken together this gives

$$\begin{aligned}
(1+G^r\Sigma^r)_{CC}\, g^<_{CC}\, (1+\Sigma^a G^a)_{CC} &= (1+G^r\Sigma^r)_{CC}\, g^<_{CC}\, (1+\Sigma^a G^a)_{CC} \\
&= -f_C G^r_{CC} \left(g^r_{CC}\right)^{-1} \left(g^r_{CC}-g^a_{CC}\right) \left(g^a_{CC}\right)^{-1} G^a_{CC} \\
&= -f_C G^r_{CC} \left[\left(g^a_{CC}\right)^{-1} - \left(g^r_{CC}\right)^{-1}\right] G^a_{CC} \\
&= -f_C G^r_{CC} \left[(E-i\eta)\, S_{CC} - H_{CC}\right. \\
&\quad \left. -\left\{(E+i\eta)\, S_{CC} - H_{CC}\right\}\right] G^a_{CC} \\
&= 2i\eta f_C G^r_{CC} S_{CC} G^a_{CC} \\
&= 0 \quad \text{for} \quad \eta \to 0
\end{aligned}$$

Now the rest terms with $W = L$ or R in Eq. (B.43) need to be considered. For the self-energies $\Sigma^a = \Sigma^r$ we note that (see Sec. A.3.3) they have only components connecting C and X ($X = L$ or R), namely[7]

$$\Sigma^a_{CX} = \Sigma^r_{CX} = t_{CX} = \left(\Sigma^a_{XC}\right)^T = \left(\Sigma^r_{XC}\right)^T . \tag{B.44}$$

Therefore the relations $(1+G^r\Sigma^r)_{CX} = G^r_{CC} t_{CX}$ and $(1+\Sigma^a G^a)_{XC} = t_{XC} G^a_{CC}$ hold, and for $g^<_{XX}$ we can again exploit Eq. (A.39) to obtain

$$\begin{aligned}
G^<_{CC} &= \sum_{X=L,R} (1+G^r\Sigma^r)_{CX}\, g^<_{XX}\, (1+\Sigma^a G^a)_{XC} \\
&= i \sum_{X=L,R} f_x G^r_{CC} t_{CX} 2\pi \rho_{XX} t_{XC} G^a_{CC} \\
&= i \sum_{X=L,R} f_x G^r_{CC} \Gamma_X G^a_{CC},
\end{aligned}$$

which is identical to Eq. (B.40).

For reasons of completeness we state here also the result for $G^>_{CC}$. The derivation is the same as for $G^<_{CC}$, but one uses Eq. (A.40) instead of Eq. (A.39) to express the unperturbed $g^>_{WW}$ components ($W = L$, C or R). The final result is

$$G^>_{CC} = iG^r_{CC} \left[\Gamma_L (f_L - 1) + \Gamma_R (f_R - 1)\right] G^a_{CC} \tag{B.45}$$

Putting together Eqs. (B.40), (B.45), and (A.31) we get

$$2\pi\rho_{CC} = G^r_{CC} \left(\Gamma_L + \Gamma_R\right) G^a_{CC} \tag{B.46}$$

This result may also be derived more directly by noting that

$$\begin{aligned}
\Gamma = \Gamma_L + \Gamma_R &= \sum_{X=L,R} i \left(\Sigma^r_X - \Sigma^a_X\right) \\
&= i \left[\left(g^r_{CC}\right)^{-1} - \left(G^r_{CC}\right)^{-1} - \left\{\left(g^a_{CC}\right)^{-1} - \left(G^a_{CC}\right)^{-1}\right\}\right] \\
&= i \left[\left(G^a_{CC}\right)^{-1} - \left(G^r_{CC}\right)^{-1}\right]
\end{aligned}$$

---

[7] Note that the self-energies Σ_X defined in Eq. (B.27) should not be confused with the self-energy Σ_{CX} defined here. The Σ_{CX} are self-energies of the Keldysh formalism, whereas Σ_X is a conveniently defined self-energy expression relevant for the central cluster. As the number of subscripts differ for both of them, no confusion should arise.

Multiplying both sides with G^a_{CC} and G^r_{CC} and using Eq. (A.31) we come to the result of Eq. (B.46).

Eq. (B.40) is valid for the general nonequilibrium situation, when $\mu_L \neq \mu_R$ and f_L and f_R differ. Therefore it can be used to obtain the density matrix for a system subject to some external bias.

$$\varrho_{ij} = \int \frac{dE}{2\pi i} G^<_{ij}(E) = \int \frac{dE}{2\pi} G^r_{CC}(E) \left[\Gamma_L(E) f_L(E) + \Gamma_R(E) f_R(E)\right] G^a_{CC}(E)$$

However, when $\mu_L = \mu_R$ further simplifications are possible

$$G^<_{CC} = i f G^r_{CC} \left(\Gamma_L + \Gamma_R\right) G^a_{CC} = i f 2\pi \rho_{CC} = -2 i f \mathrm{Im}\left[G^r_{CC}\right],$$

where we denoted with $f = f_L = f_R$ the common Fermi function of the contacts. For the density matrix, the simplification implies that

$$\varrho_{ij} = \int \frac{dE}{2\pi i} G^<_{ij}(E) = \int dE f(E-\mu) \frac{-\mathrm{Im}\left[G^r_{ij}(E)\right]}{\pi}. \tag{B.47}$$

For zero temperature the Fermi function vanishes for energies above the Fermi energy E_F, which coincides with the electrochemical potential μ, ($f(E) = 0$ for $E > \mu = E_F$) and we get

$$\varrho_{ij} = \int_{-\infty}^{E_F} dE \frac{-\mathrm{Im}\left[G^r_{ij}(E)\right]}{\pi}. \tag{B.48}$$

This formula will be employed, when we want to obtain the ground state density as needed for the construction of a charge neutral Hamiltonian in our tight-binding (TB) model or a self-consistent determination of the ground state electron density in density functional theory (DFT) for an embedded system. In our TB models, we set E_F equal to the Fermi energy of the contacts. Opposed to this in DFT we determine E_F by a charge neutrality condition of the central system, namely $N_C = \mathrm{Tr}\left[(\varrho S)_{CC}\right] = \mathrm{Tr}\left[\varrho_{CC} S_{CC} + \varrho_{CL} S_{LC} + \varrho_{CR} S_{RC}\right]$. In this expression N_C is the charge of the central system, which is analyzed in terms of a Mulliken poplation analysis [81]. These issues will be discussed further in the separate subsections.

With the help of Eq. (B.20) we generalize $G^{\overset{r}{a}}(E)$ to be a function in the complex domain by writing

$$G^{\overset{r}{a}}_{ij}(z) = \sum_\mu \frac{c_{i\mu} c_{j\mu}}{z - (\varepsilon_\mu \mp i\eta)}, \tag{B.49}$$

which fulfills the equation

$$\sum_k \left[\left(z \pm i\eta\right) S - H\right]_{ik} G^{\overset{r}{a}}_{kj}(z) = \delta_{ij}.$$

In chemistry the electron density is often presented in the form

$$\varrho(\vec{x}) = \sum_{\mu \in \{\text{occ. MOS}\}} |\psi_\mu(\vec{x})|^2 = \sum_{i,j} \varrho_{ij} \phi_i(\vec{x}) \phi_j(\vec{x}),$$

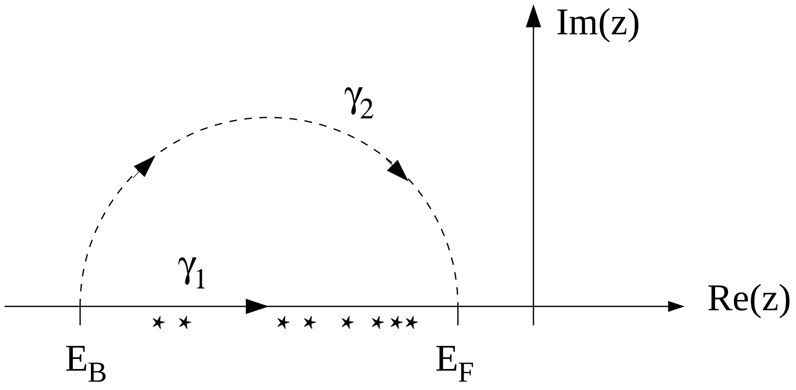

Figure B.2: Different possible integration contours γ_1 and γ_2 for obtaining the density matrix according to Eq. (B.48). While γ_1 runs along the real axis from E_B to E_F, γ_2 is a semicircle in the upper half of the complex plane with the same start and end points as γ_1. As G^r possesses only singularities below the real axis, indicated by the stars $\ast$, the joint path $\gamma_1 \cup -\gamma_2$ encloses no poles. For this reason $\varrho_{ij} = -\int_{\gamma_1} dz \mathrm{Im}\left[G^r_{ij}(z)\right]/\pi = -\int_{\gamma_2} dz \mathrm{Im}\left[G^r_{ij}(z)\right]/\pi$. (With $-\gamma_2$ we mean that we are running through the path γ_2 in the opposite direction as compared to the direction indicated in the figure.) In any practical integration E_B is chosen to be somewhat below the lowest lying energy states of the physical system considered.

where

$$\varrho_{ij} = \sum_{\mu \in \{\text{occ. MOS}\}} c_{i\mu} c_{j\mu}.$$

With $\mu \in \{\text{occ. MOS}\}$ we mean that μ is an occupied molecular orbital or, phrased differently, a state with an energy below the Fermi energy ($\varepsilon_\mu \leq E_F$). This is another access to Eq. (B.48), because with the Dirac identity (see Eq. (A.37)) one gets $-\mathrm{Im}\left[G^r_{ij}(E)\right]/\pi = \sum_\mu \delta(E-\varepsilon_\mu) c_{i\mu} c_{j\mu}$, so that the integration from $-\infty$ to E_F actually includes the contributions of all occupied states.

If one integrates along a contour in the upper (lower) half plane, where no residues of G^r (G^a) can be found, then it becomes obvious that the integral along the real axis from $-\infty$ to E_F can be replaced by the integral over this conveniently chosen complex contour (see Fig. B.2). This is of practical interest, because in this way the sharp features of the poles of G^r (G^a) can be smoothed out and less integration points are needed [254, 127, 152]. In any practical implementation, the energy integration will start from somewhat below the lowest energy states of the system considered, called E_B (B for bottom).

Appendix C

Landauer formula and current operator

Macroscopic conductors are characterized by Ohm's law, which establishes that the conductance G of a given sample is directly proportional to its transverse area S and inversely proportional to its length L, i.e.

$$G = \sigma S/L,$$

where σ is the conductivity of the sample [1]. In this work we are interested in atomic-sized conductors, which are a limiting case of mesoscopic systems. For such mesoscopic systems quantum coherence plays a central role, and simple concepts such as Ohm's law are now longer applicable.

In mesoscopic systems one can identify different transport regimes according to the relative size of various length scales. We will concentrate here on phase-coherent ballistic transport, which is the full quantum limit. In this transport regime the following inequality holds [1, 255]

$$b_0 \ll L < l \lesssim l_\phi \lesssim l_{in} \quad \text{and} \quad W \sim \lambda_F.$$

In the first inequality b_0 is the Bohr radius, standing for the atomic scale, L is the size of the mesoscopic region, l is the elastic mean free path, l_ϕ is the phase-coherence length, and l_{in} is the energy relaxation length. In the second inequality W is the contact width, and λ_F is the Fermi wavelength. (See Fig. C.1 for a schematic drawing of the system that we have in mind and the different length scales involved.)

We consider electron transport at low temperatures. Therefore electrons with energies at the Fermi level E_F with a particle length scale λ_F are involved. The phase coherence length l_ϕ is the length scale over which quantum coherence is preserved. For quantum effects to be observable it needs to be longer than our sample size L. The elastic mean free path measures the distance between elastic collisions with static impurities. If the elastic mean free path is longer than our sample size we reach the ballistic regime, in which the electron momentum can be assumed to be constant and changes only due to scattering at the boundaries of the sample. If no additional interactions are present (such as electron-vibration coupling), the energy relaxation length l_{in} shall also be bigger than L, so that

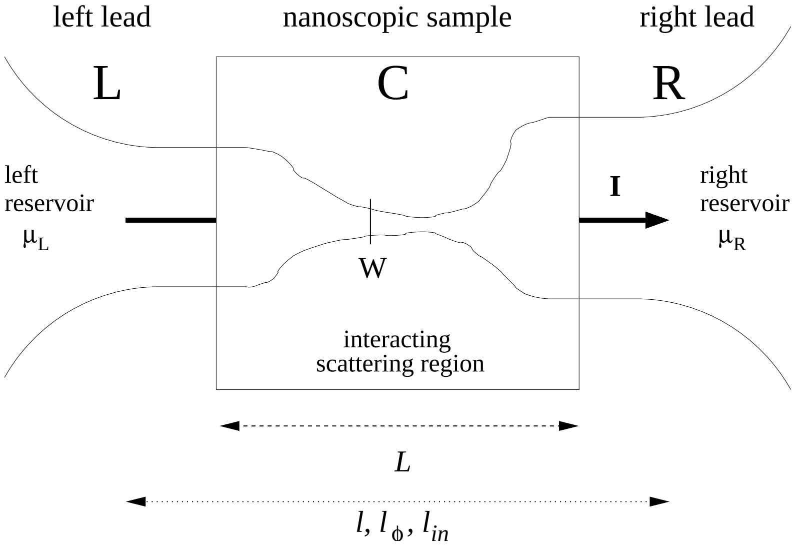

Figure C.1: Schematic diagram of the experimental configuration for which the Landauer formula for the current is derived. Two leads, characterized by chemical potentials μ_L and μ_R, are connected to a mesoscopic scattering region. If $\mu_L > \mu_R$ a current I will flow from left to right as indicated in the figure. In addition different relevant length scales are indicated. L is the sample length, l the mean free path, l_ϕ the phase-coherence length, l_{in} the energy relaxation length, and W is the width of the contact.

the transport is elastic. This means that electrons preserve their energy in the scattering events. Of course, the sample should be large on the atomic scale, characterized by the Bohr radius of around $b_0 = 0.529$ Å. If, in addition, the transverse dimension or width of the sample at the narrowest point is on the order of the Fermi wavelength, we are in the full quantum limit, which cannot simply be described by semiclassical arguments. This is the situation we are concerned with.

In Sec. C.1 of this chapter we will derive the two-terminal Landauer formula for the current through an interacting mesoscopic region [256]. This result will be of interest in Chap. 3, where inelastic corrections to the current due to electron-vibration coupling are studied. However, we will not discuss this general formula in this chapter. Instead it will serve as an intermediate step, by which we obtain the result for the two-terminal Landauer formula for the noninteracting case. We consider here the complications arising from a nonorthogonal local basis. In this sense additional complications arise as compared to the paper by Meir *et al.* [256], where the Landauer formula has been derived by means of the Keldysh nonequilibrium Green's function formalism for an orthogonal local basis. That the complications are nontrivial is manifested in the appearance of a recent paper, where the presentation of Meir *et al.* [256] has been generalized to a nonorthogonal basis by Thygesen [253]. We will shortly comment on the different procedure chosen by Thygesen as compared to ours in the end of this section.

In Sec. C.2 we will comment on general properties of the elastic current operator. The

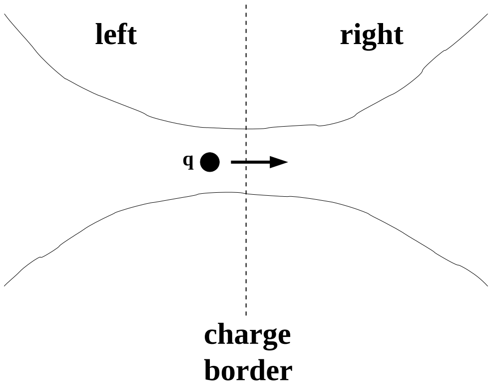

Figure C.2: In order to compute a current I, it is necessary to count charges. This requires an unambiguous attribution of charges to a certain region. As indicated in the figure a charge q is crossing the "charge border" by making a transition from the left to the right.

discussion will cover topics such as the current conservation, the conservation of transmission eigenchannels T_n, which will be shown to uniquely characterize an atomic contact for a certain energy of incident electrons, as well as the boundedness of the T_n between 0 and 1.

C.1 Two-terminal Landauer formula for the current in nanocontacts

In this paragraph we derive the Landauer formula for the current through an interacting mesoscopic region. We consider here the complications arising from a nonorthogonal local basis. The current through a system requires a clear separation of device regions, so that charges can be attributed to one of these regions. Only this allows a counting of electrons as it is necessary for a definition of the current I. In Fig. C.2 a charge q crosses the "charge border" between the left and the right region, and the current I can be determined. The attribution of charge to a certain subsystem is, however, ambiguous in a nonorthogonal basis, where different ways of assigning charges to certain regions exist [81], e.g. the Mulliken or Löwdin population analysis. In this sense additional complications arise as compared to the paper by Meir *et al.* [256], where the Landauer formula has been derived in the Keldysh Green's function formalism for an orthogonal basis set.

The presentation given below derives the current through an interacting region, as presented in Refs. [256, 253]. However, we will immediately concentrate on the noninteracting case. We mainly follow Viljas *et al.* [129], but also refer to the more detailed derivation for the current formula in the noninteracting case in Ref. [194].

The system that we have in mind is drawn schematically in Fig. C.1. A central scattering region, called C, is connected to left and right leads, called L and R respectively, which consitute noninteracting reservoirs at electrochemical potentials μ_L and μ_R. We choose a

Mulliken charge partitioning scheme [81] and get for the total charge Q and the subcharges Q_W ($W = L$, C and R)

$$Q = \sum_{W=L,C,R} Q_W = \sum_{W=L,C,R} \mathrm{Tr}_W \left[\varrho S\right] \tag{C.1}$$

where $\mathrm{Tr}_W \left[\varrho S\right] = \sum_{i\in W,j} \varrho_{ij} S_{ji}$. We want to compute the current at the interface from the left electrode (L) into the center combined with the right electrode ($C+R$). The particle currents of the L and $C+R$ parts are

$$\frac{d}{dt}\hat{Q}_L(t) = \hat{J}_L(t) \quad \text{and} \quad \frac{d}{dt}\hat{Q}_{C+R}(t) = \hat{J}_{C+R}(t).$$

In these expressions the charge operators

$$\hat{Q}_W = \sum_{i\in W,j} \hat{d}_i^+ S_{ij} \hat{d}_j$$

and the particle current operators

$$\hat{J}_W = -\hat{I}_W / q_e$$

have been introduced ($W = L$ or $C+R$). The operator $\hat{I}_W$ is the charge current operator due to charges leaving or entering the region W. The particle currents J_W are then given as the expectation values of the particle current operators $J_W = \left\langle \hat{J}_W \right\rangle$ and analogously for the charges $Q_W = \left\langle \hat{Q}_W \right\rangle$. As $\frac{d}{dt}\left(\sum_{W=L,C,R} \hat{Q}_W\right) = 0$, $\hat{J}_{C+R}(t) = -\hat{J}_L(t)$. Exploiting this, we get for the total charge current operator $\hat{I}$

$$\hat{I} = \alpha \hat{I}_L(t) + (1-\alpha)\,\hat{I}_{C+R}(t) = -q_e \frac{d}{dt}\left(\alpha \hat{Q}_L(t) - (1-\alpha)\,\hat{Q}_{C+R}(t)\right) \tag{C.2}$$

for an arbitrary α between 0 and 1 ($0 \leq \alpha \leq 1$).[1] This means that in order to get an expression for the current, we need to take time derivatives of the charge. Now, we make the specific choice of $\alpha = 1/2$ and take the time derivatives

$$\begin{aligned}
J = \left\langle \hat{J} \right\rangle &= \frac{d}{dt}\left(\left\langle \hat{Q}_L \right\rangle(t) - \left\langle \hat{Q}_{C+R} \right\rangle(t)\right)/2 \\
&= \frac{d}{dt}\left(\mathrm{Tr}\left[\varrho_{LL} S_{LL}\right] + \mathrm{Tr}\left[\varrho_{L(C+R)} S_{(C+R)L}\right]\right. \\
&\quad \left. -\mathrm{Tr}\left[\varrho_{(C+R)L} S_{L(C+R)}\right] - \mathrm{Tr}\left[\varrho_{(C+R)(C+R)} S_{(C+R)(C+R)}\right]\right)/2 \\
&= \frac{d}{dt}\left(\mathrm{Tr}\left[\varrho_{LL} S_{LL}\right] - \mathrm{Tr}\left[\varrho_{(C+R)(C+R)} S_{(C+R)(C+R)}\right]\right) \\
&= \frac{d}{dt}\left(\left\langle \hat{Q}'_L \right\rangle(t) - \left\langle \hat{Q}'_{C+R} \right\rangle(t)\right)/2.
\end{aligned}$$

---

[1] Here, the electron charge is $q_e = -e$ and $e = 1.60219 \cdot 10^{-19}$ C is the (absolute value) of the elementary charge.

In this expression we have introduced the new operators $\hat{Q}'_W = \sum_{i,j\in W} \hat{d}_i^+ \hat{d}_j S_{ji}$. This was possible by observing that the difference of the nondiagonal components cancel

$$\mathrm{Tr}\left[\varrho_{L(C+R)} S_{(C+R)L}\right] - \mathrm{Tr}\left[\varrho_{(C+R)L} S_{L(C+R)}\right] = 0$$

for a symmetric density matrix ($\varrho = \varrho^T$) because

$$\begin{aligned} \mathrm{Tr}\left[\varrho_{L(C+R)} S_{(C+R)L}\right] &= \mathrm{Tr}\left[S_{L(C+R)} \varrho_{(C+R)L}\right] \\ &= \mathrm{Tr}\left[\varrho_{(C+R)L} S_{L(C+R)}\right] . \end{aligned}$$

All density matrices considered in this work are real and symmetric due to the symmetric overlap S and Hamiltonian H (see Eqs. (B.22), (B.23)) and Eq. (B.48), so that the assumption $\varrho = \varrho^T$ is always fulfilled.

For this reason we look at the symmetric choice $\alpha = 1/2$ in Eq. (C.2) and can obtain the current from

$$\hat{I} = -q_e \frac{d}{dt}\left(\hat{Q}'_L(t) - \hat{Q}'_{C+R}(t)\right)/2 = -q_e \frac{d}{dt}\left(Q'_L\left(t\right)\right). \tag{C.3}$$

With the help of Eqs. (B.10) and (B.11) we get

$$\frac{d}{dt}\left(\hat{d}_j^+ \hat{d}_j\right) = \hat{d}_j^+ \sum_{k\neq j} \frac{1}{i\hbar}\left(H_{jk} - i\hbar S_{jk}\frac{d}{dt}\right)\hat{d}_k + \left(\sum_{k\neq j} \frac{1}{i\hbar}\left(-H_{kj} - i\hbar S_{kj}\frac{d}{dt}\right)\hat{d}_k^+\right)\hat{d}_j$$

and therefore

$$\begin{aligned} \frac{d}{dt}\left(\hat{Q}'_L\right) &= \tfrac{1}{i\hbar} \sum_{j\in L, k\in(C+R)} \left(\hat{d}_j^+ \left(H_{jk} - i\hbar S_{jk}\frac{d}{dt}\right)\hat{d}_k + \left(\left(-H_{kj} - i\hbar S_{kj}\frac{d}{dt}\right)\hat{d}_k^+\right)\hat{d}_j\right) \\ \frac{d}{dt}\left(\hat{Q}'_{(C+R)}\right) &= \tfrac{1}{i\hbar} \sum_{j\in (C+R), k\in L} \left(\hat{d}_j^+ \left(H_{jk} - i\hbar S_{jk}\frac{d}{dt}\right)\hat{d}_k + \left(\left(-H_{kj} - i\hbar S_{kj}\frac{d}{dt}\right)\hat{d}_k^+\right)\hat{d}_j\right) . \end{aligned}$$

Taken together and using that $i\left\langle \hat{d}_j(t_2)\hat{d}_k^+(t_1)\right\rangle = G_{kj}^<(t_{1,}, t_2)$ (see Eq. (A.52)) Eq. (C.3) gives

$$\begin{aligned} 2J(t) = 2\left\langle \hat{J}\right\rangle(t) &= \sum_{j\in L, k\in(C+R)} \frac{1}{i\hbar}\left(H_{jk} - i\hbar S_{jk}\frac{d}{dt}\right)\left\langle \hat{d}_j^+(t')\hat{d}_k(t)\right\rangle\Bigg|_{t'=t} \\ &\quad - \sum_{j\in(C+R), k\in L} \frac{1}{i\hbar}\left(H_{jk} - i\hbar S_{jk}\frac{d}{dt}\right)\left\langle \hat{d}_j^+(t')\hat{d}_k(t)\right\rangle\Bigg|_{t'=t} + \text{c.c.} \\ &= 2\frac{1}{\hbar}\mathrm{Re}\left[\left(\sum_{j\in L, k\in(C+R)} - \sum_{j\in(C+R), k\in L}\right)\left(H_{jk} - i\hbar S_{jk}\frac{d}{dt}\right) G_{kj}^<(t,t')\right] . \end{aligned}$$

Finally the expression for the current becomes[2] [129]

$$I(t) = \frac{2e}{\hbar}\,\mathrm{Tr}\left[\left(H_{LC} - i\hbar S_{LC}\frac{d}{dt}\right) G^<_{CL}(t,t') - \left(H_{CL} - i\hbar S_{CL}\frac{d}{dt}\right) G^<_{LC}(t,t')\right]\Bigg|_{t'=t}.$$

As we look at time independent Hamiltonians, all Green's functions depend only on the time difference (see Eq. (A.27)). In particular we are interested in the stationary current. A Fourier transformation of

$$G^<_{ij}(t,t') = G^<_{ij}(t-t') = \int_{-\infty}^{\infty} \frac{dE}{2\pi} e^{-iE(t-t')/\hbar} G^<_{ij}(E)$$

yields

$$I = \frac{2e}{h}\int dE\,\mathrm{Tr}\left[t_{LC}(E)G^<_{CL}(E) - t_{CL}(E)G^<_{LC}(E)\right] \tag{C.4}$$

with $t_{CX}(E)$ defined as in Eq. (B.25).

We will now rewrite the term in the trace of Eq. (C.4), which can be accomplished with the relations given in paragraph A.3.2 on Keldysh Green's functions. From Eq. (A.84) we get

$$\begin{aligned} G^<_{LC} &= g^<_{LL} t_{LC} G^a_{CC} + g^r_{LL} t_{LC} G^<_{CC} \\ G^<_{CL} &= G^<_{CC} t_{CL} g^a_{LL} + G^r_{CC} t_{CL} g^<_{LL}. \end{aligned}$$

Put into Eq. (C.4) the current becomes

$$\begin{aligned} I &= \frac{2e}{h}\int dE\,\mathrm{Tr}\left[t_{CL}\left(g^a_{LL} - g^r_{LL}\right) t_{LC} G^<_{CC} + t_{CL} g^<_{LL} t_{LC}\left(G^r_{CC} - G^a_{CC}\right)\right] \\ &= \frac{2e}{h}\int dE\,\mathrm{Tr}\left[i\Gamma_L G^<_{CC} + f_L \Gamma_L 2\pi\rho_{CC}\right], \end{aligned} \tag{C.5}$$

where the definition of the scattering rate $\Gamma_X = t_{CX} i\left(g^r_{XX} - g^a_{XX}\right) t_{XC}$ (see Eq. (B.42)) has been used together with the definition of the spectral density ρ (see Eq. (A.31)). The expression for I in the last line is the result for the charge current through an interacting region [256, 253]. This general result will find an application in Chap. 3, where the effects of electron-vibration interactions on the current are discussed.

We will now come to the current formula for the noninteracting case. If we use the relation between ρ_{CC} and the scattering rates $2\pi\rho_{CC} = i\left(G^r_{CC} - G^a_{CC}\right) = \left(G^r_{CC}\left(\Gamma_L + \Gamma_R\right) G^a_{CC}\right)$ (see Eqs. (A.31) and (B.46)) and the expression for $G^<_{CC} = iG^r_{CC}\left(\Gamma_L f_L + \Gamma_R f_R\right) G^a_{CC}$ from Eq. (B.40) in Eq. (C.5), we finally get

$$I = \frac{2e}{h}\int dE\,\mathrm{Tr}\left[-\Gamma_L G^r_{CC}\left(\Gamma_L f_L + \Gamma_R f_R\right) G^a_{CC} + f_L \Gamma_L G^r_{CC}\left(\Gamma_L + \Gamma_R\right) G^a_{CC}\right].$$

---

[2] Note that the additional factor of 2 arises from the summation over the degenerate spins.

This gives the final expression for the stationary elastic current

$$\begin{aligned} I &= \frac{2e}{h}\int dE T(E)\left(f(E-\mu_L)-f(E-\mu_R)\right) \qquad \text{(C.6)} \\ &= \frac{2e}{h}\int dE \mathrm{Tr}\left[\Gamma_L G^r_{CC}\Gamma_R G^a_{CC}\right](f_L-f_R) = \frac{2e}{h}\int dE \mathrm{Tr}\left[t^+t\right](f_L-f_R) \end{aligned}$$

where we have defined the transmission

$$T(E) = \mathrm{Tr}\left[\Gamma_L G^r_{CC}\Gamma_R G^a_{CC}\right] = \mathrm{Tr}\left[t^+t\right] \qquad \text{(C.7)}$$

and have introduced the transmission matrix[3]

$$t(E) = \sqrt{\Gamma_L}G^a_{CC}\sqrt{\Gamma_R}. \qquad \text{(C.8)}$$

In equilibrium the electrochemical potentials of the left and right electrode are equal ($\mu = \mu_L = \mu_R$) and Eq. (C.6) predicts a zero current. In case of a small deviation from this equilibrium state, the linear response regime, the current is proportional to the applied bias. Assuming that the electrochemical potentials satisfy $eV = \Delta\mu = \mu_L - \mu_R$, we obtain the conductance [257]

$$G = \left.\frac{dI}{dV}\right|_{V=0} = \frac{2e^2}{h}\int dE\,(-\partial_E f)\,T(E). \qquad \text{(C.9)}$$

For low temperatures $T \approx 0$, the Fermi function becomes a step function (see Eq. (A.14))

$$f(E-\mu) = \Theta(\mu - E)$$

and

$$-\partial_E f \approx \delta(E-\mu) = \delta(E-E_F).$$

Then Eq. (C.6) gives the low-bias, zero-temperature conductance

$$G = \frac{2e^2}{h}T(E_F) = G_0\mathrm{Tr}\left[t^+t\right] = G_0\sum_n T_n(E_F) \qquad \text{(C.10)}$$

with the quantum of conductance $G_0 = 2e^2/h$. In Eq. (C.10) we have introduced the transmission T_n of the transmission eigenchannel n. The T_n are the eigenvalues of the matrix t^+t of Eq. (C.7) and are energy dependent.

That the derivation of the current formula is not trivial is demonstrated by the appearance of a recent paper, where the results of Meir *et al.* [256] for the electron transport through an interacting region have been reformulated for nonorthogonal basis states $\{|\phi_i\rangle\}$ by Thygesen [253]. Thygesen arrives at exactly the same expression for the current as we do (see Eqs. (C.5) and (C.6)). He uses in his derivation the dual basis set in the center of the system $\{|\phi^i\rangle\}$. Due to the definition of the dual basis $\langle\phi_i\,|\phi^j\rangle = \delta_i^j$ (see Eq. (B.1))

---

[3] The positive definiteness of Γ_X, necessary for taking the square root of Γ_X, will be proven in Sec. C.2.

he gets rid of all overlap contributions in the perturbation between the leads and the center. However, the construction of the dual basis for the center requires the knowledge of the overlap structure of the complete system. This becomes clear when considering that $|\phi^i\rangle = g^{ij}\,|\phi_j\rangle = (S^{-1})_{ij}\,|\phi_j\rangle$. Previously we have seen that $(S^{-1})_{CC}$ contains contribution of the overlap from the left and right electrode (see Eq. (B.33)). The basis set $\{|\phi^i\rangle\}$ used by Thygesen will therefore be highly nonlocal. Our derivation on the other hand is entirely based on the covariant basis set $\{|\phi_i\rangle\}$, which is consistently used in the left electrode, the center, and the right electrode. Also in our case the question arises, how the current operator would look like if we had for example not made the symmetric choice $\alpha = 1/2$ in Eq. (C.2). However, we find our derivation more practical, in the sense that the construction of the dual basis set in terms of basis functions is in reality very complicated, because for strong overlap contributions the dual basis of the central system will involve strong contributions of basis functions of the electrodes.

C.2 General properties of the elastic current operator

In this paragraph we will prove some general properties of the elastic current operator. These will be the current conservation, meaning that the current is independent of the charge border (see Fig. C.2), the conservation of the eigenvalues T_n of the current for a fixed energy, and the boundedness of these eigenvalues T_n between 0 and 1.

Differing from the definition of the current operator in the local basis given above (see Eq. (C.2)), we will now use the continuity equation for its definition. The continuity equation relates the electron density operator $\hat{\varrho}$ (see Eq. (A.22)) and the current density operator $\hat{\vec{j}}$ (see Eq. (A.24))

$$-\frac{d}{dt}\hat{\varrho}(\vec{x},t) = \nabla\hat{\vec{j}}(\vec{x},t). \tag{C.11}$$

We can define the current operator $\hat{I}$ as the integral over a charge border surface Ω (see Fig. C.2)

$$\hat{I} = -q_e \int_{\Omega} d\vec{S}\hat{\vec{j}}(\vec{x},t). \tag{C.12}$$

From this definition of the current operator, $\hat{I}$ might appear to be a local operator. Its expectation value $I = \left\langle \hat{I} \right\rangle$ should depend on the surface Ω, over which the current density $\hat{\vec{j}}$ is integrated. Due to the continuity equation in the stationary case (see Eq. (C.11)), however, the divergence of the current density vanishes ($\nabla\hat{\vec{j}} = 0$) and the current operator $\hat{I}$ becomes independent of the surface Ω that divides the nanocontact into a left and a right region. This is nothing else but the conservation of the total current I due to the continuity equation.

We will now go on to demonstrate that not only the total current is conserved, but also the transmission at every single energy. If we define the transport direction to be the z

axis and choose surfaces Ω perpendicular to the z axis, we can parameterize the planes by their z value ($\Omega = \Omega(z)$). In second quantization the current operator reads

$$\begin{aligned} \hat{I}(z) = -q_e \hat{J}(z) &= -q_e \sum_{\lambda,\lambda'} J_{\lambda\lambda'}(z) c_\lambda^+ c_{\lambda'} \\ J_{\lambda\lambda'}(z) &= \int_{\Omega(z)} dxdy \psi_\lambda^*(x,y,z) \hat{\vec{j}}(x,y,z,t) \psi_{\lambda'}(x,y,z) \end{aligned}$$

for some appropriately chosen states $|\psi_\lambda\rangle$ with quantum numbers λ.

We are interested in elastic currents. For this reason we choose the states $|\psi_\lambda\rangle$ to be energy eigenstates. For such energy eigenstates the elastic current operator is diagonal with respect to energy ($J_{\lambda\lambda'}(z) = J_{\lambda\lambda'}(z)\delta_{E_\lambda,E_{\lambda'}}$). We will shown now that $J_{\lambda\lambda'}(z)$ does not depend on z [255]. This conclusion follows from the continuity equation

$$\begin{aligned} \langle\psi_\lambda| \frac{d}{dz}\hat{J} |\psi_{\lambda'}\rangle &= \langle\psi_\lambda| \frac{d}{dt}\hat{Q} |\psi_{\lambda'}\rangle = -\frac{i}{\hbar} \langle\psi_\lambda| \left[\hat{Q},\hat{H}\right] |\psi_{\lambda'}\rangle \\ &= -\frac{i}{\hbar}\left(E_\lambda - E_{\lambda'}\right) \langle\psi_\lambda| \hat{Q} |\psi_{\lambda'}\rangle = 0. \end{aligned} \tag{C.13}$$

This expression vanishes, because $E_\lambda = E_{\lambda'}$. This implies that $J_{\lambda\lambda'}(z) = J_{\lambda\lambda'}$ is indeed a constant. Therefore a more specific representation of the charge transfer operator $\hat{J}$ is

$$\hat{J}(z) = \sum_{\lambda,\lambda'} \delta_{E_\lambda,E_{\lambda'}} J_{\lambda\lambda'} c_\lambda^+ c_{\lambda'},$$

where the elements $J_{\lambda\lambda'}$ do not depend on z. If we diagonalize $\hat{J}$ at a fixed energy E, we get

$$\hat{J}(z,E) = \sum_\nu \delta_{E,E_\nu} J_\nu c_\nu^+ c_\nu.$$

The interpretation of this equation is that the elastic current $I = -q_e \left\langle \hat{J} \right\rangle$ possesses eigenvalues $-q_e J_\nu$, which characterize it completely at a fixed energy. To every nonzero transmission eigenvalue T_n at energy E there exists a corresponding $J_n = \frac{2}{h} T_n$, where the energy E_ν of the states $|\psi_\nu\rangle$ that diagonalize $\hat{J}$ is equal to the energy E ($E_\nu = E$). This means that eigenstates of the current operator at energy E have a constant spectrum, because the J_ν are independent of z. The transmission eigenvalues may be probed in any cut $\Omega(z)$. In particular the transmission eigenvalues at E_F are real observables in the sense that they are eigenstates of an operator, namely the elastic current operator, and they can be measured by means of the subgap I-V characteristics of the nanocontacts [19]. A certain contact is fully characterized by the energy dependent set of transmission eigenvalues $T_n(E)$.

Next, we want to proof that the spectrum of t^+t is bounded between 0 and 1. It is not difficult to see that every eigenvalue of t^+t is positive ($T_n \geq 0$ for $T_n \in \operatorname{spec}\{t^+t\}$). The reason is that t^+t is positive definite ($\vec{a}^+t^+t\vec{a} = |t\vec{a}|^2 \geq 0$), and therefore also all eigenvalues need to be positive. In order to express the transmission $T(E)$ in terms of t^+t with $t(E) = \sqrt{\Gamma_L} G^a_{CC} \sqrt{\Gamma_R}$ (see Eqs. (C.7) and (C.8)) the square root of scattering rate matrix Γ_X needs to exist. From Eq. (B.42) we note that $\Gamma_X = 2\pi t_{CX} \rho_{XX} t_{XC} = -2 t_{CX} \mathrm{Im}\left[g^r_{XX}\right] t_{XC}$ is real and symmetric. For this reason it is possible to diagonalize Γ_X by means of an orthogonal transformation. Recalling that by g^r_{XX} we actually mean the contravariant component $(g^r)^{XX}$, we can apply the proof for Eq. (B.35), which says in our lax index notation that $-\mathrm{Im}\left[g^r_{XX}\right]$ is positive definite. For this reason also Γ_X is positive definite ($\vec{a}^+ \Gamma_X \vec{a} = \left(\vec{a}^+ t_{CX} \sqrt{2}\right) \left(-\mathrm{Im}\left[g^r_{XX}\right]\right) \left(\sqrt{2} t_{XC} \vec{a}\right) = \vec{b}^+ \left(-\mathrm{Im}\left[g^r_{XX}\right]\right) \vec{b} \geq 0$ with $\vec{b} = \sqrt{2} t_{XC} \vec{a}$) and all its eigenvalues are positive. To summarize, the positive definiteness of the real and symmetric scattering matrices guarantees that we can write the transmission in terms of the transmission matrix t as t^+t. The spectrum T_n of t^+t is therefore positive and all eigenvalues T_n are real due to the hermiticity of t^+t.

Next we will give a direct proof that for all n the transmission eigenvalues T_n are less than one ($T_n \leq 1$). We write down Eq. (B.46) in the form

$$0 = -2\pi \rho_{CC} + G^r_{CC} \Gamma_L G^a_{CC} + G^r_{CC} \Gamma_R G^a_{CC}$$

Now, we multiply from the left and the right with $\sqrt{\Gamma_L}$ and add the unity on both sides

$$\begin{aligned} \mathbb{1}_{CC} &= \mathbb{1}_{CC} - \sqrt{\Gamma_L} 2\pi \rho_{CC} \sqrt{\Gamma_L} + \sqrt{\Gamma_L} G^r_{CC} \Gamma_L G^a_{CC} \sqrt{\Gamma_L} + \sqrt{\Gamma_L} G^r_{CC} \Gamma_R G^a_{CC} \sqrt{\Gamma_L} \\ &= \mathbb{1}_{CC} - \sqrt{\Gamma_L} i \left(G^r_{CC} - G^a_{CC}\right) \sqrt{\Gamma_L} + \sqrt{\Gamma_L} G^r_{CC} \Gamma_L G^a_{CC} \sqrt{\Gamma_L} + t^+t, \end{aligned}$$

where the definitions of ρ and t have been used (see Eqs. (A.31) and (C.8)). This can be brought into the final form

$$\mathbb{1}_{CC} = r^+r + t^+t \tag{C.14}$$

with the reflection matrix

$$r = \mathbb{1}_{CC} + i \sqrt{\Gamma_L} G^a_{CC} \sqrt{\Gamma_L} \tag{C.15}$$

As proven before, the square root of Γ_L exists. For any vector $\vec{a}$ we get the inequality $|\vec{a}|^2 = |r\vec{a}|^2 + |t\vec{a}|^2 \geq |t\vec{a}|^2$ so that the eigenvalues T_n of t^+t need to be bounded by one. As an "add on" of this proof, we obtain an explicit form for the reflection matrix r.

It should be noted that both the transmission matrix t and the reflection matrix r can be transformed with arbitrary unitary transformations

$$\tilde{t} = U_1 t U_2 \quad \text{and} \quad \tilde{r} = U_1 r U_2 \tag{C.16}$$

which still leaves Eq. (C.14) unchanged, because

$$\mathbb{1}_{CC} = U_1^+ U_1 = U_1^+ r^+ U_2^+ U_2 r U_1 + U_1^+ t^+ U_2^+ U_2 t U_1 = \tilde{r}^+ \tilde{r} + \tilde{t}^+ \tilde{t}.$$

As a consequence there exist many different transmission and reflection matrices t and r, which are all connected by transformations of Eq. (C.16) and their particular form is not unique.

Appendix D

Electrode Green's functions

In this chapter the details on the construction of the electrode Green's functions g_{XX} will be given as they appear in the self-energies

$$\Sigma_X(E) = (H_{CX} - ES_{CX})\, g_{XX}\, (H_{XC} - ES_{XC})$$

and as they are needed for the construction of the Green's function of the central system G_{CC} (see Eqs. (B.26) and (B.27)). There are two kinds of Green's functions that we have used within this work for the construction of the electrode Green's functions, namely bulk and surface Green's functions. In the theoretical analysis of stretching curves of metallic nanowires and conductance histograms in Sec. 2 (as published in Refs. [35, 36]) we used bulk electrode Green's functions, although we repeated part of the analysis with surface electrode Green's functions (see Sec. 2.10). In the ab-initio study of the conductance based on density functional theory (DFT) we obtained all our results by use of surface electrode Green's functions (see Secs. 5 and 6), and bulk electrode Green's functions have only been used for illustrative purposes (see the discussion in Sec. 5.1.5).

In the context of conductance calculations surface electrode Green's functions should be preferred to bulk electrode Green's functions. The reason is that the electrodes are semi-infinite systems, instead of infinite ones assumed in the construction of bulk Green's functions. The knowledge about the construction of bulk Green's functions may, however, be very useful. For example the density of states (DOS) of a crystal can be extracted from the bulk Green's function. In this way we can learn something about the electronic structure of a certain material. Additional information may be gained from the DOS by resolving its different orbital contributions or determining the crystal's Fermi energy from it (see, e.g., Fig. E.3).

In this chapter we will first present the construction of bulk Green's functions in Sec. D.1. In this context we will also discuss how to obtain the bulk DOS (see Sec. D.1.1). Finally we will present the more complicated computation of surface Green's functions in Sec. D.2.

D.1 Construction of bulk Green's functions

In this paragraph, we want to compute the bulk Green's function of a crystal. In order to accomplish this task we assume the crystal's atoms to be arranged in a regular array, the Bravais lattice. A Bravais lattice consists of all points with position vectors $\vec{R}_n$ of the form

$$\vec{R}_n = n_1\vec{a}_1 + n_2\vec{a}_2 + n_3\vec{a}_3,$$

where $\vec{a}_1$, $\vec{a}_2$, and $\vec{a}_3$ are any three vectors not all in the same plane, and n_1, n_2, and n_3 range through all integral values ($n_i \in \mathbb{Z}$). Thus the point $\vec{R}_n = \sum_i n_i\vec{a}_i$ is reached by moving n_i steps of length a_i into the direction of $\vec{a}_i$ for i = 1, 2, and 3 [184]. Here, the subscript n at $\vec{R}_n$ shall indicate the index tuple $n = (n_1, n_2, n_3)$. The vectors $\vec{a}_i$ are called primitive vectors and are said to span the direct lattice $\left\{\vec{R}_n\right\}$.

We want to emphasize right from the start that the description of a crystal as an array of atoms arranged in a perfect Bravais is an idealization. A perfect crystal consists of an infinite number of atoms while any real system is made up of a finite number of atoms and possesses surfaces. Furthermore real solids are never absolutely pure, there is a certain temperature-dependent probability of finding missing or misplaced atoms, and atoms continually undergo thermal vibrations about their equilibrium positions. All these effects destroy the perfect translational symmetry present in a crystal described as a Bravais lattice. A practical approach, however, is to assume a perfectly translationally invariant crystal (implying a perfectly periodic effective one-electron potential $U(\vec{r})$) and treating all the imperfections mentioned above as small perturbations [184, 258].

In order to model a perfectly translationally invariant system with a finite number of atoms one employs periodic boundary conditions (PBCs), also called "Born-von-Kármán" boundary conditions. It is convenient to work in a lattice commensurate with a primitive cell of the underlying Bravais lattice. All physically relevant functions $f(\vec{r})$ of the crystal (such as electronic wave functions $\psi(\vec{r})$ or the effective one-electron potential $U(\vec{r})$) need to fulfill the generalized PBCs

$$f(\vec{r}) = f(\vec{r} + N_i\vec{a}_i) \quad i = 1, 2, 3, \tag{D.1}$$

where the $\vec{a}_i$ are the three primitive vectors of the Bravais lattice and the N_i are integers of order $N^{1/3}$, where $N = N_1N_2N_3$ is the total number of primitive cells in the crystal. We concentrate now on functions $f_n = f(\vec{R}_n)$ defined at the lattice positions $\vec{R}_n$. For such functions and their Fourier transforms the following relations hold if PBCs are assumed

$$f(\vec{k}) = \sum_n f(\vec{R}_n)e^{-i\vec{k}\cdot\vec{R}_n} \tag{D.2}$$

$$f(\vec{R}_n) = \frac{1}{N}\sum_n f(\vec{k})e^{i\vec{k}\cdot\vec{R}_n}. \tag{D.3}$$

From Eq. (D.1) it follows that

$$N_i\vec{k}\cdot\vec{a}_i = 2\pi q_i N_i = 2\pi l_i, \tag{D.4}$$

where l_i is an integer ($l_i \in \mathbb{Z}$) and where we have set

$$\vec{k} = \sum_{i=1}^{3} k_i \vec{b}_i. \tag{D.5}$$

The vectors

$$\vec{b}_i = \pi \sum_{jk} \varepsilon_{ijk} \frac{\vec{a}_j \times \vec{a}_k}{\vec{a}_1 \cdot (\vec{a}_2 \times \vec{a}_3)}$$

($i = 1$, 2, and 3) are the primitive vectors of the reciprocal lattice spanned by the $\vec{a}_i$ with the totally antisymmetric tensor

$$\varepsilon_{ijk} = \begin{cases} 1 & (i,j,k) = (1,2,3) \text{ and cyclic} \\ -1 & (i,j,k) = (1,3,2) \text{ and cyclic} \\ 0 & \text{else} \end{cases}.$$

The vectors $\vec{b}_i$ are defined by the relation

$$\vec{a}_i \cdot \vec{b}_j = 2\pi\delta_{ij}. \tag{D.6}$$

Notice that, except for a factor 2π, the reciprocal lattice vectors $\vec{b}_i$ are the contravariant basis set with respect to the covariant basis spanned by the vectors $\vec{a}_i$ (see Eq. (B.1)). From Eq. (D.4) it follows that

$$k_i = \frac{l_i}{N_i}. \tag{D.7}$$

It is sufficient to limit $\vec{k}$ to the first Brillouin zone (or the primitive cell of the reciprocal lattice), because the addition of a reciprocal lattice vector $\vec{G}_m = \sum_i m_i \vec{b}_i$ to $\vec{k}$ will not alter anything in Eqs. (D.2) and (D.3) ($\exp(-i\vec{G} \cdot \vec{R}_n) = 1$). This means that the indices l_i can be restricted to the set

$$l_i \in M;\ M = \left\{ -\frac{N_i}{2}, \ldots, \frac{N_i}{2} - 1 \right\}. \tag{D.8}$$

Also other choices for each index l_i are possible such as $l_i \in M'$; $M' = \{1, \ldots, N_i\}$ [258]. Set M can be transformed into the set M' by adding the reciprocal vector $\vec{b}_i$ to one half of the indices of M, namely to $l_i \in \{-N_i/2, \ldots, 0\}$. Altogether this means that there are N different discrete vectors $\vec{k}$, which are specified by the index tuple $l = (l_1, l_2, l_3)$ and we will write from now on $\vec{k}_l$ in the same way as we did for $\vec{R}_n$. In our implementations we choose the index set M (see Eq. (D.8)) as will be explained later.

For $\vec{k}_l$ and $\vec{k}_m$ in the first Brillouin zone the following relations hold

$$\frac{1}{N} \sum_n e^{i\left(\vec{k}_l - \vec{k}_m\right) \cdot \vec{R}_n} = \delta_{\vec{k}_l, \vec{k}_m} \tag{D.9}$$

$$\frac{1}{N} \sum_l e^{i\vec{k}_l \cdot \left(\vec{R}_m - \vec{R}_n\right)} = \delta_{\vec{R}_m, \vec{R}_n}. \tag{D.10}$$

They can be proven easily by writing $\vec{R}_n = \sum_i n_i \vec{a}_i$ and $\vec{k}_l = \sum_i \frac{l_i}{N_i}\vec{b}_i$. If we exploit Eq. (D.6) and the identities $e^{2\pi i l} = 1$ and $\sum_{n=1}^{N} a^n = a\left(1-a^N\right)/(1-a)$ we get

$$\frac{1}{N}\sum_p e^{i\left(\vec{k}_m-\vec{k}_n\right)\cdot\vec{R}_p} = \prod_{i=1}^{3}\frac{1}{N_i}\sum_{p_i=1}^{N_i} e^{2\pi i(m_i-n_i)p_i/N_i} = \begin{cases} 1 & \text{if } m_i = n_i \text{ for all } i \\ 0 & \text{if } m_i \neq n_i \text{ for one } i \end{cases} .$$

Instead of the index set M' we used the equivalent set M. This proves Eq. (D.9) and Eq. (D.10) can be obtained in the same way.

Let us now assume that a set of parameters $Y_{0\alpha,j\beta}$ is available to us, where Y can either be the overlap S or the Hamiltonian H, 0 and j stand for the index of the Bravais lattice cell at point $\vec{R}_0 = \vec{0}$ and $\vec{R}_j = \sum_i j_i \vec{a}_i$, and α and β are the orbitals or basis functions for atoms in the Bravais lattice cell at position 0 and j, respectively. Such a set of parameters describes a translationally invariant system completely, because for such a system only the relative distance matters. Therefore every element $Y_{m\alpha,n\beta}$ can be brought into the form $Y_{0\alpha,j\beta}$ with $j = n - m$, because

$$Y_{0\alpha,j\beta} = Y_{0\alpha,(n-m)\beta} = Y_{m\alpha,n\beta} \quad \text{for } j = n - m. \tag{D.11}$$

If we construct the Green's function for a translationally invariant system, the Green's function G needs to be translationally invariant as well. This can be seen from the basic definition of G (see Eq. (B.13)), namely

$$\delta_{i,r} = \sum_q \left[(E+i\eta)S - H\right]_{0,q} G^r_{q+i,r} = \sum_q \left[(E+i\eta)S - H\right]_{0,q} G^r_{q+i+l,r+l} = \delta_{i+l,r+l}. \tag{D.12}$$

From this relation it can be seen that G^r only depends on the difference in its index arguments, because $G^r_{q+i,r}$ and $G^r_{q+i+l,r+l}$ obey the same equations.

According to Eq. (D.12) a Fourier transformation of the overlap $S_{0,j}$ and the Hamiltonian $H_{0,j}$ to k-space will allow the determination of the Green's function by an inversion for every $\vec{k}$ point separately. A Fourier back transformation to direct space finally yields the bulk Green's function. In formulas this recipe will be given now.

We assume that a set of parameters $Y_{0,j}$ (with $Y = S$ or H) is given to us. These matrix elements will be centered around the origin $\vec{R}_0 = \vec{0}$ and will decay with the distance $\left|\vec{R}_j\right|$. For this reason we choose a lattice $\vec{R}_n = n_1\vec{a}_1 + n_2\vec{a}_2 + n_3\vec{a}_3$, where the indices n_i run symmetrically around the origin ($n_i \in M = \{-N_i/2, \ldots, N_i/2-1\}$) and the N_i are chosen large enough. (The conditions that need to be fulfilled by the N_i will be addressed further below.) Then we Fourier transform[1] the elements $Y_{0,j}$ (see Eq. (D.2))

$$Y_{k,\alpha,\beta} = \left(Y(\vec{k}_k)\right)_{\alpha,\beta} = \sum_j \left(Y(0,\vec{R}_j)\right)_{\alpha,\beta} e^{-i\vec{k}_k\cdot\vec{R}_j} = \sum_j Y_{0\alpha,j\beta} e^{-i\vec{k}_k\cdot\vec{R}_j} \tag{D.13}$$

---

[1] All discrete Fourier transformations of this work have been carried out with the numerical routines of the fftw-package 3.0, dated April 2003. This package is available at http://www.fftw.org. For historical reasons in our implementation we first perform a backward transformation (keyword: FFTW_BACKWARD) to go to k-space and then a forward transformation (keyword: FFTW_FORWARD) to go back to direct space. This corresponds to a different sign convention of the exponents in the Fourier transformation in Eqs. (D.2) and (D.3).

or in a more compact form, when we suppress orbital indices

$$Y_k = Y(\vec{k}_k) = \sum_j Y(0, \vec{R}_j) e^{-i\vec{k}_k \cdot \vec{R}_j} = \sum_j Y_{0,j} e^{-i\vec{k}_k \cdot \vec{R}_j}. \tag{D.14}$$

The bulk Green's function in k-space is diagonal and can be determined via

$$\left[(E + i\eta) S_k - H_k\right] G^r_k(E) = \mathbb{1} \quad \text{or} \quad G^r_k(E) = \left[(E + i\eta) S_k - H_k\right]^{-1}. \tag{D.15}$$

A Fourier back transformation of G^r_k to direct space yields the bulk Green's function

$$G^r_{0,j}(E) = \sum_k G_k(E) e^{i\vec{k}_k \cdot \vec{R}_j} \tag{D.16}$$

from which, via the translational symmetry (see Eq. (D.11)), any other matrix element $G^r_{m,n}(E)$ can be obtained.

Now to the conditions that the N_i need to fulfill. The periodic boundary conditions imply a finite period in direct space. Explicitly this means that $Y_{0,j} = Y(\vec{0}, \vec{R}_j) = Y(\vec{0}, \vec{R}_j + \vec{R}_J) = Y_{0,j+J}$ where $J = (J_1, J_2, J_3) = (m_1N_1, m_2N_2, m_3N_3)$ (with $m_i \in \mathbb{Z}$). This periodicity is not wanted, because the matrix elements $Y_{0,j}$ should decay for increasing $\left|\vec{R}_j\right|$, whereas now for instance $Y_{0,0} = Y_{0,J}$. In order to avoid unphysical results, the period of the lattice in each direction needs to be chosen large enough for the system under consideration. The first condition is of course, that (i) the parallelepiped $\vec{R}_n = n_1\vec{a}_1 + n_2\vec{a}_2 + n_3\vec{a}_3$ with $n_i \in M$ centered around $\vec{R}_0 = \vec{0}$ should at least be big enough, so that all the elements $Y_{0,j}$ can be taken into account in the Fourier transformation Eq. (D.14) (see Fig. D.1 for a sketch of this situation in two dimensions). The second condition is that (ii) no matrix element $G^r_{m,n} = G^r_{0,j}$ with $j = n - m$ is needed in the construction of the bulk Green's function g_{XX} with an index $j_i \notin M$. In advance the N_i need to be chosen large enough to meet these two conditions. Of course a convergence of the results with respect to the employed period N_i or in other words the k-point number should be made.

In order to show, how the conditions (i) and (ii) can be taken care of, we write $\vec{R}_j = j_1\vec{a}_1 + j_2\vec{a}_2 + j_3\vec{a}_3 = A\vec{j}$ with $A = (\vec{a}_1, \vec{a}_2, \vec{a}_3)$. Then we can determine the maximum integer index, needed to run over all points in a sphere with radius $\left|\vec{R}\right|$, by noting that $\vec{R}_j^2 = \vec{j}^T A^T A \vec{j} \geq \lambda_{min}(A^TA)\vec{j}^2$ (where $\lambda_{min}(A^TA)$ is the smallest eigenvalue of A^TA) . Therefore an index $N_i/2 = \left\lceil \sqrt{R^2/\lambda_{min}(A^TA)} \right\rceil$ (where $\lceil x \rceil$ means the next integer $n \geq x$) is a sufficient choice for insuring that all lattice atoms $\vec{R}_j$ inside a sphere of radius R are present. If the matrix elements $Y_{0,j}$ vanish for all $\left|\vec{R}_j\right| \geq R$, then this choice of the N_i fulfills condition (i). Concerning condition (ii), the maximum index j_i needed in the construction of g_{XX} can be determined by running over differences of position vectors in the electrode X. The maximum index needed in the construction of the electrode Green's function is then given as $\max(|n_i|)$, where $\vec{n} = A^{-1}\vec{R}_n$ and $\vec{R}_n$ is a difference vector of two electrode atoms. Note that for this reason (and similarly in the construction of the surface Green's functions), all electrode positions need to coincide with positions of the Bravais lattice.

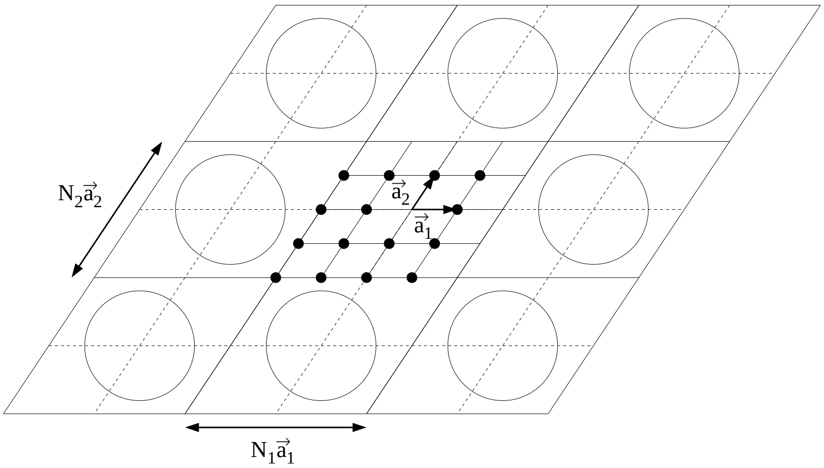

Figure D.1: A finite crystal made up of $N = N_1 \times N_2$ primitive cells with lattice vectors $\vec{a}_1$ and $\vec{a}_2$ is repeated periodically in space. In the middle all points $\vec{R}_n = n_1\vec{a}_1 + n_2\vec{a}_2$ with $n \in M$ (see Eq. (D.8)) are indicated. The period of the finite crystal is $N_1\vec{a}_1$ and $N_2\vec{a}_2$ as shown in the figure. Circles around the origin of each cell sketch the maximum radius of the elements $Y_{0,j}$ ($Y = S$ or H). The period N_i needs to be chosen large enough to accommodate all elements $Y_{0,j}$ in the lattice of one crystal cell $\vec{R}_n$.

For the special case of an fcc lattice the standard lattice vectors are

$$\vec{a}_1^{std} = \frac{a_0}{2}(\vec{e}_2 + \vec{e}_3) \quad \vec{a}_2^{std} = \frac{a_0}{2}(\vec{e}_1 + \vec{e}_3) \quad \vec{a}_3^{std} = \frac{a_0}{2}(\vec{e}_1 + \vec{e}_2) \tag{D.17}$$

with the lattice constant a_0 and the cartesian unit vectors $\vec{e_i}$ [184]. As will be explained further below, the actual $\vec{a}_i$ may be rotations thereof ($\vec{a}_i = R\vec{a}_i^{std}$ with an appropriate proper rotation R). We find for an fcc lattice with these primitive lattice vectors that $\lambda_{min}(A^T A) = a^2/4$ and therefore an index $N_i/2 = \left\lceil \frac{2R}{a} \right\rceil$ is a sufficient choice for insuring that all lattice atoms $\vec{R}_j$ inside a sphere of radius R are present. If the matrix elements $Y_{0,j}$ vanish for all $\left|\vec{R}_j\right| \geq R$, then this choice of the N_i fulfills condition (i). Notice that with the choice of the (nonorthogonal) lattice vectors $\vec{a}_i$ (see also Eq. (D.17)) only one atom is in the primitive cell of the fcc lattice. Thus the crystal structure can be described by a monatomic Bravais lattice [184].

The formalism as presented above is not restricted to an fcc lattice, but can easily be adapted to describe more complicated crystal structures, such as hcp. To tackle such a problem, PBCs need to be assumed on a Bravais lattice with a nontrivial basis describing several atoms per unit cell [184]. In essence this just increases the number of orbitals for the elements Y_{0j} where 0 and j are more generally – and as used above – indices of the primitive cell (and not simply the atom). We investigated Zn systems with an hcp structure for which this complication arises [259]. In that work our formalism, presented above, has been applied for the first time and bulk Green's functions were used to describe the electrode Green's function g_{XX}. From now on, however, we will only consider the special case of crystal structures like fcc that can be described by a monatomic Bravais lattice. Then the indices 0α and $j\beta$ of $Y_{0\alpha,j\beta}$ directly refer to the orbitals α and β at atomic positions at $\vec{R}_0$ and $\vec{R}_j$, respectively, and we will use the indices 0α and $j\beta$ from now on in this more special meaning.

Throughout this work we concentrate on fcc lattices. If bulk electrode Green's functions g_{XX} are be constructed via $G_{0\alpha,j\beta}$ (see Eq. (D.16)), in turn obtained from parameters $Y_{0\alpha,j\beta}$, it is important that the index j as well as the orbital indices α and β refer to the electrode lattice with primitive lattice vectors $\vec{a}_i$. If the parameters $Y_{0\alpha,j\beta}$ have instead been determined with respect to the standard lattice vectors $\vec{a}_i^{std}$ of Eq. (D.17), appropriate transformations of both the positional index and the orbital indices to the coordinate system of the $\vec{a}_i$ are necessary. How such transformations can be performed is described in Sec. F.1.

If the crystal lattice of the left electrode has the same lattice vectors $\vec{a}_i$ as the lattice on the right, a substantial amount of time can be saved by calculating the elements $G_{0,j}$ only once. These matrix elements can then be used for the construction of both the left and right electrode Green's functions g_{LL} and g_{RR} simultaneously. If, however, the left and right electrode lattices do not possess the same lattice vectors $\vec{a}_i$, then their fcc lattices need to be connected by an appropriate rotation R. Let's suppose the bulk Green's function elements $G_{0,j}$ for the right electrode have been computed. In order to obtain the Green's function elements for the left electrode, the $G_{0,j}$ need to be transformed appropriately, before the left Green's function can be computed (see Sec. F.1). At present, however, we implemented the separate construction of the Green's function elements of the left and right electode, which should be less efficient.

As only a finite number of k-points is actually used in any numerical construction of a bulk Green's function, the broadening η employed in the computation of G_k (see Eq. (D.15)) needs to be finite. The more k-points are used, the smaller can this broadening be. This balance between the broadening and the number of employed k-points will be illustrated at the example of the bulk DOS in the following paragraph (see Fig. D.2).

D.1.1 Density of states for a bulk atom

In order to gain some insight into the electronic structure of a solid, the DOS is a valuable quantity. As discussed in Secs. A.2, B.3, and B.3.2 (see Eqs. (A.31), (A.32), (A.36), (B.32)) the imaginary part of the Green's function contains information about available energetic states of a physical system. Eq. (B.32) shows, however, that the Green's functions contain an overlap weight, which one needs to get rid of, in order to achieve that the energy integral over a certain atomic orbital equals 1.

From Eq. (B.32)

$$-\int_{-\infty}^{\infty} \frac{dE}{\pi} \mathrm{Im}\left[G^r(E)\right] = -\int_{-\infty}^{\infty} \frac{dE}{\pi} \mathrm{Im}\left[\left((E+i\eta)\,S-H\right)^{-1}\right] = S^{-1}$$

it becomes obvious that the overlap weight can be eliminated in several ways. The two possibilities that we want to concentrate on are a multiplication from the right (or left) with the overlap S

$$-\int_{-\infty}^{\infty} \frac{dE}{\pi} \mathrm{Im}\left[G^r(E)\right] S = -\int_{-\infty}^{\infty} \frac{dE}{\pi} \mathrm{Im}\left[\left((E+i\eta)\,\mathbb{1} - S^{-1}H\right)^{-1}\right] = \mathbb{1}$$

or a symmetric multiplication from both sides with the square root of the overlap[2] $S^{1/2}$

$$-\int_{-\infty}^{\infty} \frac{dE}{\pi} S^{1/2} \mathrm{Im}\left[G^r(E)\right] S^{1/2} = -\int_{-\infty}^{\infty} \frac{dE}{\pi} \mathrm{Im}\left[\left((E+i\eta)\,\mathbb{1} - S^{-1/2}HS^{-1/2}\right)^{-1}\right] = \mathbb{1}.$$

These two possibilities correspond to a Mulliken or Löwdin analysis, respectively.

By means of the recipe for determining the bulk Green's function, the bulk DOS can be constructed by (i) a Fourier transformation of $Y_{0,j}$ ($Y = S$ or H) to the reciprocal space (see Eq. (D.14)), (ii) a construction of an orthogonal Hamiltonian[3]

$$H_k^{orth} = H_k S_k^{-1} \tag{D.18}$$

or

$$H_k^{orth} = S_k^{-1/2} H_k S_k^{-1/2}, \tag{D.19}$$

next (iii) the determination of

$$G_k^{orth,r} = \left((E+i\eta)\,\mathbb{1}_k - H_k^{orth}\right)^{-1} \tag{D.20}$$

(see Eq. (D.15)), and (iv) a subsequent Fourier back transformation (see Eq. (D.16)). The extraction of the element $G_{0,0}^{orth,r}(E)$ gives the contribution of the orbital α to the DOS

$$\mathrm{DOS}_\alpha(E) = -\frac{1}{\pi} \mathrm{Im}\left[\left(G_{0,0}^{orth,r}(E)\right)_{\alpha,\alpha}\right]. \tag{D.21}$$

The total DOS of a bulk atom is the sum over all orbital contributions of that atom

$$\mathrm{DOS}(E) = \sum_\alpha \mathrm{DOS}_\alpha(E) = -\frac{1}{\pi} \mathrm{Tr}\left[\mathrm{Im}\left[\left(G_{0,0}^{orth,r}(E)\right)_{\alpha,\alpha}\right]\right]. \tag{D.22}$$

In case that we start directly from an orthogonal Hamiltonian $H_{0,j}^{orth}$ in direct space, it is just necessary to transform it to k-space in order to obtain the orthogonal Green's function $G_k^{orth,r}$ via Eq. (D.20). Step (iv) is identical.

Let us now demonstrate the remark made at the end of Sec. D.1 that there is a connection between the broadening η and the number of k-points used for the construction of the bulk Green's function. We will show at the example of the bulk DOS of Al that more k-points allow the choice of smaller broadenings. In Fig. D.2 the DOS of Al is plotted for various broadenings and k-point numbers. In the left panel of that figure the DOS is

---

[2] Note that $S^{1/2}$ needs to exist, because S is a positive definite matrix [81]. The proof uses that $S_{ij} = \int d^3r \phi_i(\vec{r})\phi_j(\vec{r})$ from real basis functions $\phi_i(\vec{r})$. Then $\vec{d}^T S \vec{d} = \int d^3r \left(\sum_i \phi_i(\vec{r}) d_i\right)^2 \geq 0$ for an arbitrary (real) vector $\vec{d}$. Thus the eigenvalues of any overlap matrix are all positive. If s is the diagonal matrix of eigenvalues of S (with $s_i \geq 0$), we can write $S = UsU^T$ with an orthogonal matrix U (because $S^T = S$). Any power γ of S (as for instance the square root) is obtained as $S^\gamma = Us^\gamma U^T$.

[3] Note that the Fourier transformation of the identity $\mathbb{1}$ in real space is $\mathbb{1}$ in the k-space.

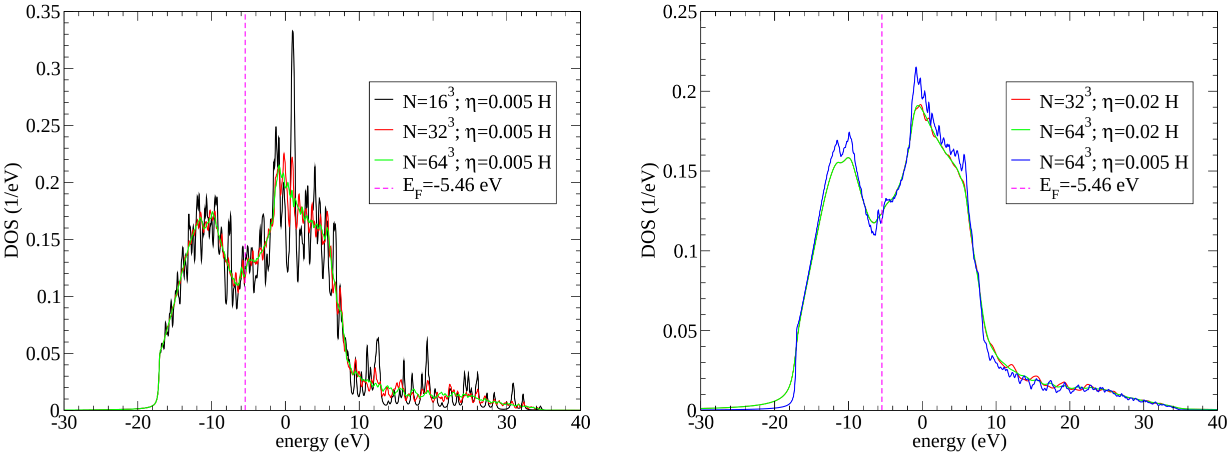

Figure D.2: DOS as obtained for Al. The parameters $Y_{0,j}$ employed in these calculations stem from an Al cluster of 683 atoms described within the al hw-min basis set and the functional BP-86 (see Sec. F.4 for details). The orthogonal Hamiltonian has been obtained from a symmetric orthogonalization (see Eq. (D.19)). In the left figure the DOS is shown for different k-point numbers of $N = 16^3$, 32^3, and 64^3 at a small broadening $\eta = 0.005$ H $=$ 0.14 eV. The figure to the right shows again the DOS, but this time for a bigger broadening of $\eta = 0.02$ H $= 0.54$ eV and $N = 32^3$ and 64^3 k-points. For reasons of comparison also the DOS for the smaller broadening of $\eta = 0.005$ H is shown with $N = 64^3$. In both figures the Fermi energy $E_F = -5.46$ eV is indicated as it is obtained from the HOMO and LUMO of the Al_{683} cluster.

shown for different numbers of total k-points[4] $N = 16^3$, 32^3, and 64^3 for a fixed broadening $\eta = 0.005$ H $= 0.14$ eV. Obviously there are many wiggles present at the selected broadening and a total k-point number of $N = 16^3$. For $N = 32^3$ many of the wiggles have decreased in amplitude, and for $N = 64^3$ they are only faintly visible. Commonly we use $N_i = 32$ in our calculations. For this reason we choose a bigger broadening in order to get rid of artifical features in the DOS. In the right panel of Fig. D.2 we show the bulk DOS for a broadening of $\eta = 0.02$ H$= 0.54$ eV as we employ it for the conductance calculations in Al contacts (see Sec. 5.2). We see that for the increased broadening $\eta = 0.02$ H the DOS for $N = 32^3$ has already converged with respect to the number of k-points and no difference is visible as compared to the curve with $\eta = 0.02$ H and $N = 64^3$. The trade-off is that, with respect to a smaller broadening, the features in the DOS are somewhat more blurred, as is visible in the comparison to the DOS curve at a k-point number of $N = 64^3$ and a broadening of $\eta = 0.005$ H.

By integrating up the DOS, the Fermi energy E_F can be determined. As indicated in Fig. D.2 we get $E_F = -5.46$ eV as the energy from the highest occupied molecular orbital (HOMO) and lowest unoccupied molecular orbtial (LUMO) of the Al_{683} cluster (see

---

[4] The number of primitive cells N_i (i = 1, 2, and 3) along each direction of the underlying fcc lattice with Bravais lattice vectors $\vec{a}_i$ (see Eq. (D.17)) is the same for all three directions ($N_1 = N_2 = N_3$), so that the total number of k-point is $N = \prod_{i=1}^{3} N_i = N_1^3$.

discussion in Secs. 4.3.1 and 4.3.3), from which the parameters for the DOS calculation stem. The integration of the DOS curves for $\eta = 0.02$ H at $N = 32^3$ and 64^3 both yield $E_F = -5.63 \pm 0.03$ eV, while for $\eta = 0.005$ H and $N = 64^3$ we get $E_F = -5.55 \pm 0.03$ eV. As E_F is somewhat dependent on the broadening chosen, we prefer to obtain the Fermi energy from the HOMO and LUMO energies of the big atomic clusters computed to obtain the bulk parameters for our DFT calculations. For the TB parameterization presented in Sec. E.1 there is, however, no other way than to obtain E_F from an integration of the bulk DOS.

D.1.2 Special k-points

If we consider the case of an infinite crystal in the thermodynamic limit ($N_i \to \infty$, $N = \prod_{i=1}^{3} N_i \to \infty$, $V \to \infty$, and $N/V =$ const.) then, the k-points become infinitely dense in the first Brillouin zone (see Eqs. (D.5), (D.7), and (D.8)). In this case, the summation over k-points in Eq. (D.3) becomes an integral. More specifically we can write in the thermodynamic limit for the Green's function in Eq. (D.16)

$$G^r_{0,j}(E) = \sum_k G_k(E) e^{i\vec{k}_k \cdot \vec{R}_j} = \frac{V}{(2\pi)^3} \int_{1.\mathrm{BZ}} d^3k G_k(E) e^{i\vec{k}_k \cdot \vec{R}_j}, \tag{D.23}$$

where 1.BZ stands for the first Brillouin zone, and we used the fact that $Nd^3k/V_{1.\mathrm{BZ}}$ is the number of k-points present in the infinitesimal volume d^3k. By exploiting that $V_{1.\mathrm{BZ}} = \left|\vec{b}_1 \cdot \left(\vec{b}_2 \times \vec{b}_3\right)\right| = (2\pi)^3 / |\vec{a}_1 \cdot (\vec{a}_2 \times \vec{a}_3)| = (2\pi)^3 N/V$ we finally arrive at Eq. (D.23) [258, 184].

Techniques have been developed to evaluate integrals over the first Brillouin zone as given in Eq. (D.23). Especially, in Ref. [260] it has been shown that such integrals can be determined in an efficient and accurate way by evaluating the integrand at sets of special k-points in the 1.BZ. Sets of such special k-points were already given in that Ref., but Monkhorst *et al.* [261] developed a more systematic approach for generating them. When special k-points are used in an integration, it is, however, very important that the integrand meets two conditions. First it needs to be periodic in k-space, and second the integrated function needs to possess the complete symmetry of the direct lattice.

Concerning $G_k(E)e^{i\vec{k}_k \cdot \vec{R}_j}$, the condition of periodicity in k-space is met. (See the discussion in the context of Eq. (D.8), from which it follows that $\exp(i\vec{k}_k \cdot \vec{R}_j)$, $f(\vec{k})$ in Eq. (D.21) and therefore also G_k (see Eq. (D.15)) are invariant with respect to additions of reciprocal lattice vectors $\vec{G}$ to their argument $\vec{k}$.) The second condition of complete lattice symmetry is, however, more restrictive. We will show now that this requirement is only fulfilled for $\vec{R}_j = 0$. In Eq. (D.12) it has been demonstrated that the translational invariance of $Y_{0,j}$ ($Y = S$ or H) carries over to $G_{0,j}$. The same is true for point group operations T_i (where T_i is a rotation or pseudo-rotation and i ranges over all operations of the point group of the underlying space group) [262]. Thus if Y is invariant with respect to T_i ($Y = T_i^{-1} Y T_i$) then we get

$$\mathbb{1} = \left[(E + i\eta) S - H\right] G^r = T_i^{-1} \mathbb{1} T_i = \left[(E + i\eta) S - H\right] T_i^{-1} G^r T_i,$$

which tells us that, because $G^r = T_i^{-1} G^r T_i$, all the point group symmetries of Y are valid for G. Taken together with the translational invariance of G we see that the elements $G_{0,j}$ obey the same symmetries as the $Y_{0,j}$, namely the elements $G_{0,j}$ for a set of js are connected via the space group of the Bravais lattice. Let us now look at the integrand $G_k e^{i\vec{k}_k \cdot \vec{R}_j}$ in Eq. (D.23). For G_k it follows from Eq. (D.2) that

$$G_k = G(\vec{k}_k) = \sum_j G_{0,j} e^{-i\vec{k}_k \cdot \vec{R}_j}. \tag{D.24}$$

Therefore G_k is lattice symmetric, because in the sum over elements $G_{0,j}$ the application of a T_i changes the order of the summation, but as all j appear in the summation, we still get $G_k = T_i^{-1} G_k T_i$. However, the phase factor $\exp(i\vec{k}_k \cdot \vec{R}_j)$ is obviously not lattice symmetric if $\vec{R}_j \neq 0$. Therefore the two requirements on the integrand $G_k(E) e^{i\vec{k}_k \cdot \vec{R}_j}$ in Eq. (D.23) are only met for $\vec{R}_j = 0$. Nevertheless, this observation has an interesting consequence for the DOS. According to Eqs. (D.21) and (D.22) the computation of the DOS requires the knowledge of (the imaginary part of) the onsite elements $G_{0,0}$ only.

To summarize, special k-points can be used to compute the DOS or, more generally, onsite elements of the Green's function by carrying out the k-space integral

$$G^r_{0,0}(E) = \sum_k G_k(E) = \frac{V}{(2\pi)^3} \int_{1.\mathrm{BZ}} d^3k G^r_k(E). \tag{D.25}$$

The set of special k-points lies in an irreducible part of the first Brillouin zone. A high symmetry of the Bravais lattice may therefore lead to an accurate integration with few k-points. Explicitly, the integral is then approximated as

$$G^r_{0,0}(E) = \frac{V}{(2\pi)^3} \int_{1.\mathrm{BZ}} d^3k G^r_k(E) \approx \sum_{i=1}^{N_k} \omega_i G^r(\vec{k}_i, E),$$

where $\vec{k}_i$ is a point in the set of special k-points, ω_i is its weight and N_k it the total number of special k-points. This set of points can be improved systematically if needed [261].[5]

D.2 Construction of surface Green's functions

In this paragraph the construction of surface Green's functions will be described. Surface Green's functions are of relevance in the calculation of the transmission properties of atomic contacts. They are Green's functions of a semi-infinite system such as an electrode. In other words the electrode Green's function g_{XX} should be modeled as a surface Green's function. Unfortunately, the construction of surface Green's functions is usually

---

[5] All other elements $G^r_{0,j}$ with $j \neq 0$ cannot be obtained from an integration with special $\vec{k}$-points. For obtaining them, a practical way is the assumption of Born-von-Kármán periodic boundary conditions in a finite crystal as explained above.

more time-consuming than the construction of bulk Green's functions. Therefore, the use of bulk Green's functions in the determination of conductances of atomic contacts may be necessary, if the system size is very big, and time is becoming an important factor. The approximation of electrode Green's functions by bulk Green's functions should reproduce correctly the general trends. This approximation has been made for the break junctions studied in Chap. 2, where the conductance histograms of different metals are studied. One should, however, be aware that the use of bulk Green's functions constitutes an uncontrolled approximation. For this reason the effort has been undertaken to implement surface Green's functions. The results of Chap. 2 have partly been reinvestigated with surface Green's functions (see Sec. 2.10). No qualitative changes have been detected, but quantitatively the modeling of the electrodes by surface Green's functions instead of bulk Green's functions changes the results. In our DFT transport method we use the improved electrode description with surface Green's functions (see Secs. 5 and 6).

The computation of surface Green's function in this work uses the decimation technique of Guinea *et al.* [263]. The derivation of the equations will be given below, as the decimation formulas are needed in a slightly more general form in this work. The generalization concerns the use of a nonorthogonal basis, a coupling which is farther than second layer, and the use of Green's function matrices instead of vectors (see Eq. (6) and the Eqs. following it in Ref. [263]). We want to thank Michael Häfner for discussions on surface Green's functions, which were very helpful, when we decided to describe the electrode Green's functions by means of surface Green's functions.

We will construct the surface Green's function from bulk parameters. At first this may appear odd, because in any self-consistent procedure, surface parameters should differ from bulk parameters. However, if the planes partitioning the system into the left (L), central (C), and right (R) part are defined such that the wire cross-sections at the left and right side are big, surface effects can be neglected for most of the atoms in the L and R part of the system. Then the construction of a surface Green's function from bulk parameters corresponds closely to the actual situation in the contact (see Fig. D.3). In any real transport calculation in this work it is of course difficult to construct a center large enough to actually achieve that a large number of atoms can be described by bulk parameters.

For the construction of surface Green's functions we need to distinguish between the left and the right surface. First we will treat the right surface. In addition, and opposed to bulk Green's functions, where all directions are equivalent, the transport direction, which shall be perpendicular to the surface plane, plays now a different role than the transverse directions spanning the surface plane. The x and y axis (transverse directions) shall be in the surface plane, while the z axis shall be perpendicular to the surface plane (see Fig. D.4).

With a rotation of the set of the standard fcc lattice vectors (see Eq. (D.17)) we will be able to describe the electrode lattice with the primitive lattice vectors $\vec{a}_i$ ($\vec{a}_i = R\vec{a}_i^{std}$ with an appropriate proper rotation R, where $\vec{a}_i^{std}$ are the primitive lattice vectors of Eq. (D.17) in the standard notation). From these $\vec{a}_i$ we construct new vectors, depending on the kind of surface present (e.g., [100], [110], or [111]), where two are located in the surface plane, we call them $\vec{c}_1$ and $\vec{c}_2$, and one is oriented along the positive z direction, $\vec{c}_3$. (In Sec. F.3

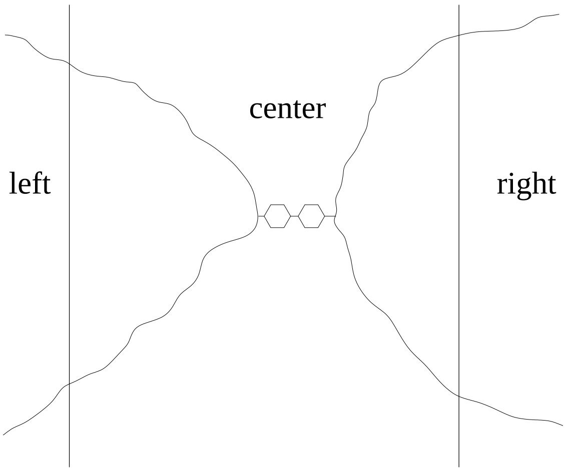

Figure D.3: Sketch of a contact as possibly present at a microscopic level in molecular electronics. If the central system called "center" in the figure is chosen large enough, the main part of atoms in the atomic layers in the left and right electrode are very similar to bulk atoms with the exception of a few atoms located at surfaces.

further details are given on how the vectors $\vec{c}_i$ are chosen for the particular surface.) As before we will assume that a parameter set $Y_{m\alpha,n\beta} = Y_{0\alpha,j\beta}$ ($Y = S$ or H and $j = n - m$) is available to us (see Eq. (D.11)) and that the parameters obey the space group symmetry of the the Bravais lattice. The matrix elements $Y_{m\alpha,n\beta}$ shall have the orientation of the electrode lattice (and a possible transformation has already been performed in oder to orientate them properly (see Sec. F.1)).[6] As before the indices $m = (m_1, m_2, m_3)$ and $n = (n_1, n_2, n_3)$ are a three-dimensional vector tuple standing for the integer indices in the spatial vectors $\vec{R}_m = \sum_i m_i \vec{a}_i$ and $\vec{R}_n = \sum_i n_i \vec{a}_i$ (see explanations in the context of Eq. (D.11)). From these indices we go over to matrix elements with indices referring to the $\vec{c}_i$, namely

$$Y_{m\alpha,n\beta} \longrightarrow Y_{t_1 p_1 \alpha, t_2 p_2 \beta},$$

where $t_1 = (t_{11}, t_{12})$ and $t_2 = (t_{21}, t_{22})$ are two-dimensional index tuples in the surface plane and p_1 and p_2 are one-dimensional index-tuples, describing the location in the plane perpendicular to the surface. More specifically we have the relation

$$\vec{R}_m = \sum_{i=1}^{3} m_i \vec{a}_i = \sum_{i=1}^{2} t_{1i} \vec{c}_i + p_1 \vec{c}_3 = \vec{R}_{t_1,p_1},$$

from which the surface index tuple (t_1, p_1) is obtained from the bulk index m as

$$(t_1, p_1) = C^{-1} A m$$

with the matrices $A = (\vec{a}_1, \vec{a}_2, \vec{a}_3)$ and $C = (\vec{c}_1, \vec{c}_2, \vec{c}_3)$. Due to the translational invariance of the parameters $Y_{m\alpha,n\beta}$ (see Eq. (D.11)) we can choose one of the transverse indices to

---

[6] In the notation of Fig. 4.4 we are dealing with the parameters $Y^{(X)}_{0\alpha,j\beta}$ with $X = L$ or R.

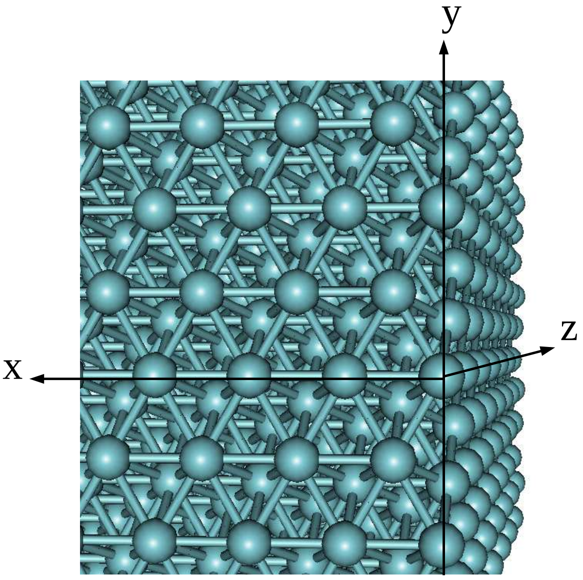

Figure D.4: Choice of the x, y and z axis in the construction of a surface Green's function. The x and y axis are located inside the surface layers and correspond to the transverse directions. The z axis is oriented perpendicular to the surface layers along the transport direction. The surface planes can be enumerated along the z axis.

be in the origin

$$Y_{t_1 p_1 \alpha, t_2 p_2 \beta} = Y_{0 p_1 \alpha, (t_2 - t_1) p_2 \beta}.$$

As explained in the context of bulk Green's functions (see Sec. D.1), we go over to k-space in the transverse direction by assuming PBCs in the surface plane. We choose a period of N_1 and N_2 lattice vectors along the directions of $\vec{c}_1$ and $\vec{c}_2$. Again care needs to be taken that these N_i are large enough to cover the full range of the hoppings $Y_{0 p_1 \alpha, (t_2 - t_1) p_2 \beta}$ in the transverse direction and that none of the indices needed in the surface Green's function g_{XX} requires a longer period N_i (see the conditions (i) and (ii) in Sec. D.1). Then a two-dimensional Fourier transformation is possible

$$Y_{\kappa, p_1 \alpha, p_2 \beta} = \sum_{j_1, j_2} Y_{0 p_1 \alpha, j p_2 \beta} e^{-i \vec{\kappa}_\kappa \cdot \vec{r}_j}$$

with the two-dimensional direct space vector $\vec{r}_j = \sum_{i=1}^{2} j_i \vec{c}_i$ and the two-dimensional k-space vector $\vec{\kappa}_\kappa = \sum_{i=1}^{2} \kappa_i \vec{d}_i$, where the $\vec{d}_i$ are the corresponding reciprocal lattice vectors of the $\vec{c}_i$ and $\kappa = (\kappa_1, \kappa_2)$. If needed, the parameters in direct space can be recovered by a Fourier back transformation

$$Y_{0 p_1 \alpha, j p_2 \beta} = \frac{1}{N} \sum_{j_1, j_2} Y_{\kappa, p_1 \alpha, p_2 \beta} e^{i \vec{\kappa}_\kappa \cdot \vec{r}_j}$$

with $N = \prod_{i=1}^{2} N_i$. From now on, all equations will be given after the two-dimensional Fourier transformation to k-space has been performed. We will suppress the k-space index κ. Also the orbital indices α and β will be suppressed if convenient, but we will keep the longitudinal layer index along $\vec{c}_3$ so that we write

$$Y_{\kappa, p_1 \alpha, p_2 \beta} = Y_{p_1, p_2}.$$

In order to construct the surface Green's function we start from the general definition of the Green's function

$$[(E+i\eta)\,S-H]\,G^r=\mathbb{1}$$

with an infinitesimal broadening $\eta>0$ (see Eq. (B.13)). More explicitly in terms of surface layers this can be written as

$$[(E+i\eta)\,S_{m,m}-H_{m,m}]\,G^r_{m,l}+\sum_{n\neq m}[(E+i\eta)\,S_{m,n}-H_{m,n}]\,G^r_{n,l}=\delta_{m,l}, \tag{D.26}$$

where the sum over n runs over all the layers, which are coupled to layer m. For the electrode Green's function of the right layer, we need all the elements of $G^r_{m,l}$ for which $m,l\in\{0,n_l\}$. Here n_l is the number of layers (in the longitudinal direction as described by the index p_i) that needs to be considered in the construction of the surface Green's function. This number is determined as the maximum of two integers, namely either n_l is the last layer (counting from 0) in the contact geometry to which the center is still coupled or n_l is chosen such that there is no coupling from layer 0 to the layer n_l+1 due to the electrode parameters Y_{p_1,p_2}.

With the help of the relations

$$Y_{m\alpha,n\beta}=Y_{0\alpha,(n-m)\beta}$$

due to translational symmetry and

$$Y_{m\alpha,n\beta}=Y^*_{n\beta,m\alpha}=Y^*_{0\beta,-(n-m)\alpha}=(Y^+_{0,-(n-m)})_{\alpha,\beta}$$

due to hermiticity, Eq. (D.26) can be brought into the form

$$\begin{aligned} WG^r_0+\tau_1G^r_1 &= \mathbb{1} && \text{(D.27)}\\ \tau_2G^r_{m-1}+WG_m+\tau_1G^r_{m+1} &= 0 \qquad \text{for } m\geq 1. && \text{(D.28)}\end{aligned}$$

with the Green's function matrices

$$G^r_m=\begin{pmatrix} G^r_{m(n_l+1),0} & G^r_{m(n_l+1),1} & \cdots & G^r_{m(n_l+1),n_l}\\ G^r_{m(n_l+1)+1,0} & G^r_{m(n_l+1)+1,1} & \cdots & G^r_{m(n_l+1)+1,n_l}\\ \vdots & \vdots & \ddots & \vdots\\ G^r_{m(n_l+1)+n_l,0} & G^r_{m(n_l+1)+n_l,1} & \cdots & G^r_{m(n_l+1)+n_l,n_l}\end{pmatrix} \tag{D.29}$$

and the coupling matrices

$$W=\begin{pmatrix} (E+i\eta)\,S_{0,0}-H_{0,0} & (E+i\eta)\,S_{0,1}-H_{0,1} & \cdots & (E+i\eta)\,S_{0,n_l}-H_{0,n_l}\\ (E+i\eta)\,S^+_{0,1}-H^+_{0,1} & (E+i\eta)\,S_{0,0}-H_{0,0} & \cdots & (E+i\eta)\,S_{0,n_l-1}-H_{0,n_l-1}\\ \vdots & \vdots & \ddots & \vdots\\ (E+i\eta)\,S^+_{0,n_l}-H^+_{0,n_l} & (E+i\eta)\,S^+_{0,n_l-1}-H^+_{0,n_l-1} & \cdots & (E+i\eta)\,S_{0,0}-H_{0,0}\end{pmatrix} \tag{D.30}$$

$$\tau_1 = \begin{pmatrix} 0 & 0 & \cdots & 0 \\ (E+i\eta)\,S_{0,n_l} - H_{0,n_l} & 0 & \cdots & 0 \\ \vdots & \vdots & \ddots & \vdots \\ (E+i\eta)\,S_{0,1} - H_{0,1} & (E+i\eta)\,S_{0,2} - H_{0,2} & \cdots & 0 \end{pmatrix} \tag{D.31}$$

$$\tau_2 = \begin{pmatrix} 0 & \cdots & (E+i\eta)\,S^{+}_{0,2} - H^{+}_{0,2} & (E+i\eta)\,S^{+}_{0,1} - H^{+}_{0,1} \\ \vdots & \ddots & \vdots & \vdots \\ 0 & \cdots & 0 & (E+i\eta)\,S^{+}_{0,n_l} - H^{+}_{0,n_l} \\ 0 & \cdots & 0 & 0 \end{pmatrix}. \tag{D.32}$$

Note that τ_2 is the Hermitian conjugate of τ_1 except for the energy argument $E + i\eta$, which remains unchanged. This is important, because in the numerical computation of Green's function η is finite. The zeros in τ_1 and τ_2 arise, because by construction the coupling between layers does not reach further than $n_l + 1$ layers.

Now the decimation scheme can be applied by first eliminating the Greens functions G^r_1, G^r_3, G^r_5, G^r_7,... and in the next step the Green's functions G^r_2, G^r_6, G^r_{10}, G^r_{14},... as described in Ref. [263]. Finally the following iterative equations are obtained (see Eqs. (14) and (15) of Ref. [263])

$$\begin{aligned} W^{(n)}_{sR} &= W^{(n-1)}_{sR} - \tau^{(n-1)}_1 \left(W^{(n-1)}_b\right)^{-1} \tau^{(n-1)}_2 && \text{(D.33)} \\ W^{(n)}_b &= W^{(n-1)}_b - \tau^{(p-1)}_1 \left(W^{(n-1)}_b\right)^{-1} \tau^{(n-1)}_2 - \tau^{(n-1)}_2 \left(W^{(n-1)}_b\right)^{-1} \tau^{(n-1)}_1 && \text{(D.34)} \\ \tau^{(n)}_1 &= -\tau^{(n-1)}_1 \left(W^{(n-1)}_b\right)^{-1} \tau^{(n-1)}_1 && \text{(D.35)} \\ \tau^{(n)}_2 &= -\tau^{(n-1)}_2 \left(W^{(n-1)}_b\right)^{-1} \tau^{(n-1)}_2, && \text{(D.36)} \end{aligned}$$

where n stands for the nth iterative step and the matrices of the 0th step are $W^{(0)}_b = W^{(0)}_{sR} = W$, $\tau^{(0)}_1 = \tau_1$, and $\tau^{(0)}_2 = \tau_2$. Note that the minus sign in the renormalization of τ_1 and τ_2 is not necessary and has been dropped in our implementation. This is possible, because in the iterative equations there always appears a multiplication of two τs in the construction of $W^{(n)}_s$ or $W^{(n)}_b$, which cancels their signs. In the iterative procedure the couplings $\tau^{(n)}_1$ and $\tau^{(n)}_2$ describe the couplings between the superlayers 0 and 2, 2 and 4, and so on for $n = 1$, between 0 and 4, 4 and 8 and so on for $n = 2$, and generally between superlayers with an index difference of 2^n after n steps (see Fig. D.5). Therefore the couplings $\tau^{(n)}_1$ and $\tau^{(n)}_2$ can be expected to decrease rapidly as a function of the number of iterative steps n. If $\tau^{(n)}_1$ and $\tau^{(n)}_2$ are negligible after ν steps, Eqs. (D.27) and (D.28) yield

$$\begin{aligned} W^{(\nu)}_{sR} G^r_0 &= \mathbb{1} && \text{(D.37)} \\ W^{(\nu)}_b G^r_{(2^\nu)} &= 0. && \text{(D.38)} \end{aligned}$$

The surface Green's function of the right side is then the solution of Eq. (D.37) for G^r_0

$$G^r_{sR} = \left(W^{(\nu)}_s\right)^{-1}. \tag{D.39}$$

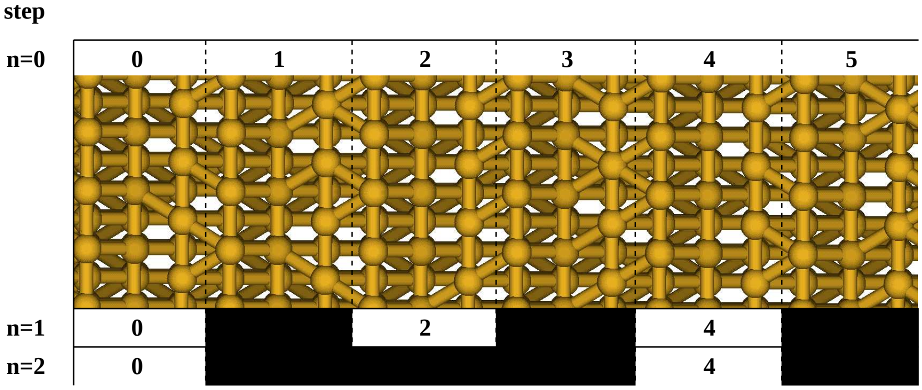

Figure D.5: Au electrode oriented along the [111] direction. In the illustration, each superlayer consists of 3 crystal layers, as indicated at the top of the figure, with indices running from 0 to 5. In the nth step of the iterative process Green's functions of the superlayers $2^{n-1}(2i-1)$ with $i \in \mathbb{N}$ are eliminated, as shown below. The renormalized couplings $\tau_1^{(n)}$ and $\tau_2^{(n)}$of Eqs. (D.31) and (D.32) describe the couplings between superlayers with an index difference of 2^n.

The decimation also provides the bulk Green's function, which is

$$G^r_{bR} = \left(W_b^{(\nu)}\right)^{-1}. \tag{D.40}$$

This last relation becomes clear, when one writes down the decimation procedure for a layer deep inside the solid state, so that no surface is reached before the coupling matrices $\tau_1^{(n)}$ and $\tau_2^{(n)}$have decayed to negligible values. This is by construction the case for superlayer 2^ν and the inversion of $W_b^{(\nu)}$ yields the bulk Green's function. Eq. (D.40) is another possibility to construct the bulk Green's function as compared to the technique of a Fourier transformation in three dimensions described before (see Sec. D.1). Results obtained in these two ways are in excellent agreement, if the number of k-points in both constructions is chosen large enough. (Usually a direct space period $N_i \geq 16$ is sufficient.)

For the left side another surface Green's function is needed. So the decimation needs to be carried out for the left side as well. The equations can be brought into a form equivalent to Eqs. (D.27) and (D.28)

$$\begin{aligned} \tau_2 G^r_{-1} + W G^r_0 &= \mathbb{1} && \text{(D.41)} \\ \tau_2 G^r_{m-1} + W G^r_m + \tau_1 G^r_{m+1} &= 0 \qquad \text{for } m \leq -1. && \text{(D.42)} \end{aligned}$$

The Green's function matrices are now

$$G^r_m = \begin{pmatrix} G^r_{m(n_l+1)-n_l,-n_l} & \cdots & G^r_{m(n_l+1)-n_l,-1} & G^r_{m(n_l+1)+1,0} \\ \vdots & \ddots & \vdots & \vdots \\ G^r_{m(n_l+1)-1,-n_l} & \cdots & G^r_{m(n_l+1)-1,-1} & G^r_{m(n_l+1)-1,0} \\ G^r_{m(n_l+1),-n_l} & \cdots & G^r_{m(n_l+1),-1} & G^r_{m(n_l+1),0} \end{pmatrix}. \tag{D.43}$$

Note that the indexing in G^r_m has changed in the sense that the surface layer 0 is now in the lower right corner of G^r_m, while in Eq. (D.29) it was in the upper left corner. The form of the matrices W, τ_1 and τ_2 (see Eqs. (D.30), (D.31), and (D.32)) remains unchanged.

Finally, the iterative equations for the left surface Green's function are the former Eqs. (D.34), (D.35), and (D.36) plus the additional relation

$$W^{(n)}_{sL} = W^{(n-1)}_{sL} - \tau^{(n-1)}_2 \left(W^{(n-1)}_b\right)^{-1} \tau^{(n-1)}_1. \tag{D.44}$$

In this way Eq. (D.33) for $W^{(n)}_{sR}$ has been replaced by Eq. (D.44) for $W^{(n)}_{sL}$. Again n stands for the nth iterative step and $W^{(0)}_{sL} = W$. If $\tau^{(n)}_1$ and $\tau^{(n)}_2$ are negligible after ν steps, Eqs. (D.41) and (D.42) yield

$$W^{(\nu)}_{sL} G^r_0 = \mathbb{1} \tag{D.45}$$

$$W^{(\nu)}_b G^r_{(2^\nu)} = 0. \tag{D.46}$$

The left surface Green's function is then the solution of Eq. (D.45) for G^r_0

$$G^r_{sL} = \left(W^{(\nu)}_s\right)^{-1} \tag{D.47}$$

and the left bulk Green's function is

$$G^r_{bL} = \left(W^{(\nu)}_b\right)^{-1}. \tag{D.48}$$

As pointed out before, it should be noted here that the indexing of the layers for the left side Green's function in the transport direction has changed in going from Eqs. (D.39) and (D.40) to Eqs. (D.47) and (D.48) (see Eqs. (D.29) and (D.43)).

If for example the crystallographic direction of the left side differs from that of the right side ([100] surfaces for the right side and [111] surfaces for the left) or the lattice orientation of the left electrode is different from that of the right side, then the matrices W, τ_1 and τ_2 differ between left and right. In such cases the matrices W, τ_1, and τ_2 need to be constructed separately, and the decimation has to be carried out for the left and right side independently. A lot of time can be saved, however, if the layers of the left and right side are planes of the same crystallographic direction, e.g., [111] planes, and if they are oriented in the same way, which means that they possess the same lattice vectors $\vec{c}_i$. Then W, τ_1, and τ_2 need to be constructed only once and Eqs. (D.33), (D.34), (D.35), (D.36), and (D.44) can all be solved simultaneously. The time saved is mainly the construction of W_b, which is needed both for W_{sL} and W_{sR}, and that the iterative procedure with a convergence criterion for the decay of $\tau^{(n)}_1$ and $\tau^{(n)}_2$ is carried out only once. In case that the left and right electrode are only oriented along the same crystallographic direction but with a possible rotation between their lattice vectors, it should be possible to obtain their surface Green's functions by appropriate rotational transformations of the Green's function of one of the two surfaces (see Sec. F.1). Presently, however, we implemented the separate

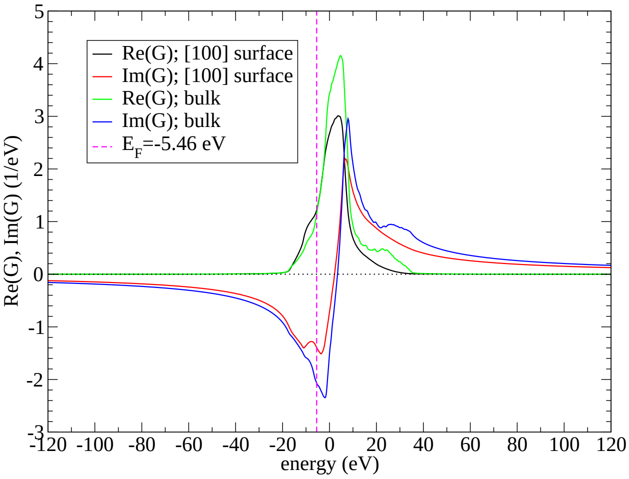

Figure D.6: Comparsion of the onsite elements of a bulk and surface Green's function. For the topmost atom of a [100] surface atom and an atom embedded in a crystal (bulk) we plot the real and imaginary parts of the sum over all onsite elements of $G^a_{0\alpha,0\beta}$ ($\mathrm{Re}\,[G(E)] = \mathrm{Re}\left[\sum_\alpha G^a_{0\alpha,0\alpha}(E)\right]$ and $\mathrm{Im}\,[G(E)] = \mathrm{Im}\left[\sum_\alpha G^a_{0\alpha,0\alpha}(E)\right]$). The total number of k-points used is $N = 32^3$, the broadening is $\eta = 0.02$ H, and the Fermi energy of $E_F = -5.46$ eV corresponds to the Al_{683} cluster, from which the parameters for this calculation have been extracted (see discussion in Secs. 4.3.1 and 4.3.3).

construction of the Green's function elements of the left and right electrode, which is less efficient, but also less error-prone.

For the convergence criterion of the decimation we have chosen in our implementation that

$$\sum_{i,j}\left|\left(\tau_1^{(n-1)}\left(W_b^{(n-1)}\right)^{-1}\tau_2^{(n-1)}\right)_{i,j}\right| < \varepsilon.$$

In this way we have a direct control, on how much the inverse surface or bulk Green's function is still modified (see Eqs. (D.33), (D.34), and (D.44)). A smallness parameter $\varepsilon = 10^{-6}$H turned out to be sufficient for the broadenings η of around 0.01 H, as used in the calculations for Au in the SVP basis set (see Secs. 5.1 and 6). In other calculations we employed an even stricter convergence criterion. In the construction of surface Green's functions for Al contacts (see Sec. 5.2) we used $\varepsilon = 10^{-8}$ H and in Sec. 2.10 we used $\varepsilon = 10^{-8}$ Ry.

To conclude the presentation of the construction of electrode Green's functions we present in Fig. D.6 a comparison between surface and bulk Green's functions for Al. For this purpose we have plotted the real and imaginary part of the sum over all onsite elements of $G^a_{0\alpha,0\beta}$ ($\mathrm{Re}\,[G(E)] = \mathrm{Re}\left[\sum_\alpha G^a_{0\alpha,0\alpha}(E)\right]$ and $\mathrm{Im}\,[G(E)] = \mathrm{Im}\left[\sum_\alpha G^a_{0\alpha,0\alpha}(E)\right]$). We compare the Green's function inside the crystal, described by a bulk Green's function, with an atom in the topmost plane of a [100] surface. Both Green's functions show a qualitatively similar behavior, although quantitatively differences can be observed especially in the imaginary parts of the Green's functions. It is also nicely visible from the plot, how the real part shows a slowly decaying behavior for $|E| \rightarrow \infty$, where a behavior $\mathrm{Re}\,[G(E)] \rightarrow c/E$ is expected (with a certain prefactor c). Instead, the imaginary part of the Green's function is only non-zero within the range of energy states of the Al crystal.

Appendix E

Metallic nanowires – methodological details

In Chap. 2 we analyzed the electrical and mechanical properties of metallic nanocontacts. The ultimate goal was the description of the characteristic peaks in low-temperature conductance histograms of different classes of metals. In this chapter we will now present more of the technical details behind that work. For this purpose we will present in Sec. E.1 the tight-binding (TB) parameterization introduced by Mehl and Papaconstantopoulos [75, 76], which we use as a starting point for the description of the electronic structure of our metallic nanocontacts. Subsequently, we present the modification of these TB parameters by the requirement of local charge neutrality in the central part of our wires (see Sec. E.2). We will then continue with Sec. E.3, where we show explicitly, how we efficiently construct our electrode geometry in the transport calculations such that all relevant atoms are included and the effort in the calculation of the conductance becomes minimal. At the end of this chapter a derivation for the force needed to break a bulklike bond in a metal is presented in Sec. E.4.

E.1 Tight-binding parameterization

In order to compute the conductance of an atomic contact, we need a description of its electronic structure. We accomplish this task by resorting to a TB parameterization developed by Papaconstantopoulos *et al.* [75, 76, 77, 79, 78]. This parameterization uses an analytic set of two-center integrals [133, 264], nonorthogonal TB parameters, and onsite parameters that change with the local environment. The method is a total energy TB method, in which the parameters were fit to the total energies and band structures obtained from first-principles calculations. The method has been demonstrated to well produce structural energy differences, elastic constants, phonon frequencies, vacancy formation energies, and surface energies for both transition metals and noble metals [75].

Density functional theory (DFT) tells us that the total energy of a system of electrons moving in a solid can be written in the form

$$E\left[n(\vec{x})\right] = \sum_i f(\varepsilon_i - \mu)\varepsilon_i + F\left[n(\vec{x})\right], \tag{E.1}$$

where the Kohn-Sham (KS) ansatz for the kinetic energy has been used. In Eq. (E.1) $n(\vec{x})$ is the electron density, ε_i is the KS eigenvalue of the ith electronic state, μ is the chemical potential, and the sum runs over all electronic states of the system. The function $f(\varepsilon - \mu)$ is chosen to have the form of a Fermi function $f(z) = (\exp(\beta z) + 1)$ (with $\beta = (kT)^{-1}$). In the functional $F\left[n(\vec{x})\right]$ the remaining part of the DFT total energy is contained, which are the ion-ion interaction energy, the parts of the Hartree and exchange-correlation energy not included in the eigenvalue sum, and the corrections for double counting in the eigenvalue sums [75].

As explained in Ref. [76], the KS method allows for an arbitrary shift in the KS potential, which leaves the noninteracting kinetic energy, the total energy, the KS wave functions and the electron density $n(\vec{x})$ unchanged. If this shift is defined to be

$$V_0 = F\left[n(\vec{x})\right]/N_e,$$

where N_e is the number of electrons in the system, then the eigenvalues ε_i are shifted by an amount V_0, to the new values

$$\varepsilon_i' = \varepsilon_i + V_0.$$

The total energy then becomes

$$E\left[n(\vec{x})\right] = \sum_i f(\varepsilon_i' - \mu')\varepsilon_i', \tag{E.2}$$

where $\mu' = \mu + V_0$ is the shifted chemical potential.

Due to the basic theorems of DFT (see Sec. 4.1), the shifted eigenvalues ε_i' can be considered to be a function of the crystal structure, including volume, primitive lattice vectors, and internal parameters. A TB method that reproduces the ε_i' over a range of structures will then solve the total-energy problem of Eq. (E.1) or Eq. (E.2) without resort to an additional term.

As explained before (see Sec. 2.2.2), the TB model is based on the following Hamiltonian written in a nonorthogonal local basis

$$\hat{H} = \sum_{i\alpha, j\beta, \sigma} H_{i\alpha, j\beta, \sigma} \hat{d}^{+}_{i\alpha,\sigma} \hat{d}_{j\beta,\sigma}, \tag{E.3}$$

where i and j run over the atomic sites, α and β denote different atomic orbitals, and $H_{i\alpha,j\beta,\sigma}$ are the onsite ($i = j$) or hopping ($i \neq j$) elements, which are spin-dependent ($\sigma = \uparrow, \downarrow$) in the case of ferromagnetic metals such as Ni. Additionally, we need the overlap integrals $S_{i\alpha,j\beta}$ of orbitals at different atomic positions. The two-center Slater-Koster (SK) formulation of TB with a nonorthogonal basis set divides the problem into the calculation of three types of integrals: (i) onsite parameters $H_{i\alpha,i\beta,\sigma}$, which represent the energy required to place an electron in a specific orbital, (ii) Hamiltonian parameters, which represent the matrix elements for electrons hopping from one site to the other ($H_{i\alpha,j\beta,\sigma}$with $i \neq j$), and (iii) overlap parameters that describe the mixing between the nonorthogonal orbitals on neighboring sites. The eigenvalues ε_i' can be determined, once the parameters have been evaluated for a given structure. The $H_{i\alpha,j\beta,\sigma}$ and $S_{i\alpha,j\beta}$ are given simple algebraic forms with parameters chosen to reproduce first-principles results over a wide range of structures.

The Hamiltonian parameters must be sensitive to the local environment around each atom. In the current parameterization the influence of the local environment is only accounted for by the onsite parameters $H_{i\alpha,i\beta,\sigma}$. For this purpose a "density" associated to atom i is defined as

$$\varrho_i = \sum_{i \neq j} q_{\tilde{j}} \exp(-\lambda^2_{\tilde{i}\tilde{j}} R_{ij}) F_c(R_{ij}) \tag{E.4}$$

where $\tilde{i}$ ($\tilde{j}$) denotes the type of atom at position $\vec{R}_i$ ($\vec{R}_j$), λ is a parameter which depends on the kind of atom, $q_{\tilde{j}}$ is an effective charge for atoms of type $\tilde{j}$, and R_{ij} is the distance between the atoms i and j ($R_{ij} = \left|\vec{R}_i - \vec{R}_j\right|$).[1] For monatomic systems the charge is taken to be $q_{\tilde{j}} = 1$ and $\lambda_{\tilde{i}\tilde{j}}$ is just a constant λ. $F_c(R_{ij})$ is a smooth cutoff function

$$F_c(R) = \begin{cases} (1 + \exp([R - R_c + 5\ell]/\ell))^{-1} & \text{if } R \leq R_c \\ 0 & \text{if } R > 0 \end{cases} \tag{E.5}$$

which is used to effectively zero all interactions more than the cuttoff radius R_c apart.[2] Typically, the cutoff radius is around $R_c = 16.5a_0 = 8.73$ Åand includes more than 5 nearest neighbor shells (see also Sec. 2.2.2).

As an additional approximation the onsite parameters are assumed to be orthogonal $H_{i\alpha,i\beta,\sigma} = \delta_{\alpha\beta}$ (and $S_{i\alpha,i\beta,\sigma} = \delta_{\alpha\beta}$). They are parameterized as

$$H_{i\alpha,i\alpha,\sigma} = a_{i\alpha,\sigma} + b_{i\alpha,\sigma}\varrho_i^{2/3} + c_{i\alpha,\sigma}\varrho_i^{4/3} + d_{i\alpha,\sigma}\varrho_i^2 \tag{E.6}$$

where $\alpha = s$, p, t_{2g}, or e_g and ϱ_i is given by Eq. (E.4). The orbitals t_{2g} and e_g arise from d states, where the crystal field in cubic crystals splits the d states at the Γ point of the Brillouin zone into states with t_{2g} (d_{xy}, d_{yz}, and d_{xz}) and e_g (x^2-y^2 and $3z^2-r^2$) symmetry. Notice that only orbitals in the energy range of interest, namely close to the Fermi energy, are considered in this approach. Depending on the valence of the considered material, the s, p, and d states may correspond to different valence orbitals, e.g., $5d$, $6s$, and $6p$, for Au or $4p$, $5s$, and $5d$ for Ag. Strictly speaking, however, no precise main quantum number can be assigned to the angular orbital functions due to the employed fitting procedure.[3]

---

[1] Notice the error in Eq. (7) of Ref. [75], where $\lambda^1_{\tilde{i}\tilde{j}}$ has been written instead of $\lambda^2_{\tilde{i}\tilde{j}}$. That this is indeed an error has been confirmed to us by email correspondence with M.J. Mehl, and in all other papers (see for example Ref. [76]) the formula is correctly denoted with $\lambda^2_{\tilde{i}\tilde{j}}$.

[2] The cutoff function in the form of Eq. (E.5) is given at http://cst-www.nrl.navy.mil/bind/notes.html.

[3] For example is is not clear, whether the $6p$ states for Au are not actually better called $5p$ states and similarly for Ag. (See also Fig. E.3 for a plot of the energetic contributions of the different orbitals to the density of states.)

Hamiltonian $H_{i\alpha,i\beta,\sigma}$ and overlap parameters $S_{i\alpha,i\beta}$ for atoms i and j at different positions ($i \neq j$) are obtained from the two-center SK approximation (see Table E.1). The interaction matrix elements P_γ for the overlap and Hamiltonian are assumed to have the same functional form

$$P_\gamma(R) = \left(e_\gamma + f_\gamma R + \bar{f}_\gamma R^2\right) \exp(-g_\gamma R) F_c(R), \tag{E.7}$$

where γ indicates the type of interaction (e.g., $ss\sigma$, $pd\pi$, $dd\delta$, etc., where σ, π, and δ refer to the component of angular momentum around the axis between the atoms i and j [133, 264]), R is the distance between the atoms i and j, and $F_c(R)$ is given by Eq. (E.5). Notice that all Hamiltonian and overlap elements given in Table E.1 are functions of the relative positions of the atoms, as it is expected for a translationally invariant crystal.

Counting the number of free parameters (per spin component σ) needed to completely specify the TB parameterization presented above, this results in an impressive number of 97 free parameters. This number originates as follows: There are 4 different onsite parameters $H_{i\alpha,i\alpha,\sigma}$ for the different orbitals ($\alpha = s$, p, t_{2g}, and e_g), and each requires 4 different parameters ($a_{i\alpha,\sigma}$, $b_{i\alpha,\sigma}$, $c_{i\alpha,\sigma}$, and $d_{i\alpha,\sigma}$ in Eq. (E.6)), which gives 16 constants. On top of this, λ needs to be specified (see Eq. (E.4)). In Eq. (E.7) there are 10 different interactions γ and each requires 4 parameters, both for the Hamiltonian and the overlap, giving another set of 80 free parameters. In total this results in 97 free parameters.[4]

These free parameters are determined by fitting the electronic band structure and total energies, as obtained by the TB model, to first principles calculations [75, 76]. Additionally there are some restrictions in this fitting procedure, namely the functions $P_\gamma(R)$ are required to decay steadily, and the overlap is forced to be positive definite.

E.1.1 Example derivation of a Slater-Koster-integral

In order to be sure about the correctness of our implementation, we derived all the two-center integrals listed in Table E.1. For the purpose of illustrating, how these integrals are obtained, we will give here a sketch of their formal origin. First we will demonstrate, how to come to an integral not listed in Table E.1. Next we will derive the form of the Hamiltonian element $H_{ix,jyz}(\vec{R}_j - \vec{R}_i)$ as given in Table E.1. As already done in Table E.1, we will henceforth suppress the angular momentum quantum number l of the orbital index and write $\alpha = \nu$, instead of l_ν. Therefore p_x becomes x and d_{yz} is yz, for example.

In case that an integral is needed, which is not listed in Table E.1 such as $H_{iyz,jyz}(\vec{R}_j - \vec{R}_i)$, we start from the analog Hamiltonian element given in Table E.1. This analog Hamiltonian element is $H_{ixy,jxy}(\vec{R}_j - \vec{R}_i)$, because it is between d states of the same symmetry as $H_{iyz,jyz}(\vec{R}_j - \vec{R}_i)$. As can be seen from change in orbital indices in the replacement $H_{ixy,jxy} \rightarrow H_{iyz,jyz}$ the role of x, y, and z in $H_{ixy,jxy}$ is now played by y, z, and x in $H_{iyz,jyz}$. For this reason it is sufficient to make the replacement $n \rightarrow l$, $l \rightarrow m$, and $m \rightarrow n$ in order to arrive get

$$H_{iyz,jyz}(\vec{R}_j - \vec{R}_i) = 3m^2n^2 P_{dd\sigma}(R_{ij}) + \left(m^2 + n^2 - 4m^2n^2\right) P_{dd\pi}(R_{ij}) + \left(l^2 + m^2n^2\right) P_{dd\delta}(R_{ij}).$$

---

[4] Considering the cutoff radius R_c and the screening length in addition, this sums up to 99 fit parameters.

$$
\begin{aligned}
H_{is,js} &= P_{ss\sigma} \\
H_{is,jx} &= lP_{sp\sigma} \\
H_{ix,jx} &= l^2 P_{pp\sigma} + \left(1 - l^2\right) P_{pp\pi} \\
H_{ix,jy} &= lmP_{pp\sigma} - lmP_{pp\pi} \\
H_{ix,jz} &= lnP_{pp\sigma} - lnP_{pp\pi} \\
H_{is,jxy} &= \sqrt{3}lmP_{sd\sigma} \\
H_{is,jx^2-y^2} &= \tfrac{1}{2}\sqrt{3}\left(l^2 - m^2\right) P_{sd\sigma} \\
H_{is,j3z^2-r^2} &= \left(n^2 - \tfrac{1}{2}\left(l^2 + m^2\right)\right) P_{sd\sigma} \\
H_{ix,jxy} &= \sqrt{3}l^2 mP_{pd\sigma} + m\left(1 - 2l^2\right) P_{pd\pi} \\
H_{ix,jyz} &= \sqrt{3}lmnP_{pd\sigma} - 2lmnP_{pd\pi} \\
H_{ix,jzx} &= \sqrt{3}l^2 nP_{pd\sigma} + n\left(1 - 2l^2\right) P_{pd\pi} \\
H_{ix,jx^2-y^2} &= \tfrac{1}{2}\sqrt{3}l\left(l^2 - m^2\right) P_{pd\sigma} + l\left(1 - l^2 + m^2\right) P_{pd\pi} \\
H_{iy,jx^2-y^2} &= \tfrac{1}{2}\sqrt{3}m\left(l^2 - m^2\right) P_{pd\sigma} - l\left(1 + l^2 - m^2\right) P_{pd\pi} \\
H_{iz,jx^2-y^2} &= \tfrac{1}{2}\sqrt{3}n\left(l^2 - m^2\right) P_{pd\sigma} - n\left(l^2 - m^2\right) P_{pd\pi} \\
H_{ix,j3z^2-r^2} &= l\left(n^2 - \tfrac{1}{2}\left(l^2 + m^2\right)\right) P_{pd\sigma} - \sqrt{3}ln^2 P_{pd\pi} \\
H_{iy,j3z^2-r^2} &= m\left(n^2 - \tfrac{1}{2}\left(l^2 + m^2\right)\right) P_{pd\sigma} - \sqrt{3}mn^2 P_{pd\pi} \\
H_{iz,j3z^2-r^2} &= n\left(n^2 - \tfrac{1}{2}\left(l^2 + m^2\right)\right) P_{pd\sigma} + \sqrt{3}n\left(l^2 + m^2\right) P_{pd\pi} \\
H_{ixy,jxy} &= 3l^2 m^2 P_{dd\sigma} + \left(l^2 + m^2 - 4l^2 m^2\right) P_{dd\pi} + \left(n^2 + l^2 m^2\right) P_{dd\delta} \\
H_{ixy,jyz} &= 3lm^2 nP_{dd\sigma} + ln\left(1 - 4m^2\right) P_{dd\pi} + lm\left(n^2 - 1\right) P_{dd\delta} \\
H_{ixy,jzx} &= 3l^2 mnP_{dd\sigma} + mn\left(1 - 4l^2\right) P_{dd\pi} + mn\left(l^2 - 1\right) P_{dd\delta} \\
H_{ixy,jx^2-y^2} &= \tfrac{3}{2}lm\left(l^2 - m^2\right) P_{dd\sigma} + 2lm\left(m^2 - l^2\right) P_{dd\pi} + \tfrac{1}{2}lm\left(l^2 - m^2\right) P_{dd\delta} \\
H_{iyz,jx^2-y^2} &= \tfrac{3}{2}mn\left(l^2 - m^2\right) P_{dd\sigma} - mn\left(1 + 2\left(l^2 - m^2\right)\right) P_{dd\pi} + mn\left(1 + \tfrac{1}{2}\left(l^2 - m^2\right)\right) P_{dd\delta} \\
H_{izx,jx^2-y^2} &= \tfrac{3}{2}nl\left(l^2 - m^2\right) P_{dd\sigma} + nl\left(1 - 2\left(l^2 - m^2\right)\right) P_{dd\pi} - nl\left(1 - \tfrac{1}{2}\left(l^2 - m^2\right)\right) P_{dd\delta} \\
H_{ixy,j3z^2-r^2} &= \sqrt{3}lm\left(n^2 - \tfrac{1}{2}\left(l^2 + m^2\right)\right) P_{dd\sigma} - 2\sqrt{3}lmn^2 P_{dd\pi} + \tfrac{1}{2}\sqrt{3}lm\left(1 + n^2\right) P_{dd\delta} \\
H_{iyz,j3z^2-r^2} &= \sqrt{3}mn\left(n^2 - \tfrac{1}{2}\left(l^2 + m^2\right)\right) P_{dd\sigma} + \sqrt{3}mn\left(l^2 + m^2 - n^2\right) P_{dd\pi} - \tfrac{1}{2}\sqrt{3}mn\left(l^2 + m^2\right) P_{dd\delta} \\
H_{izx,j3z^2-r^2} &= \sqrt{3}ln\left(n^2 - \tfrac{1}{2}\left(l^2 + m^2\right)\right) P_{dd\sigma} + \sqrt{3}ln\left(l^2 + m^2 - n^2\right) P_{dd\pi}(R_{ij}) - \tfrac{1}{2}\sqrt{3}ln\left(l^2 + m^2\right) P_{dd\delta} \\
H_{ix^2-y^2,jx^2-y^2} &= \tfrac{3}{4}\left(l^2 - m^2\right)^2 P_{dd\sigma} + \left(l^2 + m^2 - \left(l^2 - m^2\right)^2\right) P_{dd\pi} + \left(n^2 + \tfrac{1}{4}\left(l^2 - m^2\right)^2\right) P_{dd\delta} \\
H_{ix^2-y^2,j3z^2-r^2} &= \tfrac{1}{2}\sqrt{3}\left(l^2 - m^2\right)\left(n^2 - \tfrac{1}{2}\left(l^2 + m^2\right)\right) P_{dd\sigma} + \sqrt{3}n^2\left(m^2 - l^2\right) P_{dd\pi} + \tfrac{1}{4}\sqrt{3}\left(1 + n^2\right)\left(l^2 - m^2\right) P_{dd\delta} \\
H_{i3z^2-r^2,j3z^2-r^2} &= \left(n^2 - \tfrac{1}{2}\left(l^2 + m^2\right)\right)^2 P_{dd\sigma} + \sqrt{3}n^2\left(l^2 + m^2\right) P_{dd\pi} + \tfrac{3}{4}\left(l^2 + m^2\right)^2 P_{dd\delta}(R_{ij})
\end{aligned}
$$

Table E.1: Hamiltonian and overlap elements for a crystal in terms of two-center integrals (see Ref. [133]). Only the Hamiltonian elements $H_{i\alpha,i\beta,\sigma}$ are given, and the spinindex σ has been suppressed. The overlap elements $S_{i\alpha,i\beta}$ are identical in their form, and only the interaction integrals P_γ need to be replaced by different polynomials (see Eq. (E.7)). All integrals $H_{i\alpha,i\beta,\sigma}$ can be expressed as functions of the directional cosines $l = \left(R_{x,j} - R_{x,i}\right)/R_{ij}$, $m = \left(R_{y,j} - R_{y,i}\right)/R_{ij}$, and $n = \left(R_{z,j} - R_{z,i}\right)/R_{ij}$. (Here $R_{q,j}$ is the cartesian compontent q of the vector $\vec{R}_j$ and $R_{ij} = \left|\vec{R}_j - \vec{R}_i\right|$ is the distance between the atoms i and j.) Notice that the matrix elements $H_{i\alpha,i\beta,\sigma} = H_{i\alpha,i\beta,\sigma}(\vec{R}_j - \vec{R}_i)$ are functions of the relative position of the atoms i and j, while the integrals $P_\gamma = P_\gamma(R_{ij})$ are functions of their distance only. Other matrix elements are found by permuting the indices and appropriately interchanging the directional cosines. The spin index σ should not be confused with the σ which specifies the type of integral (for example $P_{ss\sigma}$), where it refers to the component of angular momentum around the axis between the atoms i and j.

For other integrals, the derivations is the same.

Next we want to derive the algebraic of the Hamiltonian element $H_{ix,jyz}(\vec{R}_j - \vec{R}_i)$. First we notice that the integrals in Table E.1 only depend on the relative distance $\vec{R}_j - \vec{R}_i$. For this reason, we set the origin into the position of atom i ($\vec{R}_i = 0$) and consider the matrix element $H_{0x,jyz}(\vec{R}_j)$. It is possible to find a new coordinate system K' in which the rotated vector $\vec{R}'_j$ is located on the z axis. The old coordinate system K is connected with the new one by means of two subsequent rotations

$$\vec{R}'_j = (0, 0, R_j)^T = D_z(\psi) D_x(\varphi) \vec{R}_j.$$

In this expression $D_z(\psi)$ ($D_x(\varphi)$) is a rotation around the z axis (x axis) with an angle ψ (φ). We observe that

$$\begin{pmatrix} x \\ y \\ z \end{pmatrix} = D_z(\psi) D_x(\varphi) \begin{pmatrix} x' \\ y' \\ z' \end{pmatrix} = \begin{pmatrix} x' \cos(\psi) - y' \sin(\psi)\cos(\varphi) + z' \sin(\psi)\sin(\varphi) \\ x' \sin(\psi) + y' \cos(\psi)\cos(\varphi) - z' \cos(\psi)\sin(\varphi) \\ y' \sin(\varphi) + z' \cos(\varphi) \end{pmatrix} \tag{E.8}$$

In terms of the direction cosines $l = x/r$, $m = y/r$, and $n = z/r$ this relation tells that for $\vec{R}'_j = (0, 0, R_j)^T$ we get $l = \sin(\psi)\sin(\varphi)$, $m = -\cos(\psi)\sin(\varphi)$, and $n = \cos(\varphi)$.

Next we consider the integrals between p and d orbitals that may arise if $\vec{R}_j$ is aligned along the positive z direction $\vec{R}_j = (0, 0, R_j)^T$, meaning that $l = m = 0$ and $n = 1$. Many Hamiltonian elements $H_{i\alpha,j\beta}(\vec{R}_j - \vec{R}_i)$ (where α is a p orbital and β a d orbital) vanish. The nonvanishing ones can be used to define the basic Hamiltonian integrals P_γ of Eq. (E.7). As sketched in Fig. E.1, there are only two nonvanishing Hamiltonian elements, namely $H_{0x,jzx}(\vec{R}_j)$, $H_{0y,jyz}(\vec{R}_j)$, and $H_{0z,j3z^2-r^2}(\vec{R}_j)$. The first two are identical and define $P_{pd\pi}(R_j)$, whereas the last one defines $P_{pd\sigma}(R_j)$. As explained before, σ and π refer to the component of angular momentum around the axis between the atoms i and j.

Equipped with this knowledge, it is now straightforward to derive the expression for the Hamiltonian matrix element

$$H_{0x,jyz}(\vec{R}_j) = \int d^3r \psi_x(\vec{r}) H \psi_{yz}(\vec{r} - \vec{R}_j).$$

The orbital functions ψ_α, where α is a p or d state, can be written as

$$\begin{aligned} \psi_x(\vec{r}) &= f_1(r)\, x \\ \psi_y(\vec{r}) &= f_1(r)\, y \\ \psi_z(\vec{r}) &= f_1(r)\, z \end{aligned}$$

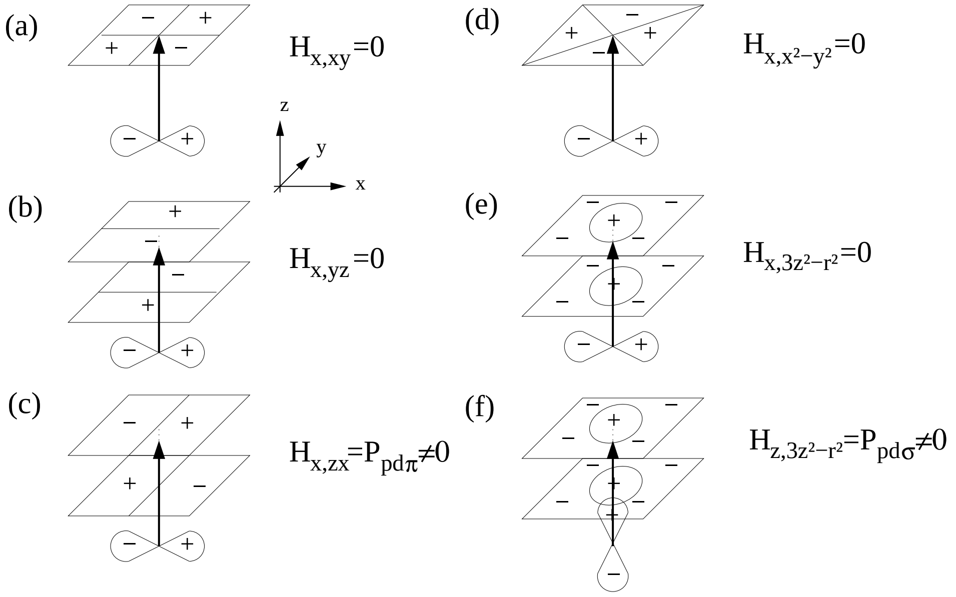

Figure E.1: Two-center Hamiltonian elements $H_{0\alpha,j\beta}(\vec{R}_j)$ for the orbitals $\alpha = x$ and (a) $\beta = xy$, (b) $\beta = yz$, (c) $\beta = zx$, (d) $\beta = x^2 - y^2$, and (e) $\beta = 3z^2 - r^2$, whereas in (f) $\alpha = z$ and $\beta = 3z^2 - r^2$. Due to the choice $l = m = 0$ and $n = 1$ in the situation sketched, the Hamiltonian elements $H_{0\alpha,j\beta}$ are equal to the basic interaction integrals P_γ for the nonvanishing integrals ($H_{0\alpha,j\beta}(\vec{R}_j) = P_\gamma(R_j)$). Only the integrals $H_{0x,jzx}(\vec{R}_j) = P_{pd\pi}(R_j)$, $H_{0y,jyz}(\vec{R}_j) = P_{pd\pi}(R_j)$, and $H_{0z,j3z^2-r^2}(\vec{R}_j) = P_{pd\sigma}(R_j)$ are nonzero and the others vanish for symmetry reasons, as is immediately obvious from the picture.

and

$$
\begin{aligned}
\psi_{xy}(\vec{r}) &= f_2(r)\,xy \\
\psi_{yz}(\vec{r}) &= f_2(r)\,yz \\
\psi_{zx}(\vec{r}) &= f_2(r)\,zx \\
\psi_{x^2-y^2}(\vec{r}) &= f_2(r)\,\frac{(x^2-y^2)}{2} \\
\psi_{3z^2-r^2}(\vec{r}) &= f_2(r)\,\frac{(3z^2-r^2)}{2\sqrt{3}}
\end{aligned}
$$

where $f_1(r)$ and $f_2(r)$ are arbitrary functions of the radius r only. The basis functions ψ_x and ψ_{yz} can be then be expressed in the coordinate system K' by use of Eq. (E.8) as

$$
\begin{aligned}
\psi_x(\vec{r}) &= f_1(r')\,(x'\cos(\psi) - y'\sin(\psi)\cos(\varphi) + z'\sin(\psi)\sin(\varphi)) \\
\psi_{yz}(\vec{r}) &= f_2(r')\,(x'\sin(\psi) + y'\cos(\psi)\cos(\varphi) - z'\cos(\psi)\sin(\varphi))\,(y'\sin(\varphi) + z'\cos(\varphi))
\end{aligned}
$$

If one uses this form of the basis functions together with the relations for the directional cosines $l = \sin(\psi)\sin(\varphi)$, $m = -\cos(\psi)\sin(\varphi)$, and $n = \cos(\varphi)$ given above, and identifies

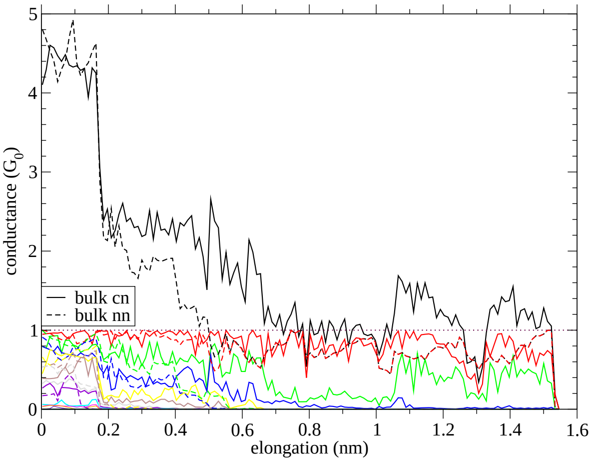

Figure E.2: Comparison of conductance traces for the contact shown in Fig. 2.18. The traces are obtained with bulk electrode Green's functions. The curve labeled "bulk cn" is the conductance together with the corresponding channel decomposition (solid lines) as presented in Fig. 2.18. The shortcut "cn" shall indicate, that the local charge neutrality has been imposed (see Sec. 2.2.2). In contrast, the curve labeled "bulk nn" is the conductance together with the corresponding channel decomposition (broken lines) as obtained, if the unmodified TB parameters are used as presented in Sec. E.1. The shortcut "nn" stands for "no local charge neutrality" and shall indicate, that the unmodified TB parameters have been used.

the different integrals according to Fig. E.1, one readily obtains

$$H_{0x,jyz}(\vec{R}_j) = \sqrt{3}lmnP_{pd\sigma}(R_j) - 2lmnP_{pd\pi}(R_j),$$

as given in Table E.1.

E.2 Local charge neutrality condition

If the TB parameters are used in conductance calculations of atomic contacts without modifications, it turns out that they yield unphysical results. This is illustrated in Fig. E.2. Here, the conductance is plotted together with its decomposition into different transmission channel contributions during the stretching of the Pt contact shown in Fig. 2.18. Two different cases are compared, namely first the conductance as obtained with the local charge neutrality imposed, labeled "cn" for local charge neutrality (see Sec. 2.2.2) and second that conductance without local charge neutrality, labeled "nn" for no local charge neutrality. In the nn case, the TB parameters are used as presented in Sec. E.1 without modification.[5] From Fig. E.2 it is evident that, as soon as the characteristic contact evolution sets in at an elongation of around 0.2 nm, the conductance of the charge neutral case differs strongly from the conductance as obtained with the original TB parameters. In addition the conductance in the chain configuration never surmounts $1G_0$ in the nn case, and there is only one open conduction channel. The conductance histogram of Pt possesses a peak at around $1.5G_0$ [20] (see Fig. 2.2), and there is strong experimental

---

[5] Note that we have included the electrode atoms in the calculation of the onsite levels of the central system (see Eqs. (E.4) and (E.6)).

and theoretical evidence that dimer and chain configurations exhibit a conductance above $1G_0$ [12, 20, 106, 107, 98, 105, 108], which requires the presence of more than a single conduction channel for these configurations. In this sense, the unmodified application of the TB parameters of Refs. [75, 76, 77] in the field of electron transport fails to describe the physics in an obvious way.

The reason for this problem can be seen in the fact that the local environment in the neck region of our contacts is very different from that in the bulk material, for which the TB parameters have been developed. This can cause large deviations from the approximate local charge neutrality that typical metallic elements must exhibit. A modification of the TB parameters is therefore justified, in which a local charge neutrality condition is imposed on the atoms in the central part of the nanowire through a self-consistent variation of the Hamiltonian. In this way the atomic levels align properly. As explained in Sec. 2.2.2, this self-consistent procedure requires the computation of the electronic density matrix ϱ_{CC}, which is obtained by integrating the Green's function of the center up to the Fermi energy E_F (for details see also Eq. B.48)

$$\varrho_{CC} = -\frac{1}{\pi}\int_{-\infty}^{E_F} \mathrm{Im}\left[\sum_{\sigma} G^r_{CC,\sigma}(E)\right] dE. \tag{E.9}$$

In this expression $G^r_{CC,\sigma}$ is the retarded Green's function of the central part of the contact

$$G^r_{CC,\sigma}(E) = \left[(E + i\eta_C) S_{CC} - H_{CC,\sigma} - \Sigma^r_{L,\sigma} - \Sigma^r_{R,\sigma}\right]^{-1}, \tag{E.10}$$

where σ stands for the spin component, S_{CC} is the overlap matrix of the center, $H_{CC,\sigma}$ is the Hamiltonian, and $\Sigma_{X,\sigma}$ (with $X = L$ or R) are the self-energies that describe the coupling of the center to the electrodes. They are given by

$$\Sigma^r_{X,\sigma}(E) = (H_{CX,\sigma} - ES_{CX})\, g^r_{XX,\sigma}(E)\, (H_{XC,\sigma} - ES_{XC}) \tag{E.11}$$

with the unperturbed, retarded electrode Green's function $g^r_{XX,\sigma}$ and the hopping (overlap) matrices between the center and the electrodes $H_{CX,\sigma}$ (S_{CX}). In the following we will give more details about the way, in which this integration is performed and how the local charge neutrality is achieved.

First, we note that in Eq. (E.9) the Fermi energy of the respective metal under investigation is required. For this purpose, we construct first the bulk density of states (DOS) (see Sec. D.1.1 for details of this construction). In Fig. E.3 the bulk DOS is plotted for the different metals investigated in this work. While in the main panel the DOS is plotted resolved in its orbital contributions (the s, p, and d states), the inset of each figure shows the total DOS, which is the sum of the different orbital contributions. As explained in Sec. D.1.1 there exists a balance between the broadening parameter η, used in the construction of the bulk DOS, and the number of k-points, which is 32^3 in the plots of Fig. E.3. It is visible, how the total DOS is getting less "peaky" if the broadening η is reduced as indicated in the insets. For all our calculations with the TB parameters, we have chosen a constant broadening of $\eta = 0.02$ Ry $= 0.272$ eV in the electrodes, in order to simulate

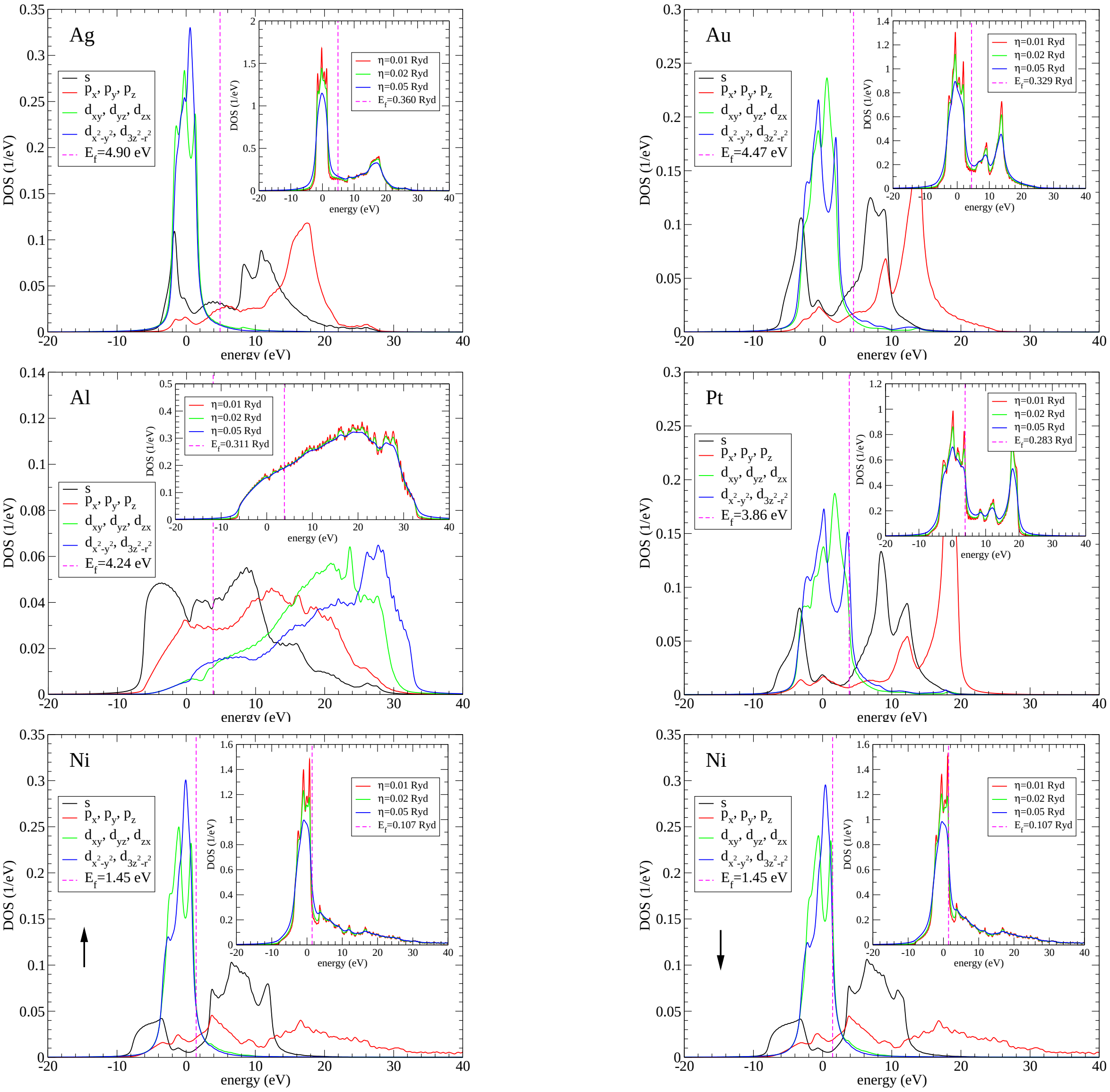

Figure E.3: DOS of a bulk atom for the metals Ag, Au, Al, Pt, and Ni. For Ni both spin components are displayed, while for the other metals the DOS is plotted for one of the degenerate spin components. In the main part of the figures the DOS for the different materials is plotted resolved in its orbital contributions for a broadening parameter $\eta = 0.02$ Ry $= 0.272$ eV. In addition, the inset of each figure shows the total DOS as the sum of all orbital contributions for broadenings of $\eta = 0.05$, 0.02, and 0.01 Ry. Furthermore the Fermi energy is indicated, as obtained by integrating the total DOS to the valence charge of the neutral atom, which is 5.5, 5.5, 1.5, and 5 per spin component for Ag, Au, Al, and Pt in this valence orbital TB model. For Ni the two spin components need to be added before the integration, where the total valence charge is 10 for the Ni atom. In every plot the number of k-points has been chosen to be 32^3. The lattice constants assumed in the plot are the same as given in Table E.2.

a continuous DOS with a characteristic structure but no artificial peaks, due to the finite number of k-points employed. From the plot of the DOS we obtain the Fermi energy via an integration to the number of valence charges provided by each atom. This Fermi energy is indicated in the legends. It is in all cases positive, which indicates that it is not of physical relevance, but only a reference point for our calculations.[6]

Let us shortly interrupt the discussion on the details of the charge neutrality and discuss the DOS of the various metals shown in Fig. E.3. For the noble metals Ag and Au a dominance of the s contribution to the DOS can be noticed at the Fermi energy E_F and a rather flat total DOS. While the DOS of Pt looks similar to that of Au, E_F is located at the edge of the d states due to the single valence electron less for Pt as compared to Au. On the other hand Al exhibits a very different DOS with respect to the aforementioned metals which is due to the fact that for this p-valent metal the d states lie mainly above E_F. The total DOS looks rather parabolic from the band bottom up to the Fermi energy. For Ni the DOS for the minority spin ($\sigma =\downarrow$) shows similarities to Pt with strong contributions of d states at E_F, while for the majority component ($\sigma =\uparrow$) the contribution of the d states is reduced, corresponding to a situation more similar to Au.

In the necessary integration of G^r_{CC} in Eq. (E.9) we distinguish three different broadening parameters. As indicated in Eq. (E.10), there is a broadening η_C for the cental part of the Green's function. In addition, the electrode Green's function $g^r_{XX,\sigma}$ needs a broadening η_X. In principle the perturbations $t_{CX} = H_{CX,\sigma} - ES_{CX}$ could also be provided with a broadening. There, however, we take the limit of zero broadening in order to obtain real perturbations (see also Sec. B.3.1). As explained before, the broadening η_X is chosen to be 0.02 Ry, in order to model a continuous DOS in the electrodes (see the plots of the DOS in Fig. E.3). Obviously, a high η results in a smooth behavior of $\mathrm{Im}\,[G]$. For this reason it facilitates the integration in Eq. (E.9), if η_C is as large as possible. However, the convergence with respect to conductance calculations needs to be checked, where η_C is always chosen to be negligible, namely $\eta_{CC} = 10^{-8}$ Ry. We will show below that in the integration $\eta_C = 10^{-4}$ Ry yields reasonably converged results for the conductance.

In order to use as few integration points as possible, it is advisable to choose an integration contour in the complex plane as explained in Sec. B.3.3. In the case of the TB parameterization discussed here, we resort to a semicircular contour in the complex plane. (Such a contour is displayed in Fig. E.7.) We have chosen the semicircle to begin on the real energy axis at $E_B = -5$ Ry, well below all energy levels of the valence electron description. Then, the radius of the semicircle in the upper half of the complex plane is chosen such that it ends on the real energy axis at the energy E_F, which is determined from an integration of the bulk DOS. The integration can thus be written

$$\varrho_{CC} = -\frac{1}{\pi}\mathrm{Im}\left[\int_\gamma dz \sum_\sigma G^r_{CC,\sigma}(z)\right] \tag{E.12}$$

---

[6] All energies in quantum chemistry are commonly measured with respect to the vacuum level and are therefore negative for electronically stable systems.

with the semicircular integration contour γ, the Green's function

$$G^r_{CC,\sigma}(z) = \left[(z + i\eta_C)\, S_{CC} - H_{CC,\sigma} - \Sigma^r_{L,\sigma}(z) - \Sigma^r_{R,\sigma}(z)\right]^{-1}, \tag{E.13}$$

and the self-energies

$$\Sigma^r_{X,\sigma}(z) = (H_{CX,\sigma} - zS_{CX})\, g^r_{XX,\sigma}(z + i\eta_X)\, (H_{XC,\sigma} - zS_{XC}), \tag{E.14}$$

where we indicate the different broadening parameters η_C and η_X explicitly.

In case that the integration in Eq. (E.12) has been carried out and ϱ_{CC} has been obtained, the charge of every atom in the central part of the system needs to be determined. For this purpose, we employ the Mulliken population analysis[7] [81] to obtain the charge N_i for the atom i

$$N_i = \sum_\alpha (\varrho S)_{i\alpha,i\alpha}. \tag{E.15}$$

where α runs over all orbitals of the atom. In principle, Eq. (E.15) includes charge contributions from both the center and the electrodes

$$N_i = \sum_{\alpha,j\in L} \varrho_{i\alpha,j} S_{j,i\alpha} + \sum_{\alpha,j\in C} \varrho_{i\alpha,j} S_{j,i\alpha} + \sum_{\alpha,j\in R} \varrho_{i\alpha,j} S_{j,i\alpha}, \tag{E.16}$$

where $j \in L$, C, or R means that j refers to an orbital in the left, central, or right part of the system. For simplicity j is restricted to C in our calculations, and charges in the electrodes are neglected, resulting in

$$N_i = \sum_\alpha (\varrho_{CC} S_{CC})_{i\alpha,i\alpha} \tag{E.17}$$

We want to point out that it is in principle possible to take into account the charge contribution of the electrodes to the central system by use of the relation (see Eq. (A.71))

$$G^r_{CX} = G^r_{CC} t_{CX} g^r_{XX}$$

The complete charge matrix N_{CC} of the center is given by

$$\begin{aligned} N_{CC} &= -\frac{1}{\pi} \sum_{W=L,C,R} \mathrm{Im} \left[\int_\gamma dz \sum_\sigma G^r_{CW,\sigma}(z) \right] S_{WC} \qquad \text{(E.18)} \\ &= -\frac{1}{\pi} \mathrm{Im} \left[\int_\gamma dz \sum_\sigma G^r_{CC,\sigma}(z) \left\{ S_{CC} + \sum_{X=L,R} t_{CX.\sigma} g^r_{XX,\sigma}(z) S_{XC} \right\} \right] \end{aligned}$$

---

[7] The Mulliken population analysis $N_i = \sum_\alpha (\varrho S)_{i\alpha,i\alpha}$ is preferred to the Löwdin analysis $N_i = \sum_\alpha (S^{1/2} \varrho S^{1/2})_{i\alpha,i\alpha}$, which would be more consistent with the LDOS calculation (see Eq. (2.12)) due to efficiency reasons. First the square root of the overlap does not need to be computed in the Mulliken population analysis. But the main advantage is the saving of an additional matrix multiplication required in every step of the iterative solution of the charge-neutrality condition, which requires that $|N_i - N_{\mathrm{atom}}| < 0.02$ for every atom i of the central part of the nanowire.

and

$$N_i = \sum_{\alpha} (N_{CC})_{i\alpha,i\alpha} \, .$$

The integral in Eq. (E.18) is not more complicated to carry out than Eq. (E.12), because all Green's functions and other matrices are known. We have implemented this kind of charge determination for testing purposes, although it results in a higher numerical effort as compared to the use of Eq. (E.17). It turned out that this charge determination has an influence on the conductance for thick contacts due to interface effects. But during the stretching process, the narrowest part of the junction plays an increasingly important role, so that finally the approximation, that only charge contributions from the center are accounted for in Eq. (E.17), becomes unimportant.

Now, that ϱ_{CC} has been obtained via Eq. (E.12) and the charge N_i for every atom i in the center is known from Eq. (E.17), we need to transform the deviation from the charge neutrality $N_i - N_{\text{atom}}$ with the reference charge N_{atom} of the neutral metal atom into a change of the matrix elements of the Hamiltonian. We define the differential shift $\delta\phi_i^{(n)}$ of the atom i in the nth loop of the self-consistent charge neutrality loop as

$$\delta\phi_i^{(n)} = d^{(n)} \left(N_i - N_{\text{atom}}\right) , \tag{E.19}$$

with a conversion factor $d^{(n)} < 1$ Ry that may depend on the number of the actual iteration. In our simulations we found that it is crucial to work with conversion factors $d^{(n)}$, which decrease with the iteration number n. The use of big $d^{(n)}$s in the first iterations may accelerate the convergence to a charge neutral solution, but no solution may be found without the use of decreasing $d^{(n)}$s. The total shift in the nth iteration is then given as

$$\phi_i^{(n)} = \phi_i^{(n-1)} + \delta\phi_i^{(n)}$$

and the Hamiltonian is modified according to the prescription

$$H_{i\alpha,j\beta}^{(n)} = H_{i\alpha,j\beta}^{(0)} + S_{i\alpha,j\beta} \frac{\phi_i^{(n)} + \phi_j^{(n)}}{2} \tag{E.20}$$

where $S_{i\alpha,j\beta}$ is the overlap matrix element between atom i with orbital α and atom j with orbital β and $H_{i\alpha,j\beta}^{(0)}$ is the original Hamiltonian element from the TB parameterization explained in Sec. E.1. In this way a constant shift of all energies $\varepsilon_\mu \rightarrow \varepsilon_\mu + \phi$ in the center is insured for a uniform shift $\phi = \phi_i^{(n)}$ of all atoms i [80] due to the Schrödinger equation $\sum_j H_{ij} c_{\mu j} = \varepsilon_\mu \sum_j S_{ij} c_{j\mu}$ (see Eq. (B.21)). The iterative procedure to determine a locally charge neutral Hamiltonian is stopped, if the charge N_i of every atom i of the central part of the nanowire differs from the reference charge N_{atom} by less then 0.02 electron charges ($|N_i - N_{\text{atom}}| < 0.02$).

If the overlap matrix is assumed to be diagonal $S_{i\alpha,j\beta} = \delta_{ij}\delta_{\alpha\beta}$, one obtains a shift of the diagonal elements only,[8] namely

$$H_{i\alpha,i\alpha}^{(n)} = H_{i\alpha,i\alpha}^{(0)} + \phi_i^{(n)} \tag{E.21}$$

---

[8] Notice that $S_{i\alpha,j\beta} = \delta_{ij}\delta_{\alpha\beta}$ is assumed in the TB parameterization for $i = j$ (see Sec. E.1)

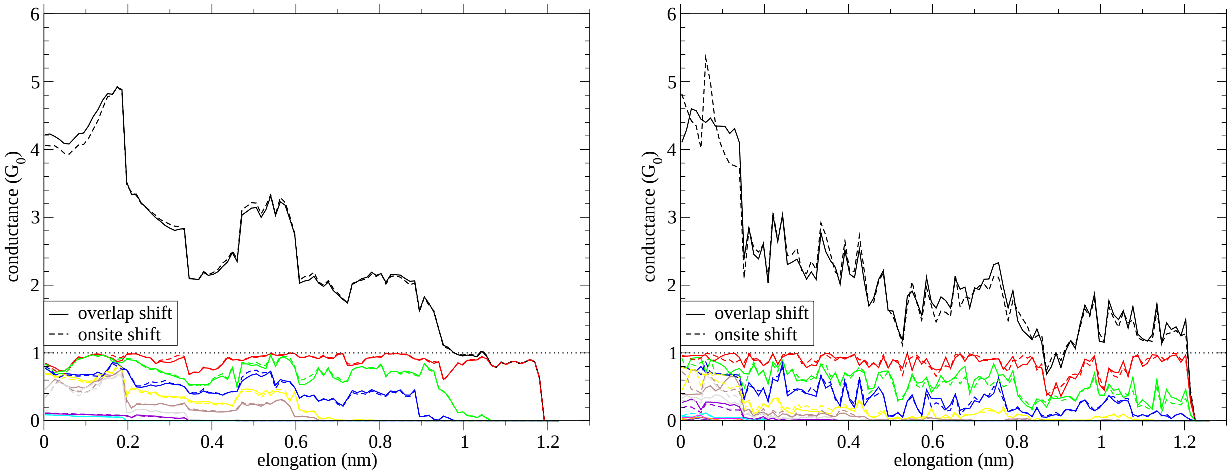

Figure E.4: Determination of the influence of the kind of shift for obtaining the local charge neutrality on the conductance. In the left panel the opening curve for the Ag contact of Fig. 2.4 is plotted. The label "overlap shift" means that the conductance is determined from a charge neutral Hamiltonian obtained by shifts considering the overlap (see Eq. (E.20)), while "onsite shift" refers to the same procedure, where the overlap is assumed to be diagonal (see Eq. (E.21)). In the right panel the same comparison is shown for the Pt contact of Fig. 2.16.

Although in this case a uniform shift in the Hamiltonian does not result in a uniform shift of all eigenvalues, this kind of shift may be more in line with the spirit of the TB parameterization. There, the local environment is only considered to modify onsite energies (see Eqs. (E.6) and (E.4)). This kind of a diagonal shift in Eq. (E.21) has been used for Au in Ref. [35] and Al in Ref. [36], while for Ag, Pt and Ni we implemented the shift as given in Eq. (E.20). For Ag and Pt we demonstrate in Fig. E.4 that these two kind of shifts yield, however, similar results. Evidently, the conductance is not very sensitive to whether Eq. (E.21) or Eq. (E.21) is used to implement the modifications needed to obtain a charge neutral Hamiltonian. The same observations can be made for the conductance histograms, which do not depend on the way the shift is implemented, as has been checked for Ag and Pt.[9]

For the complex contour integration (see Eq. (E.12)) we need appropriate integration points, in order to obtain the density matrix ϱ_{CC} in an accurate way. These integration

---

[9] The shifts of the Hamiltonian matrix elements $H_{i\alpha,j\beta}$ may also be considered as arising due to local changes of the spacial representation of an effective single-particle electronic Hamiltonian $H(\vec{r})$. The elements $H_{i\alpha,j\beta} = \int d^3r\psi_\alpha\left(\vec{r}-\vec{R}_i\right)H(\vec{r})\psi_\beta\left(\vec{r}-\vec{R}_j\right)$ can then be recalculated after a local change of $H(\vec{r})$ in a certain region around an atom l at position $\vec{R}_l$. It is clear that the new Hamiltonian elements are neither just a simple change of the diagonal elements as suggested by Eq. (E.21) nor the change as suggested by Eq. (E.20). (A uniform shift $H(\vec{r}) \to H(\vec{r}) + H_0$ yields a modification $H_{i\alpha,j\beta} \to H_{i\alpha,j\beta} + H_0 S_{i\alpha,j\beta}$ as suggested by Eq. (E.20). However, here we are interested in nonuniform shifts restricted to some spacial region.) Therefore the shifts suggested by Eq. (E.21) and Eq. (E.20) are only approximate ways to account for a, in reality, more complicated modification of Hamiltonian matrix elements.

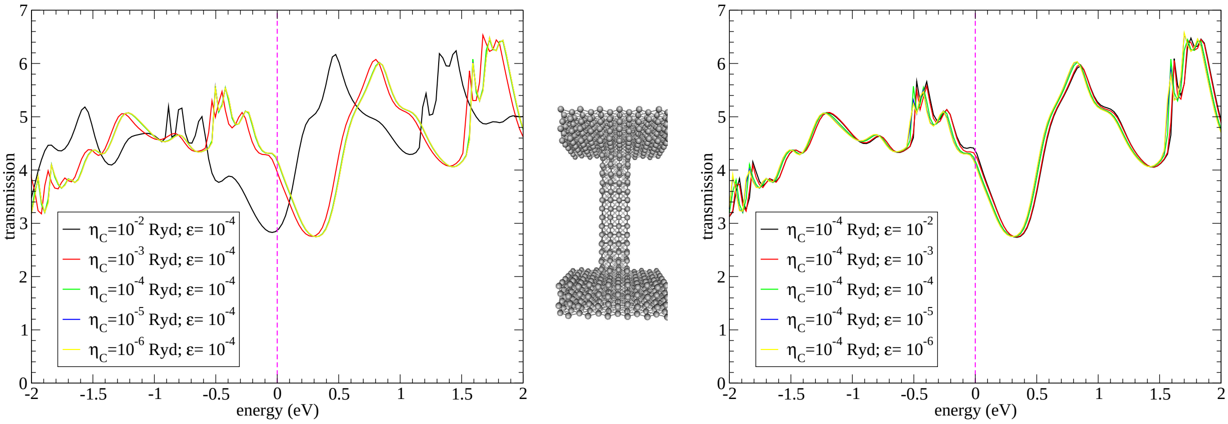

Figure E.5: Comparison of the transmissions as obtained for charge neutral Hamiltonians, determined with various broadening parameters η_C (see Eq. (E.13)) and error tolerances $\varepsilon = 10^{-2}$–10^{-6} in an adaptive integration scheme (see Eq. (E.12)). In the left panel, $\eta_C = 10^{-2}$–10^{-6} Ry is varied for a constant $\varepsilon = 10^{-4}$, in the right panel $\varepsilon = 10^{-2}$–10^{-6} is varied for a constant $\eta_C = 10^{-4}$ Ry, and in the middle the contact geometry under investigation is depicted. In this case the geometry is the starting geometry of all Ag contacts. The electrode broadening was kept constant at $\eta_X = 2 \times 10^{-2}$ Ry, mimicing a continuous electronic reservoir (see Eq. (E.14)).

points are determined by carrying out the local charge neutrality procedure for a certain configuration of a previously chosen contact with an adaptive integration routine. We use an adaptive integration scheme of the closed Newton-Cotes form [265], where a new point in the middle of an integration interval is added, if a certain error criterion is met. This error criterion is that the absolute value of the relative or absolute error in every matrix element ϱ_{ij} of ϱ_{CC} due to the new integration point, giving a contribution $d\varrho_{ij}$, needs to be smaller than ε $((|d\varrho_{ij}| < \varepsilon\, |\varrho_{ij}|) \vee (|d\varrho_{ij}| < \varepsilon))$. If this adaptive integration is applied, it turns out that configurations with a small minimum cross-section (MCS) generally require more integration points than configurations with a large MCS. For this reason we decided to carry out the adaptive integration always for two configurations of a selected contact for each metal. The first configuration was chosen to be the starting configuration of the contact, while the second configuration was either a dimer or chain configuration (see Figs. E.5 and E.6 for the configurations chosen for Ag). During every iteration n in the charge neutrality loop the integration points were written out. After the convergence to a charge neutral Hamiltonian was achieved, we took the set union of all integration points needed in this iterative process. The set union of integration points for the starting configuration always turned out to be a subset of the chain or dimer configuration studied later. For different dimer or chain configurations only few different or additional integration points were found. Thus it seems to be a good approximation to determine the set of integration points only once as the set union of integration point obtained in the charge neutrality loop for a certain chain or dimer configuration using the adaptive integration scheme. This set of integration points is then employed in a nonadaptive integration scheme in order to construct ϱ_{CC},

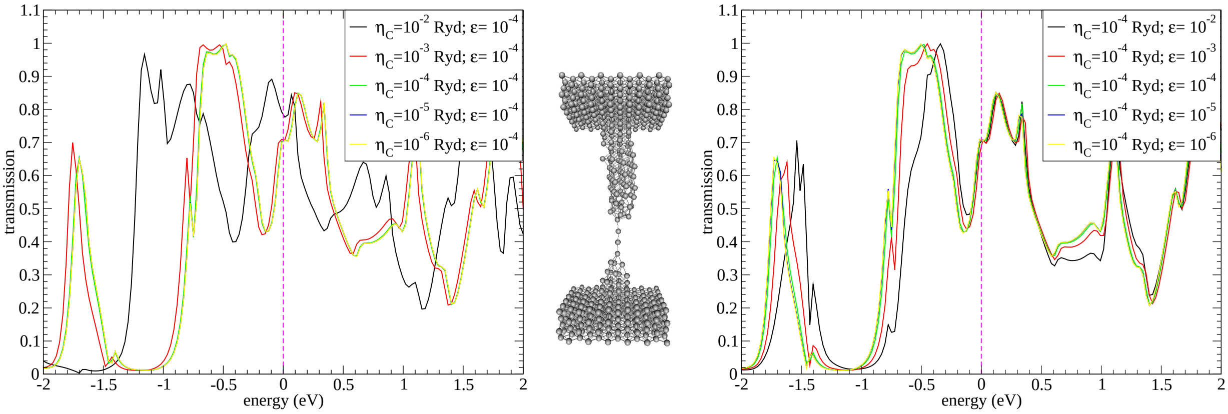

Figure E.6: The same comparison as in Fig. E.5 now for a chain configuration of an Ag contact.

when we need locally charge neutral Hamiltonians for the complete stretching process of a contact. This is mandatory, because the adaptive integration turns out to be very time consuming, and we cannot afford an adaptive integration for all the configurations, for which we need to calculate the conductance in the stretching process of our nanowires. In Fig. E.7 we show the integration point set used in the nonadaptive integration of the Ag contacts. It is remarkable that the integration points are very dense, when the semicircular integration contour γ approaches the real axis at the Fermi energy E_F. This is expected, because there are many states located at this position and the broadening of states becomes minimal. Therefore the integration needs to resolve the details of the integrand, resulting in a high number of required integration points.

As indicated in the caption of Fig. E.7 the broadening parameters $\eta_C = 10^{-4}$ Ry, $\eta_X = 2 \times 10^{-2}$ Ry (see Eqs. (E.13) and (E.14)), and a relative or absolute error tolerance of $\varepsilon = 10^{-4}$ have bee used to generate the integration points. Keeping the broadening η_X in the electrodes constant, we demonstrate in Figs. E.5 and E.6 that η_C and ε are sufficiently small in order to insure converged conductance results. It can be noted that the conductance is very sensitive to changes in η_C. A broadening of $\eta_C = 10^{-2}$ Ry, as used in Ref. [266] for the integration, yields meaningless results, while for $\eta_C = 10^{-4}$ Ry the results do not differ any more from $\eta_C = 10^{-5}$ or 10^{-6} Ry. The error criterion ε used in the integration does not have a big influence on the accuracy of the conductance for big MCS contacts (see Fig. E.5) but for a decreasing MCS an error criterion of $\varepsilon \leq 10^{-4}$ is recommendable (see Fig. E.6).

Also for all other metals, namely Au, Al, Pt, and Ni, the parameters $\eta_C = 10^{-4}$ Ry and $\varepsilon = 10^{-4}$ turned out to be sufficient for getting converged conductance results. The number of integration points used in the conductance calculations of the stretching processes for the metals Ag, Au, Al, Pt, and Ni, as determined from the adaptive integration, were 140, 149, 139, 165, and 156.

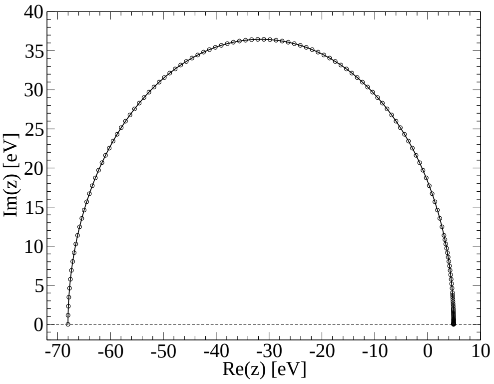

Figure E.7: Integration contour γ, as chosen in the determination of the density matrix ϱ_{CC} (see Eq. (E.12)). The semicircular path γ is shown as used for Ag. The lowest energy is located at $E_B = -5$ Ry= -68.03 eV, the Fermi energy of Ag at $E_F = 0.36$ Ry= 4.9 eV (see Fig. E.3). The integration points have been obtained as the set union of points determined in an adaptive integration of the Ag contact shown in Fig. E.6 with a broadening of $\eta_C = 10^{-4}$ Ry in the center, of $\eta_X = 2\times10^{-2}$ Ry in the electrodes and an error tolerance of $\varepsilon = 10^{-4}$ (see explanations in the text). The total number of integration points has been determined to be 140 for Ag. It can clearly be seen, how the adaptive integration routine chooses an ever denser integration point mesh, when getting close to E_F.

E.3 Electrode geometry for electron transport calculations

In Sec. 2.2.2 we explained that the left (L) and right (R) electrodes are constructed such that all the hopping elements from the 112 wire atoms, which we will call the central part or center (C) of our contact, to the electrodes are taken into account. We want to explain shortly, how this construction works.

In Fig. E.8 we display in the left panel the geometry, as used in the structure calculations of the stretching process (see Sec. 2.2.1) with 112 wire atoms and 288 slab atoms. For the conductance calculations we embed the 288 electrode atoms into [001] layers containing 1200 atoms each (see middle panel of Fig. E.8). These new electrode clusters have been checked to be big enough so that all couplings from the 112 wire atoms to the electrode are included at any time of the stretching process for all contacts of a particular metal. Due to the huge number of atoms in this geometry, the matrix multiplications in the charge neutrality loop or the computation of the conductance would become impracticable. A tremendous reduction in the number of electrode atoms results, however, if the cutoff radius R_c of the TB parameterization (see Sec. E.1) is exploited. When we consider for all wire atoms only the electrode atoms less than R_c apart, we arrive at the geometry shown in the right panel of Fig. E.8. In this particular example there are only 160 in the left and right electrode, respectively.

It is possible to exploit the cutoff radius by implementing sparse matrix multiplications (see Ref. [266]). In this case the atoms in the central part of the wire need to update the number of neighbor atoms within R_c, whenever the geometry changes during the evolution

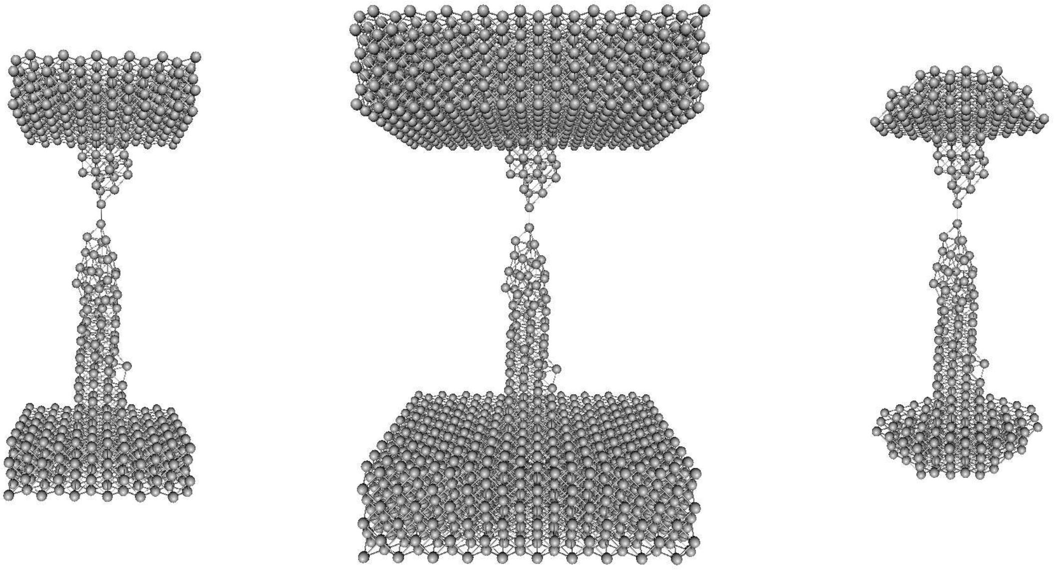

Figure E.8: To the left the geometry is shown as used in the structure determination of the molecular dynamics (MD) simulations. We consider an Ag contact. In the middle the electrode atoms have been embedded into large [001] layers, designed to include all the electrode atoms coupled to the central wire at any time of the stretching process for all contacts of the particular metal. The rightmost figure shows the atoms really needed in the computation of the conductance, namely all electrode atoms lying at most a cutoff radius R_c away from one of the atoms of the central system ($\left|\vec{R}_i - \vec{R}_j\right| < R_c$, where i is an electrode atom and there exists at least one atom j in the central part of the contact, for which their distance is less than the cutoff radius R_c).

of a stretching process. This generates a large overhead of indices that need to be taken care of. For this reason we decided not to exploit this feature. For contact geometries consisting of more atoms than studied in this work, a sparse matrix multiplication should be mandatory.

E.4 Estimate for the breaking force of a metallic bond in a crystal

In this paragraph we give a short derivation of an estimate for the force needed to break a bulklike bond in a fcc lattice (see Eq. (E.24)). The reasoning follows Ref. [70] (see Ref. 25 therein), where, however, no derivation is given.

The total energy of a crystal can approximately be written as $E_N(r) = NE(r)$, where N is the number of atoms in the volume V of the considered crystal, $E(r) = E_{\text{coh}}E^*(r^*)$ is the energy of a single atom as a function of the Wigner-Seitz radius, E_{coh} is the equilibrium cohesive energy (or enthalpy of formation), and $E^*(r^*)$ is the "universal" energy function $E^*(r^*) = -(1+r^*)\exp(-r^*)$ [124]. The Wigner-Seitz radius r is defined as $r = (3/4\pi n_A)^{1/3}$ with the atom density n_A. Because $n_A = N/V = 4/a^3$ in a fcc crystal, r is connected with the fcc lattice constant a via $r = (3/16\pi)^{1/3}\,a$. Additionally, $r^* = (r - r_0)/\ell$ is the scaled Wigner-Seitz radius and r_0 the equilibrium value of r. The length scale ℓ is related to the bulk modulus B, and it can be shown [124] that

$$\ell = \sqrt{\frac{E_{\mathrm{coh}}}{12\pi B r_0}} = \left(\frac{16\pi}{3}\right)^{\frac{1}{6}} \sqrt{\frac{E_{\mathrm{coh}}}{12\pi B a_0}} \tag{E.22}$$

with the equilibrium fcc-lattice constant a_0.

Eq. (E.22) can be proven as follows. Due to its basic definition the bulk modulus is given as

$$\begin{aligned} B &= V_0 \left.\frac{\partial^2 \bar{E}_N}{\partial V^2}\right|_{T,N,V=V_0} \\ &= V_0 \left\{ \frac{\partial^2 r}{\partial V^2} \underbrace{\left.\frac{\partial E_N}{\partial r}\right|_{r=r_0}}_{=0} + \left(\frac{\partial r}{\partial V}\right)^2 \left.\frac{\partial^2 E_N}{\partial r^2}\right|_{r=r_0} \right\}, \end{aligned}$$

where we denoted $\bar{E}_N(V) = E_N(r)$ and $V_0 = N4\pi r_0^3/3$ shall be the equilibrium volume of the crystal [267]. The first term in the second line vanishes, because $\partial E_N/\partial r|_{r=r_0} = 0$ in the equilibrium position of the atoms. If we rewrite the derivative $\partial r/\partial V = r_0/3V$ then we finally get

$$B = \frac{E_{\mathrm{coh}}}{12\pi r_0 \ell^2} = \left(\frac{16\pi}{3}\right)^{1/3} \frac{E_{\mathrm{coh}}}{12\pi a_0 \ell^2},$$

which is nothing else but Eq. (E.22).

An estimate for the maximal force F needed to break a bulklike bond may be obtained at the the inflection point of $E_N(r)$ at a Wigner-Seitz radius $r_{\mathrm{IP}} = r_0 + \ell$ (where IP stands for inflection point). If we use the relation $r = (3/16\pi)^{1/3}\sqrt{2}x$ between the Wigner-Seitz radius and the fcc nearest-neighbor distance (or interatomic bond length) x, an approximate bond length at rupture of $x_{\mathrm{IP}} = (a_0 + (16\pi/3)^{1/3}\,\ell)/\sqrt{2}$ is obtained. The absolute value of the maximal force F per bond (where there are $6N$ bonds in a fcc lattice) is then given as

$$F = \frac{1}{6N} \left.\frac{d\tilde{E}_N(x)}{dx}\right|_{x=x_{\mathrm{IP}}} = \left(\frac{3}{16\pi}\right)^{\frac{1}{3}} \frac{\sqrt{2}E_{\mathrm{coh}}}{6\exp(1)\,\ell}. \tag{E.23}$$

(where $\tilde{E}_N(x) = E_N(r)$). This finally leads to the following maximal force per bond in a fcc lattice:

$$F = \sqrt{\frac{E_{\mathrm{coh}} B a_0}{8\exp(2)}}. \tag{E.24}$$

In order to obtain numerical values from Eq. (E.24), we employ the data listed in Table E.2 for the three constants E_{coh}, B, and a_0.

metal	Ag	Au	Pt	Ni
E_{coh} (eV/atom)	2.95	3.81	5.84	4.44
B (10^{11} N/m^2)	1.007	1.732	2.783	1.860
a_0 (Å)	4.09	4.08	3.92	3.52

Table E.2: Numerical values for the constants E_{coh}, B, and a_0 as used in the computation of the bulk breaking force in Table 2.1 according to Eq. (E.24). The data is taken from Ref. [268] (see Tables 3.1, 3.3, and 1.3 therein).

Appendix F

Ab-initio quantum transport – methodological details

To this chapter of the appendix we have deferred some details of the ab-initio description of electron transport. In Sec. F.1 we derive the transformation properties of the electrode parameters under rotations. Subsequently we explain how we impose the fcc space group on the electrode parameters (see Sec. F.2), before we state in Sec. F.3, how we determine the lattice vectors as needed in the construction of surface Green's functions. The final section of this work, Sec. F.4, is listing TURBOMOLE specific details. We will specify the methods and programs employed and give information on special basis sets used for the electrode description.

F.1 Transformation properties of electrode parameters under rotations

The parameters $Y_{0\alpha,j\beta}$ ($Y = S$ or H) have been extracted from an fcc ball under the condition that they are conform with the fcc space group (see Fig. 4.4). We will refer to this spherical fcc cluster henceforth as the fcc ball. The fcc ball has a certain orientation given by the primitive lattice vectors $\vec{a}_i^{ball}$ (i =1, 2, 3). For all calculations in this work the vectors $\vec{a}_i^{ball}$, from which the lead cluster is constructed, agree with the standard primitive fcc lattice vectors $\vec{a}_i^{std}$ of Eq. (D.17) ($\{\vec{R}\,\big|\,|\vec{R}| \leq R_{ball} \wedge \vec{R} = \sum_{l=1}^{3} i_l \vec{a}_l^{ball}\}$ with $\vec{a}_i^{ball} = \vec{a}_i^{std}$ and $\vec{a}_1^{std} = (0, a_0/2, a_0/2)^T$, $\vec{a}_2^{std} = (a_0/2, 0, a_0/2)^T$, and $\vec{a}_3^{std} = (a_0/2, a_0/2, 0)^T$ with the lattice constant a_0). This orientation does not need to coincide with the orientation of the contact, through which the transport shall be computed. In Fig. F.1, for example, a Au three-atom chain between Au [111] electrodes is displayed. The [111] direction has been rotated such that it coincides with the z axis. This means that the electrodes of the contact are constructed from a set of rotated lattice vectors, which we name $\vec{a}_i^{(X)}$ (i =1, 2, 3). Here X can be L or R standing for the left or right electrode.

In TURBOMOLE, basis functions are aligned along certain axes, e.g., the p functions

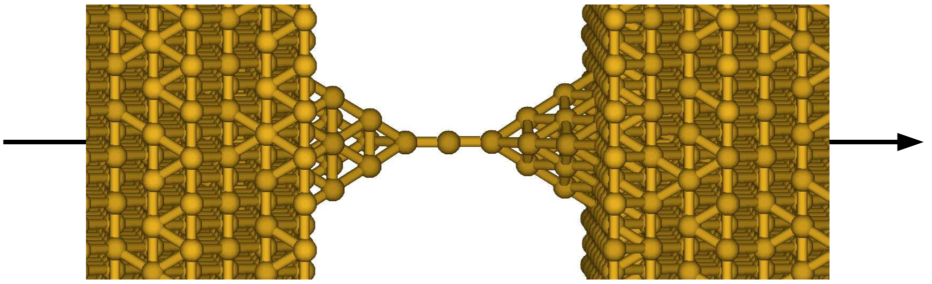

Figure F.1: Au three-atom chain between [111] pyramids, where the [111] direction has been rotated such that it coincides with the z axis.

p_x, p_y, and p_z along the x, y, and z axis, respectively. In order to employ the parameters $Y_{0\alpha,j\beta}$ in the computation of electrode Green's functions g_{XX} as needed to determine the conductance of a particular system, it is usually necessary to transform them in an appropriate way (see Fig. 4.4). This transformation includes a rotation of the atomic positions, such that the rotated vectors $\vec{a}_i^{ball}$ coincide with the vectors $\vec{a}_i^{(X)}$ of the electrode geometry ($\vec{a}_i^{(X)} = R\vec{a}_i^{ball}$). In addition, a transformation of the basis functions is required to align the basis functions again with the cartesian axes. Fig. F.2 illustrates the necessity of a transformation of the basis functions at the example of a p_y orbital.If we perform the transformation of the parameters $Y_{0\alpha,j\beta}$ according to the rotation of the lattice, we go over to the parameters $Y^{(X)}_{0\alpha,j\beta}$, where the positional index now refers to the vectors $\vec{a}_i^{(X)}$ and the orbitals have been transformed in an adequate way. In the next paragraph we will show mathematically, how the matrix elements $Y_{0\alpha,j\beta}$ transform under a rotation R.

F.1.1 Representation of rotations for s, p, and d basis functions

The parameters $Y_{0\alpha,j\beta}$ can be explicitly written as

$$\begin{aligned} Y_{0\alpha,j\beta} &= \langle 0,\alpha|\,\hat{Y}\,|j,\beta\rangle \\ &= \langle 0,\alpha|\left(\int d^3r\,|\vec{r}\rangle\,Y(\vec{r})\,\langle\vec{r}|\right)|j,\beta\rangle \\ &= \int d^3r\phi_\alpha(\vec{r})Y(\vec{r})\phi_\beta(\vec{r}-\vec{R}_j), \end{aligned}$$

where we assume that $\hat{Y} = \int d^3r\,|\vec{r}\rangle\,Y(\vec{r})\,\langle\vec{r}|$ is a single-particle operator that is diagonal in the space representation $\langle\vec{r}|\,\hat{Y}\,|\vec{r}'\rangle = Y(\vec{r})\delta(\vec{r}-\vec{r}')$ and that all basis functions ϕ_α are real. As all operators in tight-binding (TB), at the Hartree-Fock level, or in density functional theory (DFT) are effective single particle operators, all operators in this work are of this form.

Next we define for a transformation T, which takes $\vec{r}$ into $\vec{r}'$ ($\vec{r}' = T\vec{r}$), the linear

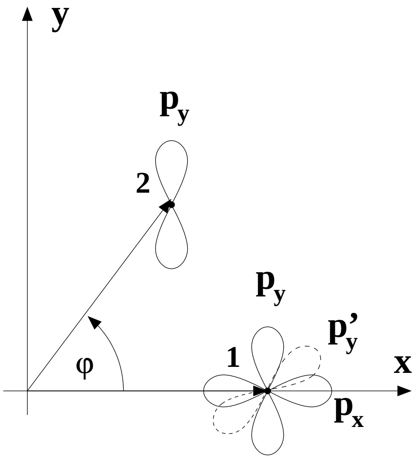

Figure F.2: The atoms 1 and 2 are related via a rotation by the angle φ in the x-y plane. A p_y orbital in the position 2 is aligned in y direction. If this p_y orbital is rotated into the position 1, now called p'_y, the orbital p'_y becomes a linear combination of the orbitals p_x and p_y in the basis of atom 1.

operator $\hat{O}_T$, which acts on a function $\psi(\vec{r})$, as [269]

$$\psi'(\vec{r}') = \hat{O}_T\psi(\vec{r}') = \psi(\vec{r}) \qquad \text{if } \vec{r}' = T\vec{r} \tag{F.1}$$

This definition can be brought into the more convenient form

$$\hat{O}_T\psi(\vec{r}) = \psi(T^{-1}\vec{r})$$

The spherical basis functions s, p, d (and higher) form a complete set of $2l+1$ linearly independent basis function for angular momentum $l = 0,\ 1,\ 2$ (and higher). For every angular momentum l a rotated basis function with angular momentum l at point $\vec{R}$ is expressible as a linear combination of the unrotated basis functions of angular momentum l at the same position, because the $2l+1$ basis functions span an invariant subspace. For this reason we can write

$$\hat{O}_R\psi^l_\nu = \psi^l_\nu(R^{-1}\vec{r}) = \sum_{\mu=1}^{2l+1} \psi^l_\mu D^l_{\mu\nu}(R), \qquad \nu = 1, ..., 2l+1 \tag{F.2}$$

where R stands for a rotation, l is the angular momentum quantum number, and $D^l_{\mu\nu}(R)$ is the representation of the rotation in terms of functions with angular momentum l. For a set of n functions (which can contain several s, p, and d functions) we can write less specifically

$$\hat{O}_R\psi_\nu = \psi_\nu(R^{-1}\vec{r}) = \sum_{\mu=1}^{n} \psi_\mu D_{\mu\nu}(R), \qquad \nu = 1, ..., n.$$

With regard to transformations of operators, it can be shown that $Y'(\vec{r}) = Y(R^{-1}\vec{r}) = \hat{O}_R Y(\vec{r}) \hat{O}_R^{-1}$, or $Y'(R\vec{r}) = Y(\vec{r})$ [269]. Using this we can analyze, how the parameters $Y_{0\alpha,j\beta}$ transform under a rotation R. Defining the transformed operator $Y'(\vec{r}) = \hat{O}_R Y(\vec{r}) \hat{O}_R^{-1}$, we get

$$\begin{aligned}
Y_{0\alpha,\vec{R}_j\beta} &= \int d^3r \phi_\alpha(\vec{r}) Y(\vec{r}) \phi_\beta(\vec{r} - \vec{R}_j) \\
&= \int d^3r \phi_\alpha(\vec{r}) Y'(R\vec{r}) \phi_\beta(\vec{r} - \vec{R}_j) \\
&= \int d^3r \phi_\alpha(R^{-1}\vec{r}) Y'(\vec{r}) \phi_\beta(R^{-1}\vec{r} - \vec{R}_j) \\
&= \int d^3r \phi_\alpha(R^{-1}\vec{r}) Y'(\vec{r}) \phi_\beta(R^{-1}\left(\vec{r} - R\vec{R}_j\right)) \\
&= \int d^3r \hat{O}_R \phi_\alpha(\vec{r}) Y'(\vec{r}) \hat{O}_R \phi_\beta(\vec{r} - R\vec{R}_j) \\
&= \int d^3r \sum_\mu \phi_\mu(\vec{r}) D(R)_{\mu\alpha} Y'(\vec{r}) \sum_\nu \phi_\nu(\vec{r} - R\vec{R}_j) D(R)_{\nu\beta} \\
&= \sum_{\mu,\nu} \left(D^T(R)\right)_{\alpha\mu} \left(\int \phi_\mu(\vec{r}) Y'(\vec{r}) \phi_\nu(\vec{r} - R\vec{R}_j)\right) D(R)_{\nu\beta} \\
&= \sum_{\mu,\nu} \left(D^T(R)\right)_{\alpha\mu} Y'_{\vec{0}\mu,R\vec{R}_j\nu} D(R)_{\nu\beta}.
\end{aligned}$$

Thus, the final result is that the matrix elements $Y_{0\alpha,j\beta}$ are obtained from the rotated matrix elements $Y'_{0\alpha,j'\beta}$ by multiplying from both sides with the representation of the rotation $D(R)$ and using $Y'_{0\alpha,j'\beta}$ at the position $\vec{R}_{j'} = R\vec{R}_j$, or in short

$$Y_{\vec{0}\alpha,\vec{R}_j\beta} = \sum_{\mu,\nu} \left(D^T(R)\right)_{\alpha\mu} Y'_{\vec{0}\mu,R\vec{R}_j\nu} D(R)_{\nu\beta}, \tag{F.3}$$

where the coordinate systems are connected by $\vec{r}' = R\vec{r}$.

In order to use this formula, the representation $D(R)$ of the rotation R needs to be obtained. In this work basis functions from s $(l = 0)$ to d $(l = 2)$ have been used. We give the representations of the rotations for these functions below.

The angular momentum l is zero $(l = 0)$ for s functions $\psi^{l=0}(\vec{r})$, their multiplicity ν is 1 $(\nu = 2l + 1 = 1)$, and they just depend on the radius $\psi^0(\vec{r}) = \psi^0(r)$. Thus we have $\hat{O}_R \psi^0(\vec{r}) = \psi^0(R^{-1}\vec{r}) = \psi^0(r) = \psi^0(\vec{r})$, and trivially the transformation for s functions is a scalar

$$D^0(R) = 1 \tag{F.4}$$

There are $\nu = 3$ p functions. In TURBOMOLE the real combinations of the angular momentum eigenfunctions $Y_{l=1}^m$ are used. They appear in the order p_x, p_y, and p_z, and can be written [245]

$$\begin{aligned} p_x(\vec{r}) &= f_1(r)x \\ p_y(\vec{r}) &= f_1(r)y \\ p_z(\vec{r}) &= f_1(r)z \end{aligned} \tag{F.5}$$

with a certain radial dependence $f_1(r)$. Therefore the rotated functions are transformed as

$$\begin{pmatrix} p'_x(\vec{r}) \\ p'_y(\vec{r}) \\ p'_z(\vec{r}) \end{pmatrix} = \begin{pmatrix} p_x(R^{-1}\vec{r}) \\ p_y(R^{-1}\vec{r}) \\ p_z(R^{-1}\vec{r}) \end{pmatrix} = \begin{pmatrix} p_x(R^T\vec{r}) \\ p_y(R^T\vec{r}) \\ p_z(R^T\vec{r}) \end{pmatrix} = R^T \begin{pmatrix} p_x(\vec{r}) \\ p_y(\vec{r}) \\ p_z(\vec{r}) \end{pmatrix}.$$

Here the orthogonality of the rotations $R^{-1} = R^T$ has been used. Therefore $\vec{p}'^T = \vec{p}R$ and from Eq. (F.2) it follows that the 3×3 representation of the rotation R for the p functions is

$$D^1(R) = R \tag{F.6}$$

For $l = 2$ there are $\nu = 5$ d functions. As for the p functions TURBOMOLE uses the real combinations of the angular momentum eigenfunctions $Y^m_{l=2}$ in the order $d_{3z^2-r^2}$, d_{xz}, d_{yz}, d_{xy}, and $d_{x^2-y^2}$, where

$$\begin{aligned} d_{3z^2-r^2} &= f_2(r)\frac{(3z^2-r^2)}{2\sqrt{3}} \\ d_{xz} &= f_2(r)xz \\ d_{yz} &= f_2(r)yz \\ d_{xy} &= f_2(r)xy \\ d_{x^2-y^2} &= f_2(r)\frac{(x^2-y^2)}{2} \end{aligned} \tag{F.7}$$

with a certain radial dependence $f_2(r)$. The transformed d functions are then given as $\vec{d}'^T = \vec{d}^T D^2(R)$ with the 5×5 representation of the rotation R for the d functions $D^2(R) =$

$$\begin{pmatrix} \left(3R_{zz}^2-1\right)/2 & \sqrt{3}R_{zx}R_{zz} & \sqrt{3}R_{zy}R_{zz} & \sqrt{3}R_{zx}R_{zy} & \sqrt{3}\left(R_{zx}^2-R_{zy}^2\right)/2 \\ \sqrt{3}R_{xz}R_{zz} & R_{xx}R_{zz}+R_{zx}R_{xz} & R_{xy}R_{zz}+R_{xz}R_{zy} & R_{xx}R_{zy}+R_{xy}R_{zx} & R_{xx}R_{zx}-R_{xy}R_{zy} \\ \sqrt{3}R_{yz}R_{zz} & R_{yx}R_{zz}+R_{zx}R_{yz} & R_{yy}R_{zz}+R_{yz}R_{zy} & R_{yx}R_{zy}+R_{yy}R_{zx} & R_{yx}R_{zx}-R_{yy}R_{zy} \\ \sqrt{3}R_{xz}R_{yz} & R_{xx}R_{yz}+R_{yx}R_{xz} & R_{xy}R_{yz}+R_{yy}R_{xz} & R_{xx}R_{yy}+R_{xy}R_{yx} & R_{xx}R_{yx}-R_{xy}R_{yy} \\ \sqrt{3}\left(R_{xz}^2-R_{yz}^2\right)/2 & R_{xx}R_{xz}-R_{yx}R_{yz} & R_{xy}R_{xz}-R_{yy}R_{yz} & R_{xx}R_{xy}-R_{yx}R_{yy} & \left(R_{xx}^2+R_{yy}^2-R_{xy}^2-R_{yx}^2\right)/2 \end{pmatrix}, \tag{F.8}$$

where the components of the rotation R have been written in the form

$$R = \begin{pmatrix} R_{xx} & R_{xy} & R_{xz} \\ R_{yx} & R_{yy} & R_{yz} \\ R_{zx} & R_{zy} & R_{zz} \end{pmatrix}$$

The use of Eq. (F.3) requires the transformation matrix $D(R)$ appropriate for the linear combination of atomic orbitals (LCAO) parameters $Y_{0\alpha,\vec{R}_j\beta}$. Usually a quantum chemistry basis set consists of several s, p, and d functions. In TURBOMOLE the basis functions are ordered according to their angular momentum number, so first come the s, then the p, and finally the d functions (or higher angular momentum functions). The functions in a basis set are all linearly independent. (The functions with the same angular momentum have a different radial dependence.) Because of this linear independence the representation of the rotation $D(R)$ can be constructed by the process of addition of representations [269]. If there are n_0 s functions, n_1 p functions, and n_2 d functions, we have

$$D(R) = \sum_{l=0}^{2} n_l D^l(R).$$

As an example the representation of the rotation for 2 s, 1 p, and 2 d functions looks like

$$D(R) = \begin{pmatrix} D^0(R) & 0 & 0 & 0 & 0 \\ 0 & D^0(R) & 0 & 0 & 0 \\ 0 & 0 & D^1(R) & 0 & 0 \\ 0 & 0 & 0 & D^2(R) & 0 \\ 0 & 0 & 0 & 0 & D^2(R) \end{pmatrix},$$

where $D^l(R)$ is the representation of the rotation for the function with angular momentum l (see Eqs. (F.4), (F.6), and (F.8)).

F.1.2 Obtaining electrode parameters for a certain contact orientation

With the results of the previous section it is now simple to obtain the parameters $Y^{(X)}_{0\alpha,j\beta}$ needed for the construction of electrode propagators g_{XX} in the contact geometry from the fcc symmetric parameters $Y_{0\alpha,j\beta}$ of a fcc ball (see Fig. 4.4). We choose the primed coordinate system in Eq. (F.3) to correspond to the fcc ball with primitive lattice vectors $\vec{a}_i^{ball}$ and the unprimed coordinate system to correspond to the electrode lattice $\vec{a}_i^{(X)}$ of the contact. According to Eqs. (F.1) and (F.3) we need the transformation $T = R$ such that $\vec{r}' = R\vec{r}$ or more concrete $\vec{r}^{ball} = R\vec{r}^{(X)}$. We construct the rotation R from electrode X (lattice vectors $\vec{a}_i^{(X)}$) to the lead cluster (lattice vectors $\vec{a}_i^{ball}$) such that the index vector $j = (j_1, j_2, j_3)$ is conserved $\sum_{q=1}^{3} j_q \vec{a}_q^{ball} = R \sum_{q=1}^{3} j_q \vec{a}_q^{(X)}$. This means that R takes the electrode vectors into the vectors of the lead cluster ($R\vec{a}_q^{(X)} = \vec{a}_q^{ball}$). The parameters $Y^{(X)}_{0\alpha,j\beta}$ for the electrode X can then be obtained via Eq. (F.3) from the parameters $Y^{ball}_{0\alpha,j\beta}$, extraced for the lead cluster, by

$$Y^{(X)}_{0\alpha,j^{(X)}\beta} = \sum_{\mu,\nu} \left(D^T(R)\right)_{\alpha\mu} Y^{ball}_{0\mu,j^{ball}\nu} D(R)_{\nu\beta}. \tag{F.9}$$

If we set $A^{(X)} = \left(\vec{a}_1^{(X)}, \vec{a}_2^{(X)}, \vec{a}_3^{(X)}\right)$ and $A^{ball} = \left(\vec{a}_1^{ball}, \vec{a}_2^{ball}, \vec{a}_3^{ball}\right)$, the transformation R is given as $R = A^{ball}\left(A^{(X)}\right)^{-1}$.

Making use of Eq. (F.9) the parameters $Y^{ball}_{0\mu,j^{ball}\nu}$ can be computed once for a certain metal and can be adapted to any electrode orientation. In this way they can be used for the transport calculation of a contact with electrodes of the same material as long as the lattice constant is kept fixed.

F.2 Imposing the fcc space group symmetry

In this paragraph we will consider, how we can impose the fcc space groups on parameters $Y^{ball}_{0\alpha,j\beta}$ ($Y = S$,H, or H^{orth}) as extracted from an fcc ball (see Figs. 4.7 and 4.8). Due to the finiteness of the clusters the translational symmetry is not exactly fulfilled and needs to be imposed. In order to avoid numerical errors, we enforce also the point group symmetry O_h in this process. Concerning the notation, we will call the original unsymmetrized parameters of the fcc ball $Y^{ball}_{0\alpha,j\beta}$. The parameters conform with the O_h point group, the translational symmetry, and the fcc space group are $Y^{O_h}_{0\alpha,j\beta}$, $Y^{trans}_{0\alpha,j\beta}$, and $Y^{fcc}_{0\alpha,j\beta}$, respectively. In the following paragraph and throughout this work we refer to the parameters $Y^{fcc}_{0\alpha,j\beta}$ also simply as $Y_{0\alpha,j\beta}$.

F.2.1 O_h point group symmetry

In paragraph F.1.1 we derived a relation, on how the parameters $Y_{0\alpha,j\beta}$ transform under a rotation R of the coordinate system (see Eq. (F.3))

$$Y_{0\alpha,\vec{R}_j\beta} = \sum_{\mu,\nu} \left(D^T(R)\right)_{\alpha\mu} Y'_{\vec{0}\mu,R\vec{R}_j\nu} D(R)_{\nu\beta}$$

where $Y'(\vec{r}) = \hat{O}_R Y(\vec{r}) \hat{O}_R^{-1}$ stands for the transformed operator, and the $D(R)$ are the representations of R in terms of the LCAO basis functions, in which Y has been expressed.

If a system possesses a certain symmetry and R is an element of this symmetry group G, the operation $Y'(\vec{r}) = \hat{O}_R Y(\vec{r}) \hat{O}_R^{-1}$ does not change the system and $Y = Y'$. For this reason a Hamiltonian with an imposed point group symmetry $Y^{ps}_{0\alpha,\vec{R}_j\beta}$ can be constructed from unsymmetric parameters $Y^{ball}_{0\alpha,\vec{R}_j\beta}$ by averaging for a certain element of $Y^{ps}_{0\alpha,\vec{R}_j\beta}$ over all $Y^{ball}_{0\alpha,\vec{R}_j\beta}$, related to it by symmetry

$$Y^{ps}_{0\alpha,\vec{R}_j\beta} = \frac{1}{N_G} \sum_{R\in G} \sum_{\mu,\nu} \left(D^T(R)\right)_{\alpha\mu} Y^{ball}_{\vec{0}\mu,R\vec{R}_j\nu} D(R)_{\nu\beta}. \tag{F.10}$$

For the special case of the O_h point group the operations in this group are [269, 262]

- the identity $\mathbb{1}$ (1 element)
- 3 rotations around 3 4-fold axes (9 elements)
- 2 rotations around 4 3-fold axes (8 elements)

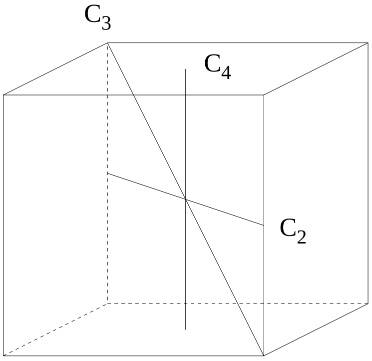

Figure F.3: Selected symmetry operations of the octahedral point group O [269]. Indicated are a two-fold (C_2), three-fold (C_3), and four-fold axis (C_4).

- 1 rotation around 6 2-fold axes (6 elements)
- inversion $-\mathbb{1}$

The 24 proper rotations listed consitute the octahedral point group O (see Fig. F.3). Combined with the inversion there are overall $N_G = 48$ elements in the O_h point group. If all the symmetry operations of the O_h point group are used in Eq. (F.10), we obtain the O_h point group symmetric matrix elements $Y^{O_h}_{0\alpha,\vec{R}_j\beta}$.

F.2.2 Translational symmetry

A translationally invariant Hamiltonian H^{trans} should only depend on the difference of atomic coordinates.[1] The Hamiltonian matrix elements therefore obey the relation

$$H^{trans}_{i\alpha,j\beta} = H^{trans}_{0\alpha,(j-i)\beta} = H^{trans}_{(j-i)\beta,0\alpha} = H^{trans}_{0\beta,-(j-i)\alpha} = H^{trans}_{j\beta,i\alpha}$$

due to the hermiticity of the Hamilton operator and purely real matrix elements. This relation is, however, not naturally fulfilled for parameters extracted from a finite cluster after a self-consistent calculation, because the selfconsistency takes surface effects into account (see Fig. F.4).The violation of the translational symmetry depends on the cluster size. The bigger the finite cluster, the smaller should be the surface effects with respect to the central atom of the cluster. Therefore also the violation decreases, and we have observed this behavior when the difference in the parameters before and after imposing the translational symmetry is compared for clusters with increasing radii (see also the discussion of Table 4.2). Nevertheless for all the clusters accessible to us, we still need to impose this symmetry. A translationally invariant Hamiltonian can be constructed via

$$H^{trans}_{0\alpha,j\beta} = \frac{1}{2}\left(H^{ball}_{0\alpha,j\beta} + H^{ball}_{0\beta,-j\alpha}\right) \tag{F.11}$$

or in terms of matrices of orbital indices

$$H^{trans}_{0,j} = \frac{1}{2}\left(H^{ball}_{0,j} + \left(H^{ball}_{0,-j}\right)^T\right)$$

Here $H^{ball}_{0,j}$ stands for the Hamiltonian extracted from the finite fcc ball.

---

[1] We consider here only a Hamiltonian because an overlap matrix depends only on relative distances and thus the translational symmetry is always fulfilled.

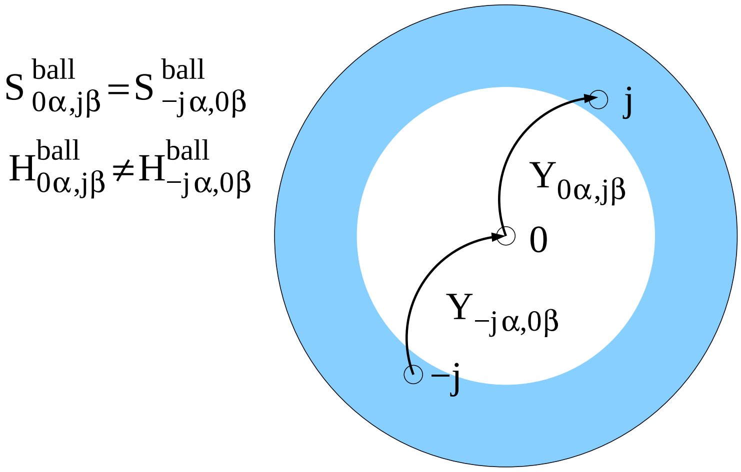

Figure F.4: Illustration of the necessity to impose the translation symmetry on the hopping elements $H^{ball}_{0\alpha,j\beta}$. A spherical cluster is displayed. In blue-shaded areas surface effects are important. While the overlap elements $S^{ball}_{0\alpha,j\beta}$, as extracted from a finite fcc ball, are translationally symmetric, this is not the case for the Hamiltonian elements $H^{ball}_{0\alpha,j\beta}$ due the self-consistent procedure that takes surface effects into account.

F.2.3 Fcc space group

The combined action of the O_h point group and the translational symmetry leads to the fcc space group symmetry. With Eqs. (F.10) and (F.11) we get the fcc space group symmetric parameters $Y_{0\alpha,j\beta} = Y^{fcc}_{0\alpha,j\beta}$ according to the prescription

$$Y^{fcc}_{0\alpha,j\beta} = \frac{1}{2N_G} \sum_{R\in G} \sum_{\mu,\nu} \left\{ \left(D^T(R)\right)_{\alpha\mu} Y^{ball}_{\vec{0}\mu,R\vec{R}_j\nu} D(R)_{\nu\beta} + \left(D^T(R)\right)_{\beta\mu} Y^{ball}_{\vec{0}\mu,-R\vec{R}_j\nu} D(R)_{\nu\alpha} \right\} \tag{F.12}$$

F.3 Determination of primitive lattice vectors for electrodes

In order to calculate the electrode Green's function g_{XX} it is necessary that the parameters $Y_{0,j}$ are in the coordinate system of the electrode X (with $X = L$ or R). The parameters $Y_{0,j}$ are calculated from the fcc ball, a spherical fcc cluster made up from standard fcc lattice vectors $\vec{a}_i^{std}$ (see Eq. (D.17)). If the lattice of the left or right electrode deviates from this standard fcc lattice, the lead electrode parameters $Y_{0,j}$ need to be transformed appropriately as explained before. In order to carry out the required transformation, the primitive vectors of the electrode geometry need to be determined. We assume here that the electrodes of the contact geometry are made up of [100], [110], or [111] planes. The [100], [110], or [111] direction shall be rotated such that it is pointing into the transport direction (which is either along the x, y, or z axis). The determination of the electrode vectors $\vec{a}_i^{(X)}$

can be done unambiguously only if two layers in the transport direction are used. This is necessary because of the [111] direction: While for the [100] and [110] directions the layers are repeated as ABABAB... in the [111] direction the sequence is ABCABC.... Just from the knowledge of layer A, it cannot be determined, whether B is the next layer or C. Therefore it is necessary to work in a set of points that contains at least two different layers along the transport direction. The following procedures are operating in this set of points from two consecutive crystal layers.

F.3.1 Bulk Green's functions from three-dimensional Fourier transformation

For obtaining the primitive vectors, when bulk Green's functions are constructed via a three-dimensional Fourier transformation as described in Sec. D.1, we can proceed in the following way: We determine a nearest neighbor $\vec{p}_2$ to the starting point $\vec{p}_1$. Next another nearest neighbor $\vec{p}_3$ to $\vec{p}_1$ is searched such that $(\vec{p}_3 - \vec{p}_1)(\vec{p}_2 - \vec{p}_1) = a_0^2/4$ with the lattice constant a_0. The primitive lattice vectors of the geometry are either $\vec{a}_1^{(X)} = \vec{p}_2 - \vec{p}_1$, $\vec{a}_2^{(X)} = \vec{p}_3 - \vec{p}_1$, and $\vec{a}_3^{(X)} = \left(\vec{a}_1^{(X)} + \vec{a}_2^{(X)}\right)/3 + 4\left(\vec{a}_1^{(X)} \times \vec{a}_2^{(X)}\right)/(3a_0)$ or $\vec{a}_1^{(X)} = \vec{p}_3 - \vec{p}_1$, $\vec{a}_2^{(X)} = \vec{p}_2 - \vec{p}_1$, and $\vec{a}_3^{(X)} = \left(\vec{a}_1^{(X)} + \vec{a}_2^{(X)}\right)/3 + 4\left(\vec{a}_1^{(X)} \times \vec{a}_2^{(X)}\right)/(3a_0)$. Which of these two sets reproduces the geometry can be checked easily by multiplying a difference vector $\vec{r} = \vec{R}_j - \vec{R}_i$ of two atoms in the electrode of the contact with $\left(A^{(X)}\right)^{-1} = \left(\vec{a}_1^{(X)}, \vec{a}_2^{(X)}, \vec{a}_3^{(X)}\right)^{-1}$ and checking, whether all components of this vector are (close to) integer values. This procedure works, because for a Bravais lattice there exists a vector of integers, such that $\vec{r} = A^{(X)}\vec{j}$ and therefore $\vec{j} = \left(A^{(X)}\right)^{-1}\vec{r}$ are only integer values for the correct primitive lattice vectors $\vec{a}_i^{(X)}$.

F.3.2 Surface and bulk Green's functions from decimation technique

If the Green's functions are constructed by use of the decimation technique (see Sec. D.2), the determination of the primitive lattice vectors $\vec{a}_i^{(X)}$ for the contact is slightly more complicated. (Notice that, as described in Sec. D.2, both surface and bulk Green's functions can be obtained from the decimation technique.) Currently our program can treat electrodes with [100], [110], or [111] surfaces which are displayed in Fig. F.5. These orientations can be distinguished by the interlayer distance of consecutive planes n and $n+1$, namely $d_{n,n+1} = a_0/2$ for the [100] direction, $d_{n,n+1} = a_0/\sqrt{8}$ for the [110] direction and $d_{n,n+1} = a_0/\sqrt{3}$ for the [111] direction. We require two vectors $\vec{c}_1^{(X)}$ and $\vec{c}_2^{(X)}$ to be located in the planes perpendicular to the transport direction. The transport direction, along the normal vector $\vec{n}$, shall be oriented into the z direction. The third vector $\vec{c}_3^{(X)}$ goes one plane forward from plane n to $n+1$ (and $\vec{n}\vec{c}_3^{(X)} > 0$ with $\vec{n}$ pointing from plane n to $n+1$ in the right electrode). The construction of the (nonorthogonal) vectors $\vec{c}_i^{(X)}$, which are

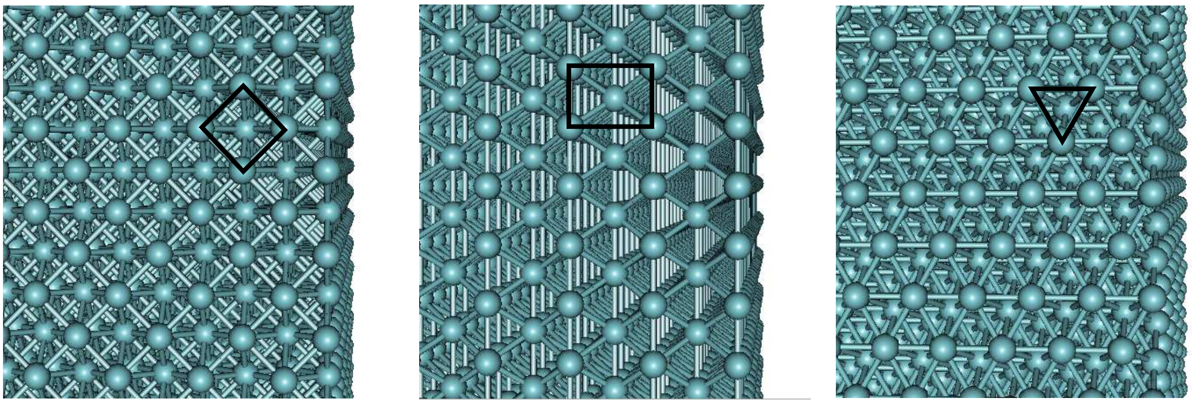

Figure F.5: Surfaces of Al oriented along the main crystallographic directions [100], [110], and [111] in the left, middle, and right panel. Some atoms of the first atomic layer are connected by dark solid lines. The atoms are located in the edges of the polygons.

required to form a right-handed coordinate system for $i = 1$ to 3 obviously needs to distinguish between the different orientations. Below we give the details of our procedure for the determination of the plane vectors $\vec{c}_i^{(X)}$ and the primitive lattice vectors $\vec{a}_i^{(X)}$ following from them.

[100]: The layer sequence is ABABAB.... The atoms in the layer are placed on a quadratic lattice with an interatomic distance of the nearest neighbor distance $a_0/\sqrt{2}$ (see the [100] surface in Fig. F.5). The vectors $\vec{c}_1^{(X)}$ and $\vec{c}_2^{(X)}$ can be chosen to be rectangular. We determine a point $\vec{p}_1$ and a nearest neighbor $\vec{p}_2$, both in layer n. Then we set $\vec{c}_1^{(X)} = \vec{p}_2 - \vec{p}_1$, $\vec{c}_2^{(X)} = \vec{n} \times \vec{c}_1^{(X)}$ and the vector connecting different planes is $\vec{c}_3^{(X)} = \frac{1}{2}\left(\vec{c}_1^{(X)} - \vec{c}_2^{(X)}\right) + a_0\vec{n}/2$. A set of right handed primitive vectors is obtained as $\vec{a}_1^{(X)} = -\vec{c}_2^{(X)}$, $\vec{a}_2^{(X)} = \vec{c}_3^{(X)}$, and $\vec{a}_3^{(X)} = \vec{c}_3^{(X)} - \vec{c}_1^{(X)}$.

[110]: The layers are stacked ABABAB... as for the [100] direction. Again the vectors $\vec{c}_1^{(X)}$ and $\vec{c}_2^{(X)}$ inside the plane can be chosen to be rectangular (see the [110] surface in Fig. F.5). However, these two rectangular vectors possess different length, namely $a_0/\sqrt{2}$ and a_0. So we search for a point $\vec{p}_2$ at one of these two distances from $\vec{p}_1$ in layer n. If we find a nearest neighbor we set $\vec{c}_2^{(X)} = \vec{p}_2 - \vec{p}_1$ and $\vec{c}_1^{(X)} = \sqrt{2}\left(\vec{c}_2^{(X)} \times \vec{n}\right)$. If instead the point $\vec{p}_2$ is a lattice constant apart, then we choose $\vec{c}_1^{(X)} = \vec{p}_2 - \vec{p}_1$ and $\vec{c}_2^{(X)} = \left(\vec{n} \times \vec{c}_1^{(X)}\right)/\sqrt{2}$. The remaining vector, connecting the different planes, can be constructed as $\vec{c}_3^{(X)} = \frac{1}{2}\left(\vec{c}_1^{(X)} + \vec{c}_2^{(X)}\right) + \frac{a}{\sqrt{8}}\vec{n}$ and the primitive vectors are obtained from $\vec{a}_1^{(X)} = \vec{c}_3^{(X)} - \vec{c}_2^{(X)}$, $\vec{a}_2^{(X)} = \vec{c}_3^{(X)}$, and $\vec{a}_3^{(X)} = 2\vec{c}_3^{(X)} - \vec{c}_1^{(X)} - \vec{c}_2^{(X)}$.

[111]: This direction is more complicated than the others, because the stacking is

ABCABCA... (see the [111] surface in Fig. F.5). So it needs to be determined, whether a layer B or C is following, if one is sitting on an atom in layer A and looks into the transport direction. Therefore information on layer n and $n+1$ is required in contrast to the previously discussed [100] and [110] directions. We determine a point $\vec{p}_3$ in layer $n+1$ as a nearest neighbor of $\vec{p}_1$ in layer n and get in this way the vector connecting different planes $\vec{c}_3^{(X)} = \vec{p}_3 - \vec{p}_1$. Next another nearest neighbor $\vec{p}_2$ of $\vec{p}_1$ is searched, but this time in layer n. We set $\vec{c}_1^{(X)} = \vec{p}_2 - \vec{p}_1$ and generate $\vec{c}_2^{(X)}$ by a rotation around the normal vector $\vec{n}$ (in a right-handed sense) by $\pi/3$. Now successive $\pi/3$ rotations of $\vec{c}_1^{(X)}$ and $\vec{c}_2^{(X)}$ around $\vec{n}$ are carried out until both scalar products of $\vec{c}_1^{(X)}$ and $\vec{c}_2^{(X)}$ with $\vec{c}_3^{(X)}$ are equal to $a_0^2/4$ ($\vec{c}_1^{(X)}\vec{c}_3^{(X)} = a_0^2/4$ and $\vec{c}_2^{(X)}\vec{c}_3^{(X)} = a_0^2/4$). The primitive vectors are then $\vec{a}_1^{contact} = \vec{c}_3^{(X)} - \vec{c}_2^{(X)}$, $\vec{a}_2^{(X)} = \vec{c}_3^{(X)}$, and $\vec{a}_3^{(X)} = \vec{c}_3^{(X)} - \vec{c}_1^{(X)}$.

F.4 TURBOMOLE details

In this chapter we give details, which are specific to TURBOMOLE. First we will list, which methods and modules of TURBOMOLE we used. Next we will provide information on basis sets employed in the electrode description. Some of these basis sets have been designed specifically for use in this work.

F.4.1 Programs and options used in TURBOMOLE

In our calculations we use TURBOMOLE V5.7 [270]. The calculations of the electronic structure are all based on density functional theory (DFT), in particular on the RI-DFT method as implemented in the module "ridft" [176, 177]. The use of RI-DFT as compared to conventional DFT calculations (as implemented in the module "dscf") gives a speedup by a factor of around 10. Structure optimizations relied on the module "relax" [271]. All optimizations were started via "jobex" with the option "-gcart 4".

We will provide now a detailed list of the options used by us in calculations with TURBOMOLE. All options not specially mentioned below are the standard options of "define" in TURBOMOLE V5.7.

In DFT we always used the generalized gradient approximation (GGA) functional BP-86 [272, 133, 273, 274, 275]. All calculations were done in a closed shell occupation, sometimes with a fractional occupation number. The various basis sets employed are listed in the next section. All our major results were consistently computed in the SVP TURBOMOLE standard basis sets [276]. If other basis sets were employed we always resorted to the standard SVP auxiliary basis set [176, 177].

Single point calculations on very large clusters (such as the large electrode cluster calculations (see Sec. 4.3) of 429 atoms or more) were mostly done with the option "$fermi", i.e., the thermal smearing of occupation numbers [277]. Starting from a conveniently chosen starting temperature, we cooled all the clusters down to temperatures of "tmend=30.0". When "$fermi" was set, we used bigger dampings of around 10.0. For such very large metallic systems we exploited the point group symmetries in order to speed up the calculations. This was of special importance in the computation of large electrode clusters (see Sec. 4.3) of more than 400 atoms, since a speedup by roughly the order of the point group is achieved. For very large systems we found it necessary to use the special option "grid 5" or even "grid 6". This was mandatory for obtaining meaningful electron densities with an integer electron number that was otherwise lost in the course of the SCF run.

We converged all calculations with the default option "$scfconv 6". Partly we resorted to the option "$marij", the multipole accelerated RI-J. With this option we encountered several problems, such as unrealistic energies with the default settings (precision parameter 10^{-6}, maximum multipole moment 10, and threshold for multipole neglect 10^{-18}) as reported to the Quantum Chemistry group, in particular P. Nova and R. Ahlrichs. Dropping the option or using more precise parameters (precision parameter 10^{-11}, maximum multipole moment 14, and threshold for multipole neglect 10^{-26}), as pointed out to us by P. Nova , helped to cure the problems.

While smaller systems were unproblematic to converge and problems could be overcome with the option "$scforbitalshift automatic 0.5", the inclusion of more metal atoms (such as for Au-h-Z in Chap. 6) was often not possible. This is most likely due to a too highly metallic systems, i.e., too small HOMO-LUMO gaps. The convergence of the huge metal contacts of Chap. 5 or the previously mentioned electrode clusters required the exploitation of point group symmetries.

F.4.2 Basis sets for the electrode description

In the following we list the basis sets used for the electrode description in this work. For Al they are given in Table F.2 and for Au in Table F.1. The SVP basis sets are listed for completeness and correspond to the TURBOMOLE standard basis sets [276]. Some non-standard basis sets with reduced overlap matrix elements have been constructed. This means that the basis functions with minimal exponents, i.e., the most diffuse functions, were left out. The two basis sets constructed in this way are "au SVP-wsp" and "al SVP-wsp-opt". The shortcut "wsp" stands for "without *s* and *p*", because we dropped the most diffuse *s* and *p* basis functions. These modified basis sets have been constructed such that the (variational) restricted open shell Hartree Fock (ROHF) total energy of a single atom does not differ by more than 40 meV from the value obtained by using the basis set of SVP quality.

For Au in the basis au SVP we obtain a total ROHF energy of $E = -134.7843224$ H and in the basis au SVP-wsp $E = -134.7589204$ H. This is an acceptable difference of 25.4 mH= 0.692 eV.

For the Al atom in the basis al SVP wet get $E = -241.786870$ H and for the corresponding basis with the dropped most diffuse *s* and *p* functions the total energy is $E = -241.592158$ H. This results in an unacceptably high difference of 194.7 mH = 5.298 eV. Thus a reoptimization of the outer two *s* and *p* functions was necessary. Their new exponents are therefore printed emphasized in Table F.2. Then we get $E = 241.750278$ H for the optimized basis al SVP-wsp-opt and an energy difference of 36.6 mH= 0.9957 eV with respect to al SVP. We need to acknowledge the help of F. Furche, who recommended the error criterion of 40 meV to us and performed the necessary reoptimization of outer basis functions for the basis set al SVP-wsp-opt.

In addition to the SVP basis sets we list in Table F.2 a minimal basis for Al, which we call al hw-min. It is constructed from the basis al hw-dz with 2*s* and 2*p* ([2s2p] {21/21}) functions by combining both outermost *s* and *p* functions. This leads to a basis set with a single *s* and *p* function ([1s1p] {3/3}), called al hw-min from now on. The basis set al hw-dz [278] is defined in TURBOMOLE and is only listed for reasons of completeness. (The electronic core potential (ECP) ecp-10 can also be found there or in Ref. [278].) The minimal basis al hw-min serves for "quick and dirty" test calculations. From DFT calculations of Al clusters of 555 atoms we obtained a HOMO energy of $E_{\mathrm{HOMO}} = -5.48$ eV, well below the HOMO of other basis sets such as al SVP with $E_{\mathrm{HOMO}} = -4.26$ eV, al SVP-wsp-opt with $E_{\mathrm{HOMO}} = -4.04$ eV, and al hw-dz with $E_{\mathrm{HOMO}} = -4.22$ eV.

au SVP {au def-SV(P)}		au SVP-wsp	
# au (7s6p5d) / [6s3p2d] {211111/411/41}		# au (6s5p5d) / [5s2p2d] {21111/41/41}	
2 s		2 s	
20.115299000	-0.15910719389	20.115299000	-0.15910719389
12.193477000	0.79105526778	12.193477000	0.79105526778
1 s		1 s	
6.0735294368	1.0000000000	6.0735294368	1.0000000000
1 s		1 s	
1.3174451569	1.0000000000	1.3174451569	1.0000000000
1 s		1 s	
0.58596768244	1.0000000000	0.58596768244	1.0000000000
1 s		1 s	
0.13875427354	1.0000000000	0.13875427354	1.0000000000
1 s		–	
0.48876985527E-01	1.0000000000	–	–
4 p		4 p	
8.6096650000	0.50053018599	8.6096650000	0.50053018599
7.3353260000	-0.72681584494	7.3353260000	-0.72681584494
1.6575296365	0.57315511417	1.6575296365	0.57315511417
0.78159310216	0.49579068859	0.78159310216	0.49579068859
1 p		1 p	
0.32384840661	1.0000000000	0.32384840661	1.0000000000
1 p		–	
0.54000000000E-01	1.0000000000	–	–
4 d		4 d	
4.1439490000	-0.37099566643	4.1439490000	-0.37099566643
3.5682570000	0.40197233762	3.5682570000	0.40197233762
1.2345757130	0.46001988624	1.2345757130	0.46001988624
0.48190232338	0.46152130958	0.48190232338	0.46152130958
1 d		1 d	
0.16490636769	1.0000000000	0.16490636769	1.0000000000

Table F.1: Au basis sets as used in this work. Official names of the TURBOMOLE basis sets are given in curly brackets.

al SVP {al def-SV(P)}		al SVP-wsp-opt	
# al (10s7p1d) / [4s3p1d] {5311/511/1}		# al (9s6p1d) / [3s2p1d] {531/51/1}	
5 s		5 s	
5887.5727030	0.13483347987E-02	5887.5727030	0.13483347987E-02
885.61225996	0.10071576809E-01	885.61225996	0.10071576809E-01
201.13604899	0.45132454056E-01	201.13604899	0.45132454056E-01
56.284974674	0.11461268043	56.284974674	0.11461268043
17.229551243	0.10159608943	17.229551243	0.10159608943
3 s		3 s	
29.340249922	0.69347454208E-01	29.340249922	0.69347454208E-01
3.0439630420	-0.42528117679	3.0439630420	-0.42528117679
1.1285539518	-0.41449832210	1.1285539518	-0.41449832210
1s		1s	
0.14234175160	1.0000000000	*0.10860263042*	1.0000000000
1 s		–	
0.54400192313E-01	1.0000000000	–	–
5 p		5 p	
145.11918809	0.63963373134E-02	145.11918809	0.63963373134E-02
33.717894833	0.44189359965E-01	33.717894833	0.44189359965E-01
10.369863083	0.15581575993	10.369863083	0.15581575993
3.5135616036	0.28635286951	3.5135616036	0.28635286951
1.1980050273	0.22921423248	1.1980050273	0.22921423248
1 p		1 p	
0.26583005913	1.0000000000	*0.11855759602*	1.0000000000
1 p		–	
0.71003361994E-01	1.0000000000	–	–
1 d		1 d	
0.30000000000	1.0000000000	0.30000000000	1.0000000000

al hw-dz {al ecp-10 dz hay & wadt}		al hw-min	
# al (2s1s2p1p) / [2s2p] {21/21}		# al (3s3p) / [1s1p] {3/3}	
2 s		3 s	
0.96150000000	-0.24840700000	0.96150000000	-0.24840700000
0.18190000000	0.61056400000	0.18190000000	0.61056400000
1s		0.65650000000E-01	0.54439000000
0.65650000000E-01	0.54439000000		
2p		3 p	
1.9280000000	-0.33757000000E-01	1.9280000000	-0.33757000000E-01
1p		0.20130000000	0.48144700000
0.20130000000	0.48144700000	0.58040000000E-01	0.62819800000
0.58040000000E-01	0.62819800000		

Table F.2: Al basis sets as used in this work. The basis set al hw-dz is only listed for reasons of completeness. Official names of the TURBOMOLE basis sets are given in curly brackets.

Bibliography

[1] N. Agraït, A. L. Yeyati, and J. M. van Ruitenbeek, Phys. Rep. **377**, 81 (2003).

[2] G. Binnig and H. Rohrer, Rev. Mod. Phys. **59**, 615 (1987).

[3] D. Abraham, H. J. Mamin, E. Ganz, and J. Clarke, IBM J. Res. Dev. **30**, 492 (1986).

[4] H. van Kempen and G. F. A. van de Walle, IBM J. Res. Dev. **30**, 509 (1986).

[5] M. F. Crommie, C. P. Lutz, and D. M. Eigler, Science **262**, 218 (1993).

[6] A. J. Heinrich, C. P. Lutz, J. A. Gupta, and D. M. Eigler, Science **298**, 1381 (2002).

[7] G. V. Nazin, X. H. Qiu, and W. Ho, Science **302**, 77 (2003).

[8] J. K. Gimzewski and R. Möller, IBM J. Res. Dev. **30**, 509 (1986).

[9] N. Agraït, J. G. Rodrigo, and S. Vieira, Phys. Rev. B **47**, 12345 (1993).

[10] J. I. Pascual, J. Méndez, J. Gómez-Herrero, A. M. Baró, N. García, and V. T. Binh, Phys. Rev. Lett. **71**, 1852 (1993).

[11] L. Olesen, E. Lægsgaard, I. Stensgaard, F. Besenbacher, J. Schiøtz, P. Stoltze, K. W. Jacobsen, and J. K. Nørskov, Phys. Rev. Lett. **74**, 2147 (1995).

[12] C. Sirvent, J. G. Rodrigo, S. Vieira, L. Jurczyszyn, N. Mingo, and F. Flores, Phys. Rev. B **53**, 16086 (1996).

[13] N. Agraït, C. Untiedt, G. Rubio-Bollinger, and S. Vieira, Phys. Rev. Lett. **88**, 216803 (2002).

[14] L. Limot, J. Kröger, R. Berndt, A. Garcia-Lekue, and W. A. Hofer, Phys. Rev. Lett. **94**, 126102 (2005).

[15] N. Néel, J. Kröger, L. Limot, K. Palotas, W. A. Hofer, and R. Berndt, Phys. Rev. Lett. **98**, 016801 (2007).

[16] J. Moreland and J. W. Ekin, J. Appl. Phys. **58**, 3888 (1985).

[17] C. J. Muller, J. M. van Ruitenbeek, and L. J. de Jongh, Phys. Rev. Lett. **69**, 140 (1992).

[18] C. J. Muller, J. M. van Ruitenbeek, and L. J. de Jongh, Physica C **191**, 485 (1992).

[19] E. Scheer, P. Joyez, D. Esteve, C. Urbina, and M. H. Devoret, Phys. Rev. Lett. **78**, 3535 (1997).

[20] A. I. Yanson, PhD thesis (Universiteit Leiden, Leiden, 2001).

[21] H. Ohnishi, Y. Kondo, and K. Takayanagi, Nature **395**, 780 (1998).

[22] A. I. Yanson, G. Rubio-Bolinger, H. E. van den Brom, N. Agraït, and J. M. van Ruitenbeek, Nature **395**, 783 (1998).

[23] J. M. Krans, J. M. van Ruitenbeek, V. V. Fisun, I. K. Yanson, and L. J. de Jongh, Nature **375**, 767 (1995).

[24] Z. Gai, Y. He, H. Yu, and W. S. Yang, Phys. Rev. B **53**, 1042 (1996).

[25] B. Mann and H. Kuhn, J. Appl. Phys. **42**, 4398 (1971).

[26] J. Reichert, R. Ochs, D. Beckmann, H. B. Weber, M. Mayor, and H. v. Löhneysen, Phys. Rev. Lett. **88**, 176804 (2002).

[27] J. Reichert, H. B. Weber, and M. Mayor, Appl. Phys. Lett. **82**, 4137 (2003).

[28] B. Xu and N. J. Tao, Science **301**, 1221 (2003).

[29] X. Xiao, L. A. Nagahara, A. M. Rawlett, and N. Tao, J. Am. Chem. Soc. **127**, 9235 (2005).

[30] M. Magoga and C. Joachim, Phys. Rev. B **56**, 4722 (1997).

[31] A. Tsuda and A. Osuka, Science **293**, 79 (2001).

[32] R. E. Martin and F. Diederich, Angew. Chem. Int. Ed. **38**, 1351 (1999).

[33] R. P. Feynman, *There's plenty of room at the bottom*, Talk given at the annual APS meeting (December 29th 1959).

[34] M. Elbing, PhD thesis (Forschungszentrum Karlsruhe, Karlsruhe, 2004).

[35] M. Dreher, F. Pauly, J. Heurich, J. C. Cuevas, E. Scheer, and P. Nielaba, Phys. Rev. B **72**, 075435 (2005).

[36] F. Pauly, M. Dreher, J. K. Viljas, M. Häfner, J. C. Cuevas, and P. Nielaba, Phys. Rev. B **74**, 235106 (2006).

[37] J. C. Cuevas, A. L. Yeyati, and A. Martín-Rodero, Phys. Rev. Lett. **80**, 1066 (1998).

[38] E. Scheer, N. Agraït, J. C. Cuevas, A. L. Yeyati, B. Ludoph, A. Martín-Rodero, G. R. Bollinger, J. M. van Ruitenbeek, and C. Urbina, Nature **394**, 154 (1998).

[39] J. C. Cuevas, A. L. Yeyati, A. Martín-Rodero, G. R. Bollinger, C. Untiedt, and N. Agraït, Phys. Rev. Lett. **81**, 2990 (1998).

[40] N. Agraït, G. Rubio, and S. Vieira, Phys. Rev. Lett. **74**, 3995 (1995).

[41] A. I. Yanson, I. K. Yanson, and J. M. van Ruitenbeek, Nature **400**, 144 (1999).

[42] A. I. Yanson, I. K. Yanson, and J. M. van Ruitenbeek, Phys. Rev. Lett. **87**, 216805 (2001).

[43] E. Medina, M. Díaz, N. León, C. Guerrero, A. Hasmy, P. A. Serena, and J. L. Costa-Krämer, Phys. Rev. Lett. **91**, 026802 (2003).

[44] A. I. Mares, A. F. Otte, L. G. Soukiassian, R. H. M. Smit, and J. M. van Ruitenbeek, Phys. Rev. B **70**, 073401 (2004).

[45] A. I. Mares and J. M. van Ruitenbeek, Phys. Rev. B **72**, 205402 (2005).

[46] V. Rodrigues, T. Fuhrer, and D. Ugarte, Phys. Rev. Lett. **85**, 4124 (2000).

[47] V. Rodrigues and D. Ugarte, Phys. Rev. B **63**, 073405 (2001).

[48] Y. Kondo and K. Takayanagi, Science **289**, 606 (2000).

[49] Y. Oshima, H. Koizumi, K. Mouri, H. Hirayama, K. Takayanagi, and Y. Kondo, Phys. Rev. B **65**, 121401(R) (2002).

[50] J. A. Torres, J. I. Pascual, and J. J. Sáenz, Phys. Rev. B **49**, 16581 (1994).

[51] A. García-Martín, J. A. Torres, and J. J. Sáenz, Phys. Rev. B **54**, 13448 (1996).

[52] A. Hasmy, E. Medina, and P. A. Serena, Phys. Rev. Lett. **86**, 5574 (2001).

[53] U. Landman, W. D. Luedtke, N. A. Burnham, and R. J. Colton, Science **248**, 454 (1990).

[54] A. P. Sutton and J. B. Pethica, J. Phys.: Condens. Matter **2**, 5317 (1990).

[55] T. N. Todorov and A. P. Sutton, Phys. Rev. Lett. **70**, 2138 (1993).

[56] A. M. Bratkovsky, A. P. Sutton, and T. N. Todorov, Phys. Rev. B **52**, 5036 (1995).

[57] T. N. Todorov and A. P. Sutton, Phys. Rev. B **54**, R14234 (1996).

[58] H. Mehrez and S. Ciraci, Phys. Rev. B **56**, 12632 (1997).

[59] M. Brandbyge, M. R. Sørensen, and K. W. Jacobsen, Phys. Rev. B **56**, 14956 (1997).

[60] A. Buldum, S. Ciraci, and I. P. Batra, Phys. Rev. B **57**, 2468 (1998).

[61] M. R. Sørensen, M. Brandbyge, and K. W. Jacobsen, Phys. Rev. B **57**, 3283 (1998).

[62] A. Nakamura, M. Brandbyge, L. B. Hansen, and K. W. Jacobsen, Phys. Rev. Lett. **82**, 1538 (1999).

[63] P. Jelínek, R. Pérez, J. Ortega, and F. Flores, Phys. Rev. B **68**, 085403 (2003).

[64] E. Z. da Silva, F. D. Novaes, A. J. R. da Silva, and A. Fazzio, Phys. Rev. B **69**, 115411 (2004).

[65] J. A. Torres and J. J. Sáenz, Phys. Rev. Lett. **77**, 2245 (1996).

[66] A. Hasmy, A. J. Pérez-Jiménez, J. J. Palacios, P. García-Mochales, J. L. Costa-Krämer, M. Díaz, E. Medina, and P. A. Serena, Phys. Rev. B **72**, 245405 (2005).

[67] K. W. Jacobsen, P. Stoltze, and J. K. Nørskov, Surf. Sci. **366**, 394 (1996).

[68] P. Stoltze, *Simulation methods in atomic-scale materials physics*, p. 258 (Polyteknisk Forlag, Lyngby, 1997).

[69] P. Stoltze, J. Phys.: Condens. Matter **6**, 9495 (1994).

[70] G. Rubio-Bollinger, S. R. Bahn, N. Agraït, K. W. Jacobsen, and S. Vieira, Phys. Rev. Lett. **87**, 026101 (2001).

[71] S. R. Bahn and K. W. Jacobsen, Phys. Rev. Lett. **87**, 266101 (2001).

[72] D. Frenkel and B. Smit, *Understanding Molecular Simulation* (Academic Press, San Diego, 1996).

[73] M. P. Allen and D. J. Tildesley, *Computer Simulation of Liquids* (Oxford University Press, Oxford, 1987).

[74] G. M. Finbow, R. M. Lynden-Bell, and I. R. McDonald, Molecular Physics **92**, 705 (1997).

[75] M. J. Mehl and D. A. Papaconstantopoulos, Phys. Rev. B **54**, 4519 (1996).

[76] M. J. Mehl and D. A. Papaconstantopoulos, *Tight-Binding Parametrization of First-Principles Results*, in Computational Materials Science, edited by C. Fong (World Scientific Publishing, Singapore, 1998).

[77] http://cst-www.nrl.navy.mil/bind/ .

[78] M. I. Haftel, N. Bernstein, M. J. Mehl, and D. A. Papaconstantopoulos, Phys. Rev. B **70**, 125419 (2004).

[79] http://cst-www.nrl.navy.mil/bind/ni_ferro_par .

[80] M. Brandbyge, N. Kobayashi, and M. Tsukada, Phys. Rev. B **60**, 17064 (1999).

[81] A. Szabo and N. S. Ostlund, *Modern quantum chemistry: introduction to advanced electronic structure theory* (Dover, New York, 1996).

[82] B. Ludoph and J. M. van Ruitenbeek, Phys. Rev. B **61**, 2273 (2000).

[83] V. Rodrigues, J. Bettini, A. R. Rocha, L. G. C. Rego, and D. Ugarte, Phys. Rev. B **65**, 153402 (2002).

[84] J. L. Mozos, P. Ordejón, M. Brandbyge, J. Taylor, and K. Stokbro, Nanotechnology **13**, 346 (2002).

[85] Y. J. Lee, M. Brandbyge, M. J. Puska, J. Taylor, K. Stokbro, and R. M. Nieminen, Phys. Rev. B **69**, 125409 (2004).

[86] B. Ludoph, M. H. Devoret, D. Esteve, C. Urbina, and J. M. van Ruitenbeek, Phys. Rev. Lett. **82**, 1530 (1999).

[87] I. K. Yanson, O. I. Shklyarevskii, S. Csonka, H. van Kempen, S. Speller, A. I. Yanson, and J. M. van Ruitenbeek, Phys. Rev. Lett. **95**, 256806 (2005).

[88] I. N. Bronstein, K. A. Semendjajew, G. Musiol, and H. Mühlig, *Taschenbuch der Mathematik* (Verlag Harri Deutsch, Frankfurt am Main, 1997).

[89] W. H. A. Thijssen, D. Marjenburgh, R. H. Bremmer, and J. M. van Ruitenbeek, Phys. Rev. Lett. **96**, 026806 (2006).

[90] G. Rubio, N. Agraït, and S. Vieira, Phys. Rev. Lett. **76**, 2302 (1996).

[91] T. Kizuka, Phys. Rev. Lett. **81**, 4448 (1998).

[92] Y. Takai, T. Kawasaki, Y. Kimura, T. Ikuta, and R. Shimizu, Phys. Rev. Lett. **87**, 106105 (2001).

[93] P. Z. Coura, S. B. Legoas, A. S. Moreira, F. Sato, V. Rodrigues, S. O. Dantas, D. Ugarte, and D. S. Galvão, Nano Lett. **4**, 1187 (2004).

[94] J. A. Torres, E. Tosatti, A. D. Corso, F. Ercolessi, J. J. Kohanoff, F. D. D. Tolla, and J. M. Soler, Surf. Sci. Lett. **426**, L441 (1999).

[95] M. Okamoto and K. Takayanagi, Phys. Rev. B **60**, 7808 (1999).

[96] D. Sánchez-Portal, E. Artacho, J. Junquera, P. Ordejón, A. García, and J. M. Soler, Phys. Rev. Lett. **83**, 3884 (1999).

[97] H. Häkkinen, R. N. Barnett, and U. Landman, J. Phys. Chem. B **103**, 8814 (1999).

[98] R. H. M. Smit, C. Untiedt, G. Rubio-Bollinger, R. C. Segers, and J. M. van Ruitenbeek, Phys. Rev. Lett. **91**, 076805 (2003).

[99] E. Scheer, W. Belzig, Y. Naveh, M. H. Devoret, D. Esteve, and C. Urbina, Phys. Rev. Lett. **86**, 284 (2001).

[100] E. Scheer, W. Belzig, Y. Naveh, and C. Urbina, Adv. in Solid State Phys. **42**, 107 (2002).

[101] D. Averin and A. Bardas, Phys. Rev. Lett. **75**, 1831 (1995).

[102] J. C. Cuevas, A. Martín-Rodero, and A. L. Yeyati, Phys. Rev. B **54**, 7366 (1996).

[103] R. H. M. Smit, Y. Noat, C. Untiedt, N. D. Lang, M. C. van Hemert, and J. M. van Ruitenbeek, Nature **419**, 906 (2002).

[104] R. H. M. Smit, C. Untiedt, A. I. Yanson, and J. M. van Ruitenbeek, Phys. Rev. Lett. **87**, 266102 (2001).

[105] L. de la Vega, A. Martín-Rodero, A. L. Yeyati, and A. Saúl, Phys. Rev. B **70**, 113107 (2004).

[106] S. K. Nielsen, M. Brandbyge, K. Hansen, K. Stokbro, J. M. van Ruitenbeek, and F. Besenbacher, Phys. Rev. Lett. **89**, 066804 (2002).

[107] S. K. Nielsen, Y. Noat, M. Brandbyge, R. H. M. Smit, K. Hansen, L. Y. Chen, A. I. Yanson, F. Besenbacher, and J. M. van Ruitenbeek, Phys. Rev. B **67**, 245411 (2003).

[108] V. M. García-Suárez, A. R. Rocha, S. W. Bailey, C. J. Lambert, S. Sanvito, and J. Ferrer, Phys. Rev. Lett. **95**, 256804 (2005).

[109] J. M. Krans, C. J. Muller, I. K. Yanson, T. C. M. Govaert, R. Hesper, and J. M. van Ruitenbeek, Phys. Rev. B **48**, 14721 (1993).

[110] A. I. Yanson and J. M. van Ruitenbeek, Phys. Rev. Lett. **79**, 2157 (1997).

[111] T. Kitamura and Y. Umeno, Modelling Simul. Mater. Sci. Eng. **11**, 127 (2003).

[112] J. L. Costa-Krämer, Phys. Rev. B **55**, R4875 (1997).

[113] F. Ott, S. Barberan, J. G. Lunney, J. M. D. Coey, P. Berthet, A. M. de Leon-Guevara, and A. Revcolevschi, Phys. Rev. B **58**, 4656 (1998).

[114] T. Ono, Y. Ooka, H. Miyajima, and Y. Otani, Appl. Phys. Lett. **75**, 1622 (1999).

[115] M. Viret, S. Berger, M. Gabureac, F. Ott, D. Olligs, I. Petej, J. F. Gregg, C. Fermon, G. Francinet, and G. LeGoff, Phys. Rev. B **66**, 220401(R) (2002).

[116] F. Elhoussine, S. Mátéfi-Tempfli, A. Encinas, and L. Piraux, Appl. Phys. Lett. **81**, 1681 (2002).

[117] V. Rodrigues, J. Bettini, P. C. Silva, and D. Ugarte, Phys. Rev. Lett. **91**, 096801 (2003).

[118] C. Untiedt, D. M. T. Dekker, D. Djukic, and J. M. van Ruitenbeek, Phys. Rev. B **69**, 081401(R) (2004).

[119] A. Martín-Rodero, A. L. Yeyati, and J. C. Cuevas, Physica C **352**, 67 (2001).

[120] A. Delin and E. Tosatti, Phys. Rev. B **68**, 144434 (2003).

[121] A. Bagrets, N. Papanikolaou, and I. Mertig, Phys. Rev. B **70**, 064410 (2004).

[122] D. Jacob, J. Fernández-Rossier, and J. J. Palacios, Phys. Rev. B **71**, 220403(R) (2005).

[123] P. García-Mochales, S. Peláez, P. A. Serena, E. Medina, and A. Hasmy, Appl. Phys. A: Mater. Sci. Process. **81**, 1545 (2005).

[124] M. M. Sigalas, J. H. Rose, D. A. Papaconstantopoulos, and H. B. Shore, Phys. Rev. B **58**, 13438 (1998).

[125] S. R. Bahn, PhD thesis (Technical University of Denmark, Lyngby, 2001).

[126] O. Guelersen, F. Ercolessi, and E. Tossatti, Phys. Rev. Lett. **80**, 3775 (1998).

[127] Y. Xue, S. Datta, and M. A. Ratner, Chem. Phys. **281**, 151 (2002).

[128] J. J. Palacios, A. J. Pérez-Jiménez, E. Louis, E. San-Fabián, and J. A. Vergés, Phys. Rev. B **66**, 035322 (2002).

[129] J. K. Viljas, J. C. Cuevas, F. Pauly, and M. Häfner, Phys. Rev. B **72**, 245415 (2005).

[130] T. Frederiksen, M. Brandbyge, N. Lorente, and A.-P. Jauho, Phys. Rev. Lett. **93**, 256601 (2004).

[131] T. Frederiksen, M. Brandbyge, A.-P. Jauho, and N. Lorente, J. Comput. Electron. **3**, 423 (2004).

[132] T. Frederiksen, M. Paulsson, M. Brandbyge, and A.-P. Jauho, Phys. Rev. B **75**, 205413 (2007).

[133] J. C. Slater and G. F. Koster, Phys. Rev. **94**, 1498 (1954).

[134] R. E. Cohen, M. J. Mehl, and D. A. Papaconstantopoulos, Phys. Rev. B **50**, 14694 (1994).

[135] R. E. Cohen, M. J. Mehl, and D. A. Papaconstantopoulos, J. Phys.: Condens. Matter **15**, R413 (2003).

[136] M. J. Montgomery, J. Hoekstra, T. N. Todorov, and A. P. Sutton, J. Phys.: Condens. Matter **15**, 731 (2003).

[137] E. G. Emberly and G. Kriczenow, Phys. Rev. B **61**, 5740 (2000).

[138] T. Mii, S. G. Tikhodeev, and H. Ueba, Phys. Rev. B **68**, 205406 (2003).

[139] A. Mitra, I. Aleiner, and A. J. Millis, Phys. Rev. B **69**, 245302 (2004).

[140] M. Galperin, M. A. Ratner, and A. Nitzan, J. Chem. Phys. **121**, 11965 (2004).

[141] G. D. Mahan, *Many-particle physics* (Plenum Publishers, New York, 2000).

[142] Y. Chen, M. Zwolak, and M. Di Ventra, Nano Lett. **3**, 1691 (2003).

[143] Y. Chen and M. Di Ventra, Phys. Rev. Lett. **395**, 166802 (2005).

[144] A. Aviram and M. A. Ratner, Chem. Phys. Lett. **29**, 277 (1974).

[145] D. M. Eigler, C. P. Lutz, and W. E. Rudge, Nature **352**, 600 (1991).

[146] C. Joachim, J. K. Gimzewski, and A. Aviram, Nature **408**, 501 (2000).

[147] M. P. Samanta, W. Tian, S. Datta, J. I. Hederson, and C. P. Kubiak, Phys. Rev. B **53**, R7626 (1996).

[148] L. E. Hall, J. R. Reimers, N. S. Hush, and K. Silverbrook, J. Chem. Phys. **112**, 1510 (2000).

[149] S. Yaliraki, A. E. Roitberg, C. Gonzalez, V. Mujica, and M. A. Ratner, J. Chem. Phys. **111**, 6997 (1999).

[150] Y. Xue, S. Datta, and M. A. Ratner, J. Chem. Phys. **115**, 4292 (2001).

[151] J. Taylor, H. Guo, and J. Wang, Phys. Rev. B **63**, 245407 (2001).

[152] M. Brandbyge, J.-L. Mozos, P. Ordejón, J. Taylor, and K. Stokbro, Phys. Rev. B **65**, 165401 (2002).

[153] P. Damle, A. W. Gosh, and S. Datta, Chem. Phys. **281**, 171 (2002).

[154] Y. Fujimoto and K. Hirose, Phys. Rev. B **67**, 195315 (2003).

[155] K. S. Thygesen, M. V. Bollinger, and K. W. Jacobsen, Phys. Rev. B **67**, 115404 (2003).

[156] P. Havu, V. Havu, M. J. Puska, and R. M. Nieminen, Phys. Rev. B **69**, 115325 (2004).

[157] T. Tada, M. Kondo, and K. Yoshizawa, J. Chem. Phys. **121**, 8050 (2004).

[158] F. Jiang, Y. X. Zhou, H. Chen, R. Note, H. Mizuseki, and Y. Kawazoe, Phys. Rev. B **67**, 155321 (2003).

[159] A. R. Rocha, V. M. García-Suárez, S. Bailey, C. Lambert, J. Ferrer, and S. Sanvito, Phys. Rev. B **73**, 085414 (2006).

[160] A. Pecchia and A. Di Carlo, Rep. Prog. Phys. **67**, 1497 (2004).

[161] D. A. Papaconstantopoulos, *Handbook of the Band Structure of Elemental Solids* (Plenum Press, New York, 1986).

[162] F. Evers, F. Weigend, and M. Koentopp, Phys. Rev. B **69**, 235411 (2004).

[163] J. Heurich, J. C. Cuevas, W. Wenzel, and G. Schön, Phys. Rev. Lett. **88**, 256803 (2002).

[164] P. Delaney and J. C. Greer, Phys. Rev. Lett. **93**, 036805 (2004).

[165] G. Fagas, P. Delaney, and J. C. Greer, Phys. Rev. B **73**, 241314 (2006).

[166] G. Stefanucci and C.-O. Almbladh, Phys. Rev. B **69**, 195318 (2004).

[167] A. P. Horsfield, D. R. Bowler, A. J. Fisher, T. N. Todorov, and C. G. Sanchez, J. Phys.: Condens. Matter **16**, 8251 (2004).

[168] S. Kurth, G. Stefanucci, C.-O. Almbladh, A. Rubio, and E. K. U. Gross, Phys. Rev. B **72**, 035308 (2005).

[169] N. Bushong, N. Sai, and M. Di Ventra, Nano Lett. **5**, 2569 (2005).

[170] N. Sai, M. Zwolak, G. Vignale, and M. Di Ventra, Phys. Rev. Lett. **94**, 146810 (2005).

[171] M. Koentopp, K. Burke, and F. Evers, Phys. Rev. B **73**, 121403 (2006).

[172] A. Arnold, PhD thesis (Forschungszentrum Karlsruhe, Karlsruhe, 2007).

[173] W. Koch and M. C. Holthausen, *A Chemist's Guide to Density Functional Theory* (WILEY-VCH, Weinheim, 2001).

[174] P. Hohenberg and W. Kohn, Phys. Rev. **136**, B863 (1964).

[175] W. Kohn and J. M. Luttinger, Phys. Rev. **118**, 41 (1960).

[176] K. Eichkorn, O. Treutler, H. Öhm, M. Häser, and R. Ahlrichs, Chem. Phys. Lett. **242**, 652 (1995).

[177] K. Eichkorn, F. Weigend, O. Treutler, and R. Ahlrichs, Theor. Chim. Acc. **97**, 119 (1997).

[178] J. J. Palacios, A. J. Pérez-Jiménez, E. Louis, and J. A. Vergés, Phys. Rev. B **64**, 115411 (2001).

[179] M. Kondo, T. Tada, and K. Yoshizawa, J. Phys. Chem. A **108**, 9143 (2004).

[180] R. Ahlrichs and S. D. Elliott, Phys. Chem. Chem. Phys. **1**, 13 (1999).

[181] F. Furche, R. Ahlrichs, P. Weis, C. Jacob, S. Gilb, T. Bierweiler, and M. M. Kappes, J. Chem. Phys. **117**, 6982 (2002).

[182] A. Köhn, F. Weigend, and R. Ahlrichs, Phys. Chem. Chem. Phys. **3**, 711 (2001).

[183] P. Nava, M. Sierka, and R. Ahlrichs, Phys. Chem. Chem. Phys. **5**, 3372 (2003).

[184] N. W. Ashcroft and N. D. Mermin, *Solid State Physics* (Harcourt, Orlando, 1976).

[185] R. Dovesi, C. Pisani, C. Roetti, and V. R. Saunders, Phys. Rev. B **28**, 5781 (1983).

[186] M. Causà, R. Dovesi, and C. Roetti, Phys. Rev. B **43**, 11937 (1991).

[187] M. Catti, G. Valerio, R. Dovesi, and M. Causà, Phys. Rev. B **49**, 14179 (1994).

[188] A. Kokalj and M. Causà, J. Phys.: Condens. Matter **11**, 7463 (1999).

[189] R. Dovesi, R. Orlando, C. Roetti, C. Pisani, and V. R. Saunders, phys. stat. sol. (b) **217**, 63 (2000).

[190] Y. Noel, C. M. Zicovich-Wilson, B. Civalleri, P. D'Arco, and R. Dovesi, Phys. Rev. B **65**, 014111 (2001).

[191] E. Louis, J. A. Vergés, J. J. Palacios, A. J. Pérez-Jiménez, and E. San-Fabián, Phys. Rev. B **67**, 155321 (2003).

[192] S.-H. Ke, H. U. Baranger, and W. Yang, Phys. Rev. B **70**, 085410 (2004).

[193] K. N. Kudin and G. E. Scuseria, Phys. Rev. B **61**, 16440 (2000).

[194] S. Wohlthat, Diploma thesis (Universität Karlsruhe, Karlsruhe, 2006).

[195] H. Riel, private communication (December 2006).

[196] L. Venkataraman, J. E. Klare, C. Nuckolls, M. S. Hybertsen, and M. L. Steigerwald, Nature **442**, 904 (2006).

[197] R. B. Capaz and M. J. Caldas, Phys. Rev. B **67**, 205205 (2003).

[198] H. B. Weber, J. Reichert, F. Weigend, R. Ochs, D. Beckmann, M. Mayor, R. Ahlrichs, and H. v. Höhneysen, Chem. Phys. **281**, 113 (2002).

[199] L. A. Bumm, J. J. Arnold, T. D. Dunbar, D. L. Allara, and P. S. Weiss, J. Phys. Chem. B **103**, 8122 (1999).

[200] S. Creager, C. J. Yu, C. Bamdad, S. O'Connor, T. MacLean, E. Lam, Y. Chong, G. T. Olsen, J. Luo, M. Gozin, and J. F. Kayyem, J. Am. Chem. Soc. **121**, 1059 (1999).

[201] T. Ishida, W. Mizutani, Y. Aya, H. Ogiso, S. Sasaki, and H. Tokumoto, J. Phys. Chem. B **106**, 5886 (2002).

[202] D. J. Wold, R. Haag, M. A. Rampi, and C. D. Frisbie, J. Phys. Chem. B **106**, 2813 (2002).

[203] D. M. Adams, L. Brus, C. E. D. Chidsey, S. Creager, C. Creutz, C. R. Kagan, P. V. Kamat, M. Lieberman, S. Lindsay, R. A. Marcus, R. M. Metzger, M. E. Michel-Beyerle, J. R. Miller, M. D. Newton, D. R. Rolison, O. Sankey, K. S. Schanze, J. Yardley, and X. Zhu, J. Phys. Chem. B **107**, 6668 (2003).

[204] V. Mujica, M. Kemp, and M. A. Ratner, J. Chem. Phys. **101**, 6849 (1994).

[205] V. Mujica, M. Kemp, and M. A. Ratner, J. Chem. Phys. **101**, 6856 (1994).

[206] C.-C. Kaun, B. Larade, and H. Guo, Phys. Rev. B **67**, 121411(R) (2003).

[207] W. Su, J. Jiang, and Y. Luo, Chem. Phys. Lett. **412**, 406 (2005).

[208] Y. Asai and H. Fukuyama, Phys. Rev. B **72**, 085431 (2005).

[209] K.-H. Müller, Phys. Rev. B **73**, 045403 (2006).

[210] H. M. McConnell, J. Chem. Phys. **35**, 508 (1961).

[211] S. B. Sachs, S. P. Dudek, R. P. Hsung, L. R. Sita, J. F. Smalley, M. D. Newton, S. W. Feldberg, and C. E. D. Chidsey, J. Am. Chem. Soc. **119**, 10563 (1997).

[212] W. B. Davis, W. A. Svec, M. A. Ratner, and M. R. Wasielewski, Nature **396**, 60 (1998).

[213] Y. A. Berlin and M. A. Ratner, Rad. Phys. Chem. **74**, 124 (2005).

[214] A. Salomon, D. Cahen, S. Lindsay, J. Tomfohr, V. B. Engelkes, and C. D. Frisbie, Adv. Mater. **15**, 1881 (2003).

[215] J.-P. Launay, Chem. Soc. Rev. **30**, 386 (2001).

[216] M. N. Paddon-Row, Aust. J. Chem. **56**, 729 (2003).

[217] C. Cohen-Tannoudji, B. Diu, and F. Laloë, *Quantenmechanik* (deGruyter, Berlin, 1997).

[218] J. W. Evenson and M. Karplus, J. Chem. Phys. **96**, 5272 (1992).

[219] M. A. Ratner, J. Phys. Chem. **94**, 4877 (1990).

[220] A. Nitzan, J. Phys. Chem. A **105**, 2667 (2001).

[221] M. A. Reed, C. Zhou, C. J. Muller, T. P. Burgin, and J. M. Tour, Science **278**, 252 (1997).

[222] X. Xiao, B. Xua, and N. J. Tao, Nano Lett. **4**, 267 (2004).

[223] K. Stokbro, J. Taylor, M. Brandbyge, J.-L. Mozos, and P. Ordejón, Comput. Mater. Sci. **27**, 151 (2003).

[224] W. Tian, S. Datta, S. Hong, R. Reifenberger, J. I. Henderson, and C. P. Kubiak, J. Chem. Phys. **109**, 2874 (1998).

[225] A. Troisi and M. A. Ratner, Nano Lett. **4**, 591 (2004).

[226] G. K. Ramachandran, T. J. Hopson, A. M. Rawlett, L. A. Nagahara, A. Primak, and S. M. Lindsay, Science **300**, 1413 (2003).

[227] L. V. Keldysh, Sov. Phys.–JETP **20**, 1018 (1965).

[228] J. Rammer and H. Smith, Rev. Mod. Phys. **58**, 323 (1986).

[229] H. Haug and A.-P. Jauho, *Quantum Kinetics in Transport and Optics of Semiconductors* (Springer, Berlin, 1996).

[230] A. M. Zagoskin, *Quantum Theory of Many-body systems: techniques and applications* (Springer, New York, 1998).

[231] R. van Leeuwen, N. E. Dahlen, G. Stefanucci, C.-O. Almbladh, and U. von Barth, Lect. Notes Phys. **706**, 33 (2006).

[232] J. C. Cuevas, PhD thesis (Universidad Autónoma de Madrid, Spain, 1999).

[233] C. Caroli, R. Combescot, P. Nozieres, and D. Saint-James, J. Phys. C: Solid St. Phys. **4**, 916 (1971).

[234] C. Caroli, R. Combescot, D. Lederer, P. Nozieres, and D. Saint-James, J. Phys. C: Solid St. Phys. **4**, 2598 (1971).

[235] C. Caroli, R. Combescot, P. Nozieres, and D. Saint-James, J. Phys. C: Solid St. Phys. **5**, 21 (1972).

[236] R. Combescot, J. Phys. C: Solid St. Phys. **4**, 2611 (1971).

[237] J. J. Sakurai, *Modern quantum mechanics* (Addison-Wesley, New York, 1995).

[238] A. L. Fetter and J. D. Walecka, *Quantum Theory of Many-Particle systems* (Dover, New York, 2003).

[239] W. Nolting, *Grundkurs theoretische Physik 7. Viel-Teilchen-Theorie* (Springer, Berlin, 2002).

[240] G. C. Wick, Phys. Rev. **80**, 268 (1950).

[241] P. Danielewicz, Ann. Phys. **152**, 239 (1984).

[242] M. Wagner, Phys. Rev. B **44**, 6104 (1991).

[243] A. I. Larkin and Y. N. Ovchinnikov, Sov. Phys.–JETP **41**, 960 (1975).

[244] D. C. Langreth, in NATO Advanced Study Institute Series B, Vol. 17, edited by J.T. Devrees and E. van Doren (Plenum, New York, 1976).

[245] P. Atkins and R. Friedman, *Molecular Quantum Mechanics* (Oxford University Press, Oxford, 2005).

[246] E. Emberly and G. Kriczenow, Phys. Rev. Lett. **81**, 5205 (1998).

[247] E. Emberly and G. Kriczenow, J. Phys.: Condens. Matter **11**, 6911 (1999).

[248] E. Klingbeil, *Tensorrechnung für Ingenieure* (B.I.-Wissenschaftsverlag, Mannheim, 1966).

[249] H. K. Iben, *Tensorrechnung* (Teubner, Stuttgart, 1999).

[250] D. Lohez and M. Lannoo, Phys. Rev. B **27**, 5007 (1983).

[251] E. Artacho and L. M. del Bosch, Phys. Rev. A **43**, 5770 (1991).

[252] K. W. Sulston and S. G. Davison, Phys. Rev. B **67**, 195326 (2004).

[253] K. S. Thygesen, Phys. Rev. B **73**, 035309 (2006).

[254] R. Zeller, J. Deutz, and P. H. Dederichs, Solid State Commun. **44**, 993 (1982).

[255] H. Bruus and K. Flensberg, *Many-body Quantum Theory in Condensed Matter Physics* (Oxford University Press, Oxford, 2004).

[256] Y. Meir and N. S. Wingreen, Phys. Rev. Lett. **68**, 2512 (1992).

[257] S. Datta, *Electronic Transport in Mesoscopic Systems* (Cambridge University Press, Cambridge, 2005).

[258] G. Czycholl, *Theoretische Festkörperphysik* (Springer, Berlin, 2004).

[259] M. Häfner, P. Konrad, F. Pauly, J. C. Cuevas, and E. Scheer, Phys. Rev. B **70**, 241404 (2004).

[260] D. J. Chadi and M. L. Cohen, Phys. Rev. B **8**, 5747 (1973).

[261] H. J. Monkhorst and J. D. Pack, Phys. Rev. B **13**, 5188 (1976).

[262] A. D. Corso, in *Quantum mechanical ab initio calculation of the properties of crystalline materials*, edited by C. Pisani, p. 77 (Springer, Berlin, 1996).

[263] F. Guinea, C. Tejedor, F. Flores, and E. Louis, Phys. Rev. B **28**, 4397 (1983).

[264] W. A. Harrison, *Electronic Structure and the Properties of Solids* (Dover, New York, 1989).

[265] W. H. Press, B. P. Flannery, and S. A. Teukolsky, *Numerical Recipes in FORTRAN 77 and FORTRAN 90: The Art of Scientific and Parallel Computing* (Cambridge University Press, Cambridge, 1996).

[266] J. Heurich, PhD thesis (Universität Karlsruhe, Karlsruhe, 2004).

[267] K.-H. Hellwege, *Einführung in die Festkörperphysik*, p. 66 (Springer, Berlin, 1988).

[268] C. Kittel, *Einführung in die Festkörperphysik* (R. Oldenbourg Verlag, München, 1999).

[269] M. Hamermesh, *Group theory and its applications to physical problems* (Dover, New York, 1989).

[270] R. Ahlrichs, M. Bär, M. Häser, H. Horn, and C. Kölmel, Chem. Phys. Lett. **162**, 165 (1989).

[271] M. von Arnim and R. Ahlrichs, J. Chem. Phys. **111**, 9183 (1999).

[272] P. A. M. Dirac, Proc. Royal Soc. (London) A **123**, 714 (1929).

[273] S. H. Voskov, L. Wilk, and M. Nusair, Can. J. Phys. **58**, 1200 (1980).

[274] A. D. Becke, Phys. Rev. A **38**, 3098 (1988).

[275] J. P. Perdew, Phys. Rev. B **33**, 8822 (1986).

[276] A. Schäfer, H. Horn, and R. Ahlrichs, J. Chem. Phys. **97**, 2571 (1992).

[277] *TURBOMOLE, User's Manual* (Karlsruhe, May 2004).

[278] W. R. Wadt and P. J. Hay, J. Chem. Phys. **82**, 284 (1985).

Abbreviations

ABL	alternating bond length
CGF	contracted Gaussian function
DBA	donor bridge acceptor
DFT	density functional theory
DOS	density of states
ECL	effective conjugated length
ECP	electronic core potential
EMT	effective medium theory
FZK	Forschungszentrum Karlsruhe
GGA	generalized gradient approximation
GTO	Gaussian type orbtial
HOMO	highest occupied molecular orbital
I-V	current-voltage
IETS	inelastic electron tunneling spectroscopy
INT	Institut für Nanotechnologie
KS	Kohn-Sham
LDOS	local density of states
LUMO	lowest unoccupied molecular orbital
MCBJ	mechanically controllable break junction
MCS	minimum cross-section
MD	molecular dynamics
MMM	metal-molecule-metal
MO	molecular orbital
NEGF	nonequilibrium Green's functions
NMR	nuclear magnetic resonance
PBC	periodic boundary condition
PCS	point contact spectroscopy
ROHF	restricted open shell Hartree Fock
SCF	self-consistent field
STM	scanning tunneling microscope
STO	Slater type orbtial
TB	tight-binding
WBL	wide-band limit

Acknowledegments

First of all I would like to thank Prof. Dr. Gerd Schön for the possibility of writing my PhD thesis in his group at the Institut für Theoretische Festkörperphysik (TFP). I appreciated a lot the excellent infrastructure provided both by the Universität Karlsruhe and the Forschungszentrum Karlsruhe (FZK). Without the computer facilities of the TFP and the Institut für Nanotechnologie (INT) at FZK this work would not have been possible in this form. I am deeply indebted to my supervisor, Juan Carlos Cuevas, for having introduced my to the topic of molecular electronics. I value highly his constant openness for discussions with me and the sharing of new interesting ideas concerning future directions of research. He proposed the projects of this work and thus put the basis for my PhD thesis. Next I want to thank Janne Viljas. His interest and expertise regarding details of any kind of physical system was an irreplaceable help during the final stage of this work. Together with him I could discuss and solve many of the uncertainties that had piled up over the years. It was also a great pleasure for me to work together with Michael Häfner and Sören Wohlthat. Michael's tight-binding studies of surface Green's functions initiated their implementation in the DFT transport program, developed during my thesis, and turned out to be crucial. Sören helped me a lot by applying the ab-initio DFT method in an efficient way to analyze the transport through various nanoscale systems. In doing so he gave further impetus to my work by demonstrating that also for his systems the method yielded good results.

In every mostly numerical work the good will and support by system administrators is inevitable. In this sense I thank a lot, at first place, Andreas Pönicke. But also Tobias Ulbricht, Daniel Hermann at Universität Karlsruhe, and Matthias Hettler at INT helped me innumberable times in solving the many technical problems that appeared in the course of my thesis. With respect to compiler problems I want to thank also Peter Schmitteckert for assistance and Günter Schneider for an initial trigger on the enforcement of the fcc symmetry with respect to the electrode description in the DFT program. In addition I want to thank Ferdinand Evers for one helpful discussion, where he showed to me how to obtain densities of states with orthogonalized parameters, and Andreas Arnold and Max Köntopp for discussions. To the rest of the members of TFP and TKM I want to say thanks for the enjoyable atmosphere, especially to my friend and room mate Carsten Hutter and to Ralph Werner for the many activities we did together.

The work on conductance histograms of various metals in the first part of this work has been carried out in a fruitful collaboration with Markus Dreher at Universität Konstanz. We successfully combined our knowledge on the simulation of molecular dynamics and electron transport, and both of us took great care to achieve correct results. Often it was a great ease to me to know you struggling through the scientific jungle with me, Markus.

Concerning my work on molecular electronics I want to acknowledge the support by the whole group for theoretical quantum chemistry at the Lehrstuhl für Theoretische Chemie at Universität Karlsruhe. Prof. Dr. Reinhart Ahlrichs provided me with a source code version of his quantum chemistry package TURBOMOLE. Without this program package my research on molecular electronics would not have been possible. Special thanks goes to Uwe Huniar. He introduced me to TURBOMOLE, and helped me with all kinds of technical issues (and there were many – like linker problems with static linking, basis set use, etc.). He was a very reliable contact person for me. Together with him I developed the description of the electrodes. Additional thanks goes to Paola Nava, who helped me a lot with her experience in the calculation of large metal clusters (marij-Problem), Dmitrij Rappoport for discussions about oligophenylenes, Marco Kattannek for support with 64bit applications and a very helpful test program, Filipp Furche for basis set related issues, and also Florian Weigend, Marek Sierka and Claudia Schrodt for several interesting discussions.

In the end thanks a lot to my parents Ilse and Manfred Pauly and my sisters and brothers Eva, Simon, and Vera. It's great to have a family like you!